Compact Radio Cores in AGN: The X-Ray Connection

Dissertation

zur Erlangung des Doktorgrades (Dr. rer. nat.)

der Mathematisch-Naturwissenschaftlichen Fakultät

der Rheinischen Friedrich-Wilhelms-Universität Bonn

vorgelegt von

Matthias Kadler

aus Brake (Unterweser)

Bonn 2005

Angefertigt mit Genehmigung der Mathematisch-Naturwissenschaftlichen Fakultät der Rheinischen Friedrich Wilhelms-Universität Bonn

Promotionskommission:
PD Dr. J. Kerp (Erstgutachter)
Prof. Dr. U. Klein (Zweitgutachter)
Prof. Dr. P. Herzog (fachnahes Mitglied)
Prof. Dr. C. Baier (fachangrenzendes Mitglied)

Contents

Summary

In this thesis, the results from an archival X-ray spectral survey of 50 radio-loud active galactic nuclei (AGN) are presented. The sample is based on MOJAVE, a statistically complete sample of radio-loud, core-dominated AGN, that is regularly monitored with the Very Long Baseline Array (VLBA) at $\lambda 2$ cm wavelength (the VLBA 2 cm Survey). Taking into account all available X-ray spectroscopic archival data of MOJAVE sources, the *2 cm-X-Sample* is defined, which represents the so far largest sample of radio-loud AGN being studied spectroscopically in the (0.2–12) keV X-ray regime with more than 200 individual observations of the X-ray observatories *ASCA*, *Beppo*Sax, *Chandra*, and *XMM-Newton*. The analysis of the *2 cm-X-Sample* accumulates over 7.5 Msec of telescope integration time and a considerable amount of previously unpublished data. The primary goal of this PhD-thesis project is to determine the characteristic properties of radio-loud, core-dominated AGN.

A fundamental question behind this study is how powerful relativistic plasma jets are formed in the environment of supermassive black holes of AGN. A wealth of information about the variable parsec-scale structure of these jets exists, obtained from Very-Long-Baseline Interferometry (VLBI), but the fundamental difference between (jet-forming) radio-loud and (jet-suppressing) radio-quiet AGN remains mysterious. This is partly due to the fact that in the past the X-ray properties of radio-loud AGN have not been studied as intensely as the X-ray characteristics of radio-quiet objects. Moreover, the radio-loud AGN samples studied so far were mostly based on properties dominated by large-scale jet structures, such as the single-dish luminosity, rather than on the compact radio cores like it is the case for the *2 cm-X-Sample*. The *2 cm-X-Sample* is demonstrated to be representative of the complete MOJAVE sample and therefore to provide a firm statistical basis for the characterization of the X-ray properties of radio-loud, core-dominated AGN.

It is found that the X-ray spectra of radio-loud, core-dominated AGN generally can be well represented by a simple absorbed power law. Soft-excess emission, in most cases below 1 keV to 2 keV, is found in 15 out of 50 sources, which can be attributed to a soft thermal plasma in two cases. In two further cases, for the BL Lac objects 0235+164 and 0716+714, the soft excess is best explained as the high-energy tail of the primary synchrotron component of the blazar emission. A possible identification for the soft excesses found in quasars is the high-energy end of the big blue bump. Only two out of 50 sources cannot be described adequately with a combination of a soft excess, a hard power-law and a thermal-plasma emission component. These two sources are NGC 1052 and Cygnus A, which both exhibit a two-sided parsec-scale jet radio morphology, indicating a large angle to the line of sight.

Radio-loud, core-dominated AGN are found to have a sharp-peaked distribution of hard-power-law photon indices with an average value of $\langle \Gamma_{\mathrm{hard-PL}} \rangle = 1.68$. The disper-

sion of the distribution of $\sigma_{\langle\Gamma_{\text{hard}-\text{PL}}\rangle} = 0.26$ can best be explained as representative of an intrinsic dispersion over the sample. Quasars show the smallest dispersion of hard-power-law photon indices, while the values for BL Lacs and galaxies lie in the range $1.4 < \Gamma^{\text{B,G}}_{\text{hard}-\text{PL}} < 2.5$. $\Gamma_{\text{hard}-\text{PL}}$ correlates weakly with the hard-power-law luminosity and with radio VLBI luminosity. The galaxies are the least powerful sources and the quasar luminosities are higher than the BL Lac luminosities.

The photon index of the soft-excess power-law component is found to correlate with the apparent speed of VLBI jet components, which may be the signature of a shifting emission maximum of the soft-excess emission component. No correlation of $\Gamma_{\text{hard}-\text{PL}}$ with the core-dominance or the radio–to–X-ray loudness is found in conflict with the discrepancy between the photon indices of radio-loud and radio-quiet AGN. Only a tentative correlation is found between $\Gamma_{\text{hard}-\text{PL}}$ and the Doppler factor as derived from radio-variability measurements. 21 out of 41 sources show excess absorption over the Galactic value of unknown origin, which is unexpected within the standard model of AGN given the type-1 character of 19 of those objects. Disk-reflection signatures and iron lines are weak or absent in the majority of core-dominated, radio-loud AGN. This can be understood as an effect of a different structure of the accretion flow in radio-loud and radio-quiet AGN or as an effect of a jet-associated emission component shining out the weaker disk emission component. A small number of exceptions from this rule is identified for which a disk reflection emission component is suggested by the available data. These sources may play an important role in future combined VLBI and X-ray studies of jet-disk coupling in radio-loud AGN.

Eight X-ray jets, four distinct X-ray emission knots, 2 hotspots, and two jet-associated halos are found in 14 out of 26 *Chandra*-observed sources of the *2 cm-X-Sample*. Predominantly flat photon indices ($\Gamma \sim 1.3$–1.5) of the X-ray jets are found sustaining the hypothesis that jet emission may dominate the X-ray spectra of radio-loud, core-dominated AGN on smaller scales, as well, giving rise to the flatter photon indices found in the *2 cm-X-Sample* compared to radio-quiet AGN.

Detailed radio and X-ray studies of four special sources have been triggered by the survey analysis. Their results are presented in this thesis, as well:

By making use of continuous Morlet wavelet transform and Lomb-Scargle periodogram methods, a strong periodicity of the long-term radio flux-density light curve of the BL Lac object PKS B0048−097 is revealed. The characteristic period of the signal is found to vary between 400 and 600 days with a slow modulation on a time scale of several years. Despite of the very compact parsec-scale radio structure, very pronounced structural variability is found from the analysis of two VLBA 2 cm Survey observations of PKS B0048−097. The parsec-scale jet is found to vary in position angle by $\sim 30°$ between both epochs and by even larger angles with respect to earlier reported VLBI-jet position angles. These findings make PKS B0048−097 a key source for tests of precessing-jet models against alternative models (e.g., shock-in-jet models) of periodic light-curve modulation in blazars.

Four epochs of VLBA 2 cm Survey observations, three epochs of Effelsberg short-term radio-variability observations and four *XMM-Newton* observations of the BL Lac object AO 0235+16 are analyzed. A kinematical model for the extremely compact parsec-scale jet structure is derived from the VLBA 2 cm Survey observations of AO 0235+16.

For the first time, X-ray short-term variability of this well known radio and optical rapidly variable source is found during a high-flux state. The X-ray light curve is investigated in several wavebands without finding any evidence for time lags or large amplitude differences, an unexpected result within standard short-term variability models.

The active galaxy NGC 1052 is studied at radio, optical, and X-ray frequencies. This study is performed on various scales from sub-parsecs to kiloparsecs and brings together observations with the Very Long Baseline Array, the MERLIN radio interferometer, the *Hubble Space Telescope (HST)* and the X-ray observatories *Beppo*Sax, *Chandra*, and *XMM-Newton*. A VLBI scrutiny of the obscuring torus of this object is presented. The well-known soft X-ray spectral excess exhibited by this source is identified with an extended region of thermal X-ray plasma emission associated with the kiloparsec-scale radio jet. The detection of a relativistic iron X-ray emission line is reported, which is the first of its kind in an object with a bright compact radio core. By taking advantage of this fact, the inter-relation between the accretion process and jet formation in a radio-loud AGN is investigated. Significantly different profiles of the relativistic iron line are found before and after the ejection of a new, bright jet component into the jet of NGC 1052. This observational signature suggests that a part of the inner accretion disk was fed into the black hole and a fraction of the material was ejected as a new jet component.

Results from 10 epochs of VLBA 2 cm Survey observations of 3C 111 and from 13 years of radio flux density monitoring observations conducted at the University of Michigan are presented. A major radio flux-density outburst of 3C 111 occurred in 1996 and was followed by the ejection of a particularly bright superluminal jet component. The ejected jet plasma gradually "stretched out" as it traveled down the jet with a leading component being visible throughout the monitoring and several trailing components forming in the wake of the leading component. A change in direction, speed and brightness temperature of the leading component can be described in terms of two ballistic regimes where the component is moving with a constant intrinsic speed but at an angle to the line of sight changing from $\sim 24°$ to $\sim 11°$ in a deflection event about 3 mas from the core.

The results of three epochs of *XMM-Newton* observations of the bright BL Lac object 0716+714 are presented. In all three epochs the source exhibits an extraordinarily steep X-ray spectrum with photon indices of 2.8–3.0 if a simple absorbed power law model is applied. In two epochs in 2001 a significantly better fit is achieved with a two-power-law model. This is interpreted as variability in the relative strength of a primary synchrotron component and a secondary inverse Compton component to the total spectrum. A relatively stable absorbing column density of $\sim (3 - 6) \times 10^{20} \, \mathrm{cm}^{-2}$ is found at all epochs. Substantial short term variability is detected with time scales of the order of ~ 1000 s and variability amplitudes up to 50%. A pronounced energy dependence of a strong flare in March 2002 is revealed. The time lag of ~ 150 s between the $(0.2–1)$ keV band and the $(1–8)$ keV band emission might reflect the travel time of a perturbation in the jet between the characteristic regions of origin for the soft and hard X-ray photons, respectively. The tentative detection of an iron line in 0716+714 is reported. The line is visible as excess emission at ~ 5.8 keV in March 2002, the epoch in which the inverse Compton component is weak. If this excess is attributed to the Fe K_α transition at 6.4 keV in the source rest frame, the redshift of 0716+714 can be determined to $z = 0.10 \pm 0.04$, significantly below previously discussed redshift ranges.

1   Introduction

1.1   Mass-Accretion and Jet-Production in Supermassive-Black-Hole Systems

The observational study of active galactic nuclei (AGN) has developed rapidly during the last decades. A broad consensus has been reached with most astronomers agreeing that the energetic phenomena observed in AGN are related to the accretion of matter onto supermassive black holes. Extreme physical conditions prevail inside (and in the immediate vicinity of) a supermassive black hole, where millions of solar masses are confined to a region of one solar diameter, i.e., the size of a star like our sun under "normal" physical conditions. In view of this, it is not surprising that supermassive black holes can trigger physical processes that make their environment enormously bright and visible over billions of light years. This fact allows the central regions of distant galaxies to be studied on a brightness level that often exceeds the emission of star light from the whole galaxy by several orders of magnitude.

The so-called standard model of AGN describes the general assembly of components associated with a supermassive black hole at the very center of an active galaxy: The matter being "trapped" in the gravitational potential of the black hole forms an accretion disk inside which the rotating matter looses angular momentum via turbulent friction, radiates, and spirals inwards, approaching the event horizon of the black hole. Inside the event horizon, the gravitational attraction of the black hole is so strong that not even light can escape from there. While the bulk of the accreting matter is being swallowed by the black hole, a relatively small fraction is being ejected from the central engine of the AGN in the form of collimated jets of relativistic plasma.

Jets are a common phenomenon, occurring not only in AGN but also in Galactic sources when a mass-accreting compact object is involved. This includes young stellar objects (YSOs) as well as nuclei of planetary nebulae, white dwarfs, neutron stars and galactic black holes. A review of galactic jets can be found in Mirabel and Rodríguez (1999). Extragalactic jets are associated ordinarily with radio-loud AGN (see Zensus 1997 for a review) but weak compact flat-spectrum radio cores indicative of jet emission have been found in an increasing number of radio-quiet AGN, as well (compare appendix F). The flat spectra of compact radio cores can be explained by the superposition of synchrotron emission coming from different unresolved regions of the parsec-scale jets. Very-Long-Baseline Interferometric (VLBI) observations, combining individual radio telescopes located at different sites, up to thousands of kilometers apart from each other (compare Sect. 2.3), yield the highest angular resolution in modern astronomy. VLBI observations typically reveal one-sided parsec-scale morphologies of extragalactic radio jets for pow-

erful radio-loud quasars, with a bright unresolved flat-spectrum core (even at milliarcsecond resolution) and a steeper-spectrum jet. Distinct features within the jet structure are commonly found to travel away from the core with apparent faster-than-light motions (superluminal). Within the standard beaming model scenario, this effect is attributed to bulk relativistic motion of jet plasma at a small angle to the line of sight, that gives further rise to strong Doppler boosting of the core and jet flux density and de-boosting of the counter-jet emission. At larger angles to the line of sight, two-sided parsec-scale jet morphologies are found with typically subluminal motions. The observational study of parsec-scale jets has seen substantial progress in recent years, in particular from the conduction of large monitoring surveys (see appendix D). However, the formation of extragalactic jets, and their different prominence in radio-loud and radio-quiet AGN remains poorly understood. A suggestive hypothesis is that the accretion flows in radio-loud and radio-quiet AGN differ in a critical way, that fosters or suppresses the production of powerful relativistic jets.

Recent years have shown that a combination of the (historically grown) different observing techniques at various regimes of the electromagnetic spectrum can yield considerably deeper insights into the physics of accreting black-hole systems than the traditionally distinct observational efforts of radio, infra-red, optical/ultra-violet, and high-energy astronomy alone. In particular, radio and X-ray astronomy make up an extremely fruitful partnership. One outcome of that is the combination of radio-interferometric and X-ray-spectroscopic methods. As outlined above, the former offers the unique possibility to image the small-scale structure of extragalactic radio jets. The latter is sensitive to emission which is originating in the most central regions of black-hole accretion flows (see Sect. 2.1.4), which are supposed to differ fundamentally in jet-forming (radio-loud) and jet-suppressing (radio-quiet) AGN. During the last one-and-a-half decades, X-ray spectroscopic data in the (0.2–12) keV regime have been gathered by various X-ray observatories (see Sect. 2.2). Contemporaneously, large VLBI monitoring surveys of radio-loud AGN have been conducted. Thus, systematical studies of large samples of radio-loud AGN with well-known parsec-scale jet properties can now be performed and compared to complementary studies of radio-quiet AGN. This approach allows the processes of mass-accretion and jet formation in AGN to be explored. In particular, one of the most fundamental questions of modern AGN research can be addressed: "What makes an AGN radio-loud?"

1.2 Scope of this thesis

In this thesis, a sample of 50 radio-loud, core-dominated AGN is investigated, based on archival X-ray spectroscopic data and VLBI data from the VLBA 2 cm Survey (see appendix D). This represents the so far largest sample of radio-loud AGN being studied spectroscopically in the (0.2–12) keV X-ray regime. It provides a large database, consolidating the X-ray characteristics of radio-loud AGN that can be interpreted in view of the structural and kinematical information available for the compact radio cores, as e.g., superluminal motion of jet features, Doppler factors, or the subparsec-scale VLBI cores. This X-ray spectral survey provides both, a unique statistical basis for characterizing the X-ray properties of radio-loud, core-dominated AGN, and a rich resource for triggered

detailed studies of individual objects based on the available radio and X-ray data.

This thesis is organized as follows: in Chap. 2, the various X-ray emission mechanisms at work in AGN are reviewed and the concepts of X-ray imaging spectroscopy and Very-Long-Baseline Interferometry are introduced. In Chap. 3, the scientific project is outlined and its relevance for AGN research is discussed in view of previous studies of radio-loud AGN in the X-ray regime. In particular, the sample definition, the data acquisition and analysis are described there and the representative character of the investigated sample (i.e., its suitability for statistical studies) is demonstrated. The results from the X-ray spectral survey are presented in Chap. 4: the characteristic X-ray spectral parameters and their distributions over the sample are compiled, and the results for the individual sources are presented in brief. In Chap. 5, X-ray spectral survey results and their implications are discussed in the context of independent, relevant research results. Detailed studies of five individual sources triggered by the survey are presented in Chap. 6. The appendices contain supplementary studies that are employed at various points of the analysis and interpretation within the main part of this thesis.

2 Background

2.1 X-Ray Emission Processes associated with AGN

One of the most common characteristics of AGN is that they are all bright X-ray sources. While a typical "normal" galaxy has an X-ray luminosity L_{X} of $10^{37}\,\mathrm{erg\,s^{-1}}$ to $10^{39}\,\mathrm{erg\,s^{-1}}$, Seyfert galaxies have luminosities in the range of $10^{43}\,\mathrm{erg\,s^{-1}}$ to $10^{45}\,\mathrm{erg\,s^{-1}}$. BL Lac objects have luminosities of $10^{44}\,\mathrm{erg\,s^{-1}}$ to $10^{46}\,\mathrm{erg\,s^{-1}}$ and quasars make up the upper luminosity class with values of $10^{45}\,\mathrm{erg\,s^{-1}}$ to $10^{48}\,\mathrm{erg\,s^{-1}}$. Most astrophysicists agree that mass accretion onto a supermassive black hole residing at the very center of these objects drives the activity and leads to the enormous observed luminosities. Thus, the primary energy-conversion process in AGN can be parametrized via the rate of accreted mass M

$$L_{\mathrm{X}} \propto \frac{\mathrm{d}M}{\mathrm{d}t} \quad . \tag{2.1}$$

Roughly speaking, the increase in luminosity from normal galaxies over Seyferts to BL Lac objects and quasars suggests a scaling of the mass-accretion rate from well below a percent of one solar mass per year to dozens of solar masses per year. Below, four specific emission processes are outlined, which are actually observed. Basically, all three processes purchase their driving force from some converted form of the primarily available mass-accretion energy. Ultimately, a characteristic form of electromagnetic radiation is set free by each process, shaping the observed spectrum.

2.1.1 Thermal Plasma Emission

The term "thermal" denotes the state of a plasma which can be fully described by the temperature T of its electrons. The X-ray emission of a thermal plasma can be dominated by various physical processes, dependent on the temperature: below $T = 5 \cdot 10^6\,\mathrm{K}$ ($\sim 0.43\,\mathrm{keV}$) line-emission dominates originating from the various elements that make up the plasma. With increasing temperature, these elements become more and more ionized and ultimately H- and He-like ion emission is observed predominantly. At temperatures above $T = 5 \cdot 10^6\,\mathrm{K}$, thermal bremsstrahlung dominates the thermal plasma emission. This kind of radiation comes from the interaction of electrons with atomic nuclei.

The exact spectral shape of a thermal plasma spectrum depends on a variety of parameters, density, pressure, metalicities and temperature. In general, a strong "line forest" is superimposed on a continuum of thermal bremsstrahlung. The relative strength of the lines to the continuum depends on the temperature. The maximal frequency of the continuum corresponds to the complete kinetic energy of a single electron transferred to a single
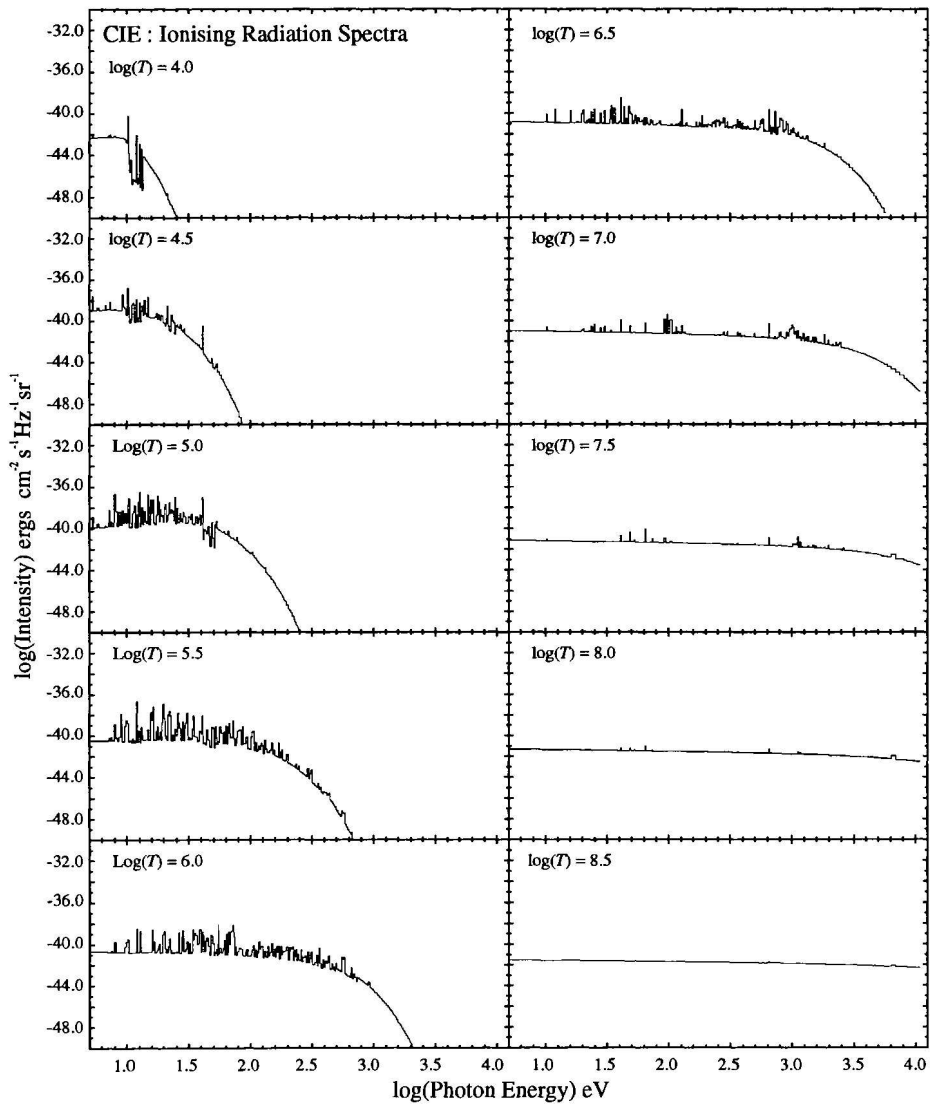
Figure 2.1: X-ray plasma spectra of a gas with solar metalicities for various temperatures. Towards higher temperatures the bremsstrahlung continuum dominates over the line emission and extends up to higher energies. (Taken from Sutherland and Dopita 1993.)

X-ray photon. This maximal frequency is roughly proportional to the plasma temperature (see Fig. 2.1). The scaling of the thermal plasma emission is proportional to the product of electron and hydrogen density integrated over the volume of the emitting plasma, the so called emission measure $EM = \int n_e n_H \mathrm{d}V$.

2.1.2   Synchrotron Emission

The frequently used term *non-thermal emission* denotes the fact that a physical process produces a spectrum that does not reproduce the shape of thermal plasma emission. The most important emission mechanism at radio frequencies is synchrotron radiation. A charged particle moving in region with an electromagnetic field encounters the Lorentz

force

$$\boldsymbol{F_L} = q\left(\boldsymbol{E} + \boldsymbol{\beta} \times \boldsymbol{B}\right) \tag{2.2}$$

with $\boldsymbol{\beta} = \boldsymbol{v}/c$, the velocity in units of the speed of light and q, the charge of the particle. In the case of a vanishing electric field ($\boldsymbol{E} = 0$) the charged particle is accelerated perpendicular to the magnetic field $\boldsymbol{B}$. For a linear magnetic field this results in a helical motion around the direction of $\boldsymbol{B}$ as a superposition of a constant velocity component along the field and a constant acceleration perpendicular to it. The particle orbits with a period $\gamma mc/2\pi qB$ corresponding to the Larmor frequency

$$\omega_B = \frac{qB}{\gamma mc} \tag{2.3}$$

with the Lorentz factor $\gamma = 1/\sqrt{1 - \beta^2}$ and the mass m of the particle. In the non-relativistic case (Cyclotron radiation) the particle emits an electromagnetic wave with this frequency. It can be shown that the emitted power for each energy is given by

$$P = 4/3\,\sigma_T\,c\,(\gamma\beta)^2\,U_B \propto \gamma^2 U_B \tag{2.4}$$

(Larmor formula, see Rybicki and Lightman 1979 for details), with $\sigma_T = 8\pi e^4/m^2 c^4$, the Thomson cross section and $U_B = B^2/8\pi$, the magnetic field density. The dependence on m^{-2} shows that in general the synchrotron emission from electrons will be much stronger than from protons ($m_p \sim 2 \cdot 10^3\,m_e$).

In the relativistic case of charges moving with a substantial fraction of the speed of light it has to be taken into account that the observed flux density S_ν is affected by the relativistic Doppler effect. The flux density S'_ν emitted in the comoving frame that is moving with a longitudinal velocity component $\beta_{||}$ relative to the observer is increased (or reduced) to[1]

$$S_\nu = D^3 S'_\nu \tag{2.5}$$

with the Doppler factor defined by

$$\delta = \frac{1}{\gamma(1 - \beta_{||}\cos\theta)} \quad . \tag{2.6}$$

The strong dependence on the viewing angle θ implies that an intrinsically isotropically emitted radiation is beamed into a cone with the half opening angle $1/\gamma$.

If an ensemble of electrons with a continuous energy distribution, rather than a single electron of fixed energy, is considered, a continuous spectrum of synchrotron radiation is emitted. An ensemble of electrons with a power-law energy distribution $N(\gamma)d\gamma = N_0 \cdot \gamma^{-s}d\gamma$ produces a power-law spectrum

$$S_\nu \propto \nu^\alpha \tag{2.7}$$

with the spectral index

$$\alpha = \frac{1-s}{2} \quad . \tag{2.8}$$

---

[1]See e.g. Rybicki and Lightman (1979). The exponent of the Doppler factor is reduced to $2 - \alpha$ for a continuous jet with spectral index α since not only the flux density but also the emitting frequencies are transformed.

It can be shown that an adiabatically expanding relativistic jet in equipartition, i.e., with equal kinetic and magnetic energy density, emits equal flux densities over a broad range of radio frequencies, i.e., a flat synchrotron spectrum with $\alpha \sim 0$ [2]. This is the spectral shape typically exhibited by compact radio cores in AGN. The highest frequencies to which the flat spectrum extends correspond to the most compact region of the jet. At higher frequencies, an optically thin synchrotron spectrum is expected that may extend far beyond the radio regime, up to optical or soft X-ray frequencies.

2.1.3   Inverse-Compton Emission

Accreting black hole systems often exhibit power-law spectra extending to hard X-ray energies, up to energies of hundreds of keV. Even in the case of blazars, radio-loud AGN with a relativistically beamed jet oriented at a small angle to the line of sight, a spectral break at high energies is usually observed, indicating a further spectral component besides the primary synchrotron emission component. Inverse-Compton scattering of photons by highly relativistic electrons is generally invoked in models of high-energy blazar spectra. The SSC (Synchrotron Self Compton) mechanism is the special case of inverse-Compton scattering where synchrotron photons scatter off the very same electrons which produced them. "Inverse" means that the photons gain energy from the electrons and are upscattered to higher frequencies. The frequency of the inverse Compton scattered photons ν' simply depends on the frequency of the seed photons ν and the Lorentz factor γ_e of the electrons responsible for the scattering (e.g. Rybicki and Lightman 1979)

$$\nu' \sim \gamma_e^2 \nu \quad . \tag{2.9}$$

Thus, in order to produce X-ray emission of $1\,\mathrm{keV}\,(\hat{=}2.4 \cdot 10^{17}\,\mathrm{Hz})$ from seed photons of $22\,\mathrm{GHz}$, high energy electrons with Lorentz factors $\gamma_e = 1600$ are needed. Since these are the same electrons which produce the seed photons, the inverse Compton spectrum reproduces the shape of the synchrotron spectrum at higher-frequencies.

It can be shown (e.g. Krolik 1999, section 9.2.1) that the luminosity of the inverse-Compton radiation P_C relative to to the initial synchrotron luminosity P_S depends simply on the ratio of the energy density in the synchrotron photon field U_S and the magnetic field energy density U_B:

$$\frac{P_C}{P_S} = \frac{U_S}{U_B} \quad , \tag{2.10}$$

with $U_B = B^2/8\pi$. Thus, compact radio cores in radio-loud AGN with high brightness temperatures (i.e., high energy densities in the photon field) are likely sites of strong SSC emission. Kellermann and Pauliny-Toth (1969) derive a limit of $10^{12}\,\mathrm{K}$ for the brightness temperature, above which the inverse-Compton effect should transfer the bulk emission into the high-frequency regime. Based on equipartition arguments, Readhead (1994) derives an even lower limit of $\sim 10^{11}\,\mathrm{K}$. High-resolution VLBI observations show that these limits are reached or even violated in a substantial fraction of all radio-loud, core-dominated AGN (e.g., Kovalev et al. 2005) so that SSC emission must play an important role.

---

[2] A brief derivation of the synchrotron spectrum emitted from an adiabatically expanding relativistic jet (Blandford and Königl 1979), based on the model developed by Falcke and Biermann (1995), can be found in Kadler (2002).
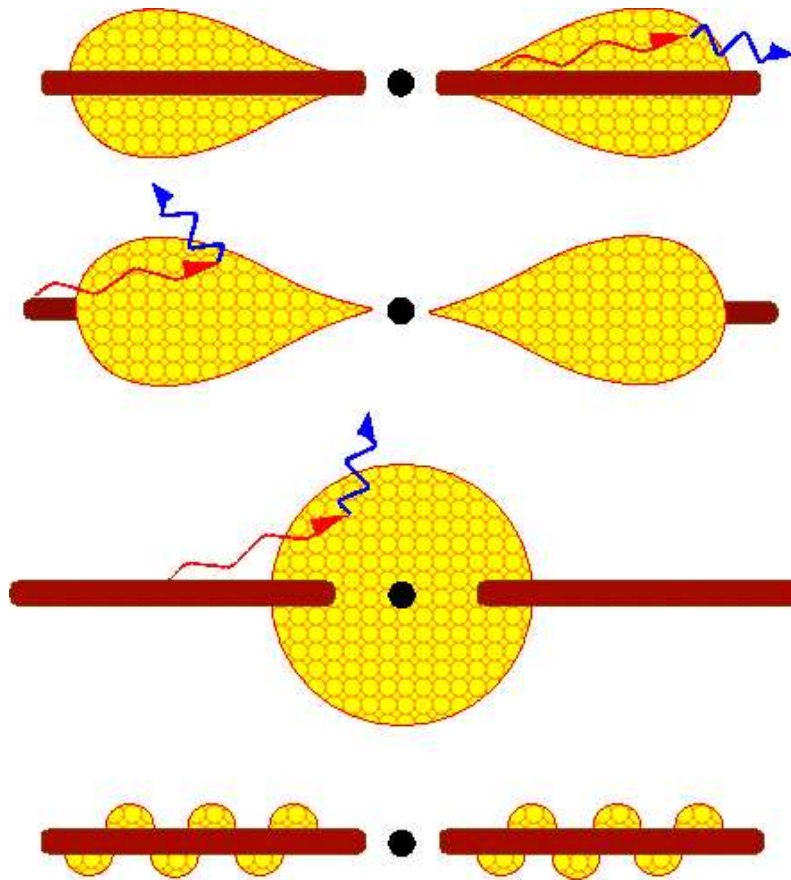
Figure 2.2: Possible geometries for accretion disk coronae. The top figure is referred to as a "slab" or "sandwich" geometry. The remaining three show "photon starved geometries" wherein the corona is less effectively cooled by soft photons from the disk. The middle two geometries are often referred to as "sphere+disk geometries", while the bottom geometry is often referred to as a "patchy corona" or "pill box" model (image taken from Reynolds and Nowak 2003).

High-energy particles, capable of scattering photons up to high energies via the inverse-Compton effect, are not only produced in jets but also in black-hole accretion disks. It is being discussed (see e.g., Reynolds and Nowak 2003 for a review) that a conversion of the accretion energy per particle into kinetic energy may produce a corona of high-energy electrons associated with accretion disks. Although the mechanism of coronal heating is not well understood at present and although the geometry of the corona is unknown, models of "Comptonisation" of optical and soft X-ray photons from the disk are naturally predicting the observed power-law spectra of radio-quiet AGN. Possible geometries of accretion-disk coronae are displayed in Fig. 2.2. For a more comprehensive discussion see Reynolds and Nowak (2003).

2.1.4   X-Ray Disk-Reflection Emission

The concept of hot coronae associated with black-hole accretion disks provides a natural explanation of a class of hard X-ray spectral features that are frequently observed in AGN

spectra. The most common of these spectral features, which are usually referred to as "X-ray reflection emission", are an absorption edge at $\sim 7\,\mathrm{keV}$, a hump-like broad spectral maximum above $10\,\mathrm{keV}$ and broadened (FWHM of $\sim 5 \times 10^4\,\mathrm{km\,s^{-1}}$) line emission at $6.4\,\mathrm{keV}$. In Fabian et al. (2000a) or Reynolds and Nowak (2003), the basic physics of X-ray reflection are being described in more detail. Adopting here the way of introducing the basic X-ray reflection model in these reviews, a hard X-ray power-law continuum (from the corona) shall be considered that illuminates a semi-infinite slab of cold gas (the accretion disk). An X-ray photon may be I) Compton scattered by free or bound electrons out of the slab, or II) photoelectrically absorbed, followed by fluorescent line emission or Auger de-excitation. The cross section for photoelectric absorption is strongly energy dependent ($\sigma_{\mathrm{pe}} \propto E^{-3}$) so that incident soft X-rays are mostly absorbed, whereas hard photons are mostly scattered back out of the slab (with a probability determined by the Thompson cross section σ_{T}). Figure 2.3 illustrates the resulting "reflection hump", below the incident power law by the (energy-dependent) factor $\sigma_{\mathrm{T}}/\sigma_{\mathrm{pe}}$. In addition, there is an emission line spectrum resulting primarily from fluorescent Kα lines of the most abundant metals. Of those, the $6.4\,\mathrm{keV}$ iron Kα line is by far the strongest because of the combination of relatively high abundance and the high photoelectric cross section of iron. The detailed shape of the reflection spectral component is a sensitive measure for the elemental abundances, the ionization of the disk surface and the geometry of the corona-disk system (see, e.g., Reynolds and Nowak (2003) for details).
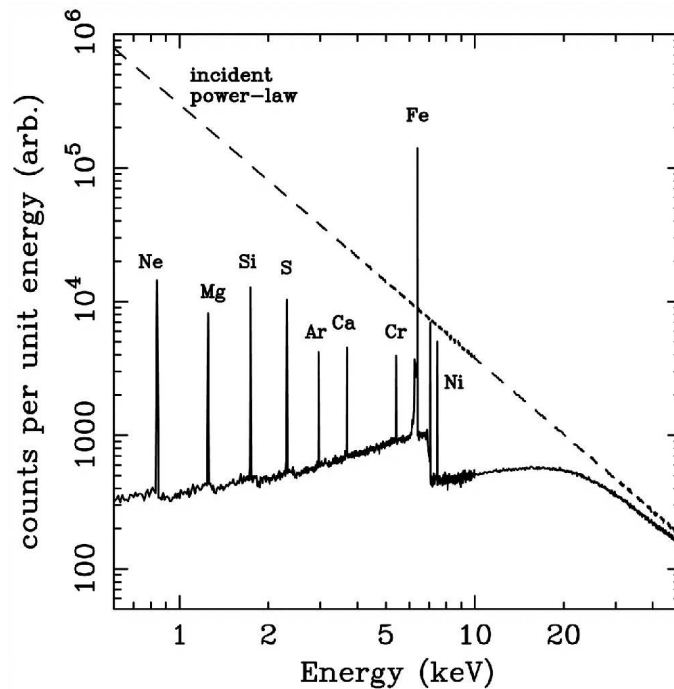
Figure 2.3: X-ray reflection from an accretion disk modeled as a semi-infinite slab of uniform density gas, irradiated by an X-ray continuum spectrum produced in the disk corona via thermal Comptonization. The dashed line shows the incident continuum, and the solid line shows the reflected spectrum (integrated over all angles). Figure (taken from Fabian et al. (2000a)) is based on Monte Carlo simulations from Reynolds (1996).

Newtonian
(Emission from a Narrow Ring)

Special Relativity
(Transverse Doppler Effect;
Rel. Beaming)

General Relativity
(Gravitational Redshift)

Line Profile
(Integration over Disk)

0.5   1   1.5
ν_{obs}/ν_{em}
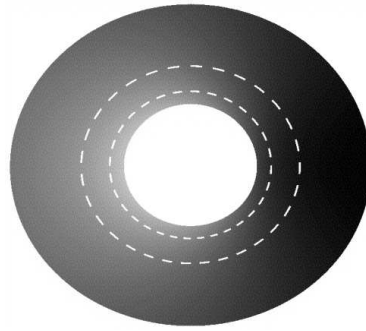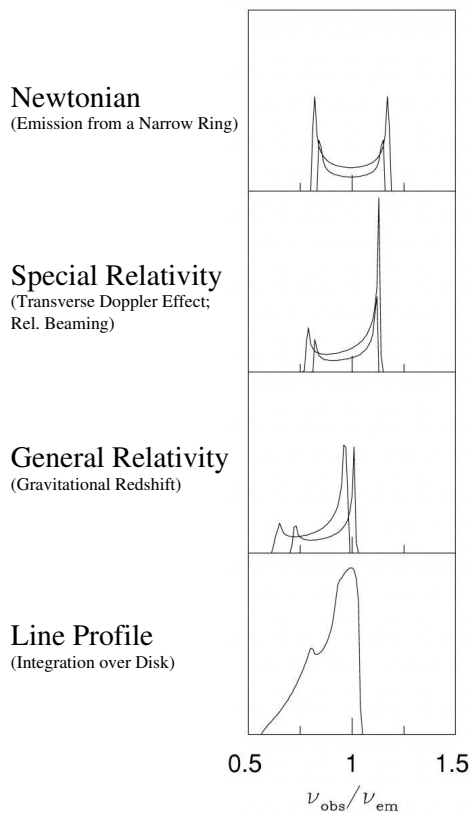
Figure 2.4: The emission from a narrow ring inside the accretion disk (top) has two peaks corresponding to the approaching and receding parts of the rotating disk (top left panel). Relativistic beaming increases the blue peak and decreases the red peak and the transverse Doppler effect (i.e., moving clocks run slowly) and gravitational redshifting transfer the line profile to lower energies (middle left panels). The broad, skewed line profile (bottom left panel) results from integrating over the whole disk. Figure adopted from Fabian et al. (2000a).

Relativistically Broadened Iron-Line Emission   Intrinsically, fluorescent iron Kα line emission has a well-defined discrete energy of 6.4 keV (in the case of neutral iron). However, its profile can become substantially broadened, double-peaked and characteristically skewed by Doppler shifts, gravitational redshifting and relativistic beaming. Figure 2.4 illustrates these effects. In the case of a Newtonian (non-relativistic) disk, each disk annulus gives rise to a symmetric double-horned line due to emission from approaching (blueshifted) and receding (redshifted) material on the opposing sides of the rotating disk. In the extreme environment close to a black hole special and general relativistic effects play an important role, enhancing the blue peak and decreasing the red peak of the line and shifting the whole line profile towards lower energies. Integrating over the full relativistic disk results to a characteristic broad, skewed line profile that can extend from below 4 keV up to $\sim$ 8 keV. The innermost part of the disk is particularly responsible for the strong red wing of the line, probing the material in the immediate vicinity of the black hole. In particular, the red wing of the line provides a probe of the black-hole spin. Since the innermost stable orbit of a non-rotating (Schwarzschild) black hole is at 6 gravitational radii, no emission is expected from inside this radius, unless the black hole is rotating (innermost stable orbit of a maximal rotating, so-called "Kerr black hole" is at $\sim$ 1r_g). Moreover, the profile of a relativistic, broad iron line provides the possibly most accurate measure of the orientation of the associated disk system with respect to the line of sight to the observer. Figure 2.5 shows the dependence of a modeled broad-line profile on the angle to the line of sight and on the black-hole spin.
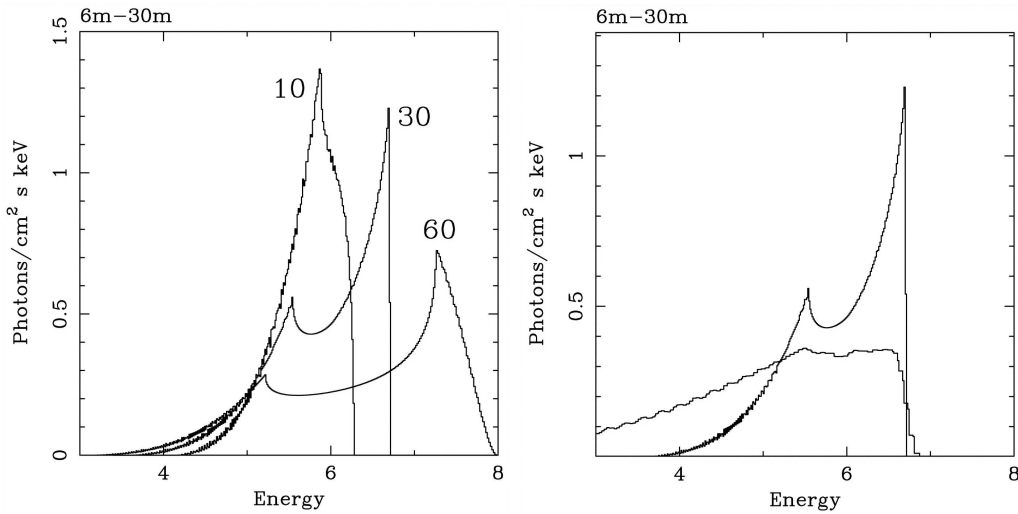
Figure 2.5: Dependence of a modeled broad-line profile on the angle to the line of sight (left, for a non-rotating black hole) and on the black-hole spin (right, for a non-rotating and a near-extremal Kerr black hole). In both panels, the emitting region is supposed to extend down to the innermost stable orbit. Figure taken from Fabian et al. (2000a).

2.2   X-Ray Imaging Spectroscopy

The most common type of detectors in X-ray astronomy until the late 1990s were proportional counters. In the case of the *ROSAT* PSPC detector, a polypropylene window with a thickness of $\sim 1\,\mu$m constrained a gas-filled chamber with argon, xenon, and methane. Via photoelectric absorption, an arriving photon creates an electron. The strong electromagnetic field inside the gas chamber accelerates the electron. Through interaction of the accelerated electron with the atoms and ions of the gas, an electron cloud forms, which causes a signal in a position (direction) sensitive array of electrode grids.

The SIS detectors onboard *ASCA*, *Chandra*'s ACIS and *XMM-Newton*'s EPIC detectors utilize CCD chips. The main advantage of these CCD detectors compared to proportional counters are the good energy resolution, the broad bandpasses and with the increasing number of pixels, the imaging capabilities. In particular the ACIS and EPIC detectors allow spatially separated regions of a given source to be spectroscopically investigated.

The basic principle of CCD detectors is similar to the way proportional counters work: an X-ray photon is absorbed in one of the pixels of the detector chip and produces electrons. The total released charge is proportional to the original photon energy. In this sense, CCDs differ from proportional counters only in the way the charge is created, collected and transferred.

For this PhD thesis project, the spectroscopic data of radio-loud, core-dominated AGN was analyzed over a broad energy band in the X-ray regime. The broad-band requirement ensures that different physical processes that might contribute to the X-ray spectrum of a given object can be disentangled, since different processes typically dominate different parts of the source spectrum. High angular resolution allows the nuclear AGN-related X-ray emission to be distinguished from extended emission originating on larger scales and the higher the sensitivity of an X-ray telescope to weak sources is, the better the spectral capabilities of its detector can be exploited. A good energy resolution (e.g.,

Table 2.1: Comparison of various X-ray missions' capabilities

Observatory Detector	*ASCA* SIS	 GIS	*Beppo*Sax LECS	 MECS	 PDS	*Chandra* ACIS-S	 ACIS-I	 HRC	*XMM-Newton* MOS	 PN
Energy Range [keV]	0.4–12	0.6–12	0.1-10	1.3-10	15-300	0.1-10	0.4-10	0.1-10	0.2-12	0.2-12
Eff. Area @0.25 keV [cm^2]	—	—	—	—	—	30	—	150	133	460
Eff. Area @0.60 keV [cm^2]	35	—	6	—	—	345	70	65	591	1061
Eff. Area @1.00 keV [cm^2]	230	50	40	—	—	615	385	215	922	1227
Eff. Area @6.00 keV [cm^2]	160	125	40	160	—	205	235	45	768	851
Eff. Area @80.0 keV [cm^2]	—	—	—	—	600	—	—	—	—	—
Angular Resolution (FWHM)	1′	1′	9.7′	1.2′	—[a]	1″	1″	0.5″	6″	6″
Field of View	22′	20′	37′	56′	1.3°	$(50 \times 8)′$	17′	31′	30′	30′

[a] Collimated Detector

$E/\Delta E \sim 20 - 50$ in the case of the EPIC detectors onboard *XMM-Newton*) allows narrow spectral features to be detected, which may carry crucial information about the underlying physical processes.

The abovementioned requirements to an ideal X-ray detector have been satisfied increasingly in the active X-ray satellite missions during the late 1990s and the early 2000s. Below, the most important characteristics of the four missions are presented, which have yielded spectroscopic data on AGN in the 0.2 keV to 12 keV range during the last one-and-a-half decades.

2.2.1 *ASCA*

ASCA (formerly named *Astro-D*) was Japan's fourth X-ray astronomy mission, and the second for which the United States have been providing part of the scientific payload. Between 1993 and 2001, *ASCA* collected spectroscopic data of hundreds of AGN, 30 of which belong to the complete sample of radio-loud, core-dominated AGN, MOJAVE, which formed the basis for the definition of the *2 cm-X-Sample* studied in this thesis. With a total of 77 analyzed epochs of observations (most of them with four independent spectroscopic detectors), *ASCA* data comprises the largest fraction of analyzed X-ray spectra.

ASCA carried four X-ray telescopes. At the focus of two of them was a Gas Imaging Spectrometer (*GIS*), while a Solid-state Imaging Spectrometer (*SIS*) was at the focus of the other two. The GIS was based on the GSPC detector that had flown on the *TENMA* satellite, while the two SIS detectors were the first Charge Coupled Device (CCD) cameras used for X-ray astronomy. The sensitivity of *ASCA*'s instruments allowed the first detailed, broad-band spectra of distant quasars to be derived.

ASCA's Solid-state Imaging Spectrometers

There have been two *SIS* cameras onboard *ASCA*, each of was based around four 420x422 square pixel front-side illuminated CCD chips. Their energy range was 0.4 keV to 10 keV, thus being the most relevant low-energy (thus soft X-ray absorption) sensitive instruments of *ASCA*. From late 1994 on, a decrease in efficiency of both SIS detectors below 1 keV
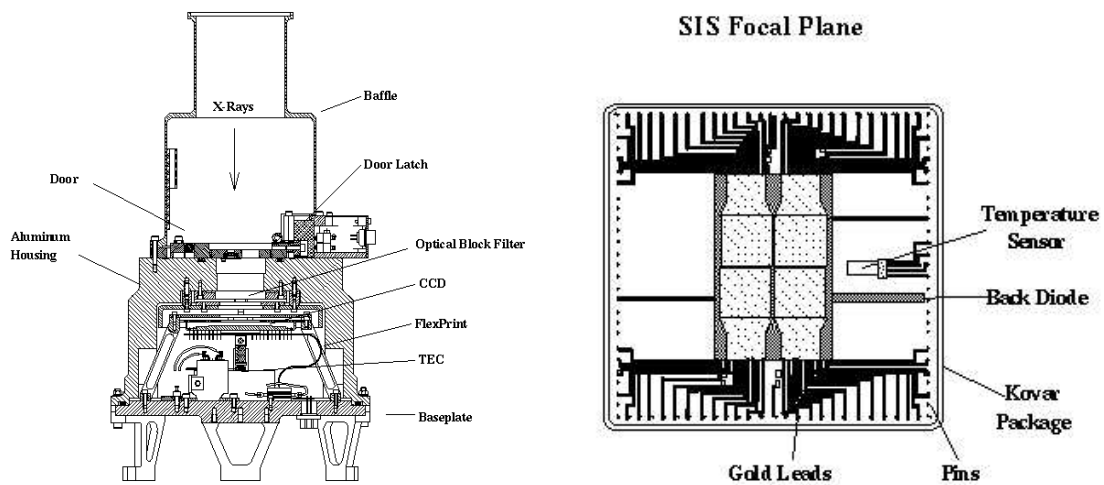
Figure 2.6: Left: Cross section of a SIS detector. Right: Four individual CCDs are combined to make a single SIS focal plane (images taken from the HEASARC website http://heasarc.gsfc.nasa.gov).

(up to about 20 %) was reported. The most plausible explanation for the occurrence of this problem is an increased residual dark current levels in the SIS and a decrease in Charge Transfer Efficiency (CTE). Due to this effect, apparent excess absorption over the Galactic value towards bright point sources need to be interpreted with caution if solely based on SIS data after late 1994[3].

ASCA's Gas Imaging Spectrometers

The ASCA *GIS* is an imaging gas scintillation proportional counter consisting of two separate detectors. The entrance window is made from beryllium and the gas chamber contains xenon with ten per cent of helium. The chamber is divided into a drift region, where the xenon atoms are ionized by incident X-ray photons, and a scintillation region, into which the photoelectrons are drifting and where they are being accelerated to excite other xenon atoms. The scintillation light, produced when the atoms de-excite, is proportional in intensity to the energy of the incident X-ray photon and detected by a position sensitive phototube. The GIS provides a larger effective area at high energies ($\gtrsim 5\,\mathrm{keV}$) compared to the SIS. With its larger field of view it was the main imaging facility of *ASCA*.

2.2.2   *Beppo*Sax

The X-ray astronomy satellite *Beppo*SAX (Boella et al. 1997a) was originally named SAX (Satellite per Astronomia X) and received his "first name" after its successful launch on April 30 1996 in honor of Giuseppe "Beppo" Occhialini. It was in operation until

---

[3]For this thesis, the SIS data below 1 keV was discarded if a significant discrepancy between GIS and SIS data could be found and the data were taken after late 1994.
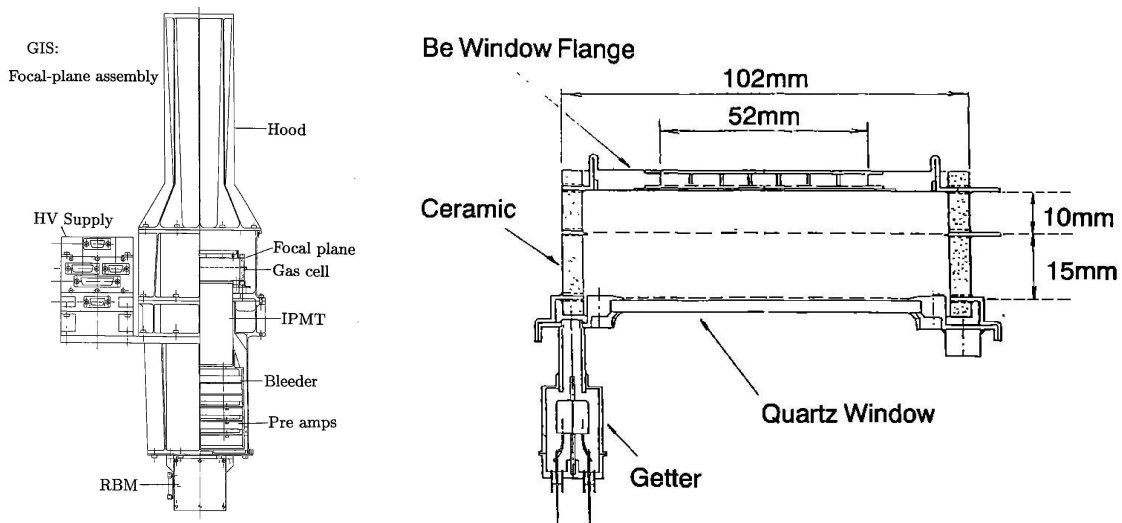
Figure 2.7: Left: Cross section of a GIS detector. Right: The structure of the gas cell. The upper 10 mm section above the mesh electrode is the drift region. The bottom 15 mm section is the scintillation region. (Image taken from Ohashi et al. 1996.)
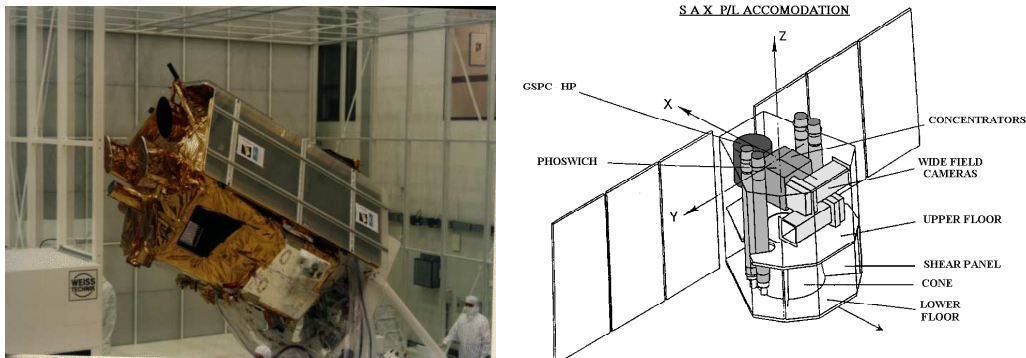
Figure 2.8: Left: *Beppo*SAX in the clean room at ESTEC; Right: Diagram of the scientific payload on-board *Beppo*SAX. (Images courtesy of the Agenzia Spaziale Italiana (ASI) and the *Beppo*SAX Science Data Center (SDC).)

April 30, 2002 and re-entered the earths atmosphere on April 29, 2003. *Beppo*Sax was a project of the Italian Space Agency (ASI) with participation of the Netherlands Agency for Aerospace Programs (NIVR). The main scientific characteristic of the *BeppoSAX* mission was its wide spectral coverage, ranging from 0.1 keV to over 200 keV. *Beppo*Sax carried three Narrow Field Instruments (NFI) relevant for individual source studies in this thesis: a Low Energy Concentrator Spectrometer (LECS), which covered the 0.1 keV to 10 keV range, a Medium Energy Concentrator Spectrometer (MECS; 1.3 keV to 10 keV), a Phoswich Detection System (PDS; 15 keV to 300 keV). The instruments of *Beppo*Sax (see Fig. 2.8) which are most relevant for this work are the two *GSPC* detectors LECS and MECS and the collimated PDS instrument.

25

The LECS detector

One of the four *Beppo*SAX GSPCs, the LECS detector (Parmar et al. 1997), was shielded with a thin window to allow transmission of low-energy X-rays into the xenon-filled detector. Inside the gas cell, a uniform electric field causes scintillation of the gas as the electrons, ionized by the incident X-ray photons, travel towards a grid. The amount of light produced is proportional to the energy of the photon but also depends on the position inside the gas cell where the absorption takes place. It is detected by a position sensitive photomultiplier. This depth can be determined by measuring the duration of the scintillation light that is produced. The LECS detector had an effective area of $20\,cm^{-2}$, $38\,cm^{-2}$, $56\,cm^{-2}$, $50\,cm^{-2}$, and $27\,cm^{-2}$ at $0.28\,keV$, $1\,keV$, $2\,keV$, $6.4\,keV$, and $9\,keV$, respectively. Its position accuracy was energy dependent, $\sim 10'$ at $0.28\,keV$ and $\sim 2'$ at $6\,keV$. The LECS provided an energy resolution of $\sim 32\%$ at $0.28\,keV$.

The MECS detector

Three of the *Beppo*SAX GSPC's had 50 micron beryllium windows, thus being sensitive in the range of 1.3-10 keV, together forming the MECS detector (Boella et al. 1997b). UV light is produced in a high electrical field region to which the electron cloud, resulting from the X-ray photon-absorption, is drifting from the absorption place. The amplitude of the signal is measured by a position sensitive photomultiplier, yielding the energy of the absorbed X-ray. The MECS detector had an effective area of $150\,cm^{-2}$ at $6.4\,keV$. and 80% of the total signal at the same energy are contained within $150''$. The MECS detector had an energy resolution of $\sim 8\%$ at $6.4\,keV$.

The PDS detector

A square array of four independent NaI(Tl)/CsI(Na) phoswich scintillation detectors made up the Phoswich Detector System (PDS) onboard *Beppo*Sax (Frontera et al. 1997). The acronym Phoswich (PHOsphor sandWICH) describes the configuration of two optically coupled crystals of NaI(Tl) and CsI(Na) in each of the four detectors. The scintillation light produced in each phoswich is collimated in a light guide of quartz and registered by a photomultiplier tube (PMT). The NaI(Tl) acts as X-ray detector, while the CsI(Na) scintillator acts as an active shield. Only events, which are exclusively detected in the NaI(Tl) crystal are accepted by the Pulse Shape Analyzer (PSA) of the analysis electronics. The phoswich configuration is providing a detector with a high efficiency at hard X-ray energies and a very low background level. The latter is further reduced by top and lateral anti-coincidence shields, which reject unwanted background counts caused by charged particles and X-rays impinging on the sides of the instrument.

2.2.3 *Chandra*

The word *Chandra* means "moon" or "luminous" in Sanskrit and in honor of the Indian-American Nobel laureate, Subrahmanyan Chandrasekhar, the NASA X-ray observatory AXAF (Advanced X-ray Astrophysics Facility) was renamed to *Chandra* after launch. Compared to earlier X-ray astronomical missions, *Chandra* provides a vast improvement in angular resolution, particularly in the regime above $2\,keV$, that was not accessible for
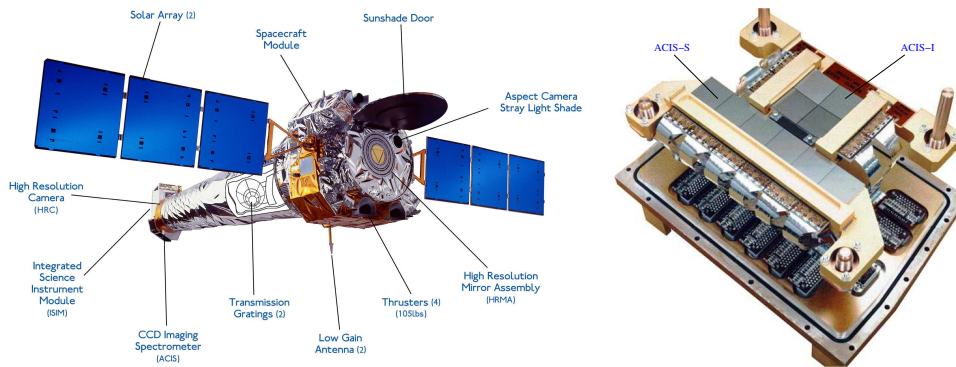
Figure 2.9: Left: The *Chandra* spacecraft with its main components labeled. Right: The Chandra Advanced CCD Imaging Spectrometer (ACIS) consists of two detectors ACIS-I and ACIS-S that both can be placed at the focus of the mirror system. ACIS-I is a 2×2 CCD array used mainly for wide-field imaging. The 1×6 CCD array of the ACIS-S can be used to investigate the linearly dispersed image of bright point sources in grating observations with the LETG or the HETG. The third chip in this 1×6 array, the S 3 chip, is backside illuminated and most often used for *Chandra* AGN observations. Images taken from `http://chandra.harvard.edu/`.

ROSAT. Both available focal plane instruments, the ACIS and the HRC (see below), achieve an unprecedented angular resolution of 0.5 arcseconds making use of the full angular-resolution power provided by the High Resolution Mirror Assembly (HRMA). The HRMA consists of 4 nested pairs of concentric grazing-incidence Wolter Type-I mirrors (the front mirror of each pair is a paraboloid and the back a hyperboloid; see Aschenbach (1985) for a review of X-ray optics), with the largest having a diameter of 1.2 m. The focal length of the HRMA is 10 m. A sketch of *Chandra* with its main components labeled is shown in Fig. 2.9.

Chandra is the prime instrument if a bright compact target source is embedded in a kiloparsec-scale extended emission region, e.g., associated with the body of the optical host galaxy of an AGN. In contrast to *ASCA*, *Beppo*Sax, and *XMM-Newton*, the *Chandra* spacecraft carries only one mirror assembly so that only one detector per observation can be used. The HRC is a micro-channel plate detector that is mainly used for high-resolution imaging, particularly if fast detector-readout (16 μs) is crucial for the successful observation. The HRC provides only a very limited energy resolution making it unattractive compared to the ACIS detector in the case of most AGN observations. An exception are AGN observations that concentrate on soft X-ray emission below 0.7 keV, particularly in combination with the Low Energy Transmission Grating (LETG). High-energy-resolution spectra ($E/\Delta E \gtrsim 1000$) down to $E = 0.08$ keV can be achieved in LETG-HRC observations.

The ACIS detector

The detector onboard *Chandra* best suited for most observations of bright, compact AGN is the AXAF CCD Imaging Spectrometer (ACIS, see Fig. 2.9). The ACIS detector consists of two arrays of identical CCD chips. Each chip provides a square field of view of 8.3×8.3 arcseconds. Four such chips make up a 2×2 array used mainly for wide-field

imaging: the ACIS-I. The other is a 1×6 CCD array, the ACIS-S, on which the linearly dispersed image of bright point source can be focused in grating observations. A special feature of the ACIS-S array is that two chips on it, in particular the third (S3) at the best focus position, are backside illuminated. The backside illuminated CCDs are sensitive down to lower energies than the front-side illuminated CCDs. The front-side illuminated CCDs are more efficient at higher energies and provided initially a better energy resolution ($E/\Delta E \sim 10 - 50$ compared to $E/\Delta E \sim 4 - 34$ for the ACIS-S3 chip) but their energy resolution varies with position since the detector was damaged in the early part of the mission. During passages of the earth's radiation-zone with the ACIS placed in focus of the HRMA, low-energy protons were reflected by the mirrors and focused onto the detector. The backside illuminated chips were not affected by this since it is far more difficult for low-energy protons being reflected from the HRMA to deposit their energy in the buried channels of the backside illuminated chips that face in the direction opposite to the HRMA. In the newest versions of the *Chandra* data reduction software CIAO (from version 2.3 on) a correction that recovers a significant fraction of the induced loss of spectral resolution of the ACIS-I can be applied.

The spatial resolution for on-axis imaging with ACIS is limited by the physical size of the CCD pixels (24.0 μm^2 corresponding to ~ 0.492 arcseconds squared) and not the HRMA. Approximately 90% of the encircled energy lies within four pixels (2 arcseconds) at 1.5 keV and within five pixels (2.5 arcseconds) at 6.4 keV. In practice, if e.g., the impact of the pileup effect in a given observation needs to be estimated (compare Sect. 3.4.3), the central nine pixels around the nominal position of a point source have to be considered to derive the source count rate.

2.2.4   *XMM-Newton*

The European Space Agency's X-ray Multi-Mirror satellite *XMM-Newton* (Jansen et al. 2001) was launched on December 10, 1999. It carries three X-ray telescopes (see Fig. 2.10), containing 58 high-precision concentric mirrors that focus incoming X-rays from a large field of view ($\sim 30'$) onto three separate European Photon Imaging Cameras (EPIC). Two of these mirror modules reflect about half of the incoming rays via the Reflection Grating Spectrometers (RGS) onto a linear array of CCDs. The MOS EPIC detectors (see below) at the end of these two mirror modules therefore can only "see" about half of the flux coming from a celestial X-ray source, while the third EPIC detector (PN, see below) is illuminated by all photons focused by the third mirror module.

Compared to *Chandra*, *XMM-Newton* provides a moderate angular resolution of $\sim 6''$ (FWHM). The high effective mirror area of *XMM-Newton* ($\sim 4300\,\mathrm{cm}^{-2}$ at 1.5 keV), however, is by far superior to all previous (and current) other X-ray astronomical observatories. Moreover, the satellite's highly eccentric orbit (traveling out to nearly one third of the distance to the Moon), allows very long and uninterrupted observations to be made making *XMM-Newton* the prime instrument for observations of relatively weak X-ray sources. In addition to the EPIC and RGS detectors, *XMM-Newton* carries a 30 cm optical/UV telescope, which can observe simultaneously the same regions as the X-ray telescopes.
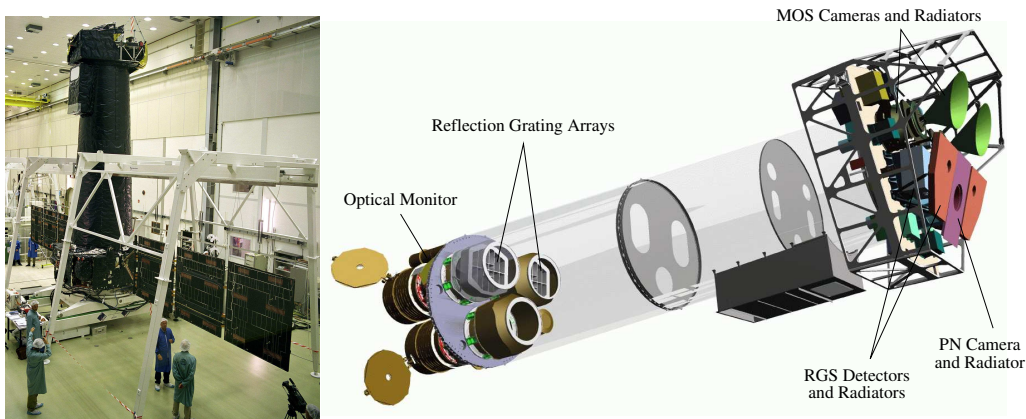
Figure 2.10: Left: Photo of the *XMM-Newton* spacecraft before launch in ESA ESTEC. The 4 tonne, 10 m long XMM-Newton spacecraft is the largest scientific satellite ever launched by the European Space Agency. (Image courtesy of ESA); Right: Sketch of the *XMM-Newton* spacecraft displaying its scientific payload components. On the left hand side of the sketch, the three telescopes are visible. At the right end, the focal plane instruments are shown: the two EPIC MOS cameras are placed at the focus of the two telescopes with Reflection Grating Arrays, the radiation collected by the third telescope is focused unattenuated onto the PN detector. (Image courtesy of Dornier Satellitensysteme GmbH)

The EPIC detectors

Two of the EPIC detectors make use metal oxide semiconductors (MOS) CCDs, consisting of seven silicon chips, each made up of a matrix of 600×600 pixels (Turner et al. 2001a). The third EPIC detector, the PN detector (Strüder et al. 2001), has been specifically developed for the *XMM-Newton* mission. In contrast to the MOS detectors, the PN detector is illuminated from the back side, which does not have insensitive layers or coatings, making it more sensitive to soft X-ray emission. Further, the individual columns of the PN chip are read out simultaneously unlike the MOS chips whose pixels are read out sequentially. This allows substantially lower read-out times to be achieved with the PN detector (1.5 ms time resolution of the MOS detectors compared to 0.03 ms of the PN detector in standard Timing Mode). The so-called Burst Mode, in which only a sub-frame of the PN detector is read out, facilitates read-out times of only 7 μs.

All three EPIC detectors allow X-ray spectroscopic observations in the energy range 0.2 keV to 12 keV to be made. The energy resolution of $E/\Delta E \sim 20 - 50$ is comparable to the *Chandra* ACIS energy resolution. The fast read-out times and the relatively large pixel size of the EPIC detectors make pileup a less severe problem for *XMM-Newton* than for *Chandra*.

2.3   Very-Long-Baseline Interferometry

The concept of this PhD thesis project combines X-ray spectroscopic observations od radio-loud AGN with the study of their milliarcsecond structure at radio wavelengths. While X-ray astronomy probes indirectly the most compact regions associated with the
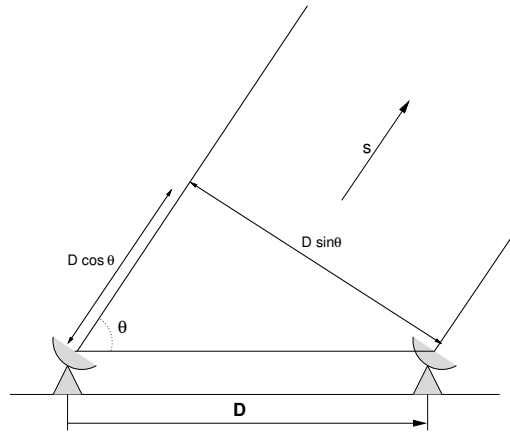
Figure 2.11: An elementary radio interferometer. Taken from Ros (1997).

accretion flows of AGN (via timing experiments or the analysis of disk-reflection spectral features; compare Sect. 2.1.4) the technique of Very Long Baseline Interferometry (VLBI) allows a direct imaging of comparably compact structures, usually associated with outflows from the central engines.

In this section, a brief introduction to VLBI, adapted from Kadler (2002), is given. More detailed information on the underlying principles of radio interferometry, can be found, e.g., in Thompson et al. (1986). A review of the development of high-resolution imaging in radio astronomy is given by Kellermann and Moran (2001). The individual steps of VLBI data calibration and analysis are described in textbooks, as e.g., Perley et al. (1989) and Taylor et al. (1999). For particular information on the VLBI data used in this thesis from the VLBA 2 cm Survey see Kellermann et al. (1998a) and Zensus et al. (2002) and compare appendix D of this thesis.

2.3.1 Fundamentals of radio aperture synthesis

Figure 2.11 shows the geometry of a simple radio Michelson interferometer consisting of two antennas, pointed at a distant radio source. If the source is far enough (in the so called far-field-pattern), the incoming rays to the different interferometer elements can be assumed to be parallel. Each of the two antennas registers a signal that produces voltages V_1 and V_2 in the telescope backend. These voltages are eventually correlated, i.e., a circuitry performs a multiplication and averaging of the (converted) voltages[4]. If the source is, for simplicity, a monochromatic emitter, then V_1 and V_2 both are sinusoidal functions. Figure 2.11 shows that the cosmic signal reaches the first antenna at a time $\tau_{\mathrm{g}} = (D/c)\cos\theta$ before it arrives at the second one, where D is the baseline of the two telescopes and c is the velocity of light. This is called the geometrical delay and the correlator output is proportional to

$$F = \sin(2\pi\nu t)\sin(2\pi\nu[t - \tau_{\mathrm{g}}]) \quad . \tag{2.11}$$

---

[4]In contrast to the simple adding interferometer, which basically receives the quantity $(V_1 + V_2)^2$, the correlator interferometer is proportional only to the correlated component of the two signals. The uncorrelated components cancel out during the time averaging process. This leads to a substantial reduction of noise in the output.

Since the Earth rotates, the projected baseline $D \sin \theta$ varies with time and so does the geometrical delay. The terms independent of τ_{g} can be filtered out, leaving for the correlator output (after some trigonometrical transformations)

$$F = \cos\left(2\pi\nu\tau_{\mathrm{g}} \cos\theta\right) \quad . \tag{2.12}$$

Therefore, the correlator output is proportional to a quasi-sinusoidal fringe pattern[5], due to the rotation of the Earth. If the cosmic source is not a point source, but has extended structure, the interferometer receives the signal not only from the direction $\boldsymbol{s}$, where it is pointed at, but from a whole area around a nominal position $\boldsymbol{s}_0$. From the position $\boldsymbol{s} = \boldsymbol{s}_0 + \boldsymbol{\sigma}$, an element of solid angle $d\Omega$ of the source then contributes the power $1/2\Delta\nu B(\boldsymbol{\sigma})A(\boldsymbol{\sigma})d\Omega$ at each of the two antennas. $\Delta\nu$ is the observing bandwidth, $B(\boldsymbol{\sigma})$ is the brightness at position $\boldsymbol{\sigma}$, $A(\boldsymbol{\sigma})$ is the reception pattern of the antenna, and the factor 1/2 represents the capability of a telescope to receive only one direction of circular polarization. Correlating the two antenna output powers and applying the fringe term of Equation (2.12), the interferometer output becomes

$$
\begin{aligned}
r(\boldsymbol{D}_\lambda, \boldsymbol{S}_0) &= \Delta\nu \int_{4\pi} A(\boldsymbol{\sigma})B(\boldsymbol{\sigma}) \cos(2\pi\boldsymbol{D}_\lambda \cdot \boldsymbol{s})d\Omega \\
&= \Delta\nu \cos(2\pi\boldsymbol{D}_\lambda \cdot \boldsymbol{s_0}) \int_{4\pi} A(\boldsymbol{\sigma})B(\boldsymbol{\sigma}) \cos(2\pi\boldsymbol{D}_\lambda \cdot \boldsymbol{\sigma})d\Omega \quad (2.13) \\
&- \Delta\nu \sin(2\pi\boldsymbol{D}_\lambda \cdot \boldsymbol{s_0}) \int_{4\pi} A(\boldsymbol{\sigma})B(\boldsymbol{\sigma}) \cos(2\pi\boldsymbol{D}_\lambda \cdot \boldsymbol{\sigma})d\Omega
\end{aligned}
$$

with $\nu\tau_{\mathrm{g}} = \boldsymbol{D}_\lambda \cdot \boldsymbol{s}$, where $\boldsymbol{D}_\lambda$ is the vector of the baseline in units of the observing wavelength. Introducing a complex quantity

$$V = |V|\mathrm{e}^{i\Phi_V} = \int_{4\pi} A_N(\boldsymbol{\sigma})B(\boldsymbol{\sigma})\mathrm{e}^{-i2\pi\boldsymbol{D}_\lambda \cdot \boldsymbol{\sigma}}d\Omega \tag{2.14}$$

with a normalized reception pattern $A_N(\boldsymbol{\sigma}) = A(\boldsymbol{\sigma})/A_0$, where A_0 is the antenna collecting area in direction $\boldsymbol{s}_0$, the correlator output is

$$r(\boldsymbol{D}_\lambda, \boldsymbol{S}_0) = A_0\Delta\nu|V| \cos(2\pi\boldsymbol{D}_\lambda \cdot \boldsymbol{s}_0 - \Phi_V) \quad . \tag{2.15}$$

V is called the complex visibility. The correlator output can be expressed in terms of a fringe pattern with the modulus and phase of V. The phase is measured relative to the phase of a hypothetical fringe pattern, received from a point source at the position $\boldsymbol{s}_0$. Both, modulus and phase of V are observables, and Equation (2.14) shows that the visibility is the Fourier transform of the brightness distribution $B(\boldsymbol{\sigma})$. In order to reconstruct B, the visibility V has to be measured with different baselines $\boldsymbol{D}_\lambda$. Usually this is expressed in terms of a two-dimensional plane with coordinates $u = \boldsymbol{D}_\lambda^{E/W} \cos\theta$ and $v = \boldsymbol{D}_\lambda^{N/S} \cos\theta$, which are basically the projected baselines in east–west and in north–south direction and are called spatial frequencies. This (u, v)–plane has to be sampled

---

[5]In reality a cosmic signal is never just composed out of one single frequency. The interference between different frequency components causes a modulation of the fringe function, which also depends on θ. This so called fringe-washing function has the shape of a sinc–function envelope, in the special case of a uniform power spectral density.

frequently enough in order to be able to perform a discrete Fourier transform[6] of the measured visibility function $V(u, v)$ and thus retrieve the brightness distribution B of the source with an angular resolution determined by the highest spatial frequency of the interferometer.

The Fourier deconvolution technique most commonly used is the CLEAN algorithm. Hybrid maps produced using this method are presented in this thesis. Special techniques are given at the appropriate section, as e.g., the production of maps of the linearly polarized emission via the imaging of the Stokes parameters Q and U in Sect. 6.3.1.

---

[6]According to the sampling theorem a discrete Fourier transformation, as an approximation to a continuous Fourier transformation of an analytically given function, can be done, if the sampling frequency is at least twice the frequency of the highest spatial frequency.

3 Project Outline

The question how powerful relativistic plasma jets are formed in the environment of supermassive black holes in active galactic nuclei (AGN) is a crucial one. Whilst a wealth of information about the jets themselves, in particular about their variable structure on parsec scales (e.g., Kellermann et al. 2004), can be obtained from VLBI, observational input that may lead to the disclosure of the fundamental difference between (jet-forming) radio-loud and (jet-suppressing) radio-quiet AGN is rare. Promising diagnostics of jet production are the accretion flows onto the central black holes. These accretion flows can be probed via X-ray spectroscopy, a technique which has dramatically benefitted from the advent of the new-generation X-ray telescopes *Chandra* and *XMM-Newton*. Their broad bandpasses, combined with the high sensitivity of *XMM-Newton* and the high angular resolution of *CHANDRA* have greatly improved our ability to identify the underlying physical processes of nuclear X-ray emission from AGN. Differences between the X-ray spectra of radio-loud and radio-quiet AGN may represent different physical properties of the accretion flows, dilution by an emission component directly associated with the jet, or even differences in the surrounding medium of their central engines.

Compared to radio-quiet AGN, little attention has been paid to radio-loud AGN in the X-ray band in the past. Kubo et al. (1998) studied a sample of 18 blazars finding that quasar-hosted blazars exhibit harder X-ray spectra than radio-quiet systems of comparable luminosity. Reeves and Turner (2000) analyzed the available archival *ASCA* data up to January 1998. In their sample, 35 radio-loud AGN and 27 radio-quiet quasars are investigated and the results suggest a a dependence of the photon index on radio loudness. Sambruna et al. (1999a; 2002) have investigated the X-ray spectra of 38 radio-loud AGN observed by *ASCA* and four sources observed by *RXTE*. Gambill et al. (2003) analyzed a sample of 17 radio-loud AGN observed with *CHANDRA*. These latter two studies were based on the integrated radio emission measured by single-dish telescopes or biased towards the presence of prominent extended radio-jet structure. To approach the characteristic differences between both classes of objects, however, it is important to avoid confusion from considering extended radio emission that arises on kiloparsec scales. In the most extreme case, emission from extended radio lobes – millions of light years away from the central engine – might still make a galaxy radio-loud when the nuclear jet-production has already been switched off for ages.

The radio emission of core-dominated radio-loud AGN is heavily affected by relativistic beaming effects due to large jet velocities and typically small angles to the line of sight. The same may be true for the X-ray emission of such objects if the jet contributes substantially to the observed X-ray flux as suggested by the relatively flatter X-ray spectra of radio-loud AGN compared to radio-quiet AGN. Thus, it is essential to study both the X-ray emission and the parsec-scale radio jets of these objects and to combine X-ray stud-

ies of core-dominated radio-loud AGN with VLBI observations of their parsec-scale radio jets to constrain the jet-system properties. Ideally, this combination promises to disentangle the contributions of "Seyfert-like" accretion-flow related emission and jet-associated (e.g., synchrotron self-Compton) emission in core-dominated radio-loud AGN.

The primary goal of this PhD thesis, is to provide a basis of uniformly analyzed X-ray spectra of a large sample of radio-loud, core-dominated AGN to consolidate the observational characteristics of this important class of AGN in the X-ray regime. The sample is selected to provide full structural and kinematical VLBI data on all sources and to represent a firm basis for statistical investigations. In this chapter, the investigated sample is introduced. The acquisition of X-ray public archival data available for this sample is outlined and the data reduction is described. In Chap. 4, the X-ray results obtained from these data are presented and discussed in Chap. 5. In particular, the X-ray characteristic quantities of the sample are compared to the multi-epoch VLBI data available for the full sample. Chap. 4 further presents results from the X-ray analysis of the individual sample sources and provides a brief review of published X-ray studies of those sources. In a number of cases, the analysis of the available VLBI and X-ray data within the scope of this thesis triggered deeper studies of individual objects. Those studies of the "special sources" PKS 0048−097, AO 0235+164, 3C 111, NGC 1052, and 0716+714 are presented in Chap. 6.

3.1   Sample Definition

The sample analyzed in this PhD thesis project is based on the statistically complete MOJAVE sample (Lister and Homan 2005), a Very Long Baseline Array (VLBA) monitored sample of the 133 brightest core-dominated radio-loud AGN in the northern sky, the continuation and extension the VLBA 2 cm Survey (see Sect. D). The primary goal of this PhD project is to compile and investigate all available X-ray spectra of MOJAVE sources taken so far with X-ray spectroscopic missions operating in the soft to medium X-ray regime ($\sim 0.2 - 12$ keV). This was achieved by making use of the publicly available archival data from the telescopes *ASCA*, *Beppo*Sax, *CHANDRA*, and *XMM-Newton*. Table 3.1 gives the 50 sources of the MOJAVE sample that have been observed at least once with one of these telescopes during the last 12 years. From here on, these 50 sources will be referred to as the *"2 cm-X-Sample"*. Throughout the next chapters, mainly the IAU (corresponding to their B 1950 coordinates)names of the individual sources are used. Common "aliases" are given in Table 1 of Kellermann et al. (2004) (reprinted in Sect. D.1), along with general properties of the *"2 cm-X-Sample"*.

Table 3.1: Journal of public archival *2cm-X-Sample* data (as of March 2005) analyzed in this work.

Source IAU Name (B 1950)	ASCA Obs. Date yyyy-mm-dd	Exposure[a] 10^3 s	PI	BeppoSax Obs. Date yyyy-mm-dd	Exposure[b] 10^3 s	PI	Chandra Obs. Date yyyy-mm-dd	Detector	Exposure[c] 10^3 s	PI	XMM-Newton Obs. Date yyyy-mm-dd	Exposure[d] 10^3 s	PI
0007+106	1997-07-01	43.7/40.4	Yaqoob								2000-07-03	8.0/8.0/14.9	Mason
0048−097				1996-12-02	0.6/2.3/10.0	Padovani							
				1997-12-19	4.7/9.9/10.0	Padovani							
0235+164	1994-02-04	12.1/10.6	Madejski	1999-01-28	25.0/29.2/30.0	Padovani	2000-08-20	ACIS-S	30.6	Turnshek	2002-02-10	19.1/19.1/16.8	Watson
	1994-02-11	12.6/10.8	Madejski								2004-01-18	29.9/29.9/29.7	Raiteri
	1994-02-16	15.4/13.5	Madejski								2004-08-02	11.7/11.7/11.5	Raiteri
	1994-02-19	13.2/12.8	Madejski										
	1998-02-11	20.6/19.3	Madejski										
0238−084	1996-08-11	42.4/39.8	Wilson	2000-01-11	26.2/63.9/75.0	Guainazzi	2000-08-29	ACIS-S	2.4	Garmire	2002-09-28	15.7/15.7/13.2	Weaver
0316+413	1993-08-06	20.4/21.1	Arnaud	1996-09-19	0/87.9/80.0	Sax-Team	1999-09-20	ACIS-I	5.4	Fabian	2001-01-30	53.7/53.7/51.3	Churazov
	1993-08-06	23.6/19.8	Arnaud				1999-10-10	ACIS-S	27.4	Canizares			
	1995-08-18	23.2/19.7	Arnaud				1999-11-28	ACIS-S	9.1	Fabian			
	1995-09-04	24.1/21.0	Arnaud				2000-01-29	ACIS-S	25.1	Fabian			
							2000-08-25	ACIS-S	25.0	Canizares			
							2002-08-08	ACIS-S	97.0	Fabian			
							2002-08-10	ACIS-S	96.7	Fabian			
							2002-08-11	ACIS-S	5.9	Fabian			
0333+321	1994-02-01	37.7/32.2	Turner	1999-08-05	17.5/50.0/60.0	Fiore							
0415+379	1996-02-13	48.2/38.1	Crawford	1998-03-08	21.0/69.6/100.0	Grandi					2001-03-14	44.0/44.0/42.3	Eracleous
0420−014	1997-08-31	20.2/20.6	Reeves										
0430+052	1994-02-17	52.9/49.9	Grandi	1997-09-20	34.7/81.6/100.0	Zdziarski	2001-01-27	ACIS-S	1.8	Wilson	2002-09-06	12.1/12.3/12.2	Mason
	1998-02-12	97.0/91.4	Inoue				2001-09-18	ACIS-S	13.1	Wilson	2003-08-26	127.0/127.0/127.5	Branduardi-Raymont
							2001-12-21	ACIS-S	58.2	Yaqoob			
0458−020							2002-10-10	ACIS-S	77.8	Bechtold			
0528+134	1994-08-28	22.0/20.0	Urry	1997-02-21	6.3/14.4/10.0	Maraschi							
	1995-03-07	24.7/21.9	Collmar	1997-02-22	5.0/13.3/10.0	Maraschi							
	1995-03-14	25.0/22.8	Collmar	1997-02-27	4.4/7.3/10.0	Maraschi							
	1995-03-19	23.2/21.1	Urry	1997-03-01	4.3/13.5/10.0	Maraschi							
				1997-03-03	5.1/14.1/10.0	Maraschi							
				1997-03-04	2.8/11.2/10.0	Maraschi							
				1997-03-06	3.1/12.7/10.0	Maraschi							
				1997-03-11	2.5/11.4/10.0	Maraschi							
0605−085							2001-05-01	ACIS-S	10.0	Sambruna			
0716+714	1994-03-16	19.8/15.9	Fujimoto	1996-11-14	16.9/122.5/100.0	Chiappetti					2001-04-13	8.1/8.0/8.5	Mulchaey
	1994-03-19	21.1/18.0	Fujimoto	1998-11-07	9.5/31.3/30.0	Giommi					2001-09-19	9.3/9.3/0	Mulchaey
	1994-03-21	24.0/22.2	Fujimoto	2000-10-30	19.2/43.5/50.0	Tagliaferri					2002-03-26	9.0/9.0/6.7	Mulchaey

Continued on next page

Table 3.1 – continued from previous page

Source IAU Name (B 1950)	ASCA Obs. Date yyyy-mm-dd	Exposure[a] 10^3 s	PI	BeppoSax Obs. Date yyyy-mm-dd	Exposure[b] 10^3 s	PI	Chandra Obs. Date yyyy-mm-dd	Detector	Exposure[c] 10^3 s	PI	XMM-Newton Obs. Date yyyy-mm-dd	Exposure[d] 10^3 s	PI
0735+178	1996-04-22	45.6/41.9	Tashiro										
0736+017	1998-10-26	39.4/36.1	Sambruna										
0738+313							2000-10-10	ACIS-S	28.0	Murray	2001-04-19	30.1/30.1/27.5	Griffiths
0827+243							2002-05-07	ACIS-S	20.1	Marscher			
0836+710	1995-03-17	20.2/14.1	Matsuoka	1998-05-27	18.5/42.6/50.0	Maraschi	1999-10-17	ACIS-S	62.3	Canizares	2001-04-12	36.1/36.1/33.5	Turner
							2000-08-25	ACIS-S	14.2	Canizares			
0851+202	1994-11-18	42.0/40.6	ASCA Team	1997-11-24	5.2/10.7/10.0	Padovani							
	1997-04-26	40.4/35.0	Idesawa	2001-11-20	23.8/39.8/100.0	Massaro							
	1997-11-18	42.0/40.6	Idesawa										
0923+392	1998-11-01	42.6/38.0	Sambruna				2002-10-19	ACIS-S	20.6	Marscher			
1038+064	1996-12-13	86.4/81.8	Yamasaki								2003-05-18	59.7/59.7/58.0	Weaver
	1996-12-20	12.5/11.5	Yamasaki										
1055+018							2001-01-09	ACIS-S	10.3	Sambruna			
1127−145				1999-06-04	18.7/47.9/50.0	Celotti	2000-05-28	ACIS-S	30.0	Bechtold	2002-07-01	29.8/29.8/28.3	Griffiths
1156+295							2000-06-29	ACIS-I	74.9	Coppi			
1222+216							2002-11-06	ACIS-S	19.7	Marscher			
1226+023	1993-06-08	39.0/35.9	Ohashi	1996-07-18	11.8/129.9/170.0	SAX Team	2000-01-09	ACIS-S	39.6	Chandra Team	2000-06-13	7.6/7.6/5.1	XMM Team
	1993-12-15	21.4/18.0	ASCA Team	1997-01-13	13.6/25.1/20.0	Maraschi	2000-01-10	ACIS-S	39.1	Chandra Team	2000-06-13	25.4/25.4/22.8	XMM Team
	1993-12-15	24.4/20.1	ASCA Team	1997-01-15	13.3/24.0/20.0	Maraschi	2000-06-14	ACIS-S	28.1	Chandra Team	2000-06-13	63.4/63.4/65.8	XMM Team
	1993-12-16	16.3/13.9	Makino	1997-01-17	12.4/27.3/20.0	Maraschi	2000-06-14	ACIS-S	27.8	Chandra Team	2000-06-15	7.4/7.4/4.9	XMM Team
	1993-12-19	22.1/19.1	ASCA Team	1997-01-22	8.8/22.2/20.0	Maraschi	2001-06-13	ACIS-S	27.1	Chandra Team	2000-06-15	27.2/27.2/29.7	XMM Team
	1993-12-20	22.3/20.3	ASCA Team	1998-06-24	27.9/72.2/0.06	SAX Team	2001-06-13	ACIS-S	30.6	Chandra Team	2000-06-15	30.0/30.0/30.0	XMM Team
	1993-12-20	12.2/10.6	Makino	2000-01-09	34.8/85.2/0.06	SAX Team	2001-06-15	ACIS-S	25.8	Chandra Team	2000-06-16	9.6/9.7/7.5	XMM Team
	1993-12-23	12.1/10.7	Makino	2000-06-13	29.6/68.1/0.06	SAX Team	2002-06-05	ACIS-S	25.0	Chandra Team	2000-06-17	58.2/58.2/60.6	XMM Team
	1993-12-27	11.9/11.6	Makino	2001-06-12	16.9/38.4/0.06	SAX Team	2002-06-05	ACIS-S	25.4	Chandra Team	2001-06-13	88.7/88.7/88.6	XMM Team
	1996-07-16	54.0/50.1	ASCA Team				2002-06-06	ACIS-S	30.2	Chandra Team	2001-12-16	5.5/5.8/5.0	Turner
	1998-06-24	77.6/72.8	ASCA Team				2002-06-04	ACIS-S	28.9	Chandra Team	2001-12-22	5.5/5.8/5.0	Turner
	2000-01-09	53.7/50.9	ASCA Team				2003-07-07	ACIS-S	27.6	Chandra Team	2002-01-09	9.2/8.9/17.7	XMM Team
							2003-07-07	ACIS-S	28.0	Chandra Team	2002-07-07	2.9/3.1/5.0	Turner
							2004-06-30	ACIS-S	30.2	Chandra Team	2002-12-17	4.9/5.2/5.0	Turner
							2004-06-30	ACIS-S	30.1	Chandra Team	2003-01-05	8.7/8.7/8.5	XMM Team
							2003-11-24	ACIS-S	41.3	Jester	2003-01-05	4.9/5.1/5.0	Turner
							2004-02-10	ACIS-S	38.4	Jester	2003-06-18	5.4/5.7/5.5	Turner
											2003-07-07	58.3/58.3/58.1	XMM Team
											2003-07-08	8.0/8.3/8.1	Turner
											2003-12-14	8.4/8.7/8.5	Turner
											2004-06-30	61.5/62.7/57.8	XMM Team
1228+126	1993-06-07	17.8/15.9	Canizares	1996-07-14	0/25.0/50.0	SAX Team	2000-04-15	ACIS-I	9.9	Fabian	2000-06-19	39.6/39.6/30.7	XMM Team

Continued on next page

Table 3.1 – continued from previous page

Source	ASCA			BeppoSax			Chandra				XMM-Newton		
IAU Name (B 1950)	Obs. Date yyyy-mm-dd	Exposure[a] 10^3 s	PI	Obs. Date yyyy-mm-dd	Exposure[b] 10^3 s	PI	Obs. Date yyyy-mm-dd	Detector	Exposure[c] 10^3 s	PI	Obs. Date yyyy-mm-dd	Exposure[d] 10^3 s	PI
							2000-04-20	ACIS-S	1.1	Wilson			
							2000-07-17	ACIS-S	38.5	Canizares			
							2000-07-29	ACIS-S	38.2	Wilson			
							2000-07-30	ACIS-S	14.2	Wilson			
							2002-01-16	ACIS-S	5.4	Harris			
							2002-02-12	ACIS-S	5.1	Harris			
							2002-03-30	ACIS-S	5.1	Harris			
							2002-06-08	ACIS-S	5.5	Harris			
							2002-07-05	ACIS-S	20.8	Cote			
							2002-07-06	ACIS-S	99.9	Cote			
							2002-07-24	ACIS-S	5.2	Harris			
							2002-11-17	ACIS-S	5.8	Harris			
							2002-12-29	ACIS-S	5.3	Harris			
							2003-02-04	ACIS-S	5.8	Harris			
							2003-03-09	ACIS-S	5.4	Harris			
							2003-04-14	ACIS-S	5.0	Harris			
							2003-05-18	ACIS-S	5.3	Harris			
							2003-07-03	ACIS-S	5.2	Harris			
							2003-08-08	ACIS-S	5.3	Harris			
							2003-11-11	ACIS-S	5.5	Biretta			
							2003-11-21	ACIS-S	37.2	Fabbiano			
							2003-12-29	ACIS-S	5.2	Biretta			
							2004-02-12	ACIS-S	5.2	Biretta			
1253−055	1993-06-21	42.5/40.5	Makino	1997-01-13	7.4/21.8/20.0	Maraschi	2002-03-21	ACIS-S	108.2	Canizares			
	1993-12-16	12.4/10.4	Makino	1997-01-15	8.4/23.9/20.0	Maraschi							
	1993-12-21	13.9/12.0	Makino	1997-01-18	0.5/2.6/20.0	Maraschi							
	1993-12-23	13.1/11.8	Makino	1997-01-21	4.2/11.7/20.0	Maraschi							
	1993-12-27	13.6/12.0	Makino	1997-01-23	11.1/24.7/20.0	Maraschi							
	1994-12-20	12.7/11.5	Kii										
	1995-01-05	10.8/10.0	Kii										
	1995-01-08	10.3/9.6	Kii										
	1995-06-27	10.8/10.9	Kii										
	1995-07-08	12.6/11.6	Kii										
	1996-01-27	22.7/21.5	ASCA Team										
1308+326	1996-06-10	19.2/17.3	Mc Breen								2002-12-10	49.3/49.3/47.6	Edge
	1996-06-11	22.8/19.6	Mc Breen										
1334−127											2003-01-31	13.7/13.7/12.0	Fiore
1413+135	1998-07-24	45.8/42.8	Perlman										

Table 3.1 – continued from previous page

Source	*ASCA*			*BeppoSax*			*Chandra*				*XMM-Newton*		
IAU Name (B 1950)	Obs. Date yyyy-mm-dd	Exposure[a] 10^3 s	PI	Obs. Date yyyy-mm-dd	Exposure[b] 10^3 s	PI	Obs. Date yyyy-mm-dd	Detector	Exposure[c] 10^3 s	PI	Obs. Date yyyy-mm-dd	Exposure[d] 10^3 s	PI
1458+718							2002-01-28	ACIS-S	18.7	Siemiginowska			
1502+106				.							2001-01-13	8.1/8.7/8.4	Turner
											2001-01-13	10.6/11.2/10.9	Petrucci
											2001-01-14	13.1/13.7/13.4	Petrucci
1510−089	1996-08-20	23.6/21.6	Singh	1998-08-03	16.2/43.8/50.0	Maraschi	2001-03-23	ACIS-S	10.2	Sambruna			
1633+382	1996-03-04	13.5/10.6	Takahashi										
	1996-03-21	10.9/9.2	Takahashi										
	1996-03-25	10.6/8.6	Takahashi										
	1996-03-27	11.0/9.5	Takahashi										
1641+399				1999-02-19	11.1/25.9/30.0	Maraschi	2001-04-27	ACIS-S	10.0	Sambruna			
1655+077							2002-04-28	ACIS-S	5.1	Marshall			
1749+096	1995-09-22	33.5/30.3	Urry										
1803+784				1998-09-28	18.7/40.5/40.0	Padovani							
1823+568				1997-10-11	4.2/13.4/10.0	Padovani							
1828+487							2002-05-20	ACIS-S	5.6	Marshall			
1928+738	1997-08-12	20.6/16.6	Yuan				2001-04-27	ACIS-S	9.3	Sambruna			
1957+405	1993-05-27	36.6/32.9	Arnaud	1999-10-27	24.3/73.0/80.0	Ettori	2000-03-08	ACIS-S	2.4	Wilson			
	1993-10-27	40.7/35.3	Arnaud				2000-05-21	ACIS-S	35.2	Wilson			
							2000-05-26	ACIS-S	10.2	Wilson			
2134+004				2000-11-25	25.9/75.1/80.0	Celotti							
2145+067	1998-12-05	41.3/36.8	Yamasaki										
2200+420	1995-11-22	31.9/29.3	Urry	1997-11-08	12.4/13.8/10.0	Padovani	2000-01-07	ACIS-I	2.1	Pesce			
	1997-07-18	65.6/36.8	*ASCA* Team	1999-06-05	45.3/54.4/50.0	Tagliaferri	2000-02-16	ACIS-I	1.1	Pesce			
	1999-06-28	89.2/82.4	Tashiro	1999-12-05	17.5/54.7/50.0	Tagliaferri							
				2000-07-26	16.9/23.3/50.0	Tagliaferri							
				2000-10-31	24.9/33.7/50.0	Tagliaferri							
2223−052				1997-11-10	9.4/16.2/20.0	Ghisellini							
2230+114	1995-12-06	22.4/19.8	Madejski	1997-11-11	11.0/23.8/20.0	Maraschi							
				1997-11-13	10.3/22.3/20.0	Maraschi							
				1997-11-16	13.2/25.7/20.0	Maraschi							
				1997-11-18	7.0/12.2/20.0	Maraschi							
				1997-11-21	9.5/19.4/20.0	Maraschi							
2243−123				1998-11-18	10.2/27.5/30.0	Maraschi							
2251+158				2000-06-05	17.7/48.5/50.0	Tavecchio	2002-11-06	ACIS-S	5.2	Marshall			

[a] Nominal Exposure of the SIS and GIS detectors; [b] Nominal Exposure of the LECS, MECS, and PDS detectors; [c] Nominal Exposure of the ACIS-S or ACIS-I detectors; [d] Nominal Exposure of the MOS 1, MOS 2, and PN detectors

3.2   Properties of the *2 cm-X-Sample*

3.2.1   Redshift Distribution

In Fig. 3.1, the redshift distribution of the sources in the *2 cm-X-Sample* is shown. A large range between $z = 0.004$ and $z = 2.286$ is covered, exhibiting an apparently bimodal distribution with a pronounced peak at small z values ($\lesssim z = 0.25$) and a second, broader maximum above $0.5 \lesssim z \lesssim 0.75$ with a wing towards higher z values. The decomposition into different source classes shows that the low-redshift peak is dominated by nearby radio galaxies, while the quasar distribution peaks above $z = 0.5$, and extends up to high z-values. The BL Lacs peak at low frequencies ($0.25 \lesssim z \lesssim 0.5$).
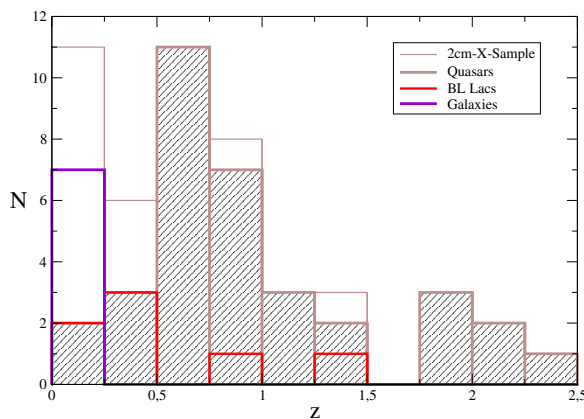
Figure 3.1: Redshift distribution of *2 cm-X-Sample* sources. The distribution is shown for the full sample (brown, solid line), quasars (hatched), BL Lac objects (red, dashed line), and galaxies (blue, solid line).

3.2.2   Comparison of the *2 cm-X-Sample* and the VLBA 2 cm and MOJAVE samples

Is the *2 cm-X-Sample* representative of the MOJAVE sample in terms of VLBI characteristics?

Figure 3.2 (top panels) shows the distribution of mean VLBI radio fluxes for the *2 cm-X-Sample* in comparison to the distribution for the whole MOJAVE sample. In the middle panels of Fig. 3.2 the comparison of the source compactness (i.e., unresolved flux on the longest VLBA baselines at 15 GHz divided by the total recovered VLBI flux) is shown. These distributions for the whole MOJAVE sample are analyzed in detail in Kovalev et al. 2005. As for the MOJAVE sample, the peak of the VLBI flux distribution for the *2 cm-X-Sample* reflects the selection limit while the low flux density wing reflects the variable nature of AGN. The distribution of the mean source compactness shows, in agreement with expectations from unification models of radio galaxies, quasars and BL Lacs, the rising compactness from galaxies to quasars to BL Lacs for both samples. The bottom panels of Fig. 3.2 display the distributions for the *2 cm-X-Sample* and the whole MOJAVE sample of the apparent linear velocity of the brightest component in each source with well determined kinematics. The apparent bimodality of speeds for the full VLBA 2 cm Survey sample and the MOJAVE sample reported in Kellermann et al. (2004) is also present for the *2 cm-X-Sample*, with a minimum (most pronounced for the quasar distribution) around $\beta_{\mathrm{app}} \sim 8$.
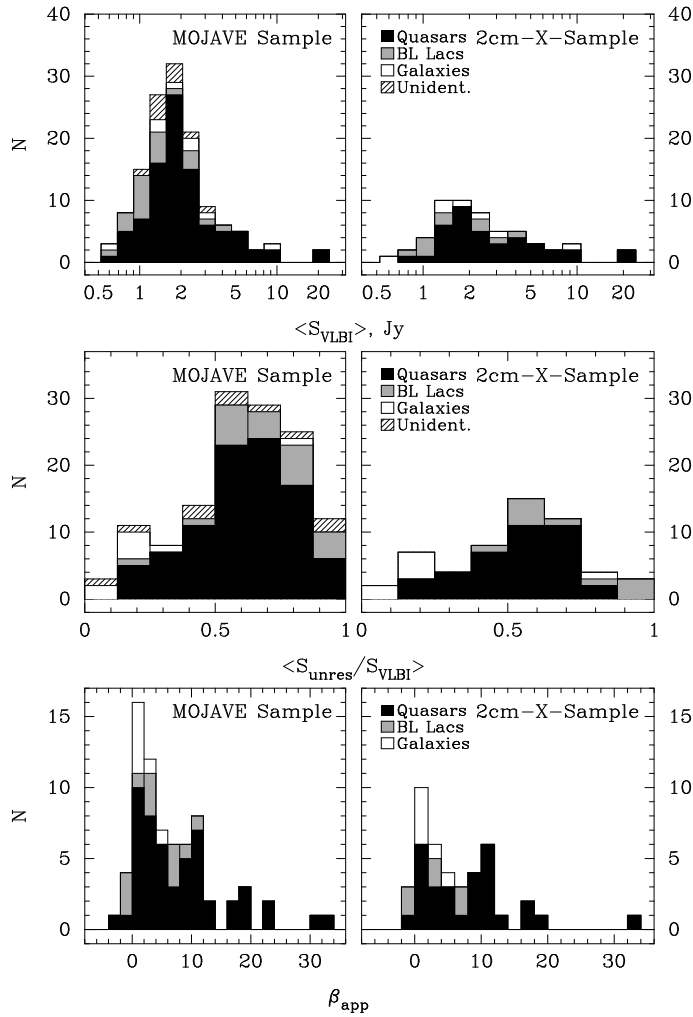
Figure 3.2: Distribution of the statistically complete MOJAVE sample and the *2 cm-X-sample* observed spectroscopically at X-rays over the mean total flux density S_{VLBI} observed by the VLBA (top), the mean compactness index S_{unres}/S_{VLBI} (middle), and the apparent linear velocity $\beta = v/c$ of well determined jet components. In all histograms the sources are divided by optical classification into quasars, BL Lac objects and galaxies.

A Kolmogorov-Smirnov (KS) test does not reveal any significant differences between the VLBI properties of both samples, so that we consider the *2 cm-X-Sample* to be representative of the statistically complete MOJAVE sample. It thus provides a firm basis for statistical investigations of core-dominated radio-loud AGN.

Is the *2 cm-X-Sample* representative of the MOJAVE sample in terms of X-ray characteristics?

To further test the representative character of the *2 cm-X-Sample* for the class of radio-loud, core-dominated AGN, in terms of X-ray characteristics, the soft X-ray flux and luminosity distributions of both samples were compared by making use of the *ROSAT* All-Sky Survey (RASS) (see Appendix B). Fig. B.4 demonstrates that the 2 cm-X-Sample is representative of the larger, complete MOJAVE sample in terms of soft X-ray luminosity. A KS-test reveals a 99.9 % probability that the 2 cm-X-Sample and the full MOJAVE sample are drawn from the same parent population in terms of soft X-ray luminosity, i.e., the *2 cm-X-Sample* is representative of the MOJAVE sample.

3.3 Data Acquisition

The open-archive policy of most relevant astronomical facilities makes it possible nowadays to conduct an archival survey like the one presented in this work. In general, observations of astronomical targets are performed either organized by the science teams of the observatories themselves for calibration and performance tests, as public observations, e.g., as Target-of-Opportunity (ToO) observations, as part of guaranteed-observing time programs of mission participating agencies and/or individuals, or as peer-reviewed and approved guest-observer projects. The data collected are stored in archives maintained by the mission teams and can in general be accessed by the astronomical community after the expiration of individual proprietary periods either via web interfaces or upon written request.

In high-energy astronomy this concept has been fostered during the last decades, in particular by embracing the Flexible Image Transport System (FITS) data format as a standard for all astrophysical missions from the late 1980s on. The *ROSAT* mission in 1990 was the first mission whose data were distributed in the FITS format, defining a number of FITS templates and keywords applicable to the different levels of data. In contrast, data from missions flown before 1990 were usually stored in mission-specific formats on a variety of media and depending on specialized software, hampering the development of multi-mission archive concepts.

The NASA High Energy Astrophysics Science Archive Research Center[1] (HEASARC) was created in 1990 and now archives high energy (X-ray and γ-ray) astrophysical data from all major satellite missions. Data from "mature" missions, i.e., from the pre-*ROSAT* era, have been restored and reformatted into the FITS format, whereas the data from missions flown after 1990 come to the HEASARC archive directly from their Science Data centers or the mission PIs.

The HEASARC website allows the user to browse observation catalogs of the individual missions and to search multiple mission catalogs for a given source name or position in the sky. For this thesis, the mission catalogs of *ASCA*, *Beppo*Sax, *Chandra*, and *XMM-Newton* were searched for observations that contained sources of the MOJAVE sample inside the mission-specific Field-of-Views (FoVs) of their X-ray spectroscopic detectors. In the case of the narrow-field instruments[2] of *ASCA* and *Beppo*Sax, this usually implied pointed observations of the AGN of interest. In the case of *Chandra* and *XMM-Newton* a number of sources were found in observations of objects or fields close to the nominal position a MOJAVE source. In these cases, however, the final judgment about the usability of these observations had to be made after a direct inspection of the data because of the roll-angle dependence of the (non circular) FoVs, e.g., of the ACIS-S detector of *Chandra*, and the different detector-modes that may reduce the useful FoV considerable, e.g., in the case of small-window mode observations with the *XMM-Newton* PN detector.

---

[1] `http://heasarc.gsfc.nasa.gov`

[2] The full FoV of the SIS, GIS, LECS, and MECS detectors onboard these two satellites is comparable to the FoVs of *Chandra* and *XMM-Newton* (compare Table 2.1). However, the ratio of their PSFs to their FoVs is in the range of 1/4 to 1/60, making it difficult or impossible to resolve neighboring sources from the generally much brighter target source at the center of the FoV.

3.4   Data Calibration and Extraction of Source Spectra

The general concept of X-ray spectral data reduction involves the following steps that, to a large degree, differ only in the use of specific software for the individual missions:

1. The data have to be downloaded from the given archive, copied and uncompressed in a local directory.

2. The data have to be inspected. In general, the FITS headers contain all relevant information on the observational details like nominal pointing position, integration time, detectors in use, etc.

3. The most recent (or most appropriate) calibration has to be used, i.e., the necessary information on how the given detector at the time of the observation responds to the incoming radiation in terms of spectral, timing and spatial response. In particular, this step provides the necessary calibration data that allows the data-reduction software to consider properly the mirror area (effective area), the mirror point-spread-function (PSF), the mirror grating diffraction efficiency and the grating line-spread function (LSF) (in case of grating facilities in use), the detector quantum efficiency (QE), the detector redistribution matrix file (RMF), and the time-dependent coordinate transformations (accounting for telescope "dithering") for the given observation.

4. The event file that contains the full information of data recorded during the observation (photon events) has to be filtered, i.e., "bad-time" intervals need to be recognized and waived. In particular, this may apply for periods of detector malfunctions, high internal or external background periods, or damaged detector pixels or sub-arrays. Filtering may also invoke the extraction of events inside a given detector or sky region (the extraction of source data) or for given time periods.

5. The spectrum, i.e., the pulse-height signal, of the source has to be extracted from the filtered event file for the time period of interest.

6. An appropriate background spectrum has to be extracted from the filtered event file for the same time period. The background should not be contaminated by other sources and should be taken from a region close to the source (ideally from an annulus around the source region). If this is not possible, standard background files provided from the mission science teams may be used.

7. Using the filtered event file and applying the proper calibration, an RMF has to be created for the detector regions and time periods of interest. The RMF accounts for detector-specific modifications of the incoming signal, in particular for the redistribution of detector channels into energy bins. The same applies for the background spectrum.

8. An ancillary response file (ARF) has to be produced, accounting for the combined mirror/filter/detector effective areas and efficiencies as a function of energy, for the regions and time periods of interest, i.e., the source and background spectra.

9. The spectra have to be binned (irreversible) or grouped (reversible) together to pro-
   vide an acceptable SNR. Usually, for the spectra analyzed in this thesis, grouping
   has been performed to yield 25 counts per bin, providing a SNR of 5 (assuming
   Poisson statistics).

10. The background-subtracted source spectra have to be fitted with a (physical) model.
    The free parameters of the spectral model are varied to find the best fitting approxi-
    mation (according to the least-squares method) of the model folded with the instru-
    mental response to the measured spectral data.

The application of the basic steps of for the individual detectors of *ASCA*, *Beppo*Sax,
Chandra, and *XMM-Newton* are described in more detail in the subsequent paragraphs.
The spectral fitting procedure is described in Sect. 3.5.

3.4.1   *ASCA* Data

All *ASCA* observing sequences with targets designated as AGN (as indicated by a leading
"7" in the observing sequence number) are contained in the TARTARUS database (Turner
et al. 2001b). TARTARUS provides source and background event files, spectra, ancillary
response files and response matrices, images and assorted light curves for all 661 *ASCA*
observing sequences designated as AGN observations.

All TARTARUS data base on the observation files available from the HEASARC
ASCA database. Screened event files have been produced using the ancillary files for the
given observation. Source and background events have been extracted from the nominal
target position for all four detectors. All TARTARUS results used in this thesis correspond
to source detections of at least 5-σ. Appropriate ancillary and response files are provided
along with the source spectra. For a full description of the data reduction applied, see
`http://astro.ic.ac.uk/Research/Tartarus`.

3.4.2   *Beppo*Sax Data

The SAX Science Data Center in Rome maintains the archive of *Beppo*Sax observational
data. This archive includes all necessary files for the *Beppo*SAX data analysis of the NFI
detectors LECS, MECS, and PDS. Along with the raw and filtered event files, the archive
provides higher-level data products, in particular the source spectra, produced following
the procedures described in the cookbook of the *Beppo*Sax NFI spectral analysis (Fiore
et al. 1999). The PDS spectra are background subtracted, while background spectra ob-
tained from blank-sky observations have to be obtained for the given source-extraction
radius from the HEASARC public ftp area[3]. The same holds for the necessary response
and ancillary files.

---

[3]`ftp://heasarc.gsfc.nasa.gov/sax`

3.4.3   *Chandra* **Data**

The *Chandra* data were obtained from the *Chandra* Data Archive (CDA[4]) and were reduced with the *Chandra* data reduction software CIAO V.3.0.2 using the CALDB 2.26 calibration files provided by the CXC.

Source and background spectra were extracted following the guidelines of the "Step-by-Step Guide to Creating ACIS Spectra for Pointlike Sources" of the *Chandra*-Science-Threads website[5]. The regions for the extraction of source spectra were defined to contain virtually all source photons. Usually circular regions with an extraction radius of 10 arcsec were used (unless contaminating sources in this field were present) for the source spectra and source-free background regions in the direct vicinity of the source region located on the same detector chip. Light curves from both regions were obtained and inspected for background flares during the observations and if necessary, the data were filtered to waive contaminated time intervals. If the source was found to be resolved into a nucleus–jet structure, the source spectra were extracted to contain both the nucleus and the jet, to allow the spectral results to be compared with the (lower-angular resolution) data from *ASCA*, *Beppo*Sax, and *XMM-Newton*. In these cases, separate jet or knot spectra have been extracted, as well. In the case of bright sources (see pileup discussion below), source spectra have been obtained for the full source and for annuli excluding the central 3×3 pixels around the source center for later comparison of pileup-modeled full source spectra and the source spectra from the wings of the PSF which are not affected by pileup. Response and ancillary matrices were calculated for the given position on the chip and a correction for the aspect motion during the observation was applied.

The Pileup Effect: CCD detectors in general, but *Chandra's* ACIS in particular, suffer from the problem of photon pileup. Pointings on bright point sources are the strongest affected observations by this effect. When multiple photons arrive at the same CCD pixel within one frame time (the read-out interval of the detector), the detector is not capable of distinguishing between one high-energy event and possible combinations of separate lower-energy events. If we consider a series of 1 keV photon pairs that arrive at the same pixel of *Chandra's* ACIS within its standard frame time of 3.2 s, two things may occur: I: the detector electronics may record one-photon events of 2 keV energy, reducing the source flux by a factor of two and artificially hardening the spectrum. II: the two photons of one pair may produce different event patterns, i.e., set free charge in neighboring pixels, resulting in an overall pattern with a "bad grade" (grade migration). In this case, the event will be discarded by the onboard electronics, again reducing the source flux and hardening the measured spectrum due to the loss of soft-energy photons. Pairs of higher-energy photons above 6 keV are lost anyway because the total energy goes above the on-board discriminators. In practice, the impact of pileup can be reduced by decreasing the frame time of the detector in observations of bright point sources. This, however, reduces substantially the efficiency of the detector performance.

The number of incident X-ray photons per detector frame can be written as

$$N_{\text{Frame}} = F_{\text{X}} \times A \times \tau_{\text{Frame}} \quad , \tag{3.1}$$

---

[4]The CDA is part of the Chandra X-Ray Observatory Science Center (CXC) which is operated for NASA by the Smithsonian Astrophysical Observatory.

[5]`http://cxc.harvard.edu/ciao/threads`

where F_X is the X-ray flux in photons/s/cm^{-2}, A is the effective area of the mirror-detector assembly including the quantum efficiency and filter transmission, and τ_{Frame} is the frame time of the detector. The degree of pileup for *Chandra* ACIS observations was determined by the AXAF X-ray Calibration Facility (XRCF) in pre-launch ACIS exposures with increasing flux of a monochromatic source (Al Kα emission, $E = 1.487\,\mathrm{keV}$). In these measurements, the intensity of the ACIS detected 1.487 keV line decreased when pileup occurred while pileup peaks at 2.974 keV, 4.461 keV, etc. could be seen. The pileup fraction is the ratio of the number of photons detected at the pileup energies at 2.974 keV, 4.461 keV, etc. to the total number of detected photons. The degree of photon pileup P_{P} of ACIS was determined from the ratio of the summed, photon-weighted areas under the pileup peaks A_n ($n = 1, 2, 3, ...$) and the primary peak A_0:

$$P_{\mathrm{P}} = \frac{\sum_{n \geq 1}(A_n \cdot n)}{\sum_{n \geq 0}(A_n \cdot n)} \tag{3.2}$$

Similarly, the degree of event pileup P_{E} is roughly a factor of two smaller than the degree of photon pileup:

$$P_{\mathrm{E}} = \frac{\sum_{n \geq 1} A_n}{\sum_{n \geq 0} A_n} \sim P_{\mathrm{P}}/2 \tag{3.3}$$

Figure 3.3 shows the determined pileup fractions as a function of the total number of photons per frame. Moreover, it shows that the data are adequately represented by a model developed by B.R. McNamara[6]. The mean encircled energy $\epsilon(R_1)$ within the central detection cell (2.1 pixel) for the pre-launch tests of the XRCF was found to be $\epsilon(R_1) = 61\%$ while the in-orbit performance of ACIS was later determined to $\epsilon(R_1) \sim 90\%$. This degradation increases the pileup fraction further by about a factor of two.

A pileup correction model has been developed by Davis (2001), which has been implemented into the standard X-ray spectral fitting programs[7] ISIS, SHERPA and XSPEC. All *Chandra* spectra analyzed for this thesis project were tested for pileup and — if necessary — modeled by invoking the PILEUP model of XSPEC. In this model, the grade morphing is expressed through a single parameter, α which presents a free parameter of the model. The fraction of good grades is assumed to be proportional to α^{p-1} where p is the number of piled photons. A typical value of $\alpha = 0.5$ corresponds to a spectrum where half of the two-photon pileup events are lost due to grade migration, as well as 3/4 of the three-photon pileup events. To ensure the robustness of the solution, the determined spectral model was compared to a spectrum obtained from the wings of the PSF, i.e., by excluding the central piled-up pixels of the PSF.

It has to be noted that pileup remains a severe problem in the analysis of bright point sources from *Chandra* ACIS observations. While the model developed by Davis (2001) has proven to reproduce sufficiently the effects of moderate pileup, heavily piled-up sources (particularly at large off-axis angles) are beyond the scope of this approach. Two spectra of 0430+052 (3C 120), eleven spectra of 1226+023 (3C 273), and one spectrum of 1957+405 (Cygnus A) were excluded from the statistical analysis since the quality of the pileup correction could not be established.

---

[6]Compare
http://cxc.harvard.edu/cal/Acis/Cal_prods/pileup/pileup_memo_b_10_2.ps.
[7]See http://space.mit.edu/CXC/analysis/PILECOMP/ for a comparison of the three implementations.
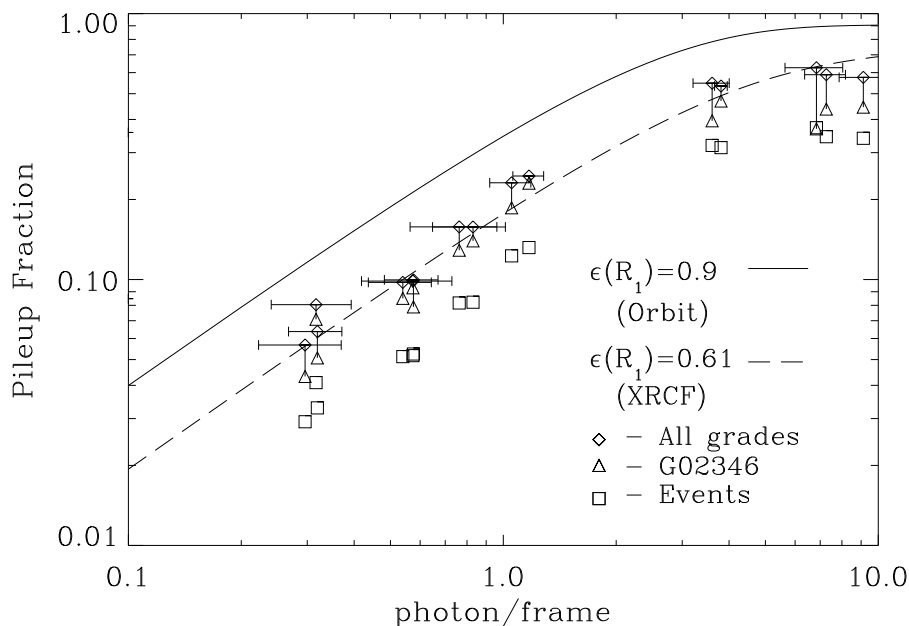
Figure 3.3: ACIS pileup fraction as a function of the number of detected photons per CCD frame. The solid and dashed lines represent the analytical pileup model developed by B.R. McNamara for $\epsilon(R_1) = 61\%$ and $\epsilon(R_1) \sim 90\%$ corresponding to the pre-launch and in-orbit performance of ACIS. Diamonds show the degree of photon pileup. Squares show the degree of event pileup. The open triangles describe the photon pileup fraction for *ASCA*-G02346-grade photons for which the pileup fraction is underestimated due to grade migration. Taken from `http://cxc.harvard.edu/cal/Acis/Cal_prods/pileup/pileup.html`.

3.4.4 *XMM-Newton* Data

The *XMM-Newton* were obtained from the *XMM-Newton* Science Archive[8]. The data were processed using the *XMM-Newton* Science Analysis System SAS V. 6.1.0 and the latest available calibration information. For that, the EPIC raw data were re-processed to obtain calibrated pipeline data products using the SAS tasks EMCHAIN and EPCHAIN. Data from all three EPIC instruments onboard *XMM-Newton* were considered when all were available: the two MOS cameras (MOS 1 & MOS 2) and the PN detector. Source and background spectra were extracted from circular regions located on the same detector chip containing virtually all source photons (usually ~ 50 arcsec in radius) and no contaminating sources, respectively. In small-window-mode observations, the background spectra were extracted from one of the outer detector chips to avoid a contamination of the background spectrum with source photons. Light curves over the full 0.3 keV to 12 keV energy range were produced for the full chip, the source- and the background region to identify time intervals contaminated by background flares, which were filtered out, subsequently. Only single and double event patterns were considered for the PN detector (PATTERN ≤ 4) and single, double, triple, and quadruple event patterns for the MOS detectors (PATTERN ≤ 4). In addition to this, the source spectra were investigated for pileup using the EPATPLOT task within SAS. If a significant pileup fraction was found, spectra

---

[8]`http://xmm.vilspa.esa.es/external/xmm_data_acc/xsa`

were extracted from annulus-regions, rejecting the central pileup-affected detector pixels at the maximal source count rate. RMF and ARF files were produced using the SAS tasks RMFGEN and ARFGEN.

3.5   Spectral Fitting

Spectral fitting was performed using the program XSPEC. For all 239 data sets investigated, a simple absorbed-power-law fit has been performed (**model I**) with the absorption being consisting of a neutral Galactic component (a WABS component in XSPEC) equal to the value determined from the LAB survey[9] (Kalberla et al. 2005) and an excess-absorption component considered to correspond to a source-intrinsic absorber located in the source rest frame (a ZWABS component in XSPEC). In some cases, excess absorption is known to correspond to Galactic molecular clouds or to intervening galactic systems. In these cases, the redshift of the ZWABS component has been set to an appropriate value (**model IZ**). These cases are marked in column 12 of Table 4.1 in Chap. 4. Due to the notorious difficulties in disentangling the relative contributions of different absorbers located at different redshifts, any possible additional contribution of source-intrinsic absorbers were neglected in these cases.

In the cases of those spectra, which are not adequately approximated by model I because of systematic trends of the residuals or a statistically unacceptable fit result ($\chi_{\mathrm{red}} \gg 1$), a second power-law component was added to the model (**model II**). If model II yielded a significant improvement of the fit according to the F-test, the model II results were used in the further analysis. Those cases are given in Table 4.2 in Chap. 4.

The sources 0316+164 (Perseus A) and 1228+126 (M 87) are known to be embedded in bright, extended thermal-plasma emitting environments (compare Sect. 4.3). The high angular resolution of *Chandra* allowed the nuclear AGN emission to be resolved from the surrounding plasma emission so that model I could be applied to the nuclear power-law spectrum. To account for the thermal emission in the lower-angular-resolution *ASCA*, *Beppo*Sax, and *XMM-Newton* spectra of those sources, a thermal-plasma model component (a MEKAL component in XSPEC) was added to the standard power-law model (**model III**).

The normalization factors for the different *ASCA* and *XMM-Newton* detectors used in the same fit (to account for inter-calibration problems or partial source masking effects on individual detectors, e.g., in the case of sources located close to detector-chip gaps) were left free to vary, yielding typically values close to unity. In some cases, particularly for data sets that are only poorly represented by a one-power-law model, the inter-calibration factors of the LECS, MECS, and PDS detectors of *Beppo*Sax had to be fixed during the fit because otherwise they diverged to unreasonable values. In these cases, the LECS/MECS factor was fixed at a value of 0.65 and the PDS/MECS factor was set to 0.85, according to the lower end of typical acceptable LECS/MECS normalization values (to avoid the spu-

---

[9]The Leiden/Argentine/Bonn Galactic HI Survey. N_{HI} values were obtained from the catalog as available in March 2005. A web interface for the LAB survey is available since July 2005 at http://www.astro.uni-bonn.de/ webrai/german/tools_labsurvey.php. See Sect. 5.2 for a discussion of the discrepancies between the March 2005 and the July 2005 versions of the LAB catalog.

rious introduction of artificial apparent absorption), and the mean PDS/MECS normalization factor, as given by Fiore et al. (1999). All spectra were grouped to have 25 counts per spectral bin (5-σ) except some cases of high background level where 50 counts per bin were chosen to increase the SNR. A considerable fraction of all *Chandra* spectra are affected by pileup. In most of these cases, invoking the PILEUP model component of XSPEC yielded a source spectrum with a photon index in agreement with the value determined from an annulus spectrum in the wings of the PSF. In some cases the pileup-corrected photon index and the annulus-determined photon index did not match, particularly in the case of extreme pileup, and the data set was waived for further analysis. All these data-set specific remarks are given in column 12 of Table 4.1 in Chap. 4. The residuals to the best-fitting spectral model I, II, or III, respectively, are shown in appendix A.

4 Results

4.1 X-ray Core Spectral Properties of Radio-Loud, Core-Dominated AGN

In this chapter, the results from the X-ray spectral fitting for the 2 cm-X-Sample are presented. The results of the one-power-law spectral fits with a fixed absorber corresponding to Galactic absorption plus a freely variable absorber in the source frame or at the redshift of an intervening system (model I) are tabulated in Table 4.1. All values in this and the following tables are listed with their 90 % confidence ranges, corresponding to $\Delta\chi = 2.7$ for one parameter of interest. For photon indices and absorbing column densities from individual spectral fits, upper and lower errors do not agree, in general, so that both values are listed. For a large fraction of all spectra model I provides an acceptable approximation (the average value of χ^2 over the whole sample is 1.43, however, with a large standard deviation of 1.22 due to a wide tail of the distribution towards high values). The largest values of χ^2 (> 3) stem from observations with the highest SNR of bright objects with complex or multiple emission, e.g., the long *ASCA*, *Beppo*Sax, and *XMM-Newton* observations of 0316+164 (Perseus A), 0430+052 (3C 120), 1228+126 (M 87), and 1957+405 (Cygnus A). Small values of $\chi^2 < 1$ occur in cases of snapshot observations or weak sources and are a sign of the transition from χ^2 statistics to Poisson statistics. In these cases, no meaningful test of more complicated spectral models is possible. A quality code is given for all model I fits in Table 4.1, with a "3" indicating an acceptable fit ($\chi_{\mathrm{red}} \sim 1$), a "2" indicating a statistically acceptable fit but the presence of systematical broad and/or narrow residuals, and a "1" indicating a statistically unacceptable fit ($\chi_{\mathrm{red}} \gg 1$). In a number of cases with quality codes "1" and "2", clear residuals at soft and/or hard energies are apparent. In other cases, these residuals show up only if the spectrum is grouped stronger, increasing the SNR. A two-power-law model with Galactic and source-intrinsic absorption (model II) has been tested in such cases but has been accepted only if the fit to the data yielded a significant improvement to model I, according to the F-test. In a small number of spectra, narrow residuals around a rest-frame energy of 6.4 keV were apparent, being accounted for by the addition of a ZGAUSS model component, a redshifted Gaussian emission line model redshifted with respect to the observer's frame. In two cases (1749+096, epoch 1995-09-22; 2200+420, epoch 1999-12-05), model II yielded no statistically significant improvement over model I but the residuals showed an apparent steepening of the continuum at hard energies. In both cases, the modified model II with a broken power law substituting the two separate power laws yields a significantly improved fit. In the nine cases of low-angular resolution observations, i.e., non-*Chandra* observations, of the sources Perseus A and M 87, a thermal plasma model component (MEKAL

component in XSPEC) has been added to the model to account for the bright intra-cluster emission into which the nuclei of these objects are embedded. All other special remarks on individual one-power-law fits (model I) are given in Table 4.1. The results of the two-power-law model II fits are given in Table 4.2. Table 4.3 gives the results of the model III fits. For further analysis, all models in Table 4.2 and Table 4.3 have been considered, waiving the statistically inferior models in Table 4.1 for these spectra. In the case of two sources (NGC 1052 and Cygnus A), neither model II nor model III provides an adequate representation of the measured spectrum. Among all *2 cm-X-Sample* sources, these are the only two jet-systems believed to be oriented close to the plane of the sky (compare Kellermann et al. (2004)). The complex X-ray spectrum of NGC 1052 is discussed in detail in Sect. 6.3.3 and the Cygnus A nucleus is known to exhibit a similarly complex spectrum invoking a heavily absorbed hard-power-law component, a soft excess composed of a power law or a bremsstrahlung-plus-narrow-emission-lines component and a strong narrow iron line (Young et al. 2002). The six observations of these two sources have not been further considered in this chapter to sustain a maximal uniformity of the analysis with only three different models. In all remaining cases, the soft power law of model II is considered as the simplest possible parametrization of a soft excess present in these sources. The nature of this soft excess and possible alternative ways to model this spectral component are discussed in Sect. 5.1. Throughout this chapter, the steeper of the two power laws in the individual model II realizations is referred to as the "soft-excess component".

For the best-fitting model of each spectrum, mean values for the photon indices of the one or two invoked power laws, for the excess absorbing column density over the Galactic value (in the source frame) and the source fluxes in the $(0.5-2.0)$ keV and $(2.0-10.0)$ keV bands have been determined. Errors have been determined as the geometrical mean of the deviations from the mean value and the mean upper and lower errors of the individual measured photon indices and column densities. For the fluxes, an absolute calibration uncertainty of 20 % has been assumed and has been used as the error for features with only one spectrum. In the cases, where more than one spectrum of the same source was available, the error of the mean fluxes was calculated as the geometrical mean of the deviations from the mean flux and the 20 % uncertainty of the mean flux. The resulting mean spectral parameters are given in Table 4.4 along with their calculated errors[1].

Table 4.1: One-power-law X-ray spectral fit results

Source[*]	Obs. Date[*]	T[†]	Sequence	N_H[★]	Γ[‡]	F_1[◇]	F_2[♣]	F_3[♠]	χ_{red}	d.o.f.	Q[♡]
0007+106	1997-07-01	A	75052000	< 0.3	$1.66^{+0.01}_{-0.02}$	5.49	10.60	−	1.00	889	2
0007+106	2000-07-03	X	0127110201	< 0.1	$1.74^{+0.02}_{-0.01}$	3.74	6.40	−	1.07	958	2[a]
0048−097	1996-12-02	B	50046003	$68.6^{+159.4}_{-68.6}$	$1.82^{+0.23}_{-0.17}$	−	1.63	−	0.15	1	3[b,c,d]
0048−097	1997-12-19	B	500460031	< 4.6	$1.95^{+0.13}_{-0.11}$	0.98	1.23	−	0.60	12	3[c,d]
0235+164	1994-02-04	A	71015000	$30.6^{+12.1}_{-15.3}$	$1.73^{+0.08}_{-0.07}$	0.63	1.41	−	1.50	86	3[e]
0235+164	1994-02-11	A	71015010	$24.1^{+11.9}_{-12.1}$	$1.82^{+0.07}_{-0.08}$	0.70	1.37	−	1.31	85	3[e]
0235+164	1994-02-16	A	71015020	$36.4^{+17.7}_{-12.3}$	$1.89^{+0.10}_{-0.07}$	0.58	1.14	−	0.72	68	3[e]

Continued on next page

[1]Note that, in contrast to Table 4.1–4.3 only one mean value for the error is given, corresponding to the upper and lower uncertainty range.

Table 4.1 – continued from previous page

Source*	Obs. Date*	T†	Sequence	N_H★	Γ‡	F_1◇	F_2♣	F_3♠	χ_{red}	d.o.f.	Q♡
0235+164	1994-02-19	A	71015030	$24.6^{+12.9}_{-13.7}$	$1.81^{+0.07}_{-0.08}$	0.86	1.69	–	0.83	73	3[e]
0235+164	1998-02-11	A	75063000	$54.6^{+9.2}_{-9.6}$	$1.76^{+0.03}_{-0.03}$	1.59	4.30	–	1.08	242	3[e]
0235+164	1999-01-28	B	50482001	$28.1^{+34.8}_{-24.6}$	$1.94^{+0.09}_{-0.09}$	0.47	0.81	–	0.98	16	3[e]
0235+164	2000-08-20	C	884	$18.7^{+2.1}_{-2.4}$	$1.55^{+0.03}_{-0.04}$	0.46	1.27	–	1.07	134	3[e]
0235+164	2002-02-10	X	0110990101	$24.5^{+0.4}_{-0.3}$	$2.40^{+0.01}_{-0.01}$	5.02	4.37	–	1.15	1103	3[e]
0235+164	2004-01-18	X	0206740101	$24.2^{+1.3}_{-0.9}$	$1.64^{+0.02}_{-0.02}$	0.78	1.98	–	0.96	755	3[e]
0235+164	2004-08-02	X	0206740501	$24.4^{+2.5}_{-2.3}$	$1.58^{+0.02}_{-0.02}$	0.79	2.18	–	0.94	344	3[e]
0235+164	2005-01-28	X	0206740701	$17.3^{+2.7}_{-2.5}$	$1.73^{+0.03}_{-0.03}$	0.39	0.82	–	1.04	244	3[e]
0238−084	1996-08-11	A	74061000	< 0.8	$0.02^{+0.01}_{-0.04}$	0.22	5.64	–	1.25	357	2[a,f]
0238−084	2000-01-11	B	50828001	$309.7^{+39.3}_{-37.1}$	$1.01^{+0.02}_{-0.02}$	0.05	3.59	30.72	2.28	84	1[a,f,g,h]
0238−084	2000-08-29	C	884	< 2.4	$0.06^{+0.08}_{-0.11}$	0.16	3.84	–	4.39	11	1[f]
0238−084	2002-09-28	X	0093630101	< 0.1	$0.45^{+0.02}_{-0.02}$	0.29	3.66	–	3.29	451	1[a,f]
0316+164	1993-08-06	A	80007000	$8.7^{+0.3}_{-0.3}$	$2.06^{+0.01}_{-0.01}$	345.36	471.75	–	2.23	1202	2[i,j]
0316+164	1993-08-06	A	80008000	$13.2^{+0.3}_{-0.2}$	$2.05^{+0.01}_{-0.01}$	306.06	473.11	–	1.72	2080	2[j]
0316+164	1995-08-18	A	83051000	$9.1^{+0.5}_{-0.5}$	$2.00^{+0.01}_{-0.01}$	310.52	464.82	–	1.69	999	2[i,j]
0316+164	1995-09-04	A	83053000	$7.9^{+0.4}_{-0.4}$	$2.01^{+0.01}_{-0.01}$	146.10	207.71	–	1.70	1061	2[i,j]
0316+164	1996-09-19	B	60009001	$37.6^{+1.7}_{-1.7}$	$2.40^{+0.01}_{-0.01}$	–	105.14	39.50	13.72	195	1[j,g′,h]
0316+164	1999-09-20	C	502	$10.7^{+3.1}_{-3.2}$	$2.13^{+0.07}_{-0.09}$	3.44	4.55	–	1.54	45	3[k,l]
0316+164	1999-10-10	C	333	$0.3^{+3.0}_{-0.3}$	$2.09^{+0.06}_{-0.03}$	18.97	19.54	–	1.25	91	3[k,l]
0316+164	1999-11-28	C	503	$12.2^{+3.4}_{-3.3}$	$2.04^{+0.12}_{-0.14}$	3.99	6.10	–	0.85	76	3[k,l]
0316+164	2000-01-29	C	1513	$10.1^{+1.6}_{-1.4}$	$2.15^{+0.07}_{-0.07}$	4.22	5.24	–	1.19	195	3[k,l]
0316+164	2000-08-25	C	428	< 2.1	$2.08^{+0.04}_{-0.04}$	8.85	9.14	–	1.17	151	3[k,l]
0316+164	2001-01-30	X	0085110101	$13.4^{+0.1}_{-0.1}$	$2.21^{+0.01}_{-0.01}$	37.95	47.01	–	3.24	2040	2[j]
0316+164	2002-08-08	C	3209	$19.8^{+0.8}_{-0.7}$	$2.58^{+0.05}_{-0.05}$	6.40	5.66	–	1.23	375	3[k,l,m]
0316+164	2002-08-10	C	4289	$18.6^{+0.8}_{-0.7}$	$2.46^{+0.05}_{-0.05}$	6.43	6.49	–	1.19	365	3[k,l,m]
0316+164	2002-08-11	C	3404	$11.7^{+1.0}_{-1.1}$	$2.45^{+0.03}_{-0.05}$	6.34	5.41	–	1.28	172	3[k,l,n]
0333+321	1994-02-01	A	71047000	$16.3^{+1.1}_{-1.0}$	$1.68^{+0.01}_{-0.01}$	3.39	9.46	–	0.98	780	3[o]
0333+321	1999-08-05	B	50997001	$17.6^{+6.0}_{-5.0}$	$1.63^{+0.02}_{-0.02}$	2.33	7.09	13.77	1.13	130	3[o]
0415+379	1996-02-13	A	74087000	$67.4^{+0.9}_{-1.0}$	$1.73^{+0.01}_{-0.01}$	7.24	39.06	–	0.97	1637	3[o]
0415+379	1998-03-08	B	50552001	$64.4^{+4.3}_{-4.1}$	$1.64^{+0.01}_{-0.01}$	4.35	25.51	51.04	1.10	226	3[o]
0415+379	2001-03-14	X	0065940101	$52.3^{+0.4}_{-0.4}$	$1.69^{+0.01}_{-0.01}$	12.61	60.03	–	1.27	1076	3[o,p]
0420−014	1997-08-31	A	75088000	$30.3^{+30.9}_{-6.5}$	$1.91^{+0.12}_{-0.02}$	1.16	1.87	–	0.99	162	3
0430+052	1994-02-17	A	71014000	$6.2^{+0.2}_{-0.2}$	$1.95^{+0.01}_{-0.01}$	32.05	47.38	–	1.27	1452	2
0430+052	1997-09-20	B	50384001	$6.9^{+0.8}_{-0.8}$	$1.86^{+0.01}_{-0.01}$	21.14	47.17	56.67	1.24	400	2
0430+052	1998-02-12	A	76009000	< 0.1	$1.85^{+0.01}_{-0.01}$	32.32	46.93	–	1.28	1895	2
0430+052	2001-01-27	C	1612	$14.4^{+2.4}_{-1.9}$	$2.49^{+0.10}_{-0.10}$	44.02	38.04	–	1.64	76	2[k′]
0430+052	2001-09-18	C	1613	$8.7^{+0.9}_{-0.9}$	$2.13^{+0.06}_{-0.06}$	6.11	7.44	–	1.09	158	2[k′]
0430+052	2001-12-21	C	3015	$6.1^{+1.4}_{-1.3}$	$2.03^{+0.02}_{-0.02}$	16.78	22.21	–	1.32	371	2[k]
0430+052	2002-09-06	X	0109131101	< 0.1	$1.84^{+0.01}_{-0.01}$	24.31	35.86	–	1.11	1255	2[q]
0430+052	2003-08-26	X	0152840101	$4.9^{+0.1}_{-0.1}$	$1.94^{+0.01}_{-0.01}$	30.73	44.55	–	4.99	2680	2[m]
0458−020	2002-10-10	C	2985	$36.7^{+7.0}_{-6.6}$	$1.64^{+0.03}_{-0.03}$	0.32	0.69	–	1.30	178	3[e′]
0528+134	1994-08-28	A	72030000	$28.9^{+3.4}_{-3.4}$	$1.69^{+0.03}_{-0.03}$	1.14	3.92	–	1.04	233	3[o]
0528+134	1995-03-07	A	73054010	$29.4^{+2.0}_{-2.0}$	$1.72^{+0.02}_{-0.02}$	2.91	9.70	–	0.93	433	3[o]
0528+134	1995-03-14	A	73054000	$27.0^{+1.8}_{-1.7}$	$1.71^{+0.02}_{-0.02}$	3.15	10.22	–	1.01	517	3[o]
0528+134	1995-03-19	A	73090000	$30.9^{+1.6}_{-1.6}$	$1.75^{+0.01}_{-0.01}$	4.08	13.40	–	1.01	508	3[o]
0528+134	1997-02-21	B	50237001	$17.7^{+24.0}_{-17.7}$	$1.41^{+0.05}_{-0.06}$	0.64	2.39	–	1.48	23	3[o,r]
0528+134	1997-02-22	B	50237002	$44.3^{+32.2}_{-20.6}$	$1.57^{+0.05}_{-0.05}$	0.56	2.54	–	0.96	22	3[o,r]
0528+134	1997-02-27	B	50237003	$24.0^{+39.1}_{-20.7}$	$1.40^{+0.10}_{-0.07}$	0.57	2.41	–	0.45	17	3[o,r]
0528+134	1997-03-01	B	50237004	$23.1^{+30.2}_{-19.9}$	$1.42^{+0.06}_{-0.05}$	0.59	2.40	–	1.09	33	3[o,r]

Continued on next page

Table 4.1 – continued from previous page

Source[*]	Obs. Date[*]	T[†]	Sequence	N_H[★]	Γ[‡]	F_1[◇]	F_2[♣]	F_3[♠]	χ_red	d.o.f.	Q[♡]
0528+134	1997-03-03	B	50237005	< 19.6	$1.27^{+0.06}_{-0.05}$	0.71	2.25	–	1.02	33	3[o,r]
0528+134	1997-03-04	B	50237006	$22.9^{+38.0}_{-21.7}$	$1.55^{+0.08}_{-0.05}$	0.70	2.36	–	1.06	27	3[o,r]
0605−085	2001-05-01	C	2132	$12.3^{+8.6}_{-6.3}$	$1.63^{+0.07}_{-0.05}$	0.60	1.32	–	1.14	46	3
0716+714	1994-03-16	A	71006000	< 0.1	$2.41^{+0.06}_{-0.05}$	2.01	1.26	–	1.02	192	3[d]
0716+714	1994-03-19	A	71006010	< 0.8	$2.17^{+0.08}_{-0.07}$	1.10	0.99	–	0.96	117	3[d]
0716+714	1994-03-21	A	71006020	< 0.5	$2.40^{+0.05}_{-0.05}$	1.62	1.04	–	1.07	211	3[d]
0716+714	1996-11-14	B	50160001	< 0.3	$2.20^{+0.03}_{-0.03}$	1.51	1.31	–	1.34	103	2[c,d,f]
0716+714	1998-11-07	B	50750002	< 0.7	$1.91^{+0.05}_{-0.04}$	1.79	2.39	2.52	1.44	44	3[c,d,f,h,s]
0716+714	2000-10-30	B	51153001	< 0.1	$2.31^{+0.04}_{-0.04}$	3.75	2.76	1.21	1.24	88	2[c,d,f,h,s]
0716+714	2001-04-13	X	0012850101	< 0.1	$2.86^{+0.11}_{-0.03}$	2.81	0.81	–	1.41	155	2[d,s]
0716+714	2001-09-19	X	0012850601	< 0.1	$2.85^{+0.06}_{-0.02}$	5.12	1.65	–	1.24	214	2[d,s,t]
0716+714	2002-03-26	X	0012850701	< 0.1	$2.66^{+0.02}_{-0.01}$	13.49	5.87	–	1.11	589	3[a′,d]
0735+178	1996-04-22	A	74005000	< 2.4	$1.74^{+0.07}_{-0.06}$	0.40	0.69	–	0.94	251	3[d]
0736+017	1998-10-26	A	76055000	$4.0^{+3.8}_{-3.3}$	$1.74^{+0.02}_{-0.02}$	1.95	3.62	–	1.03	431	3
0738+313	2000-10-10	C	377	$5.3^{+1.8}_{-2.2}$	$1.55^{+0.04}_{-0.04}$	0.35	0.84	–	1.33	113	3
0738+313	2001-04-19	X	0112850301	$6.2^{+1.5}_{-1.8}$	$1.73^{+0.04}_{-0.05}$	0.39	0.71	–	0.96	327	3
0827+243	2002-05-07	C	3047	$0.8^{+1.9}_{-0.8}$	$1.66^{+0.03}_{-0.03}$	1.04	2.01	–	1.10	160	3
0836+710	1995-03-17	A	72002010	< 33.3	$1.34^{+0.01}_{-0.01}$	4.82	15.19	–	0.89	548	3
0836+710	1998-05-27	B	50497003	$102.6^{+42.0}_{-37.3}$	$1.37^{+0.01}_{-0.01}$	7.35	25.66	87.88	0.98	224	3
0836+710	1999-10-17	C	1450	$8.8^{+15.3}_{-8.8}$	$1.37^{+0.02}_{-0.02}$	4.67	14.27	–	1.08	282	3[k]
0836+710	2000-08-25	C	1802	< 19.7	$1.39^{+0.04}_{-0.03}$	5.24	15.32	–	1.03	103	3[k]
0836+710	2001-04-12	X	0112620101	$6.5^{+0.9}_{-0.8}$	$1.34^{+0.01}_{-0.01}$	11.21	35.58	–	1.11	2686	3
0851+202	1994-11-18	A	15035000	< 0.6	$1.59^{+0.01}_{-0.01}$	2.83	6.15	–	1.13	537	3
0851+202	1997-04-26	A	75001000	< 5.2	$1.57^{+0.03}_{-0.04}$	0.88	1.96	–	1.06	260	3
0851+202	1997-11-18	A	75001010	$11.9^{+3.5}_{-2.7}$	$1.60^{+0.03}_{-0.02}$	0.89	2.22	–	1.10	380	3
0851+202	1997-11-24	B	50046002	$38.4^{+50.2}_{-29.6}$	$1.73^{+0.08}_{-0.08}$	0.76	2.16	–	1.67	11	3[c]
0851+202	2001-11-20	B	51336001	$32.6^{+27.3}_{-22.9}$	$1.86^{+0.06}_{-0.06}$	0.51	1.14	–	1.02	35	3[c]
0923+392	1998-11-01	A	76056000	$30.8^{+6.5}_{-7.0}$	$1.88^{+0.02}_{-0.02}$	2.34	4.23	–	1.01	448	3
0923+392	2002-10-19	C	3048	< 0.4	$1.69^{+0.03}_{-0.02}$	1.99	3.67	–	1.71	213	2[m]
1038+064	1996-12-13	A	74007000	$40.9^{+18.6}_{-16.1}$	$1.48^{+0.02}_{-0.02}$	0.74	2.17	–	1.04	577	3
1038+064	1996-12-20	A	74007010	$40.9^{+44.0}_{-40.9}$	$1.65^{+0.09}_{-0.06}$	0.77	1.76	–	1.27	66	3[b]
1038+064	2003-05-18	X	0151390101	< 0.2	$1.56^{+0.02}_{-0.01}$	0.64	1.45	–	0.99	943	2[f,s]
1055+018	2001-01-09	C	2137	< 0.9	$1.66^{+0.04}_{-0.03}$	1.77	3.45	–	1.08	153	3
1127−145	1999-06-04	B	50850001	$17.3^{+7.1}_{-5.5}$	$1.51^{+0.02}_{-0.02}$	2.69	8.25	20.89	0.95	147	3[e*]
1127−145	2000-05-28	C	866	$8.8^{+0.7}_{-0.7}$	$1.23^{+0.02}_{-0.02}$	1.43	6.00	–	1.31	285	3[e*]
1127−145	2002-07-01	X	0112850201	$13.0^{+0.5}_{-0.4}$	$1.32^{+0.01}_{-0.01}$	1.65	6.32	–	1.06	1233	3[e*]
1156+295	2000-06-29	C	874	$1.1^{+2.9}_{-1.1}$	$1.61^{+0.03}_{-0.03}$	0.41	0.87	–	1.22	152	3
1222+216	2002-11-06	C	3049	< 0.1	$1.41^{+0.04}_{-0.02}$	1.22	3.45	–	1.50	200	2[f]
1226+023	1993-06-08	A	70023000	< 0.1	$1.68^{+0.01}_{-0.01}$	65.46	123.47	–	2.58	373	2[f,s]
1226+023	1993-12-15	A	10022010	$2.1^{+0.2}_{-0.2}$	$1.61^{+0.01}_{-0.01}$	74.98	163.30	–	1.22	1959	2[f]
1226+023	1993-12-15	A	10022020	$1.1^{+0.2}_{-0.2}$	$1.60^{+0.01}_{-0.01}$	90.89	198.28	–	1.10	2125	2[f]
1226+023	1993-12-16	A	71038010	$2.3^{+0.2}_{-0.2}$	$1.60^{+0.01}_{-0.01}$	91.16	201.61	–	1.01	1920	3
1226+023	1993-12-19	A	10022000	$1.3^{+0.1}_{-0.1}$	$1.53^{+0.01}_{-0.01}$	73.72	178.65	–	1.13	2646	2[f]
1226+023	1993-12-20	A	10022030	$1.1^{+0.2}_{-0.2}$	$1.56^{+0.01}_{-0.01}$	71.63	165.04	–	1.08	1999	3
1226+023	1993-12-20	A	71038000	$1.5^{+0.3}_{-0.3}$	$1.60^{+0.01}_{-0.01}$	69.83	153.62	–	1.02	1754	3
1226+023	1993-12-23	A	71038020	$1.8^{+0.3}_{-0.3}$	$1.56^{+0.01}_{-0.01}$	71.27	165.72	–	1.07	1772	2[f]
1226+023	1993-12-27	A	71038030	$3.1^{+0.3}_{-0.3}$	$1.53^{+0.01}_{-0.01}$	78.24	196.72	–	1.00	1475	3

Table 4.1 – continued from previous page

Source*	Obs. Date*	T†	Sequence	N_H★	$\Gamma^\ddagger$	$F_1^\diamond$	$F_2^\clubsuit$	$F_3^\spadesuit$	χ_red	d.o.f.	Q$^\heartsuit$
1226+023	1996-07-16	A	10402000	< 0.2	$1.60^{+0.01}_{-0.01}$	35.77	75.88	–	1.12	2763	3
1226+023	1996-07-18	B	50021001	< 0.2	$1.59^{+0.01}_{-0.01}$	32.63	70.24	147.58	1.14	331	3
1226+023	1997-01-13	B	50237011	$0.8^{+0.3}_{-0.2}$	$1.58^{+0.01}_{-0.01}$	53.04	118.77	258.08	0.95	406	3
1226+023	1997-01-15	B	50237012	$0.3^{+0.2}_{-0.2}$	$1.59^{+0.01}_{-0.01}$	52.54	113.96	239.91	1.01	404	3
1226+023	1997-01-17	B	50237013	$0.9^{+0.3}_{-0.2}$	$1.63^{+0.01}_{-0.01}$	52.41	107.70	206.28	1.05	391	3
1226+023	1997-01-22	B	50237014	$0.3^{+0.3}_{-0.2}$	$1.56^{+0.01}_{-0.01}$	45.67	103.06	229.57	0.84	343	2$^\mathrm{f}$
1226+023	1998-06-24	B	50795004	< 0.1	$1.63^{+0.01}_{-0.01}$	52.93	107.00	205.59	1.26	459	2$^\mathrm{f}$
1226+023	1998-06-24	A	12601000	< 0.1	$1.64^{+0.01}_{-0.01}$	59.65	118.91	–	1.04	3062	2$^\mathrm{f}$
1226+023	2000-01-09	B	50795008	< 0.1	$1.62^{+0.01}_{-0.01}$	56.60	115.92	226.87	1.30	465	2$^\mathrm{f,u}$
1226+023	2000-01-09	A	10701000	< 0.2	$1.65^{+0.01}_{-0.01}$	62.91	123.32	–	1.07	2415	2$^\mathrm{f}$
1226+023	2000-01-09	C	1198	< 0.1	$1.83^{+0.02}_{-0.02}$	87.66	131.82	–	1.44	377	2$^{\mathrm{k}'}$
1226+023	2000-01-10	C	459	< 0.7	$1.65^{+0.04}_{-0.04}$	22.16	43.36	–	1.35	200	2$^{\mathrm{k}'}$
1226+023	2000-06-13	B	50795010	< 0.1	$1.63^{+0.01}_{-0.01}$	42.94	86.54	165.51	1.17	465	2$^\mathrm{f,u}$
1226+023	2000-06-13	X	0126700101	< 0.1	$1.79^{+0.01}_{-0.01}$	62.38	99.53	–	1.13	720	2$^\mathrm{f}$
1226+023	2000-06-13	X	0126700201	< 0.1	$1.81^{+0.05}_{-0.02}$	71.98	110.76	–	0.99	327	2$^\mathrm{f}$
1226+023	2000-06-13	X	0126700301	< 0.1	$1.81^{+0.01}_{-0.01}$	47.38	73.65	–	3.53	3002	2$^\mathrm{f}$
1226+023	2000-06-14	C	1711	< 0.2	$1.83^{+0.02}_{-0.02}$	9.98	14.92	–	1.28	280	3$^{\mathrm{k}'}$
1226+023	2000-06-14	C	1712	< 0.1	$1.51^{+0.02}_{-0.02}$	1.56	3.82	–	2.26	251	2$^{\mathrm{k}'}$
1226+023	2000-06-15	X	0126700401	< 0.1	$1.78^{+0.01}_{-0.01}$	53.46	86.22	–	1.21	1232	2$^\mathrm{f}$
1226+023	2000-06-15	X	0126700601	< 0.1	$1.81^{+0.01}_{-0.01}$	47.06	72.92	–	2.74	2691	2$^\mathrm{f}$
1226+023	2000-06-15	X	0126700701	< 0.1	$1.80^{+0.01}_{-0.01}$	45.40	71.16	–	2.63	2718	2$^\mathrm{f}$
1226+023	2000-06-16	X	0126700501	< 0.1	$1.77^{+0.01}_{-0.01}$	44.87	73.66	–	1.24	1413	2$^\mathrm{f}$
1226+023	2000-06-17	X	0126700801	< 0.1	$1.80^{+0.01}_{-0.01}$	44.60	69.70	–	4.03	2942	2$^\mathrm{f}$
1226+023	2001-06-12	B	50795011	< 0.1	$1.65^{+0.01}_{-0.01}$	50.95	100.59	186.86	1.68	416	2$^\mathrm{f}$
1226+023	2001-06-13	C	2463	< 0.6	$1.78^{+0.04}_{-0.03}$	8.78	14.23	–	1.31	183	2$^{\mathrm{k}'}$
1226+023	2001-06-13	C	2464	< 0.1	$1.93^{+0.02}_{-0.02}$	76.33	99.13	–	1.61	334	2$^\mathrm{k}$
1226+023	2001-06-13	X	0136550101	< 0.1	$1.93^{+0.01}_{-0.01}$	66.19	85.19	–	6.31	2852	2$^\mathrm{f}$
1226+023	2001-06-15	C	2471	< 0.1	$2.04^{+0.02}_{-0.02}$	93.01	101.91	–	1.46	302	2$^{\mathrm{k}'}$
1226+023	2001-12-16	X	0112770101	< 0.1	$1.85^{+0.01}_{-0.01}$	70.47	102.54	–	1.32	1673	2$^\mathrm{f}$
1226+023	2001-12-22	X	0112770201	< 0.1	$1.80^{+0.01}_{-0.01}$	67.96	107.09	–	1.38	1654	2$^\mathrm{f}$
1226+023	2002-01-09	X	0137551001	< 0.1	$1.82^{+0.01}_{-0.01}$	54.72	82.71	–	1.34	1201	2$^\mathrm{f}$
1226+023	2002-06-04	C	3574	< 0.1	$1.86^{+0.02}_{-0.02}$	30.74	43.84	–	1.66	358	2$^{\mathrm{k}'}$
1226+023	2002-06-05	C	3456	< 0.5	$2.61^{+0.04}_{-0.04}$	68.00	32.11	–	1.36	196	2$^{\mathrm{k}'}$
1226+023	2002-06-05	C	3457	< 0.6	$2.04^{+0.03}_{-0.03}$	33.78	37.13	–	1.26	227	2$^{\mathrm{k}'}$
1226+023	2002-06-06	C	3573	< 1.7	$1.92^{+0.03}_{-0.03}$	29.53	38.51	–	1.31	197	2$^{\mathrm{k}'}$
1226+023	2002-07-07	X	0112770601	< 0.1	$1.87^{+0.01}_{-0.01}$	53.27	74.96	–	1.02	1570	2$^\mathrm{f}$
1226+023	2002-12-17	X	0112770801	< 0.1	$1.96^{+0.01}_{-0.01}$	76.73	94.10	–	1.15	1602	2$^\mathrm{f}$
1226+023	2003-01-05	X	0112770701	< 0.1	$2.02^{+0.01}_{-0.01}$	64.29	72.13	–	1.10	1463	2$^\mathrm{f}$
1226+023	2003-01-05	X	0136550501	< 0.1	$1.98^{+0.01}_{-0.01}$	64.89	77.17	–	1.93	2140	2$^\mathrm{f}$
1226+023	2003-06-18	X	0112771001	< 0.1	$1.97^{+0.01}_{-0.01}$	90.36	109.89	–	1.03	859	2$^\mathrm{f}$
1226+023	2003-07-07	C	4430	< 0.7	$1.80^{+0.08}_{-0.08}$	30.53	44.14	–	1.26	188	2$^\mathrm{f,k}$
1226+023	2003-07-07	C	4431	< 0.1	$1.74^{+0.04}_{-0.04}$	37.94	61.89	–	1.52	385	2$^\mathrm{f,k}$
1226+023	2003-07-07	X	0159960101	< 0.1	$1.94^{+0.01}_{-0.01}$	75.26	96.20	–	1.99	2778	2$^\mathrm{f}$
1226+023	2003-07-08	X	0112770501	< 0.1	$1.94^{+0.01}_{-0.01}$	70.65	89.66	–	1.04	1695	2$^\mathrm{f}$
1226+023	2003-11-24	C	4876	< 0.1	$1.66^{+0.02}_{-0.02}$	38.23	73.73	–	1.20	473	3$^\mathrm{k}$
1226+023	2003-12-14	X	0112771101	< 0.1	$1.89^{+0.01}_{-0.01}$	52.53	71.45	–	1.43	1764	2$^\mathrm{f}$
1226+023	2004-02-10	C	4877	< 0.1	$1.90^{+0.02}_{-0.02}$	40.63	54.89	–	1.40	465	2$^\mathrm{f,k}$
1226+023	2004-06-30	C	5169	< 0.1	$1.70^{+0.03}_{-0.03}$	8.64	15.78	–	1.17	204	2$^{\mathrm{k}'}$
1226+023	2004-06-30	C	5170	< 0.1	$1.78^{+0.01}_{-0.01}$	29.17	47.39	–	1.35	363	3$^\mathrm{k}$
1226+023	2004-06-30	X	0136550801	< 0.1	$1.84^{+0.01}_{-0.01}$	45.80	67.65	–	1.87	3064	2$^\mathrm{f}$

Table 4.1 – continued from previous page

Source*	Obs. Date*	T†	Sequence	N_{H}*	Γ‡	$F_1^\diamondsuit$	$F_2^\clubsuit$	$F_3^\spadesuit$	χ_{red}	d.o.f.	Q$^\heartsuit$
1228+126	1993-06-07	A	60033000	$26.5^{+0.2}_{-0.2}$	$2.99^{+0.01}_{-0.01}$	134.38	84.62	–	9.37	1226	1^{j,n}
1228+126	1996-07-14	B	60010001	$97.5^{+3.5}_{-3.4}$	$3.39^{+0.01}_{-0.01}$	–	52.88	2.38	4.09	145	1$^{g',j,n}$
1228+126	2000-04-15	C	517	$11.4^{+1.3}_{-1.2}$	$2.49^{+0.07}_{-0.07}$	40.26	32.58	–	1.32	95	3^{k,v}
1228+126	2000-04-20	C	351	$4.6^{+1.0}_{-1.2}$	$2.48^{+0.13}_{-0.12}$	9.27	6.14	–	1.14	55	3^{k}
1228+126	2000-06-19	X	0114120101	$22.8^{+0.2}_{-0.2}$	$3.27^{+0.02}_{-0.02}$	12.36	5.01	–	4.69	737	1^{j,n}
1228+126	2000-07-17	C	241	$2.1^{+1.0}_{-0.8}$	$2.66^{+0.06}_{-0.05}$	3.48	1.64	–	1.77	99	3^{v}
1228+126	2000-07-29	C	352	$1.9^{+0.2}_{-0.2}$	$2.26^{+0.02}_{-0.02}$	13.20	11.01	–	3.11	207	2^{k,v}
1228+126	2000-07-30	C	1808	$1.1^{+0.3}_{-0.2}$	$2.43^{+0.03}_{-0.03}$	3.16	2.01	–	1.71	152	3^{v}
1228+126	2002-01-16	C	3085	$3.0^{+0.4}_{-0.4}$	$2.44^{+0.04}_{-0.04}$	5.07	3.41	–	1.30	122	3^{v}
1228+126	2002-02-12	C	3084	$4.3^{+0.5}_{-0.4}$	$2.53^{+0.05}_{-0.05}$	4.73	2.91	–	1.28	115	3^{v}
1228+126	2002-03-30	C	3086	$2.3^{+0.5}_{-0.4}$	$2.39^{+0.04}_{-0.04}$	4.50	3.17	–	1.25	115	3^{v}
1228+126	2002-06-08	C	3087	$5.6^{+0.5}_{-0.5}$	$2.57^{+0.04}_{-0.04}$	4.86	2.93	–	1.68	119	3^{v}
1228+126	2002-07-05	C	3717	$14.1^{+0.6}_{-0.5}$	$2.99^{+0.05}_{-0.05}$	4.66	2.08	–	1.86	181	2^{k,v}
1228+126	2002-07-06	C	2707	$2.8^{+0.2}_{-0.2}$	$2.29^{+0.02}_{-0.02}$	5.54	4.59	–	4.05	320	3^{k,v}
1228+126	2002-07-24	C	3088	$2.3^{+0.4}_{-0.4}$	$2.32^{+0.04}_{-0.04}$	5.19	4.07	–	1.46	123	3^{v}
1228+126	2002-11-17	C	3975	$4.0^{+0.4}_{-0.4}$	$2.46^{+0.04}_{-0.04}$	5.19	3.50	–	1.66	121	3^{v}
1228+126	2002-12-29	C	3976	$3.9^{+0.5}_{-0.5}$	$2.42^{+0.04}_{-0.04}$	5.13	3.63	–	1.73	119	3^{v}
1228+126	2003-02-04	C	3977	$3.9^{+0.5}_{-0.4}$	$2.42^{+0.04}_{-0.04}$	4.74	3.34	–	1.75	122	3^{v}
1253−055	1993-06-21	A	70026000	$4.0^{+1.3}_{-1.2}$	$1.78^{+0.01}_{-0.01}$	5.02	8.52	–	0.97	891	3
1253−055	1993-12-16	A	71045010	$1.7^{+1.7}_{-1.7}$	$1.75^{+0.02}_{-0.02}$	6.11	10.60	–	1.03	394	3
1253−055	1993-12-21	A	71045000	$5.2^{+2.2}_{-2.2}$	$1.73^{+0.02}_{-0.02}$	5.47	10.12	–	1.05	440	3
1253−055	1993-12-23	A	71045020	$4.6^{+2.1}_{-1.9}$	$1.79^{+0.02}_{-0.02}$	5.78	9.65	–	0.92	444	3
1253−055	1993-12-27	A	71045030	$4.5^{+2.1}_{-1.9}$	$1.78^{+0.02}_{-0.02}$	5.66	9.64	–	0.87	462	3
1253−055	1994-12-20	A	73012000	$7.3^{+3.4}_{-3.3}$	$1.69^{+0.03}_{-0.03}$	3.62	7.21	–	1.00	282	3
1253−055	1995-01-05	A	73012020	< 1.9	$1.60^{+0.02}_{-0.04}$	4.34	9.24	–	0.96	273	3
1253−055	1995-01-08	A	73012010	$2.7^{+7.5}_{-2.7}$	$1.65^{+0.03}_{-0.03}$	4.72	9.51	–	0.98	254	3
1253−055	1995-06-27	A	73012030	< 1.9	$1.61^{+0.01}_{-0.02}$	8.12	16.90	–	1.11	507	3
1253−055	1995-07-08	A	73012040	< 5.1	$1.65^{+0.02}_{-0.02}$	6.18	12.21	–	1.01	427	3
1253−055	1996-01-27	A	15401000	< 1.7	$1.63^{+0.01}_{-0.01}$	7.48	15.07	–	1.07	601	3
1253−055	1997-01-13	B	50237016	< 3.6	$1.70^{+0.03}_{-0.03}$	2.98	5.48	–	0.88	70	3^{c}
1253−055	1997-01-15	B	50237017	< 1.9	$1.68^{+0.03}_{-0.03}$	2.95	5.58	9.77	0.86	90	3^{h}
1253−055	1997-01-18	B	50237018	$12.8^{+79.2}_{-12.8}$	$1.70^{+0.09}_{-0.07}$	2.97	6.17	–	0.46	7	3^{b,c}
1253−055	1997-01-21	B	50237019	< 6.2	$1.72^{+0.04}_{-0.04}$	3.09	5.50	–	1.18	40	3^{c}
1253−055	1997-01-23	B	50237020	$7.6^{+6.9}_{-3.6}$	$1.72^{+0.04}_{-0.04}$	2.83	5.41	8.56	0.88	97	3^{h}
1253−055	2002-03-21	C	2971	$3.2^{+1.4}_{-1.3}$	$1.69^{+0.01}_{-0.01}$	5.38	10.28	–	1.58	423	3^{k}
1308+326	1996-06-10	A	74094000	$73.3^{+50.4}_{-41.4}$	$1.77^{+0.10}_{-0.08}$	0.31	0.72	–	0.98	72	3
1308+326	1996-06-11	A	74094010	< 86.2	$1.50^{+0.11}_{-0.04}$	0.33	0.82	–	0.79	103	3
1308+326	2002-12-10	X	0020540401	$0.2^{+0.9}_{-0.2}$	$1.66^{+0.01}_{-0.01}$	2.10	4.08	–	0.94	642	3
1334−127	2003-01-31	X	0147670201	$5.2^{+0.5}_{-0.5}$	$1.79^{+0.01}_{-0.01}$	1.67	2.80	–	0.92	746	3
1413+135	1998-07-24	A	76051000	$544.9^{+66.2}_{-56.0}$	$1.89^{+0.06}_{-0.06}$	0.03	0.85	–	1.16	171	3^{b}
1458+718	2002-01-28	C	3105	< 0.6	$1.59^{+0.04}_{-0.03}$	0.93	2.00	–	1.30	86	2^{f}
1502+106	2001-01-13/14	X	0112910201	< 11.6	$1.53^{+0.11}_{-0.08}$	–	–	–	0.81	52	3^{w}
1510−089	1996-08-20	A	74082000	$6.3^{+5.4}_{-5.2}$	$1.26^{+0.02}_{-0.02}$	2.43	9.32	–	0.94	422	3
1510−089	1998-08-03	B	50497004	< 3.9	$1.39^{+0.02}_{-0.02}$	1.71	5.04	16.50	0.88	96	3
1510−089	2001-03-23	C	2141	$0.1^{+1.4}_{-0.1}$	$1.39^{+0.05}_{-0.02}$	2.58	7.54	–	1.44	170	3^{k}
1633+382	1996-03-04	A	74020000	$77.3^{+150.7}_{-77.3}$	$1.39^{+0.08}_{-0.07}$	0.56	1.90	–	1.02	55	3
1633+382	1996-03-21	A	74020010	< 59.0	$1.59^{+0.07}_{-0.07}$	0.79	1.71	–	0.95	65	3
1633+382	1996-03-25	A	74020020	$0.1^{+65.7}_{-0.1}$	$1.41^{+0.08}_{-0.09}$	1.03	2.89	–	0.83	65	3

Table 4.1 – continued from previous page

Source*	Obs. Date*	T†	Sequence	$N_{\rm H}$*	Γ‡	$F_1$$^\diamond$	$F_2$$^\clubsuit$	$F_3$$^\spadesuit$	$\chi_{\rm red}$	d.o.f.	Q$^\heartsuit$
1633+382	1996-03-27	A	74020030	$1.4^{+66.3}_{-1.4}$	$1.38^{+0.07}_{-0.08}$	0.91	2.69	—	1.09	65	3
1641+399	1999-02-19	B	50727002	$0.5^{+2.3}_{-0.5}$	$1.70^{+0.03}_{-0.04}$	2.55	4.65	7.64	1.42	75	3
1641+399	2001-04-27	C	2143	< 0.3	$1.81^{+0.07}_{-0.02}$	2.78	4.28	—	1.46	148	2$^{\rm f,k,s}$
1655+077	2002-04-28	C	3122	$10.0^{+13.7}_{-10.0}$	$1.58^{+0.08}_{-0.08}$	0.53	1.28	—	1.09	28	3
1749+096	1995-09-22	A	73087000	$25.2^{+4.9}_{-4.3}$	$1.93^{+0.02}_{-0.02}$	1.96	3.63	—	0.99	412	3
1803+784	1998-09-28	B	50482004	$29.1^{+27.6}_{-18.4}$	$1.70^{+0.05}_{-0.05}$	0.80	1.83	—	1.24	41	3$^{\rm c}$
1823+568	1997-10-11	B	50046005	< 43.9	$2.22^{+0.17}_{-0.13}$	0.95	0.80	—	0.58	3	3$^{\rm c}$
1828+487	2002-05-20	C	3124	$12.5^{+4.2}_{-3.0}$	$1.81^{+0.07}_{-0.04}$	2.09	3.58	—	1.19	80	3$^{\rm k}$
1928+738	1997-08-12	A	75075000	< 2.1	$1.79^{+0.02}_{-0.03}$	3.18	5.03	—	1.03	353	3
1928+738	2001-04-27	C	2145	$2.9^{+1.1}_{-0.8}$	$2.09^{+0.05}_{-0.02}$	3.44	3.61	—	1.17	163	3$^{\rm k}$
1957+405	1993-05-27	A	70003000	$2.4^{+0.5}_{-0.4}$	$1.46^{+0.01}_{-0.01}$	28.74	79.51	—	1.47	2085	2$^{\rm j}$
1957+405	1993-10-27	A	70003010	$6.1^{+0.4}_{-0.4}$	$1.47^{+0.01}_{-0.01}$	24.45	72.95	—	1.64	2319	2$^{\rm j}$
1957+405	1999-10-27	B	51016001	$18.7^{+2.0}_{-2.0}$	$1.58^{+0.01}_{-0.01}$	17.65	57.35	126.29	3.73	343	1$^{\rm j}$
1957+405	2000-05-26	C	1707	$935.9^{+55.6}_{-46.8}$	$0.43^{+0.02}_{-0.02}$	0.01	15.74	—	3.27	105	1$^{\rm b,f}$
2134+004	2000-11-25	B	51143001	< 17.9	$1.73^{+0.04}_{-0.03}$	1.09	1.89	—	0.95	73	3$^{\rm c}$
2145+067	1998-12-05	A	76003000	< 2.9	$1.59^{+0.01}_{-0.01}$	8.00	17.23	—	1.05	956	3
2200+420	1995-11-22	A	73088000	$5.6^{+1.3}_{-1.2}$	$1.91^{+0.01}_{-0.01}$	6.03	9.38	—	0.91	732	3$^{\rm o}$
2200+420	1997-07-18	A	15505000	< 0.2	$1.44^{+0.01}_{-0.01}$	10.66	29.05	—	1.10	1287	2$^{\rm f,o}$
2200+420	1997-11-08	B	50046004	$9.9^{+4.0}_{-3.4}$	$1.90^{+0.03}_{-0.03}$	6.08	10.76	11.63	0.95	93	2$^{\rm f,o,h}$
2200+420	1999-06-05	B	50881001	$1.7^{+1.9}_{-1.6}$	$2.13^{+0.02}_{-0.02}$	5.24	5.29	3.43	1.15	182	2$^{\rm f,o,h}$
2200+420	1999-06-28	A	77000000	< 0.6	$1.87^{+0.01}_{-0.01}$	5.16	7.29	—	0.95	1136	2$^{\rm f,o}$
2200+420	1999-12-05	B	50881002	$6.0^{+3.7}_{-3.4}$	$1.65^{+0.01}_{-0.01}$	5.18	11.99	22.48	0.96	175	2$^{\rm f,o,h}$
2200+420	2000-01-07	C	843	$27.7^{+23.0}_{-16.5}$	$1.68^{+0.14}_{-0.13}$	0.98	3.47	—	0.70	9	2$^{\rm f,o,k}$
2200+420	2000-02-16	C	139	$7.5^{+24.0}_{-7.5}$	$0.73^{+0.40}_{-0.31}$	3.59	34.11	—	0.75	14	2$^{\rm f,o,k}$
2200+420	2000-07-26	B	51165001	$0.5^{+4.6}_{-0.5}$	$1.89^{+0.03}_{-0.03}$	3.92	5.49	—	0.90	62	3$^{\rm b,o}$
2200+420	2000-10-31	B	511650011	$14.4^{+1.3}_{-1.2}$	$2.62^{+0.01}_{-0.01}$	28.36	20.21	4.54	1.08	107	3$^{\rm b,o}$
2223−052	1997-11-10	B	50181006	< 99.3	$1.77^{+0.10}_{-0.09}$	0.82	1.35	—	1.06	10	3$^{\rm c}$
2230+114	1995-12-06	A	73084000	$59.5^{+23.4}_{-20.6}$	$1.52^{+0.03}_{-0.03}$	0.97	3.05	—	0.94	215	3
2230+114	1997-11-11	B	50237021	< 30.0	$1.51^{+0.04}_{-0.03}$	2.27	5.55	13.99	1.36	59	3$^{\rm h}$
2230+114	1997-11-13	B	50237022	$15.6^{+22.4}_{-15.1}$	$1.63^{+0.03}_{-0.03}$	2.66	5.88	11.50	0.74	71	3$^{\rm h}$
2230+114	1997-11-16	B	50237023	$34.3^{+29.3}_{-21.2}$	$1.61^{+0.03}_{-0.03}$	2.37	5.88	12.00	1.16	71	3$^{\rm h}$
2230+114	1997-11-18	B	50237024	$3.0^{+27.5}_{-3.0}$	$1.52^{+0.04}_{-0.04}$	2.50	6.09	14.98	1.13	47	3$^{\rm h}$
2230+114	1997-11-21	B	50237025	$9.3^{+26.6}_{-9.3}$	$1.51^{+0.04}_{-0.03}$	2.35	6.03	15.19	1.22	66	3$^{\rm h}$
2243−123	1998-11-18	B	50727005	< 8.4	$1.64^{+0.06}_{-0.06}$	0.92	1.84	—	1.21	29	2$^{\rm c,f}$
2251+158	2000-06-05	B	51220001	$46.1^{+18.6}_{-16.9}$	$1.39^{+0.01}_{-0.02}$	2.92	10.96	35.86	1.08	161	3
2251+158	2002-11-06	C	3127	$23.3^{+6.3}_{-5.8}$	$1.61^{+0.05}_{-0.04}$	4.26	10.28	—	1.12	125	3$^{\rm k}$

Continued on next page

Table 4.1 – continued from previous page

Source[*]	Obs. Date[*]	T[†]	Sequence	N_H[★]	Γ[‡]	F_1[◇]	F_2[♣]	F_3[♠]	χ_red	d.o.f.	Q[♡]

[*] B 1950.0 coordinates; [*] Date of the observation in yyyy-mm-dd format; [†] T: Telescope (A: *ASCA*, B: *Beppo*Sax, C: *Chandra*, X: *XMM-Newton*); [★] Amount of extra absorption over the Galactic value in units of $10^{20}\,\mathrm{cm}^{-2}$. Note discussion in Sect. 5.2 on the discrepancies between the used March 2005 data from the LAB survey and the data available since July 2005; [‡] Photon index; [◇] $(0.5-2.0)\,\mathrm{keV}$ flux in units of $10^{-12}\,\mathrm{erg\,s^{-1}\,cm^{-2}}$, corrected for Galactic absorption; [♣] $(2.0-10.0)\,\mathrm{keV}$ flux in units of $10^{-12}\,\mathrm{erg\,s^{-1}\,cm^{-2}}$, corrected for Galactic absorption; [♠] $(20.0-80.0)\,\mathrm{keV}$ flux in units of $10^{-12}\,\mathrm{erg\,s^{-1}\,cm^{-2}}$, corrected for Galactic absorption; [♡] Quality label of the fit (1: Inappropriate model; 2: Fair fit but model cannot account for systematic residuals; 3: Model appropriate for statistical analysis), labels 1,2 imply that the spectrum is better represented by model II or III and included in Table 4.2 or Table 4.3; [a] broad iron emission complex; [a'] narrow iron emission line residual; [b] poor statistics due to short exposure; [c] no PDS detection; [d] no redshift: $z_{zwabs}=0$; [e] intervening system at $z_{zwabs}=0.524$; [e'] intervening system at $z_{zwabs}=2.04$; [e*] intervening system at $z_{zwabs}=0.312$; [f] soft excess; [g] LECS/MECS normalization frozen at 0.65; [g'] no LECS data; [h] PDS/MECS normalization frozen at 0.85; [i] only GIS data used; [j] extended plasma emission included; [k] pileup model applied; [k'] pileup-model corrected spectrum was not in agreement with annulus spectrum taken from the wings of the PSF, data were not used in further analysis; [l] bright extended background emission; [m] broad soft residuals; [n] broad soft and hard residuals; [o] non-neutral Galactic absorption: $z_{zwabs}=0$; [p] PN data discarded due to X-ray loading (see Lewis et al. 2005 for details); [q] low-energy calibration uncertainties: data below 0.6 keV discarded; [r] PDS data discarded because of confusion; [s] hard excess; [t] no PN data; [u] spectral steepening at high energies; [v] 50 counts per grouping bin due to high background; [w] Bulk source region masked, three epochs from 2001-01-13 and 2001-01-14 combined (0112910201, 0070740101, 0070740301)

Table 4.2: Two-power-law X-ray spectral fit results

Source[a]	Obs. Date[b]	T[c]	Sequence	N_{H}[d]	Γ_1[e]	E_{Break}[f]	Γ_2[g]	$F_1^{\mathrm{soft,h}}$	$F_2^{\mathrm{soft,i}}$	$F_3^{\mathrm{soft,j}}$	$F_1^{\mathrm{hard,k}}$	$F_2^{\mathrm{hard,l}}$	$F_3^{\mathrm{hard,m}}$	χ_{red}	d.o.f.
0235+164	2002-02-10	X	0110990101	$29.8^{+0.4}_{-0.4}$	$2.70^{+0.01}_{-0.01}$	6.0	$1.34^{+0.03}_{-0.03}$	4.48	2.76	-	0.48	1.96	-	1.41	279
0430+052	1994-02-17	A	71014000	$8.8^{+0.4}_{-0.4}$	$2.63^{+0.01}_{-0.01}$	1.9	$1.47^{+0.01}_{-0.01}$	22.77	13.64	-	11.67	36.85	-	1.34	334
0430+052	1997-09-20	B	50384001	$39.5^{+0.9}_{-0.9}$	$4.64^{+0.08}_{-0.08}$	1.0	$1.79^{+0.01}_{-0.01}$	14.54	1.84	0.01	13.31	45.59	64.19	1.33	176
0430+052	1998-02-12	A	76009000	$4.8^{+0.4}_{-0.4}$	$2.32^{+0.01}_{-0.01}$	4.5	$1.01^{+0.01}_{-0.01}$	28.95	24.07	-	4.46	25.80	-	1.35	413
0430+052	2001-12-21	C	3015	$35.5^{+1.2}_{-1.7}$	$3.88^{+0.06}_{-0.06}$	2.2	$1.06^{+0.02}_{-0.02}$	10.60	2.75	-	2.08	17.78	-	1.19	369
0430+052	2002-09-06	X	0109131101	$12.1^{+0.2}_{-0.2}$	$3.48^{+0.04}_{-0.04}$	1.0	$1.56^{+0.01}_{-0.01}$	12.69	2.74	-	12.71	37.53	-	0.93	395
0430+052	2003-08-26	X	0152840101	$16.7^{+0.1}_{-0.1}$	$3.90^{+0.01}_{-0.01}$	1.0	$1.70^{+0.01}_{-0.01}$	15.19	2.23	-	16.28	43.39	-	1.48	741
0458-020	2002-10-10	C	2985	$196.2^{+7.9}_{-7.6}$	$4.09^{+0.11}_{-0.11}$	0.9	$1.38^{+0.03}_{-0.03}$	0.16	0.02	-	0.17	0.75	-	1.11	176
0716+714	1996-11-14	B	50160001	$0.1^{+0.7}_{-0.1}$	$2.41^{+0.04}_{-0.03}$	7.0	$0.78^{+0.13}_{-0.10}$	1.71	1.06	-	0.04	0.30	-	1.12	100
0716+714	1998-11-07	B	50750002	< 0.9	$2.50^{+0.26}_{-0.31}$	4.0	$1.20^{+0.09}_{-0.07}$	2.10	1.20	1.23	0.32	1.27	6.22	1.37	41
0716+714	2000-10-30	B	51153001	$0.8^{+0.5}_{-0.4}$	$3.21^{+0.23}_{-0.08}$	2.0	$1.34^{+0.02}_{-0.02}$	2.53	0.52	0.03	0.93	1.80	10.93	0.78	85
0716+714	2001-04-13	X	0012850101	< 0.3	$3.44^{+0.06}_{-0.06}$	1.6	$1.53^{+0.11}_{-0.10}$	2.11	0.30	-	0.73	1.73	-	1.08	153
0716+714	2001-09-19	X	0012850601	$0.5^{+0.3}_{-0.3}$	$3.70^{+0.05}_{-0.06}$	0.8	$2.29^{+0.06}_{-0.06}$	2.15	0.21	-	2.52	1.92	-	1.10	212
0923+392	2002-10-19	C	3048	$45.7^{+0.9}_{-0.9}$	$5.43^{+0.06}_{-0.06}$	0.8	$1.59^{+0.02}_{-0.02}$	0.66	0.01	-	1.33	3.98	-	1.40	211
1038+064	2003-05-18	X	0151390101	< 0.9	$1.67^{+0.01}_{-0.01}$	13.0	$0.43^{+0.05}_{-0.05}$	0.62	1.18	-	0.03	0.40	-	1.06	280
1222+216	2002-11-06	C	3049	$15.2^{+0.9}_{-0.8}$	$3.90^{+0.08}_{-0.09}$	0.8	$1.17^{+0.03}_{-0.02}$	0.41	0.04	-	0.83	3.93	-	1.10	198
1226+023	1993-06-08	A	70023000	$3.5^{+0.2}_{-0.2}$	$3.37^{+0.04}_{-0.04}$	0.5	$1.55^{+0.01}_{-0.01}$	64.80	125.13	-	50.16	122.55	-	1.43	371
1226+023	1993-12-15	A	10022010	$3.6^{+0.2}_{-0.2}$	$1.73^{+0.01}_{-0.01}$	20.0	$0.71^{+0.02}_{-0.02}$	75.25	169.15	-	3.78	33.43	-	1.83	440
1226+023	1993-12-15	A	10022020	$3.1^{+0.2}_{-0.2}$	$2.05^{+0.01}_{-0.01}$	0.7	$1.40^{+0.01}_{-0.01}$	91.07	203.30	-	47.53	143.94	-	1.37	516
1226+023	1993-12-19	A	10022000	$2.8^{+0.1}_{-0.2}$	$1.73^{+0.01}_{-0.01}$	8.0	$1.12^{+0.01}_{-0.01}$	73.81	183.61	-	15.81	73.60	-	1.34	668
1226+023	1993-12-23	A	71038020	$3.7^{+0.3}_{-0.3}$	$1.78^{+0.01}_{-0.01}$	7.0	$1.14^{+0.01}_{-0.01}$	71.62	172.41	-	15.16	69.44	-	1.27	270
1226+023	1997-01-22	B	50237014	$1.6^{+0.3}_{-0.2}$	$4.43^{+0.10}_{-0.17}$	0.3	$1.56^{+0.01}_{-0.01}$	45.73	108.44	179.51	42.69	99.23	222.51	0.96	130
1226+023	1998-06-24	B	50795004	$4.5^{+0.1}_{-0.1}$	$5.03^{+0.03}_{-0.03}$	0.5	$1.62^{+0.01}_{-0.01}$	52.27	125.24	176.62	44.42	100.65	200.63	1.13	179
1226+023	1998-06-24	A	12601000	< 0.4	$2.98^{+0.04}_{-0.04}$	0.4	$1.53^{+0.01}_{-0.01}$	62.41	117.91	-	14.15	3.89	-	1.41	341
1226+023	2000-01-09	B	50795008	$3.5^{+0.1}_{-0.1}$	$4.48^{+0.03}_{-0.03}$	0.4	$1.62^{+0.01}_{-0.01}$	58.85	143.74	180.91	48.47	107.48	213.60	1.26	179
1226+023	2000-01-09	A	10701000	< 0.3	$2.29^{+0.02}_{-0.02}$	0.0	$1.56^{+0.01}_{-0.01}$	64.31	125.27	-	12.96	9.70	-	1.34	676
1226+023	2000-01-09	C	1198	< 0.1	$2.88^{+0.07}_{-0.03}$	0.7	$1.27^{+0.01}_{-0.03}$	50.58	123.29	-	33.68	118.07	-	1.29	375
1226+023	2000-01-10	C	459	$8.2^{+2.0}_{-1.6}$	$2.94^{+0.13}_{-0.17}$	1.3	$1.01^{+0.03}_{-0.04}$	14.23	36.29	-	5.59	33.11	-	1.21	198

Continued on next page

Table 4.2 – continued from previous page

Source[a]	Obs. Date[b]	T[c]	Sequence	N_H[d]	Γ_1[e]	E_{Break}[f]	Γ_2[g]	$F_1^{soft,h}$	$F_2^{soft,i}$	$F_3^{soft,j}$	$F_1^{hard,k}$	$F_2^{hard,l}$	$F_3^{hard,m}$	χ_{red}	d.o.f.
1226+023	2000-06-13	B	50795010	$4.8^{+0.1}_{-0.1}$	$5.35^{+0.03}_{-0.04}$	0.4	$1.64^{+0.01}_{-0.01}$	42.76	97.10	126.88	36.66	80.20	150.86	1.12	130
1226+023	2000-06-13	X	0126700101	< 0.2	$2.83^{+0.14}_{-0.14}$	0.0	$1.70^{+0.01}_{-0.01}$	4.42	1.52	-	42.96	78.11	-	1.37	249
1226+023	2000-06-13	X	0126700201	$0.1^{+0.5}_{-0.1}$	$3.45^{+0.19}_{-0.21}$	0.3	$1.69^{+0.03}_{-0.03}$	7.54	1.06	-	63.27	117.70	-	0.94	325
1226+023	2000-06-13	X	0126700301	$0.6^{+0.1}_{-0.1}$	$2.85^{+0.05}_{-0.01}$	0.4	$1.57^{+0.01}_{-0.01}$	11.51	3.90	-	34.36	77.06	-	2.43	817
1226+023	2000-06-15	X	0126700401	< 0.1	$3.21^{+0.05}_{-0.05}$	0.2	$1.63^{+0.01}_{-0.01}$	5.80	1.14	-	46.44	93.70	-	1.08	566
1226+023	2000-06-15	X	0126700601	< 0.0	$2.75^{+0.01}_{-0.01}$	0.5	$1.53^{+0.01}_{-0.01}$	12.61	4.80	-	32.75	77.28	-	1.54	1225
1226+023	2000-06-15	X	0126700701	< 0.0	$2.91^{+0.01}_{-0.01}$	0.4	$1.56^{+0.01}_{-0.01}$	9.59	2.93	-	34.18	76.65	-	1.55	1229
1226+023	2000-06-16	X	0126700501	< 0.1	$3.53^{+0.06}_{-0.06}$	0.3	$1.61^{+0.01}_{-0.01}$	4.13	0.52	-	39.34	81.79	-	1.14	549
1226+023	2000-06-17	X	0126700801	< 0.0	$3.00^{+0.01}_{-0.01}$	0.4	$1.57^{+0.01}_{-0.01}$	8.93	2.38	-	33.94	75.54	-	1.67	1564
1226+023	2001-06-12	B	50795011	$4.0^{+0.1}_{-0.1}$	$4.93^{+0.04}_{-0.04}$	0.5	$1.64^{+0.01}_{-0.01}$	53.18	124.86	159.15	43.56	94.16	177.87	1.33	96
1226+023	2001-06-13	C	2463	< 0.7	$6.40^{+0.19}_{-0.38}$	0.3	$1.68^{+0.06}_{-0.07}$	0.76	-	-	34.54	65.43	-	1.22	181
1226+023	2001-06-13	C	2464	< 0.2	$5.34^{+0.07}_{-0.18}$	0.3	$1.65^{+0.03}_{-0.03}$	1.46	0.01	-	36.59	71.67	-	1.55	332
1226+023	2001-06-13	X	0136550101	< 0.0	$2.86^{+0.01}_{-0.01}$	0.6	$1.54^{+0.01}_{-0.01}$	22.74	7.46	-	40.34	93.94	-	1.89	1504
1226+023	2001-06-15	C	2471	$4.7^{+0.5}_{-0.4}$	$3.29^{+0.05}_{-0.06}$	1.0	$1.19^{+0.02}_{-0.02}$	12.00	2.44	-	9.97	43.09	-	1.37	300
1226+023	2001-12-16	X	0112770101	< 0.1	$2.32^{+0.01}_{-0.01}$	1.1	$1.44^{+0.01}_{-0.01}$	35.18	25.19	-	33.37	90.90	-	1.12	840
1226+023	2001-12-22	X	0112770201	< 0.1	$2.51^{+0.02}_{-0.02}$	0.4	$1.53^{+0.01}_{-0.01}$	17.03	9.23	-	38.64	90.87	-	1.24	590
1226+023	2002-01-09	X	0137551001	< 0.1	$4.08^{+0.08}_{-0.05}$	0.3	$1.70^{+0.01}_{-0.01}$	3.77	0.21	-	49.79	90.72	-	1.40	505
1226+023	2002-06-04	C	3574	< 0.2	$3.30^{+0.07}_{-0.12}$	0.3	$1.78^{+0.02}_{-0.02}$	14.01	2.43	-	86.28	140.29	-	1.93	152
1226+023	2002-06-05	C	3456	< 0.4	$5.06^{+0.17}_{-0.15}$	0.5	$1.59^{+0.05}_{-0.09}$	5.73	0.08	-	40.52	87.34	-	1.26	194
1226+023	2002-07-07	X	0112770601	< 0.1	$2.57^{+0.02}_{-0.02}$	0.2	$1.68^{+0.01}_{-0.01}$	11.93	5.96	-	40.51	75.78	-	1.31	608
1226+023	2002-12-17	X	0112770801	$1.8^{+0.1}_{-0.1}$	$2.84^{+0.01}_{-0.01}$	0.6	$1.65^{+0.01}_{-0.01}$	27.24	9.60	-	47.88	97.95	-	1.22	800
1226+023	2003-01-05	X	0112770701	< 0.1	$2.55^{+0.01}_{-0.01}$	0.9	$1.58^{+0.01}_{-0.01}$	29.98	15.34	-	32.65	71.81	-	1.12	716
1226+023	2003-01-05	X	0136550501	$1.5^{+0.1}_{-0.1}$	$3.14^{+0.01}_{-0.01}$	0.5	$1.68^{+0.01}_{-0.01}$	18.43	4.22	-	44.28	85.43	-	1.56	832
1226+023	2003-06-18	X	0112771001	$0.1^{+0.1}_{-0.1}$	$3.14^{+0.04}_{-0.05}$	0.3	$1.77^{+0.01}_{-0.01}$	14.64	3.19	-	73.47	121.16	-	1.23	363
1226+023	2003-07-07	C	4430	< 0.7	$4.86^{+0.36}_{-0.25}$	0.4	$1.69^{+0.05}_{-0.09}$	2.96	0.05	-	40.95	78.21	-	1.17	186
1226+023	2003-07-07	C	4431	< 0.4	$8.72^{+0.22}_{-1.34}$	0.2	$1.84^{+0.01}_{-0.02}$	0.04	-	-	102.35	151.41	-	1.36	383
1226+023	2003-07-07	X	0159960101	< 0.0	$2.43^{+0.01}_{-0.01}$	0.5	$1.70^{+0.01}_{-0.01}$	26.40	16.20	-	47.61	86.84	-	2.34	1400
1226+023	2003-07-08	X	0112770501	$0.4^{+0.1}_{-0.1}$	$2.15^{+0.01}_{-0.01}$	6.0	$1.28^{+0.01}_{-0.01}$	57.09	53.85	-	12.67	44.37	-	1.11	870
1226+023	2003-12-14	X	0112771101	< 0.1	$2.52^{+0.01}_{-0.01}$	0.7	$1.53^{+0.01}_{-0.01}$	20.76	11.12	-	30.22	71.74	-	1.23	892
1226+023	2004-02-10	C	4877	< 0.1	$4.81^{+0.04}_{-0.06}$	0.3	$1.67^{+0.03}_{-0.02}$	1.68	0.03	-	39.07	74.72	-	1.26	463
1226+023	2004-06-30	X	0136550801	< 0.0	$2.81^{+0.01}_{-0.01}$	0.3	$1.65^{+0.01}_{-0.01}$	8.57	3.01	-	36.07	70.47	-	2.43	1062

Continued on next page

Table 4.2 – continued from previous page

Source[a]	Obs. Date[b]	T[c]	Sequence	N_{H}[d]	Γ_1[e]	E_{Break}[f]	Γ_2[g]	$F_1^{\mathrm{soft,h}}$	$F_2^{\mathrm{soft,i}}$	$F_3^{\mathrm{soft,j}}$	$F_1^{\mathrm{hard,k}}$	$F_2^{\mathrm{hard,l}}$	$F_3^{\mathrm{hard,m}}$	χ_{red}	d.o.f.
1458+718	2002-01-28	C	3105	$53.3^{+1.9}_{-1.8}$	$5.34^{+0.09}_{-0.09}$	0.8	$1.44^{+0.03}_{-0.03}$	0.29	0.01	-	0.63	2.25	-	0.83	84
1510-089	1998-08-03	B	50497004	< 6.2	$2.22^{+0.10}_{-0.10}$	2.0	$0.99^{+0.03}_{-0.03}$	1.41	1.17	0.62	0.75	4.02	30.54	0.84	40
1641+399	2001-04-27	C	2143	$3.9^{+1.4}_{-0.8}$	$2.97^{+0.09}_{-0.09}$	0.8	$1.52^{+0.04}_{-0.04}$	0.94	0.28	-	1.36	3.37	-	1.25	147
1749+096	1995-09-22	A	73087000	< 4.4	$1.55^{+0.04}_{-0.03}$	2.1	$1.92^{+0.07}_{-0.06}$	2.23	3.76	-	-	-	-	1.16	38
2200+420	1997-07-18	A	15505000	$0.1^{+0.9}_{-0.1}$	$2.67^{+0.07}_{-0.07}$	0.7	$1.23^{+0.01}_{-0.01}$	4.28	1.63	-	7.69	28.94	-	1.17	110
2200+420	1997-11-08	B	50046004	$14.4^{+6.4}_{-2.6}$	$2.15^{+0.04}_{-0.04}$	11.0	$0.86^{+0.13}_{-0.07}$	5.24	6.76	0.25	0.30	2.63	26.94	1.08	21
2200+420	1999-06-05	B	50881001	$12.6^{+2.0}_{-1.9}$	$2.67^{+0.03}_{-0.03}$	6.0	$1.02^{+0.05}_{-0.04}$	5.89	4.36	0.74	0.33	2.17	15.59	0.91	63
2200+420	1999-06-28	A	77000000	$18.3^{+0.9}_{-1.0}$	$3.41^{+0.05}_{-0.05}$	1.1	$1.65^{+0.01}_{-0.01}$	2.73	1.19	-	2.28	6.88	-	0.79	107
2200+420	1999-12-05	B	50881002	$1.5^{+3.5}_{-1.5}$	$1.55^{+0.01}_{-0.01}$	6.8	$2.08^{+0.27}_{-0.22}$	5.24	28.66	9.52	-	-	-	0.92	86
2200+420	2000-10-31	B	511650011	$16.2^{+1.3}_{-1.2}$	$2.69^{+0.01}_{-0.01}$	25.0	$1.04^{+0.19}_{-0.12}$	24.22	16.35	1.57	0.15	1.01	6.99	1.07	105
2243-123	1998-11-18	B	50727005	< 8.2	$3.50^{+0.45}_{-0.51}$	0.8	$1.51^{+0.06}_{-0.06}$	0.70	2.60	-	0.66	1.62	-	1.00	27

[a] B 1950.0 coordinates; [b] Date of the observation in yyyy-mm-dd format; [c] T: Telescope (A: *ASCA*, B: *Beppo*Sax, C: *Chandra*, X: *XMM-Newton*); [d] Amount of extra absorption over the Galactic value in units of $10^{20}\,\mathrm{cm}^{-2}$. Note discussion in Sect. 5.2 on the discrepancies between the used March 2005 data from the LAB survey and the data available since July 2005; [e] Photon index of the soft-excess component; [f] Break Energy; [g] Photon index of the hard-power-law component; [h] $(0.5 - 2.0)\,\mathrm{keV}$ flux of the soft-excess component in units of $10^{-12}\,\mathrm{erg\,s^{-1}\,cm^{-2}}$, corrected for Galactic absorption; [i] $(2.0 - 10.0)\,\mathrm{keV}$ flux of the soft-excess component in units of $10^{-12}\,\mathrm{erg\,s^{-1}\,cm^{-2}}$, corrected for Galactic absorption; [j] $(20.0 - 80.0)\,\mathrm{keV}$ flux of the soft-excess component in units of $10^{-12}\,\mathrm{erg\,s^{-1}\,cm^{-2}}$, corrected for Galactic absorption; [k] $(0.5 - 2.0)\,\mathrm{keV}$ flux of the hard-power-law component in units of $10^{-12}\,\mathrm{erg\,s^{-1}\,cm^{-2}}$, corrected for Galactic absorption; [l] $(2.0 - 10.0)\,\mathrm{keV}$ flux of the hard-power-law component in units of $10^{-12}\,\mathrm{erg\,s^{-1}\,cm^{-2}}$, corrected for Galactic absorption; [m] $(20.0 - 80.0)\,\mathrm{keV}$ flux of the hard-power-law component in units of $10^{-12}\,\mathrm{erg\,s^{-1}\,cm^{-2}}$, corrected for Galactic absorption

Table 4.3: One-power-law plus extended plasma X-ray spectral fit results

Source[*]	Obs. Date[*]	T[†]	Sequence	$N_{\rm H}$[★]	kT[■]	Γ[‡]	F_1[◇]	F_2[♣]	F_3[♠]	$\chi_{\rm red}$	d.o.f.
0316+164	1993-08-06	A	80007000	$3.2^{+0.4}_{-0.3}$	$3.67^{+0.04}_{-0.04}$	$1.91^{+0.01}_{-0.01}$	162.29	235.24	0	1.15	1200
0316+164	1993-08-06	A	80008000	$7.8^{+0.3}_{-0.2}$	$3.84^{+0.06}_{-0.06}$	$1.95^{+0.01}_{-0.01}$	174.11	269.63	0	1.16	2078
0316+164	1995-08-18	A	83051000	$4.0^{+0.5}_{-0.5}$	$3.70^{+0.08}_{-0.06}$	$1.82^{+0.01}_{-0.01}$	146.92	251	0	1.19	997
0316+164	1995-09-04	A	83053000	$3.5^{+0.4}_{-0.4}$	$3.74^{+0.08}_{-0.06}$	$1.88^{+0.01}_{-0.01}$	166.48	253.47	0	1.13	1059
0316+164	1996-09-19	B	60009001	< 0.79	$3.16^{+0.03}_{-0.03}$	$2.06^{+0.01}_{-0.01}$	0	45.784	34.215	2.78	195
0316+164	2001-01-30	X	0085110101	$6.4^{+0.1}_{-0.1}$	$2.99^{+0.04}_{-0.04}$	$2.03^{+0.01}_{-0.01}$	21.168	28.445	0	1.43	2038
1228+126	1993-06-07	A	60033000	$7.0^{+0.2}_{-0.2}$	$1.76^{+0.01}_{-0.01}$	$2.36^{+0.01}_{-0.01}$	30.934	26.471	0	2.08	1224
1228+126	1996-07-14	B	60010001	$13.6^{+3.5}_{-3.4}$	$1.78^{+0.02}_{-0.02}$	$2.35^{+0.03}_{-0.03}$	0	11.663	6.0055	1.71	143
1228+126	2000-06-19	X	0114120101	$4.3^{+0.2}_{-0.2}$	$1.27^{+0.01}_{-0.01}$	$2.48^{+0.02}_{-0.02}$	5.8169	3.8411	0	1.57	735

[*] B 1950.0 coordinates; [*] Date of the observation in yyyy-mm-dd format; [†] T: Telescope (A: *ASCA*, B: *Beppo*Sax, C: *Chandra*, X: *XMM-Newton*); [★] Amount of extra absorption over the Galactic value in units of $10^{20}\,{\rm cm}^{-2}$. Note discussion in Sect. 5.2 on the discrepancies between the used March 2005 data from the LAB survey and the data available since July 2005; [■] temperature of thermal plasma in units of keV; [‡] Photon index; [◇] $(0.5-2.0)\,{\rm keV}$ flux in units of $10^{-12}\,{\rm erg\,s}^{-1}\,{\rm cm}^{-2}$, corrected for Galactic absorption; [♣] $(2.0-10.0)\,{\rm keV}$ flux in units of $10^{-12}\,{\rm erg\,s}^{-1}\,{\rm cm}^{-2}$, corrected for Galactic absorption; [♠] $(20.0-80.0)\,{\rm keV}$ flux in units of $10^{-12}\,{\rm erg\,s}^{-1}\,{\rm cm}^{-2}$, corrected for Galactic absorption; [a] only GIS data used; [b] extended plasma emission included; [c] no LECS data [d] PDS/MECS normalization frozen at 0.85; [e] broad soft residuals

Table 4.4: Mean X-ray spectral parameters of the *2 cm-X-Sample* sources.

Source[a]	N_2[b]	N[c]	N_H[d]	ΔN_H	Γ_1[e]	$\Delta\Gamma_1$	E_{Break}[f]	ΔE_{Break}	Γ_2[g]	$\Delta\Gamma_2$	$F_1^{soft,h}$	ΔF_1^{soft}	$F_2^{soft,i}$	ΔF_2^{soft}	$F_3^{soft,j}$	ΔF_3^{soft}	$F_1^{hard,k}$	ΔF_1^{hard}	$F_2^{hard,l}$	ΔF_2^{hard}	$F_3^{hard,m}$	ΔF_3^{hard}
0007+106	0	2	0.001	0.005	—	—	—	—	1.76	0.02	—	—	—	—	—	—	4.80	1.17	8.88	2.31	—	—
0048−097	0	2	0.001	0.346	—	—	—	—	1.91	0.09	—	—	—	—	—	—	0.98	0.20	1.43	0.32	—	—
0235+164	1	11	0.286	0.029	2.70	0.01	6.0	—	1.63	0.06	4.48	0.90	2.76	0.55	—	—	0.70	0.17	1.72	0.44	—	—
0316+164	0	14	0.064	0.017	—	—	—	—	1.97	0.07	—	—	—	—	—	—	42.85	18.54	67.49	28.82	34.22	6.84
0333+321	0	2	0.163	0.009	—	—	—	—	1.66	0.02	—	—	—	—	—	—	2.86	0.68	8.27	1.85	13.77	2.75
0415+379	0	3	0.603	0.065	—	—	—	—	1.69	0.02	—	—	—	—	—	—	7.96	2.40	41.23	11.11	51.21	10.24
0420−014	0	1	0.303	0.158	—	—	—	—	1.91	0.06	—	—	—	—	—	—	1.16	0.23	1.87	0.37	—	—
0430+052	6	6	0.161	0.059	2.39	0.55	3.8	1.6	1.68	0.16	18.93	5.20	11.29	5.77	0.01	0.00	9.12	2.94	30.83	7.85	59.87	11.97
0458−020	1	1	1.962	0.055	4.09	0.08	0.9	—	1.38	0.02	0.16	0.03	0.02	0.00	—	—	0.17	0.03	0.75	0.15	—	—
0528+134	0	12	0.292	0.036	—	—	—	—	1.69	0.06	—	—	—	—	—	—	1.37	0.44	4.65	1.45	—	—
0605−085	0	1	0.123	0.053	—	—	—	—	1.63	0.04	—	—	—	—	—	—	0.60	0.12	1.32	0.26	—	—
0716+714	5	9	0.000	0.001	3.49	0.31	3.1	1.0	2.52	0.30	2.12	0.44	0.66	0.22	0.63	0.44	2.69	1.56	1.90	0.70	8.57	3.75
0735+178	0	1	0.000	0.024	—	—	—	—	1.74	0.04	—	—	—	—	—	—	0.40	0.08	0.69	0.14	—	—
0736+017	0	1	0.040	0.025	—	—	—	—	1.74	0.02	—	—	—	—	—	—	1.95	0.39	3.62	0.72	—	—
0738+313	0	2	0.058	0.010	—	—	—	—	1.63	0.07	—	—	—	—	—	—	0.37	0.07	0.77	0.16	—	—
0827+243	0	1	0.008	0.019	—	—	—	—	1.66	0.02	—	—	—	—	—	—	1.04	0.21	2.01	0.40	—	—
0836+710	0	5	0.065	0.193	—	—	—	—	1.35	0.01	—	—	—	—	—	—	6.66	1.73	21.20	5.64	87.88	17.58
0851+202	0	5	0.009	0.023	—	—	—	—	1.60	0.01	—	—	—	—	—	—	1.17	0.44	2.73	0.96	—	—
0923+392	1	2	0.455	0.074	5.43	0.04	0.8	—	1.74	0.10	0.66	0.13	0.01	0.00	—	—	1.84	0.51	4.10	0.83	—	—
1038+064	1	3	0.002	0.192	1.67	0.01	13.0	—	1.33	0.32	0.62	0.12	1.18	0.24	—	—	0.51	0.22	1.44	0.52	—	—
1055+018	0	1	0.000	0.009	—	—	—	—	1.66	0.02	—	—	—	—	—	—	1.77	0.35	3.45	0.69	—	—
1127−145	0	3	0.117	0.021	—	—	—	—	1.33	0.07	—	—	—	—	—	—	1.92	0.50	6.86	1.49	20.89	4.18
1156+295	0	1	0.011	0.029	—	—	—	—	1.61	0.02	—	—	—	—	—	—	0.41	0.08	0.87	0.17	—	—
1222+216	1	1	0.151	0.006	3.90	0.06	0.8	—	1.17	0.02	0.41	0.08	0.04	0.01	—	—	0.83	0.17	3.93	0.79	—	—
1226+023	31	47	0.000	0.003	2.31	0.31	1.6	0.7	1.61	0.03	27.90	7.47	50.95	16.06	160.89	33.89	38.95	8.74	3.93	12.96	120.16	24.03
1228+126	0	18	0.041	0.007	—	—	—	—	2.38	0.02	—	—	—	—	—	—	6.61	2.44	4.83	1.95	—	—
1253−055	0	17	0.030	0.006	—	—	—	—	1.70	0.01	—	—	—	—	—	—	4.86	1.05	9.24	2.01	9.16	2.02
1308+326	0	3	0.003	0.243	—	—	—	—	1.66	0.07	—	—	—	—	—	—	0.91	0.52	1.88	0.98	—	—
1334−127	0	1	0.052	0.004	—	—	—	—	1.79	0.01	—	—	—	—	—	—	1.67	0.33	2.80	0.56	—	—

Continued on next page

Table 4.4 – continued from previous page

Source[a]	N_2^b	N^c	N_H^d	ΔN_H	Γ_1^e	$\Delta\Gamma_1$	E_{Break}^f	ΔE_{Break}	Γ_2^g	$\Delta\Gamma_2$	$F_1^{soft,h}$	ΔF_1^{soft}	$F_2^{soft,i}$	ΔF_2^{soft}	$F_3^{soft,j}$	ΔF_3^{soft}	$F_1^{hard,k}$	ΔF_1^{hard}	$F_2^{hard,l}$	ΔF_2^{hard}	$F_3^{hard,m}$	ΔF_3^{hard}
1413+135	0	1	5.449	0.434	—	—	—	—	1.89	0.04	—	—	—	—	—	—	0.03	0.01	0.85	0.17	—	—
1458+718	1	1	0.533	0.013	5.34	0.07	0.8	—	1.44	0.02	0.29	0.06	0.01	0.00	—	—	0.63	0.13	2.25	0.45	—	—
1502+106	0	1	0.000	0.116	—	—	—	—	1.53	0.07	—	—	—	—	—	—	—	—	—	—	—	—
1510−089	1	3	0.008	0.022	2.22	0.07	2.0	—	1.23	0.10	1.41	0.28	1.17	0.23	0.62	0.12	1.92	0.61	6.96	1.89	30.54	6.11
1633+382	0	4	0.048	0.400	—	—	—	—	1.45	0.05	—	—	—	—	—	—	0.82	0.19	2.30	0.52	—	—
1641+399	1	2	0.036	0.017	2.97	0.07	0.8	—	1.63	0.07	0.94	0.19	0.28	0.06	—	—	1.31	0.68	2.67	1.18	7.64	1.53
1655+077	0	1	0.100	0.137	—	—	—	—	1.58	0.06	—	—	—	—	—	—	0.53	0.11	1.28	0.26	—	—
1749+096	1	1	0.000	0.044	1.55	0.03	2.1	—	1.92	0.04	2.23	0.45	3.76	0.75	—	—	—	—	—	—	—	—
1803+784	0	1	0.291	0.166	—	—	—	—	1.70	0.03	—	—	—	—	—	—	0.80	0.16	1.83	0.37	—	—
1823+568	0	1	0.000	0.439	—	—	—	—	2.22	0.11	—	—	—	—	—	—	0.95	0.19	0.80	0.16	—	—
1828+487	0	1	0.125	0.026	—	—	—	—	1.81	0.04	—	—	—	—	—	—	2.09	0.42	3.58	0.72	—	—
1928+738	0	2	0.026	0.015	—	—	—	—	1.89	0.11	—	—	—	—	—	—	3.31	0.67	4.32	1.00	—	—
2134+004	0	1	0.000	0.179	—	—	—	—	1.73	0.03	—	—	—	—	—	—	1.09	0.22	1.89	0.38	—	—
2145+067	0	1	0.000	0.029	—	—	—	—	1.59	0.01	—	—	—	—	—	—	8.00	1.60	17.23	3.45	—	—
2200+420	6	10	0.101	0.027	2.22	0.26	8.4	3.3	1.44	0.15	7.93	3.40	9.83	4.46	3.02	1.98	2.30	0.94	8.55	4.01	12.38	20.27
2223−052	0	1	0.000	0.993	—	—	—	—	1.77	0.07	—	—	—	—	—	—	0.82	0.16	1.35	0.27	—	—
2230+114	0	6	0.274	0.119	—	—	—	—	1.55	0.02	—	—	—	—	—	—	2.19	0.49	5.41	1.17	13.53	4.34
2243−123	1	1	0.000	0.082	3.50	0.34	0.8	—	1.51	0.04	0.70	0.14	2.60	0.52	—	—	0.66	0.13	1.62	0.32	—	—
2251+158	0	2	0.257	0.110	—	—	—	—	1.41	0.10	—	—	—	—	—	—	3.59	0.86	10.62	2.14	35.86	7.17

[a] B 1950.0 coordinates; [b] Number of epochs in which a soft-excess component was identified; [c] Total number of epochs; [d] excess absorbing column density over the Galactic value. Note discussion in Sect. 5.2 on the discrepancies between the used March 2005 data from the LAB survey and the data available since July 2005; [e] Photon index of the soft-excess component; [f] Break Energy; [g] Photon index of the hard-power-law component; [h] $(0.5 - 2.0)$ keV flux of the soft-excess component in units of 10^{-12} erg s^{-1} cm^{-2}, corrected for Galactic absorption; [i] $(2.0 - 10.0)$ keV flux of the soft-excess component in units of 10^{-12} erg s^{-1} cm^{-2}, corrected for Galactic absorption; [j] $(20.0 - 80.0)$ keV flux of the soft-excess component in units of 10^{-12} erg s^{-1} cm^{-2}, corrected for Galactic absorption; [k] $(0.5 - 2.0)$ keV flux of the hard-power-law component in units of 10^{-12} erg s^{-1} cm^{-2}, corrected for Galactic absorption; [l] $(2.0 - 10.0)$ keV flux of the hard-power-law component in units of 10^{-12} erg s^{-1} cm^{-2}, corrected for Galactic absorption; [m] $(20.0 - 80.0)$ keV flux of the hard-power-law component in units of 10^{-12} erg s^{-1} cm^{-2}, corrected for Galactic absorption

4.1.1 Soft Excess Photon Indices

A soft-excess component is found in 13 of the 48 sources investigated in this chapter. In addition, the two objects that could not be fitted with model I, II, or III (NGC 1052 and Cygnus A) are known to exhibit pronounced soft excesses but in these cases extended thermal plasma components give rise to the soft excess (Kadler et al. 2004a, reprinted in Sect. 6.3.2; Young et al. 2002)[2]. Among the other 13 sources with a detected soft excess 9 are quasars, 3 are BL Lac objects, and 3 are radio galaxies.

In Fig. 4.1, the distribution of photon indices of the *2 cm-X-Sample* sources are shown. The soft-excess components are found to be distributed over a very broad range without a clear peak between $\Gamma_{\text{soft}-\text{excess,min}} = 1.7$ and $\Gamma_{\text{soft}-\text{excess,max}} = 5.5$. The average value is $\langle \Gamma_{\text{soft}-\text{excess}} \rangle = 3.2$ with a dispersion of $\sigma_{\langle \Gamma_{\text{soft}-\text{excess}} \rangle} = 1.2$. The numbers of objects in the quasars–, BL Lac–, and galaxy–classes are too low and the range of photon indices is too large to derive meaningful results from the individual distributions. However, it can be speculated that the untypically large scatter may be an indicator of multiple emission mechanisms and/or a curved spectral distribution of this emission component. In the case of the two BL Lac objects 0235+164 (see Sect. 6.2) and 0716+714 (see Sect. 6.5) the soft spectral component can be identified with the high-energy tail of the primary synchrotron emission component with the (secondary) inverse-Compton emission component dominating at higher energies. Another frequently considered idea is that the high-energy end of the so-called "big blue bump" may extend into the soft X-ray regime that may be better described via a black-body model rather than a power law. Even if the spectral emission maximum of the big blue bump were intrinsically located at the same frequency in the rest frame of all sources, the different source redshifts would shift its position in the observed spectrum to different values. Depending on the position of the spectral maximum of the big blue bump in the observed spectrum, the parametrization via a power law may lead to a large range of photon indices derived.

4.1.2 Hard-Power-Law Photon Indices

A range of values between $\Gamma_{\text{hard}-\text{PL,min}} = 1.2$ and $\Gamma_{\text{hard}-\text{PL,max}} = 2.5$ is found for the hard power-law components with an average photon index of $\langle \Gamma_{\text{hard}-\text{PL}} \rangle = 1.68$ and a dispersion of $\sigma_{\langle \Gamma_{\text{hard}-\text{PL}} \rangle} = 0.26$. The peak of the distribution around 1.6–1.7 is very pronounced with 15 out of 48 sources lying in this narrow range.

Figure 4.2 shows the distribution of $\Gamma_{\text{hard}-\text{PL}}$ for the separate classes of quasars, BL Lac objects and galaxies. Only the quasars exhibit the $\Gamma_{\text{hard}-\text{PL}} = 1.6 - 1.7$ peak while the hard power laws of BL Lacs range from relatively flat values ($\Gamma^{\text{B}}_{\text{hard}-\text{PL,min}} = 1.4$) to very steep slopes ($\Gamma^{\text{B}}_{\text{hard}-\text{PL,max}} = 2.5$). Among the galaxies, values between $\Gamma^{\text{G}}_{\text{hard}-\text{PL,min}} = 1.7$ and $\Gamma^{\text{G}}_{\text{hard}-\text{PL,max}} = 2.4$ occur. According to a K-S test, there is only a 16 % probability that the BL Lac and quasar distributions of $\Gamma_{\text{hard}-\text{PL}}$ are drawn from the same parent population, for the galaxies the probability to match with the quasar distribution decreases to 2 %.

---

[2]Even with consideration of the bright extended thermal plasma emission in Cygnus A, Young et al. (2002) find a soft-excess of the nuclear spectrum seen with *Chandra*.
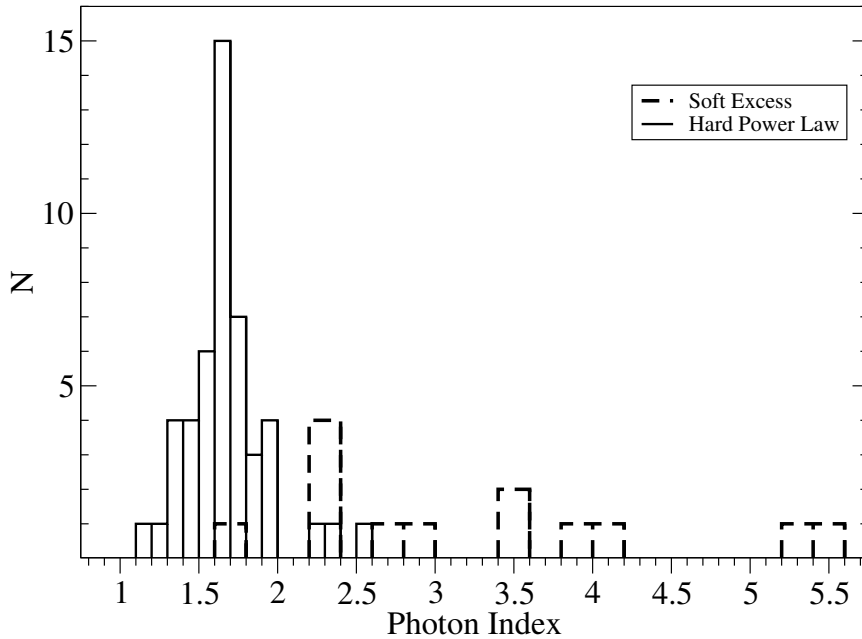
Figure 4.1: Distribution of the photon indices of the soft-excesses and the hard-power-law components found in the individual sources of the *2 cm-X-Sample*. Note the different binning sizes for the two histograms.

4.1.3 Absorbing Column Densities

In 19 out of 41 sources, a significant amount of absorption in excess of the Galactic value could be detected, that cannot be attributed to well-known intervening systems. NGC 1052 and Cygnus A are known to contain high-density absorbers obscuring the nuclear power-law source, as well (Kadler et al. (2004a), reprinted in Sect. 6.3.2; Young et al. (2002)). Including those, the detection rate of absorption towards the nuclei of *2 cm-X-Sample* sources is 51 %. 15 quasars (out of 30) are found to be absorbed, 1 (out of 7) BL Lac objects, and 5 (out of 6) radio galaxies (including NGC 1052 and Cygnus A).

In Fig. 4.3, the distribution of absorbing column densities (in the source frames) is shown for quasars, BL Lac objects, and radio galaxies. The quasar distribution ranges from $2.6 \times 10^{20} \, \mathrm{cm}^{-2}$ to $5.5 \times 10^{22} \, \mathrm{cm}^{-2}$ with an average value of $1.3 \times 10^{21} \, \mathrm{cm}^{-2}$ and a dispersion of $\sigma_{\log N_{\mathrm{H}}} = 0.57$. The galaxies seem to exhibit somewhat lower absorbing column densities but the small number of objects in this class does not allow this result to be quantified. One heavily absorbed BL Lac object is found, the source 1413+135. This peculiar case is discussed briefly in Sect. 4.3.

4.1.4 Flux and Luminosity Distribution

The absorption-corrected X-ray fluxes of the soft-excess and hard-power-law spectral components found in the *2 cm-X-Sample* are shown in Fig. 4.4. In general, the hard power laws exhibit much narrower distributions in the two bands (0.5–2.0) keV and (2.0–10.0) keV than the soft-excess spectral components. The soft-excess components are distributed in a relatively uniform way between $F_{soft-excess,min}^{(0.5-2.0)\,\mathrm{keV}} = 1.6 \times 10^{-14} \, \mathrm{erg} \, \mathrm{cm}^{-2} \, \mathrm{s}^{-1}$
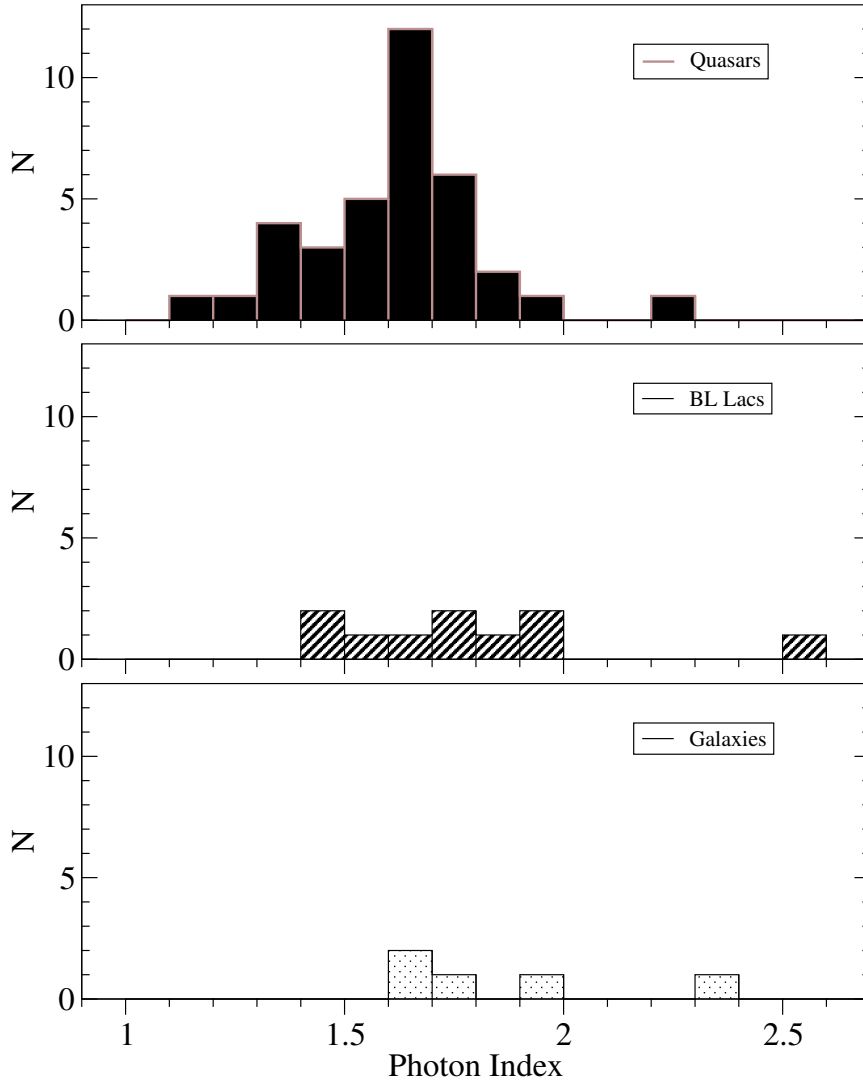
Figure 4.2: Distribution of the photon indices of the hard-power-law components for quasars (top), BL Lac objects (middle) and galaxies (bottom) of the *2 cm-X-Sample.*

and $F_{soft-excess,max}^{(0.5-2.0)\,\mathrm{keV}} = 2.8 \times 10^{-11}\,\mathrm{erg\,cm^{-2}\,s^{-1}}$ in the (0.5–2.0) keV band and between $F_{soft-excess,min}^{(2.0-10.0)\,\mathrm{keV}} = 1 \times 10^{-14}\,\mathrm{erg\,cm^{-2}\,s^{-1}}$ and $F_{soft-excess,max}^{(2.0-10.0)\,\mathrm{keV}} = 5 \times 10^{-11}\,\mathrm{erg\,cm^{-2}\,s^{-1}}$ in the (0.5–2.0) keV band. The hard-power-law components, on the other hand, exhibit distinct albeit broad maxima around $\langle F_{hard-PL}^{(0.5-2.0)\,\mathrm{keV}} \rangle = 10^{-12}\,\mathrm{erg\,cm^{-2}\,s^{-1}}$ and $\langle F_{hard-PL}^{(2.0-10.0)\,\mathrm{keV}} \rangle = 3 \times 10^{-11}\,\mathrm{erg\,cm^{-2}\,s^{-1}}$ in the two bands, respectively, with dispersions of about half a magnitude in both bands. The hard-power-law components show a clear cut-off in the harder band at $F_{hard-PL,min}^{(2.0-10.0)\,\mathrm{keV}} = 7 \times 10^{-13}\,\mathrm{erg\,cm^{-2}\,s^{-1}}$ which is most likely a selection effect related to the need for sufficiently high X-ray fluxes in the (2.0-10.0) keV band for hard-X-ray spectroscopy.

For comparison of the different source types, the X-ray flux distributions of the hard-power-law components detected in quasars, BL Lac objects and galaxies is shown in Fig. 4.5. K-S tests find low probabilities that the distributions are drawn from the same
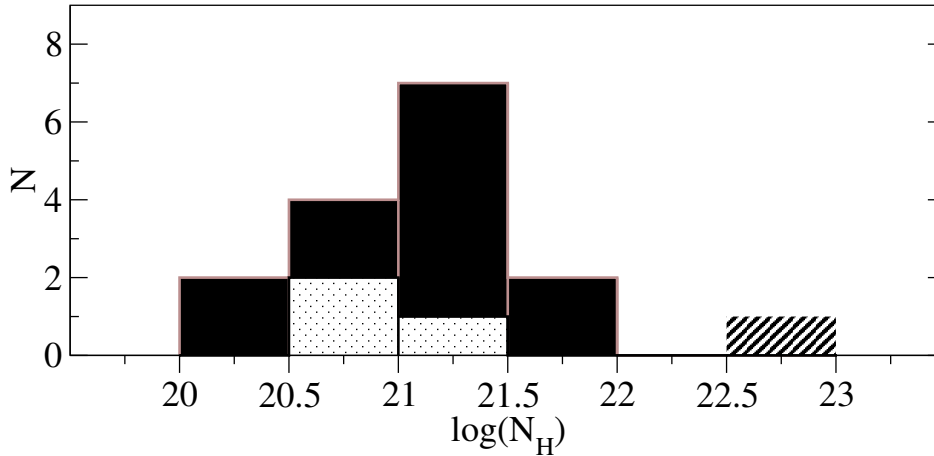
Figure 4.3: Distribution of the detected absorbing column densities in excess over the Galactic value for quasars (filled), BL Lac objects (hatched) and galaxies (dotted) in source of the *2 cm-X-Sample* where no intervening systems are known.
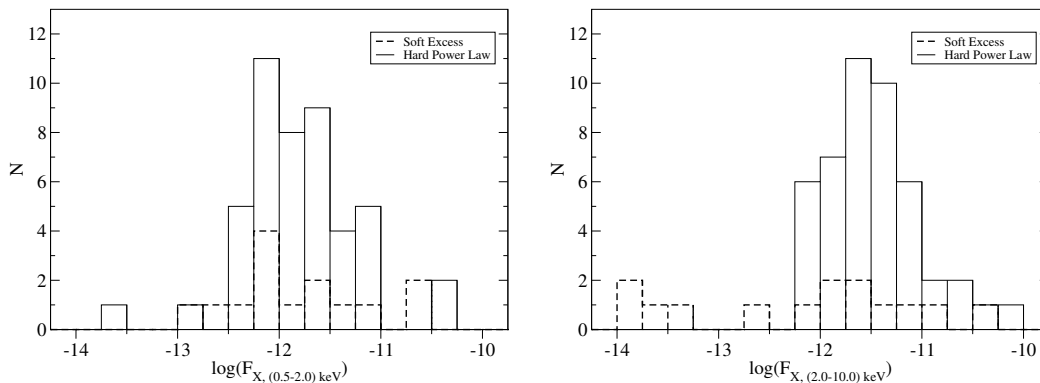
Figure 4.4: Distribution of absorption-corrected X-ray fluxes of soft-excess components and hard-power-law components of the sources of the *2 cm-X-Sample* in the (0.5–2.0) keV band (left) and in the (2.0–10.0) keV band (right).

parent population[3].

The luminosity distributions of the detected soft-excess components and the hard-power-law components are shown in Fig. 4.6. The soft-excesses and the hard-power-law components have different luminosity distributions with only 22 % and 3 % probabilities of being drawn from the same parent distribution for the (0.5–2.0) keV and (2.0–10.0) keV bands, respectively. A comparison of Figure 4.5 and Figure 4.7 shows that the X-ray brightness of galaxies is a distance effect. These sources are located at, on average, much lower redshifts compared to the BL Lacs and quasars and their luminosities are in fact

---

[3]The probabilities for a common parent population are 68 % and 38 % for the comparison of the quasars and the BL Lac objects in the (0.5–2.0) keV band and the (2.0–10.0) keV band, respectively, 0.7 % and 0.1 % for the quasar–galaxy comparisons, and 0.1 % and 2 % for the comparison of BL Lacs and galaxies.
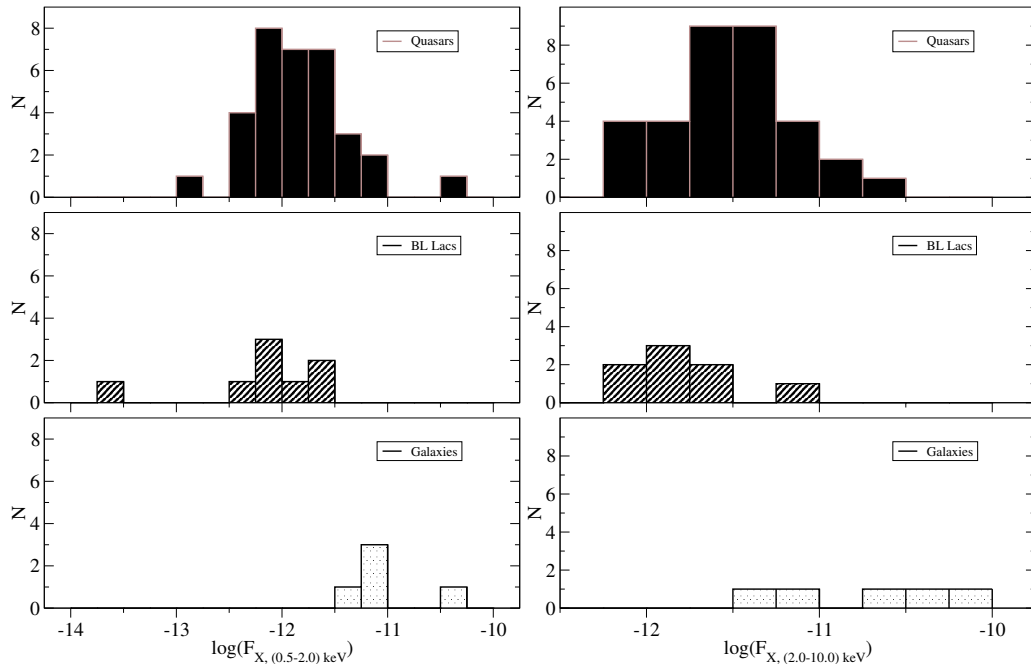
Figure 4.5: Distribution of absorption-corrected X-ray fluxes of the hard-power-law components of the sources of the *2 cm-X-Sample* in the (0.5–2.0) keV band (left) and in the (2.0–10.0) keV band (right) for quasars (filled, top), BL Lac objects (hatched, middle) and galaxies (dotted, bottom).
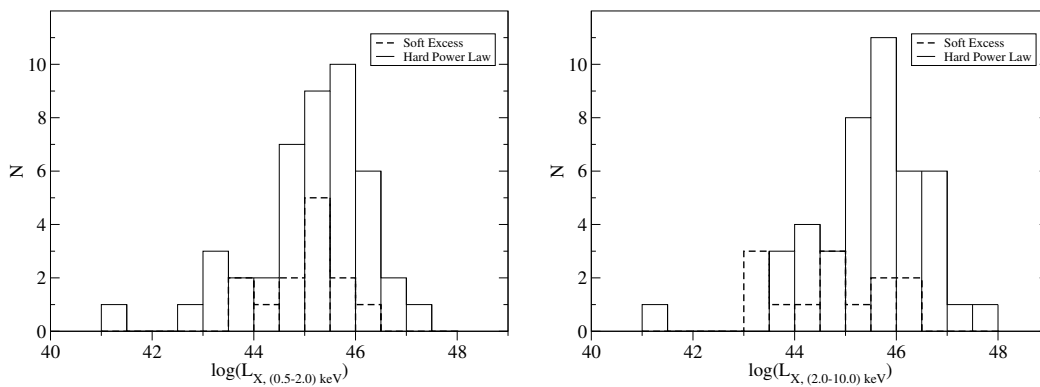
Figure 4.6: Distribution of X-ray luminosities of soft-excess components and hard-power-law components of the sources of the *2 cm-X-Sample* in the (0.5–2.0) keV band (left) and in the (2.0–10.0) keV band (right).
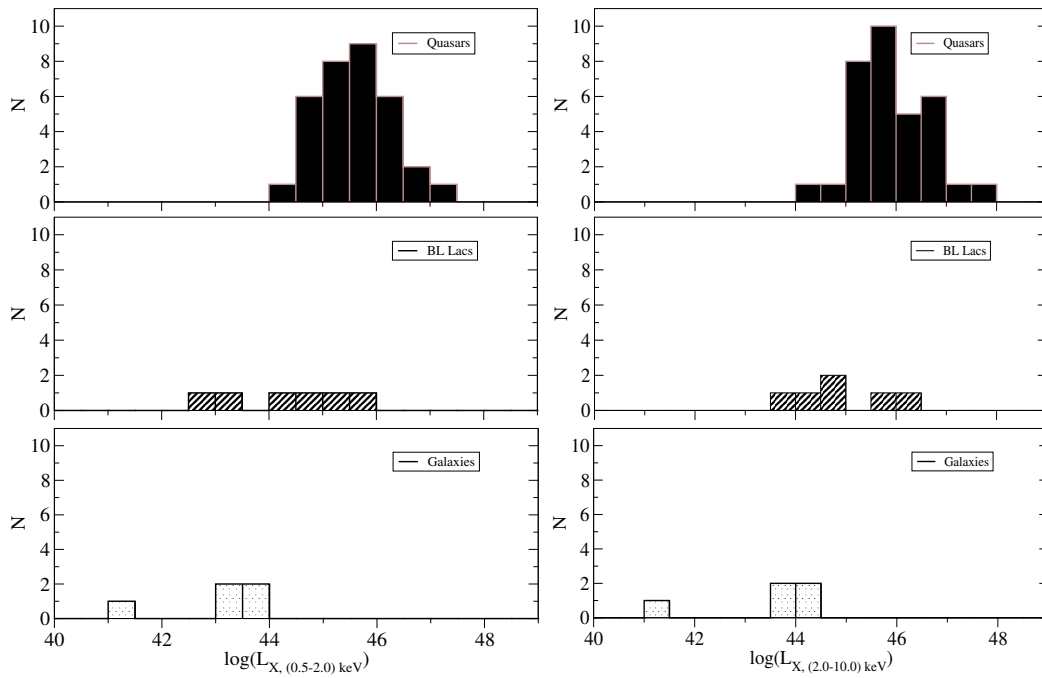
Figure 4.7: Distribution of X-ray luminosities of hard-power-law components of the sources of the *2 cm-X-Sample* in the (0.5–2.0) keV band (left) and in the (2.0–10.0) keV band (right) for quasars (filled, top), BL Lac objects (hatched, middle) and galaxies (dotted, bottom).
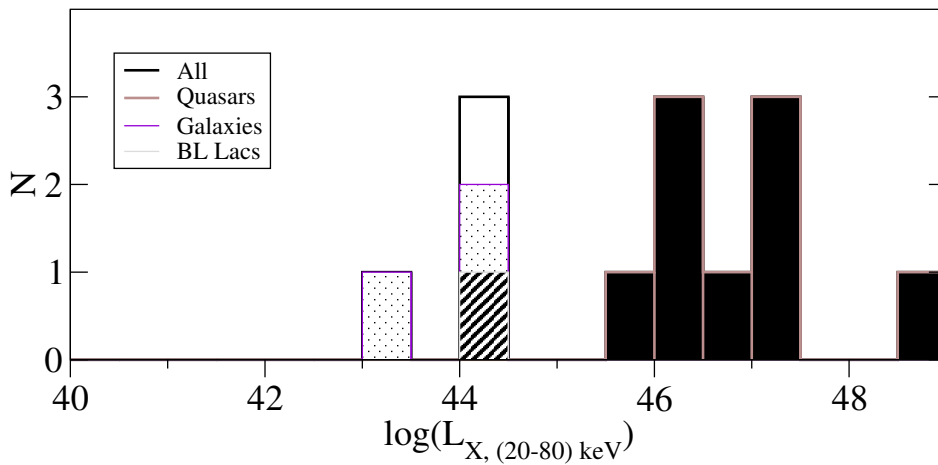
Figure 4.8: Distribution of X-ray luminosities of hard-power-law components of the sources of the *2 cm-X-Sample* detected in the in the (20–80) keV band for quasars (filled, top), BL Lac objects (hatched, middle) and galaxies (dotted, bottom).

substantially lower than the ones of the other two classes of objects. Although the number of BL Lacs with measured luminosities small[4], their luminosity distribution appears to be shifted to lower values with respect to the quasar distribution and no clear peak is visible. In fact, K-S tests find only 10 % and 3 % probabilities that both distributions are intrinsically the same.

At energies above 12 keV, the PDS detector onboard *Beppo*Sax yielded data for 15 sources. In nine cases, *Beppo*Sax failed to detect the source in any pointing with the PDS detector. In three cases (0716+714, 3C 279, and BL Lac) a detection occurred in some of the multiple pointings on those sources but not in all (compare Table 4.1) most likely due to source variability. Reflecting the limited sensitivity of the PDS detector, no (20-80) keV fluxes below $7 \times 10^{-12}\,\mathrm{erg\,s^{-1}\,cm^{-2}}$ are found among the sample sources. The luminosity distribution in Fig. 4.8 shows that the PDS-detected quasars are much more luminous in this band than the BL Lacs and the galaxies.

4.1.5 Trends with luminosity

No strong trends with the luminosity of the soft-excess component are found for the soft-excess and hard-power-law photon indices (see Fig. 4.9). However, the inspection of the $\Gamma_{\mathrm{hard-PL}}$–$L_{\mathrm{soft-excess}}$ plane shows that sources in which a soft-excess component is detected do exhibit a flatter hard-power-law slope than the average value over the full sample. The average hard-power-law photon index for those sources with a soft excess is 1.5 ± 0.2, about ~ 0.2 flatter than the overall average value for the *2 cm-X-Sample*.

A weak correlation is found between the slope of the hard power-law component $\Gamma_{\mathrm{hard-PL}}$ and the hard-power-law luminosity. Figure 4.10 shows a slightly decreasing trend of $\Gamma_{\mathrm{hard-PL}}$ with increasing $L_{\mathrm{hard-PL}}$ in the three different bands considered. A linear regression to the three relations in the $\Gamma_{\mathrm{hard-PL}}$–$L_{\mathrm{hard-PL}}$ plane yields very similar results. The correlation is not very strong with correlation coefficients of -0.44, -0.53, and -0.61 in the (0.5-2.0) keV band, the (2.0-10.0) keV band and the (20-80) keV band, respectively. The resulting values for the slopes of the three linear regressions are -0.09 ± 0.03, -0.01 ± 0.03, and -0.08 ± 0.03.

The detected absorbing column densities do not show any obvious trend with the luminosity of the hard-power-law component. The number of sources with a soft-excess and significant absorption over the Galactic value is too small to derive strong constraints on any possible correlation between $L_{\mathrm{soft-excess}}$ and N_{H}.

4.2 X-Ray Jets and Jet-Associated Extended Emission

About 50 % (26 out of 50) of the *2 cm-X-Sample* sources have been observed with *Chandra*. Among those, 14 sources exhibit extended jet-associated emission regions bright enough and far enough separated from the core emission for the extraction of spectra. The individual features are classified based on their X-ray morphology into I) jets (to the first order linear features which show a connection to the core), II) knots (distinct, unresolved regions isolated from the core or any associated jet), hotspots (unresolved regions

---

[4]0048–097 and 0716+714 have no well-established redshift measurements so that no luminosities could be obtained for these sources.
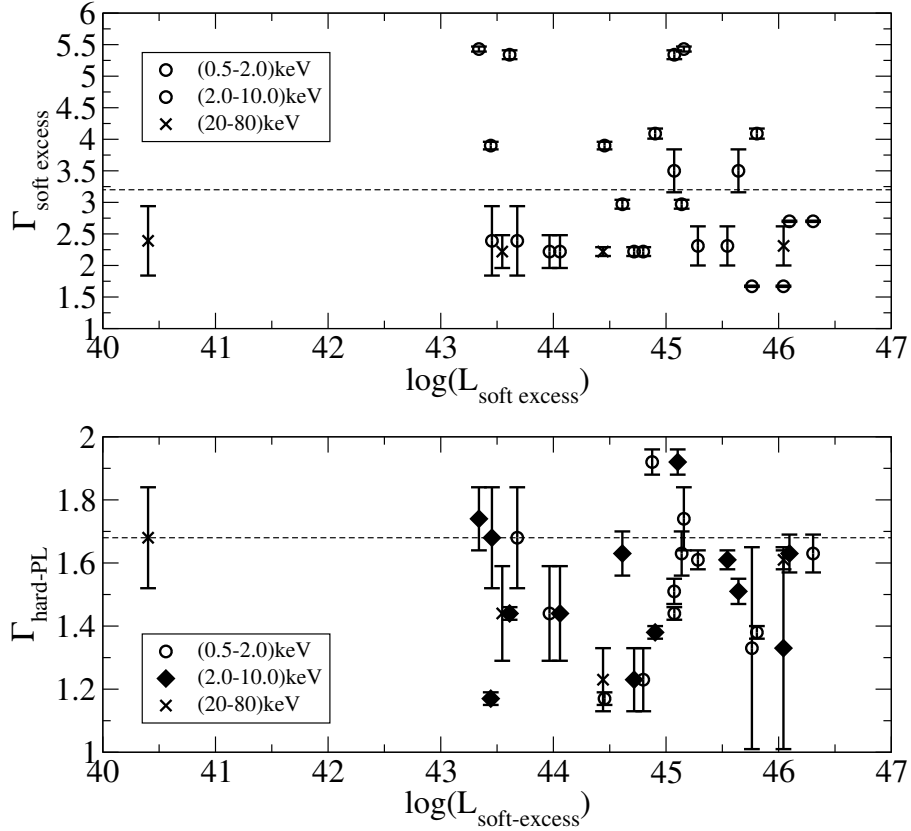
Figure 4.9: Soft-excess photon indices (top) and hard-power-law photon indices of the sources of the *2 cm-X-Sample* as a function of soft-excess X-ray luminosities. The dotted lines indicate the average soft-excess and hard-power-law photon index over the full sample.

being located beyond the end of a known radio jet), and jet-associated halos (extended, diffuse emission being correlated with a known radio jet in extent and/or direction). According to this classification scheme, the sample contains eight X-ray jets (0605−085, 0738+313, 0827+243, 1127−145, 1226+023 (3C 273), 1228+126 (M 87), 1510−089, and 1928+738), four distinct knots (0430+052 (3C 120), 1228+126 (M 87), 1253−055 (3C 279), and 2251+158 (3C 454.3)), two hotspots (both in 1957+405 (Cygnus A)), and two jet-associated halos (0238−084 (NGC 1052) and 2200+420 (BL Lac)). An additional emission knot is found in the southwest of the 0605−085 nucleus which is associated with a foreground star (Sambruna et al. 2004).

The main purpose of the spectral analysis of the extended X-ray features of *2 cm-X-Sample* sources for this thesis is to provide a set of spectral characteristic parameters describing the X-ray emission on kiloparsec scales for comparison with the nuclear emission parameters. Therefore, it has not been attempted to identify all significant features, e.g., with automatic source-detection algorithms incorporated into the *Chandra* data analysis software, CIAO. In general, only distinct features that are apparent from the inspection of the raw photon images (see Fig. 4.11 and Fig. 4.11) yield enough photons to extract spectra of sufficient SNR to compare them to the nuclear X-ray spectra of the *2 cm-X-Sample.* In the case of the two detected jet-associated halos of NGC 1052 and BL Lac,
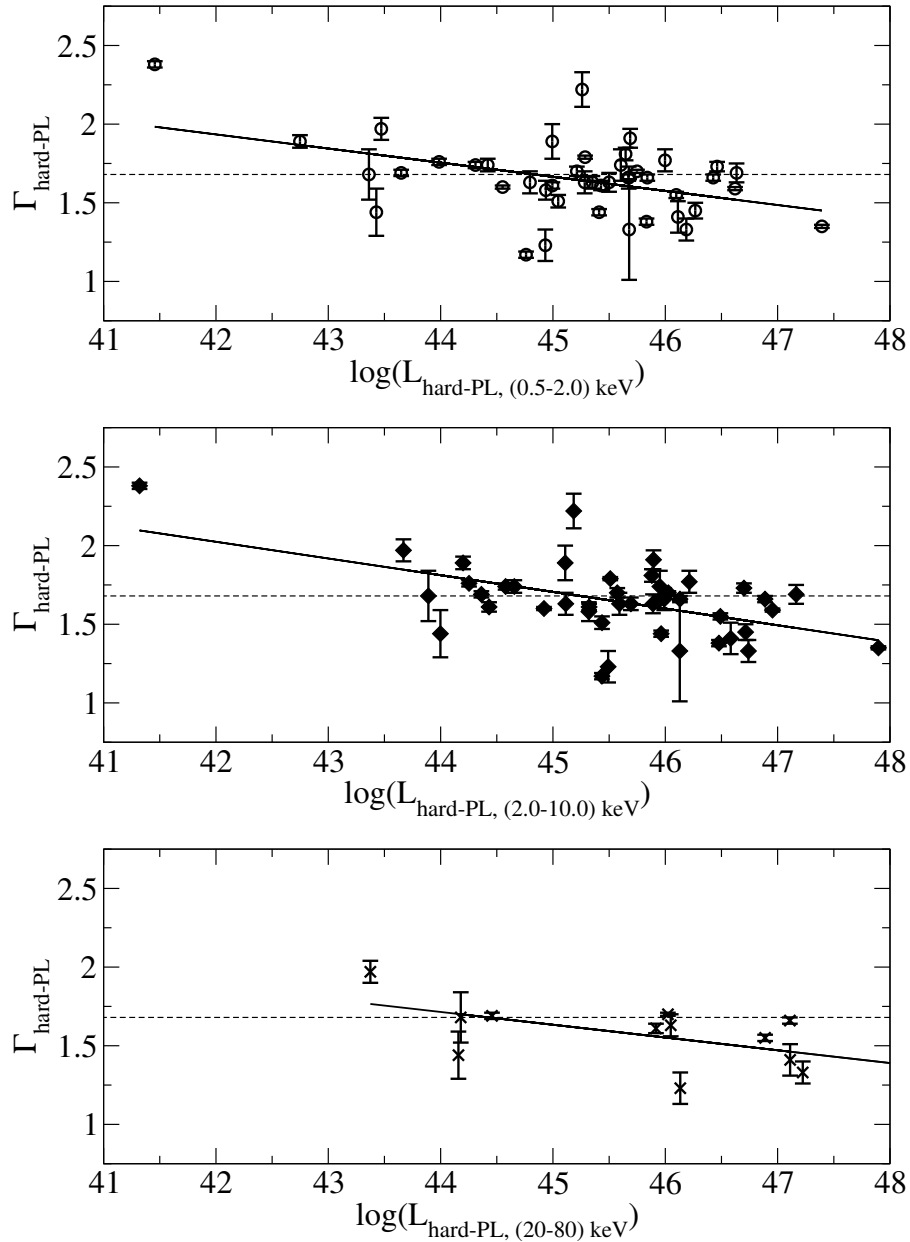
Figure 4.10: Hard-power-law photon indices of the sources of the *2 cm-X-Sample* as a function of hard-power-law X-ray luminosities in the (0.5-2.0) keV band (top), in the (2.0-10.0) keV band (middle) and in the (20-80) keV band (bottom). The dotted lines indicate the average hard-power-law photon index over the full sample and the solid lines represent a linear regression fit to the data sets.

the extended emission is diffuse and due to the short exposure times only weakly seen in raw photon images (compare Fig. 1 of Kadler et al. 2004a, reprinted in Sect. 6.3.2 and Fig. 4.12). In both cases, however, the extended emission is highly significant if an adaptive smoothing algorithm is applied, as apparent from Fig. 2 of Kadler et al. (2004a) and the right panel of Fig. 4.12.

More sophisticated detection methods of X-ray jets and associated extended features from *Chandra* observations of radio-loud AGN are applied by Sambruna et al. (2004) and Marshall et al. (2005). However, it shall be noted that the purely morphological identification and classification used here, clearly reveals four out of five of the *2 cm-X-Sample* sources in the list of Sambruna et al. (2004)[5] and two out of three *2 cm-X-Sample* objects among the twelve detected X-ray jets found by Marshall et al. (2005). With only seven objects in common with these two samples (and six sources in common between the Sambruna et al. 2004 and the Marshall et al. 2005 samples), nearly identical detection rates of extended jet-associated emission features are found: 59 %, 60 %, and 54 %, respectively. This is particularly remarkable because unlike the two other samples, the *2 cm-X-Sample* has not been selected based on the presence of a known bright kiloparsec-scale radio jet but on the milliarcsecond core properties.

X-ray spectra have been extracted from circles, annuli or rotated-box regions, depending on the shape of the emission region of the given feature (see Table 4.5 for region parameters). Appropriate background regions were selected, close to the source regions, free of contaminating sources and large enough to contain a significant number of background photons. In all cases, the background spectra were taken from the same observation as the source spectra and from the same chip. Spectral fitting was performed with the program XSPEC in the 0.3 keV to 8.0 keV band, as described in Sect. 3.5. In each case, a power-law model with Galactic absorption was used to approximate the measured spectral distribution. The results of the spectral fitting are given in Table 4.5.

As for the nuclear spectra, mean values for the photon index and the fluxes of the individual detected features in the $(0.5 - 2.0)$ keV and $(2.0 - 10.0)$ keV bands have been determined in all cases of multiply observed sources. The errors are calculated as described above for the nuclear spectra. The resulting mean spectral parameters of the investigated jet-associated extended emission features are given in Table 4.6.

In Fig. 4.14, the distribution of photon indices is shown for all extended X-ray features investigated and for the X-ray jets and knots, separately. The full sample, exhibits a broad range of photon indices between 1.3 and 3.8, with an average value of $\Gamma_{\text{extended}} = 1.8 \pm 0.6$, however, it has to be noted that the distribution is clearly non-Gaussian. It peaks at flat photon indices ≤ 1.4 and shows a broad tail towards steeper values. The extreme case of NGC 1052 with a photon index of 3.8 is better described via a thermal plasma emission model, rather than a steep power law (Kadler et al. 2004a). The exclusion of the jet-associated halos and hotspots, formally reduces the standard deviation of the distribution. Considering only the jets and knots, an average photon index of $\Gamma_{\text{jets+knots}} = 1.7 \pm 0.3$ is found. The reduced distribution is dominated by the smallest bins, peaking around 1.4 and extending up to 1.7–1.9. The only two remaining exceptions are M 87 and 1928+738 with values of 2.40 ± 0.05 and 2.2 ± 0.5, respectively. These findings are consistent with the results of Sambruna et al. (2004), who find an average photon index of 1.5 ± 0.2 for

---

[5]The X-ray jet of 1641+399 (3C 345) is visible as a weak extension of the core towards the north-west but was not bright enough and not sufficiently separated from the core to derive a spectrum.

their sample.

In Fig. 4.14, the distribution of the average luminosities of the investigated jet-associated extended X-ray emission features are shown. The jets and knots are more luminous, on average, than the hotspots and jet-associated halos, with the full distribution range of $\sim (10^{39} - 10^{45})\,\mathrm{erg\,cm^{-2}\,s^{-1}}$ in the $(0.5 - 2.0)\,\mathrm{keV}$ and $(2.0 - 10.0)\,\mathrm{keV}$ bands.

Table 4.5: X-Ray Jet Spectral Fit Results

Source[*]	M[*]	Obs. Date[†]	Sequence	$\Gamma^{\ddagger}$	$F_1^{\diamond}$	$F_2^{\clubsuit}$	χ_{red}	$d.o.f.$
0238−084	J/Halo^{I}	2000-08-29	884	$3.8^{+0.6}_{-0.7}$	9.4	1.1	0.52	22
0430+052	K^{II}	2001-09-18	1613	$1.57^{+0.09}_{-0.14}$	11.1	24.5	0.49	14
0430+052	K$^{II,\mathrm{a}}$	2001-12-21	3015	$1.41^{+0.12}_{-0.09}$	8.2	23.9	0.70	13
0605−085	J$_{\mathrm{E}}^{III,\mathrm{b}}$	2001-05-01	2132	$1.43^{+0.38}_{-0.35}$	3.0	10.3	1.13	6
0605−085	K$_{\mathrm{S}}^{IV,\mathrm{b}}$	2001-05-01	2132	$2.21^{+0.67}_{-1.10}$	3.7	3.1	1.74	2
0738+313	J$^{V,\mathrm{b}}$	2000-10-10	377	$1.43^{+0.76}_{-0.77}$	0.6	1.7	0.95	5
0827+243	J$^{VI,\mathrm{a}}$	2002-05-07	3047	$1.53^{+0.27}_{-0.24}$	2.1	4.9	0.76	6
1127−145	J$^{VII,\mathrm{a,c}}$	2000-05-28	866	$1.62^{+0.18}_{-0.16}$	2.1	4.4	0.39	13
1226+023	J^{VIII}	2000-01-09	1198	$1.85^{+0.09}_{-0.08}$	39.6	51.0	1.38	30
1226+023	J^{VIII}	2000-01-10	459	$2.02^{+0.12}_{-0.12}$	39.7	41.5	1.09	24
1226+023	J^{VIII}	2000-06-14	1711	$1.82^{+0.05}_{-0.04}$	36.6	55.4	1.10	118
1226+023	J^{VIII}	2000-06-14	1712	$1.83^{+0.04}_{-0.04}$	37.0	55.8	1.03	120
1226+023	J^{VIII}	2001-06-13	2463	$1.79^{+0.11}_{-0.13}$	29.7	47.3	1.35	14
1226+023	J^{VIII}	2001-06-13	2464	$1.83^{+0.12}_{-0.10}$	43.4	65.5	1.28	23
1226+023	J^{VIII}	2001-06-15	2471	$1.95^{+0.16}_{-0.15}$	42.4	52.7	0.40	20
1226+023	J^{VIII}	2002-06-04	3574	$1.95^{+0.15}_{-0.13}$	43.5	54.5	1.23	18
1226+023	J^{VIII}	2002-06-05	3456	$1.81^{+0.10}_{-0.12}$	35.7	54.9	0.88	14
1226+023	J^{VIII}	2002-06-05	3457	$1.87^{+0.16}_{-0.10}$	34.7	49.1	1.80	14
1226+023	J^{VIII}	2002-06-06	3573	$1.80^{+0.12}_{-0.08}$	38.3	59.7	0.62	18
1226+023	J^{VIII}	2003-07-07	4430	$1.94^{+0.15}_{-0.09}$	40.7	51.4	0.87	16
1226+023	J^{VIII}	2003-07-07	4431	$1.77^{+0.14}_{-0.11}$	39.7	65.6	0.83	17
1226+023	J^{VIII}	2003-11-24	4876	$1.84^{+0.04}_{-0.04}$	39.3	58.0	1.30	140
1226+023	J^{VIII}	2004-02-10	4877	$1.81^{+0.04}_{-0.04}$	39.5	60.8	1.11	136
1226+023	J^{VIII}	2004-06-30	5169	$2.00^{+0.12}_{-0.08}$	44.4	51.5	0.92	18
1226+023	J^{VIII}	2004-06-30	5170	$1.96^{+0.16}_{-0.12}$	41.9	51.9	0.73	17
1228+126	J$^{IX,\mathrm{d,e}}$	2000-04-15	517	$2.32^{+0.11}_{-0.10}$	983.9	709.0	1.01	61
1228+126	J$^{IX,\mathrm{d,e}}$	2000-04-20	351	$2.86^{+0.17}_{-0.18}$	588.1	190.7	0.99	31
1228+126	J$^{IX,\mathrm{e}}$	2000-07-17	241	$2.75^{+0.08}_{-0.08}$	179.4	69.1	1.39	61
1228+126	J$^{IX,\mathrm{e}}$	2000-07-29	352	$2.37^{+0.03}_{-0.03}$	152.9	101.8	2.56	167
1228+126	J$^{IX,\mathrm{e}}$	2000-07-30	1808	$2.52^{+0.04}_{-0.04}$	173.4	92.9	1.48	124
1228+126	J$^{IX,\mathrm{e}}$	2002-01-16	3085	$2.55^{+0.07}_{-0.07}$	175.6	90.3	1.45	82
1228+126	J$^{IX,\mathrm{e}}$	2002-02-12	3084	$2.50^{+0.07}_{-0.07}$	170.3	94.3	1.28	78
1228+126	J$^{IX,\mathrm{e}}$	2002-03-30	3086	$2.50^{+0.08}_{-0.08}$	164.8	91.6	1.30	76
1228+126	J$^{IX,\mathrm{e}}$	2002-06-08	3087	$2.49^{+0.07}_{-0.07}$	166.6	93.3	1.56	77
1228+126	J$^{IX,\mathrm{d,e}}$	2002-07-05	3717	$2.30^{+0.04}_{-0.04}$	142.9	106.1	1.61	143
1228+126	J$^{IX,\mathrm{d,e}}$	2002-07-06	2707	$2.32^{+0.03}_{-0.01}$	212.8	150.4	3.77	233
1228+126	J$^{IX,\mathrm{e}}$	2002-07-24	3088	$2.48^{+0.07}_{-0.08}$	172.5	97.6	1.21	74
1228+126	J$^{IX,\mathrm{e}}$	2002-11-17	3975	$2.49^{+0.06}_{-0.06}$	178.2	100.7	1.16	83
1228+126	J$^{IX,\mathrm{e}}$	2002-12-29	3976	$2.40^{+0.07}_{-0.07}$	176.1	113.3	1.81	71
1228+126	J$^{IX,\mathrm{e}}$	2003-02-04	3977	$2.43^{+0.07}_{-0.07}$	155.5	95.0	1.69	77

Table 4.5 – continued from previous page

Source[*]	M[*]	Obs. Date[†]	Sequence	Γ[‡]	F_1[◇]	F_2[♣]	χ_{red}	$d.o.f.$
1228+126	K[X,d,e]	2000-04-15	517	$2.52^{+0.14}_{-0.15}$	50.6	27.2	0.55	10
1228+126	K[X,d,e]	2000-04-20	351	$2.74^{+0.21}_{-0.29}$	175.2	67.7	0.77	10
1228+126	K[X,e]	2000-07-17	241	$2.83^{+0.11}_{-0.10}$	72.5	24.7	0.73	12
1228+126	K[X,e]	2000-07-29	352	$2.78^{+0.05}_{-0.05}$	53.7	19.6	1.49	91
1228+126	K[X,e]	2000-07-30	1808	$2.68^{+0.05}_{-0.05}$	72.0	30.6	1.88	57
1228+126	K[X,e]	2002-01-16	3085	$2.66^{+0.09}_{-0.10}$	77.8	33.9	1.12	21
1228+126	K[X,e]	2002-02-12	3084	$2.76^{+0.09}_{-0.11}$	73.3	27.6	1.41	19
1228+126	K[X,e]	2002-03-30	3086	$2.68^{+0.10}_{-0.10}$	70.5	29.7	2.30	19
1228+126	K[X,e]	2002-06-08	3087	$2.72^{+0.09}_{-0.09}$	71.2	28.6	1.05	20
1228+126	K[X,d,e]	2002-07-05	3717	$2.65^{+0.08}_{-0.05}$	128.7	57.0	1.29	52
1228+126	K[X,d,e]	2002-07-06	2707	$2.65^{+0.03}_{-0.03}$	53.0	23.5	1.58	138
1228+126	K[X,e]	2002-07-24	3088	$2.70^{+0.09}_{-0.10}$	73.8	30.2	0.89	19
1228+126	K[X,e]	2002-11-17	3975	$2.68^{+0.08}_{-0.09}$	69.4	29.5	2.08	20
1228+126	K[X,e]	2002-12-29	3976	$2.62^{+0.10}_{-0.11}$	71.6	33.4	1.43	19
1228+126	K[X,e]	2003-02-04	3977	$2.68^{+0.10}_{-0.10}$	67.4	28.7	2.70	19
1253−055	K[XI]	2002-03-21	2971	$1.36^{+0.05}_{-0.09}$	8.7	26.8	1.05	20
1510−089	J[XII,a]	2001-03-23	2141	$1.63^{+0.23}_{-0.19}$	6.2	12.7	0.50	9
1928+738	J[XIII,a]	2001-04-27	2145	$2.16^{+0.54}_{-0.37}$	3.3	3.0	0.28	2
1957+405	H$_{\mathrm{e1}}$[XIV,b]	2000-05-26	1707	$1.47^{+0.36}_{-0.18}$	5.1	13.2	0.82	13
1957+405	H$_{\mathrm{w1}}$[XV,b]	2000-05-26	1707	$1.99^{+0.54}_{-0.24}$	3.0	3.6	0.84	4
2200+420	J/Halo[XVI,b,f]	2000-01-07	843	$1.34^{+0.24}_{-0.19}$	14.8	50.7	0.25	6
2200+420	J/Halo[XVI,b,g]	2000-02-16	139	$1.32^{+0.31}_{-0.21}$	23.1	78.2	0.71	6
2251+158	K[XVII,b]	2002-11-06	3127	$1.76^{+0.77}_{-0.49}$	3.1	5.1	1.23	2

[*] B 1950.0 coordinates; [*] Morphology (J: Jet, K: Knot, H: Hotspot, J/Halo: jet-associated halo); [†] Date of the observation in yyyy-mm-dd format; [‡] Photon index; [◇] $(0.5 - 2.0)\,\mathrm{keV}$ flux in units of $10^{-14}\,\mathrm{erg\,s^{-1}\,cm^{-2}}$, corrected for Galactic absorption; [♣] $(2.0 - 10.0)\,\mathrm{keV}$ flux in units of $10^{-14}\,\mathrm{erg\,s^{-1}\,cm^{-2}}$, corrected for Galactic absorption; [I] Circular region with 10 arcsec diameter, north-west of the nucleus (compare Fig. 4.11); [II] Circular region with 4.3 arcsec diameter, east of the nucleus (compare Fig. 4.11); [III] Circular region with 4 arcsec diameter, south-west of the nucleus; associated with foreground star by Sambruna et al. (2004) and therefore not considered for further analysis; [IV] Rotated (38×8) arsec box region at $70°$ P.A., south-east of the nucleus (compare Fig. 4.11); [V] Circular region with 3.3 arcsec diameter, south of the nucleus (compare Fig. 4.11); [VI] Rotated (27.5×5.5) arsec box region at $135°$ P.A., north-east of the nucleus (compare Fig. 4.11); [VII] Circular region with 11.4 arcsec diameter, south-west of the nucleus (compare Fig. 4.11); [VIII] Circular region with 22 arcsec diameter, north-west of the nucleus (compare Fig. 4.11); [IX] Circular region with 3.3 arcsec diameter, north-west of the nucleus (compare Fig. 4.11), contained in VIII; [X] Circular region with 4 arcsec diameter, south-west of the nucleus (compare Fig. 4.11); [XI] Circular region with 6.5 arcsec diameter, south-east of the nucleus (compare Fig. 4.11); [XII] Circular region with 2.7 arcsec diameter, south of the nucleus (compare Fig. 4.11); [XIII] Circular region with 5.5 arcsec diameter, east of the nucleus (compare Fig. 4.11); [XIV] Circular region with 4 arcsec diameter, west of the nucleus (compare Fig. 4.11); [XV] Annulus region with 3 arcsec inner diameter and 30 arcsec outer diameter, surrounding the nucleus (compare Fig. 4.12); [XVI] Annulus region with 3 arcsec inner diameter and 30 arcsec outer diameter, surrounding the nucleus (compare Fig. 4.12); [XVII] Circular region with 5 arcsec diameter, north-west of the nucleus (compare Fig. 4.11); [a] 15 counts per grouping bin due to low SNR; [b] 9 counts per grouping bin due to low SNR; [c] adding extra absorption from source fit alters Γ to $1.82^{0.21}_{0.18}$; [d] pileup model applied; [e] 50 counts per grouping bin due to bright background; [f] adding extra absorption from source fit alters Γ to $1.49^{-0.18}_{+0.25}$; [g] adding extra absorption from source fit alters Γ to $1.48^{-0.32}_{+0.23}$

4.3 Notes on Individual Sources

The purpose of this section is threefold. First, peculiarities of the spectral fits to the individual spectra of the different source shall be reported to help the reader judging the individual results in the previous sections of this chapter. Second, a review of the relevant literature for each source shall be given as concise as necessary but at the same
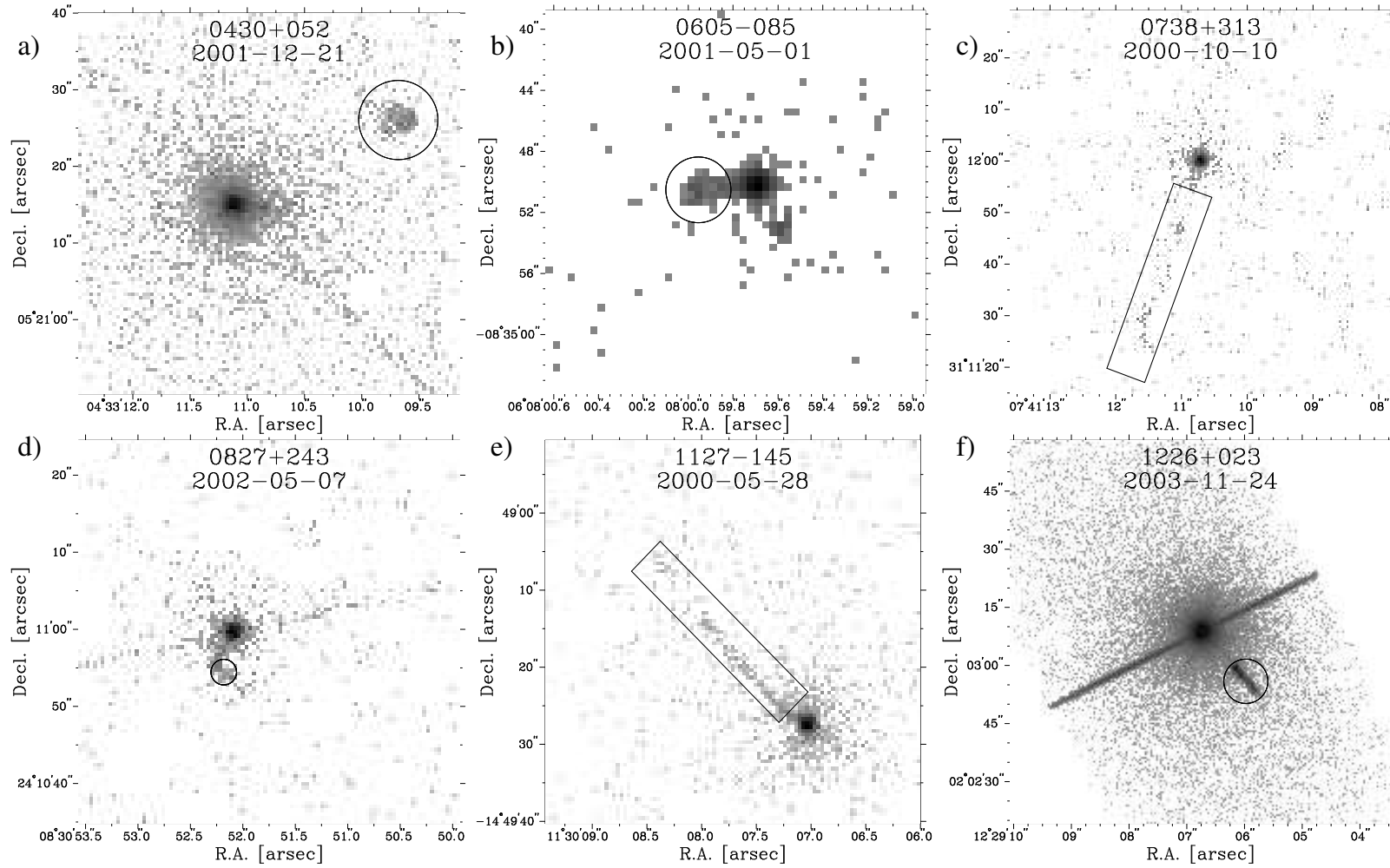
Figure 4.11: Raw *Chandra* $(0.3 - 8.0)$ keV photon images of the sources from the *2 cm-X-Sample* with jet-associated extended X-ray emission. The circles (box regions) indicate the regions over which spectra have been drawn. In the case of M 87 (a), the dotted circle indicates the region of a distinct knot, whose spectrum has been extracted in addition to the integrated jet spectrum.

a) 1228+126
2002-07-06

b) 1253-055
2002-03-21

c) 1510-089
2001-03-23

d) 1928+738
2001-04-27

e) 1957+405
2000-05-26

f) 2251+158
2002-11-06
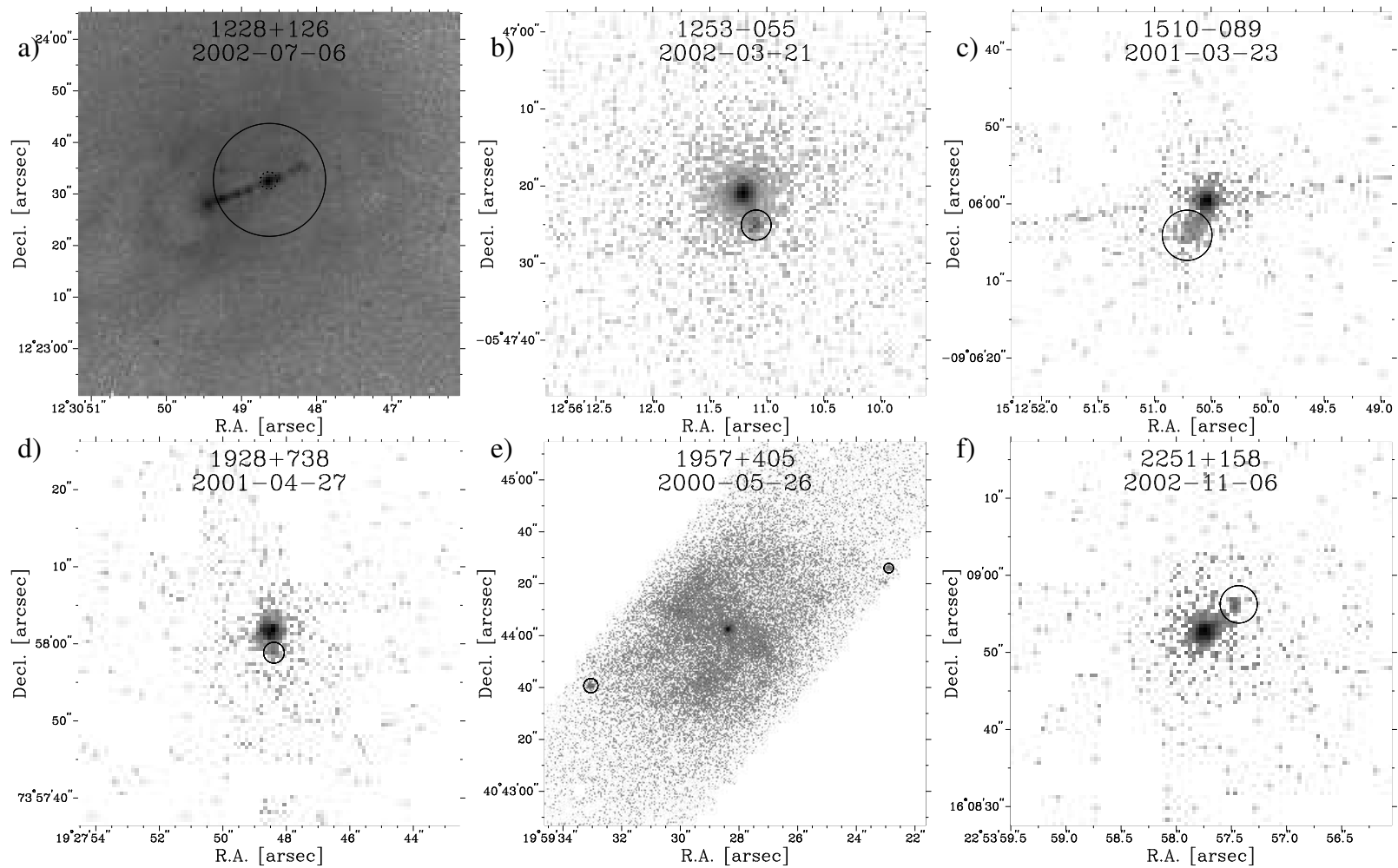
Figure 4.11: continued

Table 4.6: Mean spectral parameters for the extended jet-associated X-ray emission features of *2 cm-X-Sample* sources.

Source	M	N[a]	$\langle\Gamma\rangle$	$\Delta\langle\Gamma\rangle$	$\langle F_{(0.5-2.0)\,\mathrm{keV}}\rangle$ $[10^{-14}\,\mathrm{erg\,cm^{-2}\,s^{-1}}]$	$\Delta\langle F_{(0.5-2.0)\,\mathrm{keV}}\rangle$ $[10^{-14}\,\mathrm{erg\,cm^{-2}\,s^{-1}}]$	$\langle F_{(2.0-10.0)\,\mathrm{keV}}\rangle$ $[10^{-14}\,\mathrm{erg\,cm^{-2}\,s^{-1}}]$	$\Delta\langle F_{(2.0-10.0)\,\mathrm{keV}}\rangle$ $[10^{-14}\,\mathrm{erg\,cm^{-2}\,s^{-1}}]$
0238−084	J/Halo	1	3.80	0.65	9.4	1.9	1.1	0.2
0430+052	K	2	1.48	0.10	9.5	2.2	24.5	4.9
0605−085	J	1	1.43	0.37	4.0	0.8	3.0	0.6
0738+313	J	1	1.43	0.77	1.0	0.2	2.0	0.4
0827+243	J	1	1.53	0.25	2.0	0.4	5.0	1.0
1127−145	J	1	1.62	0.17	2.0	0.4	4.0	0.8
1226+023	J	17	1.84	0.03	666.0	202.1	928.0	281.6
1228+126	J	15	2.40	0.05	3792.0	1163.9	2196.0	674.5
1253−055	J	1	1.36	0.07	9.0	1.8	27.0	5.4
1510−089	J	1	1.63	0.21	6.0	1.2	13.0	2.6
1928+738	J	1	2.16	0.45	3.0	0.6	3.0	0.6
1957+405	H_{e1}	1	1.47	0.27	5.0	1.0	13.0	2.6
1957+405	H_{w1}	1	1.99	0.39	3.0	0.6	4.0	0.8
2200+420	J/Halo	2	1.33	0.17	45.0	18.7	121.0	50.2
2251+158	K	1	1.76	0.63	3.0	0.6	5.0	1.0

[a] Number of *Chandra* observations.
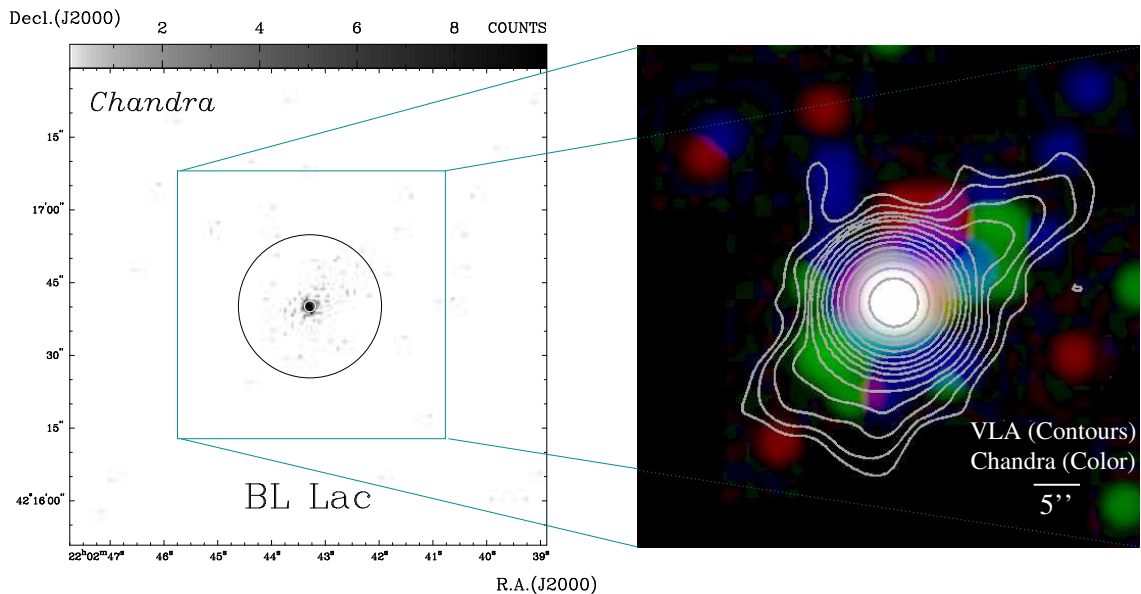
Figure 4.12: Extended X-ray emission associated with the radio jet of BL Lac. Left Panel: Raw *Chandra* photon image for the integrated energy range 0.3 keV to 8.0 keV from the 2000-01-07 2.1 ksec *Chandra* observation of BL Lac. The inner (white) and outer (black) circles indicate the annulus region from which the spectrum has been taken. Right Panel: Adaptively smoothed three-color coded *Chandra* image with radio contours superimposed. Red represents soft photons between 0.3 keV and 1.5 keV, green represents photons of medium energy between 1.5 keV to 2.5 keV and blue hard emission between 2.5 keV and 8 keV. The image has been adaptively smoothed to reveal extended structures of $3\,\sigma$–$5\,\sigma$ with a maximal allowed smoothing scale of $2''$. The radio contours have been adopted from Antonucci (1986).
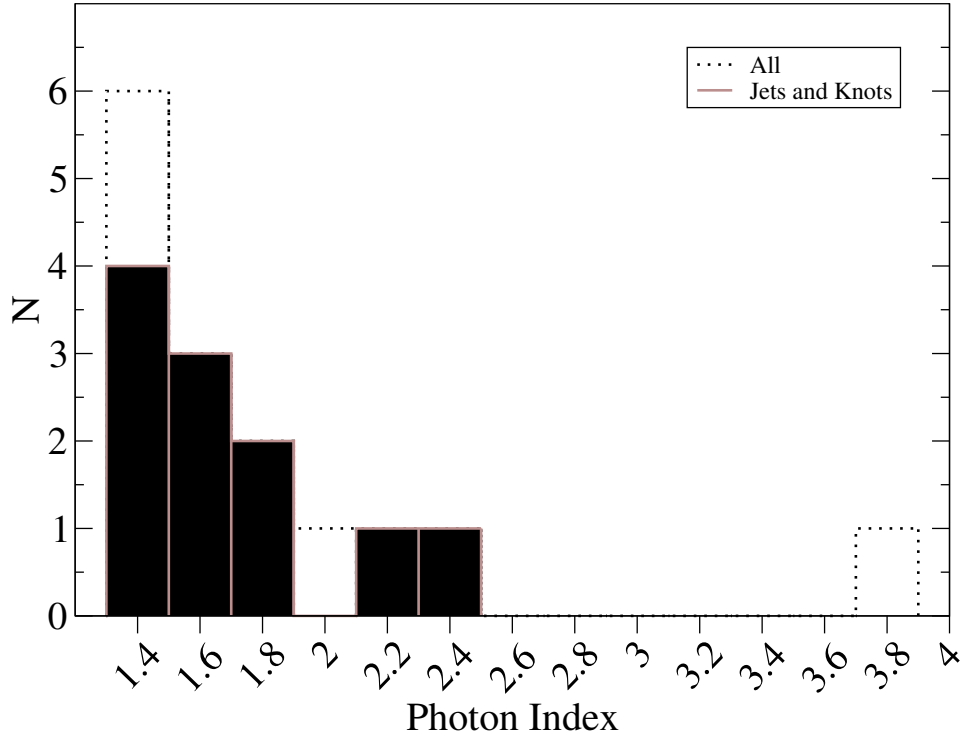
Figure 4.13: Distribution of the photon indices of jets, knots and other extended X-ray emission regions detected in *Chandra* observations of *2 cm-X-Sample* sources in the $(0.5 - 10.0)$ keV band.
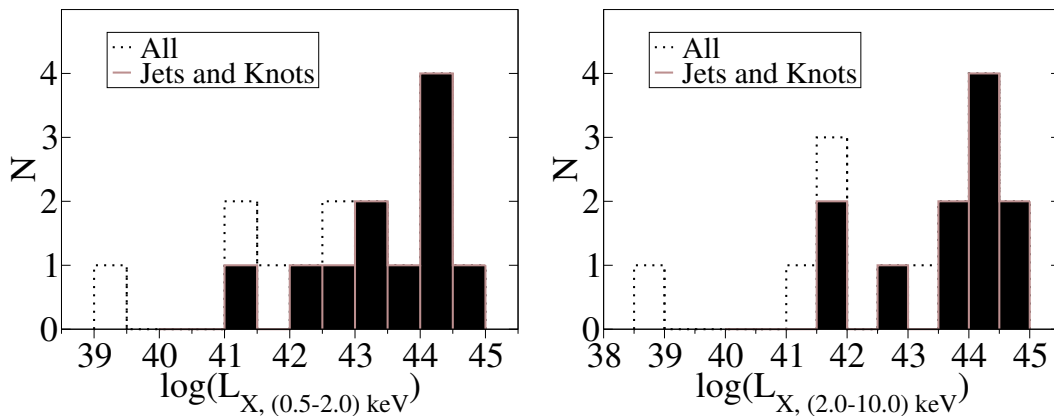
Figure 4.14: Distribution of the luminosities of jets, knots and other extended X-ray emission regions detected in *Chandra* observations of *2 cm-X-Sample* sources in the $(0.5 - 2.0)$ keV band (left panel) and in the $(2.0 - 10.0)$ keV band (right panel).

time as comprehensive as possible. These two intentions are not always compatible in view of the rich literature published on many individual sources, e.g., 3C 273. At least, each individual-source paragraph shall provide a starting point for a more complete literature search by providing references to published works that appear most relevant in the context of this thesis. Where available the X-ray spectral results shall be compared to previously published works. Relatively frequently, the results are not fully consistent and in some cases substantial differences are found. Such differences may be due to an improved calibration being available compared to the one at the time of writing of the corresponding work, to slightly or substantially different approaches in the spectral fitting procedure, or to the fact that in this work only three standard models are considered while more sophisticated spectral models may have been applied in publications dedicated to individual sources. The notes in this section shall highlight such inconsistencies, present explanations where such are obvious and refer to the corresponding works to allow the reader to compare the results directly. The third intention of this section is to collect new insights into the X-ray properties of the individual sources that have been gathered from the systematical study of the *2 cm-X-Sample* from previously unpublished data or from the uniform reanalysis of different observations at different epochs of the same source. In particular, results shall be highlighted that have a direct relevance for the general scientific context of this thesis related to the combination of radio and X-ray observational AGN research.

0007+106 — (aka III Zw 2) This X-ray bright Seyfert 1 galaxy has also been classified as a "radio-intermediate quasar" and shows correlated multiwavelength emission variability on long time scales ($\gg$ years) (Salvi et al. 2002). III Zw 2 has been observed by *ASCA* and *XMM-Newton* in July 1997 and July 2000 for ~ 44 ksec and ~ 15 ksec, respectively, exhibiting a point-like morphology to both telescopes. Both spectra are well fitted with simple absorbed power-law models at low signal-to-noise data grouping (25 counts per bin). Stronger grouping (200/250 counts per bin), however, reveals broad residuals, degrading the one-power-law fits, significantly. The *ASCA* data cannot distinguish between a two-power-law scenario ($\Gamma_1 = 2.4$, $\Gamma_2 = 1.3$) and a one-power-law plus broad-line scenario ($\Gamma = 1.7$, $E_{\mathrm{line}} = 6.99$ keV, $\sigma_{\mathrm{line}} = 1.1$ keV, $EW = 530$ eV). The *XMM-Newton* spectrum can be better fitted by a one-power-law plus broad-line model, yielding a very broad slightly redshifted line at 6 keV in the source frame with an equivalent width of ~ 890 eV.

In the radio regime, III Zw 2 is the only Seyfert galaxy, which showed superluminal motion of jet components (Brunthaler et al. 2000), although this finding could not be verified by Ros (2004). This discrepancy is of importance since the result of Brunthaler et al. led Salvi et al. (2002) to waive their best-fitting power-law plus disk-line model because it implied an almost edge-on view of the nuclear disk, in conflict with the small angle between the jet and the line of sight in superluminal-jet systems.

0048–097 — See Sect. 6.1 for a detailed discussion of the VLBI structure of 0235+164, its long-term broadband variability characteristics, and its X-ray spectrum.

0235+164   — See Sect. 6.2 for a detailed discussion of the VLBI structure of 0235+164, its long- and short-term broadband variability characteristics, and its X-ray spectrum.

0238–084   — (aka NGC 1052) See Sect. 6.3 for a detailed discussion of the VLBI structure of NGC 1052, its large-scale radio and X-ray morphology, X-ray spectrum and a probe of the jet-disk coupling in this low-luminosity AGN.

0316+164   — (aka NGC 1275, M 84, core of the Perseus cluster [aka Abell 426]). The Perseus cluster is the X-ray brightest cluster in the sky in X-rays. An unprecedented variety of structural and spectral information on the gas distribution, the relation to the radio-jet structure, shocks and gas motions have been reported on from an analysis of the large-scale X-ray emission coming from the galaxy cluster (e.g., Fabian et al. 2000b, Fabian et al. 2003, Churazov et al. 2004). The AGN itself at the center of the Perseus cluster has been considerably less well studied. Ezawa et al. (2001) found the central, non-thermal power-law source to contribute less than 1 % of the total cluster flux in the 0.7 keV to 10 keV energy bands from the analysis of *ASCA* data. Nonthermal emission, attributed to the central AGN, was found earlier by Primini et al. (1981) from *HEAO 1* observations reporting a photon index of $\sim$ 1.9 in the 20 keV–50 keV band. A flatter photon index of $\sim$ 1.25 was found by Rothschild et al. (1981) based on *OSO 7* (Peterson 1973).

The analysis of 0316+164 in this work used model III for the low-angular resolution *ASCA*, *Beppo*Sax, and *XMM-Newton* data. For the spectra taken by *Chandra* from small (10 arcsec diameter) circular regions around the central point source, model I was found to approximate the data adequately (using the Davis (2001) pileup model in XSPEC). Consistently, photon indices in the range 1.8–2.5 were found with an average value of $\Gamma = 1.97 \pm 0.07$.

0333+321   — (aka NRAO 140) This object is remarkable because of its bright, spectrally flat (or at most moderately steep) X-ray emission (Marscher 1988) but without strong γ-ray emission (Maisack et al. 1996) on a flux level detectable with the Compton Gamma Ray Observatory (CGRO).

Maisack et al. (1996) discuss a steep spectrum at MeV energies as a likely reason for the γ-ray faintness of NRAO 140 rather than a spectral break at hard X-ray frequencies. Indeed, the *Beppo*Sax spectrum of NRAO 140 shows no hints of spectral steepening in the sub-MeV regime.

NRAO 140 location in the sky is at the edge of a molecular cloud associated with the Perseus complex. The significant amount of extra absorption over the Galactic value of neutral hydrogen of $1.26 \times 10^{21} \, cm^{-2}$ is likely to occur within our own Galaxy (compare Turner et al. 1995). Assuming $z = 0$, $N_{extra} = (1.63 \pm 0.10) \times 10^{21} \, cm^{-2}$ is derived, in remarkable agreement with a value of $N_{H_2} = 1.7 \times 10^{21} \, cm^{-2}$ of molecular gas derived by Bania et al. (1991). See also Turner et al. (1995) for a more comprehensive discussion of the absorption towards NRAO 140.

0415+379   — (aka 3C 111) See Sect. 6.4 for a kinematical 2 cm-study of this source on parsec scales. A comprehensive investigation of the *XMM-Newton* view of 3C 111 is

given by Lewis et al. (2005).

0420–014 — The analysis of the available *ASCA* data for 0420–014 yielded comparable results to the study by Reeves and Turner (2000) who analyzed the same data. The γ-ray bright source exhibits a comparatively steep X-ray spectrum with $\Gamma \sim 1.9$. Significant extra absorption exceeding the Galactic value by at least a factor of two seems to be present in the quasars frame.

0430+052 — (aka 3C 120) This source is is classified as a broad-line radio galaxy and belongs to the Fanaroff and Riley type I class of radio galaxies. A detailed study of the August 2003 deep *XMM-Newton* observation of 3C 120 has been presented by Ogle et al. (2005). In contrast to previous claims, this so far highest-SNR X-ray spectrum of this source shows no evidence for relativistically broadened wings of the iron emission line in the spectrum. The source exhibits strong soft excess, which Ogle et al. (2005) ascribe to a disk corona, and an excess absorbing column density of $N_{\mathrm{H}} = (1.0 - 1.6) \times 10^{21}\,\mathrm{cm}^{-2}$ in agreement with the result presented in this thesis derived from the application of model II.

Marscher et al. (2002) find ejections of VLBI jet components in 3C 120 to be preceded by dips in the (2.4–20) keV X-ray light curve along with a hardening of the X-ray spectrum. This result is derived from a long-term radio and X-ray monitoring campaign, combining radio flux density monitoring observations from the University of Michigan monitoring program, monthly to bimonthly VLBA observations and and weekly *RXTE* X-ray flux monitoring observations. This result is interpreted by Marscher et al. (2002) as a response of the radio jet to dynamical processes within the accretion flow of 3C 120, a connection previously established for microquasars (Mirabel and Rodriguez 1998). Although the physical processes that lead to an X-ray dip are not well understood at present, the result of Marscher et al. (2002) provides the most direct link between black-hole mass accretion and jet formation in AGN that has been found so far.

0458–020 — This source is a bright distant ($z = 2.291$) quasar detected at γ-rays by EGRET. There is a pronounced ($71°$) misalignment between the inner radio jet and the kpc-scale structure and a less pronounced misalignment between individual parsec-scale jet components at different distances from the core (Paragi et al. 2000 and references therein). 0458–020 is a member of a small sample of AGN located behind a high-redshift absorption system (Wolfe et al. 1986). The $z = 2.04$ absorber in the line of sight towards 0458–020 has a particularly high column density ($5 \times 10^{21}\,\mathrm{cm}^{-2}$; Wolfe et al. 1985) and is found to have a disk-like structure that extends over several kiloparsecs in size (Briggs et al. 1989).

To my best knowledge, the *Chandra* ACIS-S spectral data derived from the only broadband spectroscopic X-ray observation of 0458–020 has not been published elsewhere at the time of writing of this thesis. A simple absorbed power law yields a moderate fit quality with $\chi_{\mathrm{red}} = 1.3$ for 178 d.o.f., a relatively flat photon index of $\Gamma \sim 1.64$, and an extra amount of photoelectric absorption over the LAB value of $(4.4 \pm 0.8) \times 10^{21}\,\mathrm{cm}^{-2}$ and $(3.7 \pm 0.7) \times 10^{21}\,\mathrm{cm}^{-2}$ if the absorber is assumed to be located at the source redshift of $z = 2.286$ or at $z = 2.04$, respectively. This is in good agreement with the value de-

rived by Wolfe et al. (1985) of $5 \times 10^{21}\,\mathrm{cm}^{-2}$ from optical and radio measurements. The spectral fit can be improved by adding either a second power-law component, a thermal plasma, or a high-energy reflection component. The two-power-law model suffers from the unphysically steep photon index of the soft component ($\Gamma > 4$), while the power-law-plus-plasma model predicts a very flat photon index ($\Gamma < 1.5$). In view of the uncertainty of the continuum model, it was not attempted to model a residual excess at $\sim 2\,\mathrm{keV}$ which might represent the tentative imprint of an iron emission line.

0528+134 — This source is a powerful, distant ($z = 2.07$), γ-ray bright blazar with a high-energy peak located between 10 MeV and 100 MeV and a low-energy peak in the far infra-red to optical regime. The X-ray band covers roughly the minimum between both emission peaks. The *ASCA* data of 0528+134 was discussed by Sambruna et al. (1997). These authors test different combinations of local (i.e. Galactic) and distant absorbers at intermediate redshifts between 0 and 2.07. They show that even under the assumption of a purely local absorber, the derived column density still exceeds the Galactic value ($N_\mathrm{H} \sim 5 \times 10^{21}\,\mathrm{cm}^{-2}$). Ghisellini et al. (1999) analyzed the 8 epochs of *Beppo*Sax data for this source taken in early 1997 during a faint state of the source. In this state, the source exhibited a flatter spectral index than in 1994/1995 of $\Gamma \sim 1.5$. Due to the low count rate, the LECS data could not further constrain the amount of absorption. Ghisellini et al. (1999) further discussed the PDS data in detail, which lies significantly above the extrapolated MECS spectrum. They explain this excess by the presence of another hard-X-ray emitting source within the FoV of the PDS detector. Adopting this explanation, the PDS spectral data of 0528+134 was discarded in the here discussed analysis.

In this work, an average value of $N_\mathrm{H} = (2.92 \pm 0.36) \times 10^{21}\,\mathrm{cm}^{-2}$ is derived from the available *ASCA* and *Beppo*Sax data, assuming of a source-intrinsic origin of the extra-amount of absorption.

0605−085 — East of the bright unresolved core of 0605−085, a compact knot is visible in the *Chandra* ACIS-S image taken in May 2001 (see Fig. 4.11). Sambruna et al. (2004) compared the *Chandra* view of 0605−085 with the A-configuration VLA observed radio source structure. They find the X-ray emission to peak about half an arcsecond before the radio-jet peaks in brightness, although matching the general extent and position angle. These authors further identified the similarly bright southern knot as a foreground star.

The 0605−085 nucleus is unaffected of pile up and dominates the integrated source emission ($\sim$90% of the total flux). The spectral parameters remain stable within their 1–σ uncertainties independent of considering only the nuclear or the integrated emission but the statistical quality of the simple absorbed power-law fit is improved significantly when the jet- and star emission is discarded (χ_red decreased from 1.14 to 0.87 with the number of degrees of freedom decreasing from 46 to 39). The high-resolution *Chandra* data of 0605−085 thus provides a good example of how small-scale sub structure can affect the statistical quality of spectral fitting.

0716+714 — See Sect. 6.5 for a detailed analysis of the X-ray properties of 0716+714 and a kinematical analysis on parsec scales.

0735+178 — This source is a BL Lac object with unknown redshift (although an absorption system at $z = 0.424$ was found by Carswell et al. (1974), providing a lower limit for the source redshift). On parsec scales, 0735+178 exhibits one of the most extreme curved morphologies observed in AGN jets with possible highly superluminal motions and free-free absorbing regions (Kellermann et al. 1998a, Gómez et al. 1999, Gómez et al. 2001b, Gabuzda et al. 2001, Agudo et al. 2002). The basic parameters of its *ASCA* spectrum (assuming a pure power-law spectrum affected by fixed Galactic absorption) have been reported by Kubo et al. (1998). The $\sim 10\%$ smaller value derived from the LAB survey yields a slightly decreased photon index of $\Gamma = 1.74 \pm 0.06$. No significant amount of excess absorption over the LAB value was found and the data show no evidence for any further spectral component besides the primary power law.

0736+017 — The *ASCA* data of this flat-spectrum quasar was previously analyzed and discussed by Sambruna et al. (2000) focusing on the apparent discrepancy between the unusually steep soft X-ray spectrum observed by *ROSAT* in the (0.2–2.4) keV band and the flatter spectrum at medium X-ray energies. The *ASCA* spectrum of 0736+017 can well be represented by a simple absorbed power law with $\Gamma = 1.74 \pm 0.02$ with only tentative evidence for a small amount of extra absorption over the neutral Galactic value.

0738+313 — (aka OI 363) Siemiginowska et al. (2003) reported on the *Chandra* detection of a 200 kpc X-ray jet in the $z = 0.63$ quasar 0738+313. The re-analysis of these data yielded quasi-identical results to Siemiginowska et al. (2003) but was restricted to a simple absorbed power-law approximation of the integrated source emission with the absorber assumed to be located in the source frame. The possible influence of two distinct intervening absorption systems is discussed in Siemiginowska et al. (2003), as well as the spectral properties of the diffuse extended emission around the nucleus. The nucleus of 0738+313 dominates the integrated source emission and its spectrum can be represented by a power law with a photon index of $\Gamma = 1.55^{+0.03}_{-0.05}$, relatively unaffected of the redshift which is assumed for the absorber.

In April 2001, six months after the *Chandra* observation, 0738+313 was observed by *XMM-Newton*. The previously unpublished data derived from this 30 ksec observation suffered heavily from a strong proton flare that affected the complete duration of the integration. Conservative flagging criteria were applied to create a good-time interval (gti) file to filter only those time intervals during which the source count rate exceeded substantially the flare-dominated background count rate. This procedure resulted to a substantially decreased effective exposure time and in somewhat larger error bars than usual. Still, the *XMM-Newton* spectrum is characterized by a significantly steeper photon index than apparent from the *Chandra* spectrum of $\Gamma = 1.73^{+0.05}_{-0.04}$.

0827+243 — *Chandra* revealed a curved kiloparsec-scale X-ray jet in this $z = 0.941$ quasar (Jorstad and Marscher 2004). The reanalysis of these *Chandra* data for this thesis yielded a good approximation with a simple absorbed power-law model of the integrated source and the jet spectrum ($\Gamma_{\rm int} = 1.66^{+0.04}_{-0.02}$; $\Gamma_{\rm jet} = 1.5^{+0.3}_{-0.2}$).

0836+710 —*ASCA* observed 0836+710 on March 17, 1995. The resulting spectral data have been presented by Cappi et al. (1997). Due to the SIS detector degradation from late 1994 on, the source-intrinsic absorption reported there, may be instrumentally altered. In the reanalysis of the *ASCA* data of 0836+710, only the SIS data between 1.0 keV and 10 keV were considered, the range that is unaffected by the detector degradation. No excess absorption over the Galactic LAB value is found and the photon index is flatter than given by Cappi et al. (1997), $\Gamma = 1.34^{+0.02}_{-0.02}$. Tavecchio et al. (2000) report on the *Beppo*Sax spectrum of 0836+710 finding a high but poorly constrained absorbing column density of several times 10^{21} cm^{-2}, in agreement with the reanalysis of the same data for this thesis. The *Chandra* data of 0836+710 suffered from strong photon pileup. Applying the PILEUP[6] model in XSPEC, spectral parameters in agreement with Fang et al. (2001) are derived, who analyzed the (pileup unaffected) HETG *Chandra* spectrum. A smaller amount of absorption is found than given by Cappi et al. (1997) and Tavecchio et al. (2000), however, within the errors in agreement with the *ASCA* and *Beppo*Sax reanalysis in this thesis (compare Table 4.1). The *XMM-Newton* spectrum of 0836+710 obtained in April 2001 provides the X-ray spectral observation with the so far highest SNR for this object. A one-power-law model provides a good approximation of the data yielding an absorbing column density of $6.5^{+0.9}_{-0.8} \times 10^{20}$ cm^{-2}.

0851+202 — (aka OJ 287) See Sect. D.1 for a study of the radio jet kinematics on parsec scales in OJ 287.

OJ 287 has been observed twice by *Beppo*Sax and three times by *ASCA* between 1994 and 2001. The first *ASCA* epoch was discussed by Idesawa et al. (1997) and Kubo et al. (1998), the latter two by Isobe et al. (2001). Massaro et al. (2003) and Padovani et al. (2001) investigated the two *Beppo*Sax spectra of OJ 287 obtained in November 1997 and 2001. While the reanalysis performed for this work in general yielded results similar to those published works, a steeper photon index is found from the 2001 *Beppo*Sax epoch ($\Gamma = 1.77^{+0.06}_{-0.05}$) compared to the values of ~ 1.6 found for the other epochs, while Massaro et al. (2003) reported a much flatter spectrum ($\Gamma \sim 1.45$). This result can be reproduced if the LECS/MECS normalization factor is fixed to 1 during the fit. In view of the usual guidelines, however, the value presented in this work may be regarded as more reliable (although the fitted normalization factor of ~ 0.58 is somewhat outside the typical range of ~ 0.65 to ~ 1).

Bearing in mind the above mentioned uncertainty for the November 2001 epoch of X-ray spectral data of OJ 287, the photon index of this optically and radio highly variable object remained remarkably stable (and comparably flat) in time. On a time scale of 7 months, no strong X-ray variability is apparent, three years earlier the source was brighter by a factor of 3 in the 2 keV to 10 keV range, although the spectral shape was similar.

0923+392 — (aka 4C +39.25) This $z = 0.698$ quasar was observed by *ASCA* and *Chandra* in November 1998 and October 2002, respectively. The *ASCA* spectrum is very sensitive to changes in the considered energy range and on whether or not an additional absorption component besides the Galactic absorption is allowed or not. Model I invokes by default an extra absorber at the source frame, yielding a relatively steep photon index

---

[6]compare Davis 2001 where the 0836+710 spectrum is used as an example of pileup correction.

of ~ 1.88. This value is in agreement with the photon index derived by Sambruna et al. (2000) from a model with freely varied absorption at $z = 0$ (predicting $\sim 1 \times 10^{21}\,\mathrm{cm}^{-2}$). While the location of the extra absorber cannot be determined unambiguously, it shall be noted that this component is required statistically with an improvement of the fit with an F-test value of 6.37 corresponding to a 99.8% reliability.

The so far unpublished *Chandra* spectrum of 4C +39.25 exhibits a flatter slope than the *ASCA* spectrum, with $\Gamma_{Chandra} \sim 1.7$ and does not require any extra amount of absorption over the Galactic value if a simple absorbed power-law model is applied. The fit is statistically not good, mainly due to residuals around $2\,\mathrm{keV}$ that may be due to detector calibration uncertainties. However, a formal improvement is achieved by adding an additional soft component to the model (model II and III). A soft excess component in 4C +39.25 was already found by Sambruna et al. (2000) based on the combination of non simultaneous *ROSAT* and *ASCA* data.

1038+064 — (aka 4C +06.41) No X-ray spectral data in the (0.5–10.0) keV band have been published so far for this object. Two *ASCA* observations of 1038+064 have been performed in December 1996 and a deeper *XMM-Newton* observation took place in May 2003. Both *ASCA* spectra can be described adequately with model I although the photon indices derived are not fully consistent ($1.48^{+0.02}_{-0.02}$ and $1.65^{+0.09}_{-0.05}$, respectively). The *XMM-Newton* spectrum reveals a similarly flat photon index for a simple absorbed PL model with $\Gamma = 1.56^{+0.02}_{-0.01}$. The residuals are weak if the data are grouped to have 25 counts per bin. However a flattening at high energies is apparent from the visual inspection. Applying a stronger grouping (125 counts/bin) reveals this flattening to be significant and model II is found to improve the fit substantially (F-test value of 25.5 with a $10^{-10}\,\%$ probability of an improvement by chance). The slope of the second PL, however, is found to be highly inverted with $\Gamma = 0.43^{+0.05}_{-0.05}$. A competitive fit is achieved with a high-energy-reflection model. The power law in this model has a slope of $\sim= 1.6$. A modest reflection fraction < 0.8 is implied and a disk at a small angle to the line of sight $< 48°$.

Based on these findings, it is likely that 1038+064 exhibits one of the most pronounced disk-reflection X-ray spectra among all core-dominated, radio-loud AGN. X-ray continuum monitoring observations, similar to the *RXTE* observing program of 3C 120 (Marscher et al. 2002) or frequent X-ray spectroscopic observations with *XMM-Newton*, thus provide a high chance of being sensitive to dynamical processes within the accretion disk of this object. Additionally, 1038+064 has a bright compact radio core, resolved into a one-sided jet with VLBI. VLBA 2 cm Survey and MOJAVE observations between 1998 and 2004 reveal at least two distinct jet components traveling at speeds of 0.11 mas/yr and 0.46 mas/yr, respectively (M. Lister, priv. communication). Future coordinated X-ray and VLBI observations of this source may have a high potential to study the connection between the accretion disk and the parsec-scale jet.

1055+018 — The here presented fit to the *Chandra* data of 1055+018 is in general agreement with the results of Gambill et al. (2003). However, it shall be noted that Gambill et al. (2003) marks the source as affected by pile up and determines the spectrum from the wings of the PSF, while the reanalysis for this work did not show a significant difference between the spectrum extracted from the whole source region and any annulus

region that excludes the PSF core. The here presented spectrum is therefore extracted from the whole source region yielding an improved SNR.

1127−145   — This distant ($z = 1.187$) gigahertz-peaked spectrum quasar was found to exhibit a 300 kiloparsec X-ray jet (Siemiginowska et al. 2002). In addition, 1127−145 is peculiar because it is located behind an intervening ($z = 0.312$) absorbing system (Bechtold et al. 2001 and references therein). The three archival X-ray spectroscopic data sets of 1127−145 from *Chandra*, *Beppo*Sax and *XMM-Newton* observations, of which the latter has not been published before, have been analyzed. In all three epochs (between June 1999 and July 2002) the source showed a flat photon index ($\Gamma = 1.2 - 1.5$). Assuming the (significant) absorber to be located at $z = 0.312$, the associated column density is consistently determined to lie in the range $\sim 9 \times 10^{20}\,\mathrm{cm}^{-2}$ to $\sim 1.7 \times 10^{21}\,\mathrm{cm}^{-2}$.

The X-ray jet of 1127−145, resolved from the core emission by *Chandra* only, can be described by a $\Gamma \sim 1.6$ power law with only Galactic absorption. If the extra absorption is fixed to the value determined from the spectral fit to the integrated source emission, the jet spectrum appears steeper ($\Gamma \sim 1.8$).

1156+295   — (aka 4C +29.45) This γ-ray loud source was observed by *Chandra* in June 2000 with the ACIS-I detector in focus of the mirror assembly. The data from this deep-field 75 ksec pointing was analyzed by the CYDER survey group (Castander et al. 2003), focusing on the field properties, particularly the faint X-ray sources, with no special emphasis on 1156+295.

The X-ray spectrum of 1156+295 is dominated by compact emission with $\Gamma = 1.61 \pm 0.03$. No significant pile up affected the observation and the absorption is consistent with the Galactic value with any extra amount of absorption in the source frame below a value of $\sim 4 \times 10^{20}\,\mathrm{cm}^{-2}$.

1222+216   — A simple power-law fit to the previously unpublished *Chandra* spectrum of this γ-ray loud quasar provides no statistically satisfactory solution ($\chi_{\mathrm{red}} = 1.5$ at 200 d.o.f.), due to systematic broad residuals across the whole $0.3\,\mathrm{keV}$ to $8\,\mathrm{keV}$ range. The addition of a thermal plasma improves the fit but leaves broad, soft residuals that disappear only if the plasma elemental abundances are assumed to be highly sub solar. This virtually corresponds to a bremsstrahlung component of $kT \sim 0.58\,\mathrm{keV}$. Both models predict an unusually flat photon index of the power-law component of $\Gamma = 1.2 - 1.3$. A fit of similar statistical quality is achieved with a two-power-law model (model II), yielding rather extreme values for the two photon indices ($\Gamma_1 \sim 3.9$, $\Gamma_2 \sim 1.2$). Although, statistically slightly inferior to the two-power-law and bremsstrahlung-plus-power-law models, a high-energy reflection component can fit the spectrum well ($\chi_{\mathrm{red}} = 1.16$ at 198 d.o.f.) and yields physically reasonable parameters: $\Gamma \sim 1.7$, and a small angle of the reflection system to the line of sight of $< 45°$.

1226+023   — (aka 3C 273) This source is the prototypical quasar, identified in 1963 with a magnitude 13, "quasi-stellar object" by Hazard et al. (1963) and the redshift measured by Schmidt (1963) to be $z = 0.158$. It has been observed in the X-ray regime ever since the early beginning of this branch of astronomy. To the first order, the X-ray spectrum

of 3C 273 is found to be a featureless continuum. High-SNR observations during the last decade have revealed a variety of relatively low-amplitude broad and narrow spectral features though. In particular, a variable soft-excess component is found (see, e.g., Page et al. 2004 and references therein). An iron emission line has been detected in a number of observations with at least one report of a broad emission profile (Yaqoob and Serlemitsos 2000 and references therein). Recently, Grandi and Palumbo (2004) presented a long-term variability study of 3C 273 based on *Beppo*Sax data, decoupling the jet and accretion-flow related emission components.

For this thesis, a total of 47 *ASCA*, *Beppo*Sax, *Chandra*, and *XMM-Newton* spectra have been analyzed. In 31 spectra, model II fitted the data significantly better than model I, revealing a soft-excess component. The average photon index of the soft-excess component is $\Gamma_{\mathrm{soft-excess}} = 2.3 \pm 0.3$ and the hard-power-law component has an average photon index of $\Gamma_{\mathrm{hard-PL}} = 1.61 \pm 0.03$ close to the average value over the full *2 cm-X-Sample*.

1228+126 — (aka M 87, core of the Virgo cluster) The active nucleus of M 87 is embedded in a bright soft X-ray emitting plasma. Distinct features within this diffuse emission region obviously result from a complex interaction of the M 87 jet and the surrounding thermal gas (e.g., Belsole et al. 2001 and references therein). To model the M 87 spectra from the "low-angular-resolution" instruments onboard *ASCA*, *Beppo*Sax, and *XMM-Newton* facilitates model III to account for this strong thermal emission component yielding consistent and reasonable values for the hard-power-law photon index in the range 2.3–2.5. The high angular resolution of *Chandra* allowed spatially resolved, background-subtracted nuclear spectra to be extracted. The *Chandra* source spectra were obtained from a circular region of 20 arcsec in size, containing the nucleus and the jet of M 87 (to allow the data to be compared with the low-resolution spectra). Background spectra were extracted from narrow annuli surrounding the source-extraction region. In good agreement with the *ASCA*, *Beppo*Sax, and *XMM-Newton* spectra, a hard power law is found (without strong distortions from the surrounding diffuse emission) with photon indices ~ 2.4 in all 15 *Chandra* observations of this source. The mean value over all 18 observations is $\Gamma_{\mathrm{hard-PL}} = 2.38 \pm 0.02$.

1253–055 — (aka 3C 279) 3C 279 has been observed 11 times with *ASCA* between 1993 and 1996, 5 times with *Beppo*Sax in 1997, and once with *Chandra* in 2002. The *Beppo*Sax data of 3C 279 has been previously analyzed by Ballo et al. (2002) and three *ASCA* observations of 3C 279 have been reported on by Kubo et al. (1998). In all cases, the spectrum was described sufficiently with model I with an average photon index of 1.70 ± 0.01.

Marshall et al. (2003) report the detection of an X-ray jet from the *Chandra* observation of 3C 279 in March 2002, that has been found independently in this study from the archival *Chandra* data and that is shown in Fig. 4.11.

1308+326 — Three archival X-ray spectroscopic observations of the high-redshift blazar 1308+326 were available for analysis for this thesis: two *ASCA* observations in June 1996 separated by only one day (see Watson et al. 2000) and one so far unpublished *XMM-Newton* observation in December 2002. Whether 1308+326 has to be classified as

a quasar or as a BL Lac object has been controversially discussed (see, e.g., Watson et al. 2000, Gabuzda et al. 1993 and references in these works): with an almost featureless optical spectrum, rapid variability and a high degree of optical polarization it exhibits typical BL Lac object peculiarities. Its FR II-like radio morphology, highly superluminal jet kinematics, high Doppler factor and an optical-UV excess over the IR continuum, however, are characteristics more typical for quasars.

The two *ASCA* observations of 1308+326 have been analyzed independently, yielding similar, albeit not within one σ coinciding spectral parameters. On June 10, the data suggested a comparatively steep spectrum ($\Gamma = 1.8 \pm 0.1$) and a relatively large amount of extra absorption in excess over the Galactic value ($N_{\mathrm{H}} = (7\pm4)\times10^{21}$ cm^{-2} assuming a source-intrinsic absorber at $z = 0.997$). The June 11 spectrum, however, can best be fitted with a flatter power law ($\Gamma \sim 1.5$) and shows no strong evidence for any extra absorption. Due to the limited sensitivity and spectral response of the *ASCA* detectors, however, the combined data of both observations can statistically sufficiently be approximated by a single model with intermediate parameters similar to the values reported by Watson et al. (2000): $\Gamma \sim 1.6$, and $N_{\mathrm{H}} \sim 3 \times 10^{21}$ cm^{-2} in the source frame, $\chi_{\mathrm{red}} = 0.85$ with 181 degrees of freedom.

The *XMM-Newton* data of 1308+326 represents a case of a serendipitous detection. The observation in December 2002 was pointed at the nearby cluster RXJ 1309.9+3222 and contained 1308+326 inside the FoV of the MOS and PN detectors. The source showed a similar spectral shape than in June 1996, although at a much higher flux level. It increased by a factor of $\sim$ in flux between 0.5 keV and 2 keV and by a factor of ~ 4.5 in the (2–10) keV range. The 2002 *XMM-Newton* spectrum can well be fitted by a simple power law with any extra absorption over the LAB survey measured Galactic neutral hydrogen value well below 10^{20} cm^{-2}. It further shows no evidence for a soft excess, reported by Watson et al. (2000) based on the analysis of combined non-simultaneous *ROSAT* data with the 1996 *ASCA* data.

1334−127   — The 14 ksec *XMM-Newton* observation of 1334−127 from January 2003 was not reported on in the literature so far. It yielded a featureless power-law spectrum, modified at low energies only by the absorption of Galactic material and a small amount of excess absorption. In the source frame, this extra absorption corresponds to a column density of $N_{\mathrm{H}} = 5.2^{+0.4}_{-0.6} \times 10^{20}$ cm^{-2}, assuming the extra absorption to take place at zero redshift, e.g., due to ionized or molecular material, yields a value of $N_{\mathrm{H}} = 2.7^{+0.2}_{-0.3} \times 10^{20}$ cm^{-2}. The extra absorber component is statistically highly significant, with an F-test value of 72.1, corresponding to a probability $> 99.9\,\%$. The coupling between the absorbing column density and the photon index is not very strong (see Fig. 4.15) and assuming a flatter photon index does not allow the extra absorption to drop below 3×10^{20} cm^{-2} in the source frame with 99 % probability.

1413+135   — This object provides the peculiar view of a bright, radio-loud, BL Lac-like AGN apparently hosted by a spiral galaxy. Perlman et al. (2002) investigated 1413+135 and its apparent host galaxy using *HST*, VLBA, and the same *ASCA* data as well analyzed for this thesis. The here derived high absorbing column density towards the X-ray nucleus of 1413+135 of $N_{\mathrm{H}} = (5.4^{+0.7}_{-0.6}) \times 10^{20}$ cm^{-2} is in rough agreement with the results
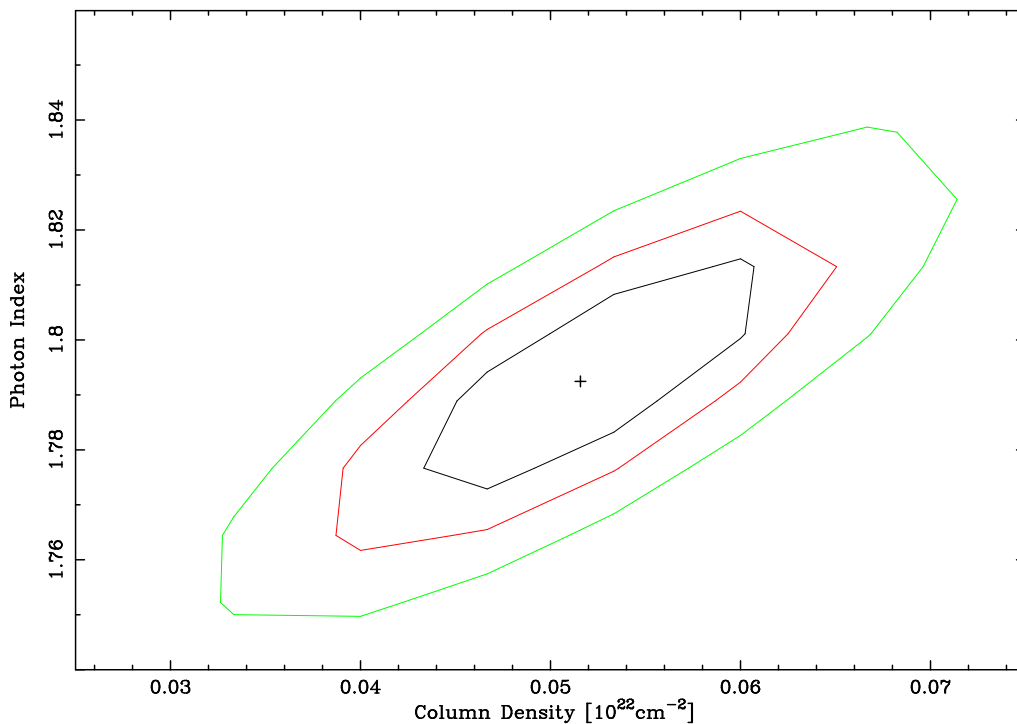
Figure 4.15: 90, 95 and 99 per cent confidence contours for the absorbing column density and the photon index of 1334−127 for the 2003, January 31 *XMM-Newton* spectrum.

of Perlman et al. (2002). Those authors point out that the absorber is unlikely to be located within the very inner region towards the nucleus of a BL Lac object like 1413+135, particularly because the *ASCA* data does not show evidence for strong reprocession features as, e.g., a strong iron line. Two alternative explanations are discussed: first, the absorber may be a molecular-cloud system within the host galaxy of 1413+135; second, the BL Lac object may in fact be a background object at higher redshift than the intervening spiral galaxy.

1458+718 — (aka 3C 309.1) The *Chandra* spectrum of this high-redshift quasar cannot be fitted statistically sufficiently with a simple absorbed power law. The fit can be improved significantly if a second power law, a thermal plasma, a black body or a reflection component is added to the model. The best fits are achieved with the two-power-law model (model II) and the black-body-plus-power-law model ($\chi_{\mathrm{red}} \sim 0.83$ at 84 d.o.f.) yielding either a very steep soft power law with $\Gamma > 5$ or a black body of $\sim 105\,\mathrm{eV}$ temperature.

1502+106 — This source is separated by only $7'$ from Mrk 841, which is brighter than 1502+106 at soft to medium hard X-rays by almost two orders of magnitude at. Although the source was therefore contained inside the field of view of three *ASCA* and two *Beppo*Sax observations, those data were not reduced for this thesis, in view of the limited angular resolution of both telescopes and the danger of blending with Mrk 841. George et al. (1994) reported the spectral characteristics of 1502+106 as derived from one of those *ASCA* observations: a simple absorbed power law with $\Gamma \sim 0.5$ affected by soft

energy absorption consistent with Galactic values.

1502+106 can further be detected in the field of view of three *XMM-Newton* observations of Mrk 841 and the resulting spectral information is presented here for the first time. In all three pointings, the PN detector was operated in small-window mode and did not collect any data of 1502+106, which was outside of the reduced FoV. The MOS cameras were operated in fast-uncompressed and small-window modes so that only a central sub array pixels on the central detector chip imaged the sky. Unfortunately, the centroid position of 1502+106 was on the central chip, close to one of the outer chips. Only a small fraction of the PSF was recorded resulting in a significant loss of source flux.

The three *XMM-Newton* observations were distributed over only two days. Within the uncertainties, no source variability could be detected between the individual observations so that the data were combined in order to improve the significance. The spectra were fitted simultaneously with an absorbed-power-law model, yielding a flat photon index of $\Gamma = 1.53^{+0.11}_{-0.08}$. Any extra absorption over the Galactic value is consistent with zero and can be constrained to be $< 10^{21}$. Due to the masking of the bulk PSF, no firm statement about the absolute source flux during these observations can be made.

1510-089 — This high-polarization quasar has been observed by *ASCA*, *Beppo*Sax, and *Chandra* on one occasion each. All three data sets reveal a very flat X-ray spectrum with a photon index of ~ 1.25 in August 1996 (Compare Singh et al. 1997) and ~ 1.4 in August 1998 and March 2001 (compare Donato et al. 2005, Gambill et al. 2003). *Chandra* resolved the source X-ray emission into a core-jet structure (see Fig. 4.11), which was investigated and compared to the kiloparsec-scale radio structure by Sambruna et al. (2004). Interestingly, the integrated jet emission has a power-law slope of ~ 1.6, a value rather steep compared to the flat nuclear continuum.

1633+382 — (aka 4C +38.41) During March 1996, four *ASCA* observations of this distant quasar have been performed (compare Kubo et al. 1998). In all of them, the source exhibited a flat spectrum. A one-power-law model with fixed Galactic plus variable source-intrinsic absorption provides an adequate approximation of the spectral data. Weak or no extra absorption over the Galactic value is required in all cases. The source varied significantly between the individual observations, both in flux and in the photon index with values of $F_{(2-10)\,\mathrm{keV}} = (1.7 - 2.9) \times 10^{-12}\,\mathrm{erg\,cm^{-2}\,s^{-1}}$ and $\Gamma = 1.3 - 1.6$. Fitting the spectral data from all four observations in March 1996 simultaneously yields a photon index of 1.5 but unacceptable statistics ($\chi_{\mathrm{red}} = 1.4$ with 315 d.o.f.), while each individual epoch can be fitted with a value of χ_{red} smaller or equal to 1. This illustrates convincingly the significance of the detected source variability.

1641+399 — (aka 3C 345) One *Beppo*Sax observation and one *Chandra* observation of this source have been performed. Tavecchio et al. (2002) reported on the *Beppo*Sax data, finding a flat power law with $\Gamma \sim 1.6$. The authors waived the LECS data of this observation mentioning a possible confusing source within the extraction region of the LECS detector, about 5 arcmin away from the target source. In the reanalysis for this thesis, the LECS data have been considered with an extraction radius of 4 arcmin providing a likely explanation for the steeper photon index of $\Gamma = 1.70^{+0.03}_{-0.04}$ derived here.
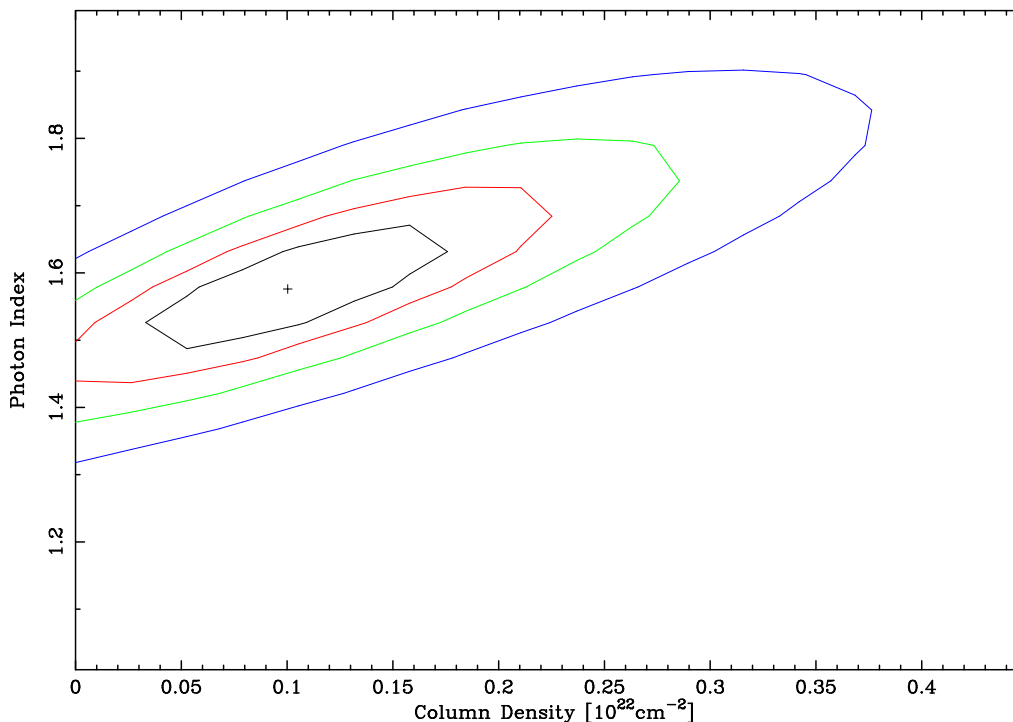
Figure 4.16: 68, 90, 95, and 99 per cent confidence contours for the absorbing column density and the photon index of 1655+077 for the 2002, April 28 *Chandra* spectrum. The source intrinsic absorption is significant on a $\sim 90\,\%$ level.

Sambruna et al. (2004) report the detection of an X-ray jet of 3C 345 but due to the short (10 ksec) exposure, the weakness of the jet and the small separation between the jet and the core, no spectrum could be extracted for this study. Gambill et al. (2003) report a soft excess of 3C 345 based on the same *Chandra* data and a best-fitting model of a broken power law with photon indices of $\Gamma_{\mathrm{soft}} \sim 2.1$, $\Gamma_{\mathrm{hard}} \sim 1.4$ and a break energy of $\sim 1.6\,\mathrm{keV}$ with no extra absorption over the Galactic value. In the reanalysis of these data for this thesis, model II provided the best fit to the data, invoking two separate power laws rather than a broken power law. The results are similar but not identical. Values of $\Gamma_{\mathrm{soft}} = 2.97^{+0.07}_{-0.04}$, $\Gamma_{\mathrm{hard}} = 1.52^{+0.04}_{-0.04}$ and a break energy of $\sim 0.8\,\mathrm{keV}$ are derived. In addition, a small amount of excess absorption is found of $N_{\mathrm{H}} = 3.9^{+1.4}_{-0.8}\,\mathrm{cm}^{-2}$.

1655+077 — Marshall et al. (2005) found no significant large-scale X-ray structure associated with the extended radio jet of 1655+077 and report an absorbed-power-law spectrum with spectral parameters similar to those found in this work ($\Gamma \sim 1.6$; $N_{\mathrm{H}} = 1.0^{+1.3}_{-1.0} \times 10^{21}\,\mathrm{cm}^{-2}$). The extra absorption in excess of the Galactic value is statistically significant at a $\sim 90\,\%$ level (compare Fig. 4.16). This is remarkable because the source shows pronounced superluminal motion on parsec scales with non-linear component trajectories (two components identified with $\sim 5c$ and $\sim 15c$ with misalignment angles of $\sim 8°$ and $\sim 60°$ relative to the mean core-component position angle) indicative of a very small angle to the line of sight (Kellermann et al. (2004)).

1749+096   — (aka 4C +09.57) This BL Lac object exhibits a spectrum that can be fitted either by I) an absorbed power-law with Galactic plus source-intrinsic (or intervening) extra absorption ($N_H = (2.5 \pm 0.5) \times 10^{21}\,\mathrm{cm^{-2}}$ in the source frame) and a rather flat photon index (for a BL Lac source) of $\Gamma = 1.93 \pm 0.3$ or by II) a broken power law affected only by Galactic absorption and indicating a spectral steepening above $\sim 2\,\mathrm{keV}$ from ~ 1.55 to ~ 1.9 (compare Sambruna et al. 1999b). Due to the poor data quality, the latter might in fact represent a gradually steepening, concave spectrum as it might be expected at the high-energy wing of the synchrotron emission component in BL Lac objects. Statistically, the broken-power-law model is only marginally superior to the absorbed-power-law model.

1803+784   — Padovani et al. (2004) reported on the *Beppo*Sax data available for this object. The authors find a one-power-law model to approximate the data sufficiently. The analysis presented here is in agreement with these results. The absorbing column density is only weakly constrained so the flatter photon index given by Padovani et al. (2004) ($\Gamma \sim 1.5$) compared to the one derived in this thesis ($\Gamma = 1.7^{+0.05}_{-0.05}$) is likely a result of a coupling with the absorbing column density.

1823+568   — (aka 4C +56.27) The photon index of 1823+568 derived in this work ($\Gamma = 2.2^{+0.2}_{-0.1}$) from a *Beppo*Sax spectrum taken in October 1997 is in agreement with the value obtained from the same observation by Padovani et al. (2001) ($\Gamma \sim 2.1$) but in contrast with the result of Donato et al. (2005) ($\Gamma \sim 1.8$).

1828+487   — (aka 3C 380) Marshall et al. (2005) find a jet-associated emission knot separated from the core by ~ 1.8 arcsec that was not sufficiently resolved from the core emission to obtain a spectrum for this thesis. The integrated source spectrum is affected by pileup and substantially absorbed with $N_H = (1.3^{+4.2}_{-3.0}) \times 10^{21}\,\mathrm{cm^{-2}}$.

1928+738   — (aka 4C +73.18) This quasar has been observed with *ASCA* (compare Yuan et al. 2000) and *Chandra* (Sambruna et al. 2004, Gambill et al. 2003). The reanalysis of the *ASCA* data for this thesis does not support the finding of Yuan et al. (2000) that a one-power-law model cannot yield an adequate fit to the data. No systematic residuals are apparent and a two-power-law model does not yield a statistically significant improvement of the fit. Gambill et al. (2003) fitted the *Chandra* spectrum with a one-power-law model invoking only a fixed amount of Galactic absorption obtained from the NED Galactic Extinction Calculator[7]. Here, model I has been used to model the *Chandra* spectrum of 1928+738 with a slightly smaller value of $N_{H,Gal.} = 6.82 \times 10^{20}\,\mathrm{cm^{-2}}$ (compared to $7.71 \times 10^{20}\,\mathrm{cm^{-2}}$ used by Gambill et al. 2003) and a freely fitted amount of extra absorption over this value. An excess absorption of $N_H = 2.9^{+1.1}_{-0.8} \times 10^{20}\,\mathrm{cm^{-2}}$ is found and a steeper photon index of $\Gamma = 2.09^{+0.05}_{-0.02}$ (compared to $\Gamma = 1.88 \pm 0.07$ derived by Gambill et al. (2003)).

---

[7]Based on Schlegel et al. (1998).

1957+405   — (aka Cygnus A) The *ASCA* and *Beppo*Sax data of this source was not analyzed because of the dominance of the extended emission and the limited angular resolution of both instruments that prohibited a separation of the core from its environment. The *Chandra* spectrum of Cygnus A is complex and cannot be approximated adequately by the models I to III considered for this study. A comprehensive analysis of the Cygnus A *Chandra* data is presented by Young et al. (2002), reporting a heavily absorbed power law with photon index $\Gamma \sim 1.5$ and an absorbing column density of $N_{\mathrm{H}} = 2.0^{+0.1}_{-0.2} \times 10^{23}\,\mathrm{cm}^{-2}$.

2134+004   — The here derived photon index of $1.73^{+0.04}_{-0.03}$ agrees within its uncertainties with the value given by Donato et al. (2005).

2145+067   — (aka 4C +06.69) Yamasaki et al. (2000) report on the *ASCA* spectrum of this quasar. The analysis presented here from model I are in agreement with the results of Yamasaki et al. (2000).

2200+420   — (aka BL Lac) BL Lac is a low-Galactic-latitude source at $b \sim -11°$. Thus, the absorbing column density due to neutral hydrogen in the direction of BL Lac is relatively large: $1.74 \times 10^{21}\,\mathrm{cm}^{-2}$. Moreover, a molecular cloud causes extra absorption of the order of $1.6 \times 10^{21}\,\mathrm{cm}^{-2}$ (Lucas and Liszt 1993 and references therein). The first *ASCA* observation of BL Lac took place in November 1995 and the derived spectrum was discussed by Sambruna et al. (1999b). The reanalysis of these data yielded similar spectral parameters than given by Sambruna et al. (1999b), although no significant improvement of the fit was achieved by considering a broken or two-power-law model over a simple absorbed one-power-law model. Five *Beppo*Sax observations of BL Lac have been performed. Padovani et al. (2001) report on the first one on November 8, 1997 finding results in agreement with the earlier *ASCA* observation analyzed by Sambruna et al. (1999b) and in rough agreement with the reanalysis performed for this thesis. The second and third *Beppo*Sax observation of BL Lac was reported on by Ravasio et al. (2002). The authors find a soft excess in June 1999 and a spectrum adequately described by a one-power-law model in December 1999. In contrast to this, the reanalysis of these data for this thesis revealed a steepening of the spectrum above $6.8\,\mathrm{keV}$ in December 1999, modeled by a broken power law. The last two epochs of *Beppo*Sax observations of BL Lac have been analyzed by Ravasio et al. (2003), whose results are confirmed by the analysis performed in this work.

The two short *Chandra* observations of BL Lac have been previously analyzed by Donato et al. (2003). These authors find evidence for weak diffuse emission around the nucleus of the source and model this emission with a radially symmetric King profile. For this thesis, a three-color coded adaptively smoothed image was produced from the same data analyzed by Donato et al. (2003). In Fig. 4.12, this image is shown with radio contours of the kiloparsec-scale radio emission of BL Lac superimposed. Although only ~ 70 photons were collected by the *Chandra* HRMA, the extended X-ray structure clearly traces the position angle of the radio jet. Preferably medium and hard photons dominate the jet and the photon index of the extended emission can be determined to $\Gamma = 1.5 \pm 0.3$.
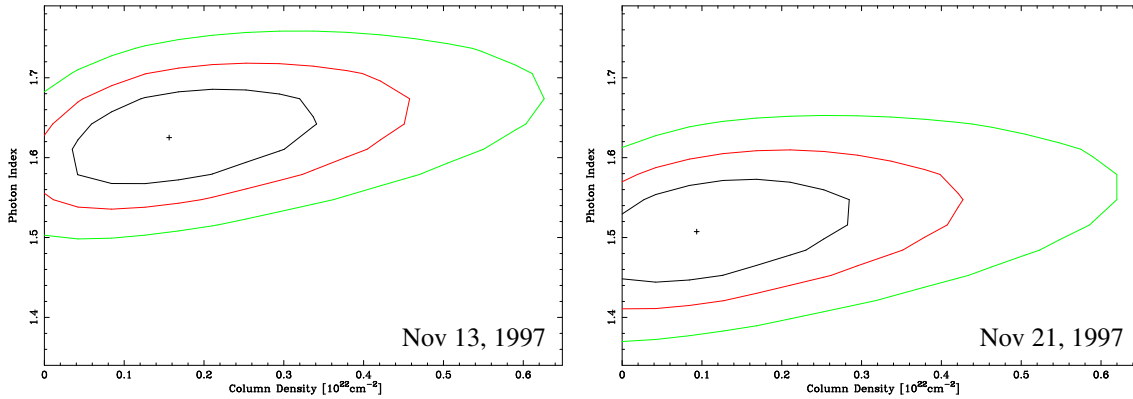
Figure 4.17: 68, 90, and 99 per cent confidence contours for $N_{\mathrm{H,extra}}$ and Γ of 2230+114 at two epochs, November 13 and 21, 1997. The difference in Γ is significant on the 68 % level.

2223−052 — (aka 3C 446) The basic absorbed-power-law model with only Galactic absorption as derived from the LAB survey yields a good fit ($\chi_{\mathrm{red}} = 1.06$ for 10 d.o.f.) with a slightly flatter photon index than derived by Tavecchio et al. (2002). The difference $\Delta\Gamma \sim 0.1$ is mainly due to different data grouping and the here used slightly more conservative LECS energy-range flagging. Within their errors, however, the two fits agree well. As pointed out by Tavecchio et al. (2002), there is little evidence for an absorption column significantly larger than the Galactic value, contrary to previous findings.

2230+114 — (aka CTA 102) One *ASCA* and five *Beppo*Sax observations (the latter being separated by only 10 days and the previous been taken about two years earlier) have been previously analyzed by Kubo et al. (1998) and Tavecchio et al. (2000). In all epochs, 2230+114 exhibited a flat X-ray spectrum, sufficiently represented by a simple absorbed power-law model with $\Gamma \sim 1.5$. In contrast to Tavecchio et al. (2000), the five *Beppo*Sax spectra have been analyzed separately, revealing a tentatively significant evolution of the power-law photon index from 1.51 ± 0.03 on November 11 over 1.61 ± 0.03 on November 13 and November 16 back to 1.51 ± 0.04 on November 18 and November 21 ($\Delta\chi_{\mathrm{red}} = 2.3$ for one parameter of interest). "Stepping" through the parameter space, however, shows that the 90 % confidence contours in the $N_{\mathrm{H}} - \Gamma$-plane intersect and that the difference between both epochs is only significant on a 1–σ level (see Fig. 4.17). Along the $N_{\mathrm{H,extra}} = 0$ axis, the difference is significant on a 90 % level, approximately.

2243−123 — Tavecchio et al. (2002) reported a simple absorbed-power-law structure of the *Beppo*Sax spectrum of 2243−123 of November 1998. The reanalysis, performed for this thesis, however, showed that a one-power-law model can fit the data only assuming an absorbing column density well below the Galactic value ($N_{\mathrm{H}} = 5.76 \times 10^{20}\,\mathrm{cm}^{-2}$). Fixing the absorption at the LAB value reveals a soft excess of 2243−123 and a fit that can be significantly improved by the addition of a soft power law (F-test value of 4.01, corresponding to a 97 % probability; compare Fig. 4.18) with a steep photon index of ~ 3.5. The dominance of a steep power law at low energies is in agreement with the results of Siebert et al. (1998) based on *ROSAT* data.
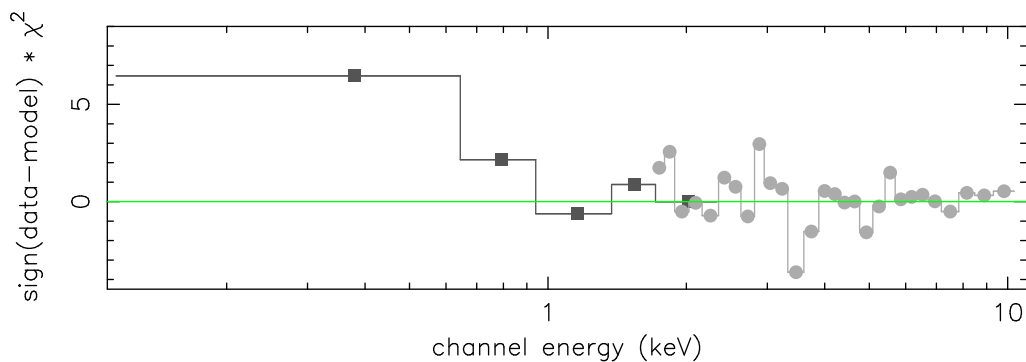
Figure 4.18: Contributions to χ^2 for the simple absorbed-power-law model to the November 1998 *Beppo*Sax spectral data of 2243−123. A soft excess is clearly visible.

2251+158 — (aka 3C 454.3) A comparably large amount of absorption towards the nuclear X-ray core of 3C 454.3 of $N_{\mathrm{H}} = 5 \times 10^{21}\,\mathrm{cm}^{-2}$ has been reported from a *Beppo*Sax observation of this source (Tavecchio et al. 2002). Alternatively, these authors suggest an intrinsic break in the continuum occurring below ∼1 keV to explain the observed lack of soft X-ray photons. The detected large amount of absorption is particularly puzzling in view of the expected small angle of the jet axis to the line of sight in superluminal quasars like 3C 454.3.

The *CHANDRA* observation of 3C 454.3 performed on Nov., 6th, 2000 reveals a resolved core-jet structure of 3C 454.3 with a bright knot of X-ray emission coinciding with strong radio emission emitted about 5 arcsec from the core (Fig. 4.19; see Murphy et al. (1993) for details of the radio structure). In addition, a significant unresolved source of X-ray emission is located at the same P.A. at a separation of ∼ 1 arcmin from the core. Deeper large-scale radio imaging is necessary to reveal the nature of this peculiar source. The X-ray spectral analysis of the integrated X-ray emission of 3C 454.3 is in agreement with the results of Marshall et al. (2005): a strongly piled-up spectrum is found with an intrinsic photon index of ∼ 1.6 and a considerable amount of extra absorption over the Galactic value of ∼ $(2.3 \pm 0.6) \times 10^{21}\,\mathrm{cm}^{-2}$, about half the value derived from the *Beppo*Sax data that had been analyzed before by Tavecchio et al. (2002). No significant improvement of the fit is achieved from considering a broken- or two-power-law model in either of the two analyzed spectra.
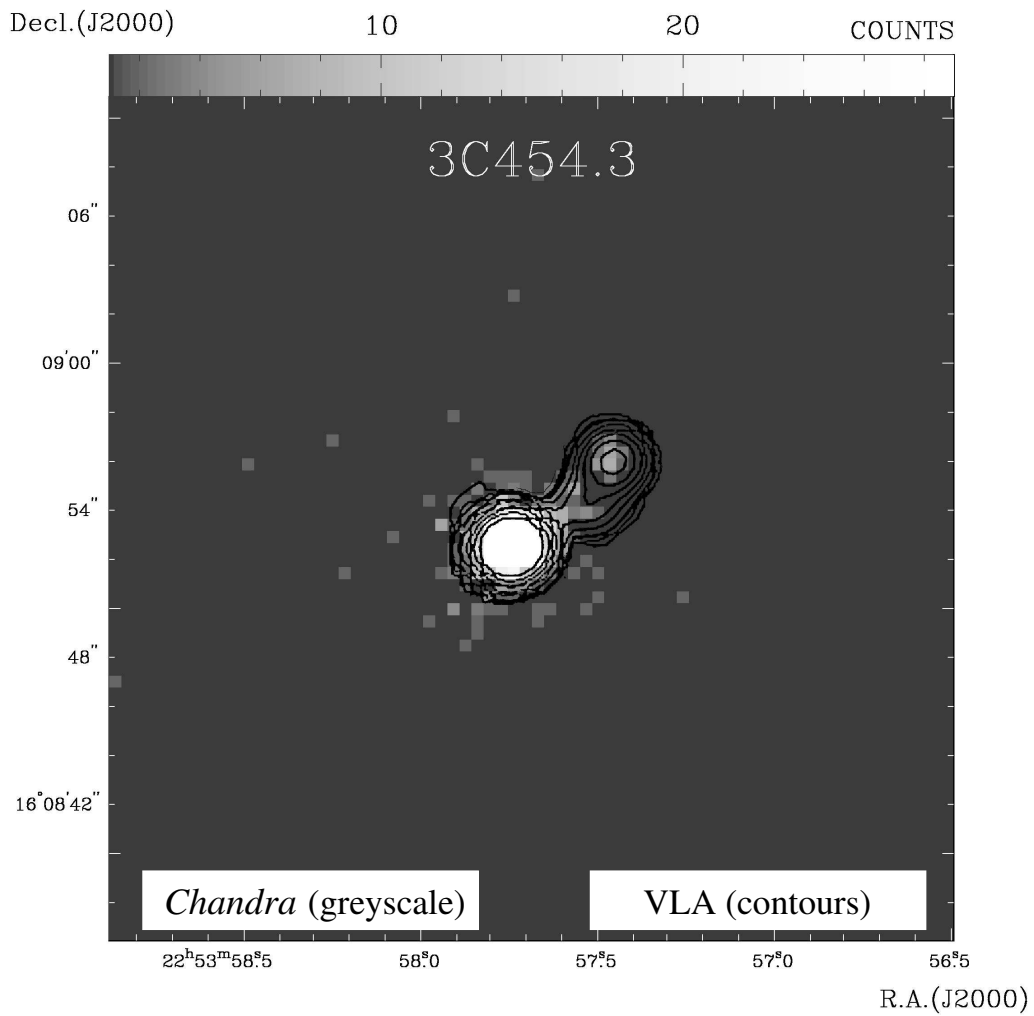
Figure 4.19: The kiloparsec-scale radio- and X-ray brightness distribution of 3C 454.3. The radio jet is displayed in contours (taken from Murphy et al. 1993) at a frequency of 1.6 GHz.

5 Discussion

5.1 Origin of the soft excess

A soft excess is found in 15 of the 50 *2 cm-X-Sample* sources. As mentioned earlier in this work (Sect. 4.1.1), these soft excesses are likely to have multiple origins. In radio galaxies, a soft X-ray thermal component is usually found (Worrall and Birkinshaw 1994, Sambruna et al. 1999a) indicative of a hot, diffuse medium into which the radio galaxies are embedded. In the case of NGC 1052, the soft excess could be associated with an extended soft X-ray emitting region that is correlated in extent and orientation with the radio jet of this object (Kadler et al. 2004a, reprinted in Sect. 6.3.2). The majority of radio-quiet AGN exhibit a soft excess that is often attributed to the high-energy end of the so-called "big blue bump" (e.g., Comastri et al. 1992, George et al. 2000, Piconcelli et al. 2005) for which thermal emission from an optically thick accretion disk is a common explanation (e.g., Czerny and Elvis 1987). The direct thermal emission from the accretion disc is expected to dominate in the optical and UV spectral regime with a fraction of the disk photons undergoing a Comptonization process, i.e., gain energy from inverse Compton scattering with hot electrons of a disk corona, and being scattered up in energy into the soft X-ray regime.

Soft-excesses in radio loud AGN, in particular in flat-spectrum radio quasars have been studied, e.g., by comparing the soft X-ray photon indices found by *ROSAT* in the (0.5–2.4) keV band and harder photon indices at higher energies revealed by *ASCA* (Sambruna et al. 2000). An explanation for soft excesses in radio loud AGN being discussed is that the inner jet may give rise to excess emission over the Seyfert-like hard X-ray continuum at soft X-ray energies via synchrotron emission. This scenario does particularly well describe the observed steep soft excesses observed in many BL Lac objects, e.g., in 0235+164 (see Sect. 6.2) and 0716+714 (see Sect. 6.5). In appendix B, it is shown that the soft X-ray luminosity of core-dominated radio-loud AGN from the MOJAVE sample correlates with the total radio luminosity and the VLBI luminosity of the parsec scale emission. It is shown there that the correlation is intrinsic and not introduced by the different redshifts of the sources from two flux-limited samples. With this information and the results presented in the last chapter, it is straightforward to test if the radio/X-ray luminosity correlation holds for the soft excess emission components detected in the *2 cm-X-Sample* and/or for the hard-power-law components. Fig. 5.1 shows the (0.5-2.0) keV luminosity of the soft-excess components and the hard-power-law components for all sources of the *2 cm-X-Sample* in which a soft excess was found (described with model II as a function of radio VLBI luminosity at 15 GHz from the VLBA 2 cm Survey). The correlation does hold for both emission components with slightly different slopes of 0.56 ± 0.11 and
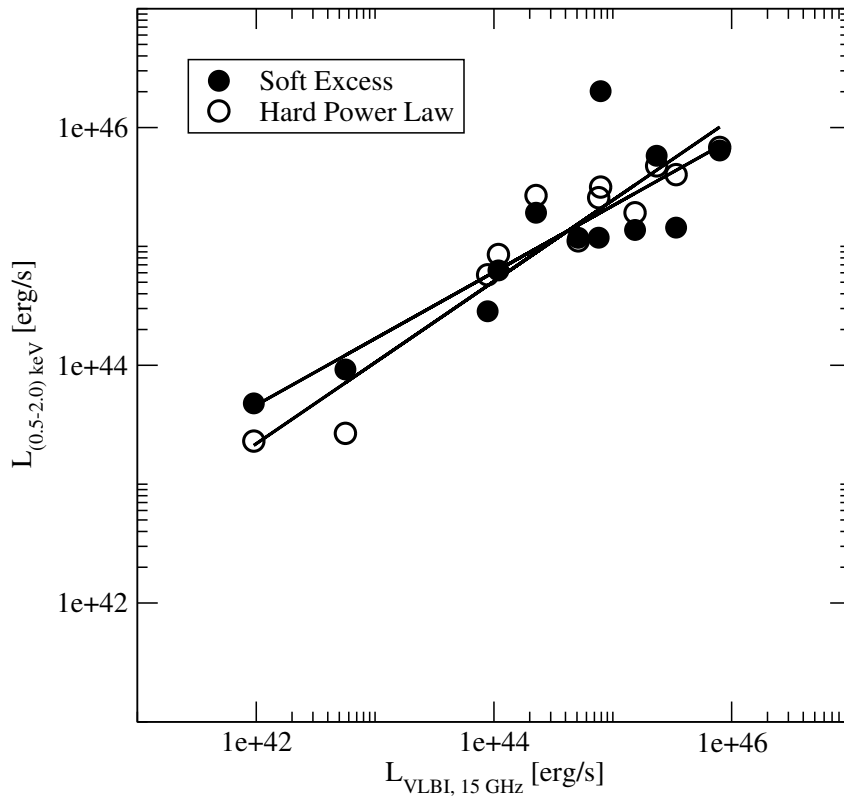
Figure 5.1: The (0.5-2.0) keV luminosity of the soft-excess components and the hard-power-law components as a function of 15 GHz VLBI luminosity for all sources of the *2 cm-X-Sample* in which a soft excess was found. The solid lines indicate linear regressions to the two data sets. The X-ray luminosity values are found in Table 4.2, the VLBI luminosities are calculated from the values for S and z given by Kovalev et al. (2005).

0.68 ± 0.07 for the soft excess and the hard power law, respectively. This shows that both emission components, the soft excess and the hard power law, typically found in the X-ray spectra of radio-loud, core-dominated AGN are coupled to the radio-jet emission on parsec scales.

It is interesting to note that the luminosity correlation between the soft-excess components and the hard-power-law components, as well as the correlation between the soft-excess luminosity and the compact radio-jet luminosity does no longer hold if one goes from the (0.5-2.0) keV band to the (2.0-10.0) keV band, while the correlation between the jet and the hard power law remains strong at these higher energies. The luminosities of the soft-excess components and the hard-power-law components as a function of radio VLBI luminosity at 15 GHz are shown for the (2.0-10.0) keV band in Fig. 5.2. The linear regression for the hard-power-law emission yields very similar values as in the softer band with a slope of 0.66 ± 0.10 while no power-law dependence of the soft-excess emission and the compact radio jet emission is seen.

A possible explanation for the disappearance of the $L_{\mathrm{softexcess}}$–L_{VLBI} correlation at high energies is that the soft excess may not adequately be represented by the power-law approximation of model II. It may rather have a spectral shape better described by a blackbody model, which is frequently invoked to model soft-excess spectra, having
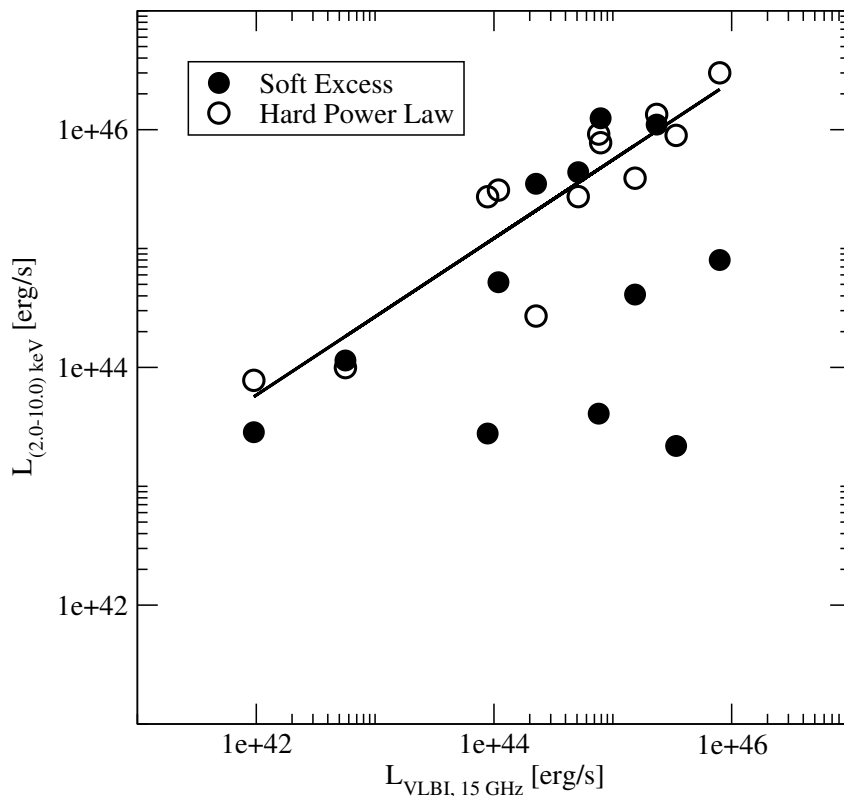
Figure 5.2: The (2.0-10.0) keV luminosity of the soft-excess components and the hard-power-law components as a function of 15 GHz VLBI luminosity for all sources of the *2 cm-X-Sample* in which a soft excess was found. The solid line indicates a linear regression to the hard-power-law data. The X-ray luminosity values are found in Table 4.2, the VLBI luminosities are calculated from the values for S and z given by Kovalev et al. (2005).

in mind a blackbody-like optically thick accretion disk as the origin of the soft-excess emission. While the different shape of a power law, as considered in model II, and a blackbody may be negligible in the rather narrow range between 0.3 keV and 1–2 keV, where the soft excess dominates the X-ray spectrum, a much faster decreasing power law may substantially underpredict the emission of this spectral component at higher energies.

While the previous result demonstrates that the validity of approximating the soft excess in core-dominated, radio-loud AGN with a power law, the slope of this soft-excess power-law representation of the soft excess is found to correlate with the apparent speed of VLBI jet components. In Fig. 5.3 the soft-excess and hard-power-law photon indices of the sources in the *2 cm-X-Sample* are shown as a function of β_{app} of the brightest component found in all epochs of VLBA 2 cm Survey observations of these sources. The hard-power-law slope of the quasars shows some weak trends with β_{app} with clustering values at $\beta_{\mathrm{app}} \sim 2$ and $\Gamma_{\mathrm{hard-PL}} \sim 1.5 - 1.9$, at $\beta_{\mathrm{app}} \sim 5$ and $\Gamma_{\mathrm{hard-PL}} \sim 1.4$, and at $\beta_{\mathrm{app}} \sim 10$ and $\Gamma_{\mathrm{hard-PL}} \sim 1.5 - 1.8$. The BL Lac and galaxy photon indices of both emission components occupy the region of low β_{app} (< 7) and steep $\Gamma \sim 1.7 - 4$, while the quasar soft-excess photon indices decrease strongly with β from very steep slopes at low β to more moderate values at the extreme end of the β distribution.
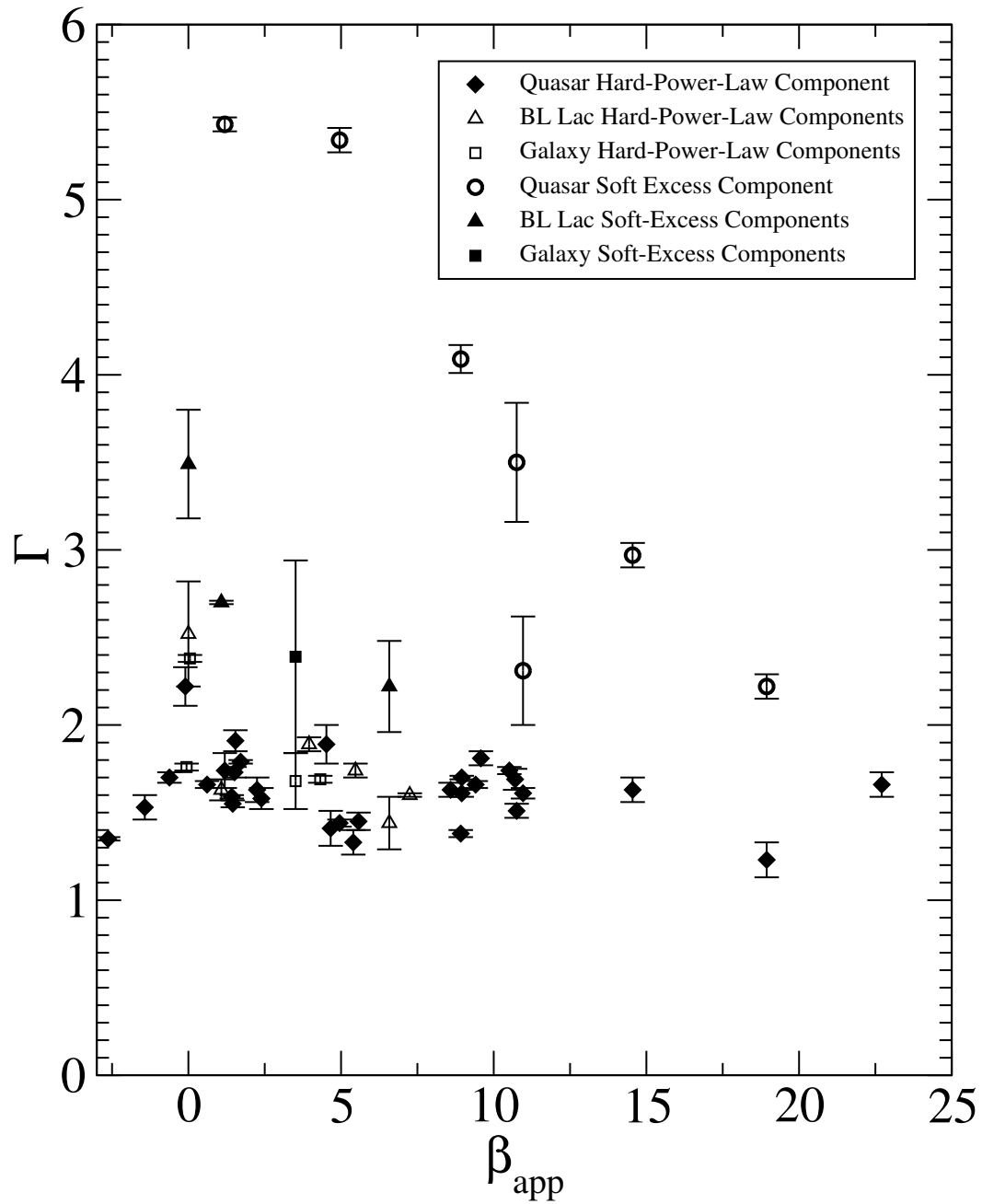
Figure 5.3: The soft-excess and hard-power-law photon indices of *2 cm-X-Sample* sources as a function of the apparent speed of jet components on parsec scale.

At present it is not clear how the finding of a strong $\Gamma_{\mathrm{softexcess}}$–$\beta_{\mathrm{app}}$ dependence has to be interpreted. Bearing in mind that the power-law approximation of the soft excess in this work may be an oversimplification and that spectral models invoking blackbody or more sophisticated disk-emission models may represent better the physical nature of these emission components, the trend of decreasing $\Gamma_{\mathrm{softexcess}}$ with beta may be the signature of a shifting emission maximum of this emission component. Models invoking the inverse Compton process to scatter photons from lower energies into the soft X-ray regime have in common that they predict a γ^2 dependence between the energy of the seed photons and the up-scattered photons ($\nu' = \gamma^2 \nu$), where γ is the Lorentz factor of the high-energy electrons scattering the radiation. This implies that any peaked spectral distribution of seed photons has a corresponding peak at higher energies where efficient inverse Compton scattering is present. It is an attractive hypothesis that the Lorentz factor of this inverse-Compton scattering medium may be related to the Lorentz factor of the jet plasma that determines the intrinsic jet speed β but obviously this issue requires deeper theoretical considerations. In addition, higher SNR X-ray spectra of a sufficiently large sample of radio-loud, core-dominated AGN with soft excesses in their X-ray spectra have to be obtained to discriminate between different spectral models for the soft-excess component and to compare the results to suited (ideally quasi-simultaneous) VLBI data.

5.2   Origin and nature of cold absorbing material towards core-dominated radio-loud AGN

The presence of cold (i.e., not ionized) absorbing material in the line towards radio-loud quasars and broad-line radio galaxies (BLRGs) has been established via X-ray spectroscopy. Sambruna et al. (1999a) found soft X-ray absorption in 6 out of 9 BLRGs (67 %) and in 3 out of 5 radio-loud quasars (60 %). These detection rates are somewhat higher than in the *2 cm-X-Sample* (46 %). Considering that all sources of the *2 cm-X-Sample* exhibit a bright compact radio core and in the most cases superluminal motions of jet components on parsec scales indicates a substantial amount of relativistic boosting, the detection rate of absorption is still remarkably high. Three different types of soft X-ray absorption of the spectra analyzed in this thesis have to be considered:

1. Absorption inside the Galaxy: If clouds inside the Galaxy contain ionized or molecular gas and/or dust, radio surveys like the LAB survey (Kalberla et al. 2005) are not sensitive to this material. Four such cases have been found from a search of the literature on the individual *2 cm-X-Sample* sources. These cases are 0333+321 (e.g., Marscher 1988 and references therein), 0415+379 (Bania et al. 1991), 0528+134 (e.g., Sambruna et al. 1997 and references therein), and 2200+420 (Lucas and Liszt 1993).

2. Absorption in intervening systems: Three sources of the *2 cm-X-Sample* are known to be located behind intervening galactic systems at intermediate redshift: 0235+164 (e.g., Madejski 1994 and references therein), 0458−020 (Wolfe et al. 1986), and 1127−145 (Bechtold et al. 2001). These so-called damped Lyα systems are thought to be galaxy-progenitor systems and provide high-column density absorption of several $10^{21}\,\mathrm{cm}^{-2}$.

3. Source-intrinsic absorption: Out of the remaining 43 sources in the *2 cm-X-Sample*, 21 exhibit soft energy absorption that is not explained via source-extrinsic origins. Potential absorbers are the obscuring torus, the broad-line region, clouds of absorbing neutral, ionized or molecular material inside the AGN host galaxy, or regions of enhanced particle density in the environment of the large-scale radio jets and lobes. However, the presence of cold absorbing gas in such a large fraction of highly beamed sources observed is surprising and particularly the cases with excess absorption being detected with column densities larger than a few times $10^{21}\,\mathrm{cm}^{-2}$ are not easy to explain. The AGN standard model predicts such obscuration effects for relatively large angles to the line of sight within the obscuring torus, which is in fact a likely explanation for the high-column density absorption in the two type-2 systems NGC 1052 and Cygnus A. With these two exceptions, the data suggest a more isotropic distribution of the absorbing material around the central X-ray source.

The fact that no obvious correlation of the absorbing column density with source luminosity is found is of interest because some AGN models predict a dependence of the solid angle subtending to the primary X-ray source on luminosity (e.g., Hill et al. 1996).

For this study, no attempt has been made to search systematically for absorption edges at low energies, frequently observed in Seyfert galaxies, and usually associated with ionized material, the so-called warm absorbers. If, for a given density, the warm absorber clouds are located at increasing distances from the central source with increasing luminosity, such a scenario could explain the apparent independence of N_H on L. The inspection of the residuals to the spectral fits with the models considered for this study shows no obvious cases of distinct warm-absorber signatures. However, most of the sources in the *2 cm-X-Sample* have redshifts considerable higher than $z = 0.4$ (compare Fig. 3.1). At this redshift, the absorption edge from highly ionized oxygen (OVII/VIII) –the usually strongest signature of warm absorbers– would be shifted from its rest energy at $0.7\,\mathrm{keV}$–$0.8\,\mathrm{keV}$ below $0.5\,\mathrm{keV}$, where it would be virtually not detectable with *ASCA* and *Beppo*Sax and where the *Chandra* calibration is less well established than at higher energies. The high-z objects in the sample from $z = 1.3$ to higher values would hide the higher continuum below the edge energy even for *XMM-Newton*, mimicking high-density cold absorption.

5.2.1   Note on the used version of the LAB catalog

The Galactic absorbing column densities, used in this thesis, are based on the LAB survey (Kalberla et al. 2005). The N_H values have been extracted from a Fits file containing the Galactic absorbing column densities for the whole sky in Ra.–Dec. coordinates, provided by P. Kalberla in March 2005. From July 2005 on, a web interface has been available[1] which can be used to determine the Galactic value of N_H for a given position in the sky. A comparison of the values used in this thesis and the ones derived from the web interface showed a discrepancy that could be explained by a coordinate-transformation problem that occured in the production of the original Fits file. Basically, the coordinates in the Fits files were in fact in B 1950 format, albeit being labeled as J 2000 coordinates in the Fits header. This introduces an error in the determined value of N_H that depends

---

[1]`http://www.astro.uni-bonn.de/ webrai/german/tools_labsurvey.php`

strongly on the local gradients of Galactic absorbing material in the vicinity of a given source. The selection criteria of the *2 cm-X-Sample* exclude sources close to the Galactic plane, however, filamentary structures are present at large Galactic latitudes that affect in a number of cases significantly the obtained values.

Table 5.1: Differences between Galactic N_H values from the LAB survey, as available in March 2005, and the values from the web interface (available from July 2005 on).

Source	$N_\mathrm{Gal.H}^{Mar05}$ [10^{20} cm^{-2}]	$N_\mathrm{Gal.H}^{Jul05}$ [10^{20} cm^{-2}]	Source	$N_\mathrm{Gal.H}^{Mar05}$ [10^{20} cm^{-2}]	$N_\mathrm{Gal.H}^{Jul05}$ [10^{20} cm^{-2}]
0007+106	5.00	5.73	1226+023	1.56	1.62
0048−097	2.98	3.22	1228+126	2.00	1.61
0235+164	8.94	6.79	1252−055	2.15	2.12
0238−084	2.91	2.96	1308+326	1.14	1.27
0316+164	12.8	13.2	1334−127	4.18	5.39
0333+321	12.6	12.1	1413+135	1.55	1.57
0415+379	26.9	29.3	1458+718	2.37	2.27
0420−014	7.11	8.12	1502+106	2.09	2.19
0430+052	10.9	10.2	1510−089	6.78	7.17
0458−020	5.65	5.97	1633+382	1.10	1.11
0528+134	24.2	23.9	1641+399	0.93	1.06
0605−085	16.8	18.5	1655+077	6.69	6.10
0716+714	3.52	3.06	1749+096	8.63	10.1
0735+178	3.66	3.86	1803+784	3.40	3.40
0736+017	7.98	7.59	1823+568	4.50	4.68
0738+313	4.60	4.31	1828+487	5.82	6.03
0827+243	3.28	2.64	1928+738	6.82	7.10
0836+710	2.94	2.76	1957+405	23.5	23.6
0851+202	2.66	2.39	2134+004	4.03	4.72
0923+392	1.28	1.34	2145+067	4.69	4.54
1038+064	2.65	2.33	2200+420	17.4	17.1
1055+018	3.61	3.03	2223−052	5.86	4.42
1127−145	3.32	3.38	2230+114	5.43	4.76
1156+295	1.87	1.50	2243−123	5.76	4.40
1222+216	2.24	1.97	2251+158	6.29	7.33

Table 5.1 lists the different values of Galactic absorption derived from the March 2005 and July 2005 versions of the LAB catalog. In the most cases, the differences between the two values is small and unlikely to have a significant influence on the spectral-fitting results. Note, that the differences cannot be compared directly to the reported source-intrinsic excess absorption values in the various tables of Chap. 4 because of the different redshifts of the various sources. However, it has to be stressed that some of the sources for which relatively small amounts of excess absorption were found from the March 2005 LAB values (10^{20} cm^{-2}–10^{21} cm^{-2}) may be artificially increased. Vice versa, a number of

sources with similar amounts of excess absorption may have been missed in the analysis because of over-estimated N_H values from the March 2005 LAB catalog.

The derived photon indices and X-ray fluxes are essentially unaffected by this problem because of the adjustment of the net absorption via the variable (source intrinsic) absorption component used in all spectral fits. As an example, the relatively strong affected *XMM-Newton* spectral fits of $1334-127$ are compared for the two LAB values of N_H: the excess absorption is decreased by $\sim 40\,\%$ from $5 \times 10^{20}\,\mathrm{cm}^{-2}$ to $3 \times 10^{20}\,\mathrm{cm}^{-2}$ but remains significant at more than $5\,\sigma$. The photon index changes from 1.79 to 1.80, being stable within the statistical uncertainty of ± 0.01, the soft X-ray flux between $0.5\,\mathrm{keV}$ and $2.0\,\mathrm{keV}$ changes by $\sim 3\,\%$ from $1.67 \times 10^{-12}\,\mathrm{erg\,s}^{-1}\,\mathrm{cm}^{-2}$ to $1.73 \times 10^{-12}\,\mathrm{erg\,s}^{-1}\,\mathrm{cm}^{-2}$, and the hard X-ray flux between $2.0\,\mathrm{keV}$ and $10\,\mathrm{keV}$ is stable at $2.80 \times 10^{-12}\,\mathrm{erg\,s}^{-1}\,\mathrm{cm}^{-2}$.

5.3   Constraints on the nature of the primary X-ray continuum

The majority of the hard X-ray spectra (above $2\,\mathrm{keV}$) of core-dominated, radio-loud AGN from the *2 cm-X-Sample* are well described by featureless power-law models with photon indices in the range 1.3–2.0 (see Fig. 4.1). The average hard-power-law photon index is $\langle \Gamma_{\mathrm{hard-PL}} \rangle = 1.68$ with a dispersion of $\sigma_{\langle \Gamma_{\mathrm{hard-PL}} \rangle} = 0.26$. The average hard-power-law photon index of quasars from the sample is $\langle \Gamma_{\mathrm{hard-PL}}^{\mathrm{Quasars}} \rangle = 1.61$ with a dispersion of $\sigma_{\langle \Gamma_{\mathrm{hard-PL}}^{\mathrm{Quasars}} \rangle} = 0.20$. BL Lac objects are found to exhibit a broader range of photon indices between ~ 1.4 and ~ 2.5 similar to the galaxy distribution, that does not reach values harder than 1.7, however. This result is in good agreement with previous studies of smaller samples of radio-loud beamed AGN. Kubo et al. (1998) investigated an *ASCA* sample of 18 blazars among which the authors identify quasar-hosted blazars as the blazar sub-class with the hardest X-ray spectra ($\Gamma \sim 1.6$). Dividing BL Lac objects into low-energy-peaked and high-energy-peaked objects (LBLs and HBLs) according to the location of the primary synchrotron peak in the spectrum, the authors find HBLs to exhibit the steepest blazar photon indices ($\Gamma \sim 2-3$) and LBLs intermediate values between quasars and HBLs. Because the *2 cm-X-Sample* is a radio-selected sample, the BL Lac objects in this study are predominantly LBLs so that the results found here for BL Lac photon indices confirms the results of Kubo et al. (1998) with the sample of LBL being increased from 4 to 9. Reeves and Turner (2000) reported on the analysis of a larger sample of 35 radio-loud AGN and 27 radio-quiet quasars based on the available *ASCA* archival data up to January 1998. The authors find an average photon index of $\Gamma \sim 1.6$ for radio-loud quasars. Considering both radio-quiet and radio-loud quasars, Reeves and Turner (2000) find a dependence of the photon index on radio loudness R_L, where R_L is defined as the logarithm of the ratio of the $5\,\mathrm{GHz}$ total radio flux density to the blue band flux (Wilkes and Elvis 1987)[2]. The authors find Γ to depend on R_L in the sense that radio-louder quasars exhibit flatter X-ray photon indices. This, together with a correlation between the X-ray luminosity and R_L, is interpreted by Reeves and Turner (2000) as an increasing importance of the jet in the more core-dominated radio-loud quasars, due to Doppler boosting. The *2 cm-X-Sample* allows this prediction to be tested by comparing

---

[2]No such correlation is found by Reeves and Turner (2000) within the radio-loud sub sample only.

the hard-power-law photon indices for sources with different core-dominance parameters. No correlation of Γ with the core-dominance, defined as the 15 GHz VLBI flux density to 15 GHz total radio flux ratio, is found[3]. The dependence of Γ on radio–to–X-ray loudness (defined as the luminosity ratio of the 15 GHz VLBI jet and the soft X-ray luminosity; compare appendix B) has been tested, as well, but no significant correlation could be found. These two results call the conclusion of Reeves and Turner (2000) into question that the radio loudness is the critical parameter that governs the slope of the hard power law. It has to be tested if the apparent radio loudness dependence found by Reeves and Turner (2000) may in fact be an effect of decreasing blue band flux, which would reconcile the two findings of a dependence of Γ on R_{L} but an independence on radio–to–X-ray loudness. Another possibility would be that the radio emission and the X-ray emission is boosted at the same level while the blue band flux may be unboosted.

Relativistic boosting of the X-ray emission is expected, if jets dominate the X-ray spectrum of radio-loud, core-dominated AGN. This hypothesis is sustained by the finding of predominantly flat photon indices from the extended X-ray jets found in the *2 cm-X-Sample* (compare Sect. 4.2). If boosting indeed has an important influence on the slope of hard X-ray spectra of core-dominated, radio-loud AGN, a direct correlation with the Doppler factor is expected. For the majority of the *2 cm-X-Sample* sources, Doppler factors have been estimated by Lähteenmäki and Valtaoja (1999) based on total radio flux density variation monitoring observations. Fig. 5.4 shows the dependence of $\Gamma_{\mathrm{hard-PL}}$ on the variability Doppler factor. Indeed, a weak trend is seen, however being only marginally significant. The correlation coefficient is -0.25 and a linear regression yields a shallow slope of -0.008 ± 0.005. Apparently, the dispersion of $\Gamma_{\mathrm{hard-PL}}$ is larger than the systematic decrease of the linear regression curve over the range of Doppler factors. On the other hand, the best determined spectral slopes, i.e., the $\Gamma_{\mathrm{hard-PL}}$ values from the statistically best fitting models with the highest SNR, the smallest error on the individual measurements of $\Gamma_{\mathrm{hard-PL}}$ and in the case of multiple observations the smallest differences between the individual $\Gamma_{\mathrm{hard-PL}}$ values for the same source, lie on average closer to the regression line than the values with larger errors. The significance of this tentative correlation needs to be tested on larger samples of high-SNR X-ray spectra, obtained from deep *Chandra* and *XMM-Newton* observations.

5.4   Disk Reflection

In general, the X-ray spectral analysis of the *2 cm-X-sample* shows that core-dominated, radio-loud AGN exhibit relatively featureless X-ray spectra with the majority of the sources being adequately characterized via a one-power-law spectral model, with soft X-ray absorption and soft excesses being exhibited by a fraction of the sources. At high energies (above 2 keV) little evidence was found for an important influence of strong iron emission lines and/or disk-reflection humps as seen in a large number of Seyfert galaxies (Nandra and Pounds 1994). A common model for the X-ray emission from Seyfert galaxies assumes that UV photons are produced from viscous dissipation in an accretion disk and that those photons are up-scattered into the X-ray energy regime via the inverse Compton process by interacting with hot electrons in a postulated disk corona above the surface of

---

[3]The values of total and VLBI flux at 15 GHz have been taken from Kovalev et al. (2005).
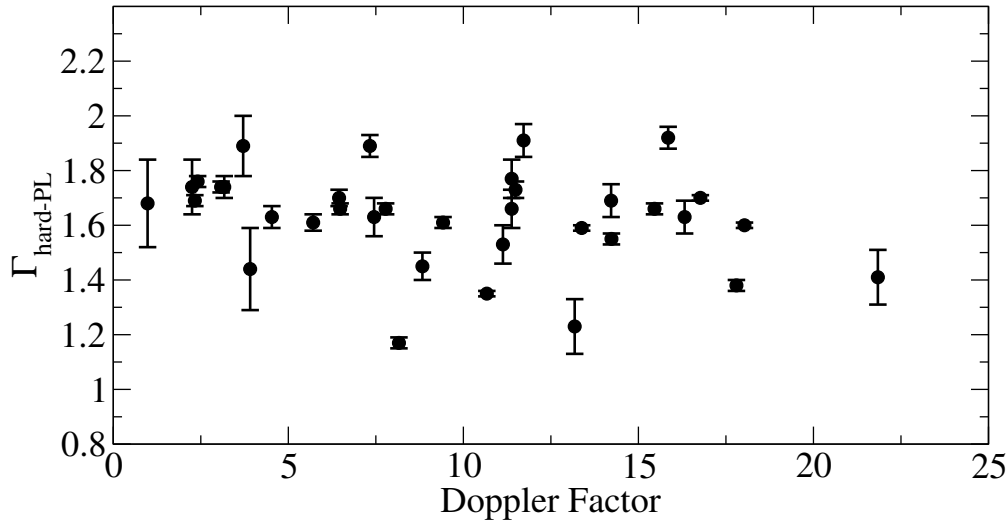
Figure 5.4: The hard-power-law photon indices found in the *2 cm-X-Sample* as a function of the Doppler factor.

the disk (Haardt and Maraschi 1993). When these hard X-ray photons illuminate in turn the disk, they can be either absorbed with Auger de-excitation following, Compton scattered back out of the disk, or reprocessed into an iron fluorescent line photon. Together, the second and third possible process is usually referred to as Compton reflection, giving rise to an iron absorption edge, an iron emission line and a Compton reflection hump in the spectrum. If this process occurs in the inner accretion disk where relativistic effects play a major role, the iron emission line is characteristically broadened and gets a skewed, double-peaked profile (compare Sect. 6.3.3 and see Fabian et al. 2000a and Reynolds and Nowak 2003 for two reviews on relativistically broadened iron lines).

Reeves and Turner (2000) found significant iron line emission in 7 out of 35 radio-loud quasars with generally smaller equivalent widths than found in Seyfert galaxies and radio-quiet quasars ($\langle EQW \rangle = (85 \pm 15)$ eV) and the reflection hump is weak or absent in most cases. Although no systematical effort has been made in the analysis of the *2 cm-X-Sample* in this thesis to apply disk-reflection models to all sources, the results presented here strengthen the findings of Reeves and Turner (2000) that both iron-line emission and Compton-reflection humps are not common in core-dominated, radio-loud AGN. However, seven sources could be identified whose X-ray spectra show some evidence of disk-reflection and where the application of HREFL and/or PEXRAV spectral models in XSPEC provided a statistically significantly better fit to the data than the standard models I to III or yielded physically more plausible parameters. The radio-intermediate quasar 0007+106 (III Zw 2) contains either a very broad relativistic iron line or a strong disk-reflection component (see Sect. 4.3 and Salvi et al. 2002). The *XMM-Newton* spectrum of the LINER galaxy 0238−084 (NGC 1052) is investigated in detail in Sect. 6.3.3. In this source not only a broad iron line is found but the profile of the line is demonstrated to be variable with a possible connection to jet-production activity on parsec scales. 0430+052 (3C 120) has been shown to exhibit a similar connection between the X-ray spectrum and the VLBI structure, with dips in the hard X-ray light curve preceding ejections of VLBI jet com-

ponents (compare Sect. 4.3 and Marscher et al. 2002). In Sect. 6.5, the *XMM-Newton* spectrum of the BL Lac object 0716+714 is discussed in detail. While this source at eight epochs of X-ray spectroscopic observations analyzed is adequately described by either model I or model II, it exhibits excess emission at $\sim 5.7\,\mathrm{keV}$ during one *XMM-Newton* observation that may be the imprint of an underlying disk component that became visible during this epoch when the inverse-Compton spectral component was weak. A very interesting case is the distant ($z = 1.265$) quasar 1038+064 (4C +06.41). As described in Sect. 4.3, the *XMM-Newton* spectrum of this source cannot easily be explained without invoking a disk-reflection spectral model component because of an unphysical inverted slope of the hard-power-law component in model II. For 1226+023 (3C 273), Grandi and Palumbo (2004) developed a model containing both a jet and a disk-emission spectral component and applied this model successfully to the available archival *Beppo*Sax data of this source. The model of Grandi and Palumbo (2004) is more complex than model II used in this thesis to account for the soft excess of 3C 273 and indeed the switch between rather low ($< 1\,\mathrm{keV}$) and high break energies ($6\,\mathrm{keV} - 20\,\mathrm{keV}$) of the 3C 273 X-ray spectrum found with model II suggests that more than two spectral components have to be considered to explain the variable X-ray spectrum of this bright quasar. Finally, the sources 0458−020, 1222+216, and 1458+718 show very steep soft excesses (compare Sect. 4.3 and unusually flat hard-power-law slopes if model II is considered. These sources may either exhibit a significant amount of disk-reflection emission and/or their soft X-ray spectra may better be described by invoking blackbody or thermal bremsstrahlung models that may be attributed to the high energy tail of the big blue bump from the quasi-thermal accretion disk spectrum.

5.5   Summary of the X-ray-spectral-survey results

The insights into the physics of core-dominated, radio-loud AGN that have been gathered from the observational results presented in Chap. 4 and their discussion in the preceding sections of this chapter shall be summarized here:

- The so far largest X-ray spectral archival survey of core-dominated, radio-loud AGN has been conducted with the analysis presented in this thesis. Data from all four X-ray observatories have been considered that have yielded X-ray spectroscopic data since the early 1990s: *ASCA*, *Beppo*Sax, *Chandra*, and *XMM-Newton*.

- The *2 cm-X-Sample* has been proven to be representative of the complete flux-limited MOJAVE sample of the brightest compact AGN in the northern radio sky, providing more reliable statistics than previous smaller samples.

- By being based on the MOJAVE sample of the VLBA 2 cm Survey, the *2 cm-X-Sample* provides a unique database of VLBI structural and kinematical information, allowing radio/X-ray correlation studies to be conducted.

- For all 237 spectra investigated, a uniform analysis has been performed with the approximation of the X-ray spectral distribution through an absorbed power law (model I). The results are given in Table 4.1. For the sources that are not adequately

represented by model I, an absorbed two-power-law model has been applied (model II, results in Table 4.2). Model II provides the simplest possible parametrization of soft excesses, a spectral feature commonly found in Seyfert galaxies. The spectrum of the radio galaxies 3C 84 and M 87 has been described via an absorbed thermal-plasma plus power-law model (Table 4.3).

- Only two out of 50 sources cannot be described sufficiently with this spectral-modeling scheme: the two heavily obscured sources NGC 1052 and Cygnus A. NGC 1052 is investigated in detail in Sect. 6.3.

- In a large number of cases, data from multiple observations of the same source with the same or different X-ray telescopes are available. Average values of the critical X-ray spectral parameters Γ, N_{H}, $F_{(0.5-2.0)\,\mathrm{keV}}$, $F_{(2.0-10.0)\,\mathrm{keV}}$, and $F_{(20-80)\,\mathrm{keV}}$ have been derived for these multiply observed sources, yielding mean values better suited for statistical purposes than one-epoch data and intrinsic dispersions of these observables.

- The majority of core-dominated, radio-loud AGN can be described by model I. A soft excess is found in 15 out of 50 sources, in two cases being attributed to a soft thermal plasma. The average hard-power-law photon index of the remaining 13 soft-excess sources is $\langle \Gamma_{\mathrm{softexcess}} \rangle = 3.2$ with a large dispersion of $\sigma_{\langle \Gamma_{\mathrm{softexcess}} \rangle} = 1.2$. For the two BL Lac objects 0235+164 and 0716+714, the soft excess is best explained as the high-energy tail of the primary synchrotron component of the blazar emission. A possible identification for the soft excesses found in quasars is the high-energy end of the big blue bump.

- A sharp-peaked distribution of hard-power-law photon indices is found with an average value of $\langle \Gamma_{\mathrm{hard-PL}} \rangle = 1.68$. Despite of the sharp peak, the dispersion of the distribution of $\sigma_{\langle \Gamma_{\mathrm{hard-PL}} \rangle} = 0.26$ can best be explained as representative of an intrinsic dispersion over the sample.

- The quasars dominate the sharp peak of $\Gamma_{\mathrm{hard-PL}}$. The hard power laws of BL Lacs and galaxies range from small to large values ($1.4 < \Gamma_{\mathrm{hard-PL}}^{\mathrm{B,G}} < 2.5$).

- The soft-excess spectral components cover a broader range in X-ray flux than the hard power laws. Quasars, BL Lacs and galaxies have different X-ray flux and luminosity distributions with the galaxies being brighter at X-rays than quasars and quasars being brighter than BL Lac objects. In luminosity, the galaxies are the least powerful sources and the quasar luminosities are higher than the BL Lac luminosities.

- $\Gamma_{\mathrm{hard-PL}}$ correlates weakly with the hard-power-law luminosity in all considered energy bands and with radio VLBI luminosity. The soft-excess luminosity correlates with both quantities in the soft (0.5-2.0) keV band but not in the higher energy bands. This may indicate that $L_{\mathrm{softexcess}}$ is not adequately represented by the power-law approximation of model II.

- The photon index of the soft-excess power-law component is found to correlate with the apparent speed of VLBI jet components. This may be the signature of a shifting emission maximum of the soft-excess emission component.

- No correlation of $\Gamma_{\mathrm{hard-PL}}$ with the core-dominance or the radio–to–X-ray loudness was found over the (all radio-loud) sources of the *2 cm-X-Sample* in conflict with the discrepancy between the photon indices of radio-loud and radio-quiet AGN.

- A tentative correlation is found between $\Gamma_{\mathrm{hard-PL}}$ and the Doppler factor. If true, this may indicate the increasing importance of relativistic boosting with flattening $\Gamma_{\mathrm{hard-PL}}$.

- 14 out of 26 *Chandra*-observed sources of the *2 cm-X-Sample* exhibit extended emission features bright enough and well-separated from the core so that their X-ray spectra could be determined. Based on their X-ray morphology, those features are classified, finding eight X-ray jets, four knots, 2 hotspots, and two jet-associated halos.

- Fitting a power-law model to the detected extended X-ray emission features yields a skewed distribution of photon indices with a peak at $\Gamma \sim 1.3$–1.5 and a wide tail towards steeper photon indices. The finding of predominantly flat photon indices from X-ray jets sustains the hypothesis that jet emission may dominate the X-ray spectra of radio-loud, core-dominated AGN on smaller scales, as well, giving rise to the flatter photon indices found in the *2 cm-X-Sample* compared to radio-quiet AGN.

- 21 out of 41 sources show excess absorption over the Galactic value of unknown origin, which is unexpected within the standard model of AGN given the type-1 character of 19 of those objects. 15 out of 30 quasars, 1 out of 7 BL Lacs and 5 out of 6 galaxies exhibit a significant amount of excess absorption. The detected absorbing column densities do not show any obvious trend with luminosity.

- No obvious cases of warm absorbers could be identified within the *2 cm-X-Sample*. In many cases, however, the presence of warm absorbers may be hidden through redshift effects.

- Disk-reflection signatures and iron lines are weak or absent in the majority of core-dominated, radio-loud AGN. This can be understood as evidence for a different structure of the accretion flow in radio-loud and radio-quiet AGN or as an effect of a jet-associated emission component shining out the weaker disk emission component. A small sample of exceptions from this rule is identified for which a disk reflection emission component has been demonstrated or is at least suggested by the available data. These sources may play an important role in future combined VLBI and X-ray studies of jet-disk coupling in radio-loud AGN.

6 Detailed Studies of Special Sources

The archival X-ray survey of radio-loud, core-dominated AGN presented in the previous chapters of this PhD thesis triggered deeper radio and/or X-ray studies of five individual sources from the *2 cm-X-Sample*. The studies of these "special" sources are presented in this Chapter.

6.1 The Quasi-Periodic Modulation of the Radio Light Curve of PKS B 0048–097

Background, observations and analysis Combined low-frequency (radio) and high-energy (X-ray, γ-ray) observations of AGN can yield important insights into the physics of relativistic outflows associated with super-massive black holes. In particular, the emission of blazars (BL Lac objects and optically violently variable objects (OVV's), see Ulrich et al. 1997 for a description on the nature of blazars) is believed to be dominated over the whole electromagnetic spectrum by the most compact regions of a relativistic jet so that a full understanding of the invoked physical mechanisms can be only achieved from quasi-simultaneous observations at different wavebands, either over long time ranges or during characteristic states of the nuclear jet.

PKS B0048−097 is a BL Lac object with unknown redshift. A lower limit of z=0.5 is postulated by Falomo (1996) from the non-detection of the host galaxy in deep optical observations. The flux density of PKS B0048−097 has been measured since 1979 at 4.8 GHz, 8.0 GHz, and 14.5 GHz as part of the UMRAO[1] program, using the University of Michigan 26 m paraboloid (Aller et al. 2003). The source is observed once every three months at all three frequencies as part of the UMRAO BL Lac Observing Program (Aller et al. 1999). The light curve since 1995 shows pronounced maxima during several well defined time periods, but a non-completely homogeneous time sampling prevents a direct derivation of the invoked time scales.

X-ray spectral analysis: PKS B 0048–097 has been observed only two times by an X-ray spectroscopic mission. Within the range of errors, no significant spectral variability could be detected on a time scale of two years between two *Beppo*Sax observations (1996-12-02 & 1997-12-19). In both epochs, the source exhibits a moderately steep photon index of $1.8 - 1.9$. The higher signal-to-noise epoch (December 1997; see also Padovani et al. 2001) yields detections in the LECS and MECS detectors but no significant PDS signal.

---

[1]University of Michigan Radio Astronomy Observatory; see
`http://www.astro.lsa.umich.edu/obs/radiotel/umrao.html`
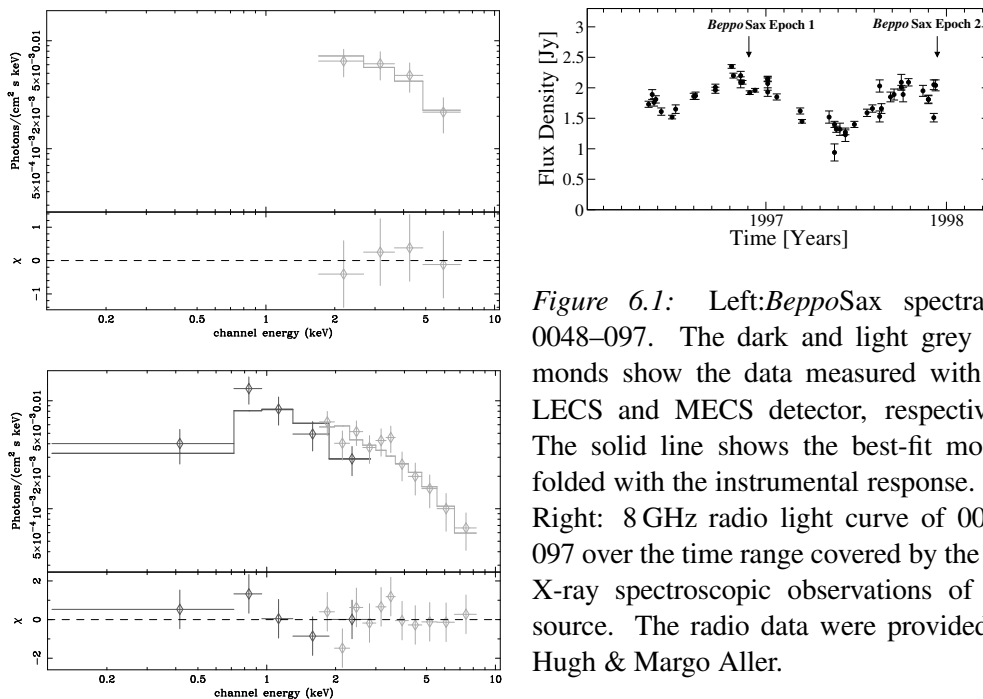
Figure 6.1: Left:*Beppo*Sax spectra of 0048–097. The dark and light grey diamonds show the data measured with the LECS and MECS detector, respectively. The solid line shows the best-fit models folded with the instrumental response. Top Right: 8 GHz radio light curve of 0048–097 over the time range covered by the two X-ray spectroscopic observations of this source. The radio data were provided by Hugh & Margo Aller.

There is no strong evidence for any extra absorption in excess over the Galactic value, in agreement with the general expectations from the standard model of AGN in type 1 sources (but compare the discussion of the detection rate of cold absorbing material in type 1 AGN in Sect. 5.2).

Interestingly, both epochs coincide with high states of the radio core, which exhibited flux-density maxima $\sim 12 - 15$ months in the time range between 1996 and 2000 (see Fig. 6.1; compare also Venturi et al. 2001). Between January 1997 and May 1997, the 8 GHz flux density of 0048–097 decreased from ~ 2.3 Jy to ~ 1.2 Jy, and rised again to ~ 2 Jy by October 1997. No X-ray data are available for the deep minimum between the two exposures or for one of the following minima.

Wavelet Analysis: Motivated by the subtle finding of similar X-ray spectra at two different epochs with similar radio states, the available UMRAO data have been investigated for periodicities that would allow for deep follow-up observations of the X-ray spectrum of PKS B0048−097 in characteristic states as it happened by chance for the two *Beppo*Sax epochs in 1996 and 1997.

A continuous wavelet analysis quantifies the behavior of a signal on different temporal scales, as a function of time, by convolving the signal with a localized wave-packet, as the packet is translated along the series, for a number of 'dilations' of the wave-packet (see Hughes et al. 1998 for a more comprehensive description). This has the great advantage of preserving temporal locality: a gap in the time series will be evident along the corresponding line in transform space, and events that are distinct in the signal will have distinct counterparts in transform space. A Morlet wavelet is particularly well suited for the analysis of time series, as it is complex, so the real part of the transform exhibits an oscillatory behavior corresponding to periodicity in the time series, while the modulus provides a measure of the power in different components of the signal.

Such an analysis has been applied to the time series for PKS B0048−097 and, as seen
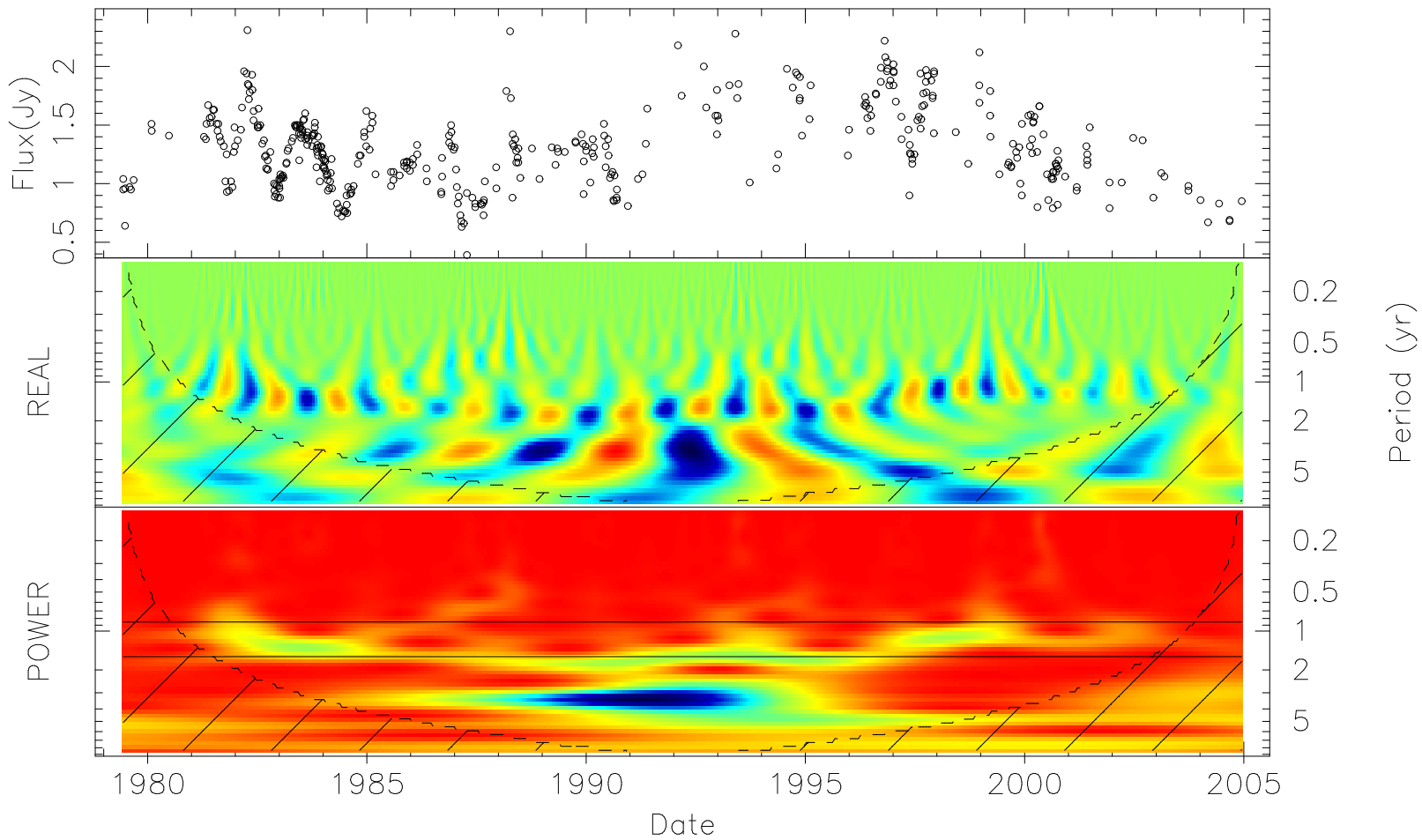
Figure 6.2: A continuous Morlet wavelet transform of the time series data of the flux density for PKS B0048−097 taken at the UMRAO at 8.0 GHz within the scope of the study presented here (illustration produced by P.A. Hughes). The panels show the flux density time series (top), the real part of the transform (middle) and the modulus (power) of the transform (bottom). The real part displays clearly the signature of a quasi-periodic component, evident at a dilation (vertical axis) with logarithmic period ∼ 2.5; a slight shortening of the period is evident in the last third of the time series, but power at this dilation extends across the entire series.

in Fig. 6.2, a distinct pattern is seen in both the real part of the source wavelet transform, and its modulus. The signal corresponds to a quasi-periodic component containing a modest fraction of the overall power. This periodicity would be masked in a Fourier power spectrum, because of small drifts in time scale across the data window, i.e., the characteristic time scale of the periodicity changes with time. The cross-wavelet transform technique is described, e.g., by Kelly et al. (2003). The continuous transform of the signal, and of a set of template periodic signals, are convolved. This analysis has been used to quantify the result (apparent on visual inspection of the top panel at Fig. 6.2), establishing a time scale of 450–470 days with a confidence of $> 99.9\%$ that this component does not arise by chance from random patterns associated with a lag-1 autoregressive process.

The varying time scale of the disclosed periodicity has been further investigated using a Lomb-Scargle periodogram analysis for different time segments during the monitoring (Lomb 1976, Scargle 1982). In a L-S periodogram, the classical discrete Fourier periodogram is redefined in such a manner to as to make it invariant to a shift of the origin of time. It is particularly designed to investigate unevenly spaced data like the UMRAO PKS B0048−097 monitoring data. The L-S periodogram analysis has been performed by E. Ros using the PERIOD software package[2].

The L-S analysis between November 1979 and September 1985 shows a strong periodicity of ~ 400–460 days and a secondary signal at ~ 580 days (see Fig. 6.3). Between October 1985 and February 1995, only one narrow peak at ~ 585 days is present. After October 1995, the strongest signal is found at a period of ~ 405 days, that is considerably less pronounced than the periodicities at the earlier time ranges. This result confirms and quantifies the result from the visual inspection of Fig. 6.2 from the Morlet wavelet analysis: a strong periodic signal is present over the full ~ 25 years of UMRAO 8 GHz radio light curve monitoring of PKS B0048−097. However, there is a small modulation in the period and its power with time.

Additional radio monitoring data of PKS B0048−097 is available from the UMRAO monitoring program at the frequencies 5 GHz and 15 GHz but because of the inferior sampling of those light curves the higher-quality 8 GHz data is better suited for a timing analysis as presented here. A comparison of the 8 GHz data with the 5 GHz and 15 GHz data will be presented elsewhere in more detail.

Structural variability on parsec scales: On parsec scales, Shen et al. (1997) and Gabuzda et al. (1999) both report a core-jet morphology of PKS B0048−097, however the southward position angles they find differ by 45 degrees. While Shen et al. (1997) report a P.A. of $\sim -160°$ (south-eastward) in epoch 1992.9 from 5 GHz VLBI observations, Gabuzda et al. (1999) find a jet at P.A. $\sim +160°$ (north-eastward) in epoch 1992.2 also from 5 GHz data. In both cases the (u, v)-coverage was not optimum. In the VLBA 2 cm Survey observations before 2002, PKS B0048−097 showed no clear resolved structure. Figure 6.4 shows the milliarcsecond structure of PKS B0048−097 in epochs 1995.57 and 2002.38. In 1995.57, a weak westward directed jet is found, partially resolved only by the longest east-west baselines. The (u, v)-data obtained in 2002.38 show clear evidence for

---

[2]The PERIOD software package is provided by the Starlink Project which was run by CCLRC on behalf of PPARC. See `http://star-www.rl.ac.uk`
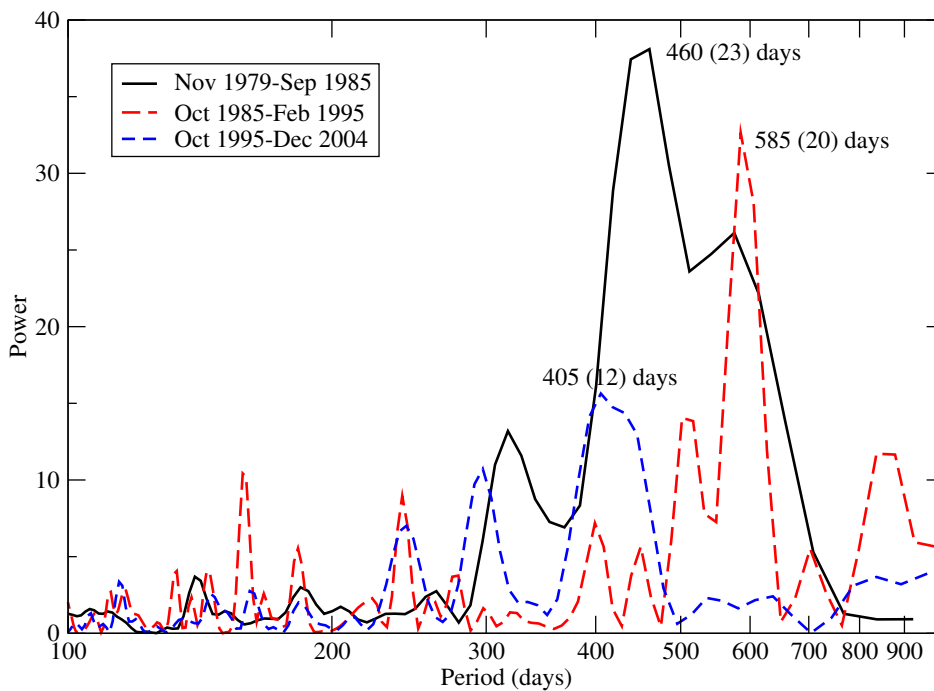
Figure 6.3: Lomb-Scargle periodogram for three different parts of the time series of UMRAO PKS B0048−097 8 GHz monitoring data. The positions of the strongest signals found are labeled with their uncertainty given in brackets.

a resolved north-south structure along P.A. $\sim -30°$ with the jet pointing in the opposite direction than reported by Gabuzda et al. (1999).

Considering these discrepancies between different works, PKS B0048−097 might exhibit an extreme jet-ejection-angle variation. This would be of particular interest in conjunction with the detected periodicity of the radio light curve. In the scenario of a precessing jet, PKS B0048−097 might represent a highly attractive target to study the broadband jet emission of a BL Lac object at different angles to the line of sight.

On the basis of the available data, it is not possible to derive the time scales of the structural variability. VLBA 2 cm Survey observations of PKS B0048−097 have been conducted during two additional epochs between 1995 and 2002 but the data quality in both cases does not allow us to compare the milliarcsecond structure directly to the two images presented here, due to shorter integration times and sub-optimal (u, v)-coverage. After 2002, the source has been observed two times as part of the VLBA 2 cm Survey continuation project, MOJAVE. An analysis of these observations, which provide full polarimetric information, is currently being performed. First images are published in Lister and Homan (2005).

6.1.1   Comparison to other blazars with known quasi-periodic behavior

Individual blazars exhibiting quasi-periodic behavior allow the relationship between the parsec-scale radio jet and the broadband spectral energy distribution to be deciphered.
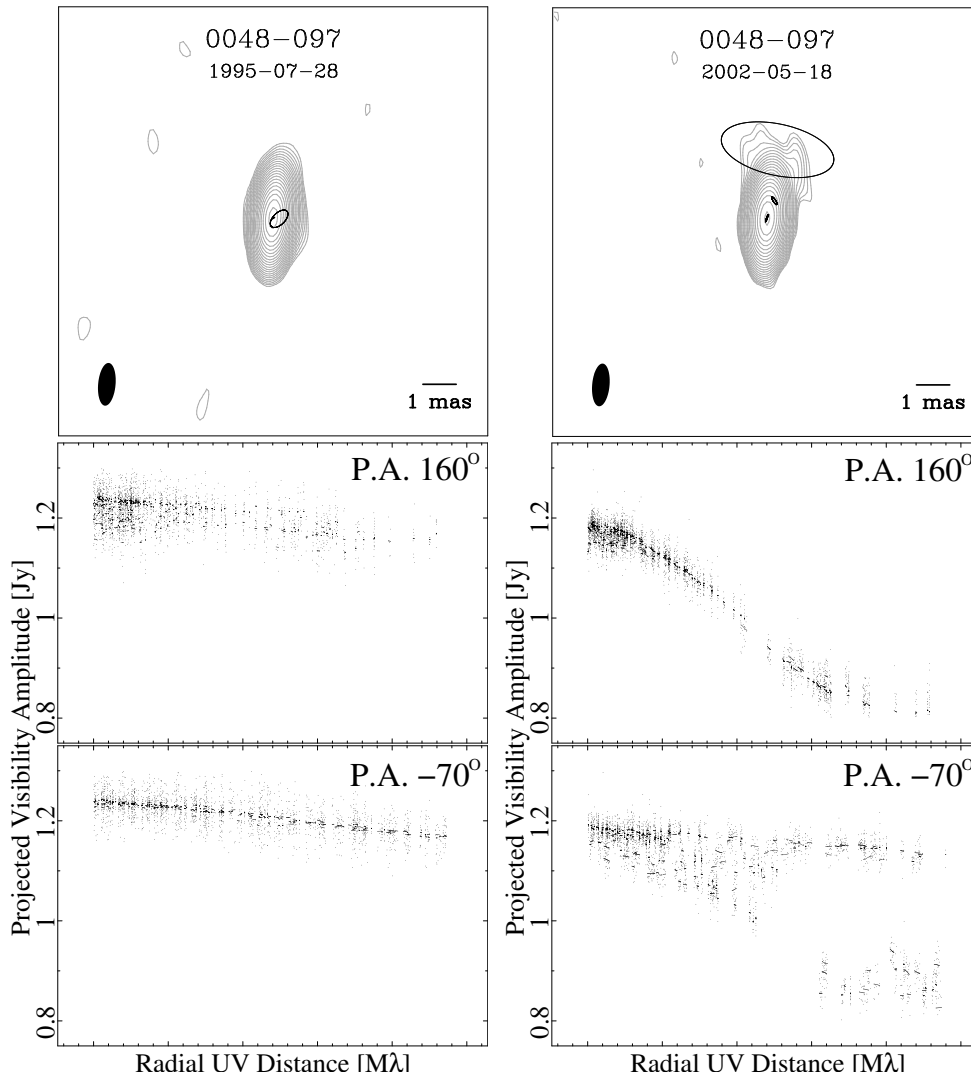
Figure 6.4: VLBI structure of PKS B0048−097 at 15 GHz. Top Panels: Naturally weighted images of 0048–097 in July 1995 (left) and in May 2002 (right) at $\lambda 2$ cm obtained from VLBA 2 cm Survey observations. Image parameters are given in Table 6.1. A jet towards the north is visible in the 2002 image while a slight extention to the west is seen in the earlier 1995 image. Best fitting Gaussian-model-component approximations to the (u, v)-data are indicated as ellipses. Middle Panels: The projected visibility along P.A. 160° for the 1995 epoch (left) and along P.A. 160° for the 2002 epoch (right). Middle and bottom panels: The projected visibility along P.A. 160° and −70° for both epochs. Clear deviations from a flat point-source visibility indicate an elongation of the source along different position angles.

Table 6.1: VLBI results for PKS B0048−097.

Epoch	Image parameters			Model fit parameters[b]			
	Beam size & P.A.	S_{peak}	rms[a]	Comp.	r	P.A.	S
	[(mas×mas),°]	[Jy/beam]	[mJy/beam]		[mas]	[°]	[Jy/beam]
1995-07-28	(1.3×0.5); -5.2	1.21	0.3	Core	0	—	1.186
				W1	0.2	−97.4	0.052
2002-05-18	(1.3×0.5); -2.6	1.09	0.2	Core	0	—	1.074
				N1	0.6	−22.2	0.110
				N2	2.1	8.7	0.012

[a] The lowest contour is in both cases 1 mJy/beam, contours increase by factors of $\sqrt{2}$. [b] Formal uncertainties in the model fits are too small and therefore are not printed in the table.

Unfortunately, such objects are rare: Hughes et al. (1998) find a persistent modulation of the total flux and polarization of the BL Lac object OJ 287. The dominating period of ∼1.12 yr in the 1980s was later displaced by a strong ∼1.66 yr periodicity during the 1990s. The relationship between these two variations was interpreted by the authors in terms of a "shock-in-jet" model. The complex periodic optical variability of OJ 287, has been interpreted in terms of a "precessing-jet" model by Abraham (2000). Stirling et al. (2003) suggest an oscillating "nozzle" structure of the inner jet of BL Lac, based on three years of optical photometric, radio millimeter flux-density monitoring and VLBI observations between 1998 and 2001. The optical and radio long-term variability of the BL Lac object AO 0235+16 has been investigated by Raiteri et al. (2001) revealing a possible 5–6 year periodicity (see Sect. 6.2.4 for a more comprehensive description of this program) based on data of the WEBT collaboration and the UMRAO database. Ostorero et al. (2004) interpreted this behavior in terms of orientation variations of a helical jet. In all these cases, attempts have been made to understand the periodic behavior as a result of jet precession possibly caused by the orbital motion of two black holes in a binary system.

6.1.2   Summary and Implications

Most multi-frequency blazar observations so far have been hampered by unpredictability of characteristic high-amplitude events within the jet flow. While post-radio-flare campaigns can be organized comparatively easy from a logistical point of view, even with the contribution of space-based missions like *Integral* (compare, e.g., the recent observing campaign on 0716+714, that was triggered in response to a major optical outburst: Pian et al. 2005), the continuous monitoring of individual objects over a long time range invokes a vast amount of telescope time and carries the danger of tracing the source during a quiescent period without the occurrence of characteristic events.

The BL Lac object PKS B0048−097 exhibits strong structural variability and pronounced radio, optical and X-ray flux variability. Here, it has been demonstrated that the radio light curve of PKS B0048−097 has a strong modulation with a characteristic period of ∼ 400–460 days and a secondary signal at ∼ 580 days. Among all sources studied so far from the UMRAO program, only OJ 287 exhibits a comparably strong persistent signal. The strength of the modulation and the comparatively short time scale

make PKS B0048−097 a prime object for coordinated broadband observing campaigns. In particular, the correlation of the varying VLBI-jet ejection angle of the source with radio (and higher energy) light-curve evolution provides a tool to test precessing-jet models against alternative models (e.g., shock-in-jet models) of periodic light-curve modulation in blazars. One may expect to find either a more or less direct one-to-one relation between the parsec-scale radio jet and the light curve at all wavelengths (indicating a precessing jet) or de-coupled structural and light-curve variability with characteristic time lags between various observing frequencies (indicating traveling shocks within the jet flow). Unlike most other sources, the short 460 day time scale of PKS B0048−097 allows these alternatives to be tested observationally in a relatively short time.

List of collaborators: H. D. Aller, M. F. Aller, P. A. Hughes, E. Ros

6.2   AO 0235+16

In this section, results are presented from the analysis of four epochs of VLBA 2 cm Survey observations, of three epochs of Effelsberg IDV observations and of the timing analysis of four *XMM-Newton* X-ray observations of the BL Lac object AO 0235+16. The Effelsberg observations and the last three *XMM-Newton* observations have been performed as part of a large observing campaign of this object organized by the Whole Earth Blazar Telescope (WEBT) collaboration (Campaign PI: C. M. Raiteri). In Sect. 6.2.1, the scientific framework of radio/optical/X-ray studies of BL Lac objects in general and the crucial role of the special source AO 0235+16 are introduced. Section 6.2.2 contains the VLBI results, presenting a kinematical model for the extremely compact parsec-scale jet structure of AO 0235+16. In Sect. 6.2.3, the analysis of an archival *XMM-Newton* is presented, reporting for the first time X-ray IDV activity of this well known radio and optical IDV source. The X-ray light curve is investigated in several wavebands without finding any evidence for time lags or large amplitude differences, an unexpected result within standard short-term variability models. A variation of the absorber can be excluded on the basis of the available data. In Sect. 6.2.4, the WEBT campaign on AO 0235+16 and the associated Effelsberg and *XMM-Newton* observations are described and results from the first observing season of this campaign are summarized, which have been published by Raiteri et al. (2005). The Effelsberg results for this first campaign season are discussed in more detail in Sect. 6.2.5. A brief discussion of the *XMM-Newton* light curves obtained during the three campaign observations of AO 0235+16 is presented, as well. Unlike in the high source state during which the archival *XMM-Newton* light curve had been taken, the source showed no evidence for pronounced short-term X-ray variability during any of these three epochs, when the source was in low-flux states.

6.2.1   Introduction

BL Lac objects belong to the blazar class of Active Galactic Nuclei (AGNs). They show variability at all wavelengths, from the radio to the γ-ray band, on a variety of time scales: in general, slow oscillations of the flux base level on time scales of years have been observed, on which fast flares lasting down to a few hours are superposed. At radio wavelengths, about 30 % of all flat spectrum radio quasars and BL Lacs are known to exhibit rapid variability (Witzel et al. 1986, Heeschen et al. 1987) on time scales of hours to days (IntraDay Variability, IDV). The cause of the variations seen in these sources is currently controversial with claims being made for either: 1) a source-intrinsic (e.g. shock-in-jet physics) or 2) extrinsic origin (scattering in the interstellar medium or gravitational microlensing) (e.g., Wagner and Witzel 1995 and references therein). Due to the involved small source sizes, interstellar scintillation (ISS) may play an important role in the cm-radio regime, while intrinsic variations require extreme high Doppler boosting (D$\sim$100) or special source geometries in order to prevent the inverse Compton catastrophe. While the variations in sources like J1819+3845 (Dennett-Thorpe and de Bruyn 2000) can be modeled by the interstellar scattering assumption, which predicts a steep frequency dependence $\nu^{-2.2}$ of the variability amplitude, this explanation fails in other sources, e.g. 0716+714, where correlated radio-optical IDV seems to be present. The different mechanisms causing rapid radio variations can only be disentangled by simultaneous monitoring

at different bands (radio–optical–X-ray). Since ISS cannot explain correlated IDV over a wide range of the electromagnetic spectrum, the detection of broad band correlations would directly role out ISS as sole explanation for radio IDV and would favor a source intrinsic contribution to the IDV pattern.

In the special case of the BL Lac object AO 0235+16 (z = 0.92), the interpretation of the observed brightness temperature requires a Doppler factor of the order of 100 (Kraus et al. 1999), which is a value significantly higher than the values of ~ 10 typical for other BL Lac objects. Very Long Baseline Interferometry (VLBI) observations reveal a compact structure only slightly resolved at milliarcsecond scales (see Fig. 6.5) and super-luminal motion (see Fig. 6.6). This milliarcsecond characteristics are in agreement with the expectations of the blazar standard model, that assumes the orientation of the nuclear jet-disk system to be very close to the line of sight.

Previous Studies of the X-Ray Spectrum of AO 0235+16:   Worrall and Wilkes (1990) and Madejski (1994) reported on observations of AO 0235+16 with the *Einstein* Observatory Imaging Proportional Counter (IPC) in 1979-1981. They attributed the substantial soft X-ray cutoff, which exceeds the absorption effects expected from our own Galaxy by several times, to photoelectric absorption in an intervening galaxy, located at $z = 0.524$. *EXOSAT* data of AO 0235+16 taken in 1984 have been discussed by Ghosh and Soundararajaperumal (1995) but the limited instrumental accuracy did not allow a pure Galactic-absorption scenario to be ruled out.

Madejski et al. (1996) verified the high absorption towards AO 0235+16 with X-ray data from *ROSAT* and *ASCA* obtained in 1993 and 1994. Substantial spectral variability was found on a time scale of months while the *ASCA* observations alone, that were spread over two weeks, revealed no significant variability on this time scale. This was interpreted by the authors as a dominating soft, steep synchrotron spectral component during bright source states and a harder inverse Compton component that becomes more important during low-flux states.

Comastri et al. (1997) found large-amplitude soft X-ray variability of AO 0235+16 from two *ROSAT* observations performed in summer 1993 without strong changes of the photon index and Webb et al. (2000) reported a very low X-ray state during a *RXTE* observation that was performed during the rising phase of a major radio-optical outburst of the source.

Junkkarinen et al. (2004) analyzed *ASCA* data of AO 0235+16 taken in 1998, about four years after the first *ASCA* epoch reporting a brighter and harder spectrum than in February 1994. A *Beppo*Sax observation in which the PDS detector did not detect the source took place in early 1999 and has been analyzed by Padovani et al. (2004).

Previous Studies of the Milliarcsecond-Scale Radio Structure of AO 0235+16:   The radio structure of AO 0235+16 can be characterized by a nearly unresolved compact component at almost all available frequencies. Chu et al. (1996) present and discuss a series of VLBI images of AO 0235+16 at 5 GHz. Frey et al. (2000) investigate the sub-milliarcsecond structural properties of the source at 1.6 GHz and 5 GHz as seen with space VLBI. They find a brightness temperature of $T_{\rm B} > 5.8 \times 10^{13}$ K at 5 GHz and hints for a slightly resolved jet to the north. However, Chen et al. (1999) report an eastward directed

jet. A resolved structure can be inferred from the $\lambda 3$ mm VLBI observations performed in 1993, during an outburst of the source (Lobanov et al. (2000)), but the data quality was not good enough to derive a source image. A follow-up $\lambda 3$ mm global VLBI observation with improved (u, v) coverage and sensitivity that has been approved to be observed after the onset of the next major flare of the source (GR 025, PI: E. Ros) might shed light on the elusive submilliarcsecond structure of this object.

6.2.2   VLBA 2 cm Survey Monitoring of AO 0235+16

Four VLBA 2 cm Survey observations of AO 0235+16 were performed between 1995 and 2001[3]. Due to the extremely compact structure of AO 0235+16, no jet speed was determined for the initial kinematical analysis of the VLBA 2 cm Survey presented by Kellermann et al. (2004). Ros (2004) presented a first update of the 2 cm Survey source kinematics, reporting speeds of additional sources for which no kinematics had been given by Kellermann et al. (2004). The partially resolved structure of AO 0235+16 was pointed out by Ros (2004), but no kinematical model was derived. Below, a reanalysis of these four epochs of VLBA 2 cm Survey observations of AO 0235+16 is presented. A kinematical model is subsequently introduced that accounts for the compact source structure by considering two overlapping Gaussian components. This model corresponds to the scenario of a jet pointing almost directly to the observer with a compact unresolved base and traveling jet plasma components that are expanding as they travel down the jet while their projection still covers the compact jet core.

CLEAN VLBI images of AO 0235+16 have been produced by applying standard self-calibration procedures (see, e.g., Kadler et al. 2004c) with DIFMAP for all four epochs. The final calibrated visibility data were fitted with uniform weighting in the (u, v)-domain with two-dimensional elliptical Gaussian functions. A single Gaussian component does not provide a good approximation of the data: the residual maps show clear evidence for missing flux (see Fig. 6.5). The structure and amplitude of the missing component is very similar in the two epochs in 1995 (that were separated by only 4.5 months) with the strongest residuals being distributed in an intermittent ring-like pattern around the central Gaussian component. The distribution of the flux residuals during the 1997 epoch is similar but with much lower amplitudes while in March 2001 a jet-like extension of the source towards the north-east is visible.

The addition of a second Gaussian modelfit component improved the fit to the data considerably in all four cases: the reduced χ^2 decreased from from 1.8 to 1.2, from 1.4 to 1.0, from 2.0 to 1.8, and from 1.3 to 1.0, respectively, and the two-Gaussian-component models became statistically competitive to the best-fitting CLEAN models. The final modelfit parameters are summarized in Table 6.2. For the first three epochs, the extended component overlaps the smaller core component in projection onto the plane of the sky. This may be indicative of a jet pointing almost directly towards the observer, with the smaller compact component representing the jet core and the extended component representing a bright region downward the jet. Such a jet component is expected to travel along a well-defined trajectory away from the core position as it increases in size and de-

---

[3]Three additional observations in March 2003, September 2004 and May 2005 have been performed as part of the VLBA 2 cm Survey extension project MOJAVE. Another MOJAVE observation is planned for mid/late 2005. The data from these epochs will be presented elsewhere.

Table 6.2: AO 0235+16 VLBI model fit parameters.

Id[a]	Flux density [mJy]	Radius[b] [mas]	P.A.[c] [°]	Major Axis [mas]	Axial Ratio	ϕ[d] [°]	$T_{\rm b}$[e] K
			Epoch 1995.57, $\chi_{\rm red} = 1.2, 7100$ *d.o.f.*				
C	614	0	—	0.21	0.54	−23	2.7×10^{11}
J1	173	0.12	−22	0.87	0.74	−13	3.3×10^{9}
			Epoch 1995.96, $\chi_{\rm red} = 1.0, 6300$ *d.o.f.*				
C	241	0	—	0.16	0[f]	−33	$> 9.9 \times 10^{10}$
J1	153	0.11	−15	0.91	0.72	−17	2.7×10^{9}
			Epoch 1997.66, $\chi_{\rm red} = 1.8, 3100$ *d.o.f.*				
C	1438	0	—	0.11	0[f]	−81	$> 1.3 \times 10^{12}$
J1	27	0.21	26	1.40	0.80	15	1.8×10^{8}
			Epoch 2001.20, $\chi_{\rm red} = 1.0, 6900$ *d.o.f.*				
C	1439	0	—	0.08	0[f]	70	$> 2.4 \times 10^{12}$
J2	118	0.23	−33	0.35	0.38	73	2.7×10^{10}

[a] Component ID: C (Core), J1 (first jet component), J1/2 (ambiguous identification as first or second jet component); [b] Distance from core component; [c] Position angle of the line connecting core and component (measured from North through East); [d] Position angle of the major axis of the elliptical Gaussian (measured from North through East); [e] Brightness temperature, calculated following XXX Kovalev et al. (2005); [f] The two-dimensional Gaussian component degenerated to a linear feature during the fitting procedure, indicative of an elongated structure that is unresolved in the direction perpendicular to ϕ. For the calculation of $T_{\rm b}$, the value of the major axis was used to derive a lower limit.

creases in flux due to adiabatic expansion. The data given in Table 6.2 are in agreement with this scenario: the extended component of the first three epochs (J1) travels with (0.048 ± 0.004) mas/yr along a curved path, its flux density and brightness temperature decrease monotonically and its size increases (compare Fig. 6.6). This sky proper motion corresponds to an apparent speed of $\beta = (2.38 \pm 0.19)$. The secondary Gaussian component found in the 2001 epoch (J2) exhibits a much higher brightness temperature and is most likely representative of a newly emerged jet feature after J1 disapeared during the long observing gap between the 1997 and the 2001 epoch. It is interesting to note that the back extrapolation of the J1 trajectory in the radius-vs-time domain predicts for the ejection epoch 1993.25, right after the onset of one of the major flares of AO 0235+16 (see below). An association of VLBI component ejections with radio flares in AO 0235+16 are of special interest since they rule out microlensing as a possible origin for the given outburst. An analysis of the new MOJAVE observations of AO 0235+16 will show if the new jet component J2 can be attributed to the 1997 outburst that remains the most promising candidate for a microlensing event in this system (compare Stickel et al. 1988, Webb et al. 2000).

6.2.3 Short-Term X-Ray IDV Activity of AO 0235+16 in February 2002

Of special interest is the variability of AO 0235+16 on short time scales. At radio wavelengths the source is known to exhibit strong intraday variability (IDV; e.g. Kraus et al.
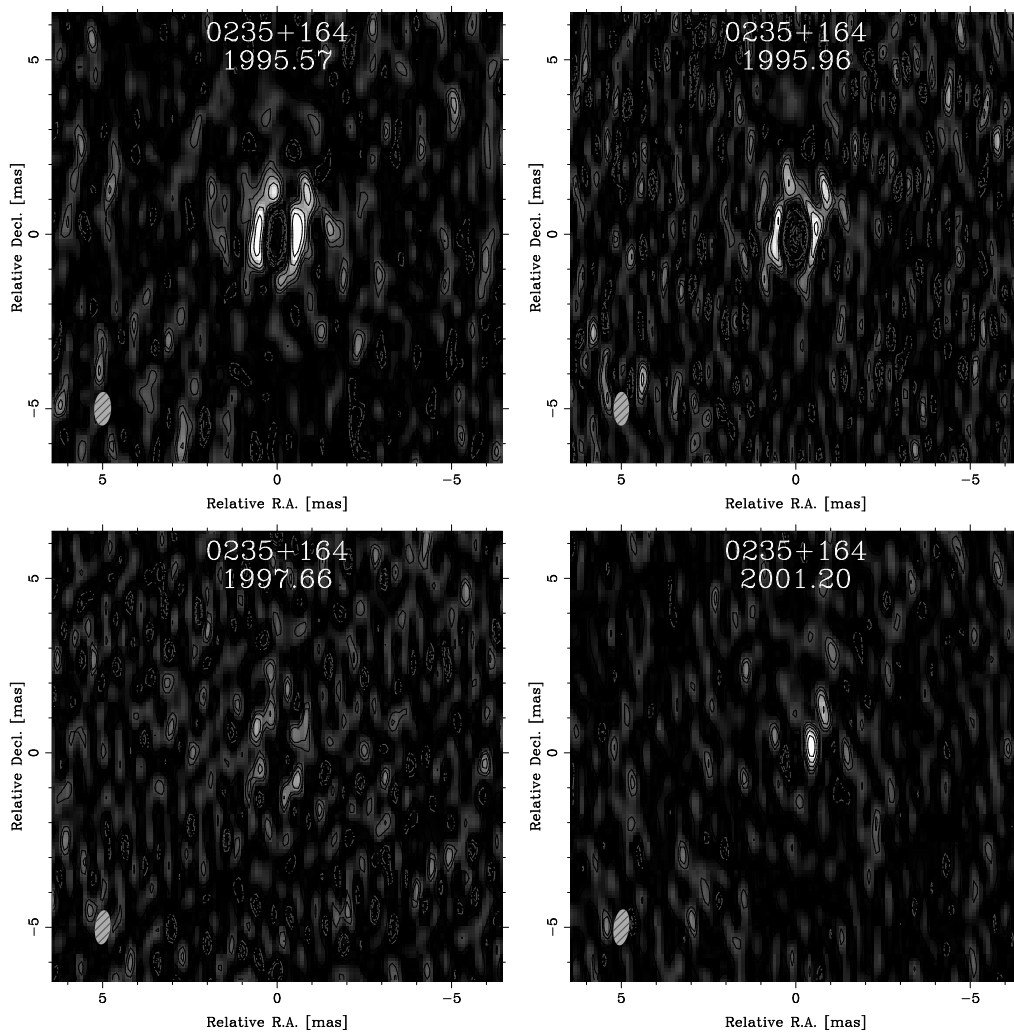
Figure 6.5: Visibility residuals for the four epochs of VLBA 2 cm Survey observations of AO 0235+16 after fitting with a single Gaussian component. Negative residual flux is shown in light-grey, dashed contours (-0.004, -0.0028, and -0.002 mJy/beam), positive residual flux is shown in black solid contours (0, 0.002, 0.0028, 0.004, and 0.0057 mJy/beam). The light-grey, hatched ellipse in the bottom left corner of each panel represents the restored beam. Note the need for an intermittent ring-like extended emission structure in the first three epochs that becomes weaker with time. In 2001, the ring-like structure has vanished and a weak jet-like structure to the north-east has formed.

1999), requiring an extremely small source size. IDV has been detected over a wide range of the electromagnetic spectrum. Besides correlated radio IDV at $\lambda 20$, $\lambda 6$ cm, and $\lambda 3.6$ cm with a possible optical correlation (Kraus et al. 1999), IDV has been seen in the IR (Takalo et al. 1992) and the optical regime (Romero et al. 2000, Raiteri et al. 2001). Below it is shown that AO 0235+16 exhibits IDV at X-ray frequencies, as well.

In February 2002, a ~ 20 ksec *XMM-Newton* observation of AO 0235+16 took place. The archival data have been obtained from the *XMM-Newton* archive and light curves for all three EPIC detectors have been produced as described in Sect. 3.4.4 from circular regions of $100''$ (accounting for the high source flux at this epoch). Count rates have been
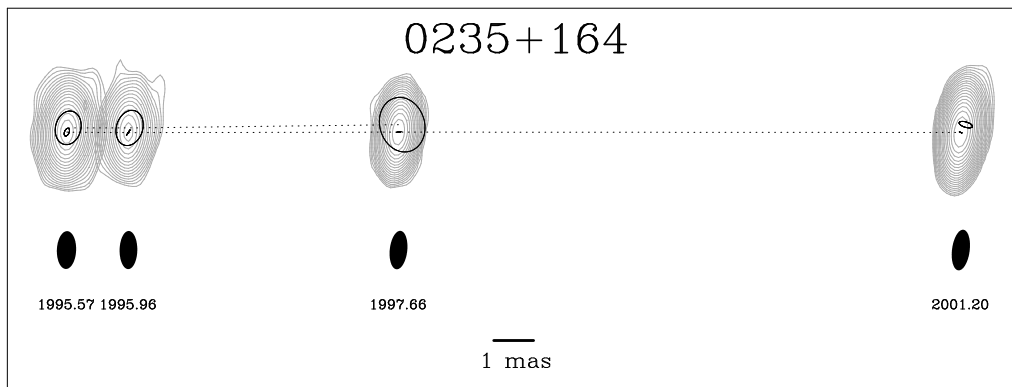
Figure 6.6: The milliarcsecond structure of the BL Lac object AO 0235+16 observed with Very-Long-Baseline Interferometry (VLBI). At a frequency of 15 GHz, 80% to 98% of the radio emission is unresolved even with a resolution below 1 mas. The quasi-concentric, variable elliptical Gaussian model components, visible in the first three epochs, can be interpreted as the trace of moving jet plasma oriented almost directly to the line of sight. The lowest contour for the first to fourth epoch is 2 mJy, 2.8 mJy, 4 mJy, and 2 mJy, respectively.

determined by averaging over 100 s bins, resulting to a SNR of each data point of ~ 17 for the PN and ~ 10 for the MOS detectors, respectively. The event list has been filtered to contain only time intervals during which the count rate in the adjacent source-free background region did not exceed 0.1 cts/s and 0.2 cts/s for the MOS and PN detectors, so that no background subtraction was necessary. Figure 6.7 shows the resulting X-ray light curve of AO 0235+16 in February 2002. Rapid X-ray variability with time scales smaller than one hour are visible with amplitudes up to $\sim 50\%$ of the source count rate.
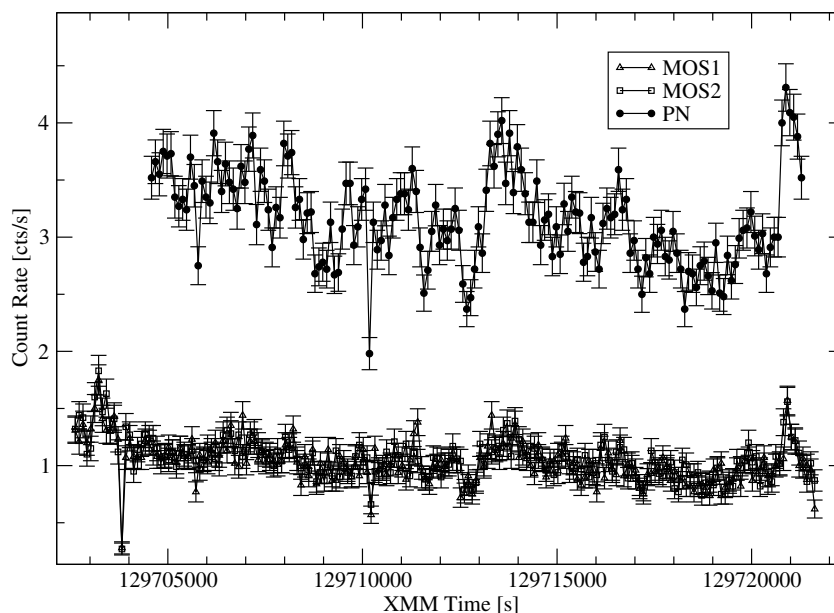
Figure 6.7: X-ray light curve (0.3 keV to 12 keV) extracted from the ~ 20 ksec *XMM-Newton* observation of AO 0235+16 in February 2002 averaged over 100 s bins.
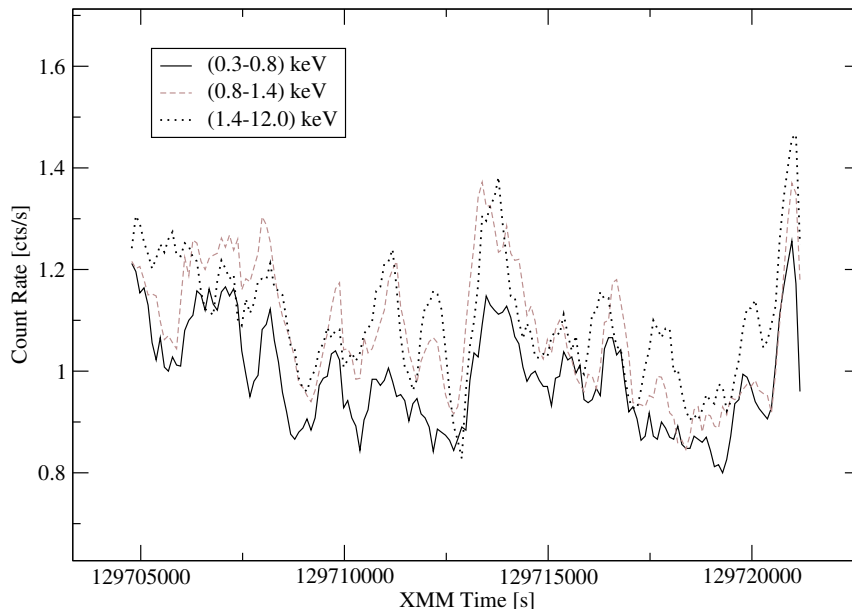
Figure 6.8: XMM-Newton PN light curve of February 2002 split into three energy bands with roughly the same count rate. No time lags between the different energy bands are detectable.

The spectral behavior of characteristic variability patterns can reveal the nature of the underlying physical mechanism. E.g., in Sect. 6.5, a $\sim 150\,\mathrm{s}$ time lag of the soft X-ray emission with respect to the hard X-ray emission is found during a pronounced short-term X-ray flare of the BL Lac 0716+714. There, a jet model is developed that naturally explains such soft lags as a result of travel times of disturbances within a compact jet. Therefore, the *XMM-Newton* 2002 light curve of AO 0235+16 has been investigated within three different energy bands that contribute roughly the same number of photons to the integrated light curve in Fig. 6.7: $(0.3-0.8)\,\mathrm{keV}$ (solid line), $(0.8-1.4)\,\mathrm{keV}$ (dashed line), and $(1.4-12.0)\,\mathrm{keV}$ (dotted line). The three individual light curves have been averaged in time via a running-average calculation over five $100\,\mathrm{s}$ bins each. The resulting three independent light curves (see Fig. 6.8) do not show any lags according to a cross-correlation analysis. The two most obvious flares (close to XMM time 129714000 and 129721000) are less pronounced in the soft band with flux increases of 35 % and 37 %, respectively, (relative to the pre-flare level) compared to the up to ~ 70 % flares in the harder energy bands. However, over the full integration time, the standard deviation of the three light curves are very similar: the variations in the normalized and running-averaged light curves are 10 %, 12 %, and 11 %. In the original light curves (i.e., before the running-average procedure) the differences are even less pronounced with variations of 16 % in all three cases. In sum, the short-term X-ray source variability of AO 0235+16 detected in the February 2002 *XMM-Newton* light curve is remarkably strong and homogeneous across the full *XMM-Newton* bandpass between 0.3 keV and 12 keV. This behavior, in particular the lack of time lags between the various energy bands, is unexpected in synchrotron or inverse Compton jet models that generally attribute the emission at different frequencies ν to different distances r_ν along the jet, with $r_\nu \propto \nu^{-1}$. A perturbation traveling along the jet is expected to need a time τ to travel from $r_{0.3\,\mathrm{keV}}$ to $r_{12\,\mathrm{keV}}$. Assuming relativisti-

cally moving jet plasma with a velocity β, the resulting time lag between the emission at 0.3 keV with respect to the emission at 12 keV is $t_{\mathrm{lag}} = \tau\beta$. In the case of AO 0235+16 in February 2002, *XMM-Newton* collected enough photons to safely detect any time lag larger than 200 s (two time bins in Fig. 6.7). With $\beta \leq 1$, we derive the X-ray emitting section along the jet to be smaller than $\delta 2 \, \mu$pc, where δ is the Doppler factor.

To further investigate the relation between the source flux variability and spectral characteristics, two separate source spectra have been determined for the low-states and the high-states of the source flux during the ~ 20 ksec observation. To achieve this, the mean 0.3 keV to 12 keV source count rate of 3.15 cts/s was used to split the event file into two approximately equally large fractions corresponding to the time intervals of low and high source flux, respectively. Two separate source spectra were produced from these two sub event files and both were fitted with a one-power-law model absorbed by a Galactic column density of 8.94×10^{20} cm^{-2} according to the LAB survey and an additional absorber located at $z = 0.524$, the redshift of the intervening system towards AO 0235+16. For this fit, the energy range was restricted to 0.6 keV to 6 keV to reduce the effect of spectral curvature and to achieve statistically good fits with only one power law component. As expected, the two spectra differ in flux ($F_{(0.6-6)\,\mathrm{keV,low\ state}} = 7.1^{+0.1}_{-0.1} \times 10^{-12}$ erg s^{-1} cm^{-2}; $F_{(0.6-6)\,\mathrm{keV,high\ state}} = 8.5^{+0.1}_{-0.1} \times 10^{-12}$ erg s^{-1} cm^{-2}; both values corrected for Galactic absorption).

The best fitting values for the excess absorption and the photon index are similar but not identical, indicating spectral differences between the two source states. There are two possible explanations for such a spectral variation: I) the absorber at $z = 0.524$ has varied and is responsible for the source variability, and II) the power law has varied, attributing the variable light curve to source intrinsic processes. The first scenario would imply extremely small (and therefore extremely compact) absorbing clouds while the second one corresponds to a source-intrinsic origin of the detected short-term X-ray. Fig. 6.9 shows the residuals for the best simultaneous fitting model to the low-state and the high-state PN spectrum. The poor fit and the systematic residuals rule out a scenario I. The detected short term variability of AO 0235+16 during the February 2002 *XMM-Newton* epoch is therefore most likely to be explained in terms of true source variability. The best fitting model for this scenario predicts that the source continuously varied between $F_{(0.3-12)\,\mathrm{keV,low\ state}} \sim 8.3 \times 10^{-12}$ erg s^{-1} cm^{-2} and $F_{(0.3-12)\,\mathrm{keV,high\ state}} \sim 9.8 \times 10^{-12}$ erg s^{-1} cm^{-2} n the full *XMM-Newton* band. During this variation the spectrum became softer as the source flux increased and harder as the source flux decreased with best fitting mean values for the photon index of $\Gamma_{\mathrm{low\ state}} = 2.29 \pm 0.02$ and $\Gamma_{\mathrm{high\ state}} = 2.35 \pm 0.02$.

6.2.4 The WEBT+Effelsberg+*XMM-Newton* Observing Campaign on AO 0235+16

The analysis of the *long-term* radio and optical light curves of AO 0235+16 has led to the conclusion that the main radio outbursts have optical counterparts, and that they repeat every 5.7 ± 0.5 yr (Raiteri et al. 2001, see Fig. 6.10). The next outburst was foreseen to peak around February–March 2004, so that a multi-wavelength radio-optical campaign
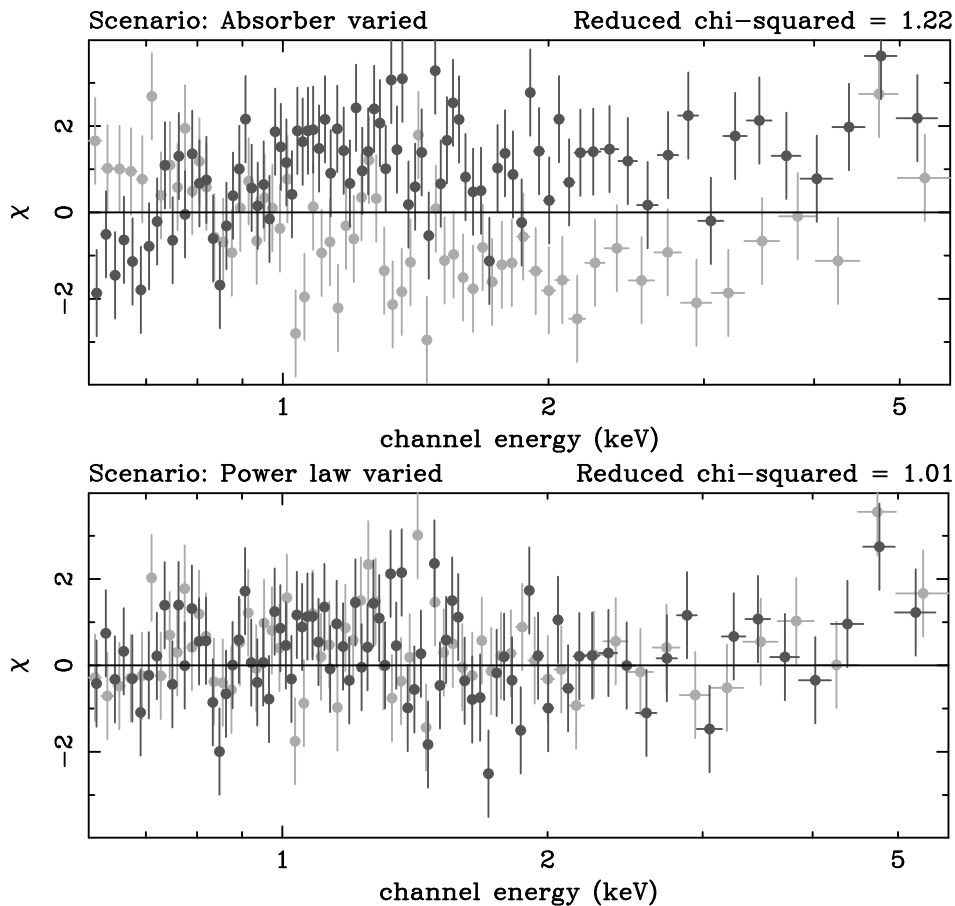
Figure 6.9: Residuals for the best simultaneous fitting model to the low-state (light grey) and the high-state (dark grey) of the *XMM-Newton* PN spectrum of February 2002, assuming that only the absorber at $z = 0.524$ has varied (top panel) and that only the power law has varied (bottom panel). For clarity, the data have been regrouped for this figure to have 250 counts per bin. Only data between 0.6 keV and 6 keV have been considered to maintain a fair approximation with a single power law.

has been organized by the Whole Earth Blazar Telescope (WEBT[4]) collaboration, involving more than 30 optical and 2 radio observatories. In addition to the WEBT participating observatories, we have successfully applied for observing time with the X-ray telescope *XMM-Newton* and the Effelsberg 100-m radio telescope. Three *XMM-Newton* pointings took place on January 18, 2004, August 2, 2004, and on January 28, 2005. During each of these pointings, simultaneous radio-light curve monitoring observations have been conducted at Effelsberg (see below).

The study of blazar flux variability to understand the elusive physical processes invoked requires simultaneous observation across the whole accessible electromagnetic spectrum. This provided the main motivation for the WEBT AO 0235+16 campaign. As an intermediate object between the two main sub-classes of high-frequency peaked (HBL) and low-frequency peaked (LBL) BL Lac objects AO 0235+16 is a particularly interesting target for such a campaign. LBLs and HBLs differ in the absolute position of

---

[4]http://www.to.astro.it/blazars/webt
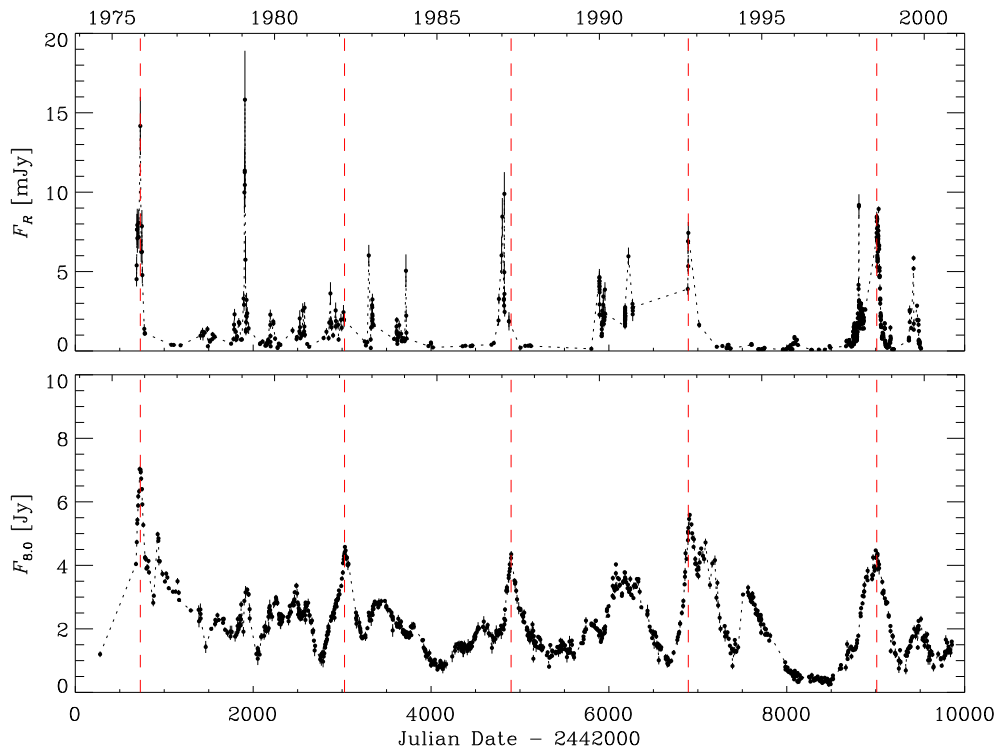
Figure 6.10: Long-term optical (R band, top) and UMRAO radio (8 GHz, bottom) light curves of AO 0235+16. Vertical dashed lines mark the recurrent outbursts. Image adopted from Raiteri et al. (2001).

the primary low-energy spectral maximum (generally assumed to be due to synchrotron jet emission) and the peak of the secondary high-energy component (originating from inverse Compton emission, e.g., Ghisellini and Madau 1996, or from hadronic processes induced by relativistic protons in the jet, e.g., Mannheim and Biermann 1989). LBLs are characterized by a low-energy peak in the near infrared or optical range and a high-energy peak at 100 MeV to 1 GeV, while in HBLs the two spectral maxima can be shifted far into the X-ray and > 100 GeV energy ranges, respectively (e.g., Fossati et al. 1998). Madejski et al. (1996) recognized a dominance of the steep tail of the synchrotron component in bright states of AO 0235+16 and a prevalence of the harder secondary component in lower states. In Fig. 6.11, the variable broadband spectral energy distribution of AO 0235+16 during past X-ray observations between 1993 and 2004 is shown. In the (optically bright) February 1998, August 2000, and in the January and August 2004 epochs, the dominance of the secondary, high-energy peaked component is very pronounced.

Until the time of writing of this thesis (early July 2005) the awaited outburst of AO 0235+16 has not happened! However, a wealth of information has been derived from the simultaneous collection of broadband spectral data between the radio and X-ray regimes. Results from the first observing season (2003-2004; including the first epoch of *XMM-Newton* and Effelsberg observations) have been published by Raiteri et al. (2005). At present, several local optical and radio telescopes of WEBT members are still monitoring the source and will continue until the awaited flare is detected. Such detection
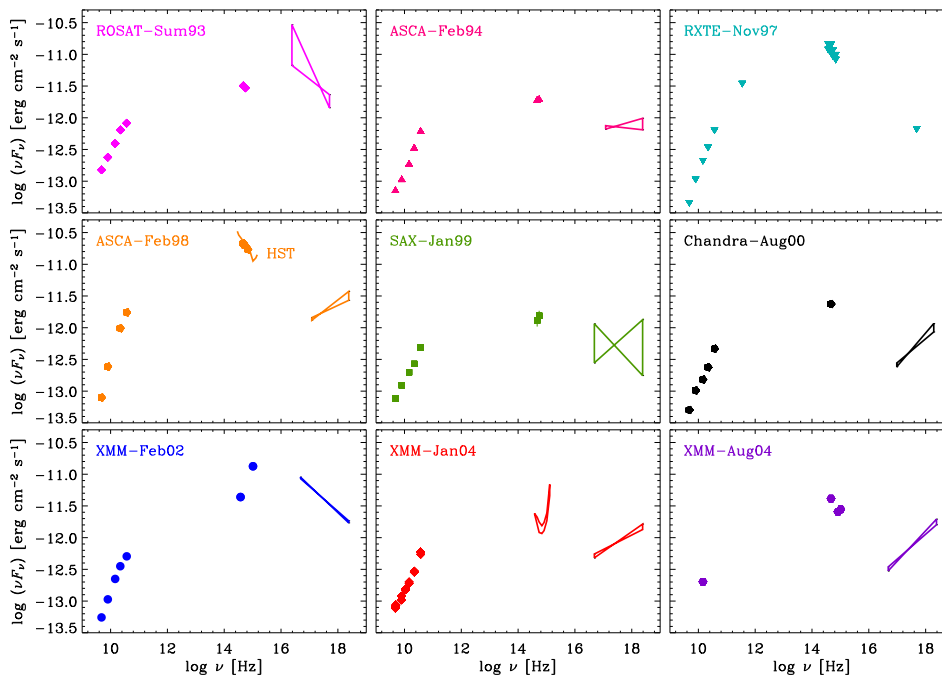
Figure 6.11: The variable broadband spectral energy distribution of AO 0235+16. The six panels show quasi-simultaneous radio, optical, and X-ray data separated by several years. The two *XMM-Newton* spectra taken in January and August 2004 (lower right panel) demonstrate the spectral variability of the source on time scales of months. Image provided by C.M. Raiteri.

would then trigger a further radio and optical dense monitoring WEBT campaign, with the expected participation of at least 20 optical telescopes.

6.2.5 Simultaneous Radio/X-ray IDV observations with the Effelsberg 100-m telescope and *XMM-Newton*:

One of the motivations for the simultaneous observation of AO 0235+16 on three occasions during the WEBT campaign in 2004/2005 was the possibility to search for simultaneous short term variability in the radio and the X-ray regime. AO 0235+16 is a well known radio IDV source and showed pronounced X-ray short-term variability during a previous *XMM-Newton* observation in 2002 (see Sect. 6.2.3). The simultaneity of radio and X-ray observations should make the campaign sensitive to correlated fast variations in both frequency bands. A direct radio/X-ray IDV correlation would have important consequences for the understanding of short-term source variability, pointing to an intrinsic origin of the IDV activity in AO 0235+16.

Radio IDV observations of AO 0235+16 with the Effelsberg 100-m telescope: On arcsecond scales, AO 0235+16 is a compact radio source and appears pointlike to the Effelsberg 100-m telescope. Its relative brightness of $\sim 1.7\,$Jy at $\lambda 6\,$cm and $\sim 1.4\,$Jy at $\lambda 2.8\,$cm in January 2004 allowed the flux-density measurements to be performed with
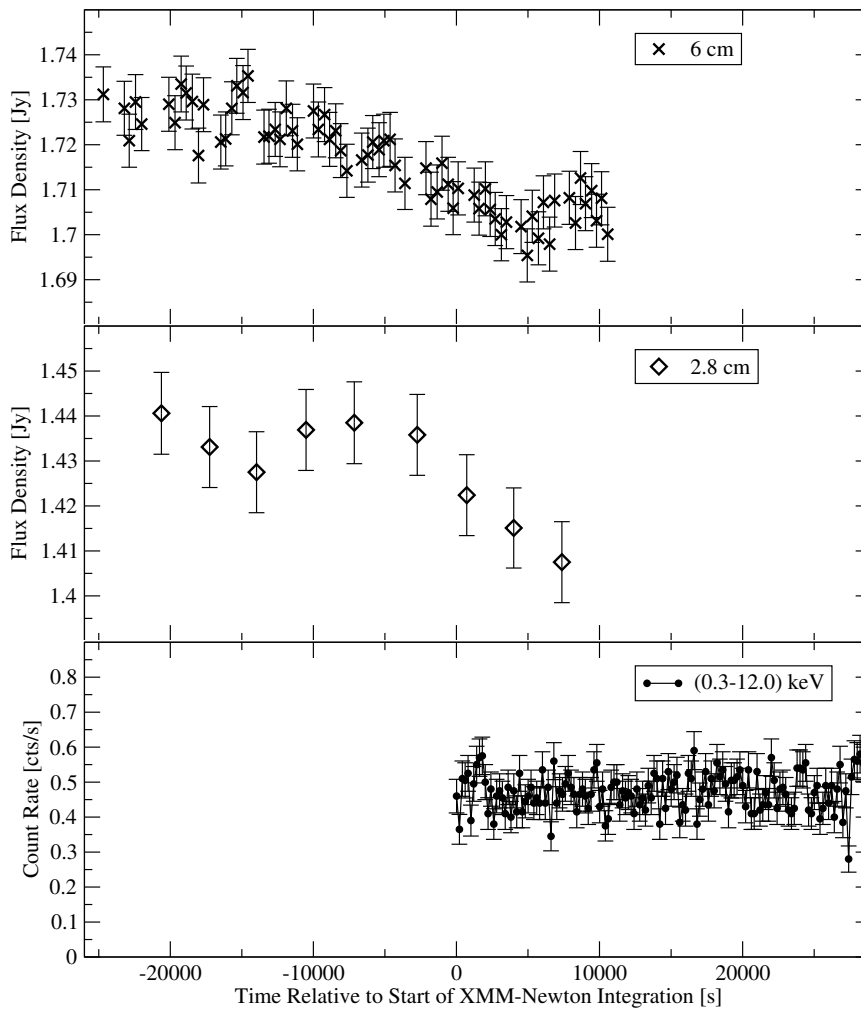
Figure 6.12: AO 0235+16 radio and X-ray light curves during the first *XMM-Newton*+Effelsberg epoch on January 18, 2004.

"cross scans" (Heeschen et al. 1987; Quirrenbach et al. 1992 for a description of the procedure) over the source position. The cross scans consisted of four individual subscans in azimuthal and elevational back-and-forth direction, respectively, which in addition were used to control the telescope pointing accuracy throughout the observations. During the measurements, lefthand- and righthand-circular polarization signals were recorded and later, offline combined. The flux density of AO 0235+16 was measured 7-8 times per hour at $\lambda 6$ cm and once per hour at $\lambda 2.8$ cm. Between the scans on the target source, the two steep-spectrum secondary calibrators, 3C 60 and 4C 08.10, were observed, alternately. As primary flux calibrators, the sources 3C 48, 3C 161, and 3C 286 were used (see Ott et al. 1994 and references therein).

Gaussian profiles were fitted to every subscan, yielding the convolution of point-like source-brightness distribution with the telescope beam. Small residual pointing errors were corrected and the amplitudes of the subscans were averaged for each scan. The secondary calibrators were used to correct for time- and elevation-dependent antenna gain effects. The absolute calibration of the measured flux-density was achieved by scaling
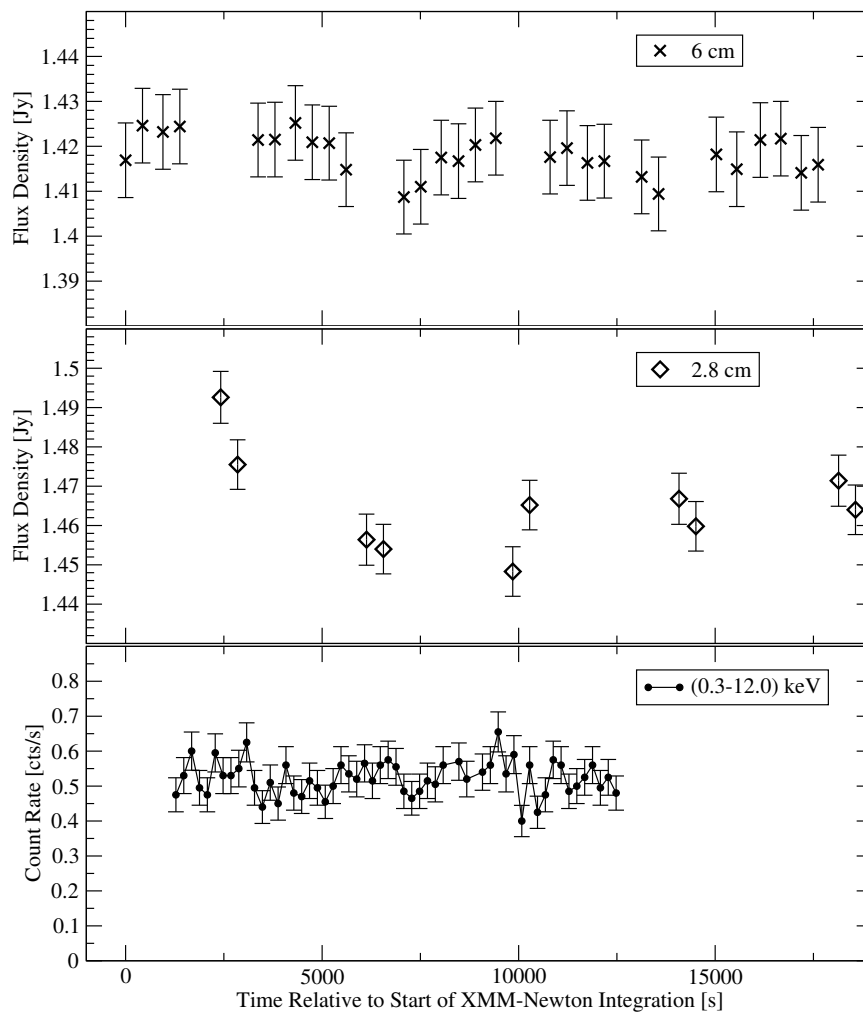
Figure 6.13: AO 0235+16 radio and X-ray light curves during the second *XMM-Newton*+Effelsberg epoch on August 2, 2004.

the registered signal from the primary calibrators to match their tabulated brightnesses. The errors of the flux-density points were estimated from the residual scatter of the non-variable secondary calibrators, which dominated over the formal statistical errors[5].

In Figure 6.12 to Figure 6.14 the resulting radio light curves of AO 0235+16 during the three *XMM-Newton*+Effelsberg observations are shown. Results from the first epoch of Effelsberg observations have been published in Raiteri et al. (2005) and are summarized below. During the second epoch, the source showed no significant short-term radio variability at $\lambda 6$ cm during the ~ 4.5 hours of Effelsberg monitoring. At $\lambda 2.8$ cm, the first and the second scan showed a flux density $\sim 2\%$ and $\sim 1\%$ above the level of the remaining scans. This may indicate that the source flux density was decreasing from a higher level when the Effelsberg monitoring started. However, it is not possible to derive meaningful results on the basis of these two data points alone. During the third epoch, on January 18, 2005, only marginal variability of AO 0235+16 at $\lambda 6$ cm was found, while

---

[5]The data reduction for the first epoch of Effelsberg observations was done by the author in collaboration with V. Impellizzeri. The second and third epoch has been reduced by V. Impellizzeri.
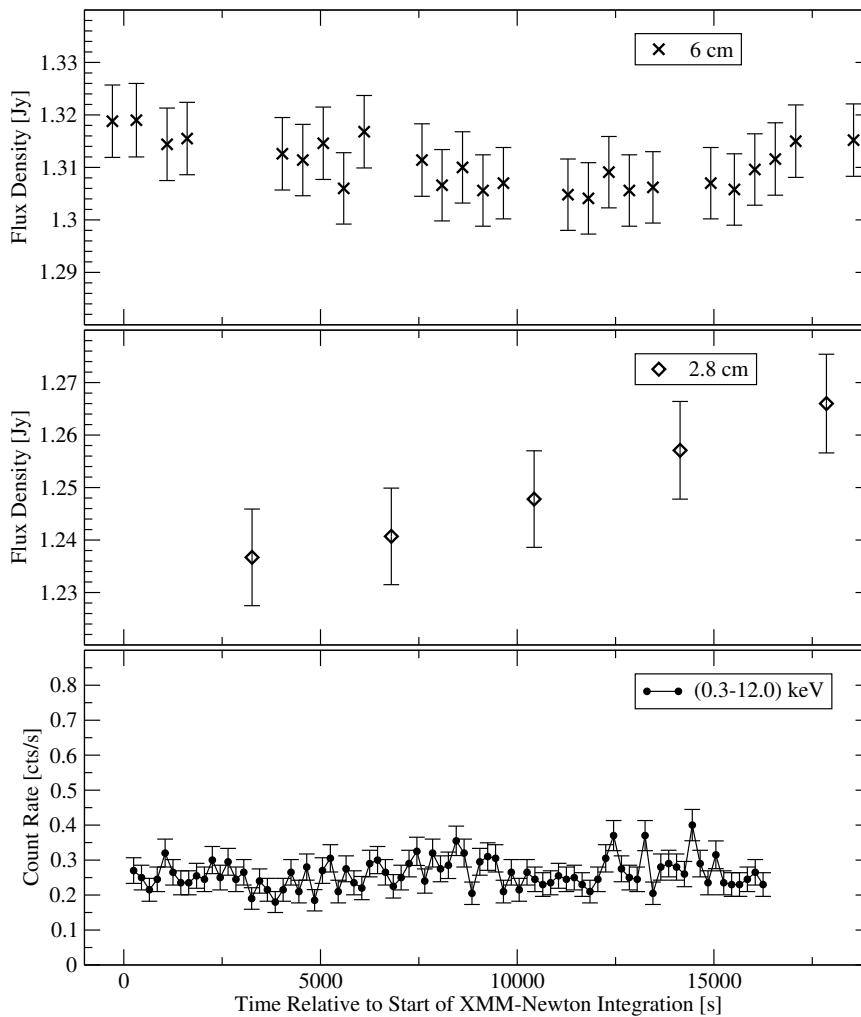
Figure 6.14: AO 0235+16 radio and X-ray light curves during the third *XMM-Newton*+Effelsberg epoch on January 28, 2005.

the $\lambda 2.8$ cm flux density increased monotonically by $\sim 2.5\%$ over ~ 4.5 hours. The light curves of AO 0235+16 for these two epochs are shown here for completeness only. A more detailed analysis will be presented elsewhere (Raiteri et al., in prep.).

AO 0235+16 exhibited short-term radio variability at both observed radio frequencies during the ~ 10 hours of Effelsberg observations on January 18, 2004, on a level of 2–3 %[6]. This corresponds to modulation indices $m = 0.5\%$ at $\lambda 6$ cm and $m = 1.2\%$ at $\lambda 2.8$ cm, where $m[\%] = 100 F/\langle F \rangle$ is defined via the standard deviation of the flux density, F, and its average value in time, $\langle F \rangle$. A higher modulation index at shorter wavelengths, as found here, is not expected if interstellar scintillation were the physical mechanism responsible for the IDV activity (e.g., Rickett 1986). This motivates the determination of formal brightness temperatures and Doppler factors from the assumption that the flux variations have a source-intrinsic origin. During the observation the flux

---

[6]The flux-density uncertainties, estimated from the residual scatter of secondary calibrators, are $\sim 0.25\%$ at $\lambda 6$ cm and $\sim 0.54\%$ at $\lambda 2.8$ cm. In Fig. 6.15, the radio light curves of the secondary calibrator 3C 67 during the first epoch are shown for comparison.

density of AO 0235+16 decreased by $\sim 30\,$mJy in ~ 7 hours at $\lambda 6\,$cm, and by $\sim 50\,$mJy in ~ 6 hours at $\lambda 2.8\,$cm. Both these variations set the same lower limit to the source brightness temperature, $T_{\mathrm{b}} \leq 10^{17}\,$K, and to the Doppler factor, $\delta \leq 46$, if the excess over the inverse-Compton limit of $10^{12}\,$K is solely attributed to Doppler boosting. The most conservative estimate of the variability time scale results from calculating the logarithmic time scale $d(\ln s)/dt$ for the observed (partially observed) light curve (e.g., Jones et al. 1974). The correction factor $<S>/\Delta S$ yields an upper limit of 14.3 days for the variability time scale, corresponding to lower limits of $T_{\mathrm{b}} \geq 5 \times 10^{14}\,$K and $\delta \geq 8$.
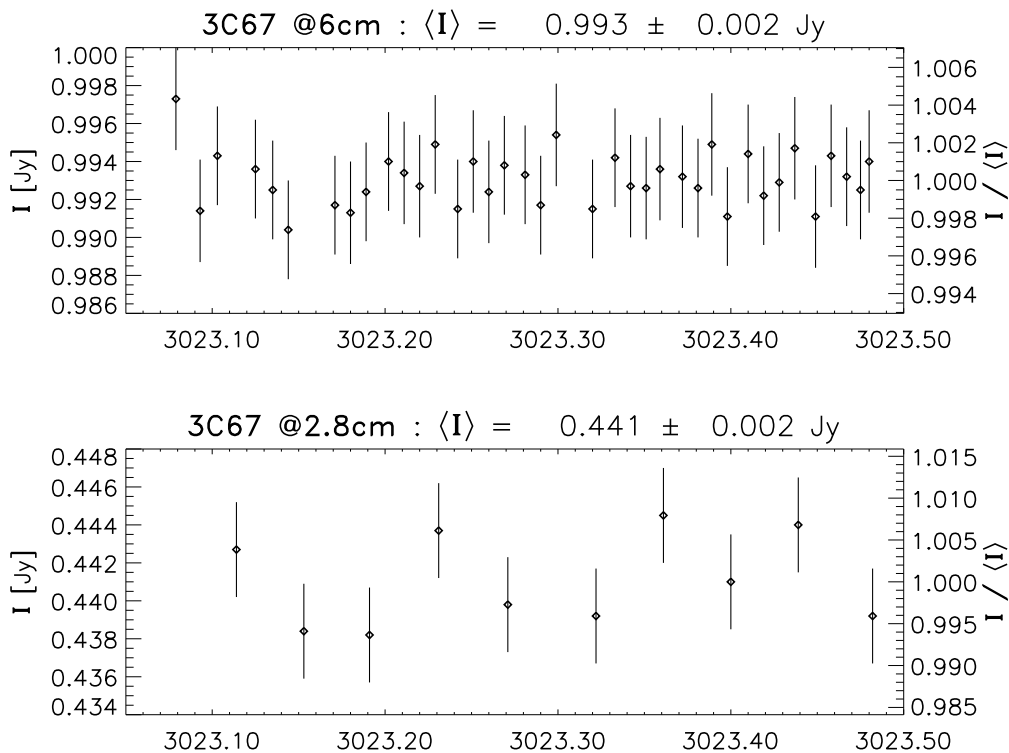
Figure 6.15: Radio light curves at $\lambda 6\,$cm (top) and $\lambda 2.8\,$cm (bottom) for the secondary calibrator 3C 67 during the first Effelsberg observation of AO 0235+16 on January 18, 2004.

Timing analysis of the three *XMM-Newton* observations The bottom panels of Figure 6.12 to Figure 6.14 show the X-ray light curves obtained during the three WEBT–Effelsberg–*XMM-Newton* epochs on 2004 January 18, 2004 August 2, and 2005 January 28. At all three epochs, the source was found in a much lower state than in February 2002 (a comparison of the spectral values in Table 4.1 shows that particularly the soft flux between 0.5 keV and 2 keV was a factor of 6 to 12 larger in 2002 than in the three 2004/2005 epochs). This lower flux level reduces the maximal time resolution of the PN detector since longer integration bins are necessary to achieve the same SNR as in brighter source states. However, in addition to this, the source showed a much more stable flux level during all three epochs: the variations after applying a running average over five 200 s bins left only weak variability with amplitudes of 4.7 %, 4.6 %, and 8.8 % for the
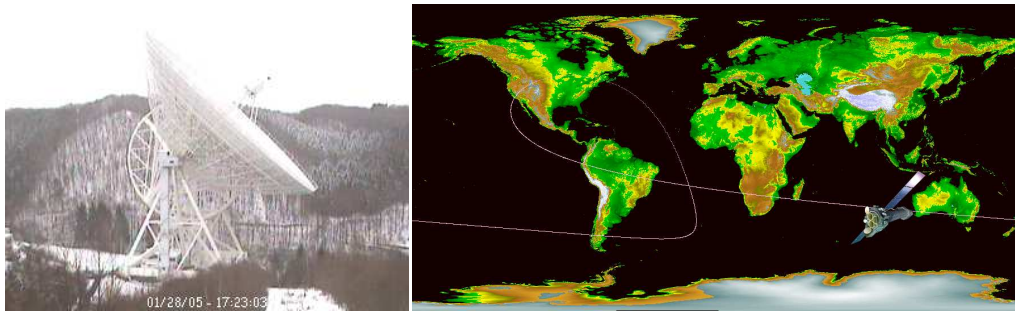
Figure 6.16: The Effelsberg 100-m radio telescope and the X-ray satellite *XMM-Newton* on 2005 January 28, 5:23 pm (MEZ) during their third simultaneous observation of the BL Lac object AO 0235+16.

three light curves, respectively. In particular, no clearly identifiable events in all three EPIC cameras are visible with the possible exception of the three short events on 2005 January 28 in the last part of the light curve.

The fact that among four performed *XMM-Newton* observations of AO 0235+16 the optically brightest epoch with the highest X-ray flux and the by far steepest X-ray photon index is the only one that exhibits clear strong X-ray IDV activity suggests that the high-energy tail of the primary jet synchrotron component was responsible for the short-term X-ray variability. This is the same behavior as exhibited by 0716+714 (see Sect. 6.5) where the strongest X-ray short term variability is found in the epoch with the brightest and steepest X-ray spectrum, as well.

No correlated short-term radio/X-ray variability could be found in any of the three epochs of simultaneous *XMM-Newton*+Effelsberg observations. Due to the general absence of strong variability patterns in the individual wavelength regimes, however, this is not a strong result. Within both bands, epochs of much higher variability amplitudes with pronounced peaks are known to occur (Radio: e.g., Kraus et al. 1999; X-ray: see Sect. 6.2.3). Ironically, the 2004-2005 observing epochs of AO 0235+16, that had been chosen because of the expectation of a major source flare, can be characterized as "extraordinary quiet" phases in the anxious being of this object.

6.3 NGC 1052

In this section the active galaxy NGC 1052 is studied at radio, optical, and X-ray frequencies. This study is performed on various scales from sub-parsecs to kiloparsecs and brings together observations with the Very Long Baseline Array, the MERLIN radio interferometer, the *Hubble Space Telescope (HST)* and the X-ray observatories *Beppo*Sax, *Chandra*, and *XMM-Newton*. Part of this work is presented in the form of reprints of already published papers. General introductions to the source NGC 1052 can be found in the first sections of Kadler et al. (2004c) (reprinted in Sect. 6.3.1) and Kadler et al. (2004a) (reprinted in Sect. 6.3.2). In particular, Sect. 6.3.1 (Kadler et al. 2004c) reviews briefly the radio properties of NGC 1052 and puts the presented VLBI scrutiny of the obscuring torus and the most compact inner part of the parsec-scale twin-jet system of this object into the context of previous radio VLBI studies. Previous X-ray studies of NGC 1052 are reported on in Sect. 6.3.2 (Kadler et al. 2004a) along with the presentation and discussion of new insights into the X-ray properties of NGC 1052 from the analysis of a short archival *Chandra* observation. Particular emphasis is put on the kiloparsec scale jet-related emission of NGC 1052 at radio, optical and X-ray frequencies, associating the soft excess exhibited by this source (compare Sect. 5.1) with an extended region of thermal X-ray plasma emission associated with the kiloparsec-scale radio jet.

In Sect. 6.3.3 the X-ray spectrum of NGC 1052 is investigated in more detail through an analysis of a deeper *XMM-Newton* pointing and a reanalysis of previously published *Beppo*Sax data. The detection of a relativistic iron line is reported, which is the first of its kind in an object with a bright compact radio core. By taking advantage of this fact, the inter-relation between the accretion process and jet formation in a radio-loud AGN is investigated in Sect. 6.3.4. Significant variability of the relativistic iron line is found between the *Beppo*Sax and the *XMM-Newton* observation which took place before and after the ejection of a new, bright jet component into the jet of NGC 1052. The observational signature suggests that it was observed how a part of the inner accretion disk was fed into the black hole and a fraction of the material was ejected as a new jet component. Sect. 6.3.4 describes the organization of a follow-up multi-mission radio/X-ray monitoring campaign of NGC 1052, invoking monitoring observations with the Effelsberg 100-m telescope, the 26-m radio telescope of the University of Michigan, and the *Rossi X-ray Timing Explorer (RXTE)* X-ray observatory and a further, deeper *XMM-Newton* observation.

6.3.1 VLBI Scrutiny of the Obscuring Torus

The VLBI study of NGC 1052 presented in this section is a continuation and completion of the work done within the scope of my Diploma-thesis project at the Rheinische Friedrich Wilhelms Universität Bonn (Kadler 2002). This work was published in the journal Astronomy & Astrophysics, Vol. 426, p.481–493 (2004) and is reprinted here.

> List of collaborators: H. Falcke, J. Kerp, A. P. Lobanov, E. Ros, & J. A. Zensus

Astronomy
&
Astrophysics

The twin-jet system in NGC 1052:
VLBI-scrutiny of the obscuring torus

M. Kadler, E. Ros, A. P. Lobanov, H. Falcke[*], and J. A. Zensus

Max-Planck-Institut für Radioastronomie, Auf dem Hügel 69, 53121 Bonn, Germany
e-mail: mkadler@mpifr-bonn.mpg.de

Abstract. NGC 1052 offers the possibility to study the obscuring torus around a supermassive black hole, predicted by the standard model of active galactic nuclei, over a wide range of wavelengths from the radio to the X-ray regime. We present a detailed VLBI study of the parsec-scale structure of the "twin-jet" system in NGC 1052 in both total and polarized intensity and at multiple frequencies. We report the detection of linearly polarized emission from the base of the eastern jet at 5 GHz. While the radio spectrum in this region might be still consistent with synchrotron self absorption, the highly inverted spectrum of the western jet base represents a clear sign of pronounced free-free absorption in a circumnuclear torus. We observe an abrupt change of the brightness temperature gradient at a distance of ∼0.2 pc to 0.3 pc east of the central engine. This might provide an observational signature of the edge of the central torus, where the transition from an external pressure-dominated jet regime to a more or less freely expanding jet takes place. We determine the absorbing column density towards the western jet core to be ∼2.2×10^{22} cm^{-2} in good agreement with the values derived from various X-ray observations. This suggests that the nuclear X-ray emission and the jet emission imaged by VLBI originate on the same scales.

Key words. galaxies: individual: NGC 1052 – galaxies: individual: PKS B0238−084 – galaxies: active – galaxies: jets

1. Introduction

Radio observations of the low-luminosity active galactic nucleus (AGN) NGC 1052 with Very Long Baseline Interferometry (VLBI) at multiple frequencies have revealed the presence of a dense circumnuclear absorber, which obscures the very center of this elliptical galaxy (Kellermann et al. 1999; Kameno et al. 2001; Vermeulen et al. 2003). Indeed, the standard model of AGNs predicts the existence of an obscuring torus, whose inner surface is expected to be photo-ionized by illumination from the accretion disk. Colder, neutral material forms the outer boundary of the obscuring torus. NGC 1052 provides the possibility to study the physical properties of this obscuring torus complementary in various wavelength regimes and with a variety of observational methods. Particularly, the combination of VLBI and X-ray spectroscopic studies is capable of addressing the same basic questions with complementary methods. Various X-ray observations of NGC 1052 imply a model-dependent column density of 10^{22} cm^{-2} to 10^{23} cm^{-2} towards the unresolved nuclear X-ray core (Guainazzi et al. 1999; Weaver et al. 1999; Kadler et al. 2004) but the angular resolution of X-ray telescopes is not sufficient to measure the accurate position and extent of the absorber. Relativistically broad iron line emission at 6.4 keV is seen in a high-quality X-ray

spectrum obtained with the *XMM-Newton* telescope (Kadler et al. in prep.). Thus, being the first radio-loud AGN with a strong compact radio core that exhibits strong relativistically broadened iron line emission from the inner accretion disk, NGC 1052 provides a unique possibility to study the inter-relation between AGN mass accretion and jet-formation. For future combined VLBI structural and X-ray spectroscopic monitoring observations, it is essential to study in detail the influence of the obscuring torus on the parsec-scale jet structure at radio wavelengths.

NGC 1052 is a moderately strong, variable source in the radio regime, with a luminosity (integrated between 1 GHz and 100 GHz) of ∼4.4×10^{40} erg s^{-1} (Wrobel 1984) and an unusually bright and compact radio core. Together with the proximity of the source of only 22.6 Mpc[1] this makes NGC 1052 a premier object for VLBI studies, aiming at the ultimate goal of revealing the physical properties of obscuring tori in AGNs. The parsec-scale structure of NGC 1052 shows a twin jet with an emission gap between the brighter (approaching) eastern jet and the western (receding) jet and free-free absorption towards the western jet (Kellermann et al. 1999). Kameno et al. (2001) suggested the presence of a geometrically thick plasma

---

[*] *Present Address*: ASTRON, PO Box 2, 7990 AA Dwingeloo, The Netherlands.

[1] We assume a Hubble constant of $H_0 = 65$ km s^{-1} Mpc^{-1} and use the measured redshift of $z = 0.0049$ by Knapp et al. (1978). This results to a linear scale of 0.11 pc mas^{-1}.

torus and a geometry of the jet-torus system in which 0.1 pc of the eastern jet and 0.7 pc of the western jet are obscured. The multi-frequency VLBI structure of NGC 1052 has been further studied by Kameno et al. (2003) and Vermeulen et al. (2003). The kinematics of both jets at 2 cm have been investigated by Vermeulen et al. (2003) who report outward motions on both sides of the gap with similar velocities around 0.6 to 0.7 mas yr^{-1} corresponding to ~0.25 c.

Besides the ionized (free-free absorbing) gas component there are multiple pieces of evidence for atomic and molecular gas in the central region of NGC 1052. H_2O maser emission occurs towards the base of the western jet (Claussen et al. 1998) within the same region that is heavily affected by free-free absorption. Atomic hydrogen is known to exist in NGC 1052 on various scales. Van Gorkom et al. (1986) imaged the distribution of the HI gas with a resolution of 1″ using the VLA. They report a structure three times the size of the optical galaxy. Recent VLBI observations resolved HI absorption features towards the nuclear jet (Vermeulen et al. 2003). Finally, an OH absorption line was also detected by Omar et al. (2002) and Vermeulen et al. (2003) but the distribution of the OH gas on parsec-scales has not been investigated so far.

In this work we analyse the multi-frequency structure of NGC 1052 on parsec-scales between 5 GHz and 43 GHz in both total and linearly polarized intensity. In Sect. 2 we describe briefly the observations with the Very Long Baseline Array (VLBA)[2] and the data reduction. Sections 3 and 4 describe the modelling of the source structure with Gaussian components and the process of aligning the images at the four frequencies. The VLBA images of NGC 1052 themselves in total and polarized intensity are presented in Sect. 5. We analyse the frequency dependence of the observed core position in both jets in Sects. 6 and 7 discusses the spectral analysis. In Sect. 8 we present the brightness temperature distribution along both jets of NGC 1052 and summarize our results in Sect. 9.

2. Observations and data reduction

NGC 1052 was observed on December 28th, 1998 with the VLBA at four frequencies (5 GHz, 8.4 GHz, 22 GHz, and 43 GHz) in dual polarization mode. The data were recorded with a bit rate of 128 Mbps at 2-bit sampling providing a bandwidth of 16 MHz per polarization hand (divided in two blocks of 16 0.5 MHz channels each). The total integration time on NGC 1052 was about one hour at 5 GHz, 8.4 GHz, and 22 GHz each, and about six hours at 43 GHz, to compensate the lower array sensitivity and the lower source flux density. 3C 345 and 4C 28.07 were used as calibrators during the observation. The correlation of the data was done at the Array Operations Center of the VLBA in Socorro, NM, USA, with an averaging time of two seconds. All antennas of the array yielded good data, except the Owens Valley antenna, which did not record data at 8.4 GHz and 22 GHz. The data at 22 GHz and 43 GHz suffered from some snow in the Brewster dish and rain at St. Croix.

---

[2] Napier (1994); the VLBA is operated by the National Radio Astronomy Observatory (NRAO), a facility of the National Science Foundation operated under cooperative agreement by Associated Universities, Inc.

The data calibration and imaging were performed applying standard methods using the programs $\mathcal{AIPS}$ and DIFMAP (Shepherd et al. 1997). The a priori data calibration and fringe fitting were performed in $\mathcal{AIPS}$ using the nominal gain curves measured for each antenna. Instrumental phase offsets and gradients were corrected using the phase-cal signals injected into the data stream during the data recording process. The data were averaged over frequency and exported from $\mathcal{AIPS}$. Then, the data were read into DIFMAP, edited, phase- and amplitude self-calibrated, and imaged by making use of the CLEAN algorithm. From a careful comparison of the uncalibrated and self-calibrated data, the absolute flux calibration can be (conservatively) estimated to be accurate on a level of ≲10 percent.

The data were corrected for the instrumental polarization of the VLBA using the method described by Leppänen et al. (1995). The absolute values of the electric vector position angles (EVPAs) at all four frequencies were calibrated using the source 3C 345, for which a large data base exists in the literature from which the EVPA in the core and jet regions of this source can be obtained (e.g., Ros et al. 2000).

3. Modeling the source structure

In VLBI imaging the absolute positional information is lost in the phase-calibration process. In the case of simultaneous multi-frequency observations this means that a priori it is not clear how the images at the different frequencies have to be aligned. The ideal method for overcoming this is to carry out phase-referencing observations, using a compact nearby object and using it to calculate the position of the target source relative to it (e.g., Ros 2004). Our VLBA observations were not phase-referenced, so another way was used to register the four maps. We model fitted the visibility data with two-dimensional Gaussian functions. Those functions, called components, were chosen to be circular to reduce the number of free model parameters and to facilitate the comparison of the models at the different frequencies. The model fitting was performed in DIFMAP using the least-squares method. The errors were determined with the program ERRFIT, a program from the Caltech VLBI data analysis package that calculates the statistical confidence intervals of the fitted model parameters by varying each parameter.

The fits were initially performed independently at the different frequencies to avoid biasing one by another. Once good fits for all four frequencies were obtained, a cross comparison of the resulting maps was made and the fits were modified to get a set of model fits as consistent as possible. Criteria for consistency were:

– regions that show emission at adjacent frequencies should be represented by the same number of components;
– extended components in the outer parts of the jets should become weaker at higher frequencies as they most likely represent optically thin synchrotron emitting regions;
– the inner edges of both jets are expected to shift inwards towards higher frequencies due to opacity effects, i.e., the corresponding model components might have no low frequency counterpart;

– optically-thin features should not show positional changes with frequency.

Table 1 gives the parameters of the final models for the four frequencies. The most distant component in the eastern jet was labeled as A 1, the adjacent inner one as A 2, and so on. The western jet was divided into three parts (B, C and D). The model fit component in the innermost part of the western jet were labeled as B 2b, B 2a, B 1 from east to west. Further out, the components C 3b, C 3a, C 2, C 1, and D follow.

4. Image alignment

The image alignment was performed in two steps. ɪ) The fitted components at the different frequencies were cross–identified and the relative shifts between the models were determined, assuming frequency-independent positions of optically thin features. ɪɪ) An origin was determined from which absolute distances could be measured. This method of alignment is not a priori definite. It is based on the assumption that optically-thin components have frequency-independent positions and that the cross identification of the model components is correct. However, all possible alternative identifications could be ruled out for consistency reasons (by making use of the component flux densities at adjacent frequencies).

We used the two most distant components (A 1 and D) to align the 5 GHz and the 8.4 GHz models by assuming that the mid-point between both components was spatially coincident. Because these two outer components are optically thin and not detectable above 8.4 GHz, the position of component A 7, which is relatively strong at all three frequencies, was used to align the three high-frequency models relative to the origin determined from the alignment of the two low-frequency models. As a natural choice, the most probable position of the true center of jet activity, namely the center between the components A 15 and B 2b, was used as the origin (compare Sect. 6). The component positions in Table 1 are given relative to this reference point.

5. The brightness distribution in total and polarized intensity

5.1. Total intensity imaging

Figure 1 shows the aligned uniformly weighted total intensity images of NGC 1052 at the four frequencies and Fig. 2 shows the images that result from applying Gaussian model-fit components to the measured visibilities. Table 2 gives the image parameters of Fig. 1.

The basic source structure is formed of two oppositely directed jets divided by an emission gap. The source can be divided into four regions: region A makes up the whole (more or less continuous) eastward-directed jet emission; region B is not visible at 5 GHz, but becomes the brightest and most compact feature at high frequencies; regions C and D are bright only at low frequencies and become faint and diffuse at high frequencies. The main source characteristics are summarized in Table 3. A sub-division can be performed based on the

Table 1. Model fit parameters.

Id	Flux density [mJy]	Radius[a] [mas]	PA [°]	*FWHM* [mas]
5 GHz, χ_{red} = 1.12				
A1	80 ± 2	14.56 ± 0.03	66.5 ± 0.1	2.14 ± 0.03
A2	54 ± 2	12.01 ± 0.04	63.6 ± 0.1	1.87 ± 0.08
A3	60 ± 2	9.61 ± 0.05	65.3 ± 0.3	1.63 ± 0.04
A4	150 ± 7	7.46 ± 0.05	71.7 ± 0.2	0.99 ± 0.02
A5	338 ± 37	6.0 ± 0.2	72.8 ± 0.1	0.93 ± 0.25
A6	447 ± 48	5.1 ± 0.1	72.8 ± 0.2	0.83 ± 0.19
A7/8	450 ± 28	4.0 ± 0.1	71.0 ± 0.2	0.69 ± 0.08
A9	397 ± 30	3.1 ± 0.2	71.1 ± 0.3	0.20 ± 0.07
A10	140 ± 37	2.3 ± 0.2	70.9 ± 0.4	0.46 ± 0.05
C3	137 ± 3	3.84 ± 0.03	−114.2 ± 0.1	1.03 ± 0.06
C2	59 ± 3	4.75 ± 0.06	−115.74 ± 0.3	0.83 ± 0.09
C1	24 ± 1	7.19 ± 0.03	−119.6 ± 0.4	1.85 ± 0.10
D	67 ± 1	11.81 ± 0.01	−114.7 ± 0.1	2.24 ± 0.05
8.4 GHz, χ_{red} = 1.76				
A1	38 ± 1	14.70 ± 0.03	66.5 ± 0.1	2.00 ± 0.03
A2	37 ± 1	12.04 ± 0.04	64.0 ± 0.1	2.34 ± 0.08
A3	36 ± 1	9.30 ± 0.05	65.9 ± 0.3	1.62 ± 0.04
A4	83 ± 4	7.34 ± 0.05	71.9 ± 0.2	0.98 ± 0.02
A5	72 ± 8	6.4 ± 0.2	72.7 ± 0.1	0.59 ± 0.25
A6	360 ± 26	5.5 ± 0.1	72.8 ± 0.2	0.81 ± 0.12
A7	396 ± 22	4.4 ± 0.1	72.3 ± 0.2	0.74 ± 0.06
A8	146 ± 8	3.8 ± 0.1	69.7 ± 0.2	0.28 ± 0.06
A9	360 ± 21	3.2 ± 0.2	71.3 ± 0.3	0.34 ± 0.05
A10	316 ± 47	2.7 ± 0.2	69.2 ± 0.4	0.31 ± 0.03
A11	137 ± 25	1.9 ± 0.2	74.3 ± 0.4	0.34 ± 0.07
B2a/b	56 ± 4	0.60 ± 0.03	−119.8 ± 0.1	0.36 ± 0.02
B1	29 ± 2	1.26 ± 0.03	−119.9 ± 0.1	0.31 ± 0.02
C3	20 ± 1	3.75 ± 0.03	−114.2 ± 0.1	1.06 ± 0.08
C2	77 ± 4	4.86 ± 0.06	−114.9 ± 0.3	0.90 ± 0.09
C1	21 ± 1	7.03 ± 0.03	−119.1 ± 0.4	1.68 ± 0.10
D	48 ± 1	11.95 ± 0.01	−114.7 ± 0.1	2.21 ± 0.05
22 GHz, χ_{red} = 0.71				
A6	138 ± 5	5.48 ± 0.03	72.4 ± 0.2	0.98 ± 0.04
A7	140 ± 7	4.39 ± 0.01	72.2 ± 0.2	0.65 ± 0.03
A8	99 ± 5	3.72 ± 0.01	68.1 ± 0.2	0.47 ± 0.03
A9	139 ± 6	3.09 ± 0.01	72.2 ± 0.2	0.32 ± 0.02
A10	144 ± 5	2.70 ± 0.01	68.5 ± 0.2	0.27 ± 0.01
A11	44 ± 8	1.98 ± 0.04	73.0 ± 0.8	0.29 ± 0.07
A12	86 ± 15	1.53 ± 0.04	72.1 ± 0.4	0.26 ± 0.06
A13	54 ± 14	1.20 ± 0.04	71.1 ± 0.9	0.22 ± 0.06
B2b	341 ± 14	0.52 ± 0.02	−123 ± 1	0.21 ± 0.01
B2a	151 ± 14	0.72 ± 0.05	−115 ± 2	0.29 ± 0.02
B1	31 ± 2	1.38 ± 0.02	−132 ± 1	0.3 ± 1.7
C3a	50 ± 4	3.34 ± 0.02	−116.4 ± 0.4	0.58 ± 0.03
C3b	86 ± 6	4.18 ± 0.07	−116 ± 1	1.95 ± 0.16
43 GHz, χ_{red} = 0.83				
A6	40 ± 2	5.36 ± 0.03	72.8 ± 0.2	0.92 ± 0.05
A7	44 ± 2	4.39 ± 0.01	72.2 ± 0.2	0.51 ± 0.03
A8	39 ± 2	3.76 ± 0.01	68.7 ± 0.1	0.46 ± 0.03
A9	37 ± 1	3.177 ± 0.003	71.8 ± 0.1	0.22 ± 0.01
A10	70 ± 1	2.772 ± 0.004	68.4 ± 0.1	0.33 ± 0.01
A11	19 ± 1	1.95 ± 0.01	71.6 ± 0.5	0.32 ± 0.03
A12	57 ± 2	1.499 ± 0.004	70.2 ± 0.2	0.22 ± 0.01
A13	43 ± 2	1.221 ± 0.006	70.8 ± 0.2	0.12 ± 0.01
A14	54 ± 1	1.017 ± 0.003	71.9 ± 0.2	0.08 ± 0.05
A15	19 ± 1	0.47 ± 0.01	61 ± 2	0.21 ± 0.03
B2b	225 ± 2	0.467 ± 0.002	−119.2 ± 0.3	0.224 ± 0.002
B2a	31 ± 2	0.779 ± 0.007	−120.9 ± 0.6	0.22 ± 0.01
C3b	27 ± 2	3.33 ± 0.05	−116.5 ± 0.8	0.95 ± 0.08

[a] The radius is measured from the center between A 15 and B 2b (see Sect. 4.6).
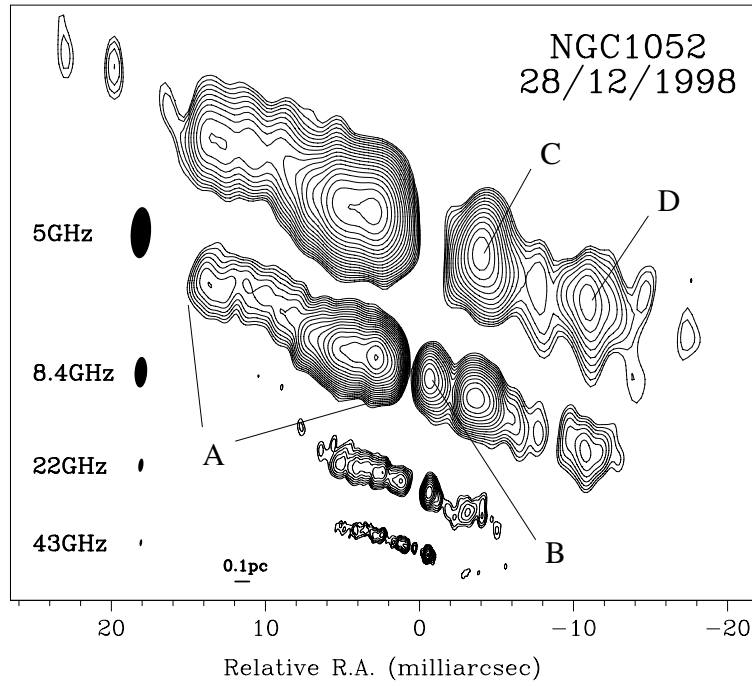
Fig. 1. The aligned VLBA images of NGC 1052 at 5 GHz, 8.4 GHz, 22 GHz, and 43 GHz. Contours and beam sizes are given in Table 2.
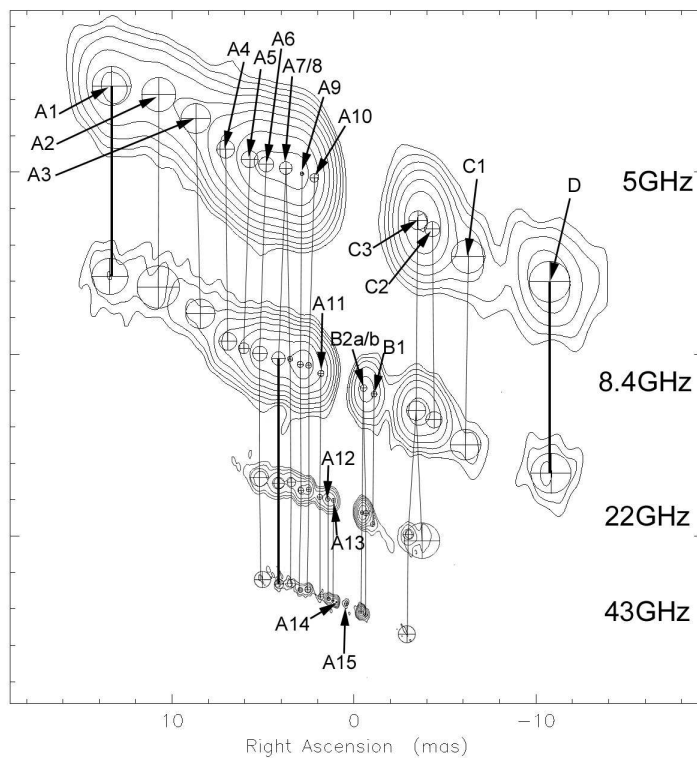
Fig. 2. The aligned model-fit maps. The circles represent the full width at half maximum (*FWHM*) of the circular Gaussians. The vertical and oblique lines join the associated components between different frequencies. The components A 1 and D between 5 GHz and 8.4 GHz and A 7 between 8.4 GHz, 22 GHz and 43 GHz (joined by a thicker trace) were used for the alignment. The lowest contours are 1.9 mJy/beam for the 5 GHz model, 2.6 mJy/beam for the 8.4 GHz model, 5.0 mJy/beam for the 22 GHz model and 3.5 mJy/beam for the 43 GHz model.

139

Table 2. Total intensity image parameters.

ν [GHz]	Beam [mas × mas,°]	S_peak [Jy/beam]	S_tot^a [Jy]	rms [mJy/beam]	Lowest contour [mJy/beam]
5	$3.30 \times 1.31, -3.74$	0.660^b	2.41	0.26	1.5
8.4	$1.98 \times 0.81, -3.87$	0.538^b	2.39	0.25	1.5
22	$0.86 \times 0.32, -7.63$	0.339^c	1.51	1.20	2.5
43	$0.45 \times 0.16, -7.93$	0.126^c	0.67	0.67	2.5

^{a} Total flux density recovered in the image.
^{b} Corresponds to the A component.
^{c} Corresponds to the B component.

Table 3. Source characteristics on mas-scales.

ν [GHz]	Mean PA	Eastern Jet length [mas]	western Jet length [mas]	Gap width [mas]	Notes
5	65°	30	30	~1.3	A dominates; B totally absorbed
8.4	65°	14	14	<0.5	A dominates; B occupies the 5 GHz gap region
22	67°	13	6	~0.5	B dominates
43	70°	5	3.5	~0.2	B dominates; western jet weak

Gaussian model fits, found to represent the source structure (see Fig. 2).

Whilst the eastern jet is only slightly curved at distances from the gap larger than 4 mas the counterjet exhibits strong curvature most pronounced at 22 GHz. The jets appear nearly symmetric in the 5 GHz and 8.4 GHz images, becoming asymmetric at higher frequencies. While the emission gap is most prominent at 5 GHz the images at 8.4 GHz, 22 GHz, and 43 GHz reveal jet components occupying this gap region, leaving a smaller but still prominent emission gap. The frequency dependence of the VLBI "core" positions, the points were the eastern and the western jet become optically thin can clearly be seen in Fig. 1. This so-called "core shift" will be analysed in detail in Sect. 6.

5.2. Linearly polarized intensity imaging

Figure 3 shows the linearly polarized intensity and its EVPA overlaid on the total intensity image at 5 GHz. A region of linearly polarized emission is visible at the base of the eastern jet. The peak is about 3 mJy per beam and the EVPA is about 70°, roughly parallel to the jet. To decide whether the region of linearly polarized emission is resolved, slices along the jet axis of both the total intensity image and the polarization image were produced, using the task SLICE in $\mathcal{AIPS}$ (inlayed panel in Fig. 3). In this plot, the polarized emission peaks about 1 mas offset from the total-intensity maximum. A comparison to Fig. 2 ascribes this part of the jet to component A 10,

which is optically thick at 5 GHz. The asymmetry of the polarized emission slice suggests the presence of at least two components. The polarized emission is thus slightly resolved and originates in the optically thick part of the eastern jet at 5 GHz.

No linearly polarized emission at a flux density level above 1 mJy could be detected at the other three frequencies. Usually, the degree of polarization rises with frequency since beam depolarization reduces the degree of polarization at lower frequencies more strongly than at higher frequencies. Thus, one expects the eastern jet to exhibit polarized emission from the region around component A 10 and A 11 at 8.4 GHz also. Assuming that the polarization has the same (flat) spectrum as the total intensity in this region, it should reach ~3 mJy per beam at 8.4 GHz (comparable to the polarized flux at 5 GHz). However, this is not observed. At higher frequencies these components become optically thin (compare Sect. 7) and thus fall in total intensity. Were their emission polarized to the same degree as at 5 GHz it would be <1 mJy per beam and would thus lie below the detection threshold. The non-detection of linear polarization at the high frequencies in our observations is consistent with the results of Middelberg et al. (2004) who report unpolarized emission from NGC 1052 at 15 GHz down to a limit of 0.4%.

6. Identifying the center of activity

The symmetry between the jet and the counterjet constrains the position of the central engine in NGC 1052. The cores of both jets are located at the distances to the central engine, r_c, where the optical depth τ has fallen to ~1. In a conical jet geometry this distance is given by: $r_\text{c} \sim \nu^{-\frac{1}{k_r}}$, (see, e.g., Lobanov 1998) where $k_r = ((2\alpha - 3)b - 2n - 2)/(5 - 2\alpha)$, with α being the spectral index and b and n the power indices of the magnetic field and the density of the emitting particles: $B \sim r^b$, $N \sim r^n$ (Lobanov 1998). Taking logarithms leads to:

$$\log(r_\text{c}) = -\frac{1}{k_r} \log(\nu) + \text{const.} \tag{1}$$

Measuring r_c at two frequencies allows one to determine k_r in the corresponding region of the jet. For a freely expanding jet in equipartition (Blandford & Königl 1979), $k_r = 1$. The value of k_r is larger in regions with steep pressure gradients and may reach 2.5, for moderate values of m and n (Lobanov 1998). If external absorption determines the apparent core position, comparable density gradients of the external medium can alter k_r to values above 2.5.

The values of k_r deduced depend crucially on the absolute values of r_c on the two sides and therefore on the assumed position of the central engine. Four scenarios have been tested with different reference points (see Fig. 4). Table 4 gives the derived values of k_r for each scenario. In each case the position of component A 14 has been assumed as the core of the eastern jet, rather than A 15. The latter is comparably weak and, thus, most likely does not represent the true jet core. A 15 might rather represent a bright but heavily self-absorbed new jet component. Formally, however, the k_r values for the scenarios 1, 2, and 4 between 22 GHz and 43 GHz change to 1.4 ± 0.06, 0.6 ± 0.03, and 1.0 ± 0.04 if A 15 instead of A 14 is used. For
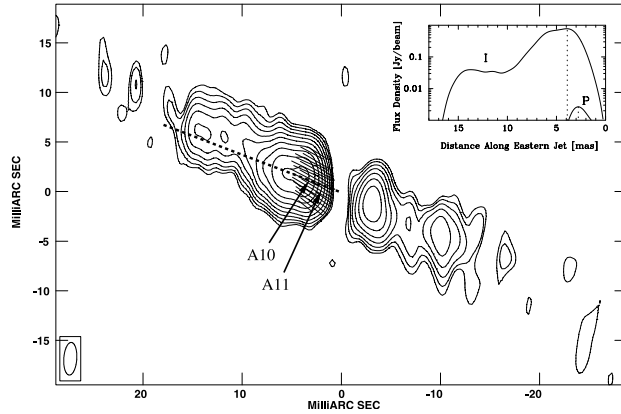
Fig. 3. 5 GHz image of the polarized emission in NGC 1052 (EVPA superimposed on the total intensity). The inlayed panel shows the total intensity and polarized emission profiles along the slice marked with the dashed line.

scenario 3, A 15 cannot be associated to the eastern jet core (compare Fig. 4).

The area between the model components A 15 and B 2b is the most likely location of the central engine and the center between both components is a natural choice for its exact position (scenario 1). Shifting the reference point eastwards (scenarios 2 and 3) alters the values of k_r into unphysically large regimes (requiring density gradients $\propto r^{-10}$ and higher). Assuming the true center of activity to be located more westwards (closer to B 2b, scenario 4), the values of k_r derived are still acceptable.

The positions of the bases of both jets at the different frequencies for the first case (scenario 1) are shown in Fig. 5. The eastern jet has rather high values of k_r below 22 GHz, although still in agreement with steep pressure gradients in the jet environment. Above 22 GHz k_r is 3.9 ± 0.8, which is a good indicator for free-free absorption affecting the jet opacity. The western jet has values of k_r as high as 6.8 ± 2.7 between 22 GHz and 43 GHz, suggesting a large contribution from free–free absorption.

The results from the core shift analysis support the picture of a free–free absorbing torus covering mainly the inner part of the western jet and also a smaller fraction of the eastern jet. The true center of activity in NGC 1052 can be determined to lie between the model components A 15 and B 2b, with an uncertainty of only ~0.03 pc.

7. Spectral analysis

Spectral information can be derived from multi-frequency VLBI data in two ways. The first approach is to use the knowledge of the proper alignment of the total intensity images to derive images of the spectral index between two adjacent frequencies. The second approach is to derive spectra of the model fit components. The approaches are somewhat complementary. The latter gives a handy number of component spectra, which can be analysed in detail, whereas the spectral index imaging gives the full course of the spectral index along the jet axis. Particularly, this yields spectral information at parts of the jet that are not adequately represented by Gaussian model compo-
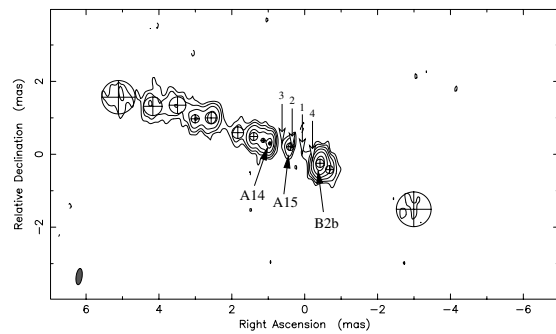
Fig. 4. Image with the model fitting results of the 43 GHz data. The innermost jet components are labeled. The putative locations of the central engine are indicated for four different scenarios (see discussion in the text).

nents. The results of both approaches will be presented in this section.

7.1. Spectral index imaging

Spectral index images have been produced using the $\mathcal{AIPS}$ task comb[3]. For this, the total intensity has been reimaged with appropriate tapering of the (u, v)-data to match the resolutions at adjacent frequencies. Information below 1 mJy/beam was discarded in both input images. Table 5 gives the restoring beams and the other relevant parameters of the derived images. The spectral index images are shown in Fig. 6.

The main feature in each image of the spectral index is an optically thick inner edge of the innermost part of both jets. Outwards along the jets, the spectral index tends to decrease. The spectral index α exceeds the value of 2.5, the theoretical upper limit for synchrotron self-absorption, on both sides of the

---

[3] At each pair of pixels of the two (coinciding) images, the spectral index α ($S \propto \nu^{\alpha}$) is calculated from the flux densities per beam S_1 and S_2 at the two frequencies ν_1 and ν_2: $\alpha = (\log S_1 - \log S_2)/(\log \nu_1 - \log \nu_2)$.
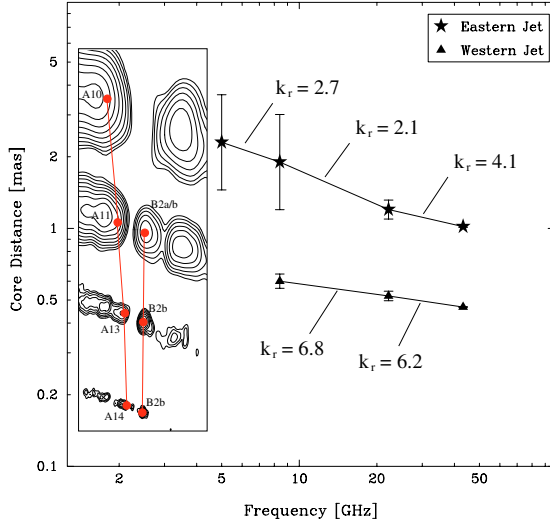
Fig. 5. Core positions in the two jets at the different frequencies for scenario 1 (see Fig. 4). Table 4 provides the values of k_r for the other two scenarios. The inset panel shows the core locations in the source at the four frequencies.

Table 4. Values of k_r for the four different putative centers of activity.

	(5–8.4) GHz		(8.4–22) GHz		(22–43) GHz	
Scenario	$k_{r,east}$	$k_{r,west}$	$k_{r,east}$	$k_{r,west}$	$k_{r,east}$	$k_{r,west}$
1	2.7 ± 1.9	–	2.1 ± 0.5	6.8 ± 3.0	4.1 ± 0.8	6.2 ± 2.2
2	2.4 ± 1.7	–	1.8 ± 0.4	9.8 ± 4.3	3.1 ± 0.6	9.3 ± 3.4
3	2.1 ± 1.5	–	1.4 ± 0.3	12.9 ± 5.2	2.2 ± 0.4	12.5 ± 4.6
4	3.0 ± 2.1	–	2.5 ± 0.6	3.7 ± 1.6	4.9 ± 1.0	3.0 ± 1.0

Table 5. Spectral index image parameters.

ν_1	ν_2	Common beam	Cutoff
[GHz]	[GHz]	[mas×mas, °]	[mJy/beam]
5	8.4	$2.64 \times 1.06, -3.81$	2
8.4	22	$1.42 \times 0.57, -5.75$	1
22	43	$0.66 \times 0.24, -7.78$	1

Fig. 6. Spectral index images of NGC 1052. The contours and beam parameters are given in Table 5. Note the different scales in the three images and that the images are centered on component B 2.

7.2. Spectral analysis of the model fit components

The flux densities of the model fit components (see Fig. 2) can be used to derive spectra of ı) the whole parsec-scale structure, ıı) the two jets separately and ııı) the model fit components themselves. In Fig. 7, the total spectrum of the parsec-scale structure of NGC 1052 between 5 GHz and 43 GHz is shown, as well as the spectra of both jets separately. All values were obtained by adding up flux densities[4] of model components (A 1 to A 15 for the eastern jet and B 2b to D for the western one).

At the high frequencies both jets show similar spectra with an optically thin decrease of the flux density above 22 GHz. The spectral index in this regime is around −1 in both jets, with the eastern jet being significantly stronger than the western one in agreement with the interpretation that the eastern jet approaches the observer whereas the western jet is the counter-jet. However, below 22 GHz the spectra of the two jets differs substantially. The eastern jet spectrum remains optically thin above 8.4 GHz and flattens around 5 GHz. The western jet, on the other hand, exhibits a sharp decrease in flux below 22 GHz.

gap in the (5–8.4) GHz spectral index image and on the eastern side of the gap also between 8.4 GHz and 22 GHz. High values of α are also reached on the western side of the gap in the (8.4–22) GHz spectral index image and on both sides between 22 GHz and 43 GHz, which however do not exceed the critical value of 2.5. Towards the outer jet regions the spectral index typically falls to values $\lesssim -1$ in the whole frequency range between 5 and 43 GHz. This suggests that the emission from these outer jet regions far from the gap is optically thin above 5 GHz.

---

[4] We estimated the statistical standard uncertainty of all quantities derived from the model component flux densities. The calculated errors are shown in the plots, when they are not negligible.
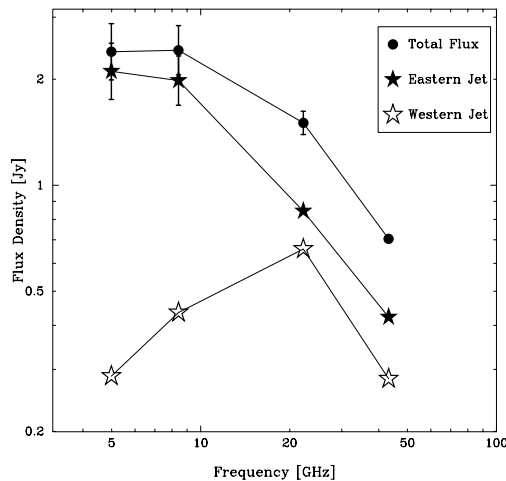
Fig. 7. Spectrum of the parsec-scale structure of NGC 1052 between 5 GHz and 43 GHz (total and for both jets separately). Errorbars are shown only if they exceed the symbol size.

Fig. 8. Spectra of the four jet regions A, B, C and D (see Fig. 1 for the definition of the jet regions). The arrows indicate that component C is partly resolved at 43 GHz and component B is not detected at 5 GHz. Thus, the shown values represent only a lower and upper limit, respectively. Errorbars are shown only if they exceed the symbol size.

Although the spectral index limit of 2.5 is not exceeded, synchrotron self-absorption seems very unlikely to be responsible for the turnover of the spectrum because of two reasons. First, the similarity of the spectra of eastern and western jet at high frequencies suggests similar intrinsic physical properties on both sides so that the self absorption frequency should not differ by a factor of three. Second, the kinematical analysis of Vermeulen et al. (2003) shows the jet axis to be close to the plane of the sky and the motions to be only weakly relativistic. There is little evidence for strong Doppler boosting. Moreover, such an effect should shift the turnover frequency of the counterjet to lower frequencies, rather than to higher ones. In Sect. 8.3 we will use the moderate velocity differences, on the one hand, and the more pronounced brightness-temperature difference of jet and counterjet, on the other hand, to constrain the orientation of the jet-counterjet system.

If the spectrum of the western jet is decomposed into the spectra of the different jet regions B, C and D (see Figs. 1 and 8) it turns out that the region B, the innermost region on the western side, is responsible for the inversion of the western jet spectrum below 22 GHz. Its spectrum between 5 GHz and 8.4 GHz is highly inverted with a spectral index >4 since it is not detectable at all at 5 GHz. Such a spectral index cannot be due to synchrotron self absorption but indicates a region of external absorption towards the core of the western, receding jet. The highly inverted spectrum of this component in NGC 1052 and the necessity of an external absorber was first mentioned by Kellermann et al. (1999) and later confirmed by Kameno et al. (2001) and Vermeulen et al. (2003).

It is not clear whether the eastern jet is also affected by external absorption. Kameno et al. (2001) proposed a geometry in which the obscuring torus covers 0.7 mas of the western jet and 0.1 mas of the eastern jet. Emission from A 11 is not detected at 5 GHz. Estimating (conservatively) a flux density of 10 mJy at 5 GHz yields a spectral index of ~5. This would suggest that the innermost part of the eastern jet is also strongly affected by external absorption. However, if the flux densities of the two components A 10 and A 11 are summed at 5 GHz and 8.4 GHz, one obtains a spectral index of 2.3, which is close to that expected for pure synchrotron self-absorption. Consequently, due to the small separations between the inner components in the eastern jet, we cannot finally judge from this approach whether free-free absorption plays an important role. Kameno et al. (2003) determined a spectral index of 3.28 ± 0.27 for the base of the eastern jet between 1.6 GHz and 4.8 GHz and attribute this to free-free absorption in the obscuring torus.

The jet-to-counterjet ratio of NGC 1052 can be determined from the model fitted flux densities of both jets. Figure 9 shows the ratio of the flux densities of the model components on either side of the gap as a function of frequency. At high frequencies the jet-to-counterjet ratio is ~1.5 and starts rising towards lower frequencies below 22 GHz. At 8.4 GHz the jet is brighter than the counterjet by a factor of ~5 and at 5 GHz the jet outshines the counterjet even by a factor of ~7. The jet-to-counterjet ratio is known to keep rising at lower frequencies up to 50 at 2.3 GHz (Kameno et al. 2001). This suggests that a much bigger part of the western jet is covered by the absorber than apparent from our high-frequency data. Alternatively, curvature effects may play an important role. In this case, the counterjet bends away from the observer at a distance of a few milliarcseconds from the core and its radiation is Doppler de-boosted.

8. Brightness-temperature gradients

In this section the brightness-temperature gradients along both jets in NGC 1052 are discussed. Starting from the assumption

143
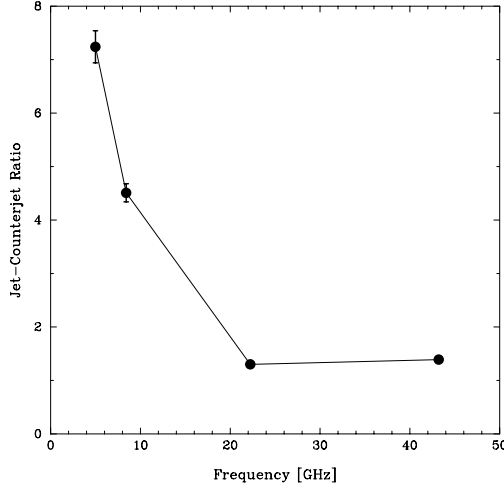
Fig. 9. The jet-to-counterjet ratio determined from the flux densities of the model fit components as a function of frequency. Errorbars are shown only if they exceed the symbol size.

that the magnetic field B, the electron density N, and the jet diameter D can be described by power-laws:

$$B \propto r^b; N \propto r^n; D \propto r^d \tag{2}$$

it can be derived that the brightness temperature, T_b, is expected to fall with increasing distance from the jet base like:

$$T_b \propto r^s, \tag{3}$$

with $s < 0$. For this, one assumes optically thin synchrotron emission with an emissivity $j_\nu \propto n_e B(\nu/\nu_B)^\alpha$ (Krolik 1999, Sect. 9.2.1) and, implicitly, a constant Lorentz factor of the emitting electrons. Under these assumptions the brightness temperature distribution is determined by the jet-geometry ($d = 1$ for a conical jet, $d < 0$ for a collimated jet, and $d > 0$ for a decelerating jet), the course of the magnetic field and the particle density via

$$s = d + n + b(1 - \alpha), \tag{4}$$

where α is the spectral index. Typically, straight and continuous jets exhibit values of $s \sim -2.5$ on parsec-scales (Kadler et al., in prep). The search for deviations from this power-law dependence provides a tool to find regions in a jet which are affected by external absorption or by abrupt changes of the jet parameters.

For a non-thermal source, the brightness temperature is a frequency-dependent quantity (see e.g., Condon et al. 1982):

$$T_b = 1.22 \times 10^{12} \, \text{K} \left(\frac{S_\nu}{\text{Jy}}\right)\left(\frac{\nu}{\text{GHz}}\right)^{-2}\left(\frac{\Theta}{\text{mas}}\right)^{-2}, \tag{5}$$

with S_ν the flux density of the source, ν the observing frequency, and Θ the apparent diameter at half maximum. In principle, the observing frequency has to be corrected for the source redshift, but due to the small distance of NGC 1052

Table 6. T_b gradient along the eastern jet.

ν [GHz]	$\hat{T}_\nu$ [K]	s
5	$2.1^{+2.4}_{-1.1} \times 10^{13}$	-4.1 ± 0.4
8.4	$5.3^{+4.2}_{-2.3} \times 10^{12}$	-4.1 ± 0.3
22	$1.9^{+1.1}_{-0.7} \times 10^{11}$	-3.8 ± 0.3
43	$3.7^{+6.6}_{-2.3} \times 10^{10}$	-4.1 ± 0.8

Note: We performed a power-law fit to T_b beyond a distance from the central engine $r = 2.5$ mas as $T_b(r) = \hat{T}_\nu \times r^s$, where $\hat{T}_\nu$ is the extrapolated brightness temperature at 1 mas and s is the power index.

($z = 0.0049$) this correction is negligible. According to Eq. (5), brightness temperatures have been computed for the model fit components at all four frequencies. The uncertainties in T_b were computed using Gaussian error propagation from the errors in flux density S and $FWHM$ of the model components Θ. We assumed conservative values of 10% for ΔS and 20% for $\Delta\Theta$.

8.1. The T_b distribution along the eastern jet

Figure 10 shows the brightness temperatures in the eastern jet as a function of distance from the central engine. The latter was assumed to lie at the center between the components A 15 and B 2b (see Sect. 6 for a detailed discussion of the central engine position in NGC 1052). T_b rises towards the center following roughly a r^{-4}-law (compare Table 6). Between 2 mas and 3 mas from the central engine, however, there is an abrupt decrease of T_b (dashed line in Fig. 10). This "cut-off" is present at all four frequencies although the inner components (only visible at 22 GHz and 43 GHz) exhibit again a rise in T_b. The value of the innermost component A 15 falls significantly below the extrapolation of the curve defined by A 12, A 13, and A 14.

8.1.1. What causes the cut-off of the T_b-distribution?

We discuss three possible origins of the frequency–independent cut-off of T_b in the eastern jet:

Free–free absorption: At a distance of ~2.5 mas from the central engine the overhanging edge of the obscuring torus might start to obscure a substantial fraction of the jet and thus reduce the brightness temperature of its components via free-free absorption. If this interpretation was correct the pronounced frequency dependence of the optical depth due to free-free absorption ($\tau_f \propto \nu^{-2.1}$) should be measurable: the free-free absorbed (i.e., observed) flux density $S_{\nu,\text{abs}}$ depends on the intrinsic flux density S_ν, the optical depth of the absorber τ_f and the observing frequency ν as

$$S_{\nu,\text{abs}} = S_\nu \cdot e^{-\tau_f}. \tag{6}$$

The calculated values of τ_f are given in Table 7 from which it is obvious that no pronounced effect of decreasing opacity with increasing frequency is present. This makes the interpretation as free-free absorption unlikely.

Table 7. Optical depth values – eastern jet.

Id	5 GHz	8.4 GHz	22 GHz	43 GHz
A 10	3.2 ± 1.1	–	–	–
A 11	–	3.0 ± 0.9	2.5 ± 1.0	3.0 ± 1.9
A 12	–	–	2.6 ± 0.9	2.3 ± 2.3
A 13	–	–	3.6 ± 1.1	2.2 ± 2.7
A 14	–	–	–	1.9 ± 3.3
A 15	–	–	–	8.2 ± 6.9

Note: Values for a distance from the central engine smaller than $r = 2.5$ mas.

Synchrotron self-absorption: The synchrotron emission from a freely expanding, relativistic jet is self-absorbed at distances smaller than

$$r_\nu = \left[\left(\frac{\nu}{K_{\text{jet}}} \right)^{\epsilon+1} \frac{1}{\delta_j^\epsilon \phi_{\text{obs}}} \right]^{1/(n+\epsilon b+1)} , \qquad (7)$$

due to the change of the optical depth along the jet (Lobanov 1998):

$$\tau_s \propto r^{n+\epsilon b+1} \delta_j^\epsilon . \qquad (8)$$

Here, $\epsilon = 3/2 - \alpha$, ν is the observing frequency, ϕ_{obs} is the observed opening angle of the jet (thus, implicitly assuming $d = 1$; compare Eq. (2)), K_{jet} is a bootstrap constant describing the jet conditions at a certain characteristic distance (Lobanov 1998), and δ_j is the jet bulk Doppler factor. Acceleration and deceleration of the flow may affect the dependence of Eq. (7), and ultimately even cause the observed abrupt decrease of the brightness temperature at shorter distances from the central engine (Fig. 10).

The effect of deceleration can be accounted for by assuming $\delta_j \propto r^f$, with $f \leq 0$, and $\phi_{\text{obs}} \propto r^c$, with $c \geq 0$. With these assumptions, the length of the self-absorbed portion of the jet becomes $r_\nu \propto \nu^\zeta$, with

$$\zeta = \frac{\epsilon + 1}{\epsilon(b+f) + n + c + 1} . \qquad (9)$$

The peak-positions of the brightness temperature distribution in the eastern jet (Fig. 10) imply $\zeta \geq -1/10$ (note that $\zeta < 0$) for the shallowest possible slope of r_ν. For a typical set of assumption about the jet flow ($b = -2$, $n = -1$, $\alpha = -1$) this requires $f \leq -8 - 2/5c$, which is implausible as it implies extremely strong deceleration ($\delta_j \propto r^{-8}$ and higher) of the flow. This scenario can therefore be ruled out.

Steep pressure gradients: Frequency-independent local maxima of the brightness-temperature distribution along the jet can also be produced by strong density and pressure gradients at the outer edge of the nuclear torus and, to a lesser degree, by the gradients of the magnetic field strength (Lobanov 1998). Such gradients may result in rapid changes of synchrotron self-absorption and external free-free absorption of the jet emission, both of them increasing the opacity at shorter distances

from the nucleus. These two factors together can in principle explain values of $\zeta \geq -1/10$, if density gradients at the outer edge of the torus are stronger than $n \approx -10$ ($N \propto r^n$). For the expected size of the nuclear torus $r_{\text{tor}} \sim 0.2$ pc to 0.3 pc (corresponding to the distance of 2 mas to 3 mas at which the brightness-temperature decrease sets on), and typical densities in the absorbing torus ($n_{\text{H}} \sim 10^6 \text{ cm}^{-3}$ to 10^{12} cm^{-3}, Cassidy & Raine 1993) and in the nuclear medium of the host galaxy ($n_{\text{H}} \sim 10^2 \text{ cm}^{-3}$ to 10^8 cm^{-3}, Ferguson et al. 1997), the density increase should occur on scales of $\sim 2.5 r_{\text{tor}}$. This seems to be the most plausible explanation for the observed brightness temperature changes in the eastern jet.

Standing shocks: The approach to describe the jet parameters B, N, and D with simple power laws (Eq. (2)) assumes, implicitly, a quasi-stationary, continuous jet flow without perturbations. This model cannot describe the influence of shocks in the jet flow on the brightness temperature distribution. Qualitatively, the occurence of a cut-off in the T_{b}-distribution at the location of a region of enhanced linearly polarized emission (compare Sect. 5.2) is in agreement with the expected observational signature of a standing shock. Part of the bulk flow energy of the jet can be converted into magnetic energy of the jet plasma in such a standing-shock region. This might cause K_{jet} to increase abruptly. Beyond the shock, the jet flow might be quasi-stationary and thus well described by our model.

8.1.2. Derivation of the spectral index

The frequency dependence of the brightness temperatures in the eastern jet of NGC 1052 (see Table 6) enables us to derive directly the value of the spectral index α: Eq. (5) shows that the brightness temperature at a given distance from the central engine depends on the spectral index as $T_{\text{b}} \propto \nu^{-2+\alpha}$, if optically thin synchrotron emission is assumed. A linear regression of the brightness temperature at a distance of 1 mas ($\hat{T}(\nu)$; see Table 6) as a function of frequency ν yielded $\hat{T}(\nu) \propto \nu^{-3.0\pm0.1}$. Thus, the spectral index is $\alpha = -1.0 \pm 0.1$. This is in good agreement with the results of the spectral index imaging (see Sect. 7.1).

8.1.3. The gradients of particle density and magnetic field

The fitted sizes of the Gaussian components at the four frequencies do not show significant deviations from a conical jet-structure so that $d = 1$ can be assumed. Applying this to Eq. (4) leads to

$$n + 2b \sim -5. \qquad (10)$$

In the most simple scenario of a conical expanding jet with a well defined particle energy distribution function (i.e. without cooling; $n = -2$) and equipartition between magnetic energy and particle energy ($b = n/2$), a relation $n + 2b = -4$ is expected. Our result thus implies that at least one of these two assumptions does not hold strictly. If one assumes that equipartion holds, energy losses (e.g. due to adiabatic
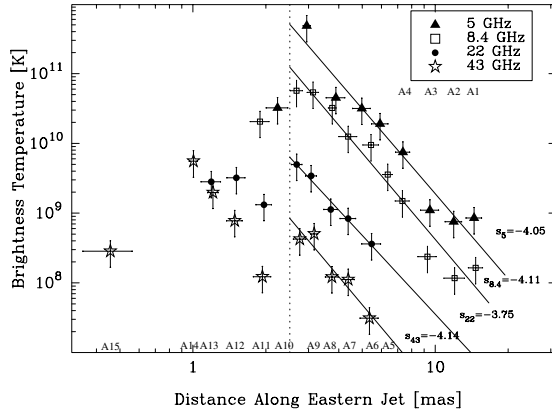
Fig. 10. Brightness temperature distribution along the eastern jet of NGC 1052. Above the cut-off distance of ~2.5 mas the data can be fitted by a power-law (see Table 6 for the fit parameters) with a power-law index of ~−4. The offset between the four data sets of brightness temperatures reflects the frequency dependence of T_b (see Eq. (5)).

Fig. 11. Brightness temperature distribution along the western jet of NGC 1052. No simple power-law can approximate the data, probably due to strong curvature effects.

expansion) might steepen the particle energy distribution effectively to $n \sim -2.5$. An alternative explanation would be that the magnetic flux of a dominant longitudinal component of the magnetic field density along the jet axis ($\pi D^2 B_z$) might be conserved so that $b = -2$. In the extreme case of no transverse magnetic field component this would lead to $n + 2b \sim -6$.

In principle, the detection of polarized emission in the eastern jet (see Sect. 5.2) allows the direction of the dominant component of the magnetic field to be determined. The linearly polarized emission originates in the region around component A 10, thus at the edge of the most compact component of the obscuring torus. Faraday rotation in this region is expected to be large so that we cannot directly derive a dominant transverse magnetic field from the alignment of the EVPAs with the jet axis. Polarimetric observations at multiple closely separated frequencies around 5 GHz would be necessary to derive the amount of Faraday rotation, which in combination with the measured opacity due to free-free absorption τ_f additionally would allow to disentangle the particle density and the magnetic field (the Faraday rotation at a given frequency is proportional to the particle density n_e, while $\tau_f \propto n_e^2$).

8.2. The T_b distribution along the western jet

The brightness-temperature distribution along the western jet of NGC 1052 is shown in Fig. 11. Here, the situation is more complex than on the eastern side. The western jet is less continuous than the eastern jet, which might be due to stronger curvature, particularly, between the regions C and D (see the counterjet structure at 22 GHz in Fig. 1). Since the equations derived above assume a straight jet geometry without abrupt bends, we do not try to approximate the brightness-temperature distribution by a single power-law. However, the course of the brightness temperature along the western jet tells something
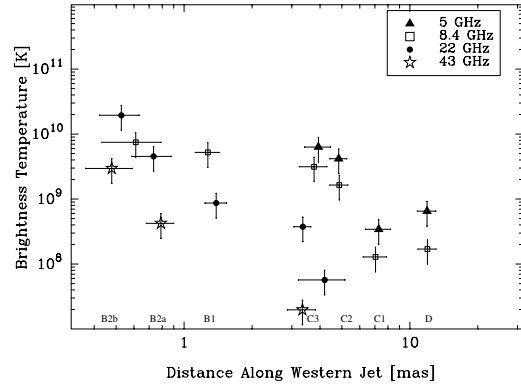
about the orientation of the jets and the structure of the obscuring torus towards the receding jet.

T_b decreases rapidly outwards between 3 and 12 mas. At a distance of about 7 mas, however, in the area of component C 1, the brightness temperature has a local minimum at 5 GHz and 8.4 GHz, which might be due to Doppler de-boosting due to a bend away from the line of sight. Inwards of 3 mas, in region B, where the strongest effects of free-free absorption were detected (see Sect. 7) the T_b distribution is flatter and the peak brightness temperatures do not exceed values of a few times 10^{10} K.

Component B 2 is strongly absorbed and, thus, its brightness temperature is substantially reduced at 8.4 GHz, dropping even below the peak value at 22 GHz (as expected due to its inverted spectrum discussed above). This can be used to estimate the absorbing column density towards component B 2, the area of the strongest effects of free-free absorption in NGC 1052. Assuming an intrinsic symmetry between jet and counterjet we can use the measured frequency-dependence of $\hat{T}(\nu)$ from the eastern jet of NGC 1052 to estimate the intrinsic brightness ratio of the counterjet at 8.4 GHz and 22 GHz. Considering the slightly different fitted slopes (compare Table 6) we derive from the best sampled region between 3 mas and 8 mas along the eastern jet that the brightness temperature at 8.4 GHz should exceed the value of T_b at 22 GHz by a factor of 15 to 20. Component B 2 has approximately the same brightness temperature at 8.4 GHz and at 22 GHz (mean value of B 2a and B 2b) which means that its flux density at 8.4 GHz is reduced by a factor of $\sim e^{-2.7}$–$e^{-3.0}$, i.e., $\tau_f^{8.4-22}$(B 2) $\sim$ 2.7 to 3.0. This is in agreement with the results of Kameno et al. (2001). These authors derive an optical depth of 300 at 1 GHz in the region corresponding to our component B 2, yielding $\tau_f \sim 3.4$ at 8.4 GHz. The optical depth due to free-free absorption is given by (e.g., Lobanov 1998)

$$\tau_f = 30 \times 10^{16} \, L \, T^{-1.35} \, \nu^{-2.1} \, \overline{n}^2. \tag{11}$$

For $\tau_f \sim 3$ at $\nu = 8.4$ GHz at a temperature of $T = 10^4$ K, and a length of the absorber of $L = 0.3$ pc (comparable to

the extent of the absorbing region in the plane of the sky) we derive a density of $\overline{n} = 2.4 \times 10^5\,\mathrm{cm}^{-3}$ and an absorbing column density of $2.2 \times 10^{22}\,\mathrm{cm}^{-2}$ towards component B 2. Depending on the unknown ionization fraction of the torus material[5] this value is consistent with various X-ray observations of NGC 1052, which imply a (model-dependent) column density of $N_H = 10^{22}\,\mathrm{cm}^{-2}$ to $N_H = 10^{24}\,\mathrm{cm}^{-2}$ towards the unresolved nuclear X-ray core (Weaver et al. 1999; Guainazzi et al. 1999; Kadler et al. 2004). Because of the smaller absolute difference between the corresponding values of T_b at 5 GHz and 8.4 GHz and the relatively larger uncertainties we do not derive opacities for the outer components of the western jet. However, from the inspection of Fig. 11 it is clear that the influence of free-free absorption is weak beyond 4 mas west of the nucleus.

8.3. Orientation of the jet-counterjet system

The ratio of brightness temperatures in the jet and in the counterjet at the same distances from the central engine can be used to constrain the angle to the line of sight of the jet/counterjet axis:

$$\frac{T_{b,j}}{T_{b,cj}} = \left(\frac{\delta_j}{\delta_{cj}}\right)^{2-\alpha}, \tag{12}$$

$$\frac{\delta_j}{\delta_{cj}} = \frac{1 + \beta \cos\theta}{1 - \beta \cos\theta}, \tag{13}$$

where δ_j and δ_{cj} are the Doppler factor of the jet and the counterjet, respectively. The mean ratio of the measured values of T_b on the western side and the fitted value at the corresponding distance on the eastern side (calculated for components between 3 mas and 5 mas distance from the center where free-free absorption effects are expected to be small) at all four frequencies is 9 ± 2. Assuming a spectral index of -1, this gives $\beta \cos\theta = 0.35^{+0.03}_{-0.04}$. Since $\beta = 1$ is an upper limit for the jet speed this results in a maximum allowed angle of $\sim72°$. The minimum allowed angle derived by Vermeulen et al. (2003) is $\sim57°$ for which $\beta = 0.64$. Thus, the jets are constrained to lie at an angle to the line of sight between 57° and 72°.

9. Discussion and summary

1. VLBI imaging of NGC 1052 exhibits a parsec-scale "twin-jet" structure, matching the standard model of AGNs if the two jets are oriented close to the plane of the sky.
2. We present accurately aligned, high-quality VLBI images of NGC 1052 at 5 GHz, 8.4 GHz, 22 GHz, and 43 GHz, the associated spectral index images between the adjacent frequencies and spectra of the various jet regions and model fit components.
3. The core of the western jet has a highly inverted spectrum with a spectral index well above 2.5, the theoretical upper limit for synchrotron self absorption, which was first mentioned by Kellermann et al. (1999) and later confirmed by Kameno et al. (2001) and Vermeulen et al. (2003).

Qualitatively, we confirm the results of those authors, particularly, the increasing opacity in the inner tens of milliarcseconds of the eastern jet.
4. We analysed the frequency dependence of the observed VLBI core position in both jets and found another clear signature of free-free absorption at the core of the western jet. The shift rate with frequency is too low to be explained in terms of synchrotron self absorption alone, while the core shift rate on the eastern side can still be explained under the assumption of steep pressure gradients increasing the synchrotron opacity. From the determination of these core shift rates we obtain an independent measurement of the position of the central engine of NGC 1052 with an accuracy as high as ~0.03 pc, superior to a kinematical derivation.
5. We find a sharp cut-off of the brightness temperature distribution along the eastern jet. Neither synchrotron self absorption nor free-free absorption can explain this behaviour. The most plausible explanation is that we see an effect of steep pressure gradients at a transition regime between the external pressure-dominated jet regime and a more or less freely expanding jet regime. Thus, the sharp cut-off of the brightness temperature distribution marks an observational sign of the overhanging edge of the obscuring torus.
6. We used the ratio of the observed brightness temperatures in the jet and the counterjet to constrain the angle to the line of sight of the "twin-jet" system. Together with the information from the kinematical study of Vermeulen et al. (2003), the angle to the line of sight can be determined to lie between $\sim57°$ and $\sim72°$.
7. The spectral index of the synchrotron jet emission was found to be -1. This result comes independently from the frequency dependence of the brightness-temperature distribution in the eastern jet and from the imaged spectral index at large distances from the core.
8. Either equipartition between the magnetic energy and the particle energy or the assumption of a single, well defined particle energy distribution without cooling is violated in the parsec-scale eastern jet of NGC 1052. Alternatively, a conserved longitudinal component might dominate the magnetic field on these scales.
9. We find a region of linearly polarized emission at the base of the eastern jet. The EVPA of the polarized emission cannot be evaluated directly since Faraday rotation at the center of this galaxy is expected to be large. We find no linear polarization of the source at higher frequencies. The simplest explanation for this behavior is that the different layers of the jet have a different degree of polarization and that the emission at higher frequencies originates in an inner, unpolarized layer of the jet. The higher column density at the more centrally located jet base at higher frequencies could cause higher Faraday depolarization than it does at 5 GHz. This idea is supported by the fact that the jet base at 5 GHz coincides with the edge of the obscuring torus. This scenario can be tested with observations at longer wavelengths and especially around 5 GHz, where the depolarization is expected to start dominating.

---

[5] Free-free absorption is an indicator of the column density N_e of free electrons in an ionised medium, rather than the column density of neutral hydrogen N_H. In a fully ionised medium, $N_e = N_H$ holds.

10. Most likely, a combination of free-free absorption, synchrotron self absorption, and the presence of steep pressure gradients determine the parsec-scale radio properties of NGC 1052. An analytical model fit to the observed spectrum of only one single absorption mechanism model seems not to be satisfactory to represent the true physical situation.

11. The absorbing column density derived from the degraded brightness temperature of the western jet core is $\sim 2 \times 10^{22}\,\mathrm{cm}^{-2}$, in good agreement with the value obtained from X-ray spectroscopy (Kadler et al. 2004). This suggests that the nuclear X-ray emission (which is unresolved for all X-ray observatories currently in orbit) originates on the same scales which are imaged by VLBI and underlines the importance of combined future radio and X-ray observations of NGC 1052.

References

Blandford, R. D., & Königl, A. 1979, ApJ, 232, 34
Cassidy, I., & Raine, D. J. 1993, MNRAS, 260, 385
Claussen, M. J., Diamond, P. J., Braatz, J. A., Wilson, A. S., & Henkel, C. 1998, ApJ, 500, L129
Condon, J. J., Condon, M. A., Gisler, G., & Puschell, J. J. 1982, ApJ, 252, 102
Ferguson, J. W., Korista, K. T., & Ferland, G. J. 1997, ApJS, 110, 287
Guainazzi, M., & Antonelli, L. A. 1999, MNRAS, 304, L15
Kadler, M., Kerp, J., Ros, E., et al. 2004, A&A, 420, 467
Kameno, S., Sawada-Satoh, S., Inoue, M., Shen, Z., & Wajima, K. 2001, PASJ, 53, 169
Kameno, S., Inoue, M., Wajima, K., Sawada-Satoh, S., & Shen, Z. 2003, Publ. of the Astron. Soc. of Australia, 20, 134
Kellermann, K. I., Vermeulen, R. C., Cohen, M. H., & Zensus, J. A. 1999, BAAS, 31, 856
Knapp, G. R., Faber, S. M., & Gallagher, J. S. 1978, AJ, 83, 139
Krolik, J. H. 1999, Active galactic nuclei: from the central black hole to the galactic environment (Princeton, NJ: Princeton University Press)
Leppänen, K. J., Zensus, J. A., & Diamond, P. J. 1995, AJ, 110, 2479
Lobanov, A. P. 1998, A&A, 330, 79
Middelberg, E., Roy, A. L., Bach, U., et al. 2004, in Future Directions in High Resolution Astronomy, ed. J. D. Romney, & M. J. Reid, ASP Conf. Ser., in press [arXiv:astro-ph/0309385]
Napier, P. J. 1994, Very High Angular Resolution Imaging, ed. J. G. Robertson, & W. J. Tango, IAU Symp., 158, 117
Omar, A., Anantharamaiah, K. R., Rupen, M., & Rigby, J. 2002, A&A, 381, L29
Ros, E. 2004, in Future Directions in High Resolution Astronomy, ed. J. D. Romney, & M. J. Reid, ASP Conf. Ser., in press [arXiv:astro-ph/0308265]
Ros, E., Zensus, J. A., & Lobanov, A. P. 2000, A&A, 354, 55
Shepherd, M. C. 1997, ASP Conf. Ser., 125, Astronomical Data Analysis Software and Systems VI, 6, 77
van Gorkom, J. H., Knapp, G. R., Raimond, E., Faber, S. M., & Gallagher, J. S. 1986, AJ, 91, 791
Vermeulen, R. C., Ros, E., Kellermann, K. I., et al. 2003, A&A, 401, 113
Weaver, K. A., Wilson, A. S., Henkel, C., & Braatz, J. A. 1999, ApJ, 520, 130
Wrobel, J. M. 1984, ApJ, 284, 531

6.3.2 Jet emission in NGC 1052 at radio, optical, and X-ray frequencies

This second part of the NGC 1052 study presented in this section has been published in the journal Astronomy & Astrophysics, Vol. 420, p.467–474 (2004). First results of this work have been given in my Diploma thesis (Kadler 2002) but the bulk part of this study has been done between 2002 and 2004 within the scope of this PhD thesis. The structure map of NGC 1052 (Fig. 4 of the paper) has been produced by R. W. Pogge from the Department of Astronomy, Ohio State University, Columbus, OH, USA. A reprint of the A&A publication is given below.

List of collaborators: H. Falcke, J. Kerp, R. W. Pogge, E. Ros, & J. A. Zensus

Astronomy
&
Astrophysics

Jet emission in NGC 1052 at radio, optical, and X-ray frequencies

M. Kadler[1], J. Kerp[2], E. Ros[1], H. Falcke[1,*], R. W. Pogge[3], and J. A. Zensus[1]

[1] Max-Planck-Institut für Radioastronomie Bonn, Auf dem Hügel 69, 53121 Bonn, Germany
[2] Radioastronomisches Institut, Universität Bonn, Auf dem Hügel 71, 53121 Bonn, Germany
[3] Department of Astronomy, Ohio State University, 140 West 18th Avenue, Columbus, OH 43210-1173, USA

Abstract. We present a combined radio, optical, and X-ray study of the nearby LINER galaxy NGC 1052. Data from a short (2.3 ks) *CHANDRA* observation of NGC 1052 reveal the presence of various jet-related X-ray emitting regions, a bright compact core and unresolved knots in the jet structure as well as an extended emitting region inside the galaxy well aligned with the radio synchrotron jet-emission. The spectrum of the extended X-ray emission can best be fitted with a thermal model with $kT = (0.4−0.5)$ keV, while the compact core exhibits a very flat spectrum, best approximated by an absorbed power-law with $N_{\rm H} = (0.6−0.8) \times 10^{22}$ cm^{-2}. We compare the radio structure to an optical "structure map" from a *Hubble Space Telescope* (*HST*) observation and find a good positional correlation between the radio jet and the optical emission cone. Bright, compact knots in the jet structure are visible in all three frequency bands whose spectrum is inconsistent with synchrotron emission.

Key words. galaxies: individual: NGC 1052 – galaxies: individual: B 0238-084 – galaxies: active – galaxies: jets

1. Introduction

NGC 1052 is a nearby[1] elliptical galaxy which harbors a low-luminosity active galactic nucleus (LLAGN) in its very center ($L_{1−100{\rm GHz}} = 4.4 \times 10^{40}$ erg s^{-1}; Wrobel 1984). It hosts a two-sided radio jet emanating from the nucleus and reaching out to kiloparsec-scales which is, however, still fully enclosed within the stellar body of the optical galaxy. In the optical, the spectrum of NGC 1052 is characterized by strong forbidden lines from low-ionization states which has made NGC 1052 the prototypical LINER (low-ionization nuclear emission line region; Heckman 1980) galaxy. As for LINERs in general, it has long been argued whether these low-ionization lines in NGC 1052 are excited by a central photo-ionizing source (e.g., Gabel et al. 2000) or if shock heating is the dominant mechanism (e.g., Sugai & Malkan 2000). While there is overwhelming evidence for the presence of an active galactic nucleus (AGN) in NGC 1052, the role of shocks in this galaxy is still unclear. The improved angular resolution in X-rays offered by *CHANDRA* makes it possible for the first time to image the distribution of

X-ray emission on the same scales as accomplished by connected radio interferometers, e.g., MERLIN (Multi-Element Radio-Linked Interferometer Network). Disentangling the contributions of compact (i.e., <1 arcsec) nuclear and extended (i.e., >1 arcsec) X-ray emitting regions to the total amount of X-ray emission of NGC 1052 can serve as an important tool to study the interaction between the radio jet plasma and the ambient interstellar medium.

NGC 1052 has been observed by all major X-ray missions of the pre–*CHANDRA* era, like *Einstein* (Mc Dowell 1994), *ASCA* and *ROSAT* (Weaver et al. 1999), and *Beppo Sax* (Guainazzi & Antonelli 1999). For these X-ray missions, NGC 1052 appeared as a point-like X-ray source. The X-ray spectrum of NGC 1052 is extremely flat, a finding that led to the proposal of an advection dominated accretion flow (ADAF) as the origin of the observed X-ray emission (Guainazzi et al. 2000). To model the AGN X-ray spectrum above $E \simeq 2$ keV absorbing column densities in excess of 10^{23} cm^{-2} have been discussed, supporting the idea of a high density obscuring torus, comparable to column densities found in other AGN (e.g., Malizia et al. 1997; Risaliti et al. 2002). Independent evidence for the existence of an obscuring torus at the center of NGC 1052 is obtained from Very Long Baseline Interferometry (VLBI) observations in the radio regime: on parsec-scales NGC 1052 exhibits a twin jet structure with a prominent emission gap between both jets (see e.g., Kadler et al. 2003b). The inner part of the western jet shows a

468   M. Kadler et al.: Jet emission in NGC 1052 at radio, optical, and X-ray frequencies

strongly inverted radio spectrum, which was first discovered by Kellermann et al. (1999) (see also Kameno et al. 2001). The cm-wavelength spectral index in this central region is larger than 2.5, exceeding the theoretical limit for synchrotron self-absorption.

Combined studies of the core region of NGC 1052 in the radio and X-ray regime are of essential importance for constraining the physical properties of the parsec-scale radio jet and the obscuring torus as well as to determine the nature of the nuclear X-ray emission. In this paper we present a combined radio, optical, and X-ray study of the jet-related emission in NGC 1052 on arcsecond scales. In particular, we focus on the soft X-ray excess in the source-spectrum below $E = 2$ keV. This soft component was identified first by Weaver et al. (1999) based on *ROSAT* PSPC data. *CHANDRAs* superior angular resolution makes it possible to present evidence that this soft excess emission is associated with the well known radio jet.

In Sect. 2 we present the *CHANDRA*, MERLIN, and *HST* data as well as their reduction. In Sect. 3 we discuss the arcsecond-scale morphology of NGC 1052 in the radio, optical, and X-ray regime and the correlations between the different wave bands. In Sect. 4 we derive models for the nuclear and extended X-ray emission and Sect. 5 summarizes our conclusions.

2. Observations and data reduction

2.1. CHANDRA data

CHANDRA observed NGC 1052 on August 29/30, 2000[2]. During the 2342 s observation, the Advanced CCD Imaging Spectrometer (ACIS) Chip S3 was in the focus of the High Resolution Mirror Assembly (HRMA). The ACIS-S3 detector offers high angular resolution as well as information on the X-ray source spectrum because of its intrinsic energy resolution and has a higher sensitivity in the soft X-ray energy regime below $E < 1$ keV then the front-side illuminated detectors of *CHANDRA*.

The nucleus of NGC 1052 is the brightest X-ray source within the field of interest. The count rate of 0.12 cts s^{-1} is sufficiently high to affect the measured AGN X-ray spectrum by the pile-up effect. The pile-up effect changes the shape of the measured X-ray spectrum as well as the measured count rate, because during a single read-out period of the chip multiple X-ray photons may be detected within a single pixel. Due to insufficient time resolution their combined signal is registered as a single photon event. The presented *CHANDRA* observation was performed using the standard timed exposure mode. Depending on the detailed shape of the AGN X-ray spectrum up to 27% of the available data can be affected by the pile-up effect. In principle, this introduces a bias which results in spectral hardening and mimics lower count rates.

The spatial distribution of photon events on the ACIS-S3 chip during the observation of NGC 1052 is shown in Fig. 1 for

---

[2] The *CHANDRA* data were taken from the public archive (http://cxc.harvard.edu/cda/chaser.html) and analyzed using standard methods within the software package CIAO 3.0 using the calibration data base CALDB 2.2.5 version.
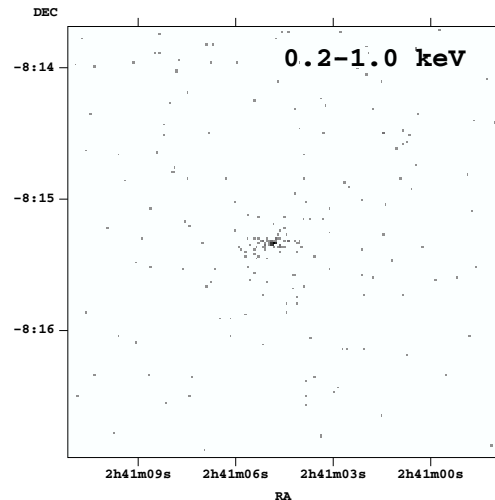
Fig. 1. Raw *CHANDRA* image of NGC 1052 showing the spatial distribution of photon events in the energy range (0.2–1.0) keV.

the energy range (0.2–1) keV. Even from the small number of counts during this snapshot observation the distribution of soft X-rays clearly differs from a point spread function. Using the CSMOOTH program which is part of the CIAO software we also produced an adaptively smoothed map of the field of interest (see Fig. 2) for which we reduced the angular resolution of the data from 0.5 arcsec to 4 arcsec and set a minimum significance threshold to 3σ.

2.2. MERLIN data

A MERLIN observation of NGC 1052 at 1.4 GHz was performed on November 22, 1995. The data from this experiment have been obtained from the public archive[3] and analyzed applying standard methods using the program DIFMAP. Two different maps of the brightness distribution of NGC 1052 at 1.4 GHz were produced. First, a strong (u, v)-taper was used to map the extended emission resulting in a restoring beam of (1.5×1.1) arcsec at a position angle (PA) of $-31°$. Second, a pure naturally weighted image was produced yielding a restoring beam of (0.5×0.3) arcsec at a PA of $27°$.

2.3. HST data

For this paper, we re-examined the archival *HST* data of NGC 1052 previously published by Pogge et al. (2000). The archival data are three narrow-band *F658N* filter images acquired with the *WFPC2* in the PC1 detector (pixels scale ~ 0.046 arcsec) with integration times of 200, 800, and 900 s, respectively. Cosmic rays were cleaned from the individual images using a version of the L.A.Cosmic Laplacian edge-detection algorithm described by van Dokkum (2001). The cleaned images were added together after registration

---

[3] http://www.merlin.ac.uk
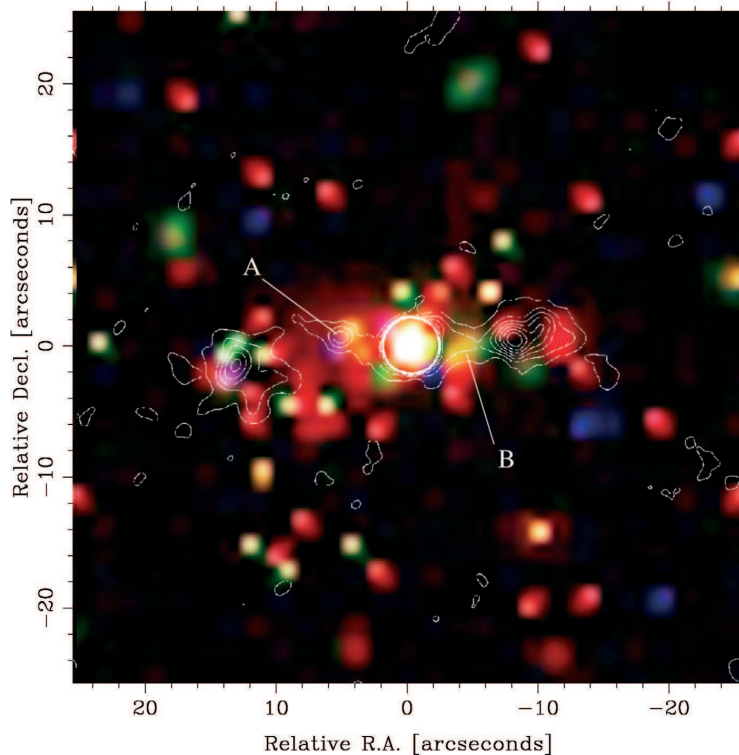
Fig. 2. Three color *CHANDRA* image of the jet-associated X-ray emission in NGC 1052 with the 1.4 GHz MERLIN radio image overlaid in contours. The *CHANDRA* image has been smoothed to a resolution of 4″ to increase sensitivity. Red represents photons between 0.1 keV and 1 keV, green between 1 keV and 2 keV and blue (2−3) keV. The clipping level is 3σ. The MERLIN image was restored with a circular beam of 1.7 arcsec *FWHM*. Contours are shown for $(0.5, 1.5, 2.5, 3.5, 4.5, 5.5, 6.5) \times 1$ mJy/beam. The jet-associated emission is dominated by soft X-rays below 1 keV, whereas the AGN appears white, representing a rather flat X-ray spectrum.

using a field star in the image to remove the inter-image offsets. To enhance the faint emission features noted by Pogge et al. (2000), we created a "structure map" of the combined, cleaned images following the technique described by Pogge & Martini (2002). We used a model point spread function for the *F*658*N* filter and PC1 camera generated using the TINYTIM package (Krist & Hook 1999). Structure mapping is an improved method of image contrast enhancement (compared to traditional unsharp masking). In brief, the technique suppresses the large-scale starlight distribution, enhancing faint emission and absorption (e.g., dust extinction) features in the image.

3. The multi-waveband jet structure

3.1. Jet-associated X-ray emission in NGC 1052

The *CHANDRA* image of NGC 1052 in the energy range (0.3−3.0) keV is shown in Fig. 2. Strong X-ray emission from the AGN is seen in this image, as well as diffuse extended emission well aligned with the radio jet, whose MERLIN image is superimposed in contours. In Sects. 4.1 and 4.2 we discuss the X-ray spectra in detail and present evidence that the soft excess component found previously in the *ROSAT* spectra of the nucleus (Weaver et al. 1999) is associated with this soft, extended jet-associated emission.

To the first order, the radio and the X-ray jet are aligned on arcsecond scales and their extent appears to be the same.

However, the intensity of synchrotron emission in the radio lobes appears to be anti-correlated with the soft X-ray intensity distribution in so far as the radio hotspots on both sides correspond to regions on the ACIS-S3 chip which did not detect any photon events. East and west of the nucleus two relatively bright X-ray emitting regions coincide with emission knots in the radio regime. Bright optical emission knots are also present in these areas (Pogge et al. 2000).

3.2. Radio emission on arcsecond scales

The large-scale radio structure of NGC 1052 visible in the tapered MERLIN image reveals some differences to the 1980 VLA image of Wrobel (1984) (see Fig. 3). The VLA, which was operated in its A configuration during the 1980 observations, was more sensitive to extended structures, which partially have been resolved out by MERLIN. The core has varied, with a flux density of ∼0.74 Jy in December 1980 and ∼1.01 Jy in November 1995. The western hot spot has increased in flux density. A knot in the western jet (labeled as B in the MERLIN image) was not visible as a local maximum in the 1980 VLA image. By aligning the core positions at both epochs, we found that the eastern knot (labeled as A), has moved about 0.5 arcsec inwards. However, an examination of the pure naturally weighted MERLIN image (see Fig. 4) reveals that knot A is composed of two isolated sub-components (A 1 and A 2) separated by the same distance of ∼0.5 arcsec.
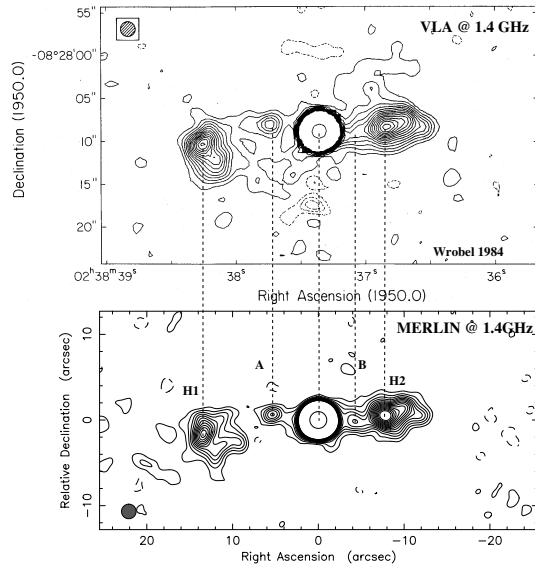
Fig. 3. Comparison between the VLA image of NGC 1052 observed in 1980 (Wrobel 1984) and the MERLIN image from 1995, both at 1.4 GHz. Both maps have been convolved with the same (circular) restoring beam of 1.7 arcsec *FWHM*. Contours at $(-1, 1, 2, 3, 4, 5, 6, 7, 8, 9, 10, 11, 12, 13, 14, 15, 800) \times 0.5$ mJy are given in both maps (the VLA map also shows negative contours at $(-4, -3, -2) \times 0.5$ mJy). The hot spots (labeled as H1 and H2) do not show any positional changes. The emission peak of the eastern knot (A) is about 0.5 arcsec closer to the core in 1995.

This suggests that the inner sub-component might have increased in flux density between 1980 and 1995, causing an apparent shift of the blended knot structure in Fig. 2. This offers a more plausible explanation than an inward motion with a velocity of $\sim 10\,c$.

3.3. Optical structure

The structure map of NGC 1052 is shown in Fig. 4 with the radio contours of the untapered, full-resolution MERLIN image superimposed. The jet–counterjet structure is aligned with the optical emission cone. The dark band perpendicular to the radio jet might be an artifact of the image processing. Two optical emission knots are located at the edges of the two radio sub-components of knot A. The optical emission knot in the west coincides roughly with a weak ($\sim 1\sigma$) radio feature while the stronger radio knot 1.5 further out has no corresponding bright optical counterpart. The origin of the optical emission remains unclear since there is no continuum image to subtract from the Hα filter image of NGC 1052. The conical morphology in this LINER 1.9 galaxy is remarkably similar to the structure of the narrow-emission-line region typically observed in Seyfert 2 galaxies (e.g., Falcke et al. 1998). This suggests that the optical emission cone is due to line emission rather than continuum emission. The optical flux density of the two eastern knots of $(68 \pm 1)\,\mu$Jy exceeds the power-law extrapolation from

the radio to the X-ray regime by almost three orders of magnitude. This is a strong argument against the synchrotron emission process, but compatible with relatively strong line emission exceeding the continuum emission of the knots in this narrow band.

4. X-ray imaging spectroscopy

Using *CHANDRA's* high angular resolution, it is possible to obtain separate spectra of the nucleus and the diffuse jet-associated X-ray emission. We selected an annulus centered at the nucleus position which excludes the nucleus itself but includes the whole area of the diffuse emission. To avoid any contamination by the nuclear X-ray emission, a diameter of 3 arcsec for the inner annulus ring was used. The nuclear X-ray spectrum was extracted up to a diameter of 2 arcsec. The extracted X-ray data of both regions were corrected for the unrelated X-ray background emission, using a region located close by without significant point sources. We also applied a correction for the quantum efficiency degeneracy of the ACIS detector.

Figure 5 reveals the much softer spectrum of the diffuse X-ray emission compared to the nuclear spectrum. The bulk emission originates below $E < 2$ keV, while the X-ray spectrum of the nucleus has an additional hard X-ray component. Remarkable is the soft X-ray emission below $E < 2$ keV towards the nucleus. *ASCA*, as well as the *ROSAT* PSPC, could not separate the nucleus and the jet spatially, but a soft excess X-ray emission had already been detected in the X-ray spectrum from the PSPC data.

4.1. The X-ray spectrum of the extended emission

To constrain the emission process of the diffuse extended emission, we fitted different models using XSPEC (version 11.2): the RAYMOND model corresponding to a Raymond/Smith plasma (Raymond & Smith 1977), the MEKAL model describing a Mewe/Kaastra plasma (e.g., Kaastra 1992) and a simple power-law. The results of the spectral fits are presented in Table 1.

Because the jet is located deep inside the stellar body of the galaxy NGC 1052, we have to determine the amount of photoelectric absorption distributed along the line of sight. Using the thermal source models, we find an attenuating column density value about one order of magnitude higher than the galactic foreground column density belonging to the Milky Way (Hartmann & Burton 1997). We attribute this additional X-ray attenuation to weakly ionized gas located inside the galaxy itself. The unabsorbed flux of the Raymond/Smith (Mewe/Kaastra) plasma in the range between 0.3 and 8 keV corresponds to an intrinsic luminosity of $L = 2.4(2.1) \times 10^{40}$ erg s^{-1} at the distance of the source of 22.6 Mpc.

Both plasma models fall below the measured count rate above 2.5 keV (see Fig. 5) suggesting some contribution of an additional hard X-ray component to the spectrum of the extended emission. Due to the low photon statistics and the large uncertainties we have not tried to account for this additional spectral component by considering more complicated models.
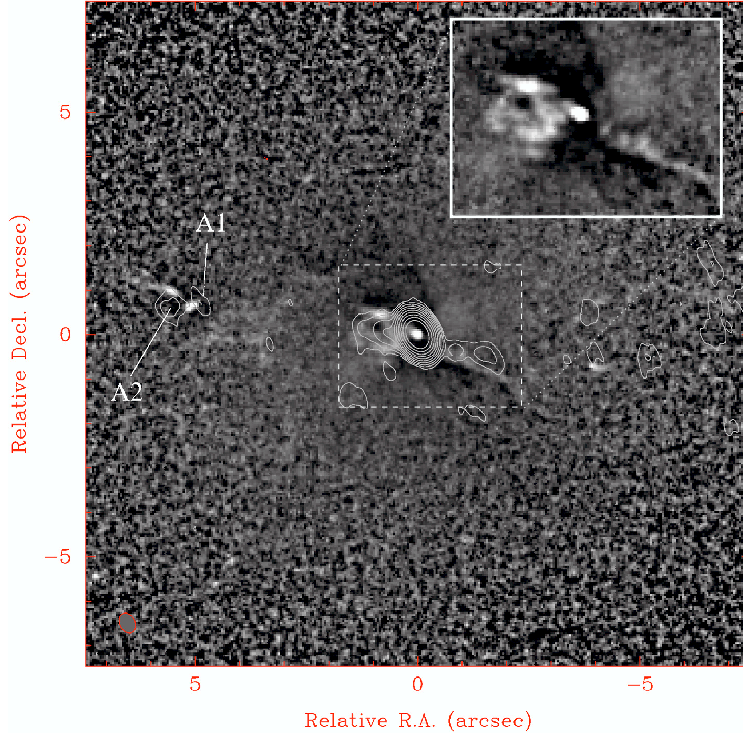
Fig. 4. *HST* structure map of NGC 1052. Dark regions represent dust obscuration while bright regions are locations of enhanced emission. Overlaid is the pure naturally weighted MERLIN map showing the core of NGC 1052 with sub-arcsecond resolution. Contours at $(-1, 1, 2, 4, 8, 16, 32, 64, 128, 256, 512, 1024) \times 0.5$ mJy/beam are shown. The inlaid panel shows an enlarged view of the marked box around the area of the optical emission cone.

Because of the low number of counts from the jet, we cannot unequivocally dismiss the power-law model, which gave an acceptable fit to the X-ray data. However, we consider the power-law fit result of the X-ray jet as unreliable because of the unusually steep photon index[4] (see Table 1).

4.2. The X-ray spectrum of the nucleus

Below $E = 2$ keV a soft excess is detected in the nuclear spectrum. Assuming that a fraction of the diffuse jet-associated emission originates within the immediate neighborhood of the nucleus, we used a hybrid model for the X-ray spectral approximation of the observed intensity distribution.

$$I_{\mathrm{obs}} = \left(I_{\mathrm{diffuse}} + I_{\mathrm{nucleus}} \times \mathrm{e}^{-\sigma \times N_{\mathrm{H(torus)}}}\right) \times \mathrm{e}^{-\sigma \times N_{\mathrm{H(gal.)}}} \qquad (1)$$

where I_{diffuse} is the X-ray spectrum of the diffuse jet-associated emission and I_{nucleus} is the spectrum of the nucleus. Here, the photoelectric absorption produced by the torus is represented by $\mathrm{e}^{-\sigma \times N_{\mathrm{H(torus)}}}$, while the X-ray absorption produced by the interstellar medium of the elliptical galaxy is $\mathrm{e}^{-\sigma \times N_{\mathrm{H(gal.)}}}$.

We assumed a power-law type X-ray spectrum of the central X-ray source and modeled the soft component as a thermal plasma spectrum of the Raymond/Smith and Mewe/Kaastra type, (model I and II) respectively. We did not try to fit for

the metallicities and fixed these during the spectral fitting procedure given the poor statistics from the short integration time. Model Ia(IIa) assumes solar abundances of the Raymond/Smith (Mewe/Kaastra) plasma and allows the other parameters to be varied. In model Ib(IIb) the temperatures of the plasma and the absorbing column density of the interstellar medium of the galaxy were fixed to the best fitting values to the extended X-ray emission (see Table 1). In model Ic(IIc) the metal abundances were additionally changed to 25% of the solar composition. Such low metal abundances typically occur only in dwarf galaxies but are found in NGC 1052 from optical line measurements of Sil'chenko (1995) who reports values [Fe/H] ~ -0.6 for the nucleus and [Fe/H] ~ -1 for the bulge of NGC 1052, corresponding to metallicities of about 25% and 10%, respectively. One way to accumulate a substantial amount of metal-poor material is a merger or close encounter with an extremely metal-poor dwarf galaxy. Evidence for such an event indeed exists from multiple observational approaches (see Forbes et al. 2001 and references therein) in the case of NGC 1052.

The statistically best fitting values are given in Table 2. For all six models we derive a luminosity of $L = 1.4 \times 10^{41}$ erg s^{-1}. Correcting for the effect of the two absorber model components increases the intrinsic (unabsorbed) value to $L = (1.7-2.0) \times 10^{41}$ erg s^{-1}. The values of $N_{\mathrm{H(gal.)}}$ and kT for the plasma component in the models Ia and IIa are very similar to the values determined for the extended plasma emission. For these models we derive best fitting values for the absorbing column density of $N_{\mathrm{H(torus)}} = (0.6-0.7) \times 10^{22}$ cm^{-2} as well as $\Gamma = 0.2-0.3$

---

[4] The photon index Γ is defined as the power-law index of the spectrum given in units of [photons s^{-1} keV^{-1}]. It is related to the energy index α, used in radio astronomy, via: $\Gamma = 1 - \alpha$.
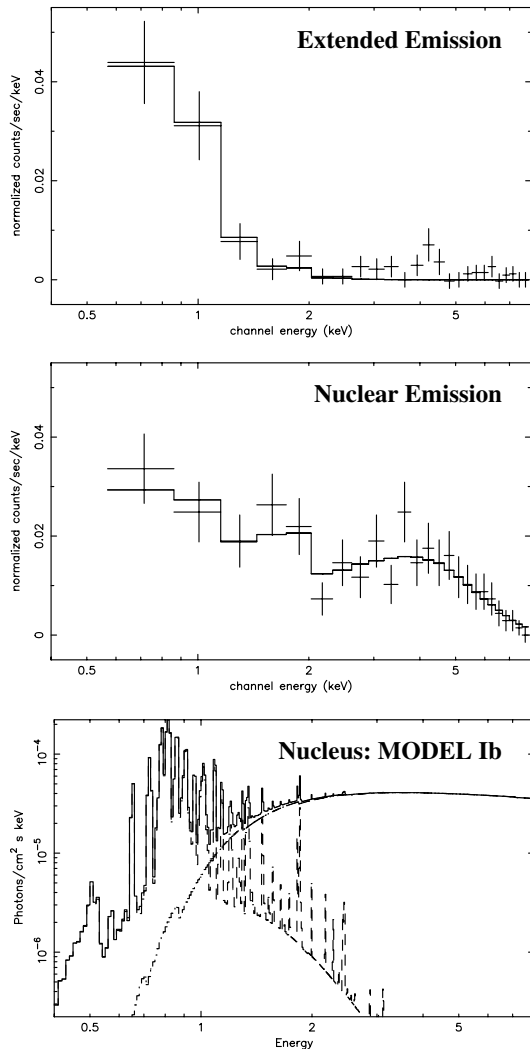
Fig. 5. *Top panel*: X-ray spectrum of the extended X-ray jet emission and the Raymond/Smith plasma model folded with the detector response matrix (solid line). *Middle panel*: X-ray spectrum of the nuclear emission and the best fit of model Ib (solid line, compare Table 4.2). *Bottom panel*: the unfolded model Ib spectrum representing an absorbed Raymond/Smith plasma whose model parameters have been held fixed at the best fitting values to the extended X-ray emission spectrum (see Table 1) plus a power-law with an additional absorber.

for the photon index. Similar values for both parameters result from fixing $N_{H(gal.)}$ and kT as described above in the models Ib and IIb. Reducing the metal abundances of the plasma component in model Ic(IIc) forces the power-law to contribute more strongly to the soft part of the spectrum resulting in higher values of $N_{H(torus)} \sim 0.8 \times 10^{22}\,\mathrm{cm}^{-2}$ and $\Gamma \sim 0.3$. These values are still rather low. Data from other X-ray observatories imply

much higher values for $N_{H(torus)}$ as well as for Γ (Weaver et al. 1999; Guainazzi & Antonelli 1999; Guainazzi et al. 2000). We note that the apparent discrepancy between previous X-ray observations and the *CHANDRA* data concerning the photon index might be due to the pile-up degradation ($\sim 30\%$) of the latter. The nuclear X-ray spectrum thus might appear artificially flattened. The determined absorbing column density, however, is not so sensitive to the pile-up effect, which mainly affects the hard part of the spectrum while the amount of absorption is determined in the soft X-ray regime. The statistical quality of all six fits is very similar, with values of χ^2_{red} ranging from 0.76 to 0.84, and the low photon statistics (reflected in the values of $\chi^2_{red} < 1$) do not allow us to dismiss any of these models.

We note that a "patchy" absorber model in which a fraction of the central source is seen directly and only a part of the source is covered by the absorber might be a more realistic model for the nuclear X-ray emission of NGC 1052, given the results of Vermeulen et al. (2003), who found that moving VLBI components in both jets show complex light curves probably caused by substantial patchiness of the absorbing screen. Additionally, they find a complex H I absorption line spectrum with compact clouds of absorbing material at different relative velocities and different locations along the parsec-scale jet structure. The absorbing column density derived from "patchy" absorber models is expected to be considerably higher ($\sim 2 \times 10^{22}\,\mathrm{cm}^{-2}$) than the values derived from uniform absorber models. However, given the low photon statistics, we omit the detailed discussion of such models with a larger number of free parameters.

5. Discussion

The *CHANDRA* data provide for the first time direct evidence for jet-associated X-ray emission in NGC 1052. The diffuse, extended X-ray emission can be best approximated with a thermal plasma model with $kT \sim 0.4-0.5\,\mathrm{keV}$. This temperature is consistent with the thermal component found earlier by Weaver et al. (1999) using *ASCA* and *ROSAT* data. Its absorbed flux is only $\sim 3\%$ of the nuclear X-ray emission but the intrinsic (absorption corrected) extended emission might contribute up to 14% to the total unabsorbed X-ray flux of NGC 1052. Because of the considerable pile-up degradation of the *CHANDRA* data, no firm conclusions on the photon index of the nucleus spectrum can be deduced. The derived column density of hydrogen towards the compact X-ray core (depending on the applied model) of $0.5-0.8 \times 10^{22}\,\mathrm{cm}^{-2}$ is in good agreement with the absorbing column density of ionized material towards the VLBI-jet derived by Kadler et al. (2002) and Kadler et al. (in prep.). This suggests that the nuclear X-ray emission of NGC 1052 might be produced on the same scales as the parsec-scale structures imaged by VLBI at high frequencies.

The detection of a diffuse region of X-ray emitting gas with a thermal spectrum and the same extent as the kiloparsec-scale radio jet suggests that jet-triggered shocks might play an important role in NGC 1052. In such a model the kinetic power of the radio jet is partially converted into X-ray emission. The optical morphology in the Hα filter substantiates this picture as was

Table 1. Best-fitting parameters for the spectral fits to the extended jet-associated emission.

Model[a]	$N_{\mathrm{H}}^{(b)}$	kT	$\Gamma^{(c)}$	$F_{\mathrm{abs}}^{(d)}$	$F_{\mathrm{unabs}}^{(d)}$	χ_{red}^2 (χ^2/d.o.f.)
	[10^{22} cm^{-2}]	[keV]		[erg s^{-1} cm^{-2}]	[erg s^{-1} cm^{-2}]	
(R&S)$^{\mathrm{abs}}$	$0.49^{+0.08}_{-0.06}$	$0.48^{+0.08}_{-0.08}$	–	0.8×10^{-13}	3.9×10^{-13}	0.49 (10.8/22)
(M&K)$^{\mathrm{abs}}$	$0.41^{+0.08}_{-0.06}$	$0.41^{+0.09}_{-0.07}$	–	0.7×10^{-13}	3.4×10^{-13}	0.53 (11.6/22)
(PL)$^{\mathrm{abs}}$	$0.06^{+0.07}_{-0.02}$	–	$3.8^{+0.6}_{-0.7}$	1.5×10^{-13}	2.0×10^{-13}	0.52 (11.5/22)

[a] R&S: Raymond/Smith plasma, M&K: Mewe/Kaastra plasma, PL: power-law; [b] absorbing column density; 2×10^{20} cm^{-2} is set as a lower limit; [c] photon index; [d] (un)absorbed X-ray flux between 0.2 keV and 8.0 keV.

Table 2. Best-fitting parameters for the spectral fits of the core emission.

Model[a]	$N_{\mathrm{H(gal.)}}^{(b)}$	kT	$Z^{(c)}$	$N_{\mathrm{H(torus)}}^{(d)}$	$\Gamma^{(e)}$	$F_{\mathrm{abs}}^{(f)}$	$F_{\mathrm{unabs}}^{(g)}$	χ_{red}^2 (χ^2/d.o.f.)
	[10^{22} cm^{-2}]	[keV]		[10^{22} cm^{-2}]		[erg s^{-1} cm^{-2}]	[erg s^{-1} cm^{-2}]	
Ia	$0.66^{+0.07}_{-0.07}$	$0.44^{+0.07}_{-0.06}$	1*	$0.74^{+0.56}_{-0.39}$	$0.30^{+0.10}_{-0.08}$	2.3×10^{-12}	3.3×10^{-12}	0.84 (15.9/19)
Ib	0.49*	0.48*	1*	$0.54^{+0.46}_{-0.34}$	$0.20^{+0.10}_{-0.08}$	2.3×10^{-12}	2.9×10^{-12}	0.76 (16.0/21)
Ic	0.49*	0.48*	0.25*	$0.84^{+0.55}_{-0.39}$	$0.28^{+0.09}_{-0.09}$	2.3×10^{-12}	3.0×10^{-12}	0.74 (15.8/21)
IIa	$0.51^{+0.09}_{-0.04}$	$0.28^{+0.03}_{-0.04}$	1*	$0.45^{+0.59}_{-0.21}$	$0.22^{+0.13}_{-0.05}$	2.5×10^{-12}	3.4×10^{-12}	0.89 (16.8/19)
IIb	0.41*	0.41*	1*	$0.62^{+0.46}_{-0.37}$	$0.23^{+0.06}_{-0.09}$	2.3×10^{-12}	2.8×10^{-12}	0.77 (16.1/21)
IIc	0.41*	0.41*	0.25*	$0.82^{+0.42}_{-0.42}$	$0.27^{+0.07}_{-0.11}$	2.2×10^{-12}	2.8×10^{-12}	0.78 (16.4/21)

* Fixed value; [a] I: (R&S + PL$^{\mathrm{abs}}$)$^{\mathrm{abs}}$, II: (M&K + PL$^{\mathrm{abs}}$)$^{\mathrm{abs}}$, (R&S$^{\mathrm{abs}}$: absorbed Raymond/Smith plasma, M&K$^{\mathrm{abs}}$: absorbed Mewe/Kaastra plasma, PL$^{(\mathrm{abs})}$: (absorbed) power–law; [b] column density of the diffuse absorber; [c] metallicity (referring to the solar value); [d] column density of the compact absorber; [e] photon index; [f] absorbed X-ray flux between 0.2 keV and 8.0 keV; [g] unabsorbed X-ray flux between 0.2 keV and 8.0 keV, i.e., $N_{\mathrm{H(gal.)}}^{(b)}$ and $N_{\mathrm{H(torus)}}^{(d)}$ are set to 0.

noted earlier by Allen et al. (1999). The alignment of the radio jet and the optical emission cone visible in Fig. 4 implies that the ionization cone might be drilled out by the radio jets, resulting in a predominantly shock-excited, conical narrow-line region (see e.g., Dopita 2002). Shocks might occur also on larger scales giving rise to the soft thermal X-ray emission associated with the radio jet/lobe structure in NGC 1052. A rough estimate (see Kadler et al. 2003a) shows that the soft thermal X-ray spectrum associated with the radio jet of NGC 1052 can be explained in terms of the kinetic jet power being partially converted into X-ray emission originating in shocks driven into the ambient medium. (A more detailed model of the relation between jet-driven shock-activity and the spectral shape of the extended X-ray emission in NGC 1052 will be discussed in a forthcoming paper.) The comparison of the large-scale distribution of radio emission in NGC 1052 between two epochs separated by ~15 years indeed shows activity on kiloparsec-scales. This substantiates the idea that shocks in the interstellar medium form at the working surfaces of active regions (hotspots and knots). Moreover, recent numerical simulations (e.g., Zanni et al. 2003) show that jets in radio galaxies can inflate over-pressured cocoons that drive shocks into the ambient gas resulting in morphologies (in the case of weak shocks) very similar to what is observed in NGC 1052: a cavity of hot X-ray emitting gas in conjunction with a local deficit of X-ray emission around the hotspots. A deeper *CHANDRA* observation with an improved photon statistic compared to the observation discussed here would provide both a higher sensitivity to the weak diffuse emission and a higher resolution. Additionally,

the full resolution of *CHANDRA* of ~0.5 arcsec would allow one to study in more detail the connection between the knots in the diffuse X-ray emission and the optical emission knots.

References

Allen, M. G., Koratkar, A. P., & Dopita, M. A. 1999, BAAS, 31, 893

Dopita, M. A. 2002, Rev. Mex. Astron. Astrofis., 13, 177

Falcke, H., Wilson, A. S., & Simpson, C. 1998, ApJ, 502, 199

Forbes, D. A., Georgakakis, A. E., & Brodie, J. P. 2001, MNRAS, 325, 1431

Gabel, J. R., Bruhweiler, F. C., Crenshaw, D. M., Kraemer, S. B., & Miskey, C. L. 2000, ApJ, 532, 883

Guainazzi, M., & Antonelli, L. A. 1999, MNRAS, 304, L15

474   M. Kadler et al.: Jet emission in NGC 1052 at radio, optical, and X-ray frequencies

Guainazzi, M., Oosterbroek, T., Antonelli, L. A., & Matt, G. 2000, A&A, 364, L80

Hartmann, D., & Burton, W. B. 1997, An Atlas of galactic neutral hydrogen (Cambridge, New York: Cambridge University Press)

Heckman, T. M. 1980, A&A, 87, 152

Kadler, M., Ros, E., Kerp, J., et al. 2002, in Proc. of the 6th European VLBI Network Symp., ed. E. Ros, R. W. Porcas, A. P. Lobanov, & J. A. Zensus (Bonn, Germany: MPIfR), 167

Kadler, M., Ros, E., Kerp, J., et al. 2003a, New Astron. Rev., 47, 569

Kadler, M., Ros, E., Zensus, J. A., Lobanov, A. P., & Falcke, H. 2003b, SRT: the impact of large antennas on radio astronomy and space science, ed. N. D'Amico, F. Fusi Pecci, I. Porceddu, & G. Tofani (Bologna: Società Italiana di Fisica), 219

Kameno, S., Sawada-Satoh, S., Inoue, M., Shen, Z., & Wajima, K. 2001, PASJ, 53, 169

Kaastra, J. S. 1992, An X-ray Spectral Code for Optically Thin Plasmas (Internal SRON-Leiden Report, updated version 2.0)

Kellermann, K. I., Vermeulen, R. C., Cohen, M. H., & Zensus, J. A. 1999, BAAS, 31, 856

Knapp, G. R., Faber, S. M., & Gallagher, J. S. 1978, AJ, 83, 139

Krist, J., & Hook, R. 1999, The Tiny Tim User's Guide, Ver. 5.0 (Baltimore: STScI)

Malizia, A., Bassani, L., Stephen, J. B., Malaguti, G., & Palumbo, G. C. C. 1997, ApJS, 113, 311

Mc Dowell, J. C. 1994, in Einstein Obs. Unscreened IPC Data Archive

Pogge, R. W., Maoz, D., Ho, L. C., & Eracleous, M. 2000, AJ, 532, 323

Pogge, R. W., & Martini, P. 2002, ApJ, 569, 624

Raymond, J. C., & Smith, B. W. 1977, ApJS, 35, 419

Risaliti, G., Elvis, M., & Nicastro, F. 2002, ApJ, 571, 234

Sil'chenko, O. K. 1995, Astron. Lett., 21, 283

Sugai, H., & Malkan, M. A. 2000, ApJ, 529, 219

van Dokkum, P. G. 2001, PASP, 113, 1420

Vermeulen, R. C., Ros, E., Kellermann, K. I., et al. 2003, A&A, 401, 113

Weaver, K. A., Wilson, A. S., Henkel, C., & Braatz, J. A. 1999, ApJ, 520, 130

Wrobel, J. M. 1984, ApJ, 284, 531

Zanni, C., Bodo, G., Rossi, P., et al. 2003, A&A, 402, 949

6.3.3   The Relativistic Iron Line of NGC 1052

While broad iron lines from radio-quiet AGNs have been extensively studied over the last decade (Reynolds and Nowak 2003), no significantly broadened lines have been detected in the X-ray spectra of radio-loud AGNs (Sambruna et al. 1999a, Gambill et al. 2003). This has been explained either via the dominance of a beamed jet component, a very high ionization of the accretion disk matter, or the occurrence of optically thin, radiatively inefficient accretion flows. In agreement with this, no clear examples of relativistic broad iron line emission have been found in the study of the *2 cm-X-Sample* (compare Sect. 5.4), with the possible exception of III Zw2 (see also Salvi et al. 2002). Due to the complexity of its X-ray spectrum, the source NGC 1052 (0238−084) was not included in the systematical analysis of the sample whose results are presented in Chap. 4 and discussed in Chap. 5 of this thesis. This subsection is dedicated to a detailed study of the X-ray spectrum of NGC 1052, analyzing in detail the available archival *XMM-Newton* and *Beppo*Sax spectra of this object. Both data sets provide a substantially higher SNR than the *Chandra* spectrum of NGC 1052, discussed in Sect. 6.3.2 and the *ASCA* spectrum previously investigated by Weaver et al. (1999) and Guainazzi and Antonelli (1999).

***XMM-Newton* and *Beppo*Sax observations of NGC 1052:**   *XMM-Newton* observed the LINER galaxy NGC 1052 on September 28, 2001 with a total exposure time of 13 ksec (PI: K. A. Weaver). A standard data analysis with most conservative data flagging criteria has been performed following the procedures described in Sect. 3.4.4. For the spectral analysis we focused on the data from the *XMM-Newton* PN detector, which has a superior sensitivity and calibration compared to the two MOS detectors. The detailed comparison of the PN and MOS data, as well as the timing analysis and the results from the *XMM-Newton* RGS spectrometers are beyond the scope of this thesis and will be presented elsewhere.

A *Beppo*Sax observation of NGC 1052 was performed on 2000 January 11 (PI: M. Guainazzi). All three NFI instruments onboard *Beppo*Sax operated in standard modes. Full observational details are given by Guainazzi et al. (2000). The X-ray spectral data from the LECS, the MECS and the PDS detectors were obtained from the *Beppo*Sax data archive and handled as outlined in Sect. 3.4.2.

X-ray spectral analysis: The 0.2 keV to 10 keV *XMM-Newton* X-ray spectrum of NGC 1052 is by far too complex to be approximated with a simple spectral model consisting of three or less spectral components. Therefore, subsequently more complex spectral models are developed in the following paragraphs to account for the complexity of the spectrum and the additional constraint that the final spectral model for the September 2001 *XMM-Newton* spectrum of NGC 1052 needs to be capable of reproducing the different spectral shape exhibited during the January 2000 *Beppo*Sax observed epoch, as well. The subsequent spectral models considered are listed in Table 6.3 along with the "code" to represent those models within XSPEC.

Simple absorbed power-law models and simple hybrid models: MODEL I to MODEL III represent attempts to fit the *XMM-Newton* spectrum of NGC 1052 with a combination

158
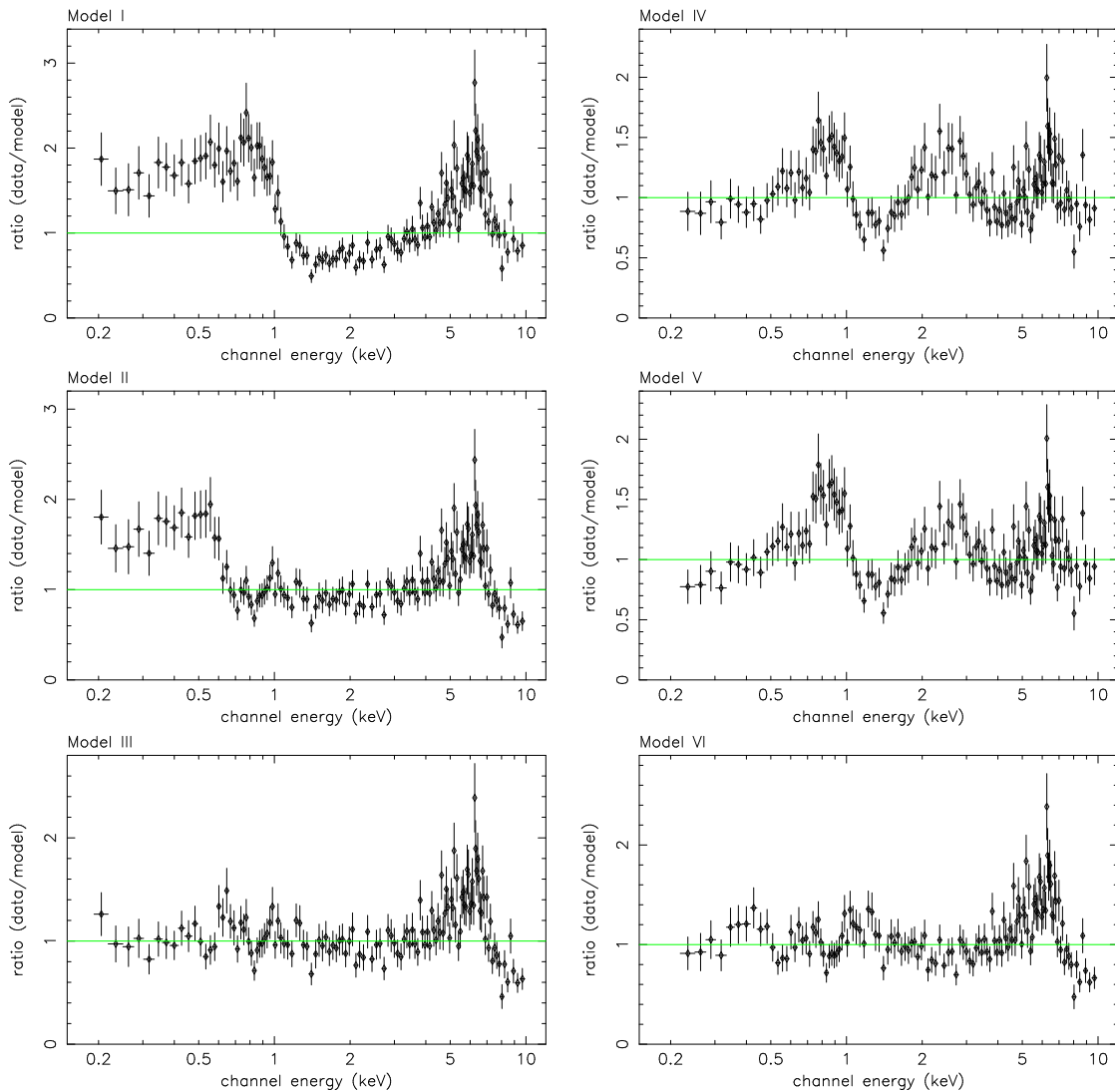
Figure 6.17: Data/model ratio for the class of simple absorbed power-law models and the three simple hybrid models for the *XMM-Newton* spectrum of NGC 1052 of September 2001 (compare Table 6.3 for model descriptions). Model parameters are given in Table 6.4.

of a simple absorbed power law and one or two thermal plasma (compare Table 6.3). Table 6.4 gives the formal best fitting values of the considered spectral components in these models. The corresponding residuals are shown in Fig. 6.17. It is obvious that the residuals are too large to derive meaningful errors. However, these simplistic models are shown and discussed here because they illustrate notably the peculiarities of NGC 1052's X-ray spectrum: the soft excess below 1 keV, which was first mentioned by Weaver et al. (1999) and later shown by Kadler et al. (2004a) (reprinted in Sect. 6.3.2) to be associated with an extended emission region, correlated in extent with the radio jet on arcsecond scales, has a much more complex spectral shape than apparent from previous *ASCA*, *Beppo*Sax, and *Chandra* observations (Weaver et al. 1999, Guainazzi and Antonelli 1999, Kadler et al. 2004a). Moreover, NGC 1052 exhibits a broad complex of emission between 4 keV and 8 keV, calling for a more sophisticated spectral model of the hard X-ray emission.

Table 6.3: Journal of models for the *XMM-Newton* X-ray spectrum of NGC 1052.

Model	XSPEC code		Description	
I	`zwabs*pow`	Globally absorbed	PL	
II	`zwabs*(mekal+pow)`	″	Plasma plus PL	
III	`zwabs*(mekal+mekal+pow)`	″	2-temp. plasma plus PL	
IV	`zwabs*(pow+zwabs`$_{torus}$`(pow))`	″	Partially absorbed PL	
V	`zwabs*(mekal+zwabs(pow))`	″	Plasma plus absorbed PL	
VI	`zwabs*(mekal+mekal+zwabs(pow))`	″	2-temp. plasma plus absorbed PL	
VII	`zwabs*(mekal+mekal+pexriv)`	″	2-temp. plasma plus reflection from ionized material	
VIII	`zwabs*(mekal+mekal+pexrav)`	″	2-temp. plasma plus reflection from neutral material	
IX	`zwabs*(mekal+mekal` `+zwabs*pow+zwabs*pow)`	″	2-temp. plasma plus PL covered by patchy absorber	
X	`zwabs*(mekal+mekal` `+zwabs*pow+zwabs*(pow+gauss))`	″	″	plus Gaussian
XI	`zwabs*(mekal+mekal` `+zwabs*pow+zwabs*(pow+diskline))`	″	″	plus rel. line in Schwarzschild metric
XII	`zwabs*(mekal+mekal` `+zwabs*pow+zwabs*(pow+laor))`	″	″	plus rel. line in Kerr metric
Xa	`zwabs*(mekal+mekal` `+zwabs*pow+zwabs*(pow+zwabs*(pow+gauss)))`	″	2-temp. plasma plus PL covered by patchy 2-component absorber	plus Gaussian
Xb	`zwabs*(mekal` `+zwabs*pow+zwabs*(pow+gauss))`	″	1-temp. low-metallicity plasma plus PL covered by patchy absorber	plus Gaussian

Table 6.4: Simple absorbed power-law models and simple hybrid models for the *XMM-Newton* spectrum of NGC 1052.

Model	Global Abs. $[10^{22}\mathrm{cm}^{-2}]$	Plasma Temp. I [keV]	Plasma Temp. II [keV]	Torus Abs. $[10^{22}\mathrm{cm}^{-2}]$	Powerlaw Γ	Flux $0.2\,\mathrm{keV}-2\,\mathrm{keV}$ $[\mathrm{erg\,s}^{-1}\mathrm{cm}^{-2}]$	Flux $2\,\mathrm{keV}-10\,\mathrm{keV}$ $[\mathrm{erg\,s}^{-1}\mathrm{cm}^{-2}]$	χ^2	d.o.f.	χ^2_{red}
I	0.02*	-	-	-	0.6**	3.2×10^{-13}	3.4×10^{-12}	864.3	130	6.65
II	0.02*		0.6**	-	0.2**	3.4×10^{-13}	3.8×10^{-12}	456.7	128	3.57
III	0.19**	0.08**	0.6**	-	0.2**	3.6×10^{-13}	3.9×10^{-12}	339.3	126	2.69
IV	0.07**	-	-	16.9	1.7**	3.5×10^{-13}	3.7×10^{-12}	297.9	127	2.35
V	0.02**	12.1**	-	19.2**	1.8**	3.6×10^{-13}	3.8×10^{-12}	311.1	126	2.47
VI	0.05**	0.15**	0.65**	0.46**	0.3**	3.5×10^{-13}	3.9×10^{-12}	326.2	124	2.63

* Parameter hit the lower boundary of $2 \times 10^{20}\,\mathrm{cm}^{-2}$; ** Unstable solution, no error determinable

MODEL IV and MODEL V correspond to the class of spectral models that were considered by Guainazzi et al. (2000) and Kadler et al. (2004a) (see Sect. 6.3.2) to model the *Beppo*Sax, and *Chandra* spectra of NGC 1052, both taken in 2000. They consist of a heavily absorbed power-law and a soft excess that is modeled via a thermal plasma (MODEL V) or via an unabsorbed fraction of the power-law emission (MODEL IV), the latter describing a partially covered or patchy absorber or torus. To account for the larger extend of the effective area into the soft regime (down to 0.2 keV) of *XMM-Newton*, an additional global absorber was added to both models. This global absorber accounts for local absorption within the Galaxy as well as for a possible absorption on larger scales within the NGC 1052 host galaxy (as the *Chandra* data suggests to be present). In MODEL VI, the soft residuals of the spectrum are modeled via a second thermal plasma component. A more complex spectral model is needed, particularly in the hard X-ray regime, as Figure 6.17 demonstrates.

Models invoking high-energy reflection: A special class of models that can be considered to be responsible for the peculiar X-ray spectral shape of NGC 1052 are models which invoke a Compton reflection of the nuclear continuum (compare Sect. 5.4). These high-energy reflection models imply that a medium, optically thick to the Compton effect, is illuminated from a primary source. Typically, this situation is thought to be representative of an X-ray radiating coronae that illuminates the accretion disk around the central black hole from above. Guainazzi et al. (2000) showed that these class of models fail to reproduce the hard X-ray spectrum of NGC 1052 as measured by the PDS detector onboard *Beppo*Sax. It was tested if this statement remains true if the additional soft-spectral information from the *XMM-Newton* observation is taken into account. A valid physical model must approximate both the high-quality data in the relatively soft bandpass of *XMM-Newton* and the medium and high-energy data taken by *Beppo*Sax about one year earlier. Due to changes in the critical physical quantities in the source, the spectral model parameters might have changed, however. In particular, MODEL VII considers a physical scenario in which a two-temperature thermal plasma dominates the soft part of the spectrum while a variable high-energy reflection component (`pexriv` in XSPEC; Magdziarz and Zdziarski 1995) contributes the bulk emission to the hard part of the spectrum. The
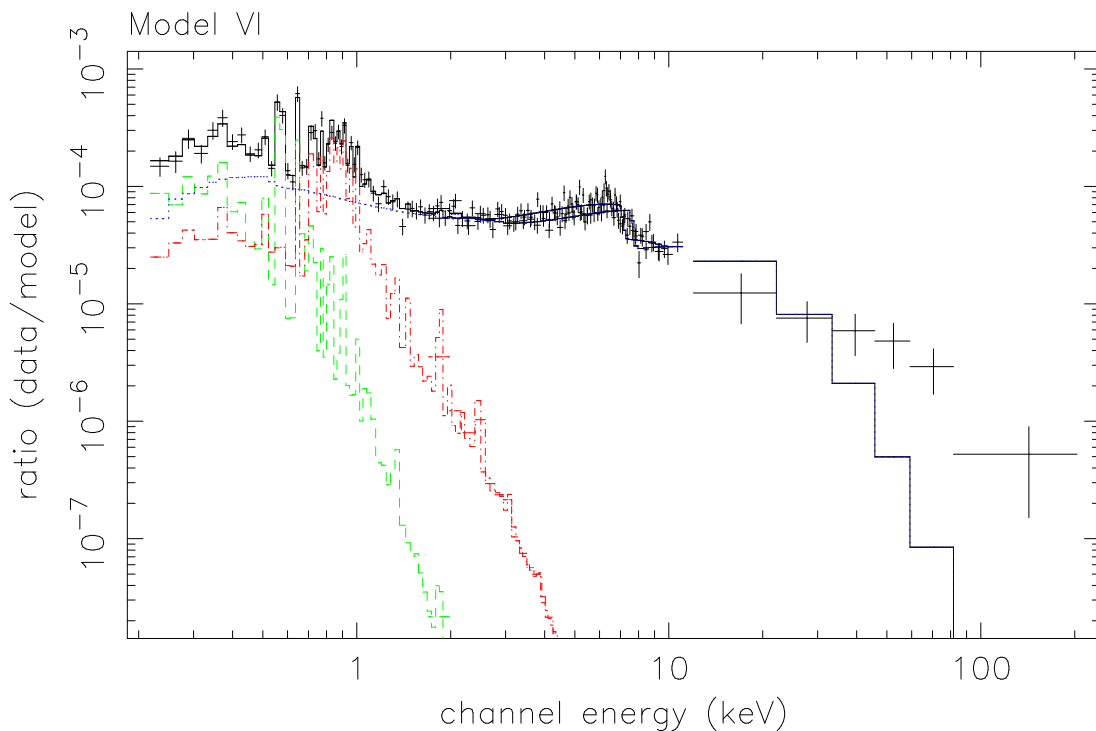
Figure 6.18: Unfolded spectral MODEL VII. While the variable model approximates correctly the broad emission complex between 4 keV and 8 keV at both epochs, the model fails to represent the spectral slope above 10 keV during the *Beppo*Sax epoch.

global absorption and the (extended) thermal plasma components are assumed to be stable in time, i.e., the corresponding model parameters of the 2001 *XMM-Newton* data and the 2000 *Beppo*Sax data have been tied to each other. Fig. 6.18 shows that this attempt fails because the model cannot at the same time approximate the 2 keV to 10 keV *Beppo*Sax MECS data and the PDS data above 10 keV for the January 2000 epoch. Table 6.5 gives the best fitting model parameters. The result of Guainazzi et al. (2000) is thus confirmed: simple high-energy reflection is unlikely to shape the X-ray spectrum of NGC 1052.

Complex-absorber models: Accepting that the X-ray spectrum of NGC 1052 cannot be described by simple models which invoke only a small number of free parameters, the task is to find a realistic physical model which explains, first, the peculiarly flat X-ray spectrum of NGC 1052, second, the soft excess below 1 keV, and third, the broad spectral bump between 4 keV and 8 keV. Moreover, this physical model should be capable of explaining both, the January 2000 *Beppo*Sax and the September 2001 *XMM-Newton* spectrum. As before, the parameters of the soft excess are modeled via a combination of thermal plasma emission regions whose parameters are held stable in time because of the large extend of this emission region. The main problem then is to describe the broad spectral bump between 4 keV and 8 keV. Having already ruled out the reflection scenario, the most likely origin of the bump is a combination of a heavily absorbed fraction of the primary power-law and an iron line. This class of spectral models assumes implicitly a patchy absorber scenario, in which the nuclear power-law source is partially covered by different absorbing column density regions. This might reflect an organization of the

Table 6.5: Models invoking high-energy reflection for the *XMM-Newton* spectrum of NGC 1052.

Model	Telescope	Global Abs. [10^{22}cm^{-2}]	Plasma Temp. I [keV]	Temp. II [keV]	Rel. Strength of Reflection	Powerlaw Γ	Cutoff Energy [keV]	Flux 0.2 keV – 2 keV [erg s^{-1} cm^{-2}]	2 keV – 10 keV [erg s^{-1} cm^{-2}]	Statistics χ^2	d.o.f.	χ^2_{red}
VII	*XMM-Newton*	$0.030^{+0.007}_{-0.006}$	$0.18^{+0.02}_{-0.02}$	$0.67^{+0.03}_{-0.04}$	150^{+5}_{-5}	$0.83^{+0.02}_{-0.02}$	$4.6^{+0.1}_{-0.1}$	3.5×10^{-13}	3.8×10^{-12}	196.0	165	1.19
	*Beppo*Sax*	″	″	″	80^{+4}_{-4}	$1.34^{+0.02}_{-0.03}$	$16.3^{+2.0}_{-1.7}$	4.8×10^{-13}	3.8×10^{-12}	″	″	″
VIII	*XMM-Newton*	$0.043^{+0.007}_{-0.006}$	$0.18^{+0.02}_{-0.02}$	$0.67^{+0.03}_{-0.04}$	250^{+9}_{-6}	$1.24^{+0.01}_{-0.02}$	$6.6^{+0.3}_{-0.2}$	3.5×10^{-13}	3.8×10^{-12}	198.3	167	1.19
	*Beppo*Sax*	″	″	″	133^{+6}_{-6}	$1.43^{+0.02}_{-0.02}$	$14.6^{+1.5}_{-1.4}$	4.8×10^{-13}	3.6×10^{-12}	″	″	″

* The parameters of the global absorption and the thermal plasma were tied between the *XMM-Newton* and the *Beppo*Sax spectral fits, the statistical quality values correspond to the simultaneous fit result.

circumnuclear matter in clouds which are small compared to the size of the source.

In MODEL IX (Table 6.6), the September 2001 *XMM-Newton* spectrum between 0.2 keV and 10 keV and the January 2000 *Beppo*Sax spectrum between 2 keV (MECS detectors) and 200 keV (PDS detector) are represented by such a patchy absorber model. The bump between 4 keV and 8 keV is shaped by a heavily absorbed component of the primary power law, which is seen through an absorbing column of $\sim 2.5 \times 10^{23}\,\mathrm{cm}^{-2}$. The photon indices for both spectra are in a range typical for Seyfert 1 galaxies (1.5 and 1.7, respectively). However, the model is statistically unacceptable, mainly because of strong residuals between 5 keV and 7 keV. The high-energy data below 100 keV is also not fitted satisfactorily. MODEL X, MODEL XI, and MODEL XII (Table 6.6) account for this by adding an iron line component to the model: a Gaussian in MODEL X and a relativistic iron line model for a Schwarzschild metric and for a Kerr metric in MODEL XI and MODEL XII, respectively. In particular, the latter yielded an excellent fit to the data and implied an iron fluorescent line emitted from an accretion disk around a rotating black hole, seen at an inclination angle of $\sim 83°$. For the September 2001 *XMM-Newton* spectrum the inner and outer radius of the disk (R_{in} and R_{out}) are derived as 4 and 57 Schwarzschild radii, while the disk seems to extend from less than 2 to 90 Schwarzschild radii in the case of the January 2000 *Beppo*Sax spectrum. The photon indices in all three cases are unusually flat with values around 1 but in all cases stable between the two epochs. These models even allow all continuum model parameters to be held stable between the two epochs without a significant degradation of the simultaneous fit statistics (the reduced χ^2 increases only slightly from 0.97 to 0.99 in the case of MODEL XII if the full discrepancy between both data sets is attributed to a change of the relativistic iron line).

It shall be noted here that, statistically, two modifications of this latter class of spectral models can adequately represent the spectral data for both X-ray epochs: MODEL Xa assumes a third component of the obscuring medium and MODEL Xb invokes only one thermal plasma component instead of two but with extremely underabundant metals (Table 6.7). In both cases, however, the equivalent width of the considered Gaussian is still very high so that the detection of a relativistic iron line in NGC 1052 is not called into question. We do not try to refine these models by invoking relativistic line models since in both cases the data quality does not allow to test more complex models. Future, high signal-to-noise spectra obtained with *XMM-Newton* (see Sect. 6.3.4) will judge, ultimately, which of these spectral models most likely represents the physical situation at the center of NGC 1052 correctly.

Notes on the radio-loudness and the LLAGN character of NGC 1052:   The detection of a relativistically broadened iron X-ray emission line in NGC 1052, demonstrated in the previous section, makes this source a unique example of a radio-loud AGN with a bright, compact radio core whose accretion flow can be probed by X-ray spectroscopy of the iron-line profile. Low-luminosity AGN (LLAGN) are generally expected to accrete on a sub-Eddington level and to have radiatively inefficient accretion flows (e.g., Falcke 2001). As such, they are not expected *a-priori* to exhibit relativistic iron line emission that is believed to originate from the inner part of geometrically thin, optically thick accretion disks. Moreover, the discrepancy between the X-ray photon indices of radio-quiet and radio-loud AGN is often being considered to be evidence for a substantially different structure of the accretion flow in both classes of objects (e.g., Reynolds and Nowak 2003).
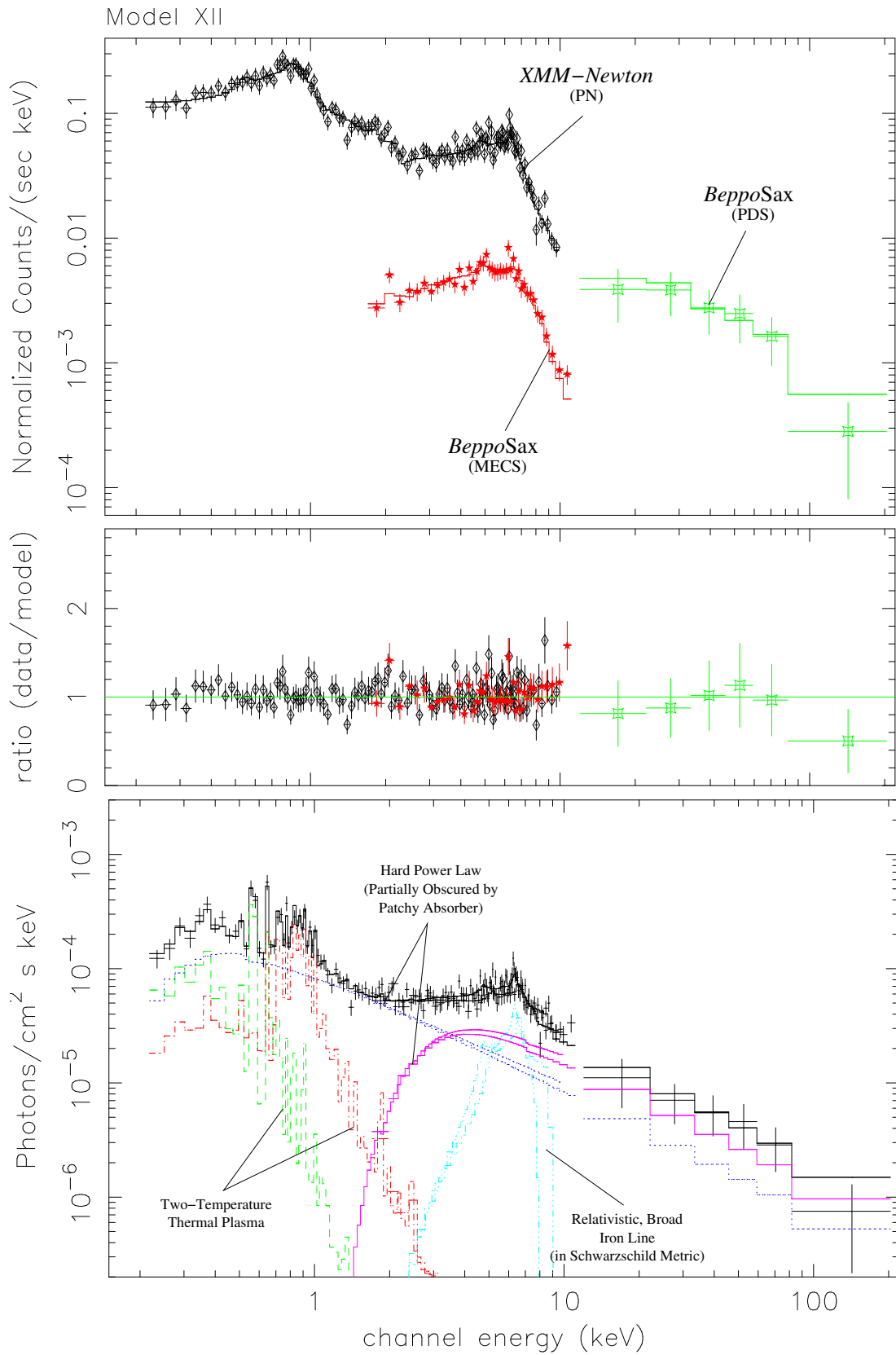
Figure 6.19: Top: *XMM-Newton* and *Beppo*Sax spectra of NGC 1052 and best fitting MODEL XII; Middle: Residuals if MODEL XII is applied to the data; Bottom: Unfolded spectral MODEL XII.

Table 6.6: Complex-absorber models for the *XMM-Newton* spectrum of NGC 1052.

Model	Telescope	Global Abs.	Plasma Temp. I	Temp. II	Torus Comp. 1	Torus Comp. 2	Powerlaw Γ	E	σ	ϵ	Iron Line R_{in}	R_{out}	θ	EW	χ^2	d.o.f.	χ^2_{red}
		$[10^{22}\mathrm{cm}^{-2}]$	[keV]	[keV]	$[10^{22}\mathrm{cm}^{-2}]$	$[10^{22}\mathrm{cm}^{-2}]$		[keV]			$[\mathrm{GM/c^2}]$	$[\mathrm{GM/c^2}]$	[°]	[keV]			
IX	*XMM-Newton*	$0.043^{+0.005}_{-0.007}$	$0.15^{+0.01}_{-0.01}$	$0.65^{+0.02}_{-0.03}$	$1.08^{+0.07}_{-0.08}$	$24.7^{+1.2}_{-1.0}$	$1.73^{+0.02}_{-0.01}$	-	-	-	-	-	-	-	247.6	170	1.46
	*Beppo*Sax*	//	//	//	//	//	$1.46^{+0.02}_{-0.02}$	-	-	-	-	-	-	-	-	//	//	//
X	*XMM-Newton*	$0.037^{+0.006}_{-0.007}$	$0.18^{+0.02}_{-0.03}$	$0.66^{+0.04}_{-0.04}$	$< 0.014^{**}$	$6.1^{+0.6}_{-0.6}$	$1.02^{+0.02}_{-0.02}$	$6.1^{+0.1}_{-0.1}$	$0.8^{+0.2}_{-0.1}$	-	-	-	-	2.35	166.0	161	1.03
	*Beppo*Sax*	//	//	//	//	//	$1.06^{+0.03}_{-0.03}$	$6.6^{+0.2}_{-0.3}$	$1.6^{+0.3}_{-0.2}$	-	-	-	-	6.52	//	//	//
XI	*XMM-Newton*	$0.035^{+0.007}_{-0.006}$	$0.18^{+0.02}_{-0.02}$	$0.66^{+0.04}_{-0.04}$	$< 0.014^{**}$	$6.5^{+0.6}_{-0.6}$	$0.96^{+0.02}_{-0.02}$	$5.7^{+0.1}_{-0.1}$	-	$-2.6^{+0.1}_{-0.2}$	$8.9^{+2.7}_{-2.5}$	114^{+71}_{-37}	$> 75^{**}$	2.76	162.0	157	1.03
	*Beppo*Sax*	//	//	//	//	//	$1.09^{+0.03}_{-0.03}$	$6.4^{+0.2}_{-0.2}$	-	//	$< 7.4^{**}$	$> 100^{***}$	//	2.76	//	//	//
XII	*XMM-Newton*	$0.035^{+0.007}_{-0.006}$	$0.18^{+0.02}_{-0.02}$	$0.66^{+0.04}_{-0.04}$	$< 0.014^{**}$	$6.3^{+0.6}_{-0.7}$	$0.96^{+0.02}_{-0.02}$	$5.6^{+0.1}_{-0.1}$	-	$-1.6^{+0.1}_{-0.2}$	$4.0^{+1.5}_{-0.8}$	57^{+7}_{-10}	83^{+2}_{-2}	3.49	152.7	157	0.97
	*Beppo*Sax*	//	//	//	//	//	$1.07^{+0.02}_{-0.03}$	$5.9^{+0.2}_{-0.2}$	-	//	$< 2.1^{**}$	80^{+30}_{-24}	//	4.35	//	//	//

* The parameters of the global absorption and the thermal plasma were tied between the *XMM-Newton* and the *Beppo*Sax spectral fits, the statistical quality values correspond to the simultaneous fit result; ** The parameter pegged against a hard limit; *** Parameter only weakly constrained

Table 6.7: Variations of model X for the *XMM-Newton* spectrum of NGC 1052.

Model	Telescope	Global Abs. [10^{22}cm^{-2}]	Plasma Temp. I [keV]	Temp. II [keV]	Metal Abundance [%]	Torus Comp. 1 [10^{22}cm^{-2}]	Torus Comp. 2 [10^{22}cm^{-2}]	Torus Comp. 3 [10^{22}cm^{-2}]	Powerlaw Γ	Iron Line E [keV]	σ [keV]	EW [keV]	Statistics χ^2	d.o.f.	χ^2_{red}
Xa	*XMM-Newton*	$0.046^{+0.007}_{-0.006}$	$0.16^{+0.03}_{-0.03}$	$0.68^{+0.06}_{-0.05}$	100[a]	$0.081^{+0.012}_{-0.011}$	$3.9^{+0.2}_{-0.3}$	$32.2^{+1.4}_{-1.3}$	$2.21^{+0.02}_{-0.02}$	$6.32^{+0.13}_{-0.13}$	$0.35^{+0.19}_{-0.11}$	0.44	154.2	158	0.98
	*Beppo*Sax[*]	//	//	//	//	//	//	//	$1.56^{+0.02}_{-0.03}$	$6.44^{+0.27}_{-0.22}$	$0.18^{+1.37}_{-0.18}$	0.30	//	//	//
Xb	*XMM-Newton*	$0.103^{+0.007}_{-0.004}$	$0.68^{+0.03}_{-0.02}$	-	$3.6^{+0.4}_{-0.5}$	-	$2.80^{+0.13}_{-0.17}$	$27.6^{+1.2}_{-1.4}$	$2.03^{+0.02}_{-0.02}$	$6.32^{+0.13}_{-0.14}$	$0.41^{+0.18}_{-0.11}$	0.57	151.0	162	0.93
	*Beppo*Sax[*]	//	//	-	//	-	//	//	$1.35^{+0.03}_{-0.02}$	$6.47^{+0.41}_{-0.44}$	$1.36^{+0.38}_{-0.27}$	3.8	//	//	//

[a] Metal abundances w.r.t. solar values; [*] The parameters of the global absorption and the thermal plasma were tied between the *XMM-Newton* and the *Beppo*Sax spectral fits, the statistical quality values correspond to the simultaneous fit result

For these two reasons it is important to consolidate the properties of NGC 1052 in terms of radio loudness and its LLAGN character.

It is not straightforward to determine the radio-loudness parameter of NGC 1052. While the prominence of the compact nuclear radio jet clearly points to a radio-loud object, the dominance of optical starlight compared to the low luminosity of the AGN in the radio and optical band makes NGC 1052 a borderline object. This, however, is a natural consequence of the proximity of the source and its low nuclear luminosity. To compare NGC 1052's radio loudness to luminous quasars it is important to avoid the contribution of the optical galaxy which is naturally negligible in distant quasars. Specifically, the integrated flux density at 4400 Angstrom is ~ 115 mJy while only ~ 1 mJy of this flux can be attributed to the central ionizing source (Gabel et al. 1999). Rejecting the star-light contribution thus alters the radio-loudness parameter (the ratio between the flux at 4400 Angstrom and the flux at 5 GHz) from ~ 20 for a maximal 5 GHz flux of 2.5 Jy during the last few years to a value larger than 2000. Alternatively, radio loudness has been classified based on the ratio of radio and X-ray brightness (Terashima and Wilson 2003). Figure F.3 (see Appendix F) displays the radio and X-ray fluxes of a sample of confirmed and candidate broad-iron-line AGN (both radio-quiet and radio-loud systems). The location of NGC 1052 in this diagram is by far above the radio-loud/quiet dividing line (applying the radio-loudness criterion of Terashima and Wilson 2003).

The bolometric luminosity of NGC 1052 of $L_{\mathrm{Bol}} = 7 \times 10^{43}$ erg s^{-1} (Woo and Urry 2002) makes up only 0.35% of the Eddington luminosity of $L_{\mathrm{Edd}} = 2 \times 10^{46}$ erg s^{-1} calculated from a black-hole mass of $10^{8.19}$ solar masses. Comparative fractions of the Eddington luminosity of $\sim 10^{-5} \times L_{\mathrm{Edd}}$ are emitted in the radio (1 GHz to 100 GHz; Wrobel 1984) and the X-ray band (2 keV to 10 keV), making NGC 1052 a low-luminosity source in both wavebands. A comparatively large amount of the power available from accretion in this system is channeled into the jet, which carries about 1% of the Eddington power or 2.7 times the bolometric luminosity as calculated from the formula for the jet jet power given by Falcke and Biermann (1995). It should be noted that for under-luminous systems like NGC 1052 flat photon indices are observed. Wang et al. (2004) give an empirical formula $\Gamma = 2.05 + 0.26 \log \epsilon$, where ϵ is the ratio between observed bolometric luminosity and Eddington luminosity. For NGC 1052, $\epsilon = 0.0035$ gives an expected photon index of 1.4.

Finally, it shall be noted that not all LLAGN accretion models predict optically thin accretion flows. Merloni and Fabian (2002) have developed a model involving strong, unbound, magnetic coronae generated by geometrically thin, optically thick accretion disks at low accretion rates. In particular, this model predicts strong thermally driven jets/outflows and hard X-ray spectra. The authors conclude that "if the jet, as is likely, radiatively inefficient, then so is the source overall, even without advection of energy into the black hole being relevant for the dynamics of the accretion flow." The observational findings on the X-ray spectrum of NGC 1052 together with its prominent jet system and its LLAGN character, make NGC 1052 a highly interesting object to test the predictions of the model of Merloni and Fabian (2002).

List of collaborators: J. Kerp, E. Ros, K. A. Weaver, & J. A. Zensus

6.3.4   Jet-Disk Coupling in NGC 1052

The formation of powerful relativistic jets, emerging from the immediate vicinity of super-massive black holes, takes place only within the radio-loud population of active galactic nuclei (AGN). The formation of these extragalactic jets is not well understood at present as well as the key question: "What makes an AGN radio loud?". Radio-loud AGNs offer the unique possibility to image the small-scale structure of extragalactic radio jets via Very Long Baseline Interferometry (VLBI) (Zensus 1997). The study of relativistically broadened iron lines in the X-ray regime (Reynolds and Nowak 2003) allows the very closest neighborhood of the black hole to be explored: its accretion disk, the resource which is thought to provide the "fuel" for the jet ejection (Meier et al. 2001).

The 2000 advent of a new jet feature in the jet of NGC 1052:   From the long-term VLBI monitoring program of NGC 1052, performed within the scope of the VLBA 2 cm Survey, it is found that a new, strong and compact radio component was ejected into the eastern (approaching) jet of the nuclear twin-jet system in 2000 (see Fig. 6.20). This new component represents one of the most violent ejections observed in NGC 1052 since the VLBI monitoring program began in 1995. A detailed analysis of the kinematical evolution of the sub-parsec-scale VLBI structure of NGC 1052 between 1999 and 2003 will be presented by Ros et al. (in prep.). There, the possible ejection of a corresponding and synchronous ejection event into the (western) counterjet of NGC 1052, which is less pronounced than the event in the eastern jet, will be discussed, as well. In Fig. 6.20, the images of the variable source structure at the last observing epoch before the ejection (1999.85) and three following epochs (2001.21, 2001.84, 2002.38) are shown. The most likely range of orientations of the jet-system derived from VLBI (Kadler et al. 2004c; reprinted in Sect. 6.3.1) is 57° to 83°, which is in remarkable agreement with the inclination of the accretion disk determined above from the X-ray spectrum (Sect. 6.3.3). The large inclination angle is further supported by the detection of strong free-free absorption at the base of the western (receding) jet occurring in an obscuring circumnuclear torus (see Sect. 6.3.1 and compare Kellermann et al. 1999a & Kameno et al. 2001). The analysis of the kinematics of the newly emerged component shows that the ejection epoch is ~ 2000.5 with an uncertainty of several months.

Before the advent of the new component in the jet of NGC 1052 in 2000.5 *Beppo*Sax observed the source at epoch 2000.03 and a rather small iron line equivalent width of only 200 eV to 300 eV was reported (Guainazzi et al. 2000). The *Beppo*Sax spectrum taken in 2000.03 shows a clear count rate deficit between 5 keV and 6.5 keV, the regime dominated by the "red wing" of the relativistic iron line, compared to the *XMM-Newton* 2001.62 spectrum. In Sect, 6.3.3, this spectral difference is shown to be due to a change of the broad-iron line profile, while the continuum remained more or less stable between the two observations. To substantiate this finding, it was tried to adjust the parameters of the continuum and the line component of the spectral model separately. Since the *Beppo*Sax data quality is insufficient to fully constrain the different parameters of the line and the continuum, the statistical improvement of the fit that can be achieved from fitting the power-law index and flux with the improvement from fitting the line energy and flux was compared. In both cases, the number of degrees of freedom changes by two, so that both fits can be compared directly with the F-test. Adjusting the continuum can only
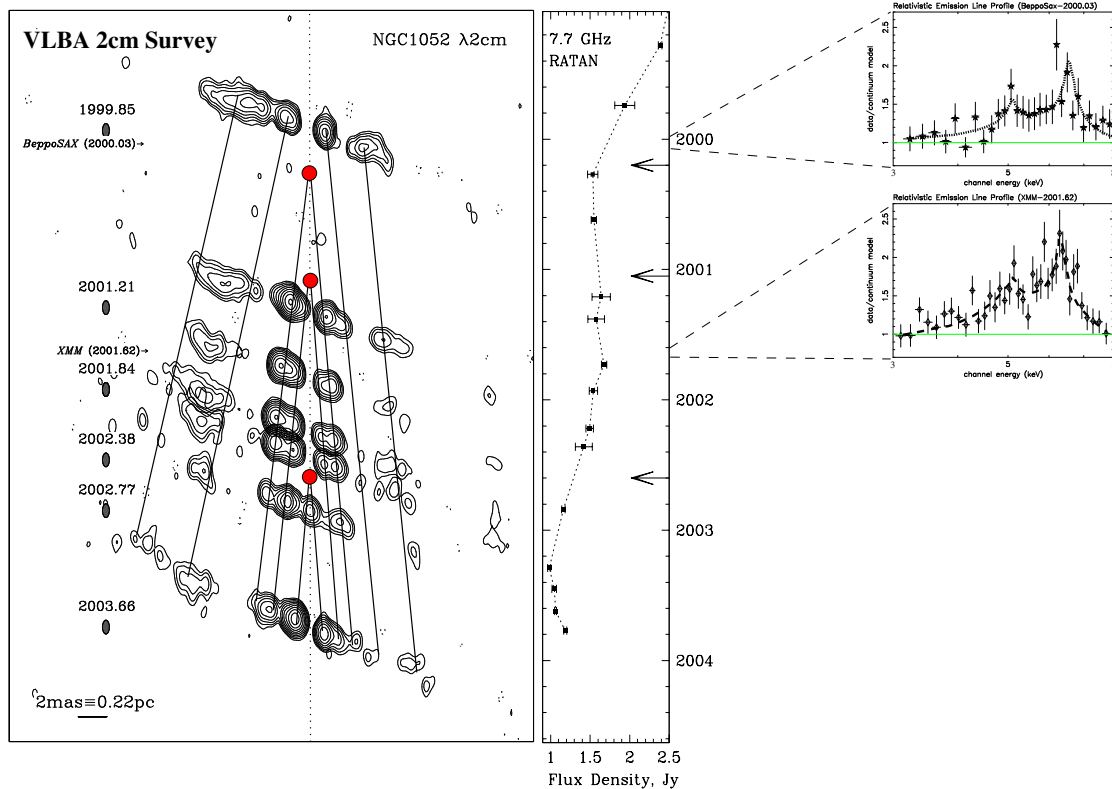
Figure 6.20: The variable relativistic X-ray iron line profile of NGC 1052 in relation to the radio jet dynamics on sub-parsec scales. Left: The varying radio jet structure on parsec scales of NGC 1052 between 1999.85 and 2002.38 observed at a wavelength of 2 cm with the VLBA. Components in jet (left) and counter-jet (right) move outwards with apparent speeds of $\sim 0.25c$ (yellow lines). The new, central jet component, first visible in the 2001.21 image, was ejected in ~ 2000.5 and moves along the eastern (approaching) jet. Top right: Relativistic, broad iron line profile of NGC 1052 in January 2000 extracted from the *Beppo*Sax data. Bottom right: Relativistic, broad iron line profile of NGC 1052 in September 2001 from the *XMM-Newton* observation. The line profiles are represented by the ratio of the measured *XMM-Newton* spectrum of the September 2001 epoch between 3 keV and 8 keV and the spectral model I of the underlying continuum. The "red wing" of the line varied substantially between both epochs, indicative of strong structural changes in the inner accretion disk.

improve the fit by $\Delta\chi^2 = 8$, while optimizing the line parameters yields a significantly larger improvement of $\Delta\chi^2 = 17$ for the spectral model XI. In the latter case, the line energy is shifted from 5.6 keV to 5.8 keV, indicative of a weaker contribution of the inner disk compared to the 2001 *XMM-Newton* epoch, and the equivalent width decreased from ~ 2 keV to ~ 1.5 keV. The presence of line-variability is also obvious from an inspection of the two panels in Fig. 6.21.

While the continuum was stable or varied only marginally between the *Beppo*Sax and the *XMM-Newton* observation, significant variability of the relativistic iron line occurred. This line variability can only be explained within the standard model of relativistic iron lines in AGNs if characteristic physical parameters of the accretion flow, e.g., the inner radius of the disk, have changed considerably between the two observations. Such a dramatic event within the accretion flow is expected to be followed by the ejection of a new jet component on parsec-scales if a coupling between jet-formation and black hole accretion exists, as is suggested by most theoretical models (Meier et al. 2001) but has not been observed prior to this work[7].

It should be stressed that it is not possible from the available data to constrain the exact epoch at which the structural change in the accretion disk took place. The time scale on which the broad iron line profile changed might be much shorter than the time period covered by our observations. Thus, the *Beppo*Sax spectrum most likely does not represent the iron line profile during or immediately after the structural change in the accretion disk happened. It is thus difficult to develop a detailed physical model, that relates the processes within the accretion disk to the jet component emergence. However, it can be concluded from our observational data that the relativistic iron line profile changed on a time scale smaller than ~ 1.5 years, most likely due to a significant event within the accretion disk, and that within the same time range a bright new jet component ejection on sub-parsec scales took place.

What happened in NGC 1052 in 2000/2001? A toy model: The data presented here imply the following scenario for the physical processes at the center of NGC 1052 between January 2000 and September 2001 (compare Fig. 6.22). Before 1999 a more or less steady, optically thick, and disk-like accretion flow feeds the central black hole and a broad iron line is emitted in the energy range between ~ 3 keV and 8 keV. Part of the accreting matter maintains a twin-jet, which transports synchrotron emitting plasma away from the central engine. In late 1999 or early 2000 a dramatic event within the accretion flow occurs, during which the inner radius of the accretion disk pulls back from the black hole. This results in a depression of the relativistic "red wing" of the iron line and a decrease of the fluorescenting disk area as observed with *Beppo*Sax. A substantial amount of the inner disk material is accreted onto the black hole, while a fraction of the same material is ejected into the jet. The ejection causes a shock within the existing jet flow, which emits self-absorbed synchrotron radio emission. While traveling along the jet with approximately 20% of the speed of light, adiabatic expansion causes the new radio-jet component to become optically thin at the highest frequencies. A wavelength-dependent radio outburst propagates through the spectrum, as the synchrotron self-absorbed peak

---

[7]The results of Marscher et al. (2002) of X-ray flux dips preceding VLBI component ejections in 3C 120 may be closely related to the results presented here for NGC 1052. However, a varying profile of a relativistic iron line is theoretically much better understood than the occurrence of X-ray dips.

171
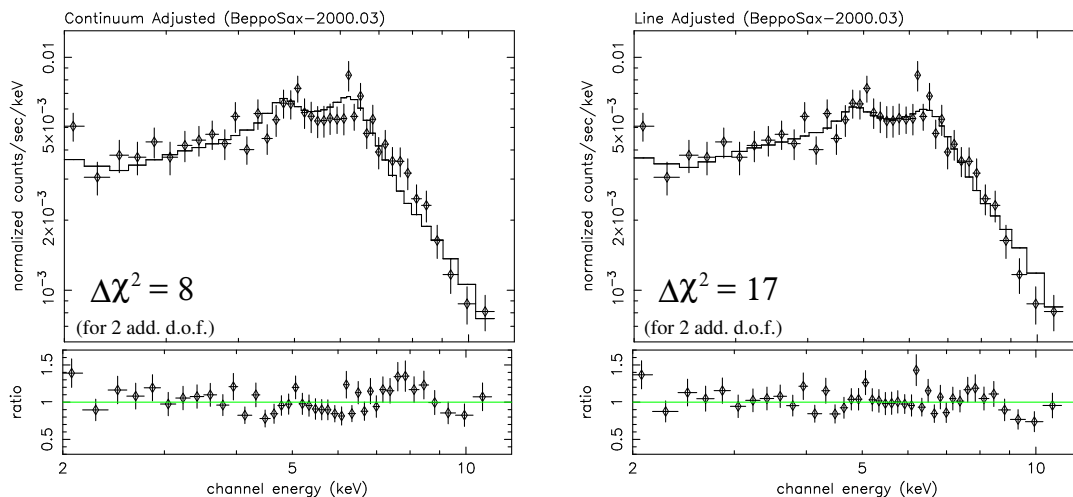
Figure 6.21: Iron line variability vs. continuum variability in NGC 1052. The 2 keV to 12 keV X-ray spectrum of NGC 1052 extracted from the *Beppo*Sax observation in January 2000. Only the data from the *Beppo*Sax MECS detectors are shown. In the left panel, the solid line represents the best model which can be achieved by adjusting the continuum parameters (corresponding to continuum variability between the two observations). The right panel shows the best model which results from adjusting the line energy and flux instead. Statistically, the line-variability model provides a much better approximation to the data with an improvement of 17 for χ^2 compared to an improvement of 8 in the continuum-variability model.

shifts to lower frequencies (Kovalev priv. comm.). In early 2001 the emission of the new jet component becomes optically thin at 15 GHz and is first visible in the VLBI image at epoch 2001.21. After the accretion-ejection event the inner disk slowly replenishes so that the broad, relativistic line profile is visible during the September 2001 *XMM-Newton* observation with a stronger "red wing" compared to the January 2000 *Beppo*Sax observation.

List of collaborators: J. Kerp, E. Ros, K. A. Weaver, & J. A. Zensus

Organization of a Multi-Mission Radio/X-ray Observing Campaign of NGC 1052:
The only observational link between accretion disks and jet activity in AGNs established so far is the occurrence of dips in the X-ray light curve of the radio galaxy 3C 120 correlated with ejections of superluminal knots in the radio jet (Marscher et al. 2002). Relativistic, broad iron lines, however, are much better understood than those dips in X-ray light curves and provide the closest probe of black hole accretion that can be accessed observationally. The observed line variability in correlation with jet-production activity provide the first direct view of an accretion-ejection event in an active galaxy. Future combined VLBI and X-ray observations of radio-loud AGNs may reveal the details of the inter-play between accretion disk dynamics, the primary X-ray continuum, high energy reflection processes, and jet formation. A major task for future AGN research will be to consolidate a corporate knowledge of accretion-ejection phenomena observed by VLBI and X-ray astronomy. Such joint efforts have been neglected prior to the detection of the first broad iron line in a radio-loud AGN, reported in this work. Ultimately, this
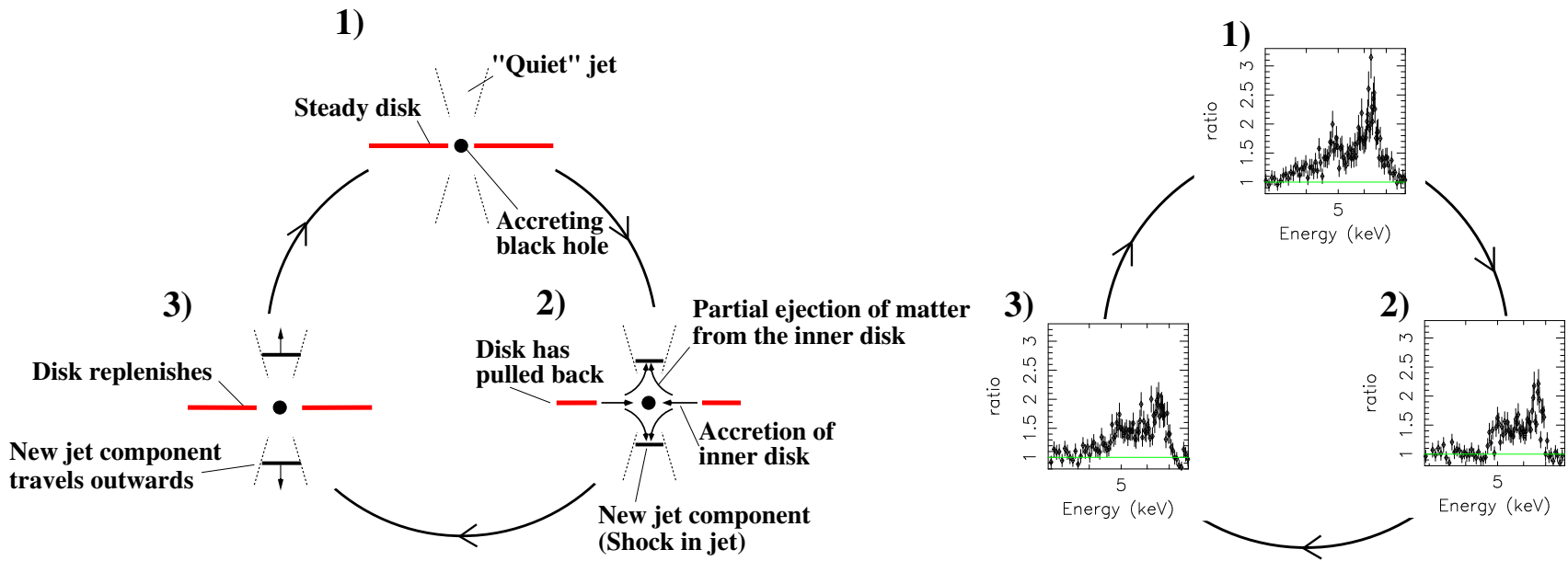
Figure 6.22: Sketch of the accretion-ejection event and the variable iron line profile of NGC 1052. Left: Sketch of the physical processes during the reported accretion-ejection event. 1) Initial system with a steady accretion disk and a "quiet" jet; 2) The inner edge of the disk pulls back from the black hole. Enhanced accretion takes place and a fraction of the inner disk material is ejected into the jet. A new jet component is formed; 3) The disk slowly replenishes while the new jet component travels outwards. Right: Simulated 30ksec XMM-Newton spectra for the three stages from the left panel. 1) Inner accretion disk extends to 6 gravitational radii; 2) Inner edge at 20 gravitational radii, line flux reduces, line energy shifts bluewards; 3) Inner edge at 12 gravitational radii, line flux and energy replenish.

new observational approach of combined VLBI- and X-ray spectroscopic observations of NGC 1052, has the power to reveal the fundamental difference between radio-loud and radio-quiet AGNs, from dedicated monitoring campaigns and the comparison to timing analysis studies of broad iron lines in radio-quiet AGNs.

To address these important questions, a large multi-mission observing campaign of NGC 1052 has been set up for the time period spring 2005 to spring 2006. The goal of this campaign is to explore the triggering processes leading to the formation of relativistic jets in radio-loud AGNs. The project includes: I: 54 hours of VLBA observations of NGC1052, with dynamically scheduled observations at $\lambda 1.3$ cm and $\lambda 0.7$ cm every six weeks (PI: E. Ros), II: 15 ToO epochs of *Rossi X-ray Timing Explorer* (*RXTE*) observations for X-ray light curve monitoring every three weeks, III: Radio-spectral monitoring observations with the Effelsberg 100-m telescope, covering the full cm- to mm-wavelength regime, quasi-simultaneous to the *RXTE* pointings (PI: M. Kadler), IV: two deep Chandra/XMM-Newton pointings separated from each other by five months to derive high-spectral-resolution profiles of the broad iron line at two different epochs (PIs: J. A. Irwin & M. Kadler), V: long-term radio monitoring with the RATAN-600 telescope and the 26 m telescope of the University of Michigan (PIs: H. D. & M. F. Aller).

We expect to find dips in the X-ray light curve in the *RXTE* monitoring program that precede imminent plasma ejections into the VLBI jet, the "classical" behavior displayed by 3C 120 (Marscher et al. 2002). Our program will allow us to determine accurately the ejection epochs of the expected new jet components and any possible change in the broadband radio to X-ray light curve correlation due, e.g., to the onset of enhanced SSC emission from the flaring compact base of the jet.

> List of collaborators: H. D. Aller, M. F. Aller, J. A. Irwin, J. Kerp, Y. Y. Kovalev, A. Kraus, A. P. Marscher, E. Ros, K. A. Weaver, & J. A. Zensus

6.3.5   Summary

In this section, the LINER galaxy NGC 1052 has been studied from sub-parsec to kilo-parsec scales, combining various observational techniques and observing frequencies and invoking data from an assortment of modern astronomical observational facilities. The main results from this study are summarized below.

- A VLBI scrutiny the parsec-scale "twin-jet" of NGC 1052 and the nucleus-obscuring torus of this system has been conducted. Confirming and quantifying the results of Kellermann et al. (1999a) and Kameno et al. (2001), the high-density circumnuclear environment of the NGC 1052 nucleus revealed free-free absorption along with steep pressure gradients increasing the synchrotron opacity. Applying the methods developed in appendix C, the brightness temperature gradients along the jets are studied. A sharp cut-off along the eastern (approaching) jet can be explained as an effect of steep pressure gradients at a transition regime between the external pressure-dominated jet regime and a more or less freely expanding jet regime. The T_B gradients reveal that either equipartition holds between the magnetic energy and the particle energy or the assumption of a single, well defined particle energy distribution without cooling is violated. Alternatively, a conserved longitudinal

component might dominate the magnetic field. The angle to the line of sight of the "twin-jet" system NGC 1052 was determined to lie between $\sim 57°$ and $\sim 83°$. A region of linearly polarized emission is found along the eastern jet at 5 GHz but not at higher frequencies, providing a possible sign of jet stratification. An absorbing column density towards the base of the counter jet of $\sim 2 \times 10^{22}\,\mathrm{cm}^{-2}$ is derived.

- Data from a short (2.3 ksec) *Chandra* observation of NGC 1052 reveal the presence of a diffuse thermal X-ray emitting gas inside the galaxy. A MERLIN study of the kiloparsec-scale radio jet shows that the thermal plasma is well aligned with the radio synchrotron jet-emission. This suggests an origin from an interaction of the jet with its ambient medium, heating the gas to $kT = (0.4 - 0.5)\,\mathrm{keV}$. The soft excess of NGC 1052 (compare Sect. 5.1) is identified with this extended jet-associated emission component.

- The kiloparsec-scale radio structure of NGC 1052 is found be aligned with an optical emission cone. Bright, compact knots in the jet structure are visible at radio, optical and X-ray energies with a spectrum incompatible with synchrotron emission

- A heavily absorbed and unusually flat nuclear X-ray spectrum is found with *Chandra* in agreement with earlier *ASCA* and *Beppo*Sax studies of this source but the data quality did not allow the continuum emission model to be fully constrained.

- A deeper, higher SNR X-ray spectrum of NGC 1052 is obtained from an archival 13 ksec *XMM-Newton* observation. The X-ray spectrum is found to be complex and not adequately approximated via simple continuum models like the models I to III which represent well the majority of radio-loud, core dominated AGN as found from the analysis of the *2 cm-X-Sample* presented in this thesis. The *XMM-Newton* spectrum sustains the presence of a high-density nuclear absorber obscuring the primary nuclear X-ray source.

- Combining the *XMM-Newton* data with the data from an earlier X-ray spectral observation of NGC 1052 with *Beppo*Sax, the continuum model is further constrained. Pure high-energy reflection models are ruled out on this basis. The X-ray spectrum of NGC 1052 is found to be best described via a heavily absorbed hard-power-law model with the absorber covering the source only partially (patchy absorber).

- Broad residual emission in the range between 4 keV and 8 keV is found that can only be explained by the addition of a further spectral emission component dominating this energy range. Relativistic, broad iron line emission models are found to yield the best approximation to the data. While the data does not allow the black-hole spin to be constrained, the competing relativistic line models consistently predict a large inclination to the line of sight, larger than $75°$, in agreement with the VLBI results presented in Sect. 6.3.1.

- The developed models that can explain both the *XMM-Newton* and the *Beppo*Sax spectrum of NGC 1052 yield significantly different parameter values. The discrepancy can be explained if either the continuum and the broad iron line or only the broad line has varied between the two epochs. In both cases, it must be concluded

that a change in the inner accretion disk has caused the line variation. A pure continuum variation can be ruled out.

- The detection of a relativistic, broad iron line in NGC 1052 is the first of its kind in a radio-loud AGN with a bright compact radio core. This discovery provides for the first time the opportunity to study dynamical processes in the accretion disk and their immediate impact on jet production.

- It is found that the broad-iron-line variability was accompanied by a violent ejection of relativistic plasma in the radio jet of NGC 1052 that occurred in 2000. This observational signature suggests that the source was caught in the act of feeding a part of the accretion disk into the black hole while a fraction of the material was injected into the jet.

- A large multi-mission and multi-waveband observing campaign of NGC 1052 has been set up for the time period spring 2005 to spring 2006. At the time of writing of this thesis, this campaign has already started invoking VLBA observations of NGC1052 at $\lambda 1.3$ cm and $\lambda 0.7$ cm every six weeks, 15 ToO epochs of *RXTE* X-ray light curve monitoring observations every three weeks, Radio-spectral monitoring observations with the Effelsberg 100-m telescope, covering the full cm- to mm-wavelength regime, quasi-simultaneous to the *RXTE* pointings, two deep Chandra/XMM-Newton pointings separated from each other by five months to derive high-spectral-resolution profiles of the broad iron line at two different epochs, and long-term radio monitoring with the RATAN-600 telescope and the 26 m telescope of the University of Michigan. The results of this campaign promise to yield substantially new, deep insights into the phenomena of black-hole mass accretion and jet formation in radio-loud AGN and will provide a critical test for the jet-disk coupling interpretation of the observational data available so far.
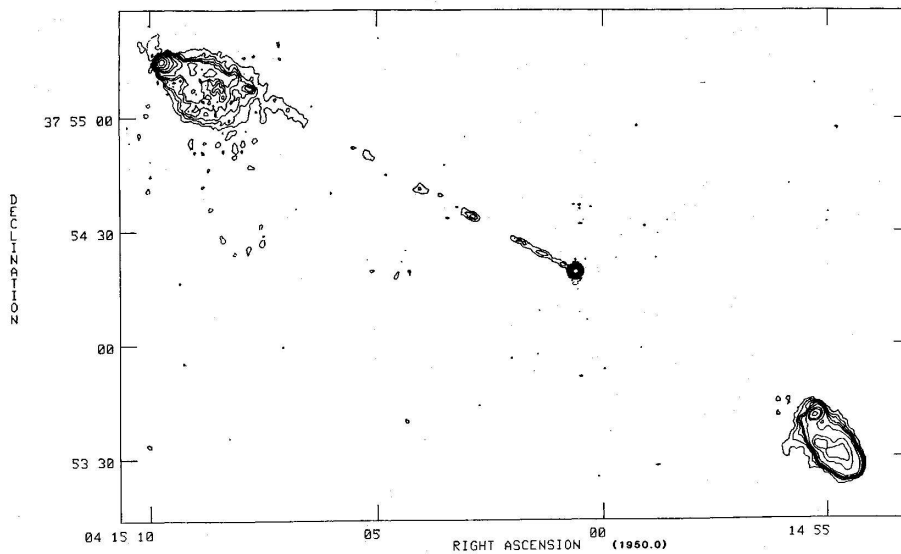
Figure 6.23: 3C 111 at 1.4 GHz observed with the VLA. Image taken from Linfield and Perley (1984).

6.4   The Trail of a Superluminal Jet Component in 3C 111

6.4.1   Introduction

The nearby (z=0.049)[8] broad-line radio galaxy 3C 111 (0415+379) shows a classical FR II morphology on kiloparsec-scales spanning more than 200″ with a highly collimated jet connecting the central core and the northeastern lobe in position angle 63° while no counterjet is observed towards the southwestern lobe (see Fig. 6.23 from Linfield and Perley 1984). This asymmetry, which is usually explained via relativistic boosting of the jet and de-boosting of the counter-jet, is even more pronounced on parsec-scales: 3C 111 exhibits the brightest compact radio core at cm/mm wavelengths of all FR II radio galaxies. It was the first lobe-dominated extragalactic radio source in which superluminal motion was detected (Goetz et al. 1987, Preuss et al. 1988). High-radio-frequency VLBI data of 3C 111 have been reported on by Alef et al. (1998) and Kharb et al. (2003) finding remarkably rapid structural changes on a time scale of months, being obtained after a major radio-flux-density outburst in 1996 (see below).

6.4.2   Observations and data analysis

3C 111 has been monitored as part of the VLBA 2 cm Survey program. The observational details are given in Kellermann et al. (1998a) and Zensus et al. (2002). Following standard methods of VLBI data reduction as described, e.g., in Kadler et al. (2004c), the data from 10 epochs of VLBI observations of 3C 111 between 1995 and 2002 (see Table 6.8) were phase and amplitude self calibrated and the brightness distribution was determined via hybrid mapping. Two dimensional Gaussian components were fitted in the (u, v)-domain

---

[8]Assuming a Hubble constant of $H_0 = 71\,\mathrm{km\,s^{-1}\,Mpc^{-1}}$, $\Omega_\mathrm{M} = 0.3$, $\Omega_\Lambda = 0.7$, this results to a linear scale of $1.0\,\mathrm{pc\,mas^{-1}}$.

177

to the fully calibrated visibility data of each epoch using the program DIFMAP. The parameters of the various model fits at the various epochs are given in Table 6.9. The models were aligned at the various epochs by assuming the westernmost component (namely, the core) to be stationary so that the position of jet components can be measured relative to the location of the core component. Because of the coupling of the flux densities of nearby model components, the true flux-density errors are larger than the formal (statistical) errors in most cases (unless the given model component is far enough separated from its closest neighbor). Throughout this section, conservative errors of 10 %–20 % are assumed for the flux densities of individual model-fit components. Positions and component sizes are assumed to have uncertainties of one fifth of a beam size and one fifth of the component diameter, respectively.

6.4.3 The 1996 Radio Outburst of 3C 111

A strong flux density outburst occurred in 1996, which was first visible at the highest frequencies and some months later at the lower frequencies. In fact, this outburst was first detected at 90 GHz with the IRAM interferometer at Plateau de Bure in January 1996 with flux densities > 10 Jy (Alef et al. 1998), at 37 GHz in March 1996, and at 22 GHz in August 1996 (Teräsranta et al. 2004). Figure 6.24 shows the single-dish radio light curves of 3C 111 at 4.8 GHz, 8 GHz, and 14.5 GHz obtained from the UMRAO radio-flux-density monitoring program (Aller et al. 2003). These data show that from early 1996 on the radio-flux density of 3C 111 was rising at 14.5 GHz, reaching its maximum in late 1996. At the two lower frequencies, the flux-density maximum was reached at subsequent later times, in mid 1997 at 8 GHz and in late 1997 at 4.8 GHz. The flare propagated through the spectrum as qualitatively expected by standard jet theory with the high-frequency radio emission coming from the most compact regions of the jet and the emission peak shifting to lower frequencies as a newly ejected jet component travels down the jet becoming optically thin. The shift rate with frequency in the case of the 1996 outburst of 3C 111 is ~ 10 GHz/yr.

6.4.4 VLBI Monitoring Results

Figure 6.25 shows the variable parsec-scale structure of 3C 111 at 10 different epochs[9] of VLBA 2 cm Survey observations between 1995.27 and 2002.19. The variable source structure can be described by a classical one-sided core-jet morphology in the first two epochs with typical velocities of the outward moving jet components of $\sim 0.8-1.9$ mas yr^{-1} corresponding to $2.6 - 6.2\,c$. In epoch 1997.19 a new bright jet component dominates the source structure shining out even the core. In the following epochs this new component travels along the jet while it is gradually stretched out.

Model Fitting: In Fig. 6.26 the radial distance of the various model fit components is shown as a function of time. The component identification was conducted, based on a comparison of the positions and flux densities, and a linear regression of the core distances

---

[9]The data of an eleventh epoch (1996.82) suffer from a calibration problem and are not used for this study.
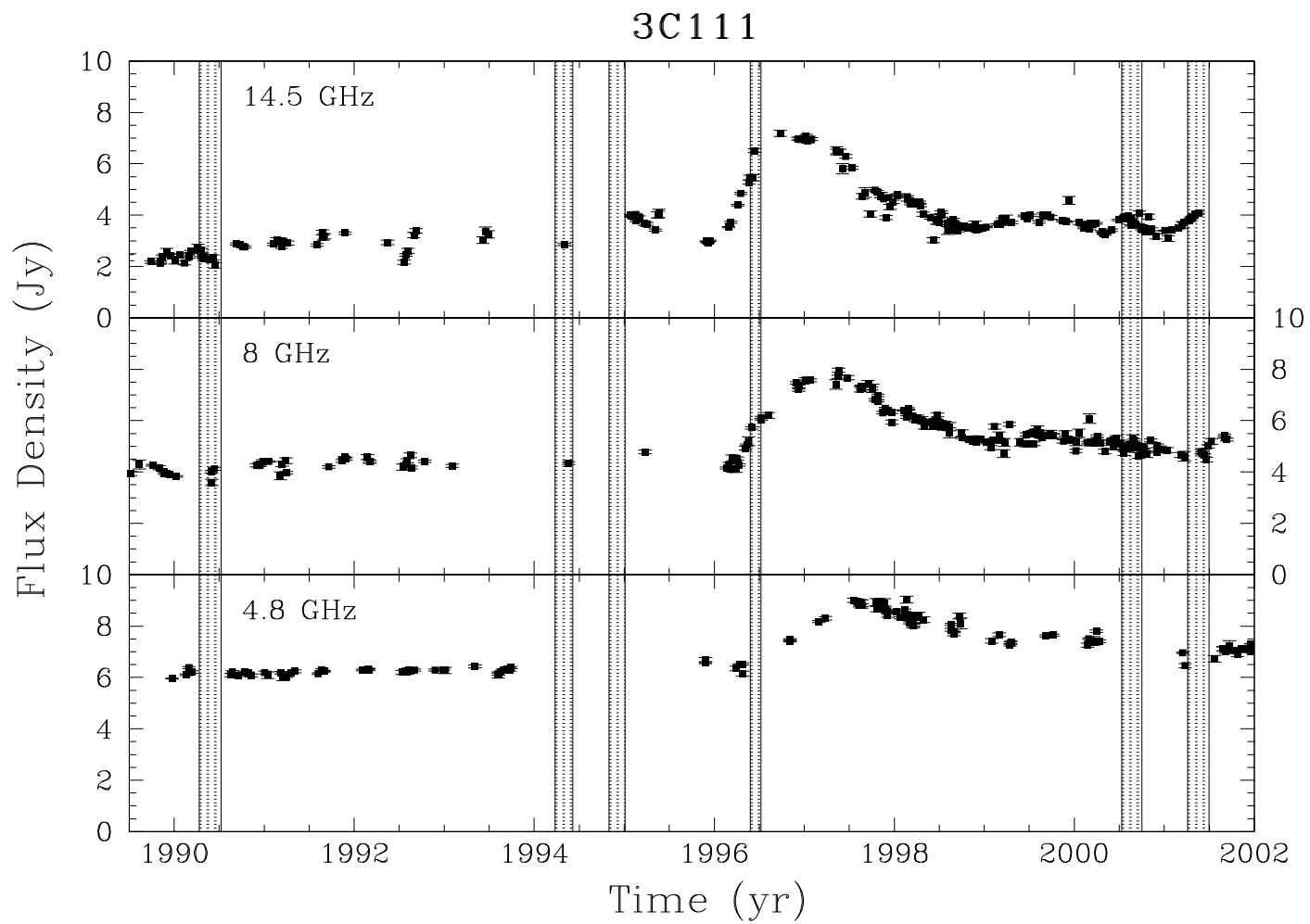
Figure 6.24: Radio-light curves of 3C 111 at 4.8 GHz, 8 GHz, and 14.5 GHz from the UMRAO monitoring program. The shaded areas indicate the ejection epoch of the components A, B, C, E 1, F, and G (see text).
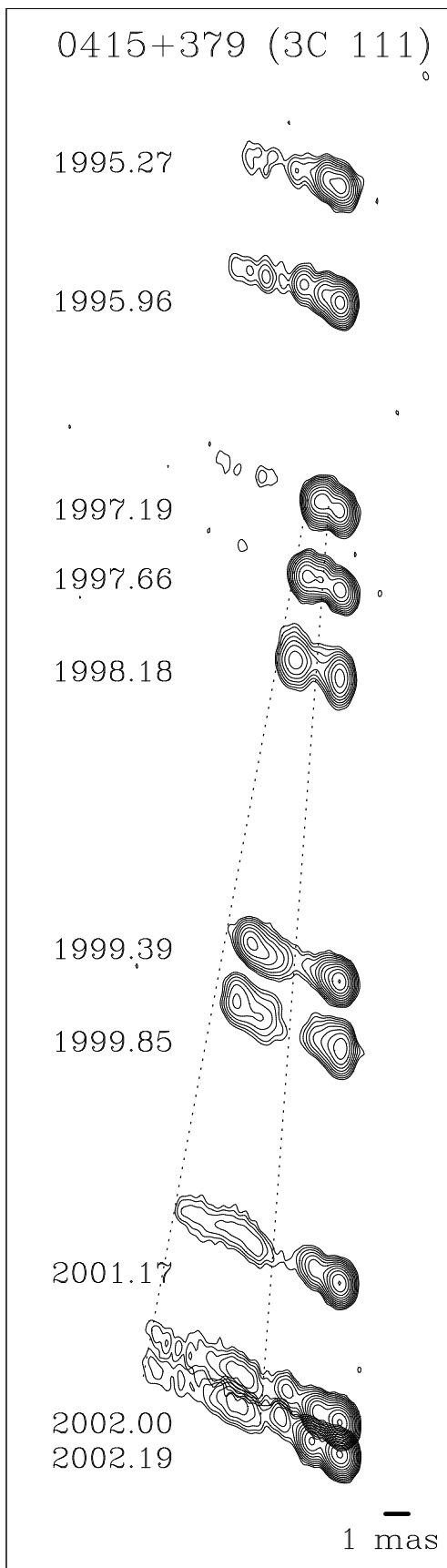
Figure 6.25: Uniformly weighted images of the parsec-scale jet of 3C 111 between 1995.27 and 2002.19. The restoring-beam sizes, the total recovered flux density in each image and the rms are given in Table 6.8. The lowest contours are 10, 5, 10, 10, 10, 5, 10, 5, 2.5, and 2.5 mJy/beam, respectively, and increase by factors of $\sqrt{3}$. The dashed lines mark the evolution of component E 1 and its trail.

Table 6.8: Journal of VLBA 2 cm Survey observations of 3C 111 analyzed in this study.

Epoch	Code	Beam [mas × mas, °]	S_{tot} [Jy]	rms [mJy/beam]
1995.27	BK 016	0.86×0.45, +5.0	2.6	1.8
1995.96	BK 037A	1.05×0.57, +25.0	1.8	1.1
1997.19	BK 048	0.94×0.55, −3.2	6.0	1.3
1997.66	BK 052A	0.92×0.52, +1.3	4.1	1.6
1998.18	BK 052B	0.85×0.54, −10.1	2.0	2.1
1999.39	BK 068A	0.88×0.51, +2.4	2.6	0.6
1999.85	BK 068C	0.91×0.50, +4.0	2.4	1.3
2001.17	BK 068E	0.96×0.52, −4.8	2.1	0.4
2002.00	BR 077D	1.07×0.55, −3.5	2.2	0.4
2002.19	BR 077I	0.95×0.54, −6.0	2.2	0.3

as a function of time was performed to determine the kinematics. The derived component velocities are tabulated in Table 6.10. The outer jet components (A, B, C) of the 1995.27 epoch can be traced over two to four epochs before their flux densities fall below the detection threshold. In 1997.19, the source structure is dominated by the emission of the core and the newly emerged jet component E 1, which travels outwards in the subsequent epochs with a mean apparent velocity of $1.6\,\mathrm{mas\,yr^{-1}}$. In the following epochs, three additional slower moving components (E 2, E 3, E 4) form behind E 1, of which only E 2 is consistent with being ejected from the core. E 3, and E 4 form at distances of 3–4 mas from the core and thus most likely represent trailing components rather than ejections into the jet at the jet base. In later epochs, two new components (F,G) are ejected from the core into the jet.

Flux Density Evolution: Figure 6.27 shows the brightness evolution of the core and the jet components with time. Apparently, the trailing components E 3 and E 4 appear in a rising state, i.e., they first increase in flux before they become fainter in later epochs. Component E 2 shows an extraordinary steep decrease in brightness during the first two epochs in which it was observed and exhibits a local maximum in flux in the next epoch. It cannot be excluded that this behavior represents two distinct jet components, the first being already invisible due to the rapid decrease in flux in the 1998.18 epoch. The flux density evolution is shown in Fig. 6.28 as a function of measured core distance. E 3 and E 4 reach their flux density maximum at different core distances.

Component Trajectories: The apparent paths of the various jet components in the plane of the sky are shown in Fig. 6.29. All components emerged from the jet base travel along approximately linear paths with the position angle varying with time clockwise. Particularly, the paths of the "early" components A and B are south of the path of E 1, while the "late" components F and G travel north of it. The interpretation of the components E 2, E 3, and E 4 as trailing components is substantiated by the fact that their

Table 6.9: 3C 111 VLBI model fit parameters.

Id	Flux density [mJy]	Radius [mas]	P.A.[a] [°]	FWHM [mas]	Axis ratio	φ [°]	Id	Flux density [mJy]	Radius[a] [mas]	P.A. [°]	FWHM [mas]	Axis ratio	φ [°]
		1995.27							*1999.39*				
0	1324	–	–	0.3	0.53	46.4	0	1480	–	–	0.4	0[c]	64.4
A	84	3.9	70.2	1.2	1[b]	–	E1	421	4.2	66.3	0.6	0.53	40.3
B	199	1.7	67.3	1.0	1[b]	–	E2	166	3.5	69.1	0.4	1[b]	–
C	981	0.6	61.8	0.4	0.40	61.2	E3	182	3.0	70.0	0.7	1[b]	–
							X	53	1.3	65.7	0.6	1[b]	–
							X	256	0.6	62.9	0.3	0[c]	56.6
		1995.96							*1999.85*				
0	873	–	–	0.3	0.58	25.4	0	1067	–	–	0.8	0.42	−3.8
A	41	4.5	70.4	0.8	1[b]	–	E1	275	5.1	64.3	0.8	0.42	−8.6
B	48	3.3	70.7	0.3	1[b]	–	E2	130	4.6	65.9	0.8	0.46	−17.1
C	124	1.7	63.5	0.4	1[b]	–	E3	332	3.7	68.2	1.2	0.74	45.7
D	677	0.4	63.5	0.9	0.34	62.0	X	376	0.7	75.5	1.3	0.25	49.4
							X	257	0.5	43.1	0.8	0.43	16.9
		1997.19							*2001.17*				
0	2577	–	–	0.4	0[c]	68.1	0	1597	–	–	0.4	0[c]	61.4
B	41	5.3	68.2	1.1	1[b]	–	E1	45	7.2	64.2	0.9	0.83	76.0
C	39	3.5	64.7	1.0	1[b]	–	E2	45	6.2	66.1	0.9	0.92	55.4
E1	3353	0.9	63.9	0.6	0.49	−82.4	E3	100	5.2	62.9	1.2	0.54	65.2
							E4	91	4.0	66.4	1.1	0.35	48.3
							F	244	1.1	59.4	0.9	0.22	54.9
		1997.66							*2002.00*				
0	1630	–	–	0.5	0[c]	58.9	0	1514	–	–	0.5	0.09	61.2
B	21	6.3	70.0	1.0	1[b]	–	E1	24	8.4	65.1	1.0	1[b]	–
C	17	4.6	64.8	0.5	1[b]	–	E2	22	7.0	64.0	1.1	1[b]	–
E1	1483	1.5	68.3	0.4	0.87	38.9	E3	20	5.9	65.9	0.8	1[b]	–
E2	961	0.9	61.1	0.4	0.21	71.2	E4	121	4.7	64.7	1.4	0.35	47.8
							F	061	2.6	58.8	0.9	0.33	50.6
							G	425	1.0	64.7	0.5	0.39	66.9
		1998.18							*2002.19*				
0	1129	–	–	0.8	0.47	6.3	0	1691	–	–	0.6	0.10	62.9
E1	816	2.1	67.9	0.9	0.65	11.9	E1	14	8.7	65.8	0.7	1[b]	–
E2	132	1.3	60.4	0.6	1[b]	–	E2	17	7.8	64.3	1.0	1[b]	–
							E3	12	6.2	67.5	0.5	1[b]	–
							E4	117	4.9	64.2	1.5	0.36	52.5
							F	34	3.1	57.1	0.7	0[c]	11.6
							G	314	1.3	64.1	0.5	0.57	65.2

[a] The PA is measured from north through east; [b] Axis ratio fixed at 1; [c] Component degenerated to a linear feature during the fit.

Table 6.10: 3C 111 VLBI jet kinematics.

Component	# of epochs	μ [mas yr^{-1}]	β_{app}	Peak Flux [mJy]
A	2	0.8	2.6	84
B	4	1.9	6.2	199
C	4	1.6	5.2	981
D	1	–	–	676
E 1	8	1.6	5.2	3353
E 2	7	1.5	4.9	961
E 3	5	1.1	3.6	332
E 4	3	0.9	2.9	121
F	3	1.9	6.2	244
G	2	1.6	5.2	425
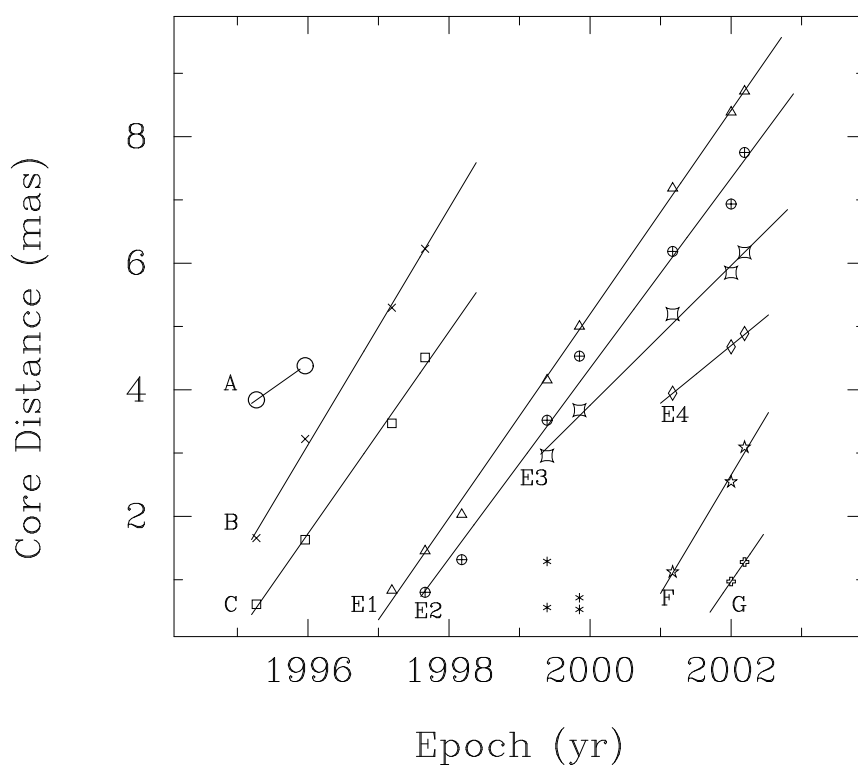
Figure 6.26: Core separation vs. time. The trailing components E3 and E4 are not ejected from the core but form behind the leading component E1. Asterisks represent components which could not be cross identified over the epochs.
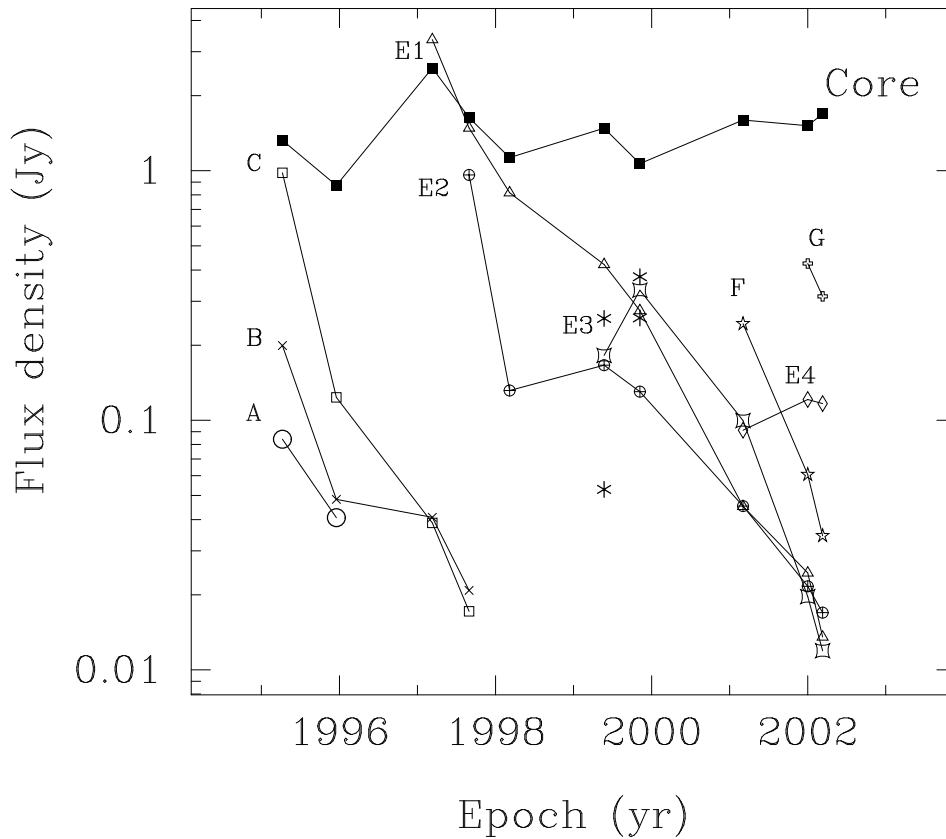
Figure 6.27: Flux-density evolution of the core and the jet components with time. Asterisks represent components which could not be cross identified over the epochs.

trajectories resemble the E 1 trajectory.

A Jet Reflection Event in 1999?   The radial velocity of component E 1 changes abruptly from $1.2 \, \mathrm{mas \, yr^{-1}}$ between 1997.19 and 1998.18 to $1.6 \, \mathrm{mas \, yr^{-1}}$ between 1999.39 and 2002.19 (see Fig. 6.30). This behavior is similar to the collimation event in the jet of 3C 279 reported by Homan et al. (2003) and enables us to constrain the orientation of the jet and the jet Lorentz factor γ. Assuming that the Lorentz factor before and after the change in apparent speed is the same, a change in the angle to the line of sight can simply explain this behavior. Physically, this may correspond to an elastical reflection of the jet in a jet-cloud interaction. If the jet Lorentz factor $\gamma = (1 - \beta^2)^{-1/2}$ is constant, the maximal apparent speed of a jet component is achieved for an angle θ that fulfills $\partial \beta_{\mathrm{app}} / \partial \theta = 0$. From $\beta_{\mathrm{app}} = \beta \sin \theta / (1 - \beta \cos \theta) = 5.235$ one derives $\beta_{\mathrm{app}} = \beta \gamma$ and therefore $\gamma = 5.33$. This is the minimal jet Lorentz factor that is required to explain the observed apparent speeds. The trajectory of E 1 can be parametrized via a piecewise linear regression to $x(t)$ and $y(t)$ in the sky for the intervals 1997-1999 (radial distance smaller than 3 mas) and 1999-2003 ($r > 3$ mas). This yields values of $\dot{x} = (1.14 \pm 0.11) \, \mathrm{mas/yr}$ and $1.46 \pm 0.02 \, \mathrm{mas/yr}$, respectively, for the gradients of $x(t)$ and $\dot{y} = (0.40 \pm 0.01) \, \mathrm{mas/yr}$ and $0.67 \pm 0.05 \, \mathrm{mas/yr}$ for the gradients of $y(t)$. This implies vector motions of $\dot{r}(t < 1999) = (1.20 \pm 0.11) \, \mathrm{mas/yr}$ and $\dot{r}(t > 1999) = (1.46 \pm 0.05) \, \mathrm{mas/yr}$ before and after the 1999 event, corresponding to apparent linear speeds of $(3.9 \pm 0.4)c$ and $(5.2 \pm 0.2)c$,
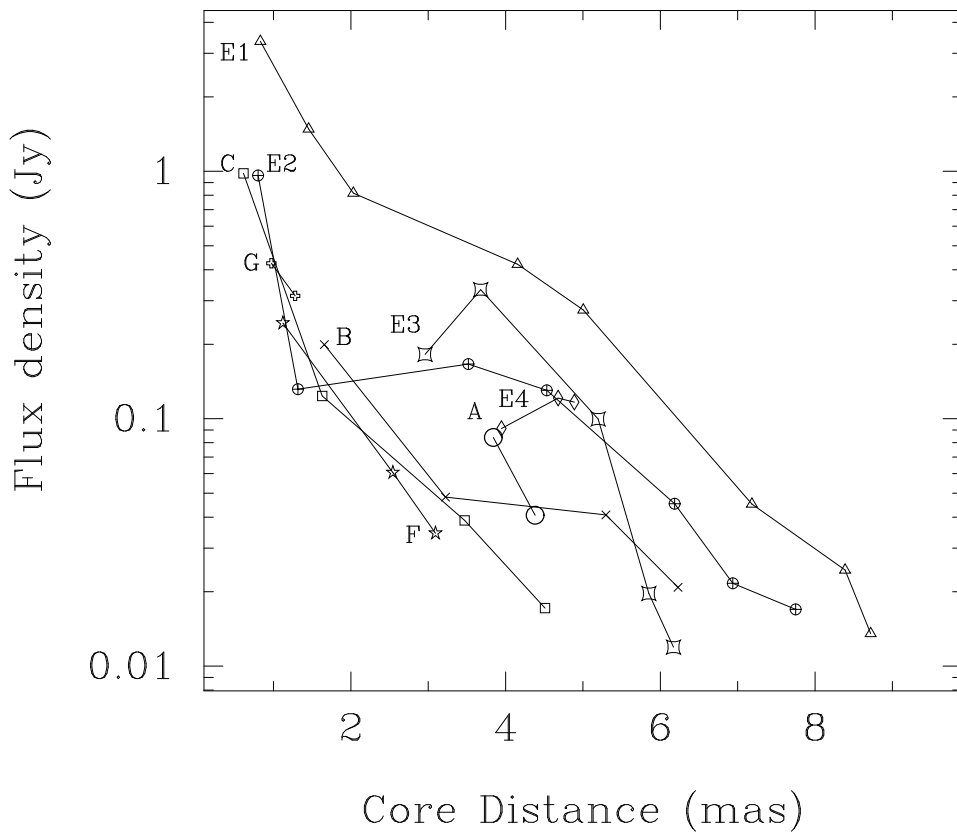
Figure 6.28: Flux densities of jet components as a function of core distance. E3 and E4 rise in flux density after their first occurrence and reach their maximal brightness after a travel distance along the jet of about one milliarcsecond.
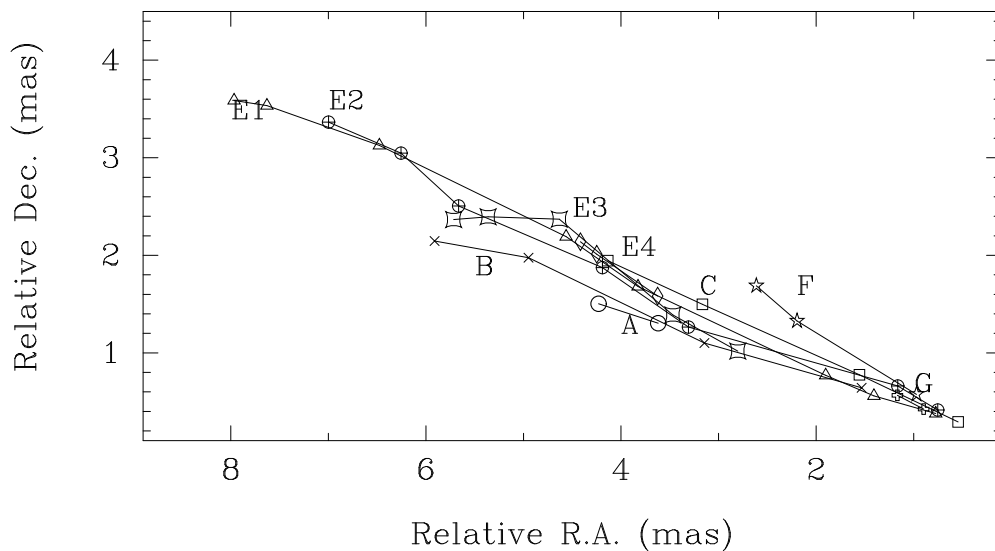
Figure 6.29: Relative position of jet components at the various epochs in the sky. The trailing components E2, E3, and E4 travel along the same (curved) path as the leading component E1. The jet components A, B, F, and G travel along different paths. The ejection angle gradually shifts towards the north.
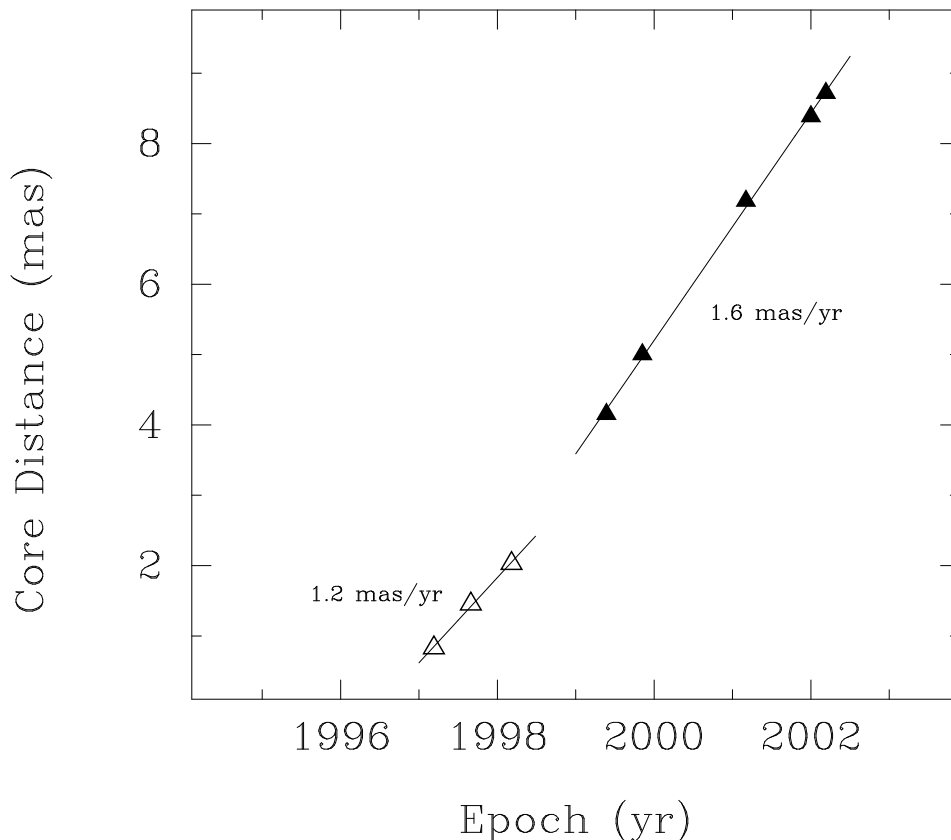
Figure 6.30: Core separation vs. time for component E 1 during 1997.19–1998.18 (open triangles) and during 1999.39–2002.19 (filled triangles). The solid lines represent linear-regression fits to the first three and the last five data points, respectively.

respectively. The viewing angle in this model changes from $\theta \sim 24°$ in the time interval 1997–1999 to $\theta \sim 11°$ after 1999[10]. The Doppler factor varied from a moderate value of 1.85 before the event to a larger value of 5.23 after the event. Interestingly, Lähteenmäki and Valtaoja (1999) derive a Doppler factor of 2.33 for 3C 111 from total flux density variability studies at 22 GHz and 37 GHz.

One can now further assume that the trailing components travel along the same path as E 1 and thus have the same angle to the line of sight. Table 6.11 gives the apparent velocities of the trailing components E 2, E 3, and E 4, which exhibit a gradually smaller apparent velocity compared to the leading component. This behavior is already apparent from the visual impression of stretching (compare Figure 6.25). This can be explained if these trailing components indeed are intrinsically slower than the leading shock represented by E 1 and have smaller Lorentz and Doppler factors. The formation of such trailing components behind the leading perturbation propagating within a jet flow are indeed predicted by numerical simulations of the response of a relativistic jet and its ambient medium to the formation and propagation of superluminal shocks (Agudo et al. 2001).

---

[10]A formal second solution for θ yields values $< 5°$. This solution is not considered further due to the inconsistency of such a blazar-like orientation with the large-scale radio morphology, the lack of observed fast variability patterns and the X-ray spectroscopic results of Lewis et al. (2005).

The T_b gradient along the jet: Figure 6.31 shows the brightness temperatures of the various jet components as a function of their core distance. In general, the brightness temperature of all components decreases as the components travel outwards but an approximation with a simple power law does not yield a good fit in the most cases. This behavior is different then expected for a straight jet geometry in which the power-law dependences of the particle density, the magnetic field strength and the jet diameter on the core distance predicts that the brightness temperature along the jet can be described with a well defined and stable gradient of T_b. In Appendix XX it is shown that most jets in the CJ 1/2 survey (Polatidis et al. 1995, Thakkar et al. 1995, Xu et al. 1995), which do not show apparent effects of curvature, show a power-law decrease with increasing distance from the core and power-law indices typically around -2.5. Since a change in apparent velocity of the E 1 component is observed, which most likely provides a signature of jet bending, the measured brightness temperatures at different distances from the core are altered by different Doppler factors depending on the local inclination of the jet. One can correct for this in the case of component E 1 by calculating the Doppler factors in the two ranges before and after the reflection event and determine from these the boosting-corrected brightness temperature for each epoch. A free parameter in this procedure is the Jet Lorentz factor, for which only a lower limit of 5.33 exists (from the maximal observed apparent velocity).

Assuming a jet inclination of $23.82°$ before and $10.98°$ after the reflection (compare Table 6.10) we calculated a corrected brightness temperature T_b^* for E 1 in each epoch

$$T_b^* = T_b \times \delta^{-3.5} \tag{6.1}$$

and the linear distance from the core

$$R = \begin{cases} r \sin \theta_1 & r < r_* \\ r_* \sin \theta_1 + (r - r_*) \sin \theta_2 & r > r_* \end{cases} \tag{6.2}$$

where r_*=3 mas is the projected core distance where the reflection takes place. Linear regressions were performed for the T_b^* vs. R dependence for different values of γ and determined the correlation coefficient ρ^2 for each γ (ρ^2 is the regression sum of squares, S_{reg}, divided by the total sum of squares where S_{reg} is the difference between the total sum of squares and the sum of the squared differences between the fit and the data). Figure 6.32 shows the resulting distribution, which falls rapidly with γ, thus suggesting that the minimal value of $\gamma \sim 5.4$ yields the best power-law dependence of T_b^* on R. In Fig. 6.33, the measured dependence of T_b as a function of r is shown in comparison to the corrected dependence of T_b^* on R. The correction yields a smooth power-law decrease of T_b^* with a power-law index of -3.75 ± 0.18 and only a small residual scatter. This value is at the extreme end of the distribution of brightness temperature gradients derived in Appendix C, implying very steep gradients of the particle density, the magnetic field and/or the spectral index (compare Fig. C.9). Recalling that E 1 is the relict of a major plasma ejection in the 3C 111 jet, a steep particle density gradient with respect to the ambient material seems plausible.

Summary and comparison with other published results: The model developed in this chapter describes with a small number of parameters the observed kinematics of the
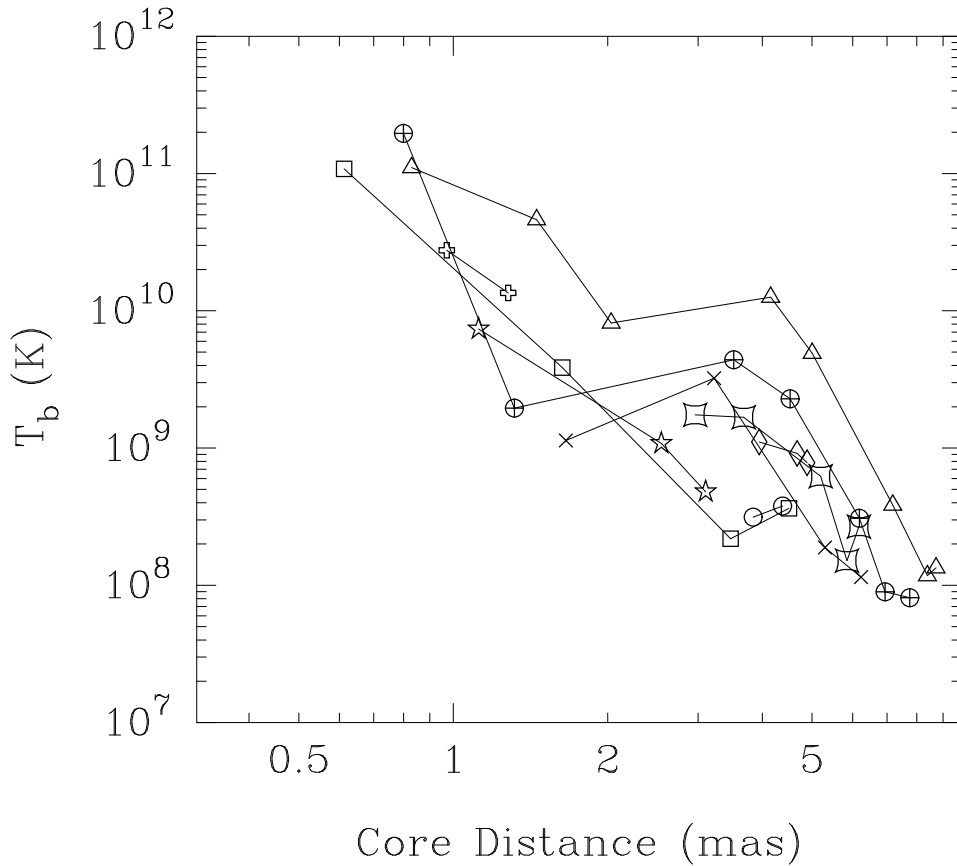
Figure 6.31: Brightness temperatures of jet components as a function of core distance. The local maximum for each component around (3-5) mas core distance indicates a change of the local jet direction relative to the angle to the line of sight resulting to a varying Doppler factor. Symbols used are the same as in Fig. 6.27–6.29.

Table 6.11: 3C 111 kinematical parameters for E 1 and its trailing components.

	E1		E2	E3	E4
	$[r < 3\,\mathrm{mas}]$	$[r > 3\,\mathrm{mas}]$			
$\beta_{\mathrm{app}}^{\dagger}$	*3.92*	*5.24*	*4.87*	*3.57*	*3.01*
γ	**5.33***	**5.33***	4.99	3.89	3.46
ϑ	23.71°	10.81°	**10.81°**	**10.81°**	**10.81°**
δ	1.85	5.23	5.33	5.06	4.84

Note: Values in boldface in the family $(\gamma, \vartheta, \delta)$ were fixed and the other two were determined from them.
† Values determined from the proper motions (via a linear regression of r vs t); * $\gamma_{\mathrm{min}} = (1 + \beta_{\mathrm{app}}^2)^{1/2}$; value that minimizes β for an observed β_{app};
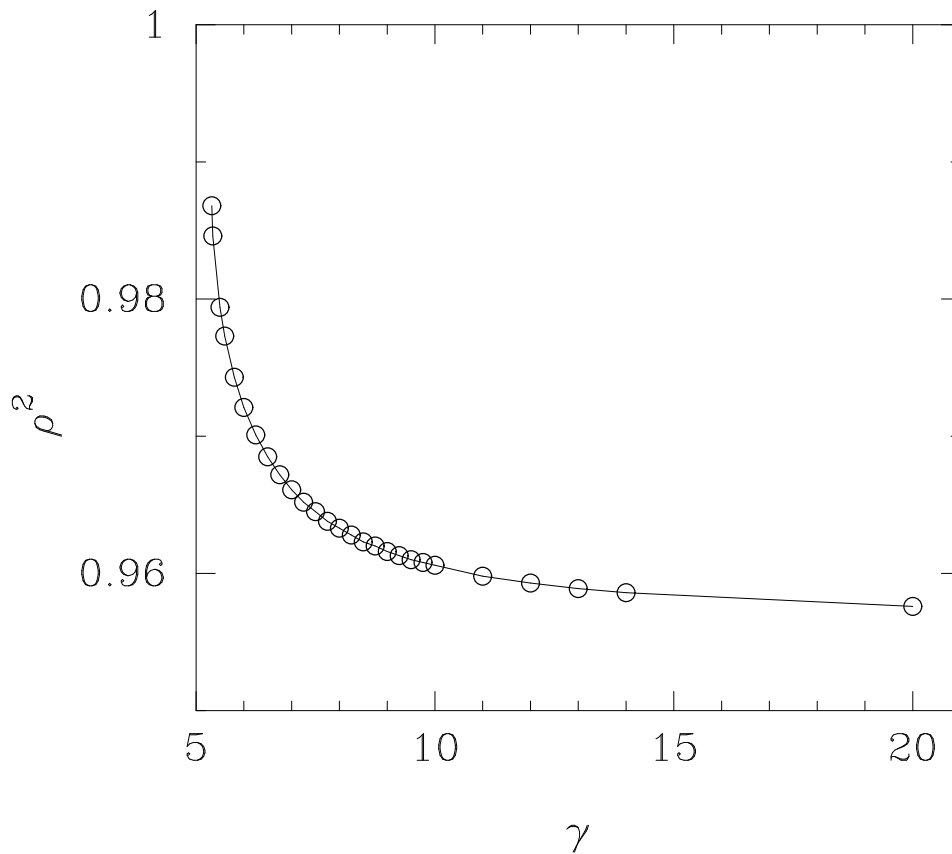
Figure 6.32: Correlation coefficient between $\log T_{\mathrm{b}}$ and $\log \mathrm{r}$ as a function of the assumed Lorentz factor.

leading component E 1 and its trailing components associated with a major flux-density outburst of 3C 111 in 1996. The trajectory of E 1 is described in terms of two ballistic regimes where the component is moving with a constant intrinsic speed but at different angles to the line of sight. The value derived for the angle of the jet to the line of sight is in good agreement with the *XMM-Newton* X-ray spectrum of 3C 111 analyzed by Lewis et al. (2005), suggesting a partial-covering model of the primary X-ray continuum source. As pointed out by Lewis et al. (2005), it is not clear which structure could be obscuring the primary X-ray source, given the small angle of the jet axis to the line of sight. In this context, it is interesting to note that I: there are bent component trajectories in the inner few milliarcseconds of the 3C 111 jet and II: that the abrupt change change in speed of component E 1 may be the result of a jet-collimation event at a boundary between the jet outflow and some kind of ambient medium (as suggested by Homan et al. (2003) in the case of the bent in the trajectory of the component C 4 in 3C 279). It is further remarkable that the model yields the best correction of the distorted brightness temperature gradient of component E 1 as it travels along the jet for a maximal boosted jet, i.e., the minimal allowed Lorentz factor. The assumption of a maximal boosted jet is made often, particularly in the case of radio galaxies with bright compact radio cores. But observational evidence for maximal boosted jets is rare.

The appearance of trailing components behind bright superluminal VLBI components has been observed earlier with VLBI. Gómez et al. (2001a) identified several knots ap-
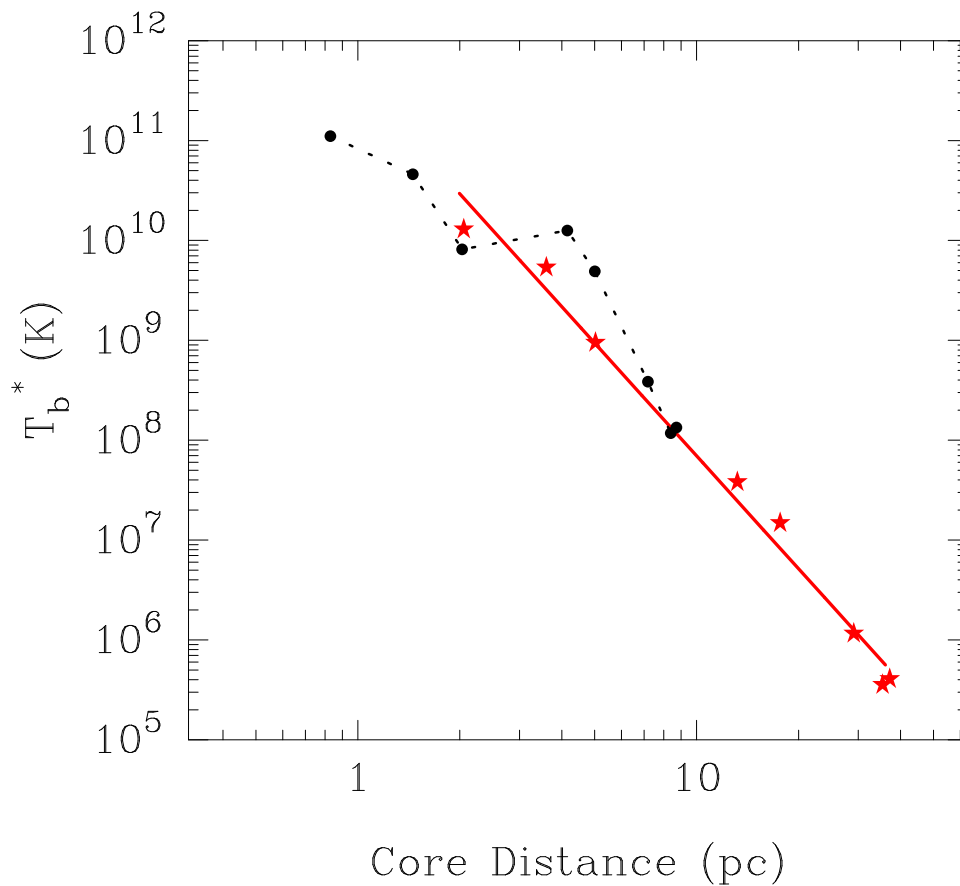
Figure 6.33: Stars: Boosting-corrected brightness temperatures of component E 1 as a function of deprojected core distance. A power-law fit to the data is indicated by the solid line (power-law index -3.75 ± 0.18). Circles: Measured brightness temperatures of component E 1 as a function of the measured core distance.

pearing in the wake of a bright superluminal component, moving at slower speeds than the typical jet velocity observed in 3C 120. Recently, Jorstad et al. (2005) have presented an independent VLBI kinematical study of 3C 111 (among 14 other AGN monitored with the VLBA at 43 GHz from 1998 March to 2001 April. The authors report trailing components at distances of $\sim 6\,mas$ and ~ 5 mas from the core in early 2001 having formed behind a leading jet component at ~ 7 mas at the same epoch. Comparing the distances and trajectories, their leading component can be identified with E 1 and their trailing components with E 2 and E 3 (following the nomenclature used throughout this section). Jorstad et al. (2005) find similar leading-shock–trailing-components patterns for several other sources in their study.

List of collaborators: H. D. Aller, M. F. Aller, K. I. Kellermann, Y. Y. Kovalev, E. Ros

6.5   0716+714

0716+714 is one of the best studied BL Lac objects and a key object in understanding the long and short term variability of active galactic nuclei (AGNs) across the whole electromagnetic spectrum. It belongs to the S5 polar cap sample of compact radio sources defined, e.g., in Eckart et al. (1986). At radio wavelengths 0716+714 exhibits strong intraday variability (IDV) and is the best candidate for source-intrinsic IDV in the ongoing debate whether the IDV phenomenon has to be explained in terms of intrinsic or extrinsic processes (e.g. Wagner and Witzel 1995) or a combination of both. The reason for the outstanding status of 0716+714 within the framework of this debate is the detection of simultaneous radio-optical variability by Quirrenbach et al. (1991) and a correlation between the radio spectral index and optical variability (Qian et al. 1996). Moreover, Giommi et al. (1999) found correlated optical and soft X-ray variability of 0716+714. Wagner et al. (1996) derived a brightness temperature of $T_b = 1.4 \times 10^{17}$ K from 5 GHz measurements implying a violation of the inverse Compton limit by several orders of magnitude. These authors assumed an intrinsic origin of the observed variability and used a redshift of $z = 0.3$, suggested as a lower limit of the redshift of 0716+714 by the non-detection of an optical host galaxy, to calculate T_b. These results implied extraordinarily high Doppler factors of the order of ~ 50 to explain the violation of the Compton limit in terms of the beamed jet model. Indeed, 0716+714 shows a core-jet morphology on parsec-scales as imaged by Very Long Baseline Interferometry (VLBI) at centimeter wavelengths. The measurement of proper motion of jet components in 0716+714 suffers from the absence of bright, compact jet features which allow to be traced unambiguously over longer periods (years) and the long gaps of typically several months between the adjacent VLBI epochs. However, several authors report superluminal motion with component velocities up to $\sim 1 \, \text{mas yr}^{-1}$ (e.g., Jorstad et al. 2001, Bach et al. 2005) but from these measurements the Doppler factor cannot be derived unambiguously due to the lack of a well determined redshift.

In the X-ray domain 0716+714 has been observed by *Einstein* (Biermann et al. 1981), *ROSAT* (e.g. Wagner et al. 1996), and *Beppo*SAX (Tagliaferri et al. 2003). As in all other wavelength regimes 0716+714 is rapidly variable at X-rays with the highest amplitude below 3 keV (Tagliaferri et al. 2003, Giommi et al. 1999). The *Beppo*SAX data suggest two distinct components contributing to the (0.1–100) keV X-ray spectrum of 0716+714. A very steep power law with a photon index of 2.5 to 3.5 dominates below (2–3) keV while a flatter power law with a photon index of $\sim$1.7 characterizes the spectrum at higher energies. These observational characteristics can be explained if the soft X-ray emission is attributed to the highly variable tail of synchrotron jet emission and an inverse Compton spectral component (which varies only on longer time scales) dominates the hard X-ray emission.

In Sect. 6.5.1, a kinematical model for the 15 GHz VLBI structure of 0716+714, derived from four epochs of VLBA 2 cm Survey observations between August 1994 and March 2001. The most plausible component identification allows 2 components to be traced over more than 3 epochs with velocities of 0.5–0.7 mas yr^{-1}.

In Sect. 6.5.2, results are reported from three epochs of observations of 0716+714 with the X-ray observatory *XMM-Newton* (see Jansen et al. 2001 for a general description of the satellite). In all three epochs the source exhibits an extraordinarily steep X-ray

0716+714

1994.67   1996.52   1999.55   2001.17

1 mas
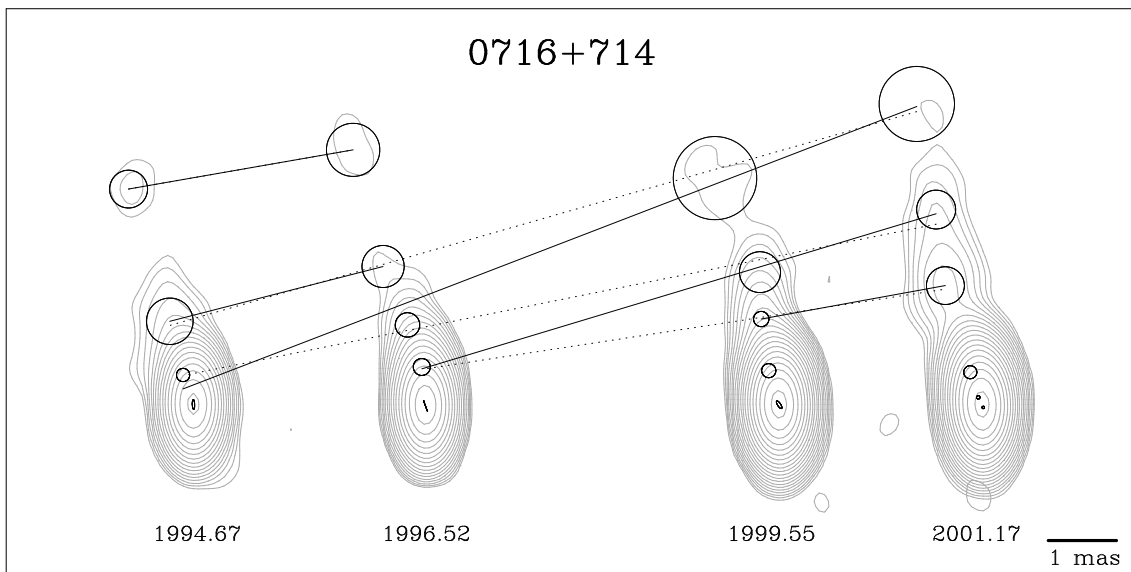
spectrum with photon indices of 2.7–3.0 if a simple absorbed-power-law model is applied. In two epochs in 2001 a significantly better fit is achieved with a two-power-law model. This is interpreted as variability in the relative strength of a primary synchrotron component and a secondary inverse Compton component to the total spectrum the latter being weak or absent in the third epoch. A relatively stable absorbing column density of $\sim (3 - 5) \times 10^{20}\,\mathrm{cm}^{-2}$ is found at all epochs while the absorbed source flux varies between $0.6 \times 10^{-11}\,\mathrm{erg\,cm^{-2}\,s^{-1}}$ and $3 \times 10^{-11}\,\mathrm{erg\,cm^{-2}\,s^{-1}}$. Short term source variability is detected with time scales of the order of $\sim 1000\,\mathrm{s}$ and variability amplitudes up to $50\,\%$. A strong flare in March 2002 exhibits a pronounced energy dependence. The soft lag of $\sim 150\,\mathrm{s}$ between the (0.2–1) keV band and the (1–8) keV band emission might reflect a travel time of a perturbation in the jet. Moreover, the tentative detection of a red-shifted iron line in 0716+714 is reported. The line is visible as excess emission at $\sim 5.7\,\mathrm{keV}$ in March 2002, the epoch in which the inverse Compton component is weak. If this excess is attributed to the $\mathrm{Fe\,K}_{\alpha}$ line at $6.4\,\mathrm{keV}$ in the source rest frame, the redshift of 0716+714 can be determined to $z = 0.12^{+0.04}_{-0.06}$.

6.5.1   VLBA 2 cm Survey Observations of 0716+714

0716+714 has been observed five times between 1994 and 2001 with the VLBA as part of the 2 cm Survey: 1994, August 31, 1996, July 10, 1996 October 27, and 2001 March 4[11].

The disclosure of the kinematics of this source on parsec scales is complicated by a variety of problems[12]: 1) The source can be described by an extraordinarily bright core and a weak jet without characteristic morphological features that can be cross-identified unambiguously over the epochs. 2) No VLBA 2 cm Survey observation of 0716+714 took place between October 1996 and July 1999. Moreover, the data from from October 1996 had to be discarded since the data quality in this epoch was substantially lower than in

---

[11]After 2001 0716+714 monitoring observations have continued as part of the VLBA 2 cm Survey follow-up project MOJAVE. At present, data from four additional epochs between August 2003 and January 2005 have been acquired and will be analyzed elsewhere.

[12]Compare Sect. D.1
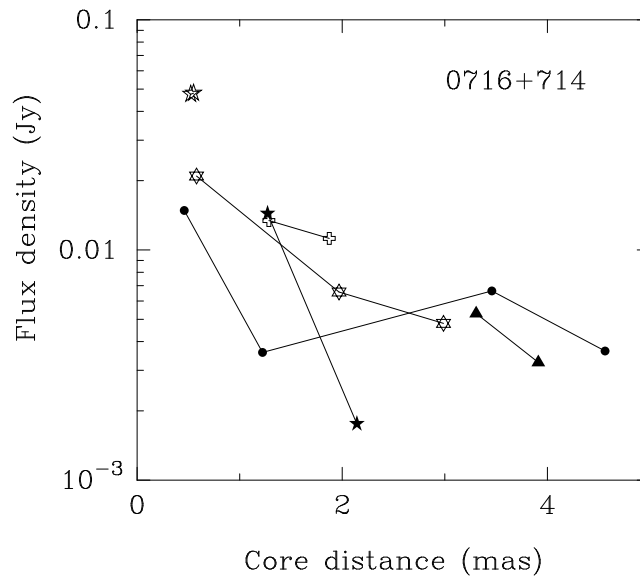
Figure 6.34: Flux density of different model components in 0716+714 as a function of core distance (see Fig. D.1 for the positions).

the other epochs. Thus, a gap of 3 years without usable data has to be bridged. 3) There is no common consensus on the proper motion of jet features in 0716+714 yet. Gabuzda et al. (1998) and Witzel et al. (1988) measured subluminal velocities below $1 \, \text{mas yr}^{-1}$. However, their results were based on only a small number of observing epochs which were separated by several years and thus not sensitive to superluminal motions. Jorstad et al. (2001) measured velocities of moving jet components of 0.9–$1.2 \, \text{mas yr}^{-1}$ from multiple, densely sampled observations at 22 GHz. Recently, Bach et al. (2005) presented a kinematical model of 0716+714 based on multiple observations at multiple frequencies at 5, 8.4, 15, and 22 GHz spread over ten years and derived smaller velocities than Jorstad et al. (2001) of 0.3–$0.9 \, \text{mas yr}^{-1}$.

The four epochs of observations of 0716+714 between August 1994 and March 2001 have been imaged, calibrated, and (u, v)-model fitted by applying standard VLBI data reduction procedures using the software packages AIPS and DIFMAP as described, e.g., in Kadler et al. (2004c). It turned out that at least 3–5 jet components were needed to adequately model the complex visibilities. The most plausible component identification allows 2 components to be traced over more than 3 epochs with velocities of 0.5–$0.7 \, \text{mas yr}^{-1}$. However, an alternative identification cannot be ruled out with smaller velocities (indicated by dashed lines in Fig D.1) of 0.3–$0.5 \, \text{mas yr}^{-1}$. The rapid decrease of the flux density of component C (see Fig. 6.34), however, suggests that the fast-speeds identification scenario is correct and component C has vanished by July 1999.

6.5.2 *XMM-Newton* Observations of 0716+714

Observations and data analysis: 0716+714 is contained within the field of view of three archival *XMM-Newton* observations performed in April 2001 (epoch 1), September 2001 (epoch 2), and March 2003 (epoch 3). These observations (see Table 6.12) aimed at the nearby group of galaxies C 0720.8+7109 from which 0716+714 is separated by only
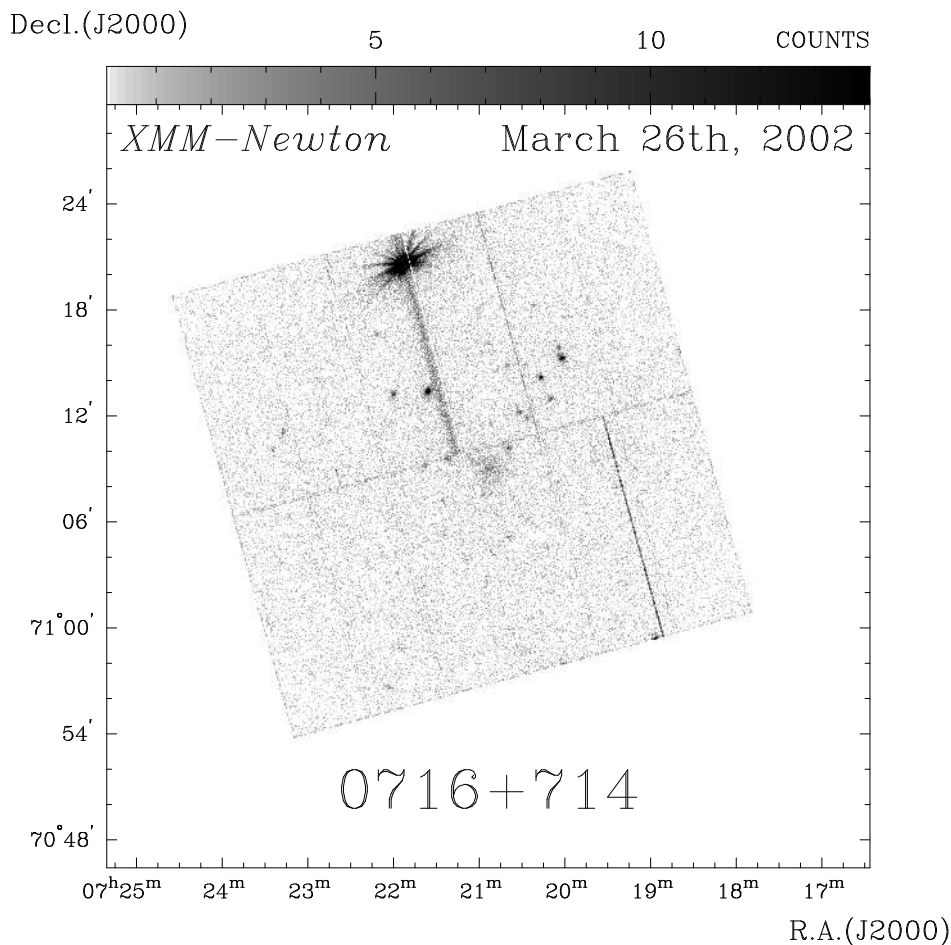
Figure 6.35: Raw photon image of the *XMM-Newton* pn-chip during the 6.6 ksec observation of the galaxy cluster C 0720.8+7109 in March 2002. 0716+714 is visible as a bright point source close to the top edge of the image.

$\sim 12'$. All three observations make use of the EPIC cameras (Turner et al. 2001a, Strüder et al. 2001) in full frame mode. In epoch 1 the net exposure time of the PN chip was more affected by a strong proton flare than the net exposure time of the MOS chips and in epoch 2 the PN camera did not collect any data, so that only the combined MOS data are used for the analysis of these two epochs. For epoch 3, the MOS and PN detector data are analyzed. The data have been reprocessed using the SAS 5.4.1 software package and only single and double events (PATTERN ¡= 4) have been considered for the PN data sets to reduce the effect of pile-up. Questionable photon events have been rejected for the spectral analysis by setting FLAG == 0. This most conservative flagging criterion ensures that the spectral results are not artifically degraded by events, e.g., on or next to bad pixels or rows, close to the edges of the chips, by electronic noise, or pile-up. Mainly the PN data of epoch 3 are affected by this, since a fraction of the source close to the edges of CCD 1 and CCD 4 of the PN detector and another region close to a row with strong readout noise is rejected. This mimics a lower source flux due to a partial masking of the source. Therefore, also the PN spectrum that includes all events is shown for comparison (in the following denoted as "unflagged" spectrum). The formal results of the spectral

Table 6.12: Journal of *XMM-Newton* observations of 0716+714.

Date	Obs. ID	Analyzed Data Set	Start of Exposure (UT)	Effective Exp. Time
13.04.2001 (*Epoch 1*)	0012850101	MOS1/2	17h:09m:15s	7950 s
19.09.2001 (*Epoch 2*)	0012850601	MOS1/2	06h:58m:20s	9200 s
26.03.2002 (*Epoch 3*)	0012850701	PN MOS1/2	06h:17m:26s 05h:44m:34s	6650 s 8900 s

fitting are given in Table 6.13. In the case of both MOS detectors only FLAG == 0 events were considered, given that only a small number of events are rejected. Circular regions with radii of 62″, 76″, and 115″ around the source in epoch 1, 2, and 3, respectively, and annuli around these regions were selected to extract source and background spectra. Response matrices and ancillary files have been calculated using the tasks RMFGEN and ARFGEN and the spectra were binned to obtain a minimum of 25 counts per bin using GRPPHA (the unflagged PN spectrum of epoch 3 is binned to 50 counts per bin to obtain a high-signal-to-noise signal for the individual data points, which are by definition stronger affected by noise than the individual data points of the flagged spectrum.). The spectral fitting was performed within XSPEC 11.2.0. Errors of fit parameters have been determined at 90% confidence range for one parameter of interest ($\Delta\chi^2 = 2.706$).

Spectral Analysis Results: In this section the fits to the (0.2–8) keV X-ray spectra of the three epochs of *XMM-Newton* observations of 0716+714 are presented. For each
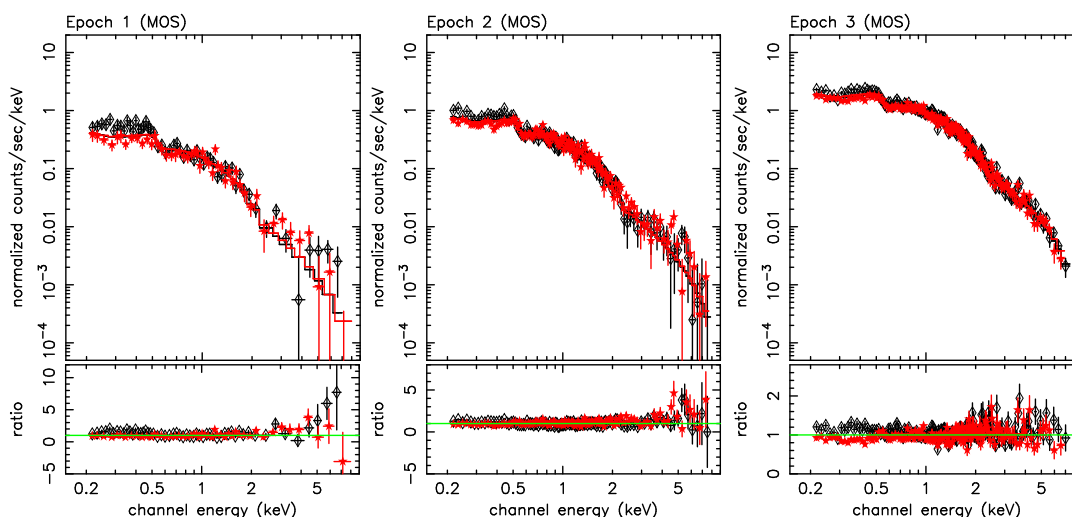
Figure 6.36: X-ray spectra of 0716+714 between 0.2 keV and 8 keV from the two MOS detectors at all three epochs (top panels). Diamonds mark MOS 1 and stars mark MOS 2 data, respectively. The solid line indicates the single-power-law model (see Table 6.13). The residuals are shown in the bottom panels.
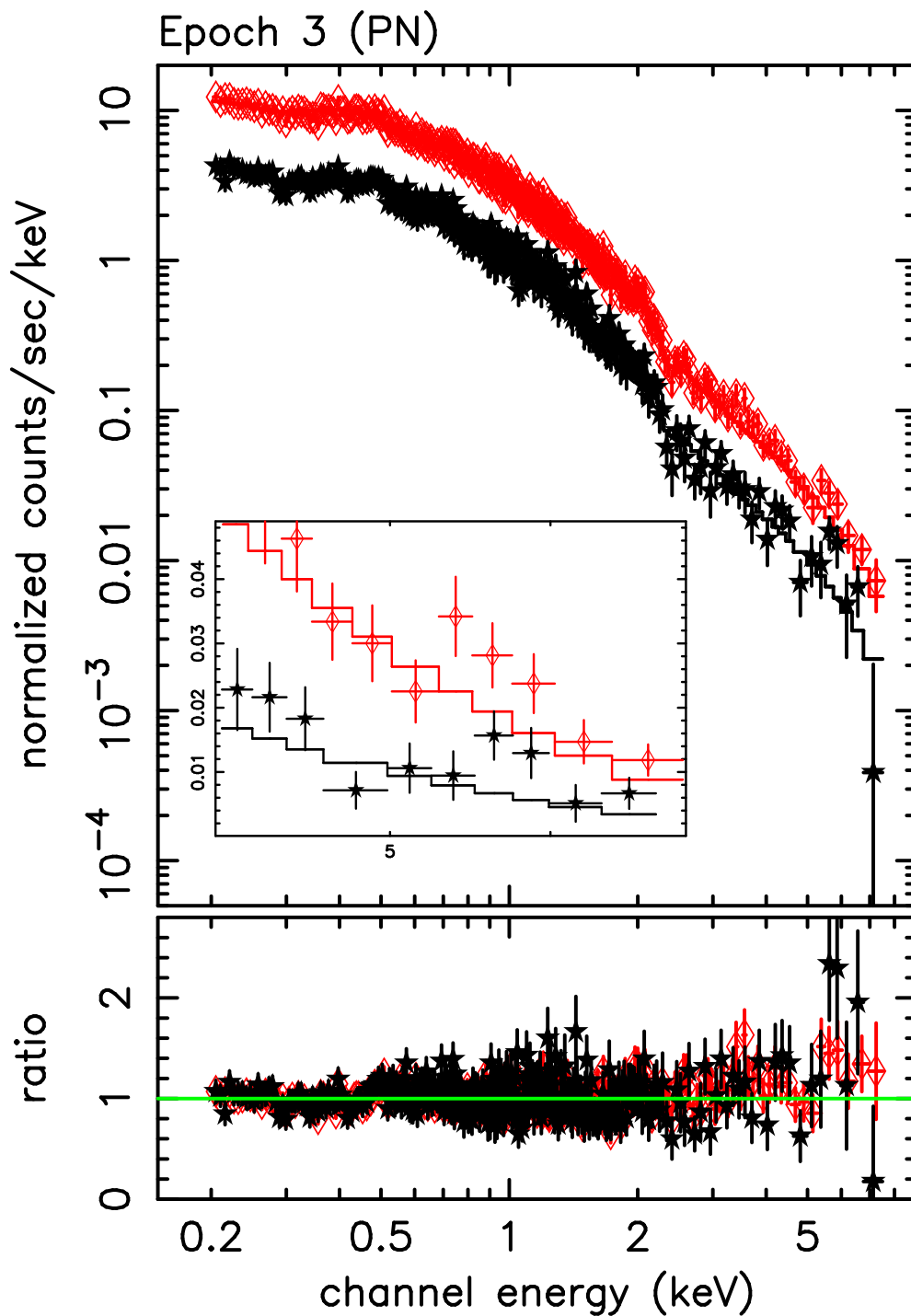
Figure 6.37: X-ray spectrum of 0716+714 between 0.2 keV and 8 keV at epoch 3 from the PN detector (top panel). Diamonds correspond to the unflagged spectrum, while stars show the spectrum extracted with FLAG == 0. The solid line indicates the single-power-law models (see Table 6.13) without the contribution of the Gaussian line component to make the line visible as excess emission in the residuals (bottom panel). The offset between the two curves is due to the rejection of a substantial fraction of the area covered by the source by the flag. An enlarged view of the 4 to 7 keV range of the spectrum is shown in the inlaid panel (with linear scaling).

Table 6.13: X-ray spectral fit parameters for the three epochs of *XMM-Newton* observations of 0716+714.

	Abs. Power-Law				Best Model							
Detector	N_H $[10^{20}\,\text{cm}^{-2}]$	Γ	Flux$_{(0.2-8)}$ $[\text{erg}\,\text{cm}^{-2}\,\text{s}^{-1}]$	χ^2_{red}/d.o.f.	N_H $[10^{20}\,\text{cm}^{-2}]$	Γ_1	Γ_2	Line Center [keV]	Line FWHM [keV]	Flux$_{(0.2-8)}$ $[\text{erg}\,\text{cm}^{-2}\,\text{s}^{-1}]$	χ^2_{red}/d.o.f.	P†
			Epoch 1					*Epoch 1*				
MOS 1/2	3.35*	$2.98^{+0.06}_{-0.07}$	0.6×10^{-11}	1.66/101	$4.52^{+0.38}_{-0.38}$	$4.08^{+0.08}_{-0.09}$	$2.20^{+0.12}_{-0.13}$	-	-	0.6×10^{-11}	1.52/99	0.4%
			Epoch 2					*Epoch 2*				
MOS 1/2	3.35*	$2.95^{+0.02}_{-0.03}$	0.9×10^{-11}	1.31/247	$3.37^{+0.18}_{-0.18}$	$3.21^{+0.03}_{-0.04}$	$1.85^{+0.12}_{-0.12}$	-	-	1.0×10^{-11}	1.23/243	0.06%
			Epoch 3					*Epoch 3*				
MOS 1/2	3.35*	$2.70^{+0.02}_{-0.01}$	3.0×10^{-11}	1.70/333	-	-	-	-	-	-	-	-
PN$_{Flagged}$	$4.70^{+0.15}_{-0.16}$	$2.84^{+0.02}_{-0.03}$	-	0.92/294	$4.81^{+0.17}_{-0.15}$	$2.85^{+0.03}_{-0.02}$	-	$5.7^{+0.2}_{-0.1}$	$0.19^{+0.31}_{-0.15}$	-	0.90/291	0.7%
PN$_{Unflagged}$	$4.30^{+0.09}_{-0.09}$	$2.77^{+0.01}_{-0.01}$	3.0×10^{-11}	1.21/335	$4.37^{+0.09}_{-0.10}$	$2.78^{+0.01}_{-0.01}$	-	$5.7^{+0.3}_{-0.2}$	$0.26^{+1.35}_{-0.13}$	3.0×10^{-11}	1.20/332	9.7%

* Parameter hit the lower bound of Galactic absorption

† Probability that the statistical superiority of the best model over the absorbed power-law model occurred by chance calculated from an F-test in XSPEC. Note the discussion in the text.

epoch the data of the two MOS detectors were fitted simultaneously. First, a single absorbed power law was fitted to each data set. The resulting parameters are given in Table 6.13. Where necessary, the models have been modified by introducing additional spectral components to account for apparent systematic residuals. The absorbing column density was fitted with the value of Galactic absorption of $3.35 \times 10^{20}\,\mathrm{cm}^{-2}$ (Hartmann and Burton 1997) set as a lower boundary of the parameter space.

In epoch 1 and 2 a single absorbed power law gives no satisfactory fit to the (0.2–8) keV spectrum of 0716+714. In both cases large residuals indicate the presence of an additional hard spectral component. The reduced χ^2 decreases significantly if a second power law is introduced (compare Table 6.13). While the first power law, which dominates the soft part of the spectrum, is very steep ($\Gamma > 3$), the second power law is comparatively flat. The overall X-ray spectrum of 0716+714 during these two epochs in 2001 is similar to the reported spectral shape during several *Beppo*SAX observations of this source (Tagliaferri et al. 2003, Giommi et al. 1999). A value of $4.5^{+0.3}_{-0.3} \times 10^{20}\,\mathrm{cm}^{-2}$ for the absorbing column density is derived in epoch 1 from the best fitting two-power-law model, while no excess over the galactic value is derived for the single-power-law model. In epoch 2 neither fit shows any evidence for additional, source-intrinsic absorption. No stable two-power-law model could be established for the MOS data of epoch 3 since in all iterations the slopes of the two power laws converged to the same value while the flux was divided between the two. The results of the spectral fitting of a single-power-law model are comparable to the other two epochs apart from a higher data quality due to the higher brightness of the source during this epoch.

The inspection of the residuals of the MOS data in all three epochs shows a systematic discrepancy between the MOS 1 and the MOS 2 detector in the soft energy range (see Fig. 6.36). This might be due to residual calibration uncertainties at large off-axis angles, which, however, do not affect the main results of this analysis.

In Fig. 6.37 the (0.2–8) keV X-ray spectrum extracted from the PN data of the epoch 3 observation of 0716+714 is shown. Although it has to be noted that the spectral information derived from the flagged data is more reliable than the one from the unflagged data, the results of the spectral fitting agree very well in both cases. A simple absorbed power law gives a very good fit to the data with a reduced χ^2 of 0.92 and 1.21 for the flagged and unflagged spectrum, respectively. The absorbing column density was fitted to $\sim 4.5 \times 10^{20}\,\mathrm{cm}^{-2}$. The photon index is very steep ($\Gamma \sim 2.8$) and there is no apparent flattening of the spectrum at high energies. However, there is a significant excess around 6 keV, which will be discussed below. As for the MOS data the PN spectrum of epoch 3 could not be approximated by a stable two-power-law model.

From the fitted spectral models (absorbed) fluxes in the (0.2–8) keV range of (0.6–1.0)$\times 10^{-11}\,\mathrm{erg\,cm}^{-2}\,\mathrm{s}^{-1}$ during epoch 1 and 2 are derived. In epoch 3 the source was considerably brighter with a flux of $\sim 3.0 \times 10^{-11}\,\mathrm{erg\,cm}^{-2}\,\mathrm{s}^{-1}$. The intrinsic ratio of unabsorbed fluxes of the two power-law spectral component is 2.3 and 5.6 in epoch 1, and 2, respectively, i.e., the soft and steep power law, which can be identified with a primary synchrotron component, dominates the hard and flat power law, which we attribute to a secondary inverse Compton component, in both epochs.

Tentative detection of an iron line in 0716+714:   The PN *XMM-Newton* spectrum of 0716+714 in epoch 3 shows significant excess emission around 6 keV (see Fig. 6.37)

which is well approximated by a Gaussian component. The fitting procedure of the flagged data set gives an energy of $5.7^{+0.2}_{-0.2}$ keV for the line center and a full width at half maximum (FWHM) of ~ 0.2 keV. Statistically, the introduction of the line component improves the reduced χ^2 from 0.92 (for 294 degrees of freedom) to 0.90 (for 291 degrees of freedom) corresponding to a probability of 0.7% that the improvement of the fit occurred by chance according to the F-test performed with XSPEC. It has to be noted that the application of the F-test is not strictly correct if the presence of a spectral line shall be tested (see Protassov et al. 2002) but should be considered as a simple mean to estimate a lower bound for the line significance. For comparison, we show in Fig. 6.37 also the unflagged PN spectrum, which exhibits positive residuals around 6 keV as well. The significance in this case, however, is smaller, with a 9.7% chance probability. The combined MOS spectra of the same observation do not show evidence of an additional line component (see Fig. 6.36). We do not find any significant evidence for the presence of a line feature in the (5-6) keV energy regime in any of the other two epochs.

If the excess emission around 5.8 keV in epoch 3 is interpreted as the signature of iron line emission at a rest energy of 6.4 keV, a formal redshift of $z = 0.12^{+0.04}_{-0.06}$ can be inferred. This is considerably lower than the expected redshift of 0716+714 of $z > 0.3$ derived by Wagner et al. (1996). Their lower limit was based on the non-detection of an optical host galaxy down to a magnitude of -21. The average brightness of BL Lac host galaxies is indeed much higher ($M_R = -23.9 \pm 0.8$, Nilsson et al. 2003). If the measured redshift of the line feature in the *XMM-Newton* spectrum indeed reflects the true distance to 0716+714, its host galaxy has to be of unusual low luminosity.

Timing Analysis Results: Fig. 6.38 shows the light curve of 0716+714 during epoch 3 recorded by the PN and the (merged) MOS cameras, respectively. No long proton flares occurred during the exposure, only a short spike after 7000 s of observations did occur in the background light curve and affects also the source light curve at high energies ($> \sim 2$ keV). In the timing analysis of the (3-8) keV band, in which this background flare becomes more prominent, a filtered light curve was used to reject the affected time range. The source itself was variable during the whole exposure time with characteristic time scales from a few hundred to ~ 1000 seconds. The light curve exhibits a broad maximum during the first 4000 s, a pronounced increase of the count rate by more than 50% within 1000 s, and a slight decrease during the last 2000 s of the observation. Local maxima are present after ~ 5000 s and ~ 6000 s, as well as a local minimum just before the end of the exposure after ~ 6500 s. The photon statistics for the light curve analysis can be improved by reconsidering the events that were rejected by the FLAG == 0 criterion, which in principle, does not introduce significant uncertainties in the photon count rates. For comparison, Fig. 6.38 shows the PN light curve for both cases: qualitatively, the course of the count rate is the same but the photon statistics benefit considerably from the inclusion of the additional events, especially from the photons close to the edges of the chips. This unflagged light curve can be considered as representative of the true source variability, the more so as it exhibits the same trend as the MOS light curve. The same general behavior of the light curve is found in several energy bands between 0.2 keV and 8 keV. Above 8 keV, however, no firm statement about source variability can be made due to the low count rate in the (8–12) keV band. In Fig. 6.39 the PN light curves for epoch 3 in two separate bands between 0.2 keV and 1 keV, and between 1 keV and 8 keV is shown. Unflagged light
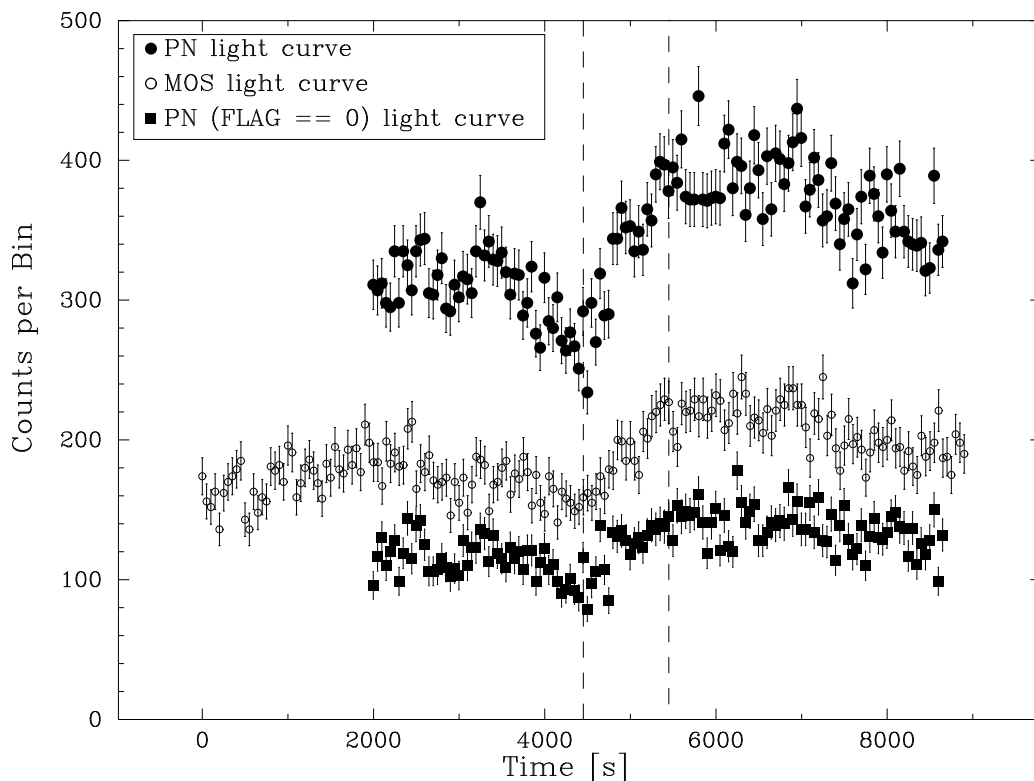
Figure 6.38: X-ray Light curves of 0716+714 between 0.2 keV and 12 keV during epoch 3. Filled circles indicate single and double photon events recorded by the PN chip integrated over 50 s bins. Filled squares represent the remaining events if the most conservative flagging criterion (FLAG == 0) is applied. Open circles show the (0.2–12) keV light curve recorded by the MOS chips (event lists of the MOS 1 and MOS 2 chip are merged) integrated over 100 s bins. The pronounced 1000 s rise of the light curve is indicated by dashed lines.

curves were used in order to maintain a sufficient signal-to-noise ratio especially in the high energy band. The mean count rate of the (1–8) keV light curve was rescaled to match the mean value of the (0.2–1) keV light curve. The running mean of both light curves was calculated with the software GRACE 5.1.4 using bins of 5 data points. This procedure basically removes the short term variability (the source intrinsic noise) from the power spectrum of the light curves and allows a cross correlation of the resulting smoothed light curves. We found a high maximal cross correlation coefficient of > 0.8 at a time lag of (150 ± 25) s by which the soft-band light curve follows the hard-band light curve while the relative amplitudes in both bands are approximately the same. It is remarkable that the light curves from both bands resemble each other so well since Giommi et al. (1999) and Tagliaferri et al. (2003) find no variability above 3 keV during pronounced flares of the soft band light curve. To test, if the (1–8) keV light curve variability is dominated solely by photons below 3 keV, a time filtered source light curve for the (3–8) keV band was produced (see Fig. 6.40). To achieve sufficient photon statistics the data had to be integrated over 250 s bins. This results to a poor temporal sampling and prevents one from studying the time delay between these high energy photons and the softer photons in the (0.2–1) keV and the (1–3) keV bands. However, the data show weak evidence for
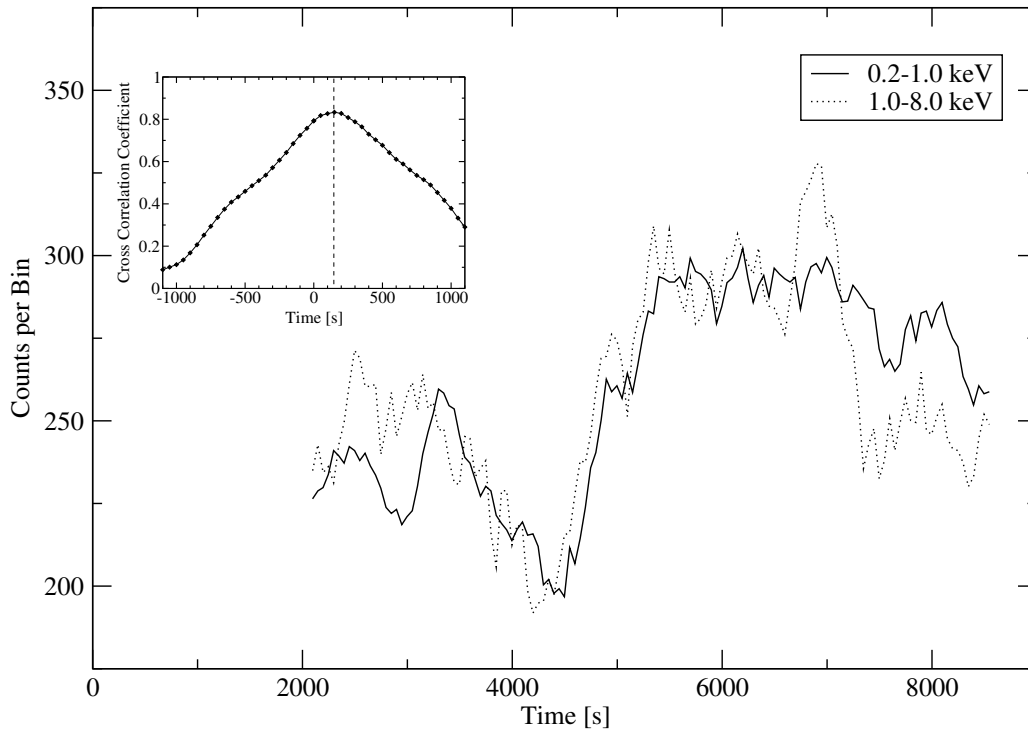
Figure 6.39: X-ray light curves of 0716+714 during epoch 3 recorded by the PN chip in 50 s bins of two separate energy bands between 0.2 keV and 1 keV (solid line) and between 1 keV and 8 keV (dotted line). The mean value of the count rate in the hard band has been rescaled to the mean value in the soft band and a running mean calculation (using bins of 5 data points) has been applied to both light curves. The soft-band light curve follows the hard-band light curve with a time lag of $\sim$150 s. The inlaid panel shows the cross correlation function of the two curves.

source variability also above 3 keV with a relatively stable count rate of $\sim 0.18\,\mathrm{cts\,s^{-1}}$ during the first 4000 sec of the observation and strong variations between $\sim 0.10\,\mathrm{cts\,s^{-1}}$ and $\sim 0.24\,\mathrm{cts\,s^{-1}}$ during the last 5000 sec. The significance of the variability during the latter *post-flare* state is obvious. For illustration, the expected 1-σ scatter range for a stable source is drawn in Fig. 6.40. Qualitatively, the low-sampled (3–8) keV band light curve resembles the soft band light curves with a local maximum after 5000 s of observations, a systematic increase between 5000 s and 6000 s of observations and a local minimum at the end of the exposure time but the low number of photons above 3 keV do not allow one a more quantitative analysis.

The strong correlation between the (0.2–1) keV and the (1–8) keV light curve shows that during epoch 3 only one physical process, most likely synchrotron emission from the jet, contributes considerably to the X-ray spectrum of 0716+714 below 8 keV. Lags between soft and hard X-rays have been reported for a small number of other BL Lac objects, e.g. in Mrk 421 (Fossati et al. 2000; Takahashi et al. 2000; Brinkmann et al. 2003), Mrk 501 (e.g., Tanihata et al. 2001), and PKS 2155-304 (Zhang et al. 1999; Kataoka et al. 2000), often in combination with spectral changes during intensity variations. Although, soft lags are more common, Tanihata et al. (2001) showed that also hard lags do occur during several flares. Moreover, Brinkmann et al. (2003) present evidence that the dura-
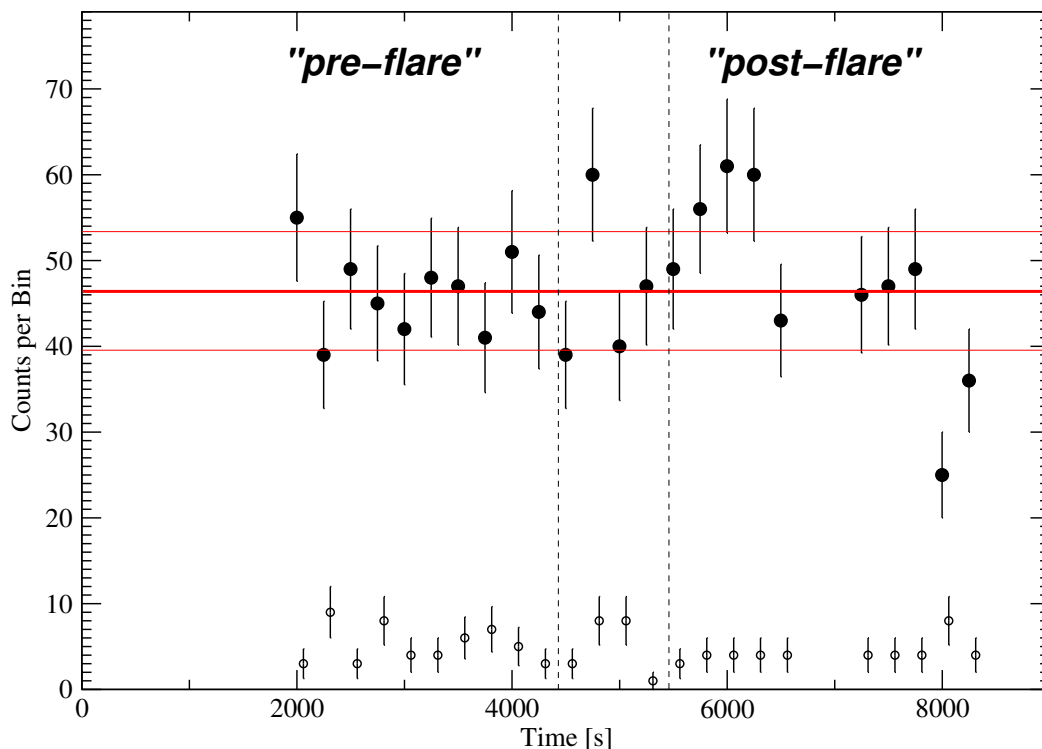
Figure 6.40: Filtered X-ray light curve of 0716+714 between 3 keV and 8 keV during epoch 3 (filled circles). Only single and double photon events recorded by the PN chip were considered and integrated over 250 s bins. The 1000 s lasting rise of the soft light curve (*flare*) is indicated by dashed lines, dividing the hard light curve into a *pre-flare* and a *post-flare* state. The measured background level for each time bin is shown with open circles. The thick solid line indicates the mean value, averaged over the whole observing range (46.6 counts/bin), the thin solid lines indicate the corresponding 1-σ scatter range for a stable source.

tion of a flare and the size of the delay between soft and hard photons may be related, with the shorter flares typically exhibiting smaller time lags. The short-term spectral variability of 0716+714 at X-rays is typical for a BL Lac objects in this sense and the additional simultaneity of radio/optical correlations (Quirrenbach et al. 1991; Qian et al. 1996) and optical/X-ray variability (Giommi et al. 1999) demonstrate its key role in understanding the wealth of broadband variability phenomena in BL Lac objects.

Discussion: The analysis of three epochs of *XMM-Newton* observations of 0716+714 in April and September 2001, and in March 2002 demonstrates clearly the interplay between two main spectral components in the spectral energy distribution of this prominent BL Lac object. The results are consistent with the idea of a variable relative strength of synchrotron and inverse Compton emission induced by the jet. In epoch 1 and 2 a spectral break at ~ 1.5 keV is observed between a steep synchrotron component and a flatter inverse Compton component. In epoch 3 the synchrotron component dominates the whole spectrum up to 8 keV while the inverse Compton component is not detectable. The comparison of the determined column densities, particularly between epoch 2 and 3, suggest

that, in addition to the source flux, the absorber may be variable, as well.

The result that both the soft and the hard part of the spectrum is produced by the same emission mechanism in epoch 3 is underlined by the high correlation between variations in the (0.2–1) keV band and the (1–8) keV band during this epoch. The significant time lag between the (0.2–1) keV and the (1–8) keV light curve of (150 ± 25) s during this synchrotron dominated epoch may reflect a characteristic travel time of a perturbation in the jet flow. In a simple "one-zone-model" the hard photons are expected to respond earlier to changes of physical parameters due to the stronger radiation losses and correspondingly shorter life time of the radiating particles, i.e., the hard photons are "newer" than the soft photons. Alternatively, in a "two-zones-model" the hard X-ray photons may be produced from highly relativistic, energetic electrons within a region 1 centered around position r_1 close to the central engine. Within a region 2, centered around r_2 further down the jet, these high energy electrons are considerably attenuated (due to synchrotron or inverse Compton cooling) and the bulk emission of soft X-ray photons is maintained from less energetic electrons from region 2. Region 1 might be contained in the larger region 2 (since the low energy electrons need to travel a longer distance until they loose their energy), however, $r_1 < r_2$ will still hold. The time lag between the soft- and the hard-band light curve then reflects the travel time for the perturbation from r_1 to r_2. From the measured time delay of 150 s an upper limit for the travel distance $r_2 - r_1$ of $\sim \delta 1.5 \, \mu$pc can be estimated, where δ is the bulk Doppler factor of the of the jet. Implicitly, this also provides an upper limit for the physical size of the two X-ray emitting zones themselves.

The X-ray spectrum of 0716+714 obtained during epoch 3 exhibits excess emission at 5.7 keV over a power law spectral fit. This excess emission is not detected during the epochs 1 and 2, when the inverse Compton component was stronger. One may interpret this as the tentative imprint of a redshifted ($z = 0.12^{+0.04}_{-0.06}$) Fe K_α line. The absence of this line emission at the two epochs 1 and 2 can be understood in terms of the stronger inverse Compton continuum emission shining out the comparatively weak line. However, it is puzzling that line emission is detected during the synchrotron dominated epoch 3 since synchrotron emission is *a-priori* not expected to produce line emission. A possible explanation might be the contribution of a third emission process to the (0.2–8) keV spectrum of 0716+714 as, e.g., Compton reflected disk emission, from which, in principle, iron line emission is expected. Alternatively, the line might originate from the interaction of the jet with circumnuclear clouds, e.g., in the broad line region. Within this scenario it can not be excluded that the line might be intrinsically blueshifted due to dynamical processes of the region of cloud-jet interaction and that the measured net-redshift might not reflect the true distance of the source.

A consecutive monitoring of the X-ray spectrum of 0716+714 with *XMM-Newton* in conjunction with simultaneous optical, radio, and ideally also γ-ray observations is necessary to understand in detail the interplay between the synchrotron and inverse Compton emission in this source.

A   Residuals of Best-Fitting Spectral Models

In this appendix chapter, the residuals to the best-fitting spectral models from continued from Fig. A.1.in Chap. 4 are shown. The residuals are plotted for a common energy range to allow specific energies to be directly compared between the plots (e.g., the expected energy of a 6.4 keV iron line for a given object observed at multiple epochs).

For *ASCA* spectra, residuals for the two SIS detectors are shown in dark gray and GIS data in light grey. For *Beppo*Sax data, residuals for the LECS and MECS detectors are shown in dark and light gray, respectively, while PDS residuals in the energy range above 10 keV are shown in black. In *Chandra* observations, residuals are shown in dark gray for the ACIS-I or the ACIS-S detector, depending on which one was used in the observation (compare Table 3.1). The residuals of the two *XMM-Newton* MOS cameras are shown in light gray, whereas the *XMM-Newton* PN detector residuals are shown in dark gray. Note the different y-axis scalings in the different plots, that were adjusted to the range covered by the residuals. For illustration clarity, the spectra have been re-grouped to have less than 500 d.o.f. for these figures.
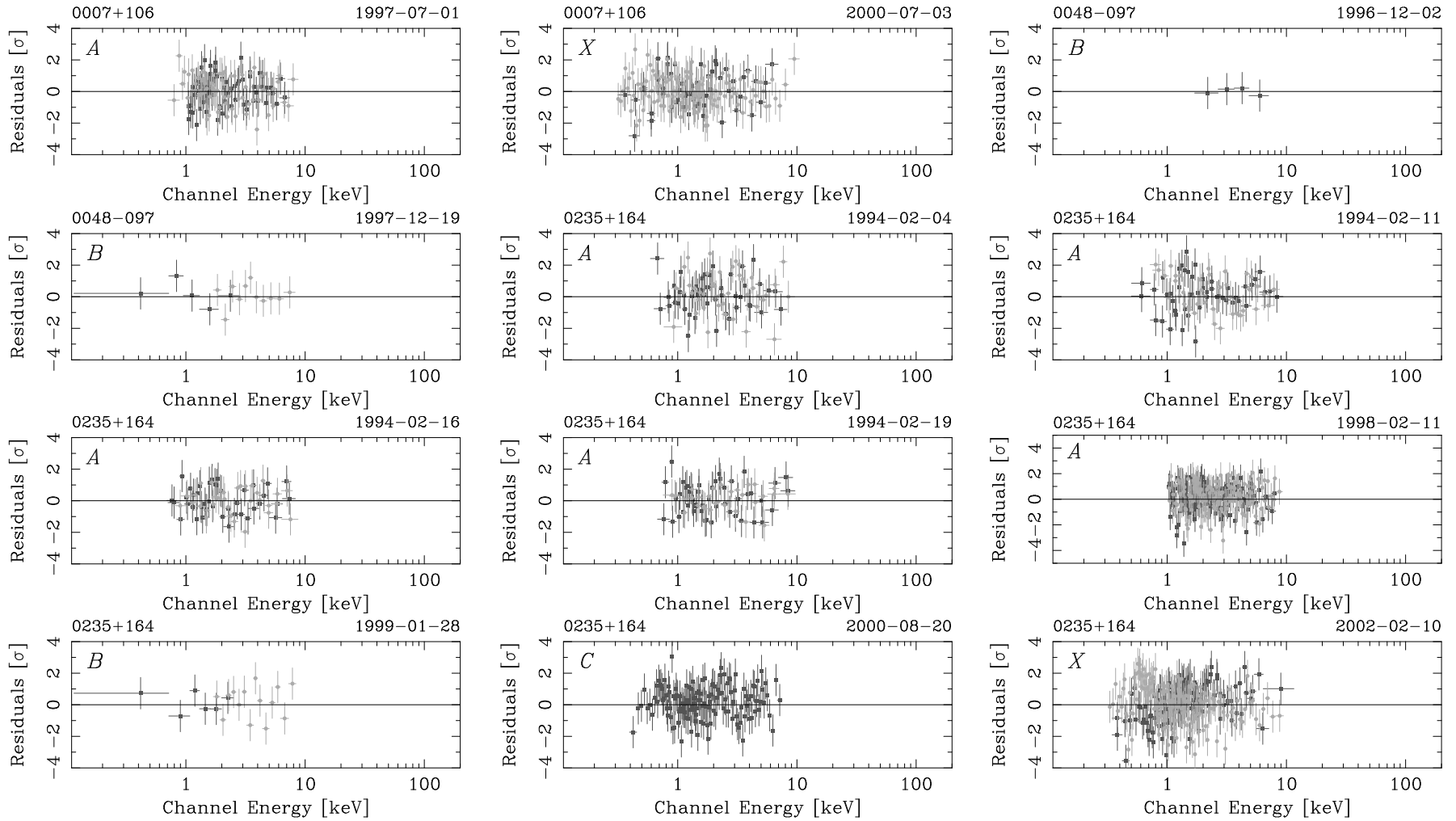
Figure A.1: Residuals of the best-fitting spectral models from Table 4.1–4.3.
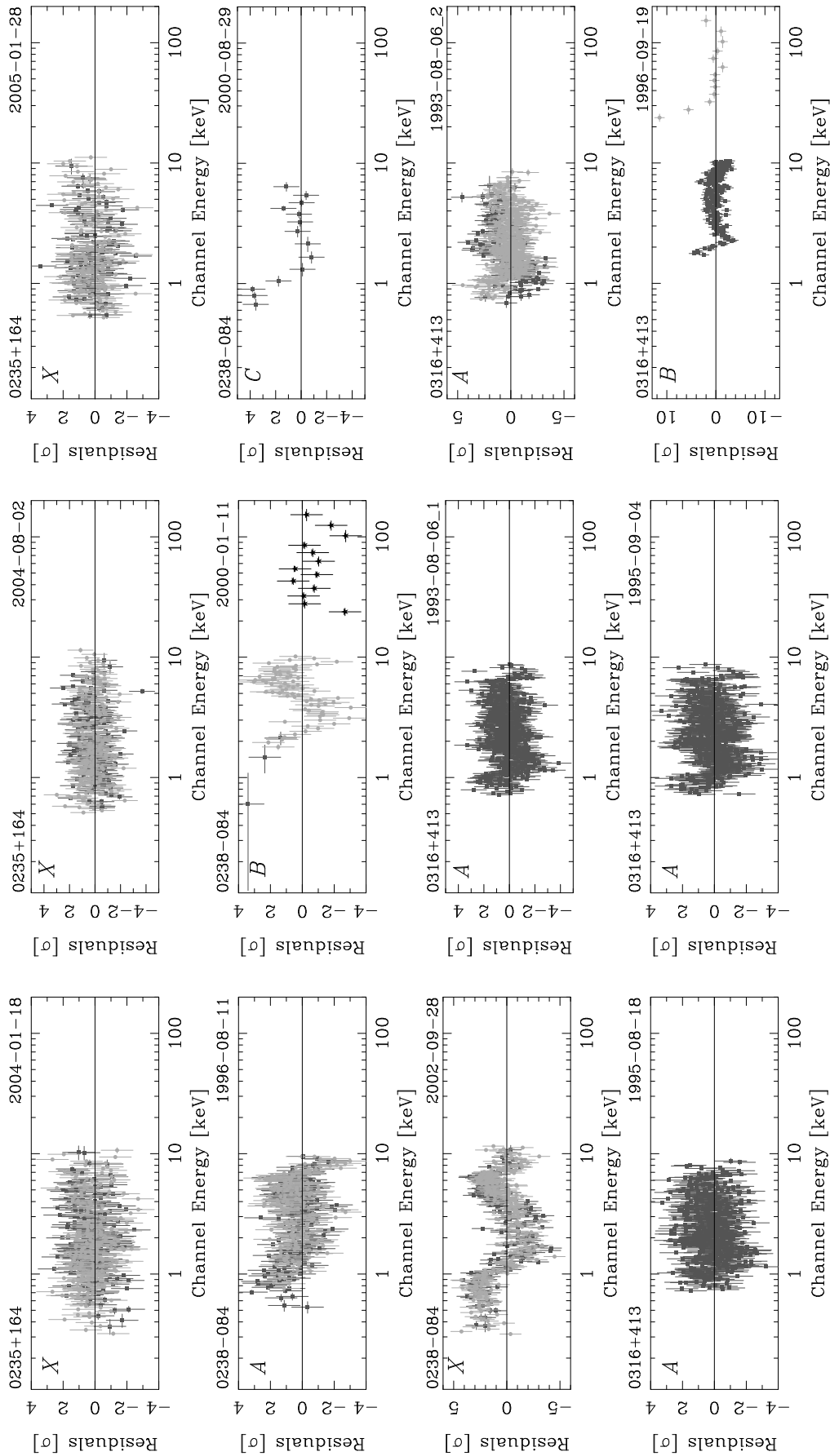
Figure A.1: continued
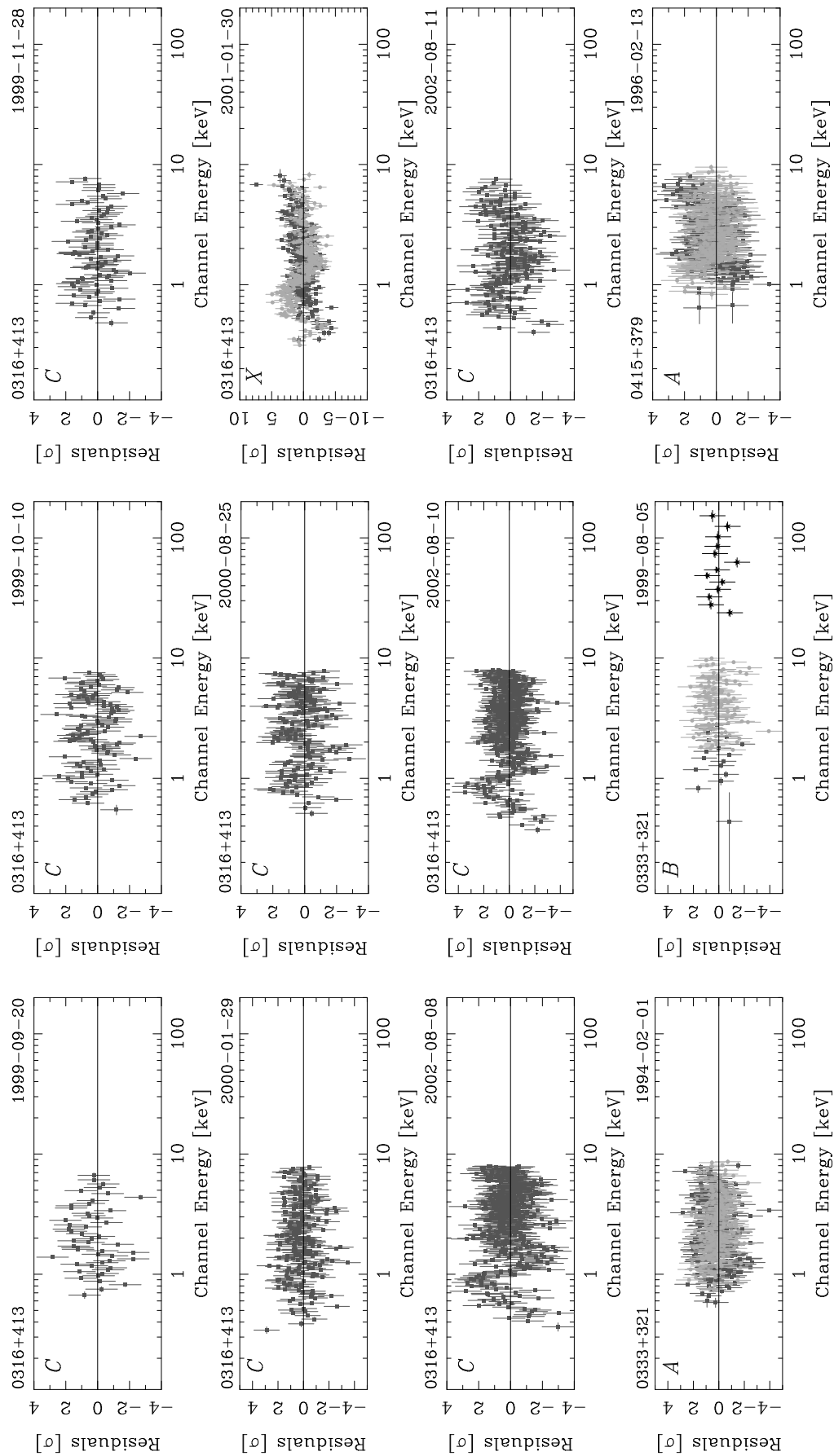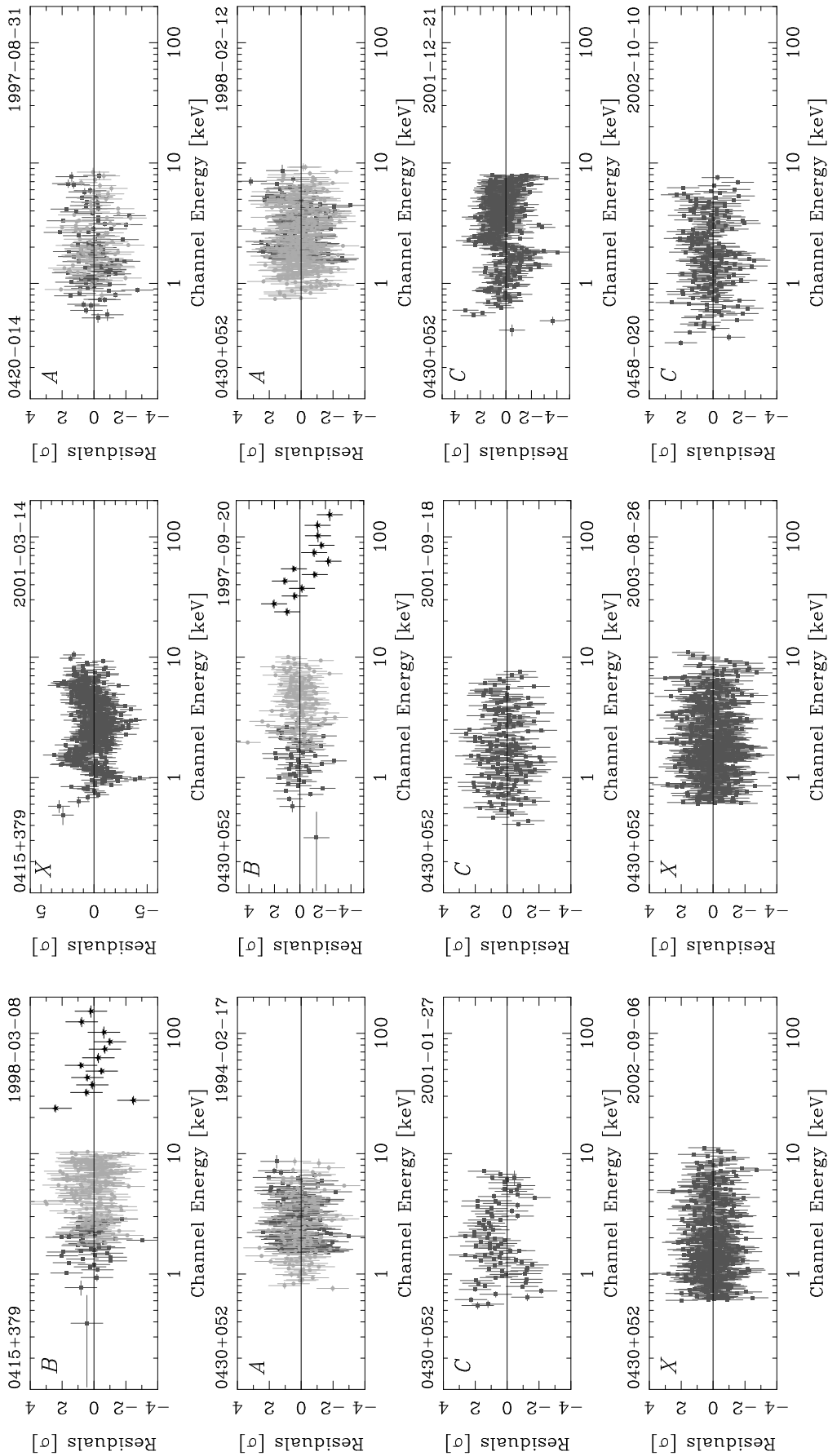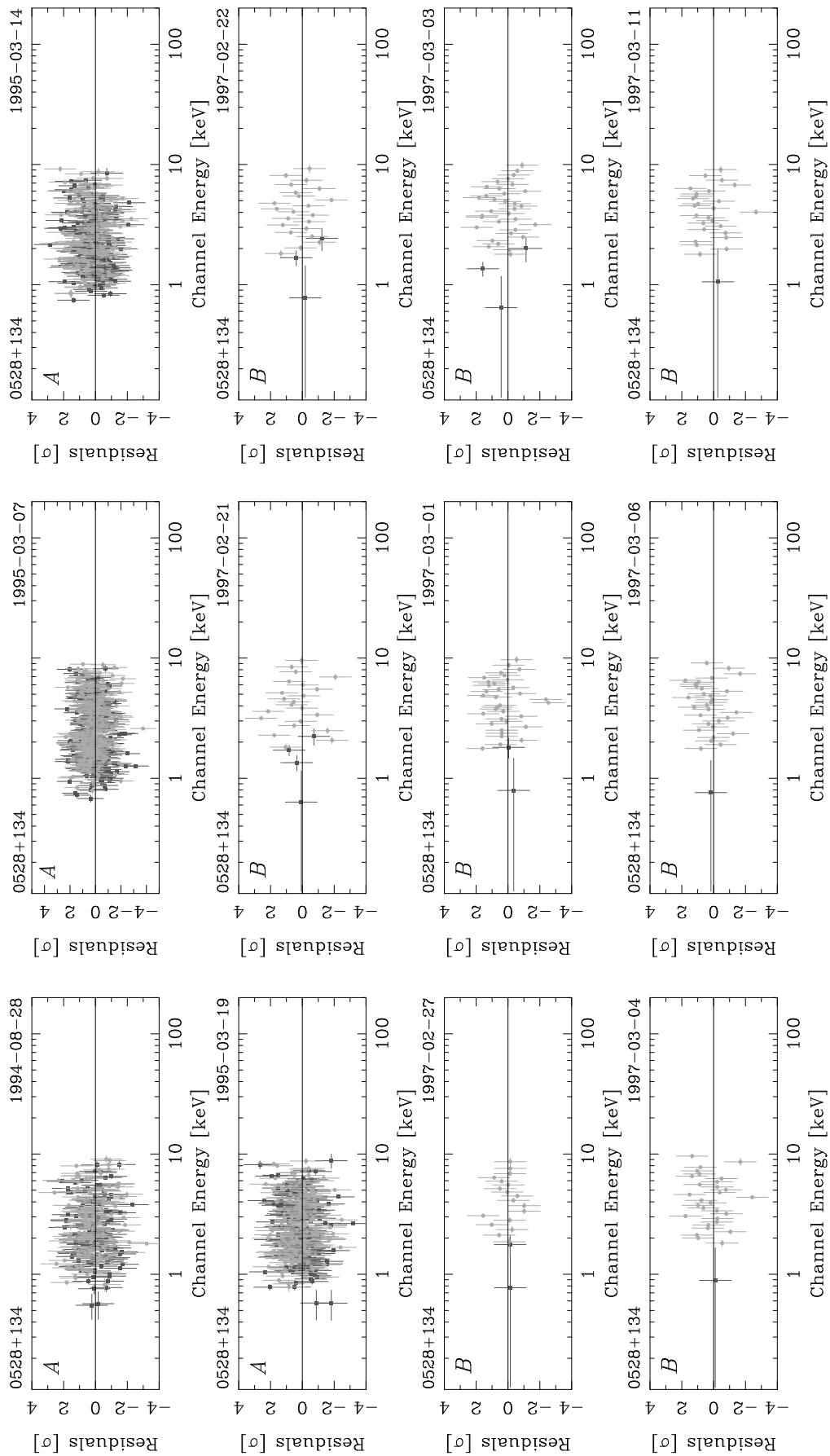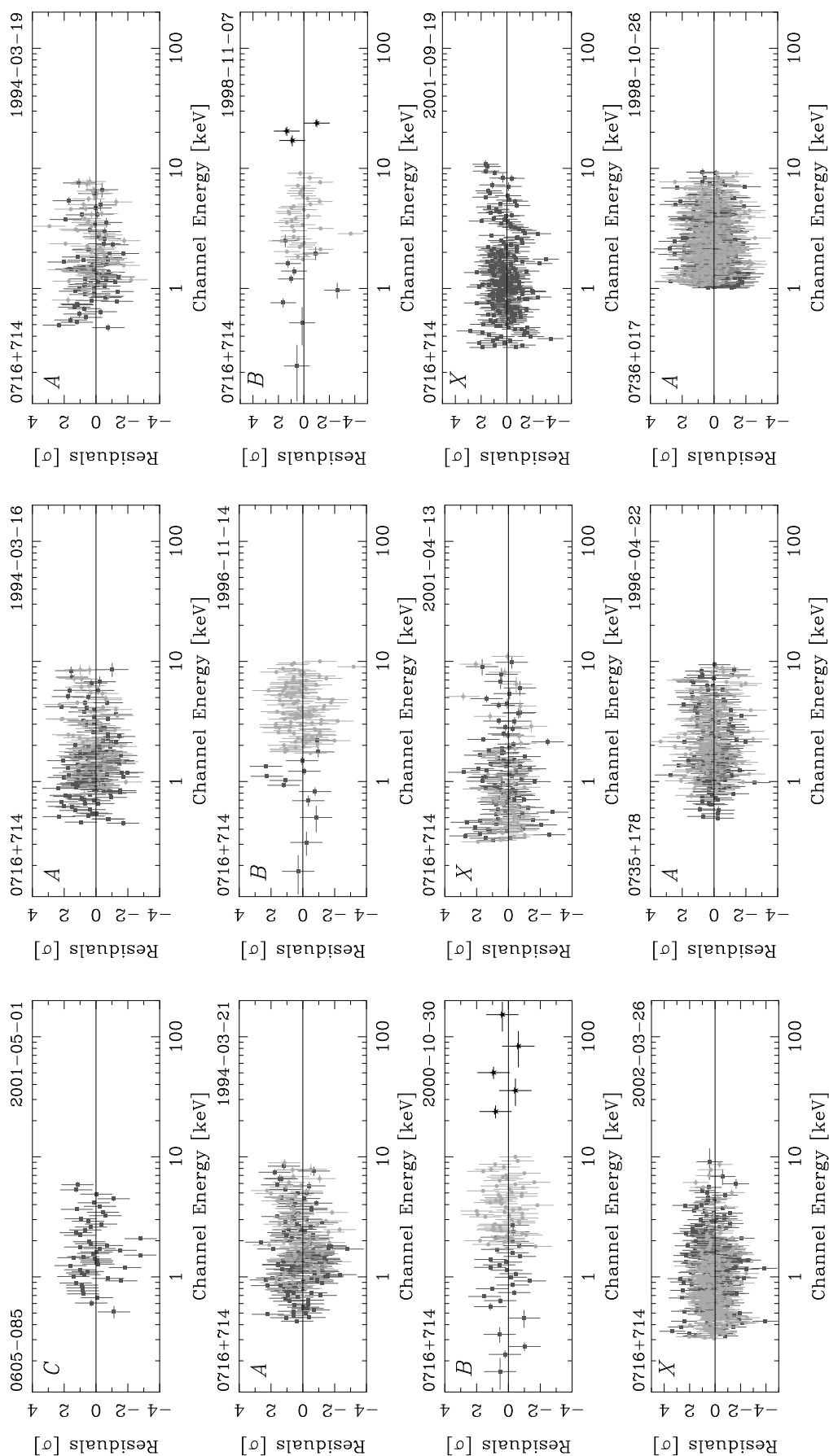
207

Figure A.1: continued

Figure A.1: continued

Figure A.1: continued

Figure A.1: continued

211

Figure A.1: continued

Figure A.1: continued

Figure A.1: continued

Figure A.1: continued

Figure A.1: continued

216

Figure A.1: continued

Figure A.1: continued

Figure A.1: continued

Figure A.1: continued

220

Figure A.1: continued

Figure A.1: continued

Figure A.1: continued

223
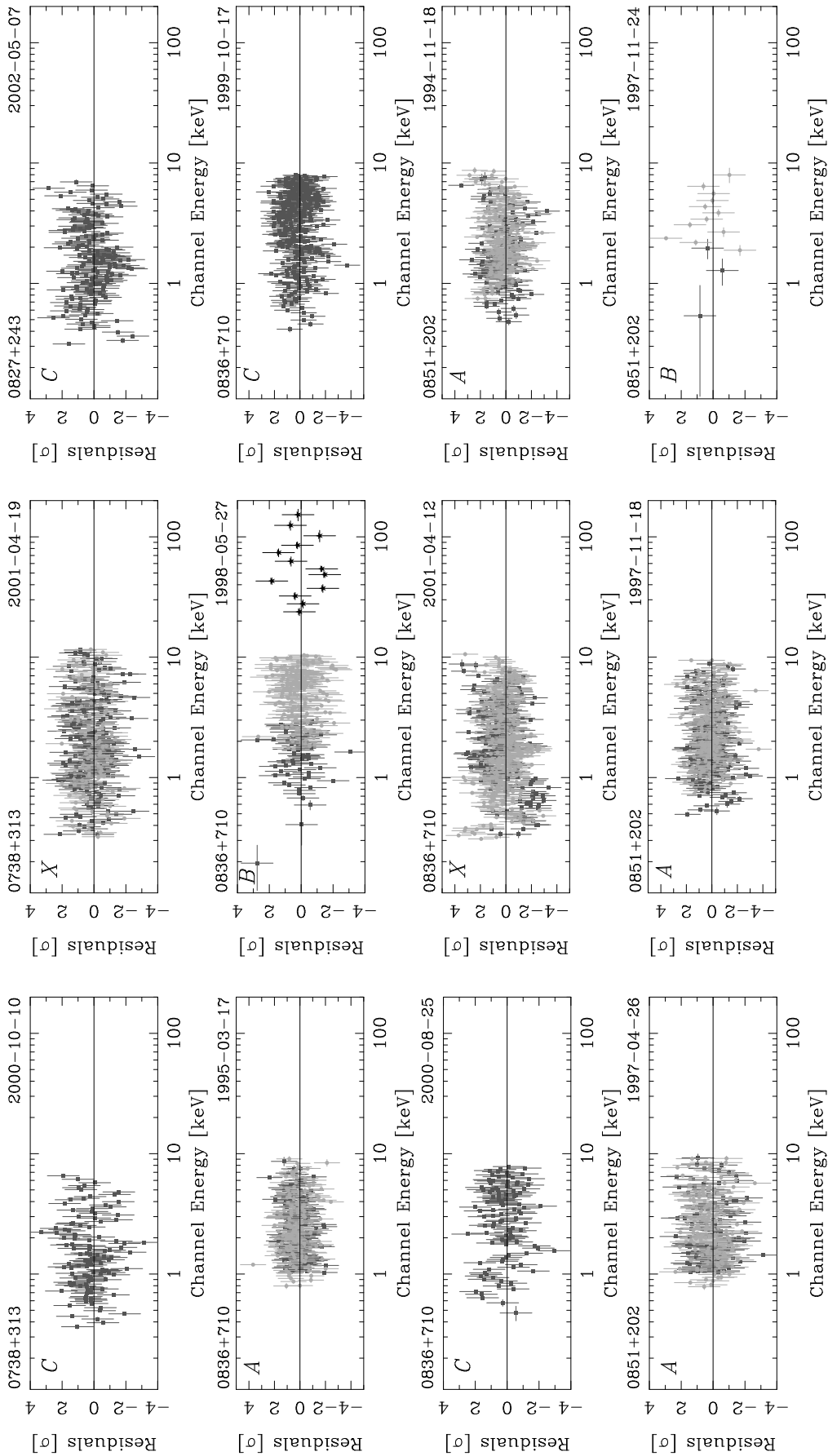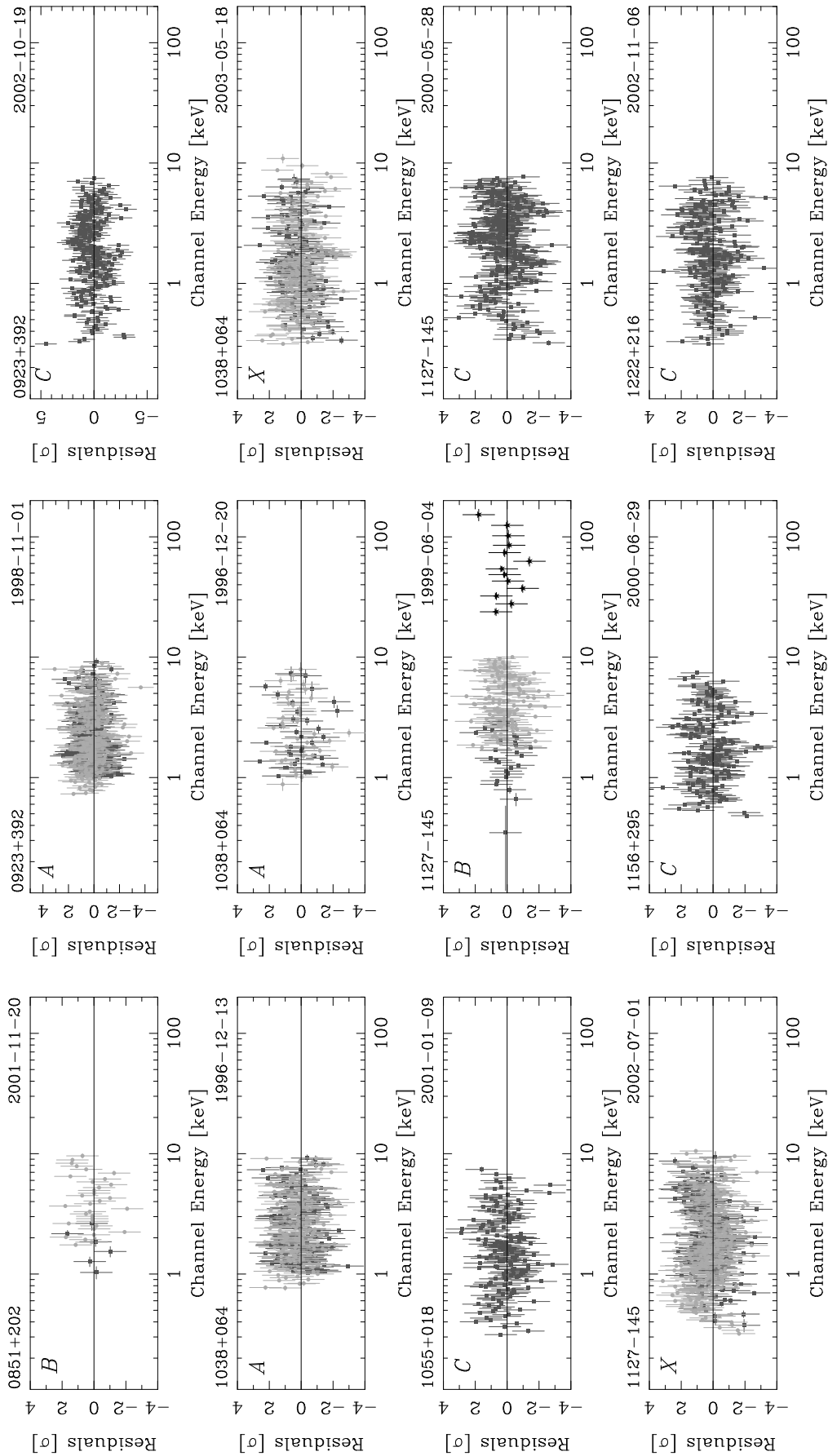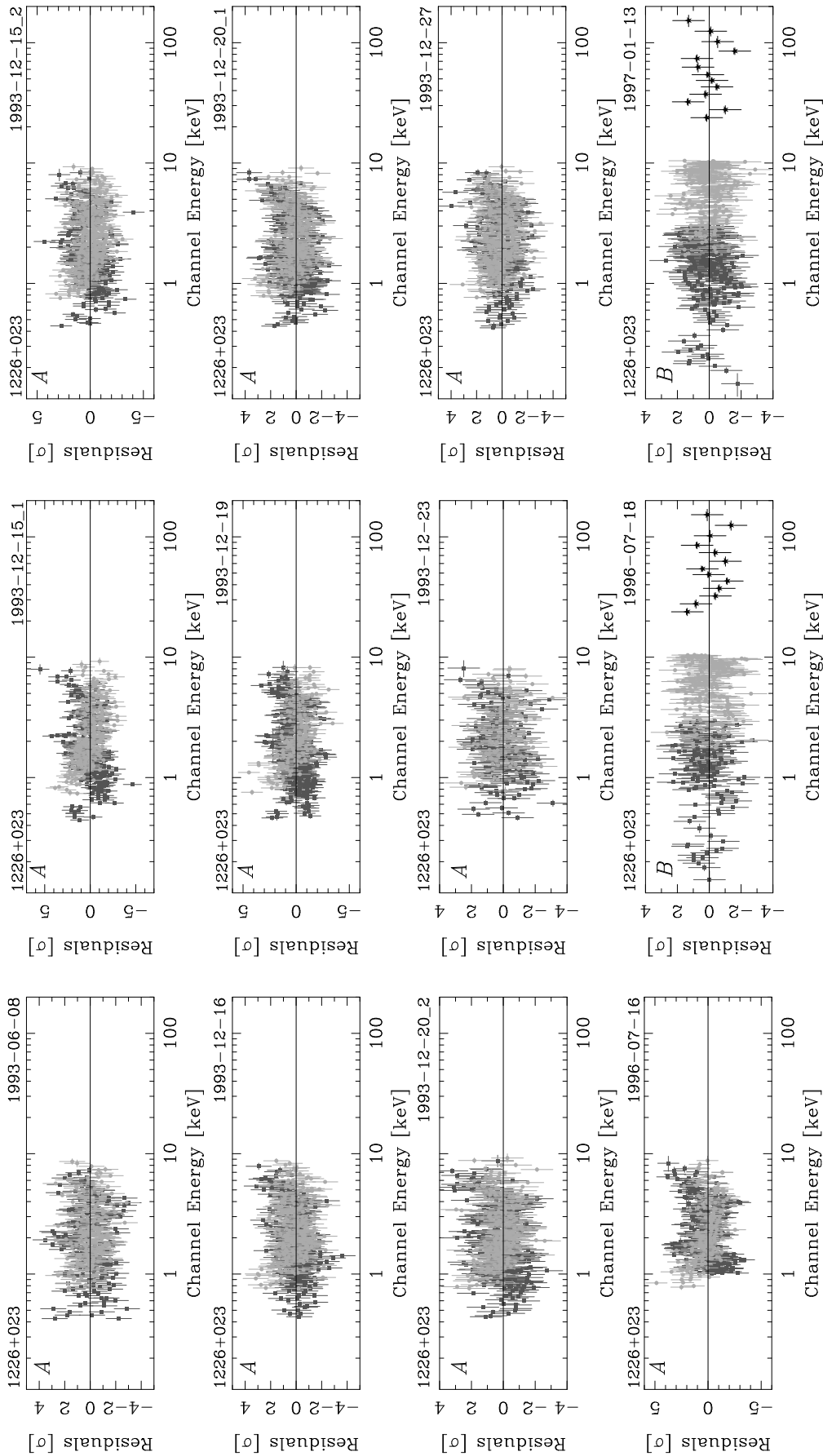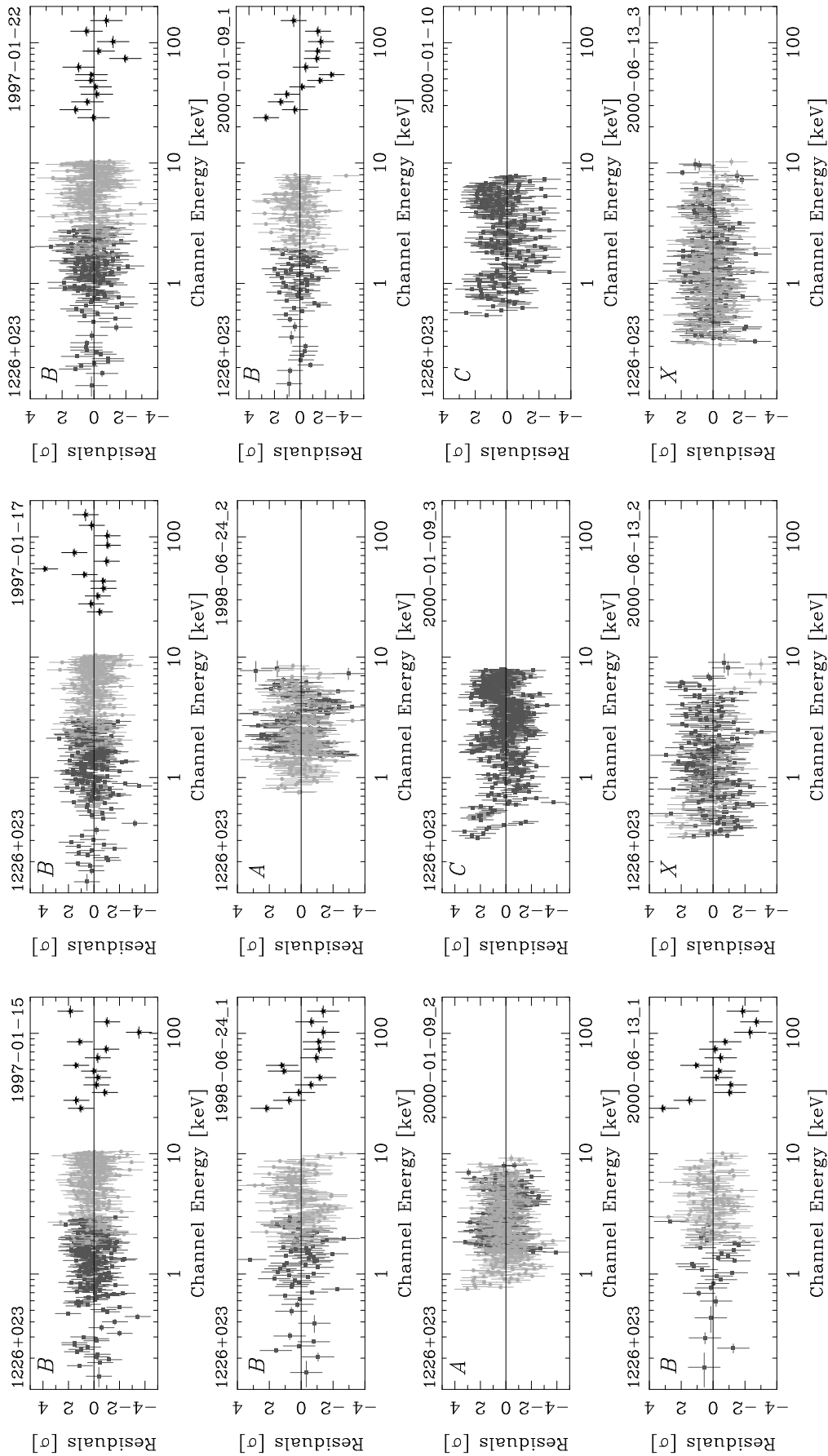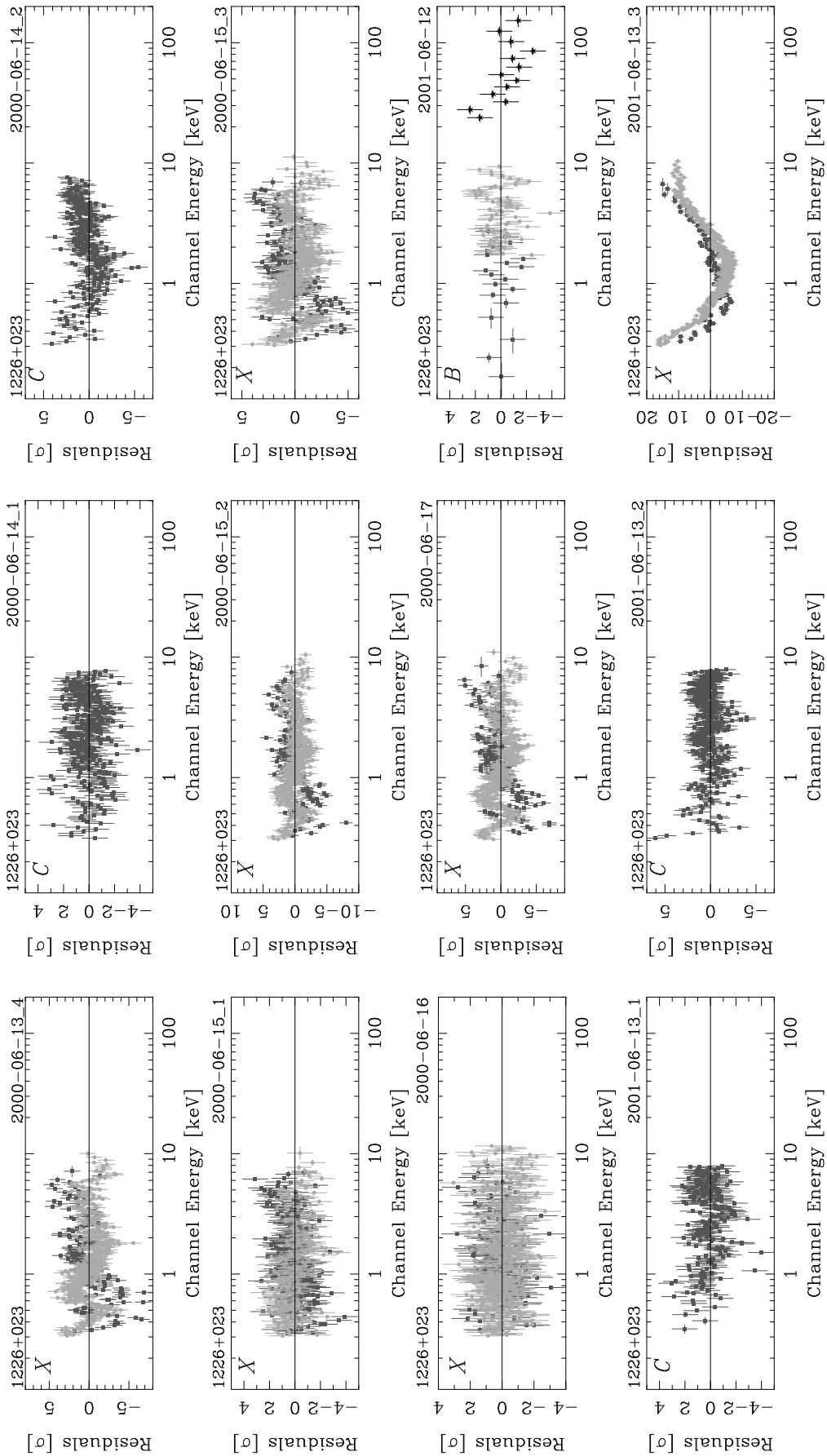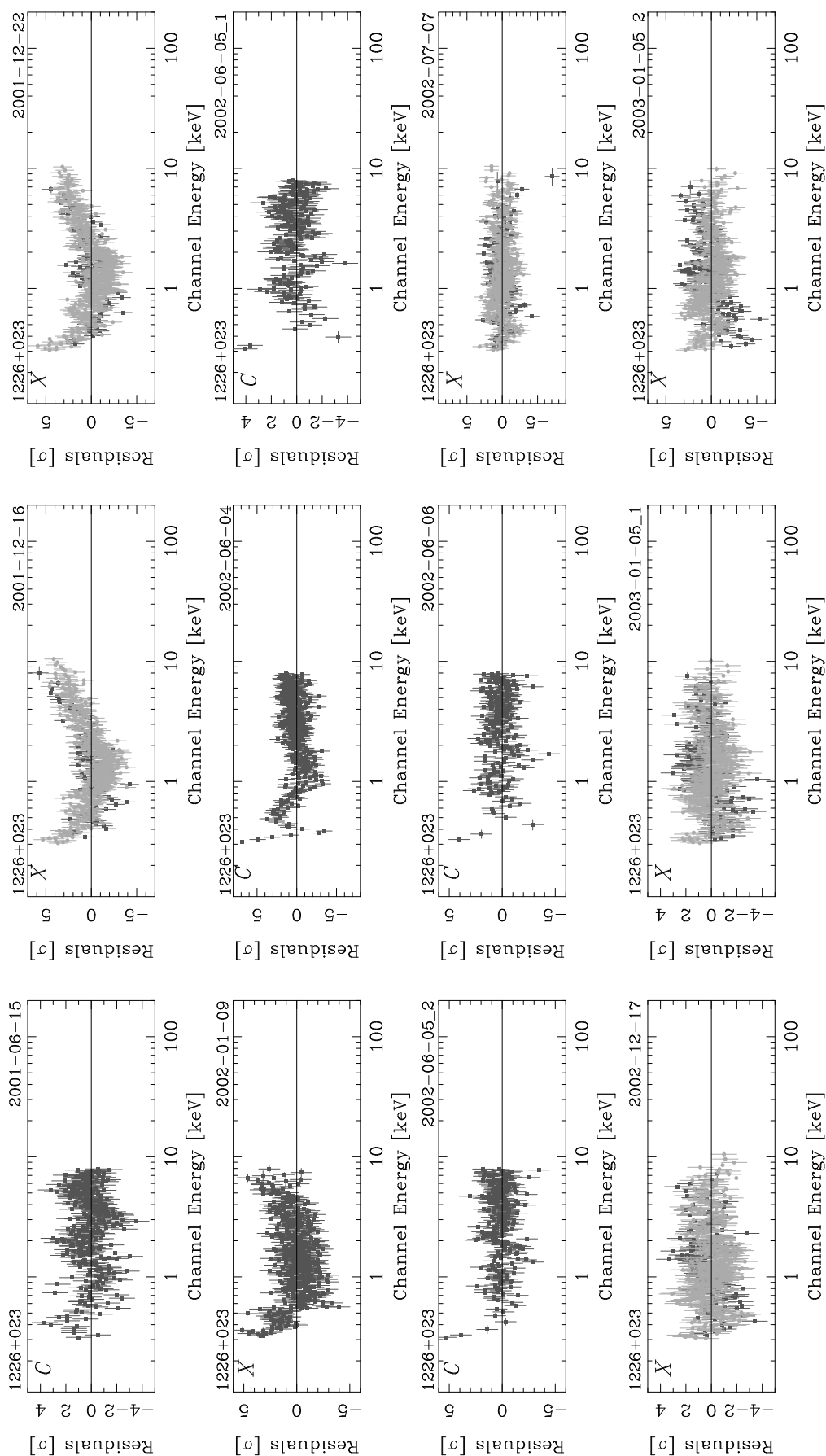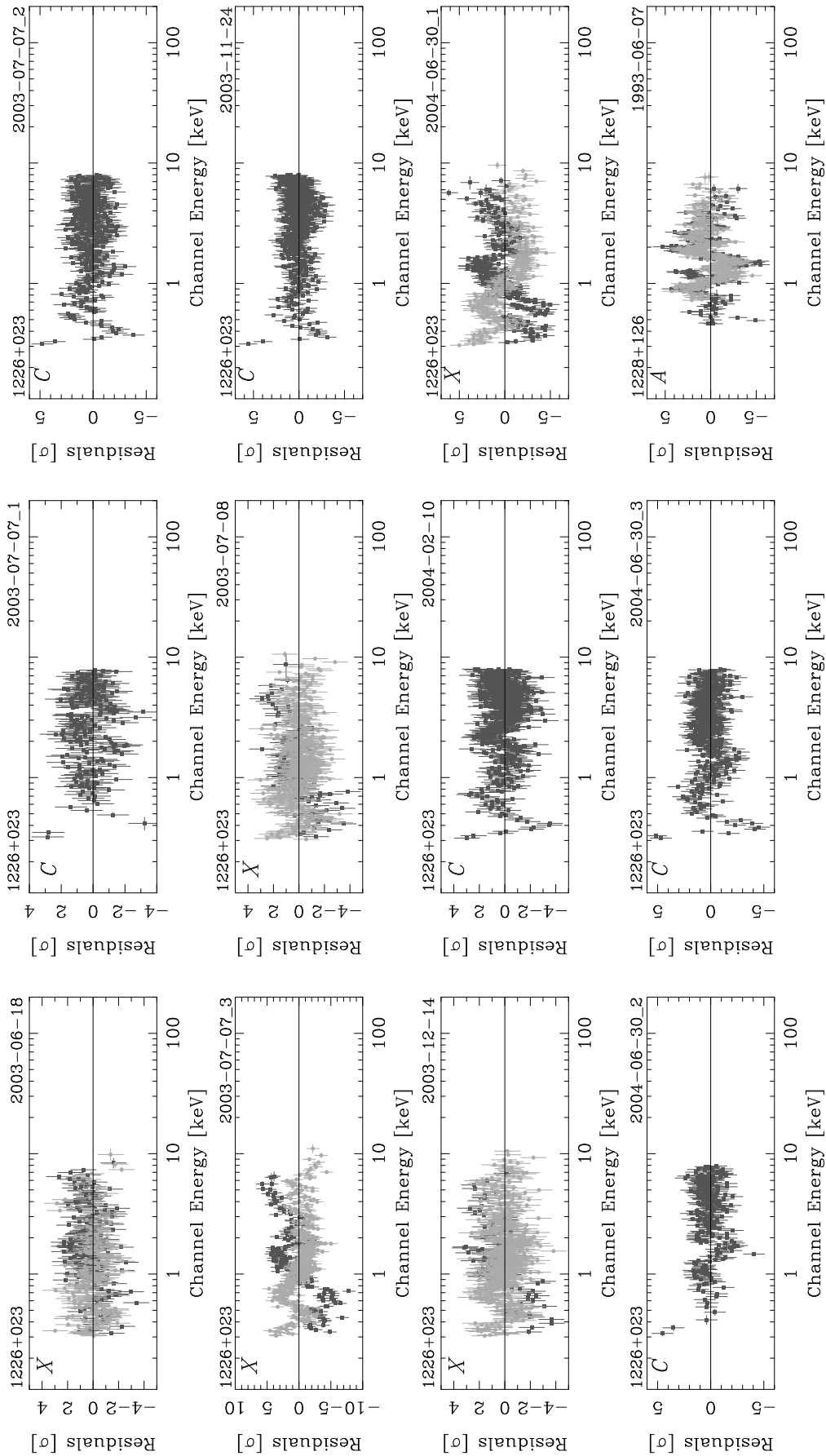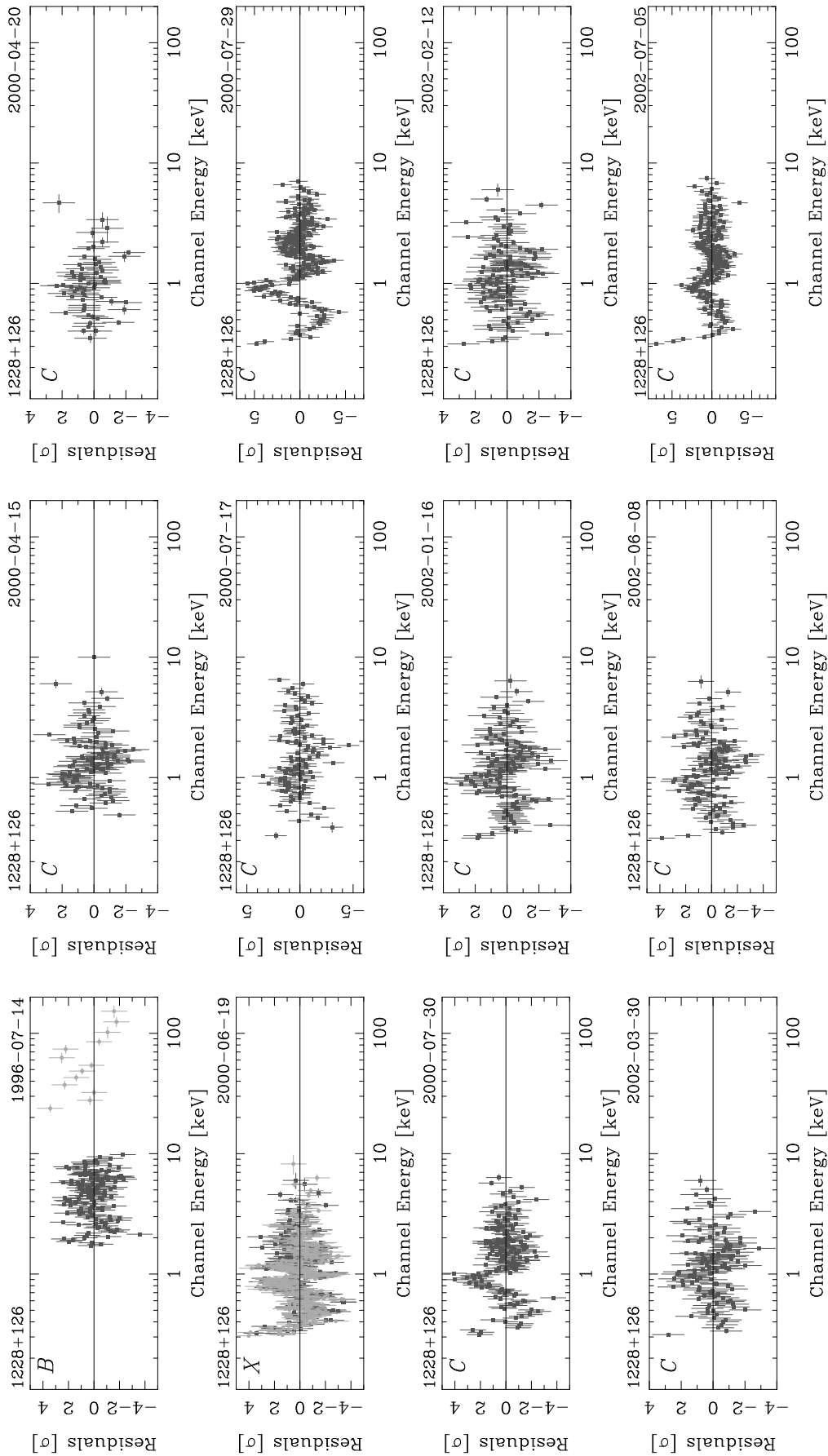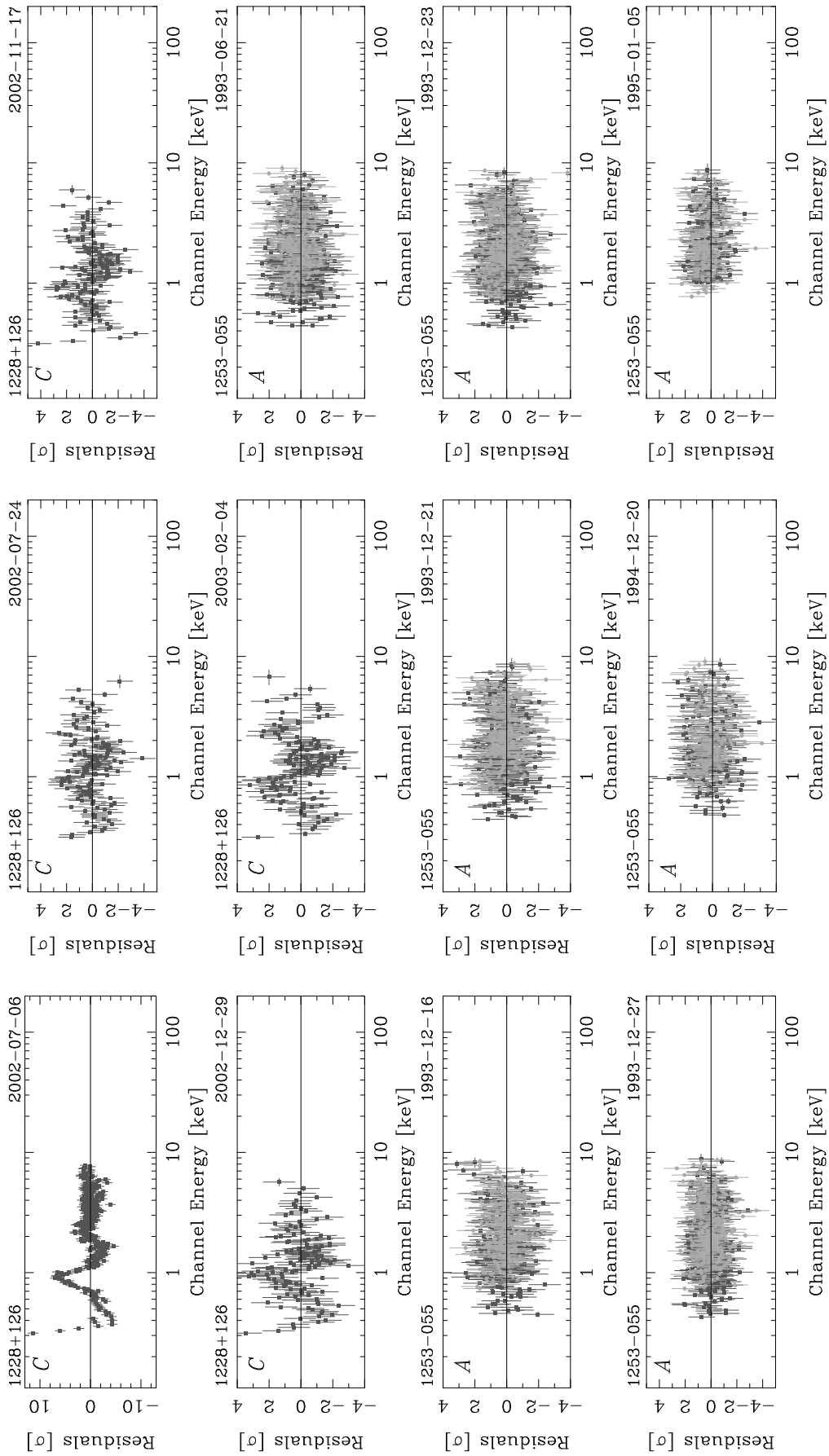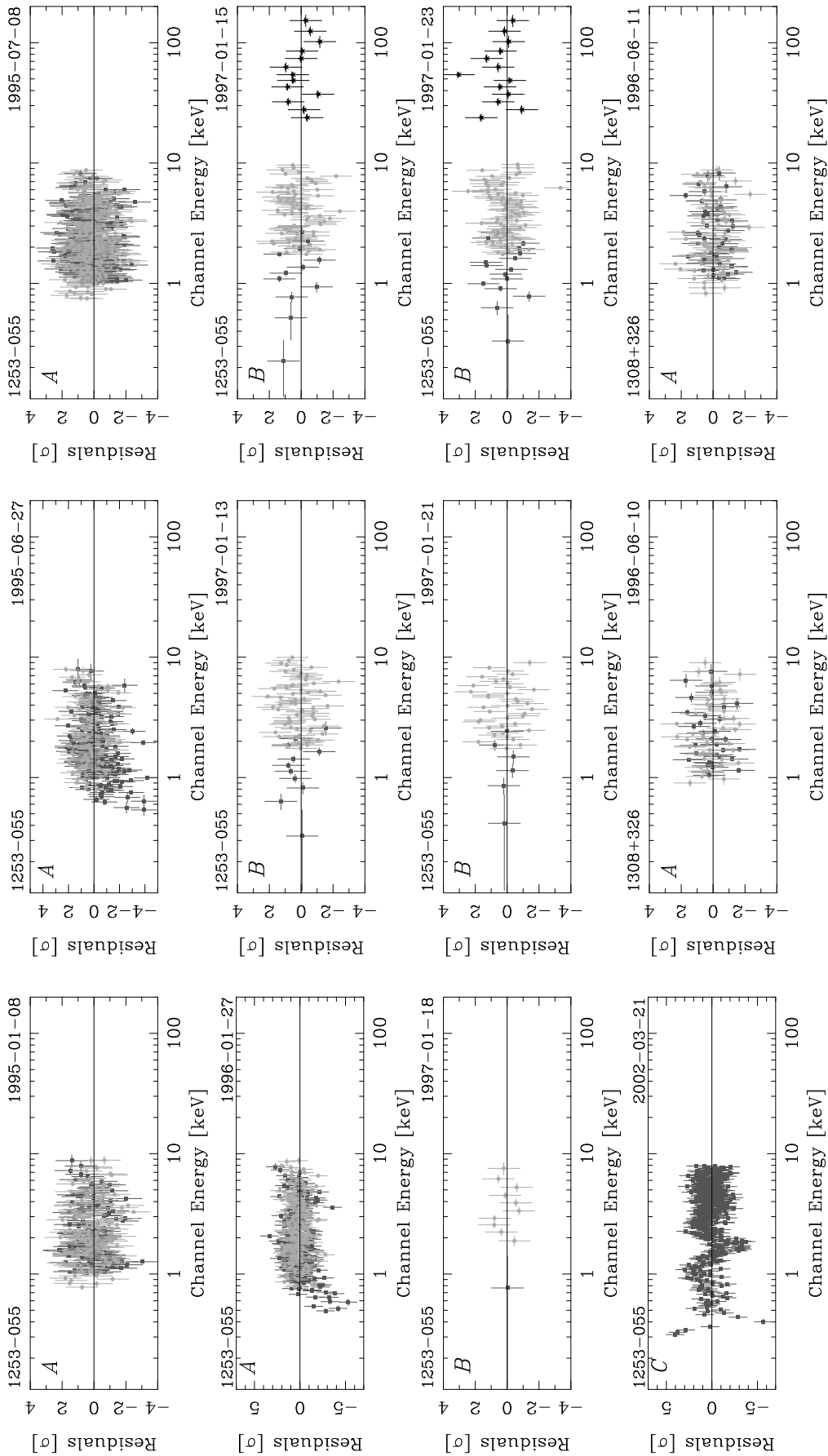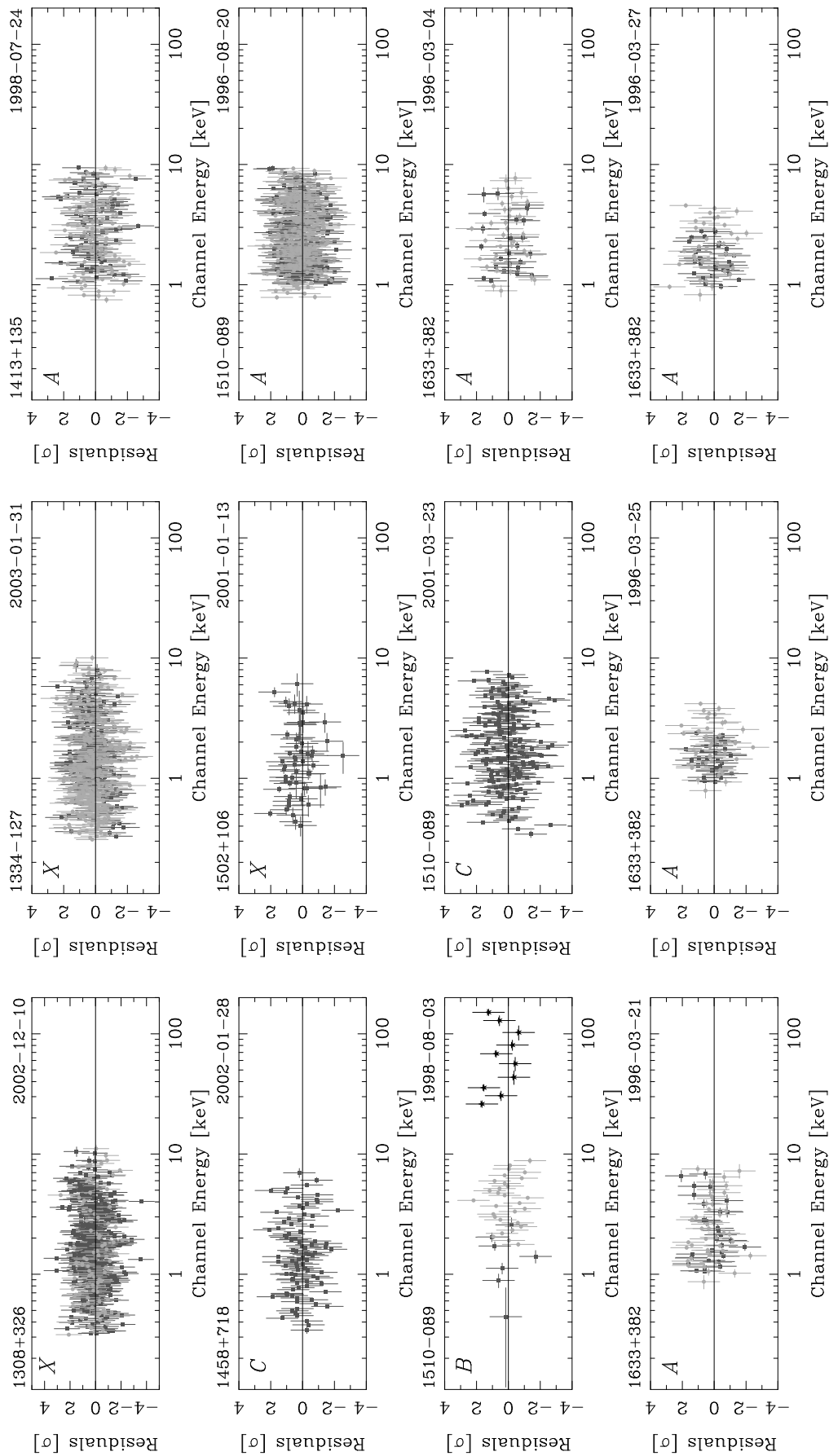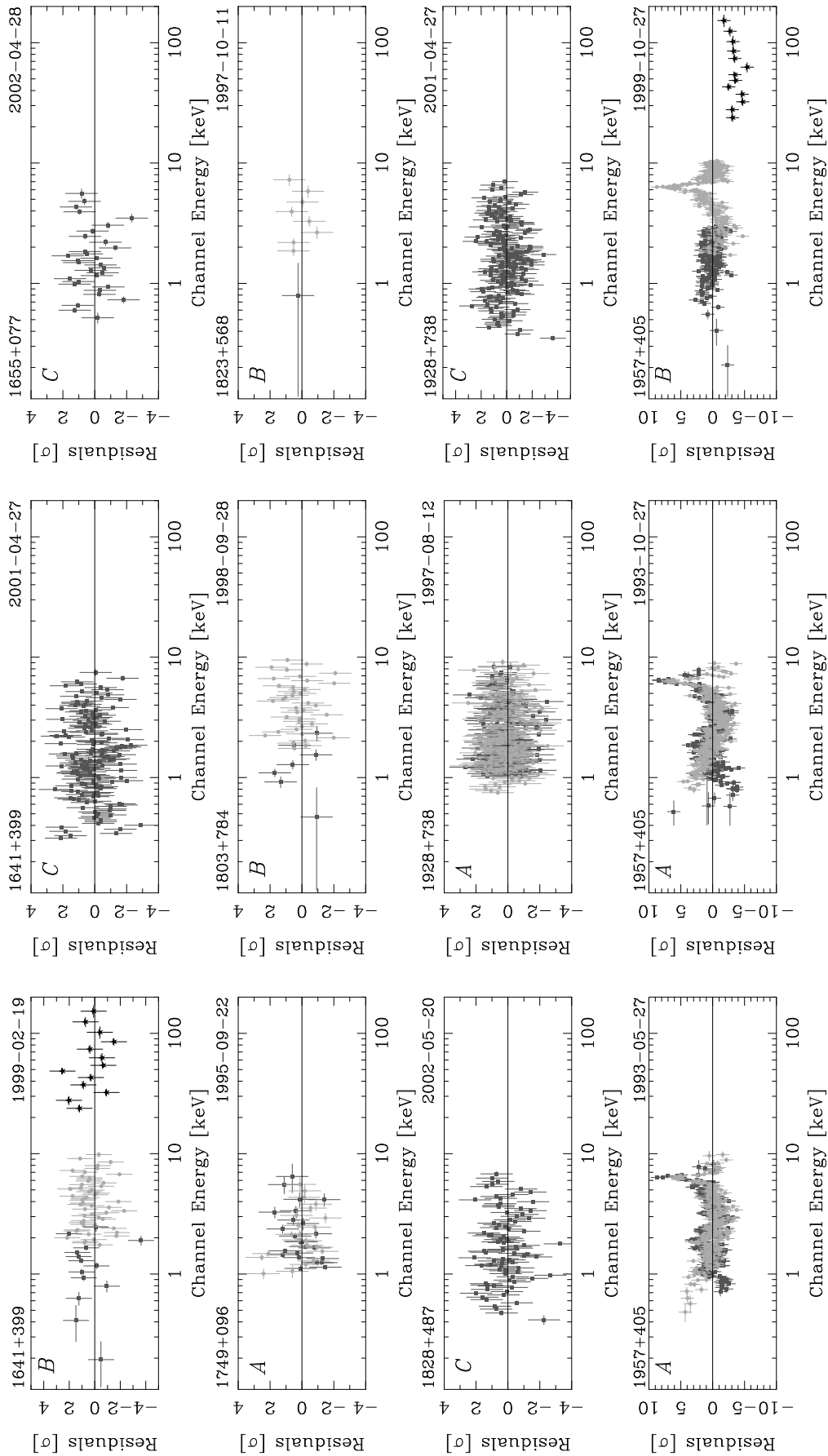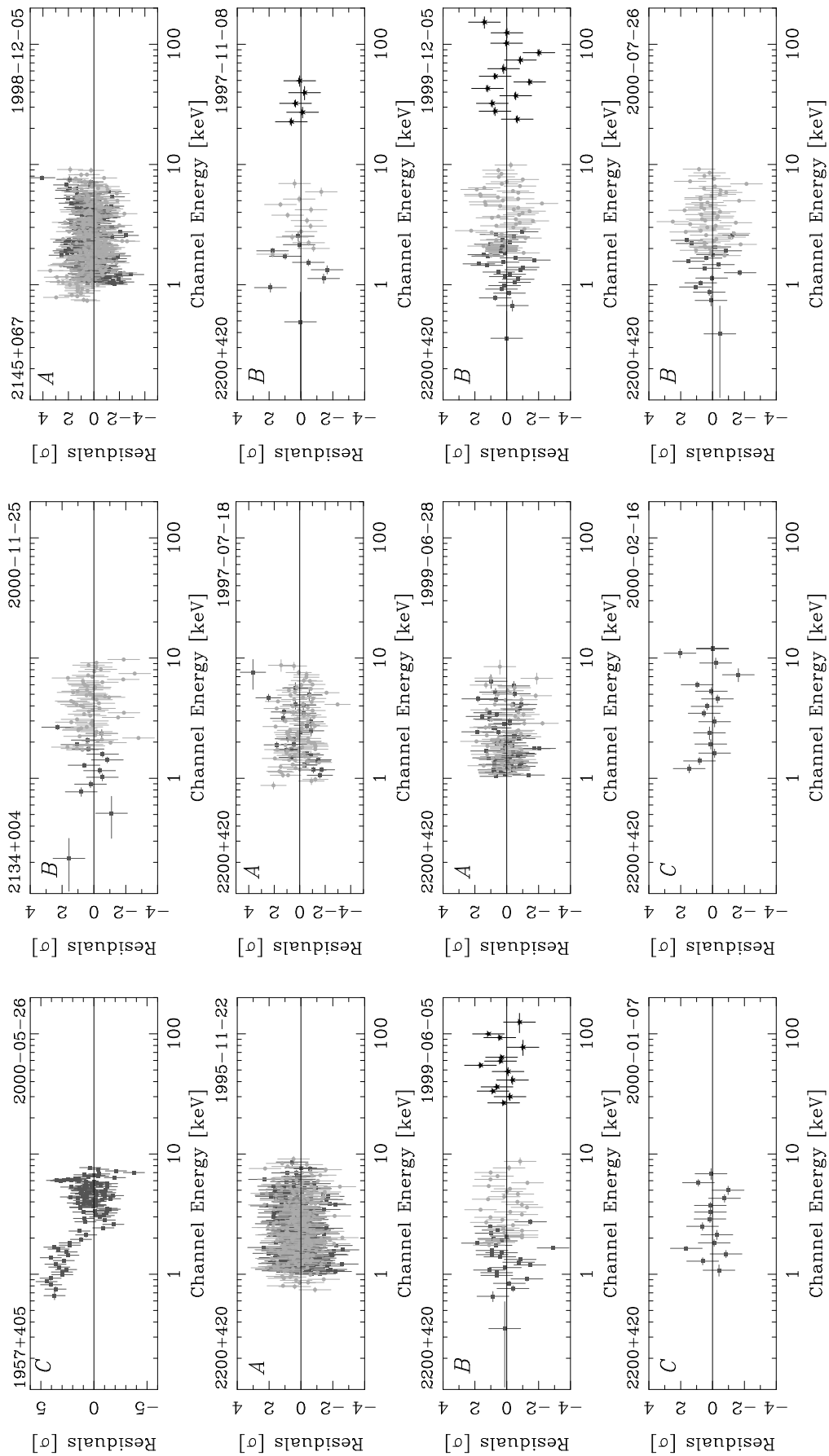
Figure A.1: continued
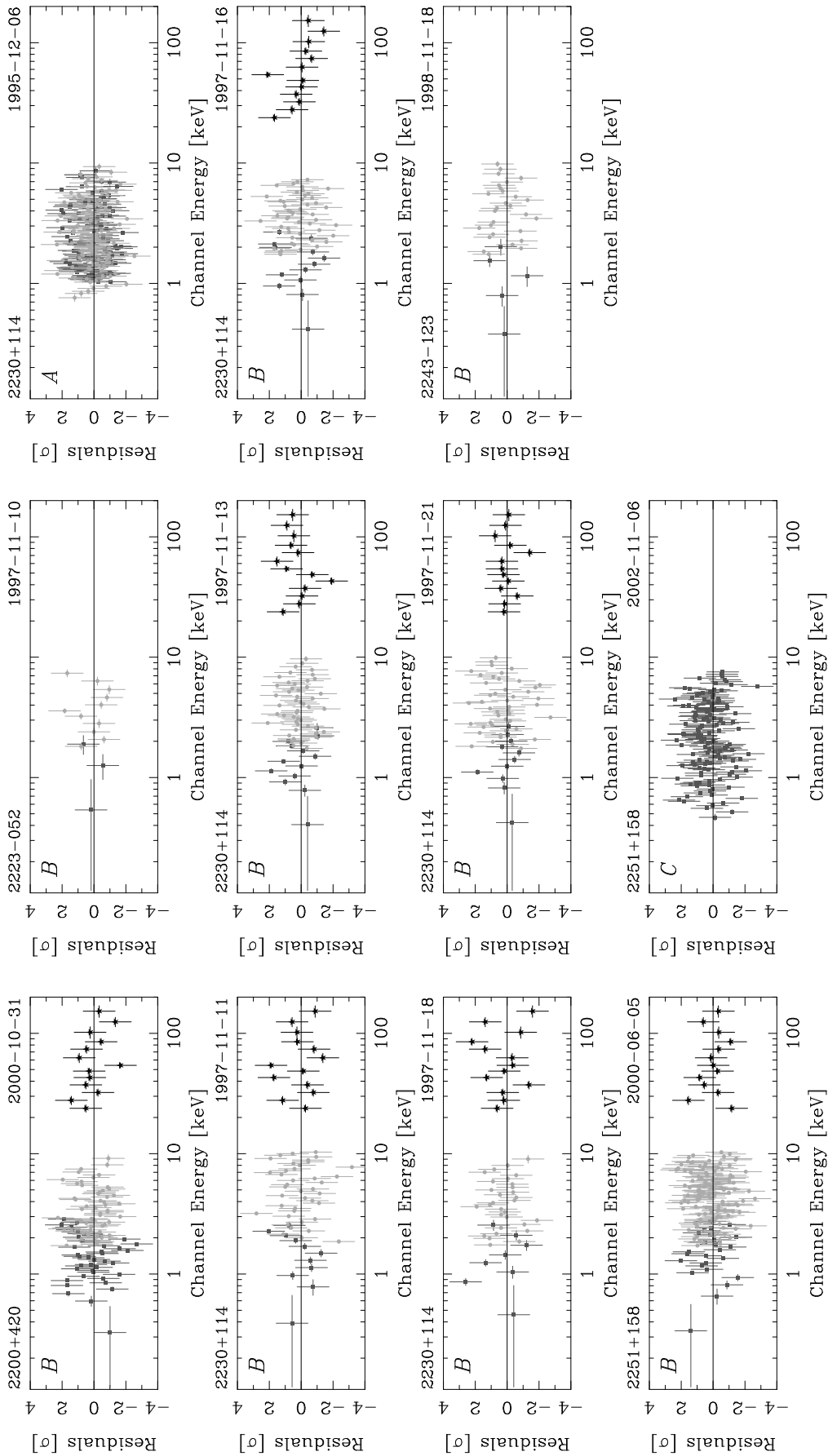
Figure A.1: continued

B Radio–X-ray Correlation Analysis

This chapter concentrates on the soft X-ray flux and luminosity characteristics of radio-loud, core-dominated AGN. Data from the *ROSAT* All-Sky Survey (RASS) are used to investigate the well known radio–X-ray luminosity–luminosity correlation of radio-loud AGN for the VLBA 2 cm Survey and the MOJAVE samples. It is shown that this correlation holds for the total (integrated) radio emission, for the parsec-scale VLBI emission and even for the sub-parsec scale most compact radio emission.

B.1 Data Acquisition and Analysis

Soft X-ray fluxes for most of the VLBA 2 cm Survey sources could be obtained from the Brinkmann et al. (1997b) catalog of *ROSAT*-observed radio-loud quasars[1]. Due to the (position dependent) flux limit of the RASS, a considerable fraction of the VLBA 2 cm Survey sources with soft X-ray fluxes below a few times $10^{-13}\,\mathrm{erg\,s^{-1}\,cm^{-2}}$ was not detected by *ROSAT*, and therefore these sources are not included in the Brinkmann et al. (1997b) catalog. In addition, however, a number of well known bright X-ray sources like, e.g., Mrk 421, AO 0235+16, or Cygnus A are missing in the catalog, as well. In a large fraction of these cases, the reason is an optical classification as a BL Lac object, or as a Seyfert galaxy. Very bright, or extended sources might be misidentified in position and highly variable sources might have been observed during a deep minimum at one specific *ROSAT* epoch, while they may be well detected at another epoch. 13 sources were found in the list of Siebert et al. (1998), the data for an additional set of five sources were provided by E. Ferrero (priv. comm.) from a cross-correlation of the missing-sources list with the *ROSAT* source catalog (*ROSAT*-SRC: Voges 1994) based on pointed observations. For the remaining 51 sources, RASS fits images of the appropriate region in the sky were obtained from the RASS website[2]. From these fits images the RASS integration time at this sky region, and the corresponding background count rate were determined. In nine cases, the source was significantly detected above the surrounding noise level (see Table B.1). For the non-detected sources (Table B.2) it was assumed that a source with a total of nine counts over the background level would have been detected to derive a source count-rate limit. Unabsorbed fluxes for the *ROSAT* $(0.2 - 2.4)\,\mathrm{keV}$ band were determined from these count-rate limits using the HEASARC provided WEBPIMMS tool[3] and assuming a power-law source spectrum with photon index 2.1 and Galactic absorption. These

---

[1]Access to the Brinkmann et al. (1997b) catalog is provided via the HEASARC website: `http://heasarc.gsfc.nasa.gov`

[2]`http://www.xray.mpe.mpg.de/cgi-bin/rosat/rosat-survey`

[3]`http://heasarc.gsfc.nasa.gov/Tools/w3pimms.html`

Table B.1: Additional VLBA 2 cm Survey sources detected in the RASS.

Source[a]	R.A.[b]	Dec.[b]	t^c [s]	Background [cts/s]	Source Counts [cts]	Source Count Rate [cts/s]	$F_{abs.}$[d] [erg/s/cm^2]	Gal. N_H[e] [cm^{-2}]	$F_{unabs.}$[d] [erg/s/cm^2]
0109+224	01:12:05.8	+22:44:39	420	0.20	86	0.20	$4.74\times10^{+20}$	2.515×10^{-12}	5.128×10^{-12}
0133−203	01:35:37.5	−20:08:46	400	0.29	42	0.10	$1.18\times10^{+20}$	7.992×10^{-13}	1.183×10^{-12}
0355+508	03:59:29.7	+50:57:50	570	0.27	34	0.06	$8.86\times10^{+21}$	1.161×10^{-12}	9.542×10^{-12}
0716+714	07:21:53.4	+71:20:36	435	0.22	113	0.26	$3.81\times10^{+20}$	3.092×10^{-12}	5.943×10^{-12}
1228+126	12:30:49.4	+12:23:28	430	0.70	18781	43.68	$2.54\times10^{+20}$	4.587×10^{-10}	7.982×10^{-10}
1324+224	13:27:00.9	+22:10:50	320	0.24	21	0.07	$1.49\times10^{+20}$	5.694×10^{-13}	8.827×10^{-13}
1751+288	17:53:42.5	+28:48:05	730	0.41	12	0.02	$5.07\times10^{+20}$	2.041×10^{-13}	4.242×10^{-13}
1901+319	19:02:55.9	+31:59:42	666	0.33	13	0.02	$1.18\times10^{+21}$	2.610×10^{-13}	7.171×10^{-13}
2010+463	20:12:05.6	+46:28:56	940	0.58	293	0.31	$5.14\times10^{+21}$	4.961×10^{-12}	2.819×10^{-11}

[a] B 1950 IAU name; [b] J 2000 coordinates; [c] RASS integration time; [d] (un)absorbed $(0.2-2.4)$ keV Flux limit; [e] Galactic neutral hydrogen column density (from Dickey and Lockman (1990)).

assumptions are made to match the flux-determination procedures of Brinkmann et al. (1997b) and Siebert et al. (1998). For all values, the errors on flux due to possible variations in photon index are small, typically below 5 % (E. Ferrero, priv. comm.). The influence of absorption (either source intrinsic or due to intervening systems) is larger for many sources and considering further the statistical error, particularly for the weakest sources, a 20 % error is a reliable common estimation of the flux uncertainties.

Table B.2: VLBA 2 cm Survey sources not found in the RASS.

Source[a]	R.A.[b]	Dec.[b]	t^c [s]	Background [cts/s]	Limiting Count rate [cts/s]	$F_{abs.}$[d] [erg/s/cm^2]	Gal. N_H[e] [cm^{-2}]	$F_{unabs.}$[d] [erg/s/cm^2]
0026+346	00:29:14.2	+34:56:32	365	0.12	0.028	$5.60\times10^{+20}$	3.64	7.786×10^{-13}
0039+230	00:42:04.5	+23:20:01	140	0.05	0.068	$3.51\times10^{+20}$	7.89	1.486×10^{-12}
0059+581	01:02:45.8	+58:24:11	350	0.18	0.030	$3.76\times10^{+21}$	4.47	2.113×10^{-12}
0108+388	01:11:37.3	+39:06:28	450	0.18	0.024	$5.80\times10^{+20}$	3.14	6.783×10^{-13}
0149+218	01:52:18.1	+22:07:07	233	0.10	0.042	$7.38\times10^{+20}$	5.66	1.318×10^{-12}
0202+319	02:05:04.9	+32:12:30	240	0.23	0.046	$6.17\times10^{+20}$	6.09	1.341×10^{-12}
0224+671	02:28:50.1	+67:21:03	625	0.21	0.017	$4.21\times10^{+21}$	2.66	1.339×10^{-12}
0300+470	03:03:35.2	+47:16:16	520	0.19	0.021	$1.81\times10^{+21}$	2.85	9.333×10^{-13}
0310+013	03:12:43.6	+01:33:18	500	0.30	0.023	$8.54\times10^{+20}$	3.19	7.789×10^{-13}
0316+161	03:18:57.8	+16:28:33	550	0.35	0.022	$1.13\times10^{+21}$	3.03	8.198×10^{-13}
0429+415	04:32:36.5	+41:38:28	475	0.21	0.023	$4.11\times10^{+21}$	3.48	1.729×10^{-12}
0446+112	04:49:07.7	+11:21:29	385	0.16	0.027	$1.52\times10^{+21}$	3.74	1.135×10^{-12}
0524+034	05:27:32.7	+03:31:32	440	0.20	0.025	$1.58\times10^{+21}$	3.38	1.045×10^{-12}
0529+075	05:32:39.0	+07:32:43	440	0.15	0.024	$1.91\times10^{+21}$	3.26	1.094×10^{-12}
0529+483	05:33:15.9	+48:22:53	410	0.15	0.025	$2.73\times10^{+21}$	3.59	1.430×10^{-12}
0648−165	06:50:24.6	−16:37:40	450	0.16	0.023	$3.20\times10^{+21}$	3.36	1.457×10^{-12}
0707+476	07:10:46.1	+47:32:11	350	0.13	0.029	$8.08\times10^{+20}$	3.94	9.462×10^{-13}
0727−115	07:30:19.1	−11:41:13	340	0.18	0.031	$3.79\times10^{+21}$	4.66	2.213×10^{-12}
0730+504	07:33:52.5	+50:22:09	420	0.16	0.025	$6.07\times10^{+20}$	3.27	7.172×10^{-13}
0741−063	07:44:21.6	−06:29:36	260	0.13	0.039	$1.24\times10^{+21}$	5.38	1.506×10^{-12}
0742+103	07:45:33.1	+10:11:13	125	0.12	0.080	$3.37\times10^{+20}$	9.24	1.722×10^{-12}
0805−077	08:08:15.5	−07:51:10	165	0.11	0.061	$9.82\times10^{+20}$	8.29	2.128×10^{-12}
0834−201	08:36:39.2	−20:17:00	350	0.16	0.030	$6.60\times10^{+20}$	3.97	8.930×10^{-13}
0919−260	09:21:29.3	−26:18:43	500	0.22	0.022	$8.34\times10^{+20}$	2.99	7.241×10^{-13}
1036+054	10:38:46.8	+05:12:29	110	0.08	0.088	$3.14\times10^{+20}$	9.90	1.813×10^{-12}
1144+402	11:46:58.3	+39:58:34	335	0.23	0.033	$1.97\times10^{+20}$	3.15	5.171×10^{-13}
1155+251	11:58:25.8	+24:50:18	460	0.32	0.026	$1.63\times10^{+20}$	2.30	3.629×10^{-13}
1213−172	12:15:46.8	−17:31:45	62	0.06	0.154	$4.27\times10^{+20}$	18.97	3.739×10^{-12}
1251−407	12:53:59.5	−40:59:31	330	0.20	0.033	$7.97\times10^{+20}$	4.44	1.060×10^{-12}
1323+321	13:26:16.5	+31:54:10	530	0.42	0.024	$1.15\times10^{+20}$	1.91	2.816×10^{-13}
1345+125	13:47:33.4	+12:17:24	280	0.26	0.041	$1.90\times10^{+20}$	3.81	6.207×10^{-13}
1404+286	14:07:0.4	+28:27:15	430	0.35	0.028	$1.40\times10^{+20}$	2.39	3.654×10^{-13}
1424+366	14:26:37.1	+36:25:10	600	0.62	0.024	$1.07\times10^{+20}$	1.89	2.738×10^{-13}
1504+377	15:06:09.5	+37:30:51	685	0.53	0.020	$1.21\times10^{+20}$	1.62	2.409×10^{-13}
1607+268	16:09:13.3	+26:41:29	660	0.35	0.018	$4.21\times10^{+20}$	2.25	4.440×10^{-13}
1908−201	19:11:09.6	−20:06:55	270	0.18	0.039	$1.31\times10^{+21}$	5.41	1.548×10^{-12}
2005+403	20:07:44.9	+40:29:49	775	0.58	0.018	$6.01\times10^{+21}$	3.08	1.928×10^{-12}
2021+317	20:23:19.0	+31:53:02	665	0.27	0.017	$5.80\times10^{+21}$	2.85	1.746×10^{-12}
2021+614	20:22:06.7	+61:36:59	1025	0.57	0.014	$1.44\times10^{+21}$	1.90	5.640×10^{-13}
2128+048	21:30:32.9	+05:02:17	255	0.15	0.041	$5.21\times10^{+20}$	5.21	1.091×10^{-12}
2209+236	22:12:06.0	+23:55:41	498	0.21	0.022	$6.53\times10^{+20}$	2.91	6.516×10^{-13}
2351+456	23:54:21.7	+45:53:04	380	0.16	0.027	$1.05\times10^{+21}$	3.77	9.909×10^{-13}

[a] B 1950 IAU name; [b] J 2000 coordinates; [c] RASS integration time; [d] (un)absorbed $(0.2 - 2.4)$ keV Flux limit;
[e] Galactic neutral hydrogen column density (from Dickey and Lockman (1990)).

Table B.3: Soft X-ray and radio-finescale properties of VLBA 2 cm Survey sources.

Source[a]	Classification[b]	z[c]	M[d]	2 cm-X[e]	$F^{\rm f}_{(0.2-2.4)\,{\rm keV}}$ [erg s^{-1} cm^{-2}]	$L^{\rm g}_{(0.2-2.4)\,{\rm keV}}$ [erg s^{-1}]	Ref.[h]	$S^{\rm i}_{\rm tot}$ [Jy]	$L_{\rm tot}$ [erg s^{-1}]	$S^{\rm j}_{\rm VLBA}$ [Jy]	$L_{\rm VLBA}$ [erg s^{-1}]	$S^{\rm k}_{\rm core}$ [Jy]	$L_{\rm core}$ [erg s^{-1}]
0003−066	B	0.347	Y	0	1.44×10^{-12}	$5.85\times10^{+44}$	1	2.46	$1.50\times10^{+44}$	2.17	$1.32\times10^{+44}$	1.23	$7.51\times10^{+43}$
0007+106	G	0.089	Y	X	1.74×10^{-11}	$3.51\times10^{+44}$	1	0.60	$1.81\times10^{+42}$	0.61	$1.84\times10^{+42}$	0.47	$1.42\times10^{+42}$
0014+813	Q	3.366	N	0	2.20×10^{-12}	$2.24\times10^{+47}$	1	0.50	$7.65\times10^{+45}$	0.47	$7.19\times10^{+45}$	0.24	$3.67\times10^{+45}$
0016+731	Q	1.781	Y	0	5.40×10^{-13}	$1.17\times10^{+46}$	1	0.92	$3.00\times10^{+45}$	0.83	$2.71\times10^{+45}$	0.52	$1.70\times10^{+45}$
0026+346	G	0.517	N	0	7.41×10^{-13}	$7.76\times10^{+44}$	4	0.70	$1.10\times10^{+44}$	0.48	$7.54\times10^{+43}$	0.06	$9.43\times10^{+42}$
0035+413	Q	1.353	N	0	8.50×10^{-13}	$9.39\times10^{+45}$	1	0.46	$7.62\times10^{+44}$	0.44	$7.29\times10^{+44}$	0.22	$3.65\times10^{+44}$
0039+230	U	0.000	N	0	1.46×10^{-12}	——	4	0.42	—	0.45	—	0.13	—
0048−097	B	0.000	Y	X	9.20×10^{-12}	——	3	1.41	—	1.14	—	1.04	—
0055+300	Q	0.016	N	0	1.18×10^{-12}	$7.29\times10^{+41}$	1	0.71	$6.61\times10^{+40}$	0.67	$6.23\times10^{+40}$	0.22	$2.05\times10^{+40}$
0059+581	U	0.000	Y	0	2.10×10^{-12}	——	4	3.12	—	3.32	—	2.72	—
0106+013	Q	2.107	Y	0	5.10×10^{-13}	$1.67\times10^{+46}$	1	2.16	$1.06\times10^{+46}$	2.07	$1.02\times10^{+46}$	1.17	$5.76\times10^{+45}$
0108+388	G	0.669	N	0	6.44×10^{-13}	$1.26\times10^{+45}$	1	0.53	$1.55\times10^{+44}$	0.44	$1.29\times10^{+44}$	0.15	$4.40\times10^{+43}$
0109+224	B	0.000	Y	0	4.96×10^{-12}	——	4	0.82	—	0.84	—	0.66	—
0112−017	Q	1.365	N	0	4.30×10^{-13}	$4.86\times10^{+45}$	1	0.83	$1.41\times10^{+45}$	0.73	$1.24\times10^{+45}$	0.32	$5.42\times10^{+44}$
0113−118	Q	0.672	N	0	1.31×10^{-12}	$2.59\times10^{+45}$	1	1.09	$3.23\times10^{+44}$	1.05	$3.11\times10^{+44}$	0.72	$2.13\times10^{+44}$
0119+041	Q	0.637	N	0	2.10×10^{-13}	$3.64\times10^{+44}$	1	1.08	$2.81\times10^{+44}$	1.03	$2.68\times10^{+44}$	0.44	$1.14\times10^{+44}$
0119+115	Q	0.570	Y	0	9.75×10^{-13}	$1.29\times10^{+45}$	1	1.35	$2.68\times10^{+44}$	1.26	$2.50\times10^{+44}$	0.85	$1.69\times10^{+44}$
0122−003	Q	1.070	N	0	1.41×10^{-12}	$8.73\times10^{+45}$	1	1.62	$1.50\times10^{+45}$	1.55	$1.44\times10^{+45}$	0.40	$3.71\times10^{+44}$
0133+476	Q	0.859	Y	0	2.16×10^{-12}	$7.78\times10^{+45}$	4	0.49	$2.65\times10^{+44}$	0.41	$2.22\times10^{+44}$	0.20	$1.08\times10^{+44}$
0133−203	Q	1.141	N	0	1.20×10^{-12}	$8.71\times10^{+45}$	1	3.35	$3.65\times10^{+45}$	3.13	$3.41\times10^{+45}$	2.73	$2.97\times10^{+45}$
0138−097	B	0.501	N	0	4.42×10^{-13}	$4.29\times10^{+44}$	1	0.49	$7.14\times10^{+43}$	0.52	$7.58\times10^{+43}$	0.26	$3.79\times10^{+43}$
0146+056	Q	2.345	N	0	2.43×10^{-13}	$1.04\times10^{+46}$	2	1.07	$6.84\times10^{+45}$	1.10	$7.03\times10^{+45}$	0.50	$3.19\times10^{+45}$
0149+218	Q	1.320	N	0	1.30×10^{-12}	$1.35\times10^{+46}$	4	1.21	$1.89\times10^{+45}$	1.18	$1.84\times10^{+45}$	1.05	$1.64\times10^{+45}$
0153+744	Q	2.338	N	0	5.90×10^{-13}	$2.50\times10^{+46}$	1	0.44	$2.79\times10^{+45}$	0.35	$2.22\times10^{+45}$	0.18	$1.14\times10^{+45}$
0201+113	Q	3.610	N	0	1.03×10^{-12}	$1.24\times10^{+47}$	1	0.67	$1.21\times10^{+46}$	0.67	$1.21\times10^{+46}$	0.50	$9.04\times10^{+45}$
0202+149	Q	0.405	Y	0	5.45×10^{-13}	$3.19\times10^{+44}$	1	2.37	$2.08\times10^{+44}$	1.79	$1.57\times10^{+44}$	1.18	$1.04\times10^{+44}$
0202+319	Q	1.466	Y	0	1.30×10^{-12}	$1.75\times10^{+46}$	4	1.51	$3.05\times10^{+45}$	1.51	$3.05\times10^{+45}$	1.16	$2.34\times10^{+45}$
0212+735	Q	2.367	Y	0	1.23×10^{-12}	$5.36\times10^{+46}$	1	2.68	$1.75\times10^{+46}$	2.35	$1.54\times10^{+46}$	0.85	$5.56\times10^{+45}$
0215+015	Q	1.715	Y	0	9.39×10^{-13}	$1.86\times10^{+46}$	1	0.76	$2.26\times10^{+45}$	0.69	$2.05\times10^{+45}$	0.47	$1.40\times10^{+45}$
0218+357	Q	0.944	N	0	7.74×10^{-13}	$3.52\times10^{+45}$	1	1.05	$7.16\times10^{+44}$	0.77	$5.25\times10^{+44}$	0.17	$1.16\times10^{+44}$
0221+067	Q	0.510	N	0	1.73×10^{-12}	$1.75\times10^{+45}$	1	0.72	$1.10\times10^{+44}$	0.71	$1.08\times10^{+44}$	0.33	$5.02\times10^{+43}$
0224+671	U	0.000	Y	0	1.31×10^{-12}	——	4	1.20	—	1.30	—	0.82	—
0234+285	Q	1.213	Y	0	1.42×10^{-12}	$1.20\times10^{+46}$	1	2.53	$3.20\times10^{+45}$	2.42	$3.06\times10^{+45}$	1.53	$1.94\times10^{+45}$
0235+164	B	0.940	Y	X	2.46×10^{-12}	$1.11\times10^{+46}$	1	1.24	$8.37\times10^{+44}$	1.17	$7.90\times10^{+44}$	0.92	$6.21\times10^{+44}$
0238−084	G	0.005	Y	X	6.28×10^{-13}	$3.31\times10^{+40}$	3	1.85	$1.46\times10^{+40}$	1.51	$1.20\times10^{+40}$	0.16	$1.27\times10^{+39}$
0248+430	Q	1.310	N	0	9.86×10^{-13}	$1.01\times10^{+46}$	1	0.80	$1.22\times10^{+45}$	0.65	$9.95\times10^{+44}$	0.25	$3.83\times10^{+44}$
0300+470	B	0.475	Y	0	9.47×10^{-13}	$8.10\times10^{+44}$	4	1.36	$1.75\times10^{+44}$	1.28	$1.64\times10^{+44}$	1.01	$1.30\times10^{+44}$
0310+013	Q	0.664	N	0	7.70×10^{-13}	$1.48\times10^{+45}$	4	0.20	$5.76\times10^{+43}$	0.16	$4.61\times10^{+43}$	0.10	$2.88\times10^{+43}$

Source[a]	Classification[b]	z[c]	M[d]	2 cm-X[e]	$F^{\mathrm{f}}_{(0.2-2.4)\,\mathrm{keV}}$ [erg s^{-1} cm^{-2}]	$L^{\mathrm{g}}_{(0.2-2.4)\,\mathrm{keV}}$ [erg s^{-1}]	Ref.[h]	$S^{\mathrm{i}}_{\mathrm{tot}}$ [Jy]	L_{tot} [erg s^{-1}]	$S^{\mathrm{j}}_{\mathrm{VLBA}}$ [Jy]	L_{VLBA} [erg s^{-1}]	$S^{\mathrm{k}}_{\mathrm{core}}$ [Jy]	L_{core} [erg s^{-1}]
0316+161	Q	0.000	N	0	8.26×10^{-13}	——	4	0.83	—	0.24	—	0.03	—
0316+413	G	0.018	Y	X	1.98×10^{-10}	$1.37\times10^{+44}$	1	16.35	$1.69\times10^{+42}$	10.39	$1.08\times10^{+42}$	1.73	$1.79\times10^{+41}$
0333+321	Q	1.263	Y	X	5.67×10^{-12}	$5.29\times10^{+46}$	1	1.66	$2.32\times10^{+45}$	1.51	$2.11\times10^{+45}$	0.86	$1.20\times10^{+45}$
0336−019	Q	0.852	Y	0	9.90×10^{-13}	$3.50\times10^{+45}$	1	2.51	$1.33\times10^{+45}$	2.38	$1.26\times10^{+45}$	1.20	$6.36\times10^{+44}$
0355+508	U	0.000	N	0	9.16×10^{-12}	——	4	4.86	—	4.64	—	2.85	—
0402−362	Q	1.417	N	0	1.96×10^{-12}	$2.43\times10^{+46}$	1	2.20	$4.09\times10^{+45}$	1.60	$2.97\times10^{+45}$	1.25	$2.32\times10^{+45}$
0403−132	Q	0.571	Y	0	2.49×10^{-12}	$3.31\times10^{+45}$	1	2.37	$4.73\times10^{+44}$	1.22	$2.44\times10^{+44}$	1.15	$2.30\times10^{+44}$
0405−385	Q	1.285	N	0	8.20×10^{-13}	$7.98\times10^{+45}$	1	1.30	$1.90\times10^{+45}$	1.10	$1.61\times10^{+45}$	0.69	$1.01\times10^{+45}$
0415+379	G	0.049	Y	X	1.04×10^{-11}	$5.82\times10^{+43}$	1	4.24	$3.55\times10^{+42}$	2.77	$2.32\times10^{+42}$	0.70	$5.86\times10^{+41}$
0420+022	B	2.277	N	0	5.00×10^{-13}	——	1	5.18	$3.08\times10^{+46}$	4.64	$2.76\times10^{+46}$	3.48	$2.07\times10^{+46}$
0420−014	Q	0.915	Y	X	2.93×10^{-12}	$1.23\times10^{+46}$	1	1.14	$7.20\times10^{+44}$	1.09	$6.88\times10^{+44}$	0.75	$4.74\times10^{+44}$
0422+004	B	0.000	Y	0	1.64×10^{-12}	——	1	1.40	—	1.44	—	1.25	—
0429+415	Q	1.023	N	0	1.69×10^{-12}	$9.37\times10^{+45}$	4	1.79	$1.49\times10^{+45}$	1.06	$8.81\times10^{+44}$	0.14	$1.16\times10^{+44}$
0430+052	G	0.033	Y	X	6.46×10^{-11}	$1.63\times10^{+44}$	1	3.31	$1.25\times10^{+42}$	2.53	$9.55\times10^{+41}$	0.56	$2.11\times10^{+41}$
0438−436	Q	2.852	N	0	1.20×10^{-12}	$8.21\times10^{+46}$	1	2.50	$2.57\times10^{+46}$	1.77	$1.82\times10^{+46}$	1.01	$1.04\times10^{+46}$
0440−003	Q	0.844	N	0	3.77×10^{-12}	$1.30\times10^{+46}$	1	1.24	$6.42\times10^{+44}$	0.99	$5.12\times10^{+44}$	0.37	$1.91\times10^{+44}$
0446+112	Q	1.207	Y	0	1.15×10^{-12}	$9.59\times10^{+45}$	4	1.77	$2.21\times10^{+45}$	1.71	$2.14\times10^{+45}$	1.31	$1.64\times10^{+45}$
0454+844	B	1.340	N	0	1.54×10^{-13}	$1.66\times10^{+45}$	1	2.67	$4.32\times10^{+45}$	2.42	$3.92\times10^{+45}$	0.51	$8.26\times10^{+44}$
0454−234	B	1.003	N	0	5.38×10^{-13}	$2.84\times10^{+45}$	1	0.32	$2.53\times10^{+44}$	0.26	$2.06\times10^{+44}$	0.15	$1.19\times10^{+44}$
0458−020	Q	2.286	Y	X	9.59×10^{-13}	$3.84\times10^{+46}$	1	1.57	$9.43\times10^{+45}$	1.32	$7.93\times10^{+45}$	0.99	$5.95\times10^{+45}$
0521−365	G	0.055	N	0	1.88×10^{-11}	$1.36\times10^{+44}$	1	4.76	$5.17\times10^{+42}$	1.96	$2.13\times10^{+42}$	0.72	$7.82\times10^{+41}$
0524+034	B	0.000	N	0	1.05×10^{-12}	——	4	0.75	—	0.75	—	0.65	—
0528+134	Q	2.070	Y	X	4.96×10^{-12}	$1.56\times10^{+47}$	1	4.53	$2.14\times10^{+46}$	4.36	$2.06\times10^{+46}$	2.06	$9.71\times10^{+45}$
0529+075	U	0.000	N	0	1.11×10^{-12}	——	4	1.56	—	1.48	—	0.08	—
0529+483	Q	1.162	Y	0	1.44×10^{-12}	$1.09\times10^{+46}$	1	1.04	$1.18\times10^{+45}$	1.03	$1.17\times10^{+45}$	0.80	$9.11\times10^{+44}$
0537−286	Q	3.104	N	0	1.04×10^{-12}	$8.73\times10^{+46}$	1	1.55	$1.95\times10^{+46}$	0.82	$1.03\times10^{+46}$	0.59	$7.43\times10^{+45}$
0552+398	Q	2.363	Y	0	2.95×10^{-12}	$1.28\times10^{+47}$	1	4.52	$2.94\times10^{+46}$	4.29	$2.79\times10^{+46}$	1.21	$7.88\times10^{+45}$
0602+673	Q	1.970	N	0	7.91×10^{-13}	$2.20\times10^{+46}$	1	0.74	$3.09\times10^{+45}$	0.76	$3.17\times10^{+45}$	0.53	$2.21\times10^{+45}$
0605−085	Q	0.872	Y	X	8.10×10^{-13}	$3.03\times10^{+45}$	1	2.31	$1.30\times10^{+45}$	1.82	$1.02\times10^{+45}$	0.73	$4.09\times10^{+44}$
0607−157	Q	0.324	Y	0	2.48×10^{-12}	$8.62\times10^{+44}$	1	7.09	$3.69\times10^{+44}$	5.55	$2.89\times10^{+44}$	3.73	$1.94\times10^{+44}$
0615+820	Q	0.710	N	0	3.10×10^{-13}	$7.00\times10^{+44}$	1	0.43	$1.46\times10^{+44}$	0.43	$1.46\times10^{+44}$	0.11	$3.73\times10^{+43}$
0642+449	Q	3.406	Y	0	7.20×10^{-13}	$7.55\times10^{+46}$	1	3.01	$4.73\times10^{+46}$	2.95	$4.64\times10^{+46}$	1.19	$1.87\times10^{+46}$
0648−165	U	0.000	Y	0	1.45×10^{-12}	——	4	2.22	—	1.81	—	1.02	—
0707+476	Q	1.292	N	0	9.30×10^{-13}	$9.17\times10^{+45}$	4	0.67	$9.91\times10^{+44}$	0.58	$8.58\times10^{+44}$	0.38	$5.62\times10^{+44}$
0710+439	G	0.518	N	0	5.83×10^{-13}	$6.14\times10^{+44}$	1	0.73	$1.15\times10^{+44}$	0.54	$8.53\times10^{+43}$	0.12	$1.89\times10^{+43}$
0711+356	Q	1.620	N	0	3.80×10^{-13}	$6.55\times10^{+45}$	1	0.40	$1.03\times10^{+45}$	0.40	$1.03\times10^{+45}$	0.09	$2.33\times10^{+44}$
0716+714	B	0.000	Y	X	5.84×10^{-12}	——	4	1.03	—	0.89	—	0.85	—
0723−008	B	0.127	N	0	1.27×10^{-12}	$5.43\times10^{+43}$	1	1.02	$6.52\times10^{+42}$	0.96	$6.14\times10^{+42}$	0.51	$3.26\times10^{+42}$
0727−115	Q	1.591	Y	0	2.18×10^{-12}	$3.59\times10^{+46}$	4	3.65	$9.02\times10^{+45}$	3.29	$8.13\times10^{+45}$	1.76	$4.35\times10^{+45}$

Table B.3 – continued from previous page

Source[a]	Classification[b]	z[c]	M[d]	2 cm-X[e]	$F^{\mathrm{f}}_{(0.2-2.4)\,\mathrm{keV}}$ [erg s^{-1} cm^{-2}]	$L^{\mathrm{g}}_{(0.2-2.4)\,\mathrm{keV}}$ [erg s^{-1}]	Ref.[h]	$S^{\mathrm{i}}_{\mathrm{tot}}$ [Jy]	L_{tot} [erg s^{-1}]	$S^{\mathrm{j}}_{\mathrm{VLBA}}$ [Jy]	L_{VLBA} [erg s^{-1}]	$S^{\mathrm{k}}_{\mathrm{core}}$ [Jy]	L_{core} [erg s^{-1}]
0730+504	Q	0.720	Y	0	6.93×10^{-13}	$1.62\times10^{+45}$	4	0.99	$3.47\times10^{+44}$	1.10	$3.86\times10^{+44}$	0.94	$3.30\times10^{+44}$
0735+178	B	0.424	Y	X	1.95×10^{-12}	$1.28\times10^{+45}$	1	1.33	$1.30\times10^{+44}$	1.10	$1.08\times10^{+44}$	0.49	$4.80\times10^{+43}$
0736+017	Q	0.191	Y	X	3.19×10^{-12}	$3.34\times10^{+44}$	1	1.69	$2.65\times10^{+43}$	1.49	$2.34\times10^{+43}$	0.85	$1.33\times10^{+43}$
0738+313	Q	0.630	Y	X	6.40×10^{-12}	$1.08\times10^{+45}$	1	2.23	$5.65\times10^{+44}$	2.06	$5.22\times10^{+44}$	0.75	$1.90\times10^{+44}$
0741−063	U	0.000	N	0	1.51×10^{-12}	——	4	—	—	—	—	—	—
0742+103	Q	2.624	Y	0	1.71×10^{-12}	$9.57\times10^{+46}$	4	1.62	$1.36\times10^{+46}$	1.22	$1.02\times10^{+46}$	0.25	$2.10\times10^{+45}$
0745+241	Q	0.410	N	0	2.76×10^{-12}	$1.66\times10^{+45}$	1	0.76	$6.87\times10^{+43}$	0.69	$6.24\times10^{+43}$	0.41	$3.71\times10^{+43}$
0748+126	Q	0.889	Y	0	1.72×10^{-12}	$6.75\times10^{+45}$	1	2.66	$1.56\times10^{+45}$	2.50	$1.47\times10^{+45}$	1.53	$9.00\times10^{+44}$
0754+100	B	0.266	Y	0	2.02×10^{-12}	$3.82\times10^{+45}$	3	1.62	$4.59\times10^{+44}$	1.42	$4.03\times10^{+44}$	1.02	$2.89\times10^{+44}$
0804+499	Q	1.432	Y	0	1.32×10^{-12}	$1.68\times10^{+46}$	1	0.79	$1.51\times10^{+45}$	0.74	$1.41\times10^{+45}$	0.60	$1.14\times10^{+45}$
0805−077	Q	1.837	Y	0	2.14×10^{-12}	$5.02\times10^{+46}$	4	1.62	$5.70\times10^{+45}$	1.57	$5.52\times10^{+45}$	1.17	$4.12\times10^{+45}$
0808+019	B	0.930	Y	0	6.67×10^{-13}	——	1	1.16	$7.62\times10^{+44}$	0.99	$6.51\times10^{+44}$	0.91	$5.98\times10^{+44}$
0814+425	B	0.245	Y	0	6.36×10^{-13}	$1.16\times10^{+44}$	1	1.13	$3.10\times10^{+43}$	1.01	$2.77\times10^{+43}$	0.69	$1.89\times10^{+43}$
0821+394	Q	1.217	N	0	2.47×10^{-12}	$2.10\times10^{+46}$	1	1.57	$2.00\times10^{+45}$	1.24	$1.58\times10^{+45}$	1.12	$1.43\times10^{+45}$
0823+033	B	0.506	Y	0	3.12×10^{-12}	$3.10\times10^{+45}$	1	1.36	$2.03\times10^{+44}$	1.20	$1.79\times10^{+44}$	0.86	$1.28\times10^{+44}$
0827+243	Q	0.941	Y	X	2.31×10^{-12}	$1.04\times10^{+46}$	1	1.63	$1.10\times10^{+45}$	1.65	$1.12\times10^{+45}$	1.24	$8.39\times10^{+44}$
0829+046	B	0.180	Y	0	1.05×10^{-12}	$9.64\times10^{+43}$	1	1.13	$1.55\times10^{+43}$	1.00	$1.37\times10^{+43}$	0.56	$7.70\times10^{+42}$
0831+557	G	0.240	N	0	2.39×10^{-12}	$4.18\times10^{+44}$	1	1.61	$4.22\times10^{+43}$	0.91	$2.38\times10^{+43}$	0.04	$1.05\times10^{+42}$
0834−201	Q	2.752	N	0	8.65×10^{-13}	$5.43\times10^{+46}$	4	2.71	$2.55\times10^{+46}$	2.24	$2.11\times10^{+46}$	0.95	$8.95\times10^{+45}$
0836+710	Q	2.218	Y	X	9.81×10^{-12}	$3.65\times10^{+47}$	1	1.98	$1.10\times10^{+46}$	1.96	$1.09\times10^{+46}$	0.83	$4.63\times10^{+45}$
0838+133	G	0.684	N	0	1.17×10^{-12}	$2.41\times10^{+45}$	1	1.05	$3.25\times10^{+44}$	0.73	$2.26\times10^{+44}$	0.37	$1.14\times10^{+44}$
0850+581	Q	1.322	N	0	3.90×10^{-13}	$4.07\times10^{+45}$	1	0.63	$9.86\times10^{+44}$	0.51	$7.98\times10^{+44}$	0.27	$4.23\times10^{+44}$
0851+202	B	0.306	Y	X	3.15×10^{-12}	$9.59\times10^{+44}$	1	2.41	$1.10\times10^{+44}$	2.11	$9.63\times10^{+43}$	1.19	$5.43\times10^{+43}$
0859+470	Q	1.462	N	0	5.14×10^{-13}	$6.88\times10^{+45}$	1	1.46	$2.93\times10^{+45}$	1.15	$2.31\times10^{+45}$	0.70	$1.40\times10^{+45}$
0859−140	Q	1.327	N	0	1.46×10^{-12}	$1.54\times10^{+46}$	1	0.86	$1.36\times10^{+45}$	0.64	$1.01\times10^{+45}$	0.41	$6.48\times10^{+44}$
0906+015	Q	1.018	Y	0	1.21×10^{-12}	$6.63\times10^{+45}$	1	1.92	$1.58\times10^{+45}$	1.96	$1.61\times10^{+45}$	1.18	$9.69\times10^{+44}$
0917+449	Q	2.180	N	0	1.84×10^{-12}	$6.56\times10^{+46}$	1	1.32	$7.06\times10^{+45}$	1.22	$6.53\times10^{+45}$	0.89	$4.76\times10^{+45}$
0917+624	Q	1.446	Y	0	3.60×10^{-13}	$4.69\times10^{+45}$	1	0.79	$1.54\times10^{+45}$	0.80	$1.56\times10^{+45}$	0.50	$9.77\times10^{+44}$
0919−260	Q	2.300	N	0	7.24×10^{-13}	$2.94\times10^{+46}$	4	1.68	$1.02\times10^{+46}$	1.33	$8.11\times10^{+45}$	0.80	$4.88\times10^{+45}$
0923+392	Q	0.699	Y	X	5.50×10^{-12}	$1.20\times10^{+46}$	1	11.03	$3.60\times10^{+45}$	10.47	$3.41\times10^{+45}$	2.65	$8.64\times10^{+44}$
0945+408	Q	1.252	Y	0	4.70×10^{-13}	$4.29\times10^{+45}$	1	1.53	$2.09\times10^{+45}$	1.41	$1.93\times10^{+45}$	0.72	$9.86\times10^{+44}$
0953+254	Q	0.712	N	0	8.30×10^{-13}	$1.89\times10^{+45}$	1	1.03	$3.51\times10^{+44}$	1.03	$3.51\times10^{+44}$	0.40	$1.36\times10^{+44}$
0954+658	B	0.367	N	0	1.23×10^{-12}	$5.69\times10^{+44}$	1	0.51	$3.56\times10^{+43}$	0.55	$3.83\times10^{+43}$	0.46	$3.21\times10^{+43}$
0955+476	Q	1.873	Y	0	7.60×10^{-13}	$1.87\times10^{+46}$	1	1.67	$6.16\times10^{+45}$	1.70	$6.27\times10^{+45}$	1.05	$3.88\times10^{+45}$
1012+232	Q	0.565	N	0	7.50×10^{-13}	$9.73\times10^{+44}$	1	1.02	$1.99\times10^{+44}$	0.94	$1.83\times10^{+44}$	0.61	$1.19\times10^{+44}$
1015+359	Q	1.226	N	0	4.40×10^{-13}	$3.81\times10^{+45}$	1	0.61	$7.93\times10^{+44}$	0.60	$7.80\times10^{+44}$	0.47	$6.11\times10^{+44}$
1032−199	Q	2.180	N	0	4.18×10^{-13}	$1.49\times10^{+46}$	2	1.14	$6.10\times10^{+45}$	1.09	$5.83\times10^{+45}$	0.31	$1.66\times10^{+45}$
1034−293	Q	0.312	N	0	1.88×10^{-12}	$5.98\times10^{+44}$	1	1.44	$6.88\times10^{+43}$	1.49	$7.11\times10^{+43}$	1.09	$5.20\times10^{+43}$
1036+054	U	0.000	Y	0	1.82×10^{-12}	——	4	2.69	—	2.66	—	2.33	—

Table B.3 – continued on next page

Source[a]	Classification[b]	z[c]	M[d]	2 cm-X[e]	$F^{\mathrm{f}}_{(0.2-2.4)\,\mathrm{keV}}$ [erg s^{-1} cm^{-2}]	$L^{\mathrm{g}}_{(0.2-2.4)\,\mathrm{keV}}$ [erg s^{-1}]	Ref.[h]	$S^{\mathrm{i}}_{\mathrm{tot}}$ [Jy]	L_{tot} [erg s^{-1}]	$S^{\mathrm{j}}_{\mathrm{VLBA}}$ [Jy]	L_{VLBA} [erg s^{-1}]	$S^{\mathrm{k}}_{\mathrm{core}}$ [Jy]	L_{core} [erg s^{-1}]
1038+064	Q	1.265	Y	X	1.36×10^{-12}	$1.27\times10^{+46}$	1	1.62	$2.27\times10^{+45}$	1.67	$2.34\times10^{+45}$	1.22	$1.71\times10^{+45}$
1045−188	Q	0.595	Y	0	1.44×10^{-12}	$2.12\times10^{+45}$	1	1.23	$2.71\times10^{+44}$	1.29	$2.84\times10^{+44}$	1.14	$2.51\times10^{+44}$
1048−313	Q	1.429	N	0	2.09×10^{-13}	$2.64\times10^{+45}$	2	—	—	—	—	—	—
1049+215	Q	1.300	N	0	5.50×10^{-13}	$5.51\times10^{+45}$	1	1.12	$1.68\times10^{+45}$	1.02	$1.53\times10^{+45}$	0.36	$5.41\times10^{+44}$
1055+018	Q	0.888	Y	X	2.22×10^{-12}	$8.68\times10^{+45}$	1	3.37	$1.98\times10^{+45}$	2.88	$1.69\times10^{+45}$	1.73	$1.01\times10^{+45}$
1055+201	Q	1.110	N	0	1.95×10^{-12}	$1.32\times10^{+46}$	1	0.55	$5.59\times10^{+44}$	0.33	$3.36\times10^{+44}$	0.23	$2.34\times10^{+44}$
1101+384	G	0.030	N	0	9.30×10^{-11}	$1.94\times10^{+44}$	1	0.61	$1.91\times10^{+41}$	0.44	$1.38\times10^{+41}$	0.32	$1.00\times10^{+41}$
1116+128	Q	2.118	N	0	8.50×10^{-13}	$2.83\times10^{+46}$	1	1.12	$5.58\times10^{+45}$	0.79	$3.94\times10^{+45}$	0.39	$1.94\times10^{+45}$
1124−186	Q	1.048	Y	0	1.07×10^{-11}	$6.31\times10^{+46}$	1	1.87	$1.65\times10^{+45}$	1.85	$1.63\times10^{+45}$	1.56	$1.38\times10^{+45}$
1127−145	Q	1.187	Y	X	2.26×10^{-12}	$1.81\times10^{+46}$	1	2.81	$3.37\times10^{+45}$	2.26	$2.71\times10^{+45}$	0.83	$9.96\times10^{+44}$
1128+385	Q	1.733	N	0	5.20×10^{-13}	$1.06\times10^{+46}$	1	0.91	$2.78\times10^{+45}$	0.86	$2.62\times10^{+45}$	0.71	$2.17\times10^{+45}$
1144+402	Q	1.088	N	0	5.23×10^{-13}	$3.37\times10^{+45}$	4	0.81	$7.84\times10^{+44}$	0.78	$7.55\times10^{+44}$	0.62	$6.00\times10^{+44}$
1145−071	Q	1.342	N	0	3.80×10^{-13}	$4.12\times10^{+45}$	1	0.74	$1.20\times10^{+45}$	0.60	$9.75\times10^{+44}$	0.23	$3.74\times10^{+44}$
1148−001	Q	1.982	N	0	9.02×10^{-13}	$2.55\times10^{+46}$	1	0.90	$3.81\times10^{+45}$	0.73	$3.09\times10^{+45}$	0.12	$5.09\times10^{+44}$
1150+812	Q	1.250	Y	0	4.80×10^{-13}	$4.36\times10^{+45}$	1	1.50	$2.05\times10^{+45}$	1.47	$2.00\times10^{+45}$	0.94	$1.28\times10^{+45}$
1155+251	Q	0.202	N	0	3.68×10^{-13}	$4.34\times10^{+43}$	4	0.32	$5.66\times10^{+42}$	0.18	$3.19\times10^{+42}$	0.06	$1.06\times10^{+42}$
1156+295	Q	0.729	Y	X	1.29×10^{-12}	$3.11\times10^{+45}$	1	1.93	$6.98\times10^{+44}$	1.81	$6.54\times10^{+44}$	1.43	$5.17\times10^{+44}$
1213−172	U	0.000	Y	0	3.64×10^{-12}	——	4	2.07	—	2.00	—	0.82	—
1219+044	Q	0.965	Y	0	2.44×10^{-12}	$1.17\times10^{+46}$	1	0.88	$6.33\times10^{+44}$	0.90	$6.48\times10^{+44}$	0.88	$6.33\times10^{+44}$
1219+285	B	0.102	N	0	2.24×10^{-12}	$5.97\times10^{+43}$	1	0.63	$2.52\times10^{+42}$	0.46	$1.84\times10^{+42}$	0.21	$8.40\times10^{+41}$
1222+216	Q	0.435	Y	X	3.60×10^{-12}	$2.50\times10^{+45}$	1	1.04	$1.08\times10^{+44}$	0.85	$8.85\times10^{+43}$	0.62	$6.45\times10^{+43}$
1226+023	Q	0.158	Y	X	9.09×10^{-11}	$6.25\times10^{+45}$	1	29.56	$3.05\times10^{+44}$	21.96	$2.26\times10^{+44}$	3.90	$4.02\times10^{+43}$
1228+126	G	0.004	Y	X	8.03×10^{-10}	$3.47\times10^{+43}$	4	28.41	$1.84\times10^{+41}$	2.11	$1.37\times10^{+40}$	0.46	$2.98\times10^{+39}$
1244−255	Q	0.638	N	0	3.11×10^{-12}	$5.42\times10^{+45}$	1	1.60	$4.18\times10^{+44}$	1.35	$3.53\times10^{+44}$	1.18	$3.08\times10^{+44}$
1251−407	Q	4.464	N	0	1.06×10^{-12}	$2.11\times10^{+47}$	4	—	—	—	—	—	—
1253−055	Q	0.538	Y	X	6.64×10^{-12}	$7.65\times10^{+45}$	1	21.88	$3.78\times10^{+45}$	18.93	$3.27\times10^{+45}$	7.92	$1.37\times10^{+45}$
1255−316	Q	1.924	N	0	5.06×10^{-13}	$1.33\times10^{+46}$	2	1.90	$7.49\times10^{+45}$	0.91	$3.59\times10^{+45}$	0.38	$1.50\times10^{+45}$
1302−102	Q	0.278	N	0	7.22×10^{-12}	$1.76\times10^{+45}$	1	0.75	$2.74\times10^{+43}$	0.63	$2.31\times10^{+43}$	0.37	$1.35\times10^{+43}$
1308+326	Q	0.997	Y	X	9.10×10^{-13}	$4.73\times10^{+45}$	1	2.64	$2.06\times10^{+45}$	2.62	$2.04\times10^{+45}$	1.45	$1.13\times10^{+45}$
1313−333	Q	1.210	N	0	4.53×10^{-13}	$3.80\times10^{+45}$	2	1.30	$1.64\times10^{+45}$	1.02	$1.28\times10^{+45}$	0.57	$7.17\times10^{+44}$
1323+321	G	0.370	N	0	2.85×10^{-13}	$1.35\times10^{+44}$	4	1.01	$7.17\times10^{+43}$	0.57	$4.05\times10^{+43}$	0.02	$1.42\times10^{+42}$
1324+224	Q	1.400	Y	0	8.96×10^{-13}	$1.08\times10^{+46}$	4	0.63	$1.14\times10^{+45}$	0.62	$1.12\times10^{+45}$	0.44	$7.93\times10^{+44}$
1328+254	Q	1.055	N	0	6.40×10^{-13}	$3.83\times10^{+45}$	1	—	—	—	—	—	—
1328+307	Q	0.849	N	0	2.80×10^{-13}	$9.80\times10^{+44}$	1	3.48	$1.83\times10^{+45}$	1.04	$5.46\times10^{+44}$	0.07	$3.68\times10^{+43}$
1334−127	Q	0.539	Y	X	2.87×10^{-12}	$3.32\times10^{+45}$	1	5.78	$1.00\times10^{+45}$	5.62	$9.76\times10^{+44}$	4.72	$8.20\times10^{+44}$
1345+125	G	0.122	N	0	6.28×10^{-13}	$2.46\times10^{+43}$	4	1.40	$8.22\times10^{+42}$	0.80	$4.70\times10^{+42}$	0.06	$3.52\times10^{+41}$
1354+196	Q	0.720	N	0	1.46×10^{-12}	$3.41\times10^{+45}$	2	1.10	$3.86\times10^{+44}$	0.95	$3.33\times10^{+44}$	0.57	$2.00\times10^{+44}$
1354−152	Q	1.890	N	0	6.22×10^{-13}	$1.56\times10^{+46}$	2	0.72	$2.72\times10^{+45}$	0.65	$2.45\times10^{+45}$	0.58	$2.19\times10^{+45}$
1354−174	Q	3.147	N	0	5.59×10^{-13}	$4.85\times10^{+46}$	1	—	—	—	—	—	—

Table B.3 – continued from previous page

Source[a]	Classification[b]	z[c]	M[d]	2 cm-X[e]	$F^{\rm f}_{(0.2-2.4)\ {\rm keV}}$ [erg s^{-1} cm^{-2}]	$L^{\rm g}_{(0.2-2.4)\ {\rm keV}}$ [erg s^{-1}]	Ref.[h]	$S^{\rm i}_{\rm tot}$ [Jy]	$L_{\rm tot}$ [erg s^{-1}]	$S^{\rm j}_{\rm VLBA}$ [Jy]	$L_{\rm VLBA}$ [erg s^{-1}]	$S^{\rm k}_{\rm core}$ [Jy]	$L_{\rm core}$ [erg s^{-1}]
1402+044	Q	3.193	N	0	2.00×10^{-13}	$1.80\times10^{+46}$	1	0.69	$9.30\times10^{+45}$	0.58	$7.81\times10^{+45}$	0.29	$3.91\times10^{+45}$
1404+286	G	0.077	N	0	3.71×10^{-13}	$5.44\times10^{+42}$	4	1.16	$2.55\times10^{+42}$	1.02	$2.24\times10^{+42}$	0.45	$9.89\times10^{+41}$
1413+135	B	0.247	Y	X	5.30×10^{-14}	$9.88\times10^{+42}$	1	1.43	$4.00\times10^{+43}$	1.33	$3.72\times10^{+43}$	0.70	$1.96\times10^{+43}$
1417+385	Q	1.832	Y	0	3.16×10^{-13}	$7.35\times10^{+45}$	1	0.92	$3.22\times10^{+45}$	0.99	$3.46\times10^{+45}$	0.76	$2.66\times10^{+45}$
1418+546	B	0.151	N	0	1.25×10^{-12}	$7.79\times10^{+43}$	1	0.95	$8.86\times10^{+42}$	0.94	$8.77\times10^{+42}$	0.60	$5.60\times10^{+42}$
1424+366	B	1.091	N	0	2.77×10^{-13}	$1.80\times10^{+45}$	4	0.40	$3.90\times10^{+44}$	0.35	$3.41\times10^{+44}$	0.16	$1.56\times10^{+44}$
1442+101	Q	3.522	N	0	6.00×10^{-13}	——	1	—	—	—	—	—	—
1458+718	Q	0.904	Y	X	1.44×10^{-12}	$5.88\times10^{+45}$	1	2.08	$1.27\times10^{+45}$	1.24	$7.60\times10^{+44}$	0.66	$4.05\times10^{+44}$
1502+106	Q	1.833	Y	X	2.90×10^{-13}	$6.77\times10^{+45}$	1	1.58	$5.53\times10^{+45}$	1.45	$5.08\times10^{+45}$	0.78	$2.73\times10^{+45}$
1504+377	G	0.672	N	0	2.44×10^{-13}	$4.81\times10^{+44}$	4	2.13	$6.30\times10^{+44}$	1.81	$5.35\times10^{+44}$	1.18	$3.49\times10^{+44}$
1504−167	Q	0.876	Y	0	2.82×10^{-12}	$1.07\times10^{+46}$	1	0.68	$3.86\times10^{+44}$	0.56	$3.18\times10^{+44}$	0.35	$1.99\times10^{+44}$
1508−055	Q	1.185	N	0	1.13×10^{-12}	$9.00\times10^{+45}$	2	1.11	$1.33\times10^{+45}$	0.58	$6.93\times10^{+44}$	0.28	$3.35\times10^{+44}$
1510−089	Q	0.360	Y	X	5.46×10^{-12}	$2.43\times10^{+45}$	1	1.96	$1.31\times10^{+44}$	1.63	$1.09\times10^{+44}$	1.26	$8.40\times10^{+43}$
1511−110	Q	1.513	N	0	1.04×10^{-12}	$1.51\times10^{+46}$	2	1.22	$2.66\times10^{+45}$	1.12	$2.45\times10^{+45}$	0.46	$1.00\times10^{+45}$
1514−241	G	0.052	N	0	2.64×10^{-12}	$1.70\times10^{+43}$	1	1.01	$9.76\times10^{+41}$	0.96	$9.27\times10^{+41}$	0.80	$7.73\times10^{+41}$
1514+004	B	0.049	N	0	1.93×10^{-12}	$1.09\times10^{+43}$	1	2.15	$1.82\times10^{+42}$	1.97	$1.66\times10^{+42}$	1.01	$8.54\times10^{+41}$
1519−273	B	0.071	N	0	4.21×10^{-12}	$5.22\times10^{+43}$	1	1.60	$2.98\times10^{+42}$	1.40	$2.61\times10^{+42}$	0.95	$1.77\times10^{+42}$
1532+016	Q	1.435	N	0	7.30×10^{-13}	$9.33\times10^{+45}$	1	0.69	$1.32\times10^{+45}$	0.52	$9.97\times10^{+44}$	0.25	$4.79\times10^{+44}$
1538+149	Q	0.605	Y	0	1.49×10^{-12}	$2.29\times10^{+45}$	1	1.02	$2.34\times10^{+44}$	0.75	$1.72\times10^{+44}$	0.62	$1.42\times10^{+44}$
1546+027	Q	0.412	Y	0	1.60×10^{-12}	$9.76\times10^{+44}$	1	2.08	$1.90\times10^{+44}$	1.97	$1.80\times10^{+44}$	1.54	$1.41\times10^{+44}$
1548+056	Q	1.422	Y	0	5.00×10^{-13}	$6.25\times10^{+45}$	1	2.81	$5.27\times10^{+45}$	2.59	$4.85\times10^{+45}$	1.46	$2.74\times10^{+45}$
1555+001	Q	1.770	N	0	2.20×10^{-13}	$4.71\times10^{+45}$	2	0.71	$2.28\times10^{+45}$	0.68	$2.18\times10^{+45}$	0.35	$1.12\times10^{+45}$
1606+106	Q	1.226	Y	0	6.00×10^{-13}	$5.20\times10^{+45}$	1	1.62	$2.11\times10^{+45}$	1.59	$2.07\times10^{+45}$	0.87	$1.13\times10^{+45}$
1607+268	G	0.473	N	0	4.32×10^{-13}	$3.66\times10^{+44}$	4	0.42	$5.33\times10^{+43}$	0.31	$3.94\times10^{+43}$	0.04	$5.08\times10^{+42}$
1611+343	Q	1.401	Y	0	1.62×10^{-12}	$1.95\times10^{+46}$	1	3.98	$7.19\times10^{+45}$	3.88	$7.01\times10^{+45}$	2.09	$3.78\times10^{+45}$
1622−251	Q	0.786	N	0	1.90×10^{-12}	$5.51\times10^{+45}$	1	2.23	$9.69\times10^{+44}$	1.62	$7.04\times10^{+44}$	1.36	$5.91\times10^{+44}$
1622−297	Q	0.815	N	0	1.83×10^{-12}	——	1	2.00	$9.50\times10^{+44}$	1.73	$8.22\times10^{+44}$	1.04	$4.94\times10^{+44}$
1624+416	Q	2.550	N	0	1.41×10^{-13}	——	1	0.57	$4.46\times10^{+45}$	0.49	$3.84\times10^{+45}$	0.18	$1.41\times10^{+45}$
1633+382	Q	1.807	Y	X	1.80×10^{-12}	$4.06\times10^{+46}$	1	2.63	$8.89\times10^{+45}$	2.31	$7.81\times10^{+45}$	1.37	$4.63\times10^{+45}$
1637+574	Q	0.751	Y	0	1.45×10^{-12}	$3.76\times10^{+45}$	1	1.66	$6.45\times10^{+44}$	1.69	$6.57\times10^{+44}$	1.27	$4.94\times10^{+44}$
1638+398	Q	1.666	Y	0	2.80×10^{-13}	$5.17\times10^{+45}$	1	1.15	$3.18\times10^{+45}$	1.08	$2.99\times10^{+45}$	0.73	$2.02\times10^{+45}$
1641+399	Q	0.594	Y	X	3.86×10^{-12}	$5.65\times10^{+45}$	1	8.05	$1.77\times10^{+45}$	7.01	$1.54\times10^{+45}$	2.71	$5.95\times10^{+44}$
1642+690	Q	0.751	N	0	7.20×10^{-13}	$1.87\times10^{+45}$	1	1.15	$4.47\times10^{+44}$	0.89	$3.46\times10^{+44}$	0.71	$2.76\times10^{+44}$
1652+398	G	0.034	N	0	6.07×10^{-11}	$1.59\times10^{+44}$	1	1.17	$4.60\times10^{+41}$	0.74	$2.91\times10^{+41}$	0.38	$1.49\times10^{+41}$
1655+077	Q	0.621	Y	X	3.28×10^{-13}	$5.35\times10^{+44}$	2	1.64	$4.01\times10^{+44}$	1.55	$3.79\times10^{+44}$	1.07	$2.62\times10^{+44}$
1656+053	Q	0.879	N	0	3.02×10^{-12}	$1.15\times10^{+46}$	1	0.83	$4.75\times10^{+44}$	0.53	$3.03\times10^{+44}$	0.19	$1.09\times10^{+44}$
1656+477	Q	1.622	N	0	3.50×10^{-13}	$6.05\times10^{+45}$	1	1.06	$2.75\times10^{+45}$	1.05	$2.72\times10^{+45}$	0.60	$1.56\times10^{+45}$
1726+455	Q	0.714	Y	0	4.63×10^{-13}	$1.06\times10^{+45}$	1	1.67	$5.74\times10^{+44}$	1.62	$5.57\times10^{+44}$	1.38	$4.74\times10^{+44}$
1730−130	Q	0.902	Y	0	5.76×10^{-12}	$2.34\times10^{+46}$	1	6.83	$4.16\times10^{+45}$	5.62	$3.43\times10^{+45}$	3.50	$2.13\times10^{+45}$

Source[a]	Classification[b]	z[c]	M[d]	2 cm-X[e]	$F^{\mathrm{f}}_{(0.2-2.4)\,\mathrm{keV}}$ [erg s^{-1} cm^{-2}]	$L^{\mathrm{g}}_{(0.2-2.4)\,\mathrm{keV}}$ [erg s^{-1}]	Ref.[h]	$S^{\mathrm{i}}_{\mathrm{tot}}$ [Jy]	L_{tot} [erg s^{-1}]	$S^{\mathrm{j}}_{\mathrm{VLBA}}$ [Jy]	L_{VLBA} [erg s^{-1}]	$S^{\mathrm{k}}_{\mathrm{core}}$ [Jy]	L_{core} [erg s^{-1}]
1739+522	Q	1.379	Y	0	1.10×10^{-12}	$1.27\times10^{+46}$	1	1.29	$2.24\times10^{+45}$	1.32	$2.29\times10^{+45}$	0.71	$1.23\times10^{+45}$
1741−038	Q	1.057	Y	0	3.72×10^{-12}	$2.23\times10^{+46}$	1	5.90	$5.32\times10^{+45}$	5.64	$5.08\times10^{+45}$	3.90	$3.51\times10^{+45}$
1749+096	B	0.320	Y	X	2.12×10^{-12}	$7.16\times10^{+44}$	1	3.75	$1.90\times10^{+44}$	3.56	$1.80\times10^{+44}$	3.22	$1.63\times10^{+44}$
1749+701	B	0.770	N	0	1.41×10^{-12}	$3.88\times10^{+45}$	1	0.63	$2.60\times10^{+44}$	0.48	$1.98\times10^{+44}$	0.33	$1.36\times10^{+44}$
1751+288	U	0.000	Y	0	4.09×10^{-13}	——	4	1.77	—	1.95	—	1.76	—
1758+388	Q	2.092	Y	0	1.12×10^{-12}	$3.61\times10^{+46}$	1	1.39	$6.72\times10^{+45}$	1.39	$6.72\times10^{+45}$	1.08	$5.22\times10^{+45}$
1800+440	Q	0.663	Y	0	9.50×10^{-13}	$1.82\times10^{+45}$	1	1.08	$3.10\times10^{+44}$	1.01	$2.90\times10^{+44}$	0.90	$2.58\times10^{+44}$
1803+784	Q	0.680	Y	X	1.48×10^{-12}	$3.02\times10^{+45}$	1	2.42	$7.38\times10^{+44}$	2.15	$6.56\times10^{+44}$	1.16	$3.54\times10^{+44}$
1807+698	B	0.051	N	0	3.70×10^{-12}	$2.30\times10^{+43}$	1	1.52	$1.42\times10^{+42}$	1.18	$1.10\times10^{+42}$	0.51	$4.76\times10^{+41}$
1821+107	Q	1.364	N	0	1.70×10^{-12}	$1.92\times10^{+46}$	1	0.48	$8.12\times10^{+44}$	0.38	$6.43\times10^{+44}$	0.24	$4.06\times10^{+44}$
1823+568	Q	0.663	Y	X	2.31×10^{-12}	$4.42\times10^{+45}$	1	1.65	$4.73\times10^{+44}$	1.54	$4.42\times10^{+44}$	1.18	$3.38\times10^{+44}$
1828+487	Q	0.692	Y	X	3.73×10^{-12}	$7.91\times10^{+45}$	1	3.05	$9.71\times10^{+44}$	1.84	$5.86\times10^{+44}$	0.98	$3.12\times10^{+44}$
1845+797	G	0.056	N	0	1.05×10^{-11}	$7.93\times10^{+43}$	1	1.59	$1.80\times10^{+42}$	0.37	$4.18\times10^{+41}$	0.21	$2.37\times10^{+41}$
1849+670	Q	0.657	Y	0	1.27×10^{-12}	$2.37\times10^{+45}$	1	1.60	$4.49\times10^{+44}$	1.74	$4.88\times10^{+44}$	1.52	$4.26\times10^{+44}$
1901+319	Q	0.635	N	0	7.23×10^{-13}	$1.24\times10^{+45}$	4	1.27	$3.28\times10^{+44}$	1.00	$2.58\times10^{+44}$	0.50	$1.29\times10^{+44}$
1908−201	Q	1.119	N	0	1.56×10^{-12}	$1.08\times10^{+46}$	4	3.30	$3.42\times10^{+45}$	2.82	$2.92\times10^{+45}$	2.20	$2.28\times10^{+45}$
1921−293	Q	0.352	N	0	6.27×10^{-12}	$2.64\times10^{+45}$	1	14.55	$9.20\times10^{+44}$	11.83	$7.48\times10^{+44}$	5.30	$3.35\times10^{+44}$
1928+738	Q	0.303	Y	X	7.09×10^{-12}	$2.11\times10^{+45}$	1	3.62	$1.62\times10^{+44}$	3.07	$1.37\times10^{+44}$	1.71	$7.63\times10^{+43}$
1936−155	Q	1.657	Y	0	1.20×10^{-12}	$2.19\times10^{+46}$	1	1.53	$4.18\times10^{+45}$	1.27	$3.47\times10^{+45}$	0.94	$2.57\times10^{+45}$
1937−101	Q	3.787	N	0	7.20×10^{-13}	$9.72\times10^{+46}$	1	0.42	$8.51\times10^{+45}$	0.29	$5.88\times10^{+45}$	0.15	$3.04\times10^{+45}$
1954+513	Q	1.220	N	0	1.40×10^{-12}	$1.20\times10^{+46}$	1	2.70	$3.47\times10^{+45}$	2.76	$3.54\times10^{+45}$	1.84	$2.36\times10^{+45}$
1954−388	Q	0.630	N	0	1.08×10^{-12}	——	1	0.93	$2.36\times10^{+44}$	0.87	$2.20\times10^{+44}$	0.41	$1.04\times10^{+44}$
1957+405	G	0.056	Y	X	6.25×10^{-11}	$4.71\times10^{+44}$	1	94.31	$1.07\times10^{+44}$	1.49	$1.68\times10^{+42}$	0.14	$1.58\times10^{+41}$
1958−179	Q	0.652	Y	0	3.27×10^{-12}	$6.00\times10^{+45}$	1	2.04	$5.62\times10^{+44}$	1.86	$5.12\times10^{+44}$	1.50	$4.13\times10^{+44}$
2000−330	Q	3.773	N	0	3.50×10^{-13}	$4.69\times10^{+46}$	1	0.54	$1.08\times10^{+46}$	0.39	$7.83\times10^{+45}$	0.15	$3.01\times10^{+45}$
2005+403	Q	1.736	Y	0	1.83×10^{-12}	$3.74\times10^{+46}$	4	2.46	$7.53\times10^{+45}$	2.33	$7.14\times10^{+45}$	0.35	$1.07\times10^{+45}$
2007+776	B	0.342	N	0	1.08×10^{-12}	$4.27\times10^{+44}$	1	1.17	$6.92\times10^{+43}$	1.01	$5.97\times10^{+43}$	0.51	$3.02\times10^{+43}$
2008−159	Q	1.180	Y	0	2.96×10^{-12}	$2.33\times10^{+46}$	1	1.77	$2.09\times10^{+45}$	1.74	$2.06\times10^{+45}$	1.38	$1.63\times10^{+45}$
2010+463	U	0.000	N	0	2.71×10^{-11}	——	4	0.33	—	0.28	—	0.23	—
2021+317	U	0.000	Y	0	1.66×10^{-12}	——	4	1.42	—	1.29	—	0.52	—
2021+614	G	0.227	Y	0	5.71×10^{-13}	$8.79\times10^{+43}$	4	2.55	$5.89\times10^{+43}$	2.24	$5.17\times10^{+43}$	0.60	$1.38\times10^{+43}$
2029+121	B	1.215	N	0	1.39×10^{-12}	$1.18\times10^{+46}$	1	0.95	$1.21\times10^{+45}$	0.99	$1.26\times10^{+45}$	0.60	$7.63\times10^{+44}$
2037+511	Q	1.687	Y	0	4.69×10^{-13}	$8.92\times10^{+45}$	1	2.57	$7.34\times10^{+45}$	2.22	$6.34\times10^{+45}$	1.46	$4.17\times10^{+45}$
2059+034	Q	1.013	N	0	1.01×10^{-12}	$5.46\times10^{+45}$	1	0.91	$7.38\times10^{+44}$	0.95	$7.71\times10^{+44}$	0.78	$6.33\times10^{+44}$
2113+293	B	1.514	N	0	4.63×10^{-13}	$6.74\times10^{+45}$	1	0.77	$1.68\times10^{+45}$	0.74	$1.62\times10^{+45}$	0.58	$1.27\times10^{+45}$
2121+053	Q	1.941	Y	0	9.78×10^{-13}	$2.63\times10^{+46}$	1	2.10	$8.46\times10^{+45}$	2.27	$9.14\times10^{+45}$	1.81	$7.29\times10^{+45}$
2126−158	Q	3.268	N	0	4.20×10^{-12}	$3.99\times10^{+47}$	1	1.25	$1.78\times10^{+46}$	1.19	$1.70\times10^{+46}$	0.88	$1.25\times10^{+46}$
2128+048	G	0.990	N	0	1.05×10^{-12}	$5.37\times10^{+45}$	4	0.78	$5.98\times10^{+44}$	0.49	$3.76\times10^{+44}$	0.02	$1.53\times10^{+43}$
2128−123	Q	0.501	Y	0	5.26×10^{-12}	$5.11\times10^{+45}$	1	2.88	$4.20\times10^{+44}$	2.58	$3.76\times10^{+44}$	0.87	$1.27\times10^{+44}$

Table B.3 – continued from previous page

Source[a]	Classification[b]	z^{c}	M[d]	2 cm-X[e]	$F^{f}_{(0.2-2.4)\,keV}$ [erg s^{-1} cm^{-2}]	$L^{g}_{(0.2-2.4)\,keV}$ [erg s^{-1}]	Ref.[h]	S^{i}_{tot} [Jy]	L_{tot} [erg s^{-1}]	S^{j}_{VLBA} [Jy]	L_{VLBA} [erg s^{-1}]	S^{k}_{core} [Jy]	L_{core} [erg s^{-1}]
2131−021	Q	1.285	Y	0	3.84×10^{-13}	$3.74\times10^{+45}$	1	1.84	$2.69\times10^{+45}$	1.75	$2.55\times10^{+45}$	0.39	$5.69\times10^{+44}$
2134+004	Q	1.932	Y	X	1.53×10^{-12}	$4.06\times10^{+46}$	1	6.47	$2.58\times10^{+46}$	5.65	$2.25\times10^{+46}$	1.26	$5.02\times10^{+45}$
2136+141	Q	2.427	Y	0	7.20×10^{-13}	$3.33\times10^{+46}$	1	1.95	$1.35\times10^{+46}$	1.81	$1.26\times10^{+46}$	0.78	$5.42\times10^{+45}$
2144+092	Q	1.113	N	X	2.69×10^{-13}	$1.84\times10^{+45}$	2	0.67	$6.86\times10^{+44}$	0.66	$6.76\times10^{+44}$	0.37	$3.79\times10^{+44}$
2145+067	Q	0.999	Y	0	5.57×10^{-12}	$2.91\times10^{+46}$	1	8.50	$6.66\times10^{+45}$	7.90	$6.19\times10^{+45}$	2.53	$1.98\times10^{+45}$
2155−152	Q	0.672	Y	0	5.70×10^{-13}	$1.13\times10^{+45}$	1	2.17	$6.43\times10^{+44}$	1.96	$5.81\times10^{+44}$	1.11	$3.29\times10^{+44}$
2200+420	B	0.069	Y	X	5.55×10^{-12}	$6.46\times10^{+43}$	1	3.60	$6.29\times10^{+42}$	3.22	$5.63\times10^{+42}$	1.83	$3.20\times10^{+42}$
2201+171	Q	1.076	Y	0	5.00×10^{-13}	$3.14\times10^{+45}$	1	1.92	$1.81\times10^{+45}$	2.01	$1.89\times10^{+45}$	1.56	$1.47\times10^{+45}$
2201+315	Q	0.297	Y	0	1.01×10^{-11}	$2.87\times10^{+45}$	1	2.64	$1.13\times10^{+44}$	2.54	$1.08\times10^{+44}$	1.87	$7.97\times10^{+43}$
2203−188	Q	0.620	N	0	1.60×10^{-13}	$2.59\times10^{+44}$	1	—	—	—	—	—	—
2209+236	Q	1.125	Y	0	6.31×10^{-13}	——	4	1.16	$1.22\times10^{+45}$	1.17	$1.23\times10^{+45}$	0.74	$7.78\times10^{+44}$
2215+020	Q	3.550	N	0	1.38×10^{-13}	$1.59\times10^{+46}$	3	—	—	—	—	—	—
2216−038	Q	0.901	Y	0	1.35×10^{-12}	$5.47\times10^{+45}$	1	2.13	$1.29\times10^{+45}$	2.02	$1.23\times10^{+45}$	1.09	$6.63\times10^{+44}$
2223−052	B	1.404	Y	X	1.79×10^{-12}	$2.17\times10^{+46}$	1	5.39	$9.79\times10^{+45}$	4.11	$7.46\times10^{+45}$	1.96	$3.56\times10^{+45}$
2227−088	Q	1.561	Y	0	5.00×10^{-13}	$7.86\times10^{+45}$	1	1.36	$3.21\times10^{+45}$	1.25	$2.95\times10^{+45}$	1.03	$2.43\times10^{+45}$
2230+114	Q	1.037	Y	X	2.24×10^{-12}	$1.28\times10^{+46}$	1	3.90	$3.35\times10^{+45}$	3.26	$2.80\times10^{+45}$	1.69	$1.45\times10^{+45}$
2234+282	Q	0.795	N	0	6.38×10^{-13}	$1.90\times10^{+45}$	1	1.05	$4.69\times10^{+44}$	1.08	$4.83\times10^{+44}$	0.55	$2.46\times10^{+44}$
2243−123	Q	0.630	Y	X	3.11×10^{-12}	$5.25\times10^{+45}$	1	2.29	$5.80\times10^{+44}$	2.02	$5.12\times10^{+44}$	1.50	$3.80\times10^{+44}$
2251+158	Q	0.859	Y	X	7.16×10^{-12}	$2.58\times10^{+46}$	1	9.81	$5.30\times10^{+45}$	8.54	$4.62\times10^{+45}$	2.24	$1.21\times10^{+45}$
2255−282	Q	0.926	N	0	6.20×10^{-13}	$2.69\times10^{+45}$	1	6.39	$4.15\times10^{+45}$	6.30	$4.10\times10^{+45}$	4.74	$3.08\times10^{+45}$
2318+049	Q	0.623	N	0	1.24×10^{-12}	$2.03\times10^{+45}$	1	0.90	$2.21\times10^{+44}$	0.91	$2.24\times10^{+44}$	0.62	$1.53\times10^{+44}$
2329−162	Q	1.153	N	0	2.69×10^{-13}	$2.00\times10^{+45}$	2	1.05	$1.17\times10^{+45}$	0.83	$9.27\times10^{+44}$	0.21	$2.35\times10^{+44}$
2331+073	U	0.000	Y	0	2.11×10^{-12}	——	3	1.16	—	1.15	—	0.66	—
2345−167	Q	0.576	Y	0	8.40×10^{-13}	$1.14\times10^{+45}$	1	2.15	$4.38\times10^{+44}$	1.81	$3.69\times10^{+44}$	0.78	$1.59\times10^{+44}$
2351+456	Q	1.986	Y	0	9.97×10^{-13}	$2.83\times10^{+46}$	4	2.10	$8.95\times10^{+45}$	1.70	$7.24\times10^{+45}$	0.97	$4.13\times10^{+45}$

[a] B 1950 coordinates; [b] Optical classification according to the Véron-Cetty and Véron (2003) catalog, where Q = quasar, B = BL Lac object, G = active galaxy, and U = unidentified; [c] Redshift from Véron-Cetty and Véron (2003) (the redshift of 0202+149 is from Stickel et al. 1996, that of 0727−115 is from Zensus et al. 2002, that of 0742+103 is from Best et al. 2003, that of 0754+100 is from Carangelo et al. 2003, that of 0808+019 is from Jackson et al. 2002, and that of 2209+236 is from Sowards-Emmerd et al. 2003.); [d] Flag, indicating whether the source belongs to the MOJAVE sample; [e] Flag, indicating whether the source belongs to the 2 cm-X-Sample; [f] Unabsorbed $(0.2-2.4)$ keV flux from RASS. Errors are typically $\sim 20\,\%$; [g] Source-intrinsic $(0.2-2.4)$ keV luminosity assuming isotropic emission; [h] Reference for RASS Flux values. 1: Brinkmann et al. (1997b), 2: Siebert et al. (1998), 3: E. Ferrero (priv. comm.), 4: this thesis; [i] Mean total 15 GHz flux taken from Kovalev et al. (2005); [j] Mean total 15 GHz flux taken from Kovalev et al. (2005); [k] Mean total 15 GHz flux taken from Kovalev et al. (2005)

B.2   Soft X-Ray Flux Distributions of the Full 2 cm Survey Sample, MOJAVE and the 2 cm-X-Sample

The soft X-ray fluxes for the full VLBA 2 cm Survey are given in Table B.3 and their distribution for the MOJAVE and the *2 cm-X-Sample* are shown in Fig. B.3. The (0.1–2.4) keV fluxes were derived from *ROSAT* all-sky-survey and pointed observations as outlined above and were corrected for Galactic absorption. In the case of non-detections, upper limits are plotted in Fig. B.3 The quasar distribution for the statistically complete MOJAVE sample appears remarkably symmetric around a median flux value of $(1.0 - 1.8) \times 10^{-12}\,\mathrm{erg\,s^{-1}\,cm^{-2}}$. This is remarkable since the MOJAVE is essentially a flux-limit selected sample and if radio- and soft X-ray flux were directly correlated one would expect a skewed distribution of X-ray fluxes with a maximum at low fluxes as exhibited by the VLBI-flux distribution (compare Fig 3.2). The full VLBA 2 cm Survey sample exhibits such a skewed distribution, considering the relatively large fraction of upper limits that correspond to fluxes left of the median, while the *2 cm-X-Sample* is biased towards objects with high X-ray flux. The distribution peaks at $\sim (1.8-3.2) \times 10^{-12}\,\mathrm{erg\,s^{-1}\,cm^{-2}}$ and is skewed towards high fluxes.

Although the quasi-Gaussian (in logarithmic units) distribution of X-ray fluxes of MOJAVE quasars argues against a direct "one-to-one" correlation between radio and X-ray fluxes, it is worth noting that the detection rate of MOJAVE quasars ($\sim 90\%$) is higher than the detection rate of the less-bright sources of the VLBA 2 cm Survey that do not belong to MOJAVE ($\sim 76\%$). The high detection rate of the *2 cm-X-Sample* ($\sim 94\%$) reflects the fact that in the class of radio-loud AGN preferably bright, well known objects have been observed during the last decade of X-ray astronomy.

The detection rates for all three samples are higher than the *ROSAT* detection rate of most other radio selected AGN samples and much higher than the detection rate of radio-quiet AGN ($\sim 5.5\%$: Yuan et al. 1998). A large mixed sample of steep- and flat-spectrum radio-loud quasars shows a detection rate of 33.2 % (Brinkmann et al. 1997b). A 47 % detection rate is reported by Siebert et al. (1998) for flat-spectrum PKS quasars from the half-Jansky Drinkwater et al. (1997) sample. This is surprising because those authors applied selection criteria similar to the ones of MOJAVE: a flat spectral index and high (total) radio flux. Apart from covering mainly the southern sky ($-45° < \delta < +10°$), the main difference to MOJAVE is the lower limiting flux of 0.5 Jy at 2.7 GHz and the fact that the selection was based on total radio flux and not on the correlated VLBI flux. In Fig. B.1, the detection rate for the full 2 cm Survey sample is displayed as a function of total-, and VLBI- flux density. In addition, the detection rates are shown for the flux density of the most compact[4] structures S_{unres} and the resolved (i.e., jet) flux density $S_{\mathrm{jet}} = S_{\mathrm{VLBI}} - S_{\mathrm{unres}}$. A clear trend of decreasing detection probability with decreasing flux is seen for the total, integrated VLBI, and unresolved VLBI flux. In contrast to this, no obvious trend of the detection rate with the VLBA-resolved parsec-scale jet emission can be seen. The tentative correlation between VLBA-jet flux density and *ROSAT* detection rate is most likely introduced by the fact that the sources with the

---

[4]The term compact means here unresolved with the VLBA at 15 GHz; compare Kovalev et al. (2005): "The unresolved (compact) flux density S_{unres} is defined as the upper envelope (with 90 % of the visibilities below it) of the visibility function amplitude S_c at projected baselines $r_{uv} > 360\,\mathrm{M}\lambda$."

strongest VLBI cores tend to have strong parsec-scale radio jets. It can be concluded that the flux density of the most compact emission regions (which dominates the total flux density) is responsible for this correlation. The low detection rate of other radio-selected AGN samples compared to the 2 cm Survey sample can therefore be interpreted as a result of weaker sub-parsec scale VLBI radio structures in those samples. For the Yuan et al. (1998) sample of radio-quiet objects and the Brinkmann et al. (1997b) sample, that contains flat- and steep-spectrum sources this is apparent. The Siebert et al. (1998) sample is expected to contain a large number of weaker compact VLBI cores compared to the "average" 2 cm Survey VLBI core because of the lower flux limit and the selection at lower radio frequencies.

All this suggests that the soft X-ray brightness of an AGN and therefore its detection probability for *ROSAT* is markedly increasing if the object harbors a bright compact radio core and sub-parsec-scale radio structure. Figure B.2 shows that indeed the soft X-ray flux and the radio flux density of VLBA 2 cm Survey sources are correlated (quantified below). The correlation is clearly visible for the total 15 GHz emission, for the full VLBI flux density, for the unresolved VLBI flux density and even for the on parsec scales resolved jet emission. This is particularly remarkable since the VLBA 2 cm Survey sources are known to be strongly variable and the radio and X-ray fluxes seen in Fig. B.2 have not been obtained simultaneously. In fact, most of the *ROSAT* data have been obtained between 1990 and 1991, while the 2 cm Survey observations have been carried out between 1994 and 2003. It is obvious that the correlations are further distorted by a population of very X-ray bright sources that have only moderate radio-flux densities. This population is dominated by galaxies, in most cases by their associated bright extended soft emission. For homogeneity, the flux–flux correlation analysis was performed only for quasars. The correlation coefficient ρ is similar for the $S_{\mathrm{tot}} - F_{\mathrm{X}}$, $S_{\mathrm{VLBI}} - F_{\mathrm{X}}$, and $S_{\mathrm{unres}} - F_{\mathrm{X}}$ correlations ($\rho = 0.52$, 0.51, and 0.50, respectively). The correlation between resolved VLBI jet flux density and soft X-ray flux $S_{\mathrm{VLBIJet}} - F_{\mathrm{X}}$ is less pronounced with $\rho = 0.35$. Similarly, the fitted slopes a of the linear-regressions for quasars for total-, integrated VLBI-, and unresolved VLBI flux density are in a similar range: $a_{\mathrm{tot}} = 0.64 \pm 0.09$, $a_{\mathrm{VLBI}} = 0.62 \pm 0.09$, $a_{\mathrm{unres}} = 0.56 \pm 0.08$; The $S_{\mathrm{VLBIJet}} - F_{\mathrm{X}}$ regression has a flatter slope: $a_{\mathrm{VLBIJet}} = 0.33 \pm 0.07$,).

In comparison to the quasars, the BL Lac objects of all three samples are X-ray brighter (the MOJAVE flux distribution peaks at $\sim (1.8 - 3.2) \times 10^{-12}\,\mathrm{erg\,s^{-1}\,cm^{-2}}$) and the detection rate is higher (2 cm Survey/non-MOJAVE: $\sim 88\%$; MOJAVE sample: $\sim 94\%$; 2 cm-X-Sample: 100%). The radio galaxies have a much smaller detection probability at X-rays which is, however, most pronounced for the full 2 cm Survey sample (2 cm Survey/non-MOJAVE: $\sim 50\%$; MOJAVE sample: $\sim 88\%$; 2 cm-X-Sample: 100%) and therefore probably not a significant characteristic of the galaxy class. More noteworthy is the fact that the galaxies cover a very broad range in X-ray flux – unlike the other classes – with extremely bright X-ray sources and a large fraction of sources that are too dim to be detected by *ROSAT*. The unclassified objects have low detection rates (2 cm Survey/non-MOJAVE: $\sim 50\%$; MOJAVE sample: $\sim 78\%$) and less bright than classified objects.
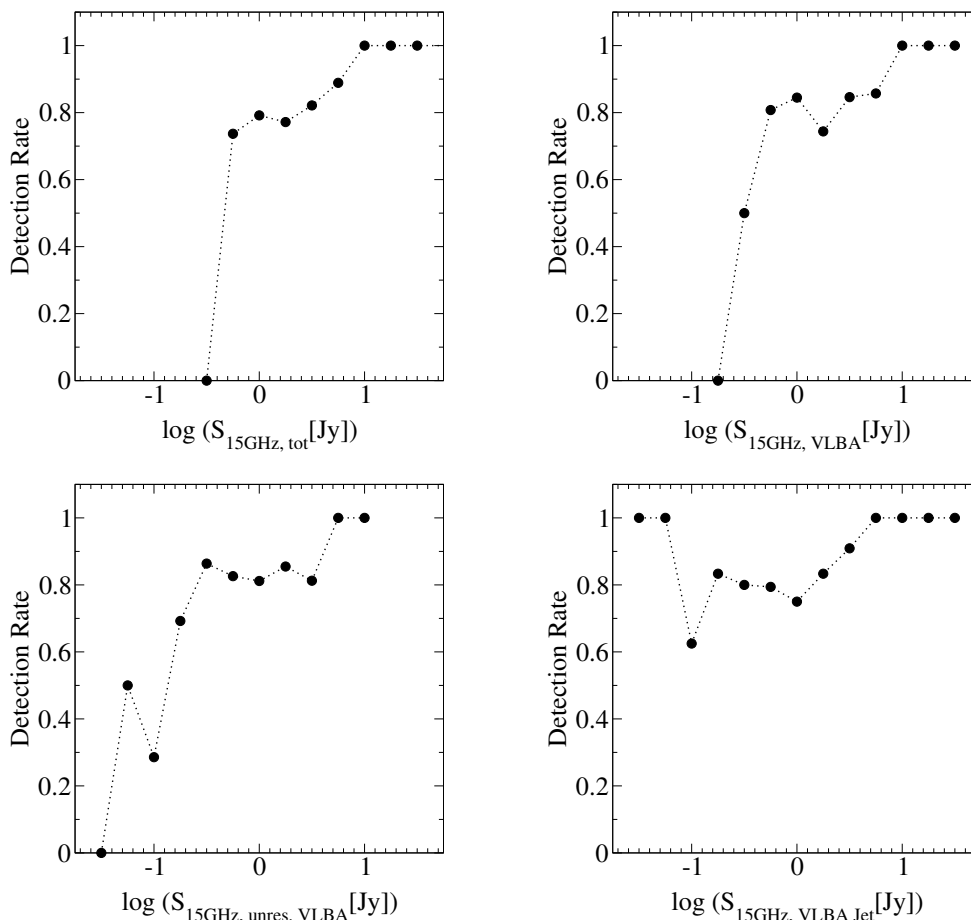
Figure B.1: ROSAT detection rates. The distributions for total radio emission (top left), full VLBI flux density (top right), unresolved VLBI flux density (bottom left) and the on parsec scales resolved emission from the radio jet (bottom right) are shown.

B.3   Radio–X-ray Luminosity Correlation Analysis

The X-ray (0.1-2.4) keV luminosity distribution of the VLBA 2 cm Survey sources covers a broad range: almost eight orders of magnitude between $10^{40}\,\mathrm{erg\,s^{-1}}$ and $10^{48}\,\mathrm{erg\,s^{-1}}$. Figure B.4 shows the individual distributions for all quasars, BL Lac objects and galaxies with known redshift (all unidentified objects have no redshift, and thus no luminosity could be determined). The quasars (in particular the MOJAVE quasars) have a Gaussian distribution in soft X-ray luminosity, with a median of $\sim 5 \times 10^{45}\,\mathrm{erg\,cm^{-2}\,s^{-1}}$. The *2 cm-X-Sample* appears consistent with being drawn unbiased and representatively from MOJAVE, i.e., the skewed flux distribution (towards bright objects) is not transfered into the luminosity domain!

It is known that the soft X-ray luminosity of flat- and steep-spectrum AGN correlates with radio luminosity (e.g., Akritas and Siebert 1996, Baker et al. 1995, Siebert et al. 1996, Siebert et al. 1998, Brinkmann et al. 1997b). The radio core, i.e. the sub-arcsecond scale region unresolved for connected radio interferometers like the VLA, has been identified as the most likely origin of the observed correlations, which typically still hold when going from total radio luminosity to sub-arcsecond scale radio-core luminosity.
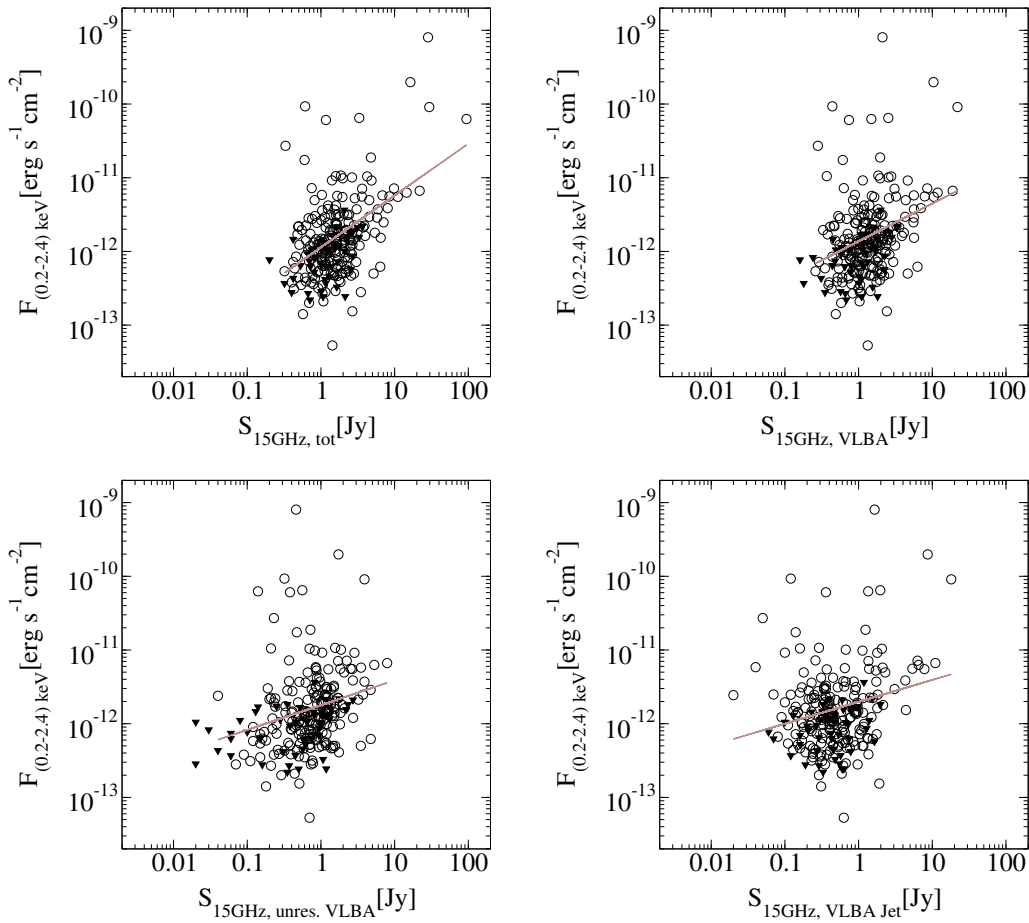
Figure B.2: Radio vs. X-ray fluxes. The distributions for total radio emission (top left), full VLBI flux density (top right), unresolved VLBI flux density (bottom left) and the on parsec scales resolved emission from the radio jet (bottom right) are shown. Upper limits are marked by filled triangles. The solid lines indicate a linear regression to the full sample of *Rosat*-detected sources.

The VLBA 2 cm Survey allows us to test the radio–X-ray luminosity correlation of radio-loud, core-dominated AGN down to thousand-times smaller scales: the finescale structure of the sources of the VLBA 2 cm Survey have been studied by Kovalev et al. (2005), providing a full set of average flux densities for the most compact sub-milliarcsecond scale regions in those sources. Table B.3 lists these average unresolved VLBI fluxes together with average values for the total radio flux and the integrated VLBI-recovered flux density, all at 15 GHz. Figure B.5 displays the soft X-ray luminosities of VLBA 2 cm Survey sources as a function of the radio luminosities of these various components of the total radio emission. Strong correlations with the soft X-ray luminosity are found for the total radio luminosity, the parsec-scale jet luminosity, and the sub-parsec scale unresolved VLBI luminosity (compare Table B.4).

The interpretation of these correlations needs caution due to the strong dependence of both quantities on redshift. Such a redshift-dependence, in particular when dealing with flux-limited samples, can draw out the points in luminosity space, causing spurious correlations. A totally uncorrelated set of radio and X-ray fluxes would then appear as if

Quasars

BL Lac Objects

Galaxies

Unclassified Objects
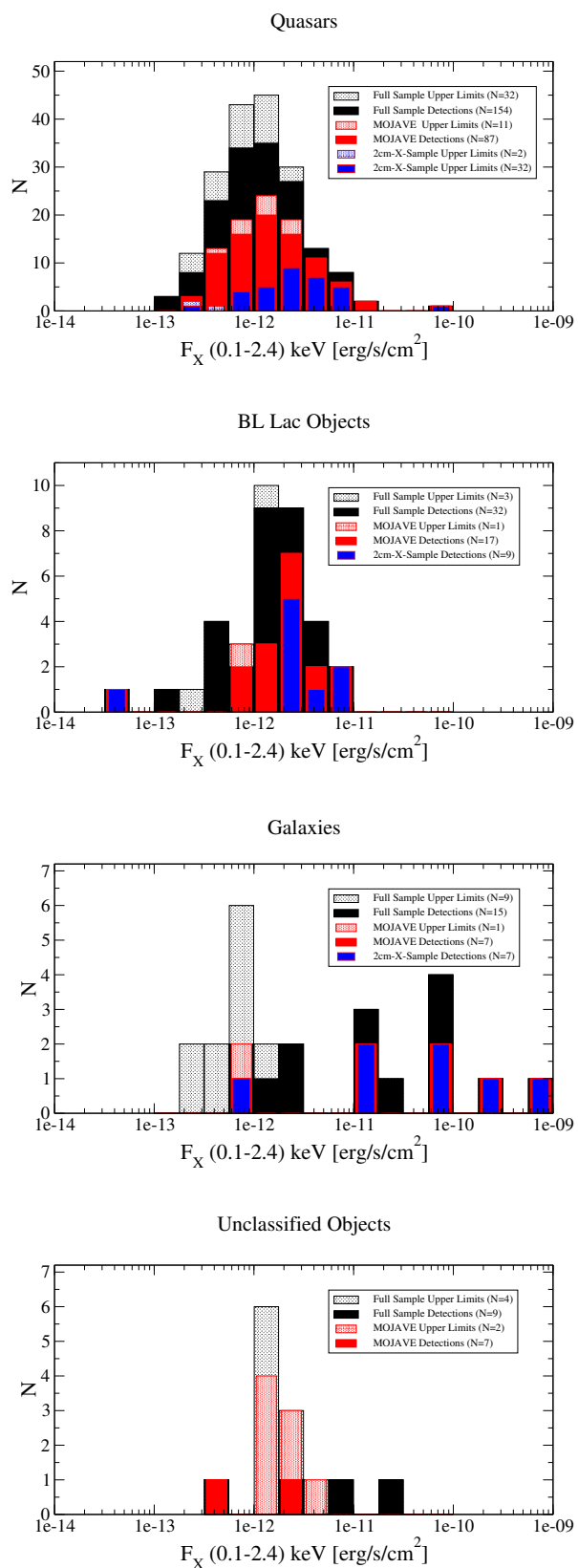
Figure B.3: Soft X-ray fluxes of all sources in the VLBA 2 cm Survey (black), of the complete MOJAVE sub-sample (red), and of 2 cm-X-Sample sources (blue). For undetected sources upper limits are plotted as dotted areas. From top to bottom the distributions for quasars, BL Lac objects, galaxies, and unclassified objects are shown.

strongly correlated due to the multiplication of a z-dependent "stretching factor" to both axes. Feigelson and Berg (1983) showed that in spite of these difficulties in interpretation, luminosity-luminosity plots can yield more accurately the underlying relationship than possible in the flux-flux plane, particularly if the relation is non-linear. An important issue, however, is the inclusion of all upper limits in the analysis. Akritas and Siebert (1996) have developed a procedure to perform a so-called partial-correlation analysis to estimate the significance of apparent correlations in the presence of upper limits and dependences on third variables like z. A code to perform a partial correlation analysis according to this procedure is provided by the Pennsylvania State University Center for Astrostatistics[5].

The results of the partial correlation analysis are summarized in Table B.4. Considering the full 2 cm Survey sample, all but the correlations for the galaxies are highly significant. In particular the $L_{\mathrm{unres}} - L_{\mathrm{X}}$ correlation falls below the 5 % probability of random occurrence. Considering the smaller but statistically complete MOJAVE sample, none of the correlations for the galaxies remains significant, what might be a result of the small number of galaxies in the MOJAVE sample. It is consistent, however, with the result derived above that a non-compact emission component dominates the galaxies soft X-ray emission. Slopes of the various correlations have been determined by considering only detections and neglecting the upper limits. The two classes for which the radio–X-ray correlations are clearly significant, quasars and BL Lacs, have very similar slopes of $a \sim 0.8$ if $L_{\mathrm{X}} \propto L_{\mathrm{r}}^{a}$. The BL Lac slope of the MOJAVE objects appears to be flatter but due to the small sample size it is consistent with the steeper slope of the full sample within $1 - \sigma$. The similar dependence of the soft X-ray flux of quasars and BL Lacs suggests that the VLBI properties are more relevant for radio–X-ray correlation analysis than optical classification. At very high luminosities, however, the $L_{\mathrm{unres}} - L_{\mathrm{X}}$ correlations seems to steepen. Restricting the fit to $L_{\mathrm{unres}} > 9 \times 10^{44}$ erg s^{-1} yields a slope of ~ 1. A similar trend was noted before by Brinkmann et al. (1997b). It should be noted that this is not a redshift effect. A restriction to quasars with $z > 1.75$, e.g., shows no significant steepening compared to the full range of redshifts.

List of collaborators: E. Ferrero, J. Kerp, Y. Y. Kovalev, E. Ros

---

[5]http:astrostatistics.psu.edu/statcodes/sc_regression.html

Table B.4: Soft X-ray/radio luminosity partial correlation analysis.

	N[a]	$L_X vs....$[b]	a[c]	ρ[d]	τ[e]	σ[f]	P[g]	$Sig.$[h]
Full 2cm Sample								
All Types	234	L_{tot}	0.77 ± 0.03	0.91	0.446	0.038	$< 4.4 \times 10^{-6}$	Y
		L_{VLBI}	0.73 ± 0.03	0.89	0.448	0.038	$< 4.4 \times 10^{-6}$	Y
		L_{Core}	0.69 ± 0.03	0.89	0.454	0.038	$< 4.4 \times 10^{-6}$	Y
		L_{Jet}	0.70 ± 0.03	0.87	0.412	0.038	$< 4.4 \times 10^{-6}$	Y
Quasars	178	L_{tot}	0.80 ± 0.04	0.74	0.388	0.042	$< 4.4 \times 10^{-6}$	Y
		L_{VLBI}	0.80 ± 0.04	0.85	0.376	0.042	$< 4.4 \times 10^{-6}$	Y
		L_{Core}	0.77 ± 0.04	0.85	0.385	0.042	$< 4.4 \times 10^{-6}$	Y
		L_{Jet}	0.68 ± 0.04	0.79	0.346	0.042	$< 4.4 \times 10^{-6}$	Y
BL Lacs	30	L_{tot}	0.79 ± 0.07	0.81	0.597	0.142	2.66×10^{-5}	Y
		L_{VLBI}	0.79 ± 0.07	0.90	0.627	0.141	8.6×10^{-6}	Y
		L_{Core}	0.78 ± 0.07	0.91	0.602	0.126	$< 4.4 \times 10^{-6}$	Y
		L_{Jet}	0.78 ± 0.09	0.87	0.572	0.159	3.18×10^{-4}	Y
Galaxies	24	L_{tot}	0.71 ± 0.16	0.73	0.209	0.085	0.014	Y
		L_{VLBI}	0.67 ± 0.18	0.72	0.173	0.075	0.021	Y
		L_{Core}	0.6 ± 0.1	0.70	0.177	0.094	0.060	N
		L_{Jet}	0.6 ± 0.2	0.68	0.177	0.075	0.018	Y
MOJAVE Sample								
All Types	120	L_{tot}	0.79 ± 0.04	0.8983753	0.472	0.057	$< 4.4 \times 10^{-6}$	Y
		L_{VLBI}	0.72 ± 0.04	0.8814678	0.448	0.057	$< 4.4 \times 10^{-6}$	Y
		L_{Core}	0.66 ± 0.04	0.8689925	0.427	0.058	$< 4.4 \times 10^{-6}$	Y
		L_{Jet}	0.69 ± 0.04	0.8533062	0.439	0.054	$< 4.4 \times 10^{-6}$	Y
Quasars	98	L_{tot}	0.73 ± 0.06	0.807471	0.385	0.042	$< 4.4 \times 10^{-6}$	Y
		L_{VLBI}	0.71 ± 0.06	0.8043694	0.368	0.058	$< 4.4 \times 10^{-6}$	Y
		L_{Core}	0.73 ± 0.06	0.7429785	0.357	0.060	$< 4.4 \times 10^{-6}$	Y
		L_{Jet}	0.55 ± 0.05	0.7429785	0.362	0.055	$< 4.4 \times 10^{-6}$	Y
BL Lacs	14	L_{tot}	1.00 ± 0.17	0.8728936	0.602	0.126	$< 4.4 \times 10^{-6}$	Y
		L_{VLBI}	1.0 ± 0.2	0.8721165	0.512	0.213	0.016	Y
		L_{Core}	0.99 ± 0.16	0.8138816	0.473	0.208	0.023	Y
		L_{Jet}	1.0 ± 0.2	0.8138816	0.566	0.204	5.6×10^{-3}	Y
Galaxies	8	L_{tot}	1.0 ± 0.3	0.8261774	0.177	0.094	0.060	N
		L_{VLBI}	1.1 ± 0.4	0.7655677	0.251	0.138	0.069	N
		L_{Core}	1.0 ± 0.3	0.7309808	0.137	0.179	0.45	N
		L_{Jet}	1.1 ± 0.4	0.7309808	0.012	0.149	0.93	N

[a] Number of objects per class; [b] Considered radio quantity; [c] Slope from linear regression; [d] Correlation coefficient; [e] Partial Kendall τ following Akritas and Siebert (1996) with the effect of redshift taken into account; [f] Variance following Akritas and Siebert (1996); [g] Probability of erroneously rejecting the null hypothesis (i.e., no correlation) ; [h] Label indicating the significance of the correlation.

Quasars

BL Lac Objects

Galaxies
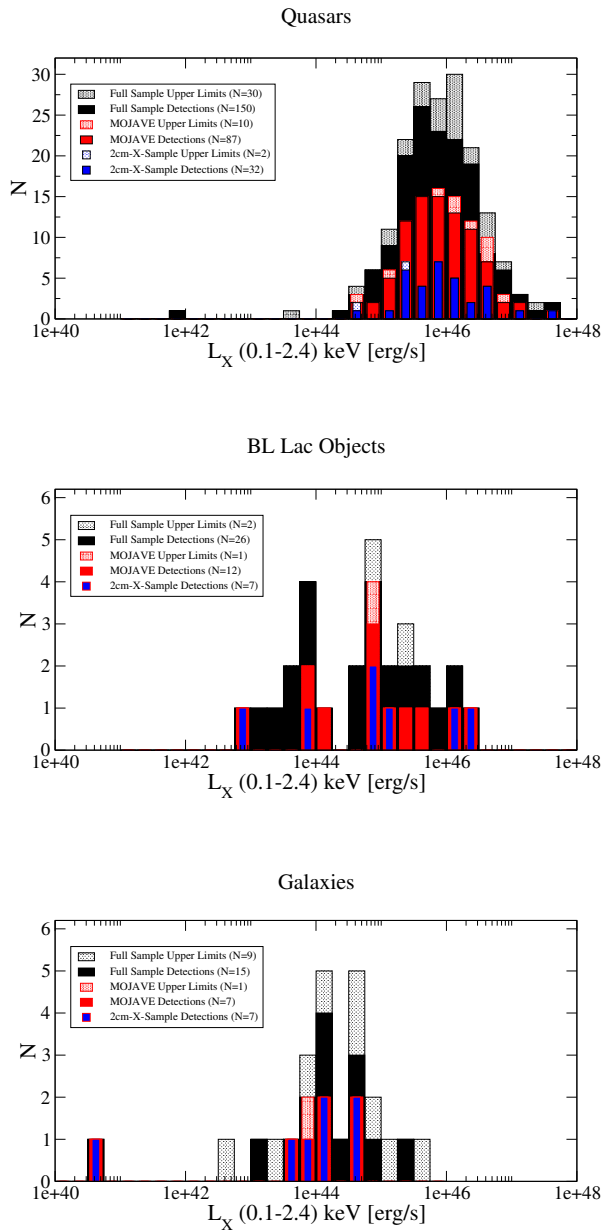
Figure B.4: (0.1-2.4) keV X-ray luminosities for the full VLBA 2 cm Survey (black), the complete MOJAVE sub-sample (red), and the 2 cm-X-Sample (blue). For undetected sources upper limits are plotted as dotted areas. From top to bottom the distributions for quasars, BL Lac objects, and galaxies are shown.
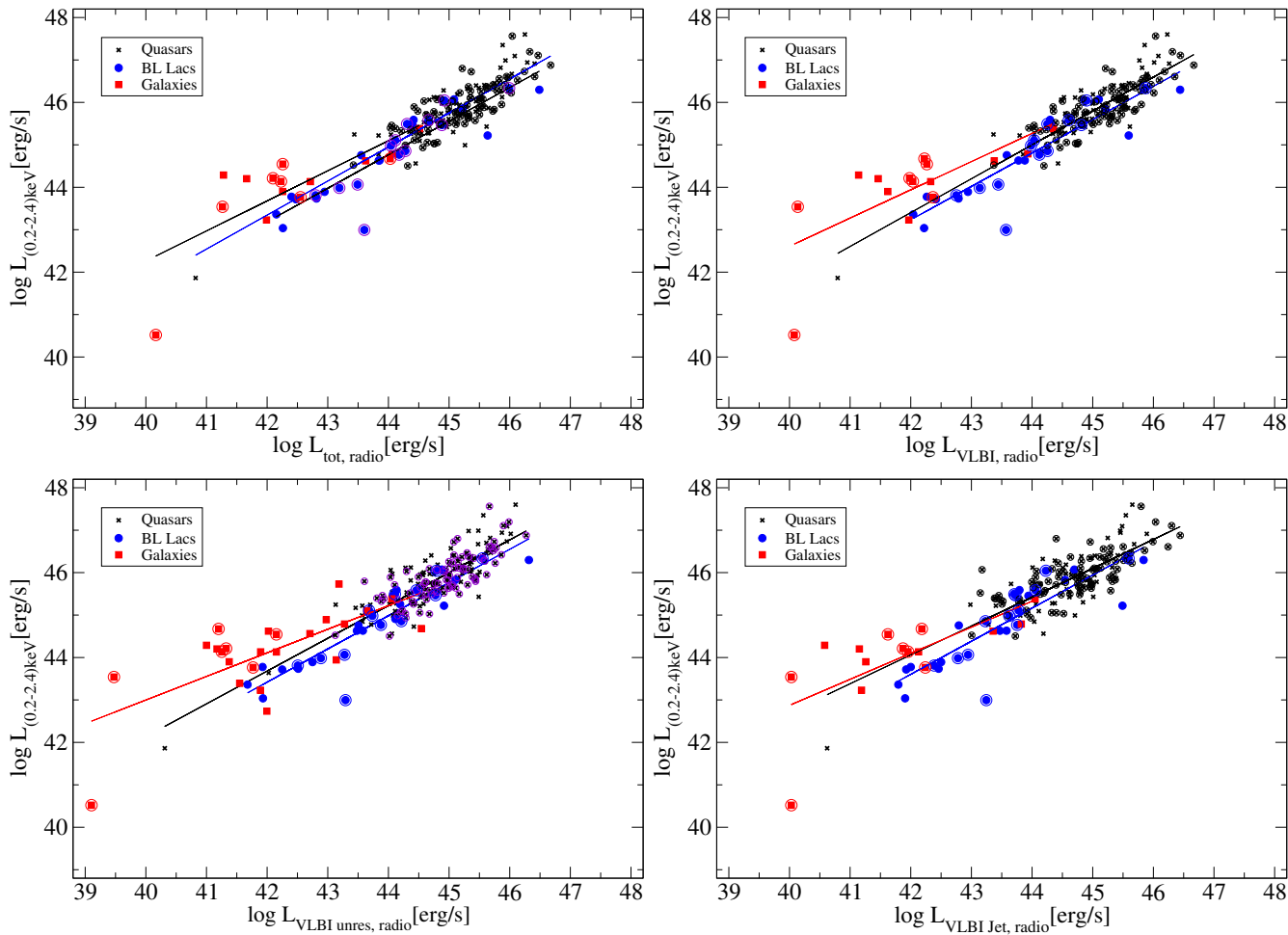
Figure B.5: Luminosity correlations between the soft (0.1–2.4) keV X-ray luminosity and the various components of the core-dominated radio emission for the full VLBA 2 cm Survey sample (filled symbols and the statistically complete MOJAVE sample (circles around filled symbols).

C   The Brightness Temperature Gradients Along Parsec-Scale Radio Jets

Abstract: The brightness temperature gradients along extragalactic jets are measured on parsec scales for a sample of AGN from the combined PR/CJ1 sample. Below, it is shown that the brightness temperature as a function of distance from the jet core can be described well with a simple power law for most of the sources with continuous and more or less straight jets. The power law index s varies from source to source with values typically between -1.5 and -3. Using only basic assumptions of synchrotron theory and jet physics it is shown that a power law in the brightness temperature distribution along parsec-scale radio jets follows naturally if the magnetic field, the particle density, and the diameter of the jet as functions of radius are assumed to be power laws.

Introduction: In the special case of NGC 1052 it was shown that the brightness temperature along the eastern jet can be well approximated by a simple power law (Kadler et al. 2004c, reprinted in Sect. 6.3.1). Does this hold for other radio jets and how do the brightness temperature gradients in various sources differ. The combined PR/CJ1 sample is complete and contains observations not only at 6 cm but also at 18 cm, where many sources exhibit pronounced jet structure. Moreover, the study of each source at two different frequencies allows one to compare the derived gradients, which are *a-priori* expected to be equal assuming optically thin synchrotron emission. Differences may occur if the jets are seen over substantially different scales at the two frequencies due to self absorption and/or resolution effects or if the source has evolved between the two observation epochs. Originally, a sample of 29 sources with classical core-jet structures and continuous jets was chosen. These selection criteria should ensure that at least 4 model components could be fitted to the parsec-scale jet structure of the sample sources to allow the T_b gradients to be determined from a power-law approximation of the data. In one case (BL Lac) this requirement was fulfilled only at $\lambda 18$ cm, while at $\lambda 6$ cm only two jet components were found. The gradient at $\lambda 6$ cm has been tabulated but was not used in the further analysis.

The calibrated (u, v)-data from the CJ-survey (Polatidis et al. 1995, Thakkar et al. 1995, Xu et al. 1995) were provided by A. Polatidis. Two-dimensional Gaussian functions were fitted to the data in the (u, v)-domain with the program DIFMAP, using only circular components to avoid the degeneration of individual components to linear features for which no meaningful brightness temperature can be derived. Distances were measured

relative to the core component which leaves 3 or more jet components for the regression. This kind of distance measurement introduces a systematic error to a power law fit since the "true" base of the jet is located somewhat inwards of the core component but is not observable due to self absorption. However, it can be estimated that this error only affects significantly the innermost components and can be neglected for most components located several milliarcseconds away from the core.

For eleven sources from the original sample, no satisfactory fit to the brightness temperature distribution along the jet was found with a simple power law model. Most of these sources were either CSOs or showed very strong bending or other signs of strong interaction with the jet environment. The analysis of these more complicated source will be presented elsewhere.

Results: The parameters of the model fits are given in Table C.1. The images at $\lambda 18\,\text{cm}$ and $\lambda 6\,\text{cm}$ of the 18 sources of the final sample that result from applying the Gaussian-component models to the (u, v)-data are shown in Fig. C.1–C.1 and the map parameters are given in Table C.2. In Fig. C.2 the brightness temperature gradients are shown measured at $\lambda 6\,\text{cm}$ and $\lambda 18\,\text{cm}$, respectively. The gradients are obtained from power-law fits to the brightness temperatures the individual model fit components in the jets as a function of their distance to the core. For Fig. C.2, uniform errors of a fifth of the beam size at the given frequency ($\sim 1\,\text{mas}$ at $\lambda 18\,\text{cm}$ and $\sim 0.2\,\text{mas}$ at $\lambda 6\,\text{cm}$) were assumed for the error in position. The error of the component diameter was estimated to be one fifth of the beam width in the case of unresolved components and one fifth of the component diameter for extended components. No redshift correction had to be applied to the measured values which would only change the scaling but not the gradients of the power-law distributions. All sources show a decrease in T_b which can be fitted with a simple power law and approximately the same power-law index s at both frequencies. In general, the brightness temperature at $6\,\text{cm}$ is lower than at $18\,\text{cm}$ at each given position along the jets as expected for optically thin synchrotron emission. The measured gradients for each source are given in Table C.3.

Table C.1: VLBI model fit parameters for the sources from the CJ sample.

	$\lambda 18\,\text{cm}$					$\lambda 6\,\text{cm}$			
Flux density	Core distance	P.A.	FWHM	T_b	Flux density	Core distance	P.A.	FWHM	T_b
[Jy]	[mas]	[°]	[mas]	$[10^{10}\,\text{K}]$	[Jy]	[mas]	[°]	[mas]	$[10^{10}\,\text{K}]$
				0716+714					
0.177	0	–	<1.0	>8.418	0.565	0	–	<0.2	>69.095
0.038	2.17	10.3	1.05	1.631	0.065	0.53	20.0	0.30	35.303
0.005	6.43	20.3	1.67	0.087	0.018	1.75	8.5	0.45	4.301
0.017	10.42	18.1	4.95	0.033	0.008	4.59	16.6	0.93	0.460
					0.009	10.98	13.0	4.90	0.019
				0740+828					
0.312	0	–	<1.0	>34.578	0.134	0	–	<0.2	>38.800
0.368	2.27	−15.5	0.97	18.565	0.156	0.51	172.69	0.13	44.861
0.144	8.10	−3.9	3.05	0.738	0.143	0.97	11.50	0.37	5.149
0.101	18.81	−10.3	7.59	0.083	0.259	2.95	−5.60	1.08	1.089
0.030	35.94	−9.5	14.11	0.007	0.062	8.89	−4.84	2.85	0.037

Table C.1 – continued from previous page

| | λ18 cm | | | | | λ6 cm | | | |
Flux density [Jy]	Core distance [mas]	P.A. [°]	FWHM [mas]	T_b [10^{10} K]	Flux density [Jy]	Core distance [mas]	P.A. [°]	FWHM [mas]	T_b [10^{10} K]
					0.041	18.80	−5.40	5.57	0.006
				0746+483					
0.243	0	–	<1.0	11.602	0.271	0	–	<0.2	<33.219
0.363	1.02	−68.6	0.77	29.100	0.350	0.70	−87.3	0.43	9.297
0.106	3.47	−94.3	0.67	11.167	0.138	1.33	−81.0	0.52	2.504
0.030	6.32	−94.9	1.34	0.788	0.056	3.10	−93.2	0.91	0.333
0.004	12.99	−76.8	1.79	0.062	0.025	4.15	−94.6	1.36	0.065
0.005	30.38	−97.6	3.18	0.024	0.010	6.62	−90.4	1.46	0.022
0.008	54.9	−100.5	7.19	0.007					
				0820+560					
0.699	0	–	0.43	33.334	1.135	0	–	0.18	138.967
0.169	3.11	81.4	1.03	7.591	0.161	0.68	102.4	0.60	2.212
0.088	6.50	70.0	2.12	0.938	0.099	2.62	100.3	1.17	0.356
0.173	16.77	69.0	5.59	0.264	0.042	4.60	73.8	2.14	0.045
0.155	22.45	80.2	6.24	0.190	0.021	5.57	70.1	1.41	0.052
					0.121	20.67	77.3	7.33	0.011
				0906+430					
0.300	0	–	0.54	49.816	0.472	0	–	0.24	41.617
0.108	4.24	149.3	1.70	1.790	0.107	1.19	150.1	0.24	8.773
0.017	13.39	129.2	2.49	0.131	0.066	3.21	154.2	0.73	0.596
0.017	27.55	144.9	3.48	0.067	0.012	5.49	142.9	0.73	0.107
0.019	39.6	148.9	4.70	0.042	0.015	6.88	141.7	0.83	0.104
0.029	97.64[a]	150.4	5.73	0.043	0.010	18.33	142.5	2.73	0.007
0.025	116.41[a]	148.5	6.00	0.033					
0.166	144.59[a]	154.0	17.67	0.025					
				0917+449					
0.509	0	–	<1.0	<24.241	0.868	0	–	0.32	407.623
0.225	1.31	179.9	1.15	8.176	0.420	1.08	175.2	0.53	71.933
0.090	5.68	−160.4	2.97	0.488	0.069	6.21	−162.6	3.42	0.283
0.061	18.01	−162.5	4.34	0.154	0.051	19.32	−161.8	6.60	0.056
0.031	22.71	−145.6	11.13	0.012					
0.026	44.65	−138.0	18.14	0.004					
0.007	71.37	−121.1	19.98	0.001					
				0945+408					
0.274	0	–	<1.0	13.0551	1.317	0	–	0.37	47.670
0.253	1.53[b]	31.7	0.87	16.050	0.030	1.79	115.1	0.65	0.338
0.407	7.14	119.0	2.92	2.281	0.169	6.33	131.1	2.43	0.140
0.374	9.83	111.4	2.68	2.472	0.193	8.41	118.3	2.69	0.130
0.179	16.88	111.7	6.30	0.215	0.037	14.50	106.2	2.32	0.034
0.071	24.04	113.7	5.91	0.097	0.078	21.5	118.7	9.61	0.004
0.028	42.86	101.2	11.84	0.009					
0.032	73.90	100.3	21.11	0.003					
				1020+400					
0.158	0	–	0.70	15.196	0.708	0	–	0.19	92.355
0.127	3.13	−37.6	0.93	7.069	0.025	1.42	−44.3	0.30	1.300
0.040	9.31	−36.9	1.98	0.485	0.075	3.22	−40.5	1.11	0.303

Table C.1 – continued from previous page

λ18 cm					λ6 cm				
Flux density [Jy]	Core distance [mas]	P.A. [°]	FWHM [mas]	T_b [10^{10} K]	Flux density [Jy]	Core distance [mas]	P.A. [°]	FWHM [mas]	T_b [10^{10} K]
0.077	13.82	−33.0	3.40	0.318	0.013	6.22	−42.1	2.50	0.010
0.006	30.73	−27.6	3.13	0.027	0.050	12.65	−33.4	4.21	0.014
0.027	93.79	−21.7	7.78	0.021	0.009	89.77	−20.9	7.42	0.001
0.016	159.78	−21.2	26.0	0.001					
0.023	204.55	−15.7	30.9	0.001					
1101+384									
0.250	0	−	0.78	19.717	0.358	0	−	0.16	67.071
0.043	4.72	−34.8	2.24	0.407	0.057	1.21	−25.5	0.83	0.407
0.062	15.26	−48.3	10.77	0.026	0.020	5.14	−36.5	1.58	0.040
0.035	30.18	−60.2	17.93	0.005	0.016	10.89	−36.6	5.07	0.003
0.084	67.35[a]	−52.3	34.70	0.003	0.029	19.93	−56.9	9.41	0.002
					0.101	58.48[a]	−58.0	50.58	0.0002
1216+487									
0.166	0	−	0.470	35.875	0.304	0	−	0.19	43.100
0.338	1.74	101.1	1.34	8.936	0.101	1.07	99.4	0.49	2.086
0.058	4.69	112.3	1.84	0.812	0.146	1.97	100.7	1.12	0.572
0.040	18.17	113.3	9.76	0.020	0.037	3.68	106.8	1.21	0.125
0.047	9.12	112.5	3.33	0.203	0.029	8.10	109.7	3.94	0.009
					0.010	20.95	107.7	4.39	0.002
1347+539									
0.247	0	−	1.40	5.220	0.421	0	−	0.20	52.095
0.098	12.05	137.1	3.10	0.471	0.056	0.84	144.8	0.34	2.322
0.076	6.75	138.8	2.13	0.816	0.046	1.95	141.7	1.06	0.203
0.091	18.33	123.4	3.34	0.384	0.030	4.97	139.9	1.34	0.082
0.097	3.50	135.5	1.23	2.380	0.030	6.45	139.4	1.01	0.145
0.124	57.15[a]	140.0	10.09	0.058	0.021	9.24	143.1	1.66	0.037
					0.029	12.44	138.3	2.39	0.025
					0.049	19.36	124.5	3.13	0.025
					0.094	59.35[a]	141.5	14.07	0.002
1418+546									
1.020	0	−	0.66	111.830	1.506	0	−	0.36	57.806
0.243	2.73	124.2	1.86	3.338	0.409	1.07	129.6	0.40	12.234
0.109	15.34	126.2	9.04	0.064	0.051	1.97	126.6	0.73	0.465
0.034	37.09	125.8	22.27	0.003	0.130	3.65	125.4	2.10	0.145
					0.024	7.00	131.5	0.97	0.125
					0.072	16.69	121.8	7.36	0.007
1504+377									
0.469	0	−	1.20	15.541	0.325	0	45.3	<0.2	>39.826
0.123	3.02	−137.1	2.83	0.734	0.182	1.06	46.7	0.44	4.626
0.209	9.93	−135.9	5.53	0.326	0.068	2.02	45.6	1.11	0.271
0.095	54.16	−137.8	19.09	0.012	0.043	5.66	46.9	1.85	0.062
0.032	107.94	−136.8	27.17	0.002	0.042	10.31	−131.4	2.01	0.051
					0.017	13.8	−140.4	1.63	0.032
1642+690									
0.400	0	−	0.63	44.219	0.923	0	−	0.20	115.784
0.274	2.22	−165.3	0.74	22.128	0.315	0.79	179.7	0.26	22.735

Continued on next page

Table C.1 – continued from previous page

λ18 cm					λ6 cm				
Flux density [Jy]	Core distance [mas]	P.A. [°]	FWHM [mas]	T_b [10^{10} K]	Flux density [Jy]	Core distance [mas]	P.A. [°]	FWHM [mas]	T_b [10^{10} K]
0.094	5.20	−164.1	0.94	4.671	0.143	1.52	−174.2	0.41	4.157
0.136	8.95	−162.8	1.69	2.119	0.084	2.58	−167.9	0.75	0.729
					0.115	5.52	−166.4	2.50	0.090
					0.012	12.10[a]	−156.6	1.36	0.032
1807+698									
0.444	0	–	<1	>21.143	0.637	0	–	0.20	74.617
0.316	1.73	−90.2	0.59	43.936	0.383	0.61	−97.7	0.16	71.418
0.105	4.45	−90.6	0.69	10.593	0.118	1.39	−105.6	0.23	11.052
0.038	6.91	−91.2	1.40	0.934	0.076	2.36	−102.2	0.19	10.235
0.070	13.11	−92.0	3.77	0.235	0.046	3.43	−98.5	0.46	1.069
0.218	33.35	−94.6	8.60	0.140	0.039	4.69	−95.1	0.99	0.197
0.031	59.86	−98.8	15.71	0.006	0.045	12.42	−100.6	2.71	0.030
					0.146	26.82	−98.7	5.01	0.0284
					0.072	35.21	−101.9	4.84	0.015
1842+681									
0.440	0	–	<1	>20.985	0.472	0	–	0.18	70.095
0.397	1.14	143.0	1.01	18.464	0.239	0.47	116.2	0.47	5.251
0.035	4.74	150.0	1.17	1.202	0.127	1.69	137.8	0.70	1.252
0.070	10.47	156.8	6.21	0.086	0.023	8.59	154.1	6.38	0.003
0.018	36.42	152.8	29.79	0.001					
1954+513									
0.625	0	–	0.55	98.325	0.711	0	–	0.23	67.546
0.107	2.55	−64.2	1.75	1.679	0.546	0.60	−65.2	0.33	24.856
0.018	7.43	−75.2	4.25	0.474	0.051	1.60	−61.8	0.01	6.197
0.141	10.86	−67.8	2.43	1.128	0.005	2.71	−46.8	0.04	0.669
0.077	18.25	−63.5	2.78	0.066	0.027	4.67	−56.7	1.20	0.091
0.049	25.79	−62.8	5.85	0.048	0.018	5.90	−65.4	0.69	0.183
0.019	42.76	−75.0	3.92	0.061	0.031	8.29	−62.8	1.14	0.117
0.030	54.66	−73.9	7.48	0.026	0.031	10.08	−65.3	1.29	0.091
0.072	86.13	−73.8	31.26	0.004	0.057	11.63	−68.9	1.98	0.072
					0.007	17.84	−76.1	0.95	0.038
					0.008	22.59	−76.5	1.32	0.023
					0.007	26.54	−73.2	1.12	0.027
2200+420									
0.810	0	–	1.08	33.354	1.189	0	–	0.65	13.599
0.852	1.79	3.9	1.27	25.339	0.571	2.83	−177.6	1.35	1.526
0.722	1.26	152.4	4.26	1.894	0.250	5.91	172.4	3.50	0.100
0.119	1.08	142.7	6.81	0.123					
0.101	1.03	165.7	27.51	0.006					

[a] Partially resolved component not considered in the determination of gradients; [b] Innermost component falls significantly below the power-law extrapolation from larger radii.

In Figure C.3 the distribution of power law indices at $\lambda 6$ cm in the sample are plotted as a function of the corresponding values at $\lambda 18$ cm. The distribution ranges from ~ -1 to ~ -3 with approximately the same values at 18 cm and 6 cm. This shows that the determination of s is in general independent of the observing frequency.
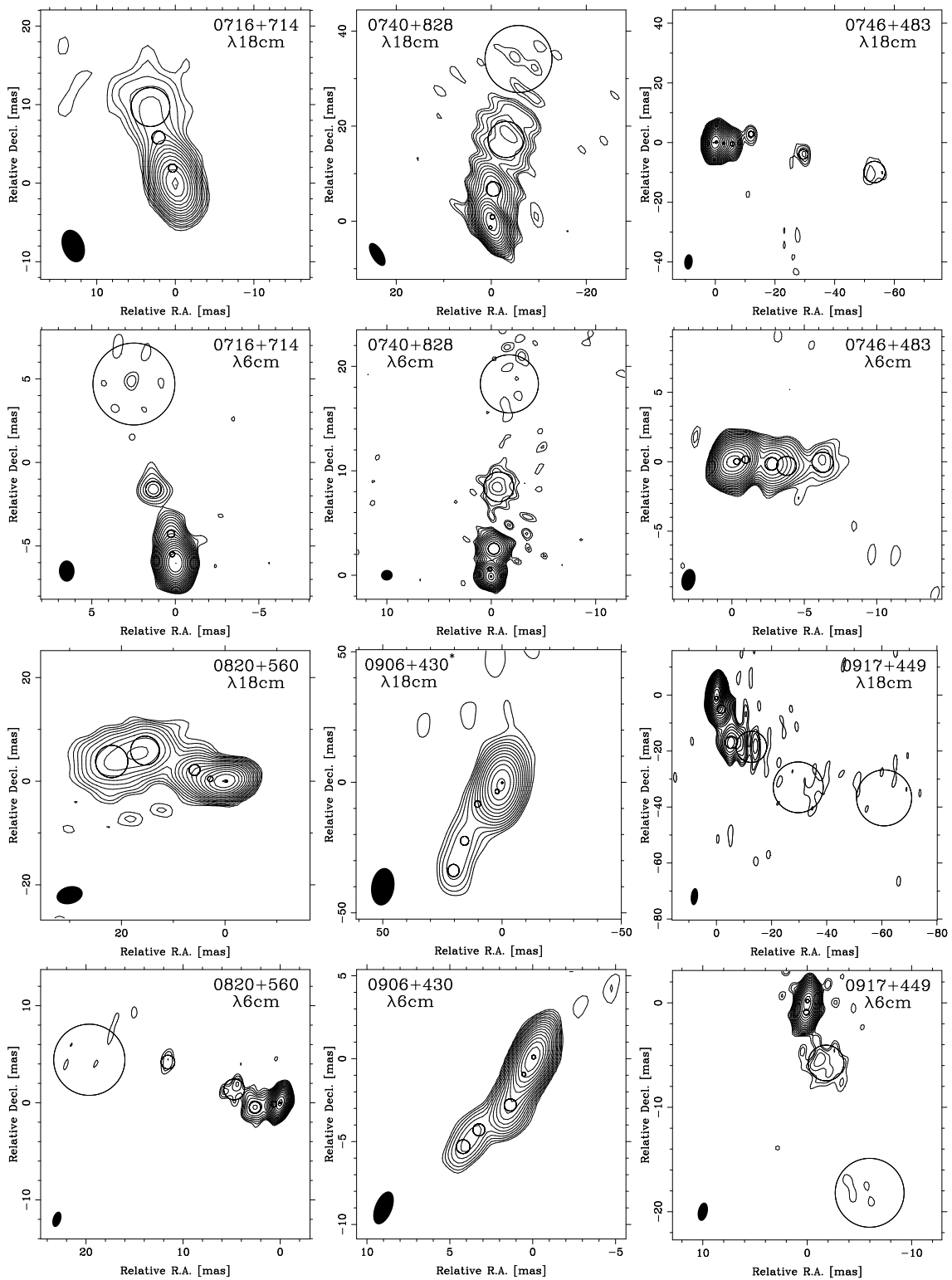
Figure C.1: Hybrid images from applying the Gaussian-component models given in Table C.1 to the calibrated visibility data and adding the residual map for the final sample. Asterisks mark sources for which the most extended components are not used in the T_b fits due to resolution effects. In the case of 0945+408, the innermost jet component fell below the power-law extrapolation from the more distant components, probably due to self absorption, and was not used in the fits either.
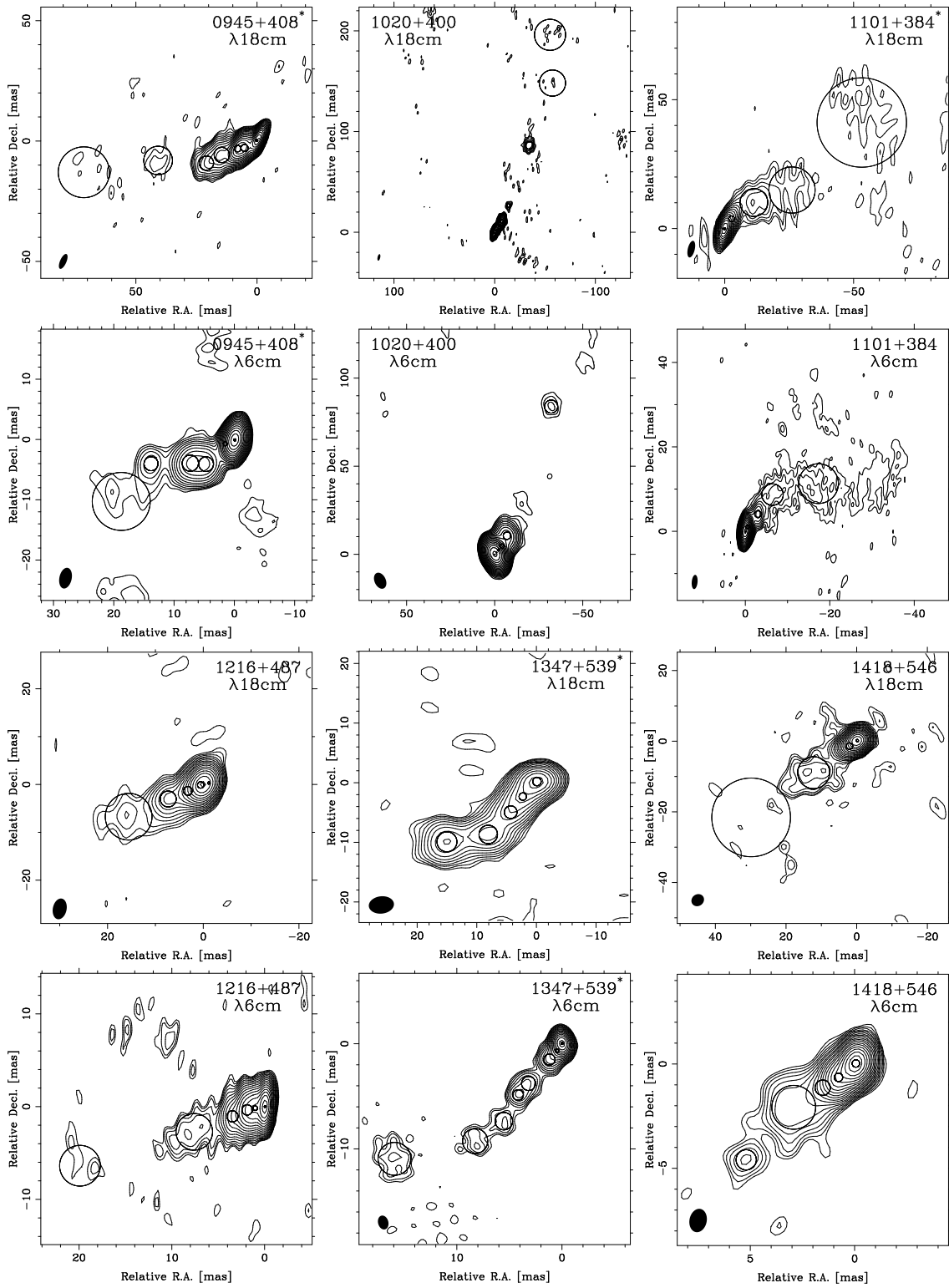
Figure C.1: continued
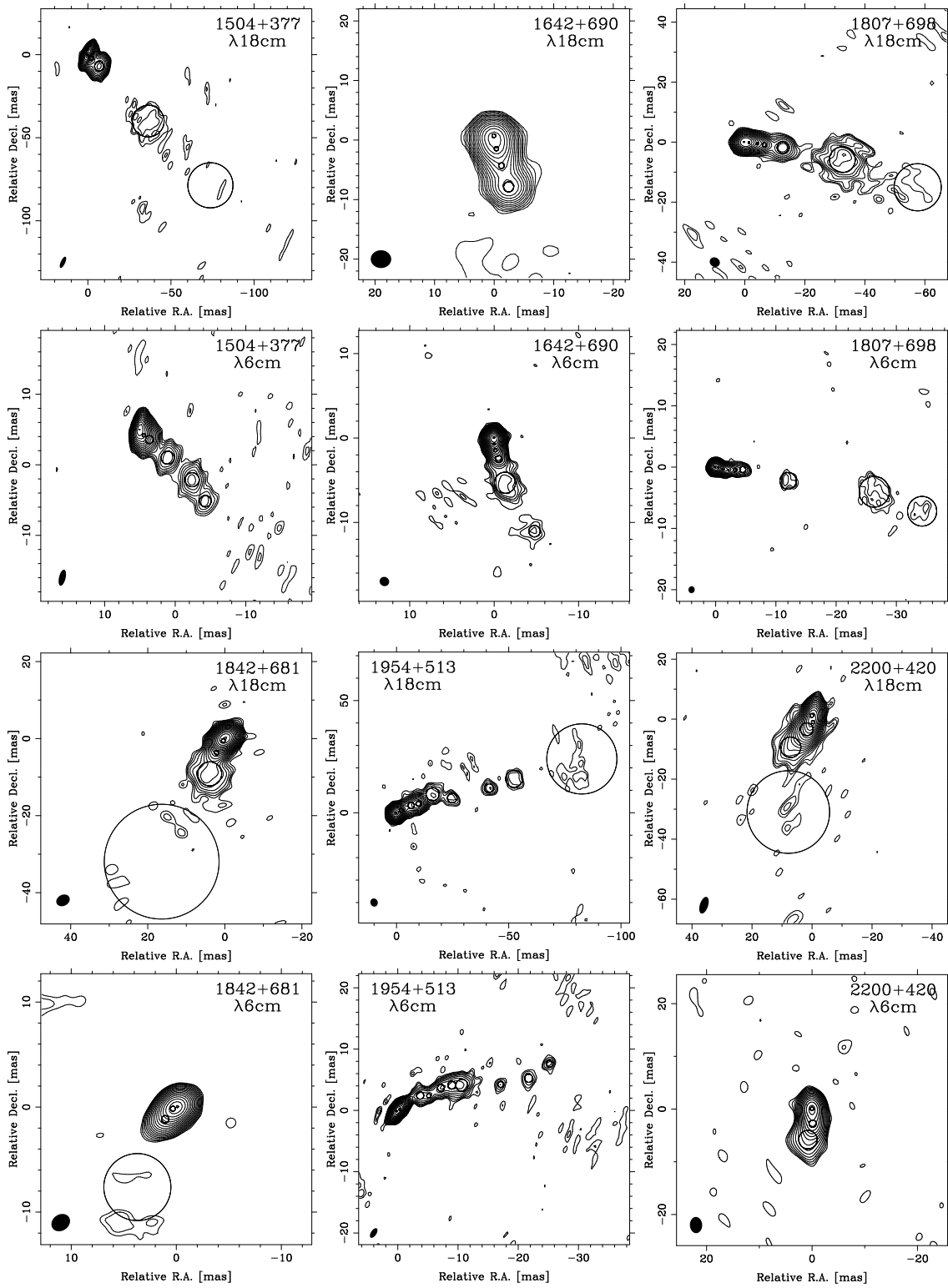
Figure C.1: continued
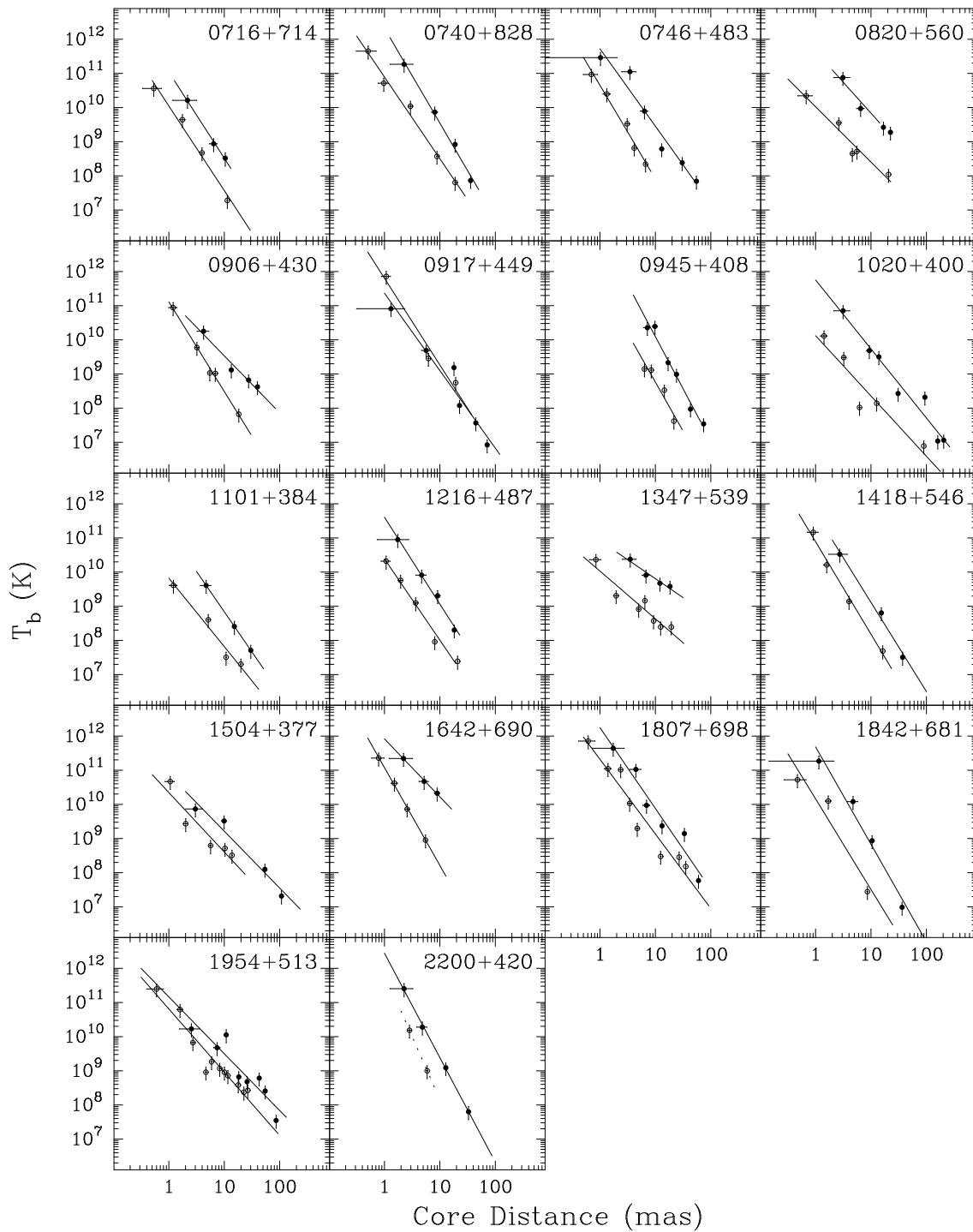
Figure C.2: Brightness temperature gradients along the jets of 18 sources in the combined PR/CJ1-sample. Filled symbols are used for data at 18 cm, open ones for 6 cm. In each plot the result of a power-law fit to the data is shown as a thick line for the measurements at 18 cm and 6 cm, respectively (compare Table C.3).

Table C.2: VLBI model fit map parameters for the sources from the CJ sample.

Source	$\lambda18\,cm$			$\lambda6\,cm$		
	Epoch [dd/mm/yy]	Lowest Contour [mJy/beam]	Beam [mas × mas, °]	Epoch [dd/mm/yy]	Lowest Contour [mJy/beam]	Beam [mas × mas, °]
0716+714	17/11/91	0.0014	$2.8 \times 4.3, +19.4$	24/09/92	0.001	$0.9 \times 1.3, 0.7$
0740+828	16/06/91	0.002	$2.5 \times 5.5, +30.9$	10/03/90	0.002	$1.0 \times 1.1, -81.9$
0746+483	16/11/91	0.001	$2.8 \times 5.1, -5.2$	08/06/91	0.001	$1.0 \times 1.6, -10.9$
0820+560	25/09/91	0.004	$3.4 \times 5.1, -76.2$	11/03/90	0.004	$0.9 \times 1.6, -17.0$
0906+430	21/09/90	0.0057	$9.7 \times 14.5, -10.4$	05/06/86	0.002	$1.0 \times 2.1, -22.0$
0917+449	16/11/91	0.0014	$2.6 \times 6.1, -6.1$	08/06/91	0.003	$0.9 \times 1.8, -12.3$
0945+408	16/06/91	0.002	$2.6 \times 6.7, -23.6$	23/11/86	0.004	$2.0 \times 3.5, -12.1$
1020+400	16/11/91	0.001	$2.6 \times 6.7, -12.4$	19/09/91	0.002	$6.4 \times 9.6, 24.8$
1101+384	16/11/91	0.0014	$2.7 \times 6.6, -13.5$	19/09/91	0.001	$1.4 \times 3.4, -5.1$
1216+487	17/06/91	0.002	$2.9 \times 4.4, -11.8$	29/03/92	0.001	$1.0 \times 2.9, -3.7$
1347+539	16/06/91	0.0028	$2.9 \times 4.2, -83.7$	11/03/90	0.002	$1.0 \times 1.3, 15.2$
1418+546	22/09/90	0.0028	$3.3 \times 3.7, -54.8$	11/03/90	0.003	$0.8 \times 1.1, -11.8$
1504+377	21/09/90	0.002	$2.6 \times 7.4, -24.3$	06/06/92	0.001	$0.9 \times 2.3, -13.4$
1642+690	21/09/90	0.0028	$3.0 \times 3.4, +88.5$	05/06/86	0.0028	$1.1 \times 1.1, 60.1$
1807+698	21/09/90	0.0028	$3.1 \times 3.5, -59.3$	05/06/86	0.0028	$1.0 \times 1.1, -8.1$
1842+681	16/06/91	0.0014	$2.9 \times 3.7, -62.1$	11/03/90	0.002	$1.5 \times 1.9, -55.7$
1954+513	20/09/90	0.002	$3.3 \times 3.7, -20.6$	24/09/87	0.0014	$0.9 \times 1.8, -33.8$
2200+420	20/09/90	0.004	$2.7 \times 5.8, -18.1$	11/12/78	0.008	$2.3 \times 3.1, 2.3$
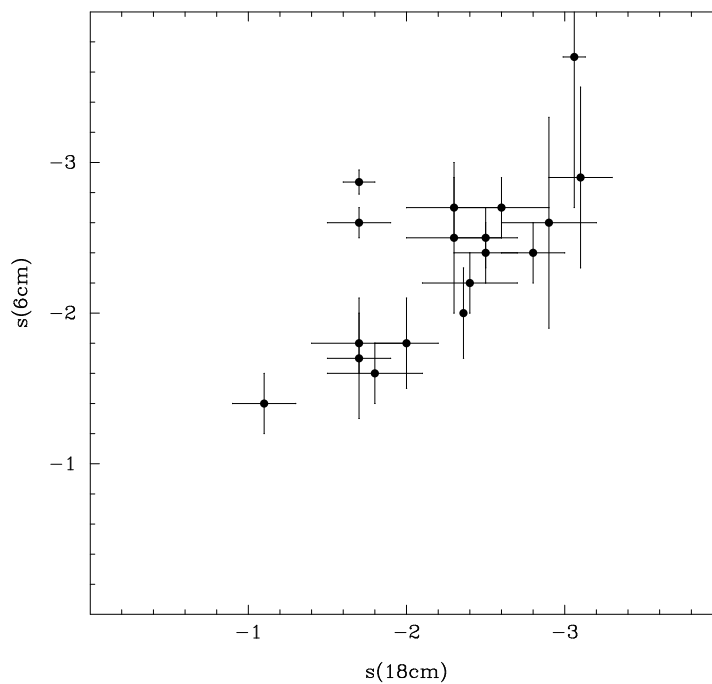
Figure C.3: Comparison of brightness temperature gradients with core distance at $\lambda18\,cm$ and at $\lambda6\,cm$ ($T_{\mathrm{b}} \propto r^s$).

Table C.3: Summary of the T_b-vs.-r and the T_b-vs.-d analysis ($T_\mathrm{b} \propto r^s$; $T_\mathrm{b} \propto d^{s_d}$; $d \propto r^l$).

Source	s(18cm)[a]	s(6cm)[a]	s_d(18cm)[b]	s_d(6cm)[b]	l(18cm)[c]	l(6cm)[c]
0716+714	-2.5 ± 0.2	-2.5 ± 0.2	-2.2 ± 1.2	-2.6 ± 0.4	0.90 ± 0.43	0.91 ± 0.22
0740+828	-2.8 ± 0.2	-2.4 ± 0.2	-2.9 ± 0.2	-2.4 ± 0.2	0.97 ± 0.02	1.00 ± 0.06
0746+483	-2.3 ± 0.3	-2.7 ± 0.2	-3.1 ± 0.6	-4.5 ± 0.4	0.57 ± 0.11	0.60 ± 0.07
0820+560	-1.8 ± 0.3	-1.6 ± 0.2	-1.9 ± 0.3	-2.1 ± 0.4	0.94 ± 0.05	0.71 ± 0.13
0833+585	-1.8 ± 0.2	-2.0 ± 0.1	-2.5 ± 0.4	-2.1 ± 0.5	0.74 ± 0.13	0.81 ± 0.14
0906+430	-1.7 ± 0.2	-2.6 ± 0.1	-3.6 ± 0.9	-3.0 ± 0.4	0.44 ± 0.06	0.83 ± 0.12
0917+449	-2.3 ± 0.3	-2.5 ± 0.5	-3.0 ± 0.2	-2.9 ± 0.1	0.75 ± 0.10	0.89 ± 0.13
0945+408	-3.1 ± 0.2	-2.9 ± 0.6	-3.2 ± 0.4	-2.6 ± 0.1	0.88 ± 0.10	0.93 ± 0.58
1020+400	-2.0 ± 0.2	-1.8 ± 0.3	-2.4 ± 0.3	-2.3 ± 0.4	0.80 ± 0.10	0.73 ± 0.18
1101+384	-2.36 ± 0.01	-2.0 ± 0.3	-2.0 ± 0.3	-2.4 ± 0.3	1.15 ± 0.15	0.80 ± 0.15
1216+487	-2.5 ± 0.2	-2.4 ± 0.2	-2.8 ± 0.6	-3.0 ± 0.4	0.82 ± 0.21	0.76 ± 0.14
1347+539	-1.1 ± 0.2	-1.4 ± 0.2	-1.9 ± 0.3	-2.2 ± 0.2	0.57 ± 0.10	0.62 ± 0.10
1418+546	-2.6 ± 0.3	-2.7 ± 0.2	-2.8 ± 0.2	-2.4 ± 0.1	0.95 ± 0.03	1.12 ± 0.04
1504+377	-1.7 ± 0.2	-1.7 ± 0.4	-2.6 ± 0.3	-2.98 ± 0.05	0.65 ± 0.03	0.50 ± 0.16
1642+690	-1.7 ± 0.1	-2.87 ± 0.08	-2.6 ± 1.1	-2.4 ± 0.3	0.56 ± 0.21	1.16 ± 0.15
1807+698	-2.4 ± 0.3	-2.2 ± 0.2	-2.3 ± 0.3	-2.3 ± 0.3	1.01 ± 0.11	0.98 ± 0.11
1842+681	-2.9 ± 0.3	-2.6 ± 0.7	-2.6 ± 0.4	-2.9 ± 0.1	1.02 ± 0.28	0.92 ± 0.30
1954+513	-1.7 ± 0.3	-1.8 ± 0.2	-2.2 ± 0.3	-2.3 ± 0.5	0.64 ± 0.18	0.53 ± 0.14
2200+420	-3.06 ± 0.07		-2.8 ± 0.3		1.07 ± 0.15	

[a] See Fig. C.2; [b] See Fig. C.5; [c] See Fig. C.4.

Table C.4: List of the 11 sources (out of 29) which do not show a power-law decrease of Tb.

Source	Comments
0248+430	Jet dominated by a very bright, compact component
0620+389	Relatively strong curvature
0833+585	T_b vs. r has a power-law shape but T_b vs. d not, Resolved source?
1058+726	
1435+638	Sharp bend in jet structure
1624+416	
1652+398	Sharp bend in jet structure, partially resolved
1719+357	Weak jet, resolved?
1800+440	
1823+568	
2229+695	

A basic model for the T_b-distribution in radio jets: The flux F_ν of one circular model component with the diameter d and the radiating area $\Phi \propto d^2$ can be written as

$$F_\nu = \Phi^2 \cdot d \cdot j_\nu \quad , \tag{C.1}$$

with the emissivity j_ν of optically thin synchrotron emission. The latter is proportional to

$$j_\nu \propto n_e \cdot B \cdot \left(\frac{\nu}{\nu_B} \right)^\alpha \tag{C.2}$$

(Krolik 1999) with the particle density n_e, the magnetic field B ($\nu_B \propto B$), and α the spectral index of optically thin synchrotron emission. We assume that the jet diameter d, the magnetic field B, and the particle density n_e all are functions of radius along the jet r and can be described by power laws:

$$d \propto r^l, \quad B \propto r^b, \quad n_e \propto r^n \quad , \tag{C.3}$$

expecting $l \le 1$ ($l > 1$ can hold only for decelerating jets). Note that these are the only critical assumptions for the further interpretation of the observed brightness temperature gradients in the following paragraphs. They imply that the flux of the model component itself has a power law dependence on the radius

$$F_\nu \propto r^{5l+n+b(1-\alpha)} \tag{C.4}$$

and the brightness temperature $T_b \propto F_\nu / \Phi^2$ can be written as

$$T_b \propto r^{l+n+b(1-\alpha)} \quad . \tag{C.5}$$

Thus, the power-law index of the brightness temperature distribution along the jet can be parametrized as

$$s = l + n + b(1 - \alpha) \quad . \tag{C.6}$$

The typical values, expected to be found for s can be estimated by setting the parameters n and b to (physically motivated) "first-guess values": if no cooling and no adiabatic losses occur in the expanding jet and if the particle flux through the jet cross section is conserved, it follows that $n_e \propto d^{-2} (\Rightarrow n = -2l)$. This simplifies Equation C.5 to

$$T_b \propto r^{b(1-\alpha)-l} \quad . \tag{C.7}$$

Conservation of magnetic energy along the jet implies a constant energy partition along the jet

$$B^2 \propto n_e, \Rightarrow b = -l \quad . \tag{C.8}$$

In this case the brightness temperature distribution can be characterized exclusively in terms of the jet geometry implied by l and the spectral index:

$$T_b \propto r^{l(\alpha-2)} \quad . \tag{C.9}$$

A conical jet with $l = 1$ thus should show a decrease in brightness temperature as $r^{\alpha-2}$. Typical values of s are thus expected to lie in the range -2.5 to -3 for spectral indices of -0.5 to -1.

Alternatively to the equations C.5 and C.6 one can parametrize the brightness temperature gradient as a function of the jet diameter, which yields the relation

$$T_b \quad \propto \quad d^{s_d} \quad , \text{with} \tag{C.10}$$

$$s_d \quad = \quad 1 + \frac{n + b(1 - \alpha)}{l} = \frac{s}{l} \tag{C.11}$$

because of $d \propto r^l$. Equation C.11 implies that the ratio of the two power-law indices s and s_d is determined by the jet geometry via

$$\frac{s}{s_d} = l \quad . \tag{C.12}$$

The power law indices s and s_d from Table C.3 can now be compared with the theoretical expectations described above.

The correlation between T_b distribution and the jet geometry: From Equation C.12 follows that the linear relationship between the T_b gradients with r at $\lambda 18$ cm and $\lambda 6$ cm (seen in Fig. C.3) should hold also for for the T_b gradients with d if the jets are conical ($l = 1$). Indeed, Fig. C.6 shows the dependence of s_d at $\lambda 18$ cm on s_d at $\lambda 6$ cm which is considerably less pronounced than for the gradients with distance. This already suggests that the assumption of an equal value of l for all jets, i.e., a standard jet geometry is not valid. In a diagram that shows s_d as a function of s, sources with $l < 1$ are expected to populate the upper left triangle of the plot. This is seen in Fig. C.7 where most of the data points lie significantly above the slope-one line. In fact only 8 out of 31 points lie below this level and most of these are consistent with $s_d > s$ within their errors.

The power law index l which describes the jet geometry (via $d \propto r^l$, where d is the jet diameter) can be approximated by the size measurement of different model components along the jet as a function of radius. Figure C.4 shows the results of power law fits to the component sizes as a function of core distance for the 18 sources in the sample. Equation C.7 implies that there should be a linear relation between s and l for sources with the same spectral index α and equal gradients of the magnetic field. On the other hand, s_d is expected to depend inversely on l (see Equation C.11). Figure C.8 shows that the measured values of s, s_d, and l indeed fulfill a linear relation as expected from Equation C.12.

The values of s, s_d, and l measured for each source (except 2200+420, where only $\lambda 18$ cm were considered) at $\lambda 18$ cm and $\lambda 6$ cm were averaged to derive one set of values for each source. Figure C.9 and Fig. C.10 show the calculated mean values of s and s_d, respectively, as a function of l together with the expected ranges for reasonable values of the characteristic source parameters n, b, and α. In the jet model, assumed in this section (Equation C.3), n, b, and α along with the jet geometry (parametrized via l) are the characteristic quantities that determine the jet physics of a given source. The dashed lines in Fig. C.9 and Fig. C.10 indicate the range of values for n, b, and α typically assumed to occur in AGN jets on parsec scales (e.g., Lobanov 1998). The figures show that the brightness temperature gradients measured in this study are in good agreement with the particle density n_e falling with r^{-1}–r^{-2}, the magnetic field B falling with $r^{-0.5}$–r^{-1} and the spectral index lying in the range $-1 < \alpha < -0.5$ in the optically thin part

of extragalactic radio jets on parsec scales. Figure C.9 further shows that the steepest decreases in T_b occur in sources which are freely expanding ($l \sim 1$). Due to the coupling between s and s_d via l (Equation C.12), it is not possible to disentangle n, b, and α from the measurement of brightness temperature gradients but only the quantity $n + b(1 - \alpha)$ even though α can in principle be determined from the offset between the T_b values at the two measured frequencies. However, a linear regression to the s_{mean}–vs–l distribution in Fig. C.9 suggests that s falls proportional to l with a slope $q = (-2.5 \pm 0.2)$ and an axis intercept of $s_{l=0} = (-0.25 \pm 0.22)$. Comparing this to Equation C.6 yields a dependence of: $n + b(1 - \alpha) = -3.5l - 0.25$.
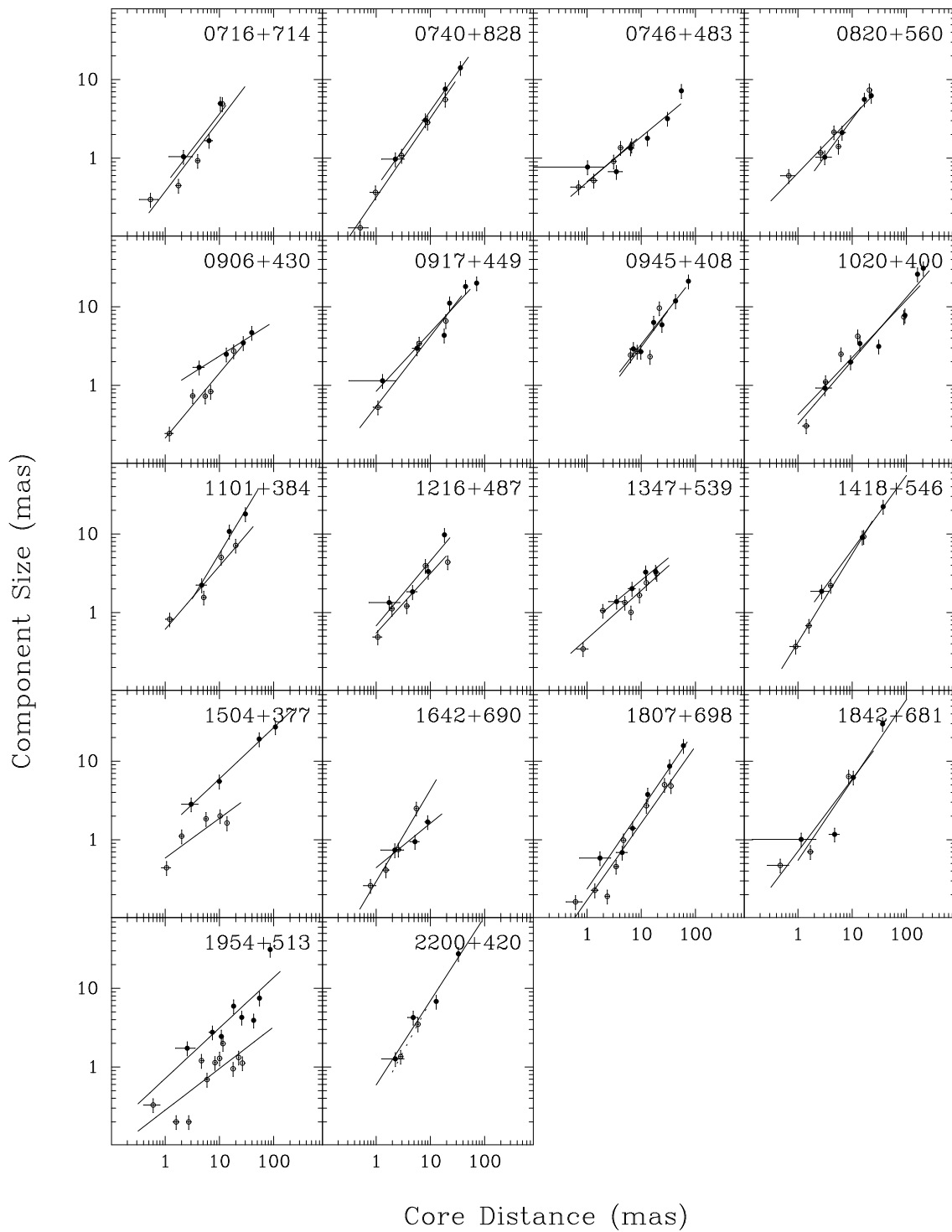
Figure C.4: Size of the model components as a function of distance along the jets in the sample sources ($d \propto r^l$). The thick line indicates a power-law fit to the data in each plot. Filled symbols show data at 18 cm, open ones data at 6 cm.
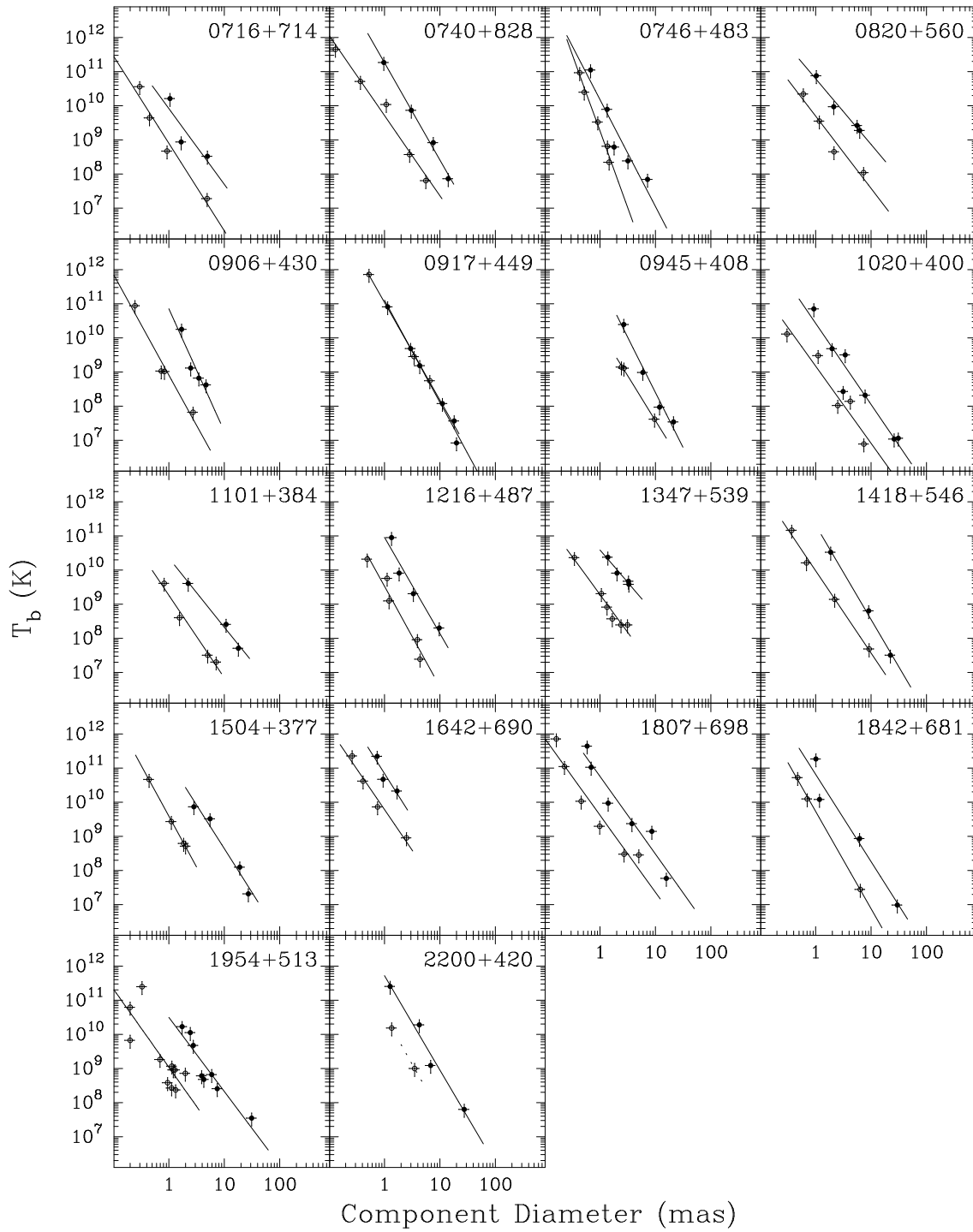
Figure C.5: Brightness temperature gradients with jet diameter ($T_\mathrm{b} \propto d^{s_d}$). The thick line indicates a power-law fit to the data in each plot. Filled symbols show data at 18 cm, open ones data at 6 cm.
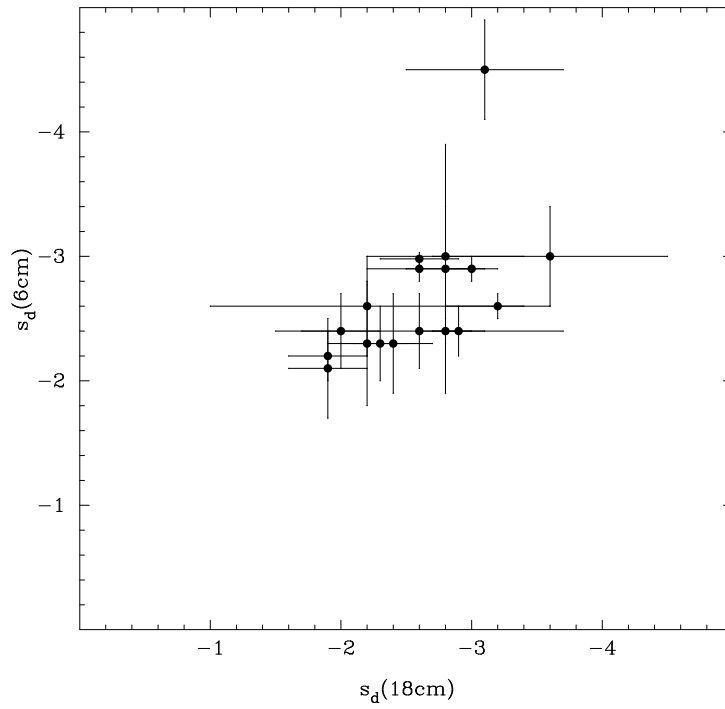
Figure C.6: Comparison of brightness temperature gradients with jet diameter at $\lambda 18\,\text{cm}$ and at $\lambda 6\,\text{cm}$ ($T_\text{b} \propto d^{s_d}$).
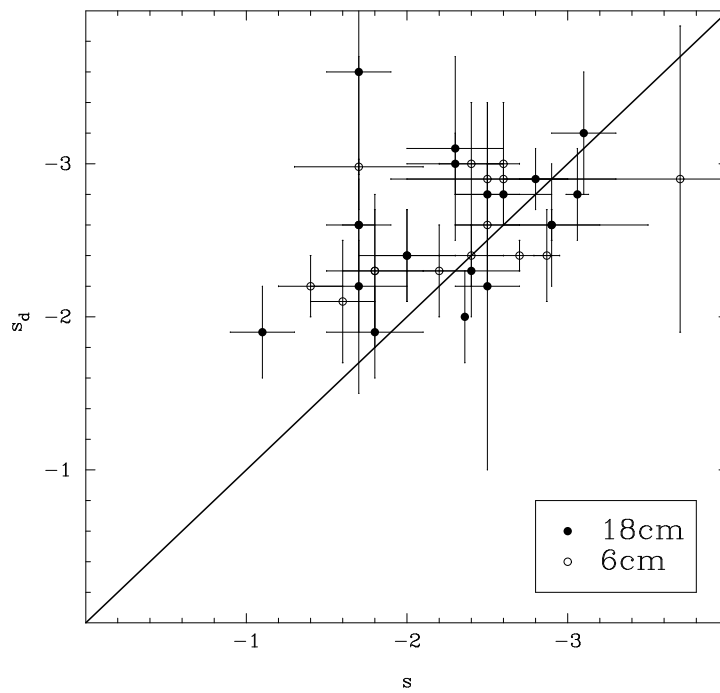
Figure C.7: Brightness temperature gradients at $\lambda 18\,\text{cm}$ and $\lambda 6\,\text{cm}$ with core distance ($T_\text{b} \propto r^s$) and with jet diameter $T_\text{b} \propto d^{s_d}$.
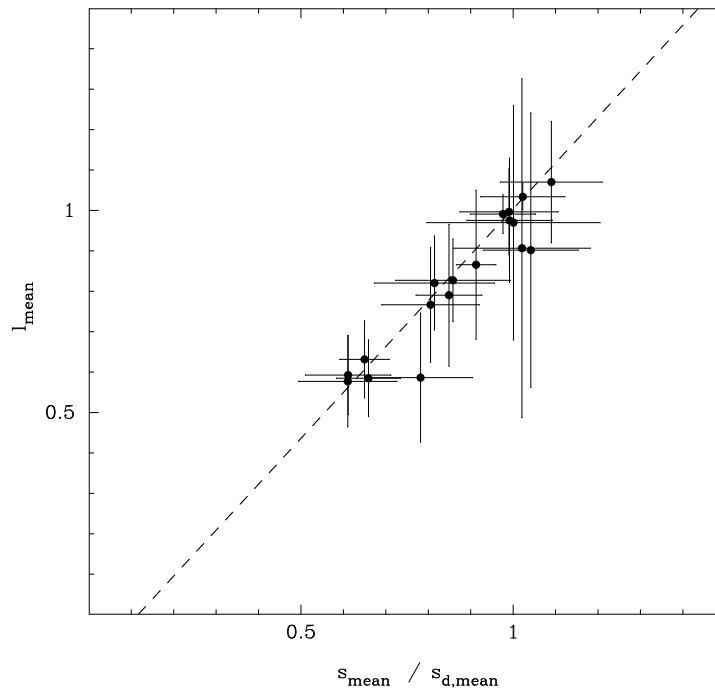
Figure C.8: The measured ratio $s_{\mathrm{mean}}/s_{d,\mathrm{mean}}$ as a function of l_{mean}. As predicted by Equation C.12 the plot shows a one-to-one correspondence. The dashed line shows a linear regression.
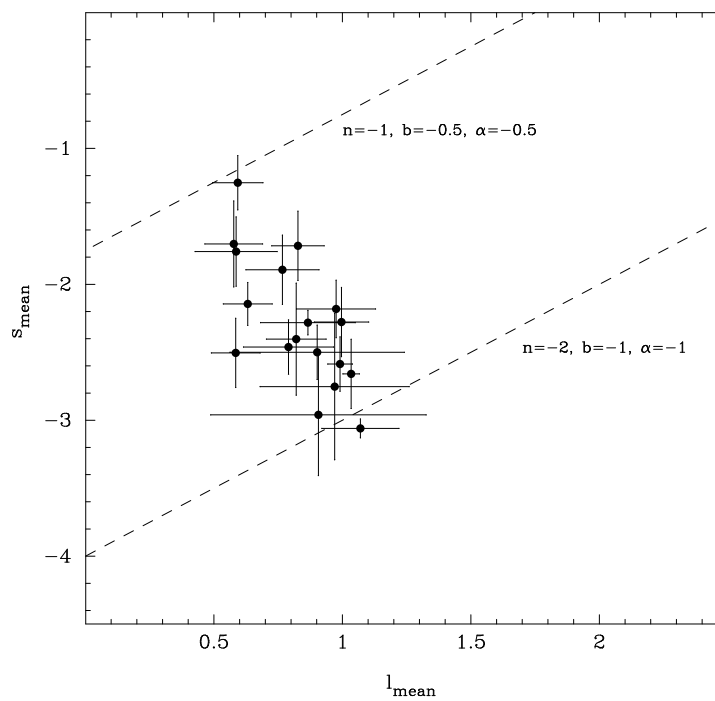
Figure C.9: The mean power-law index s as a function of the measured value of l ($d \propto r^l$). The steepest decreases of T_{b} occur in sources which are freely expanding ($l \sim 1$). The dashed lines indicate the expected dependence on l for some values of n, b, and α.
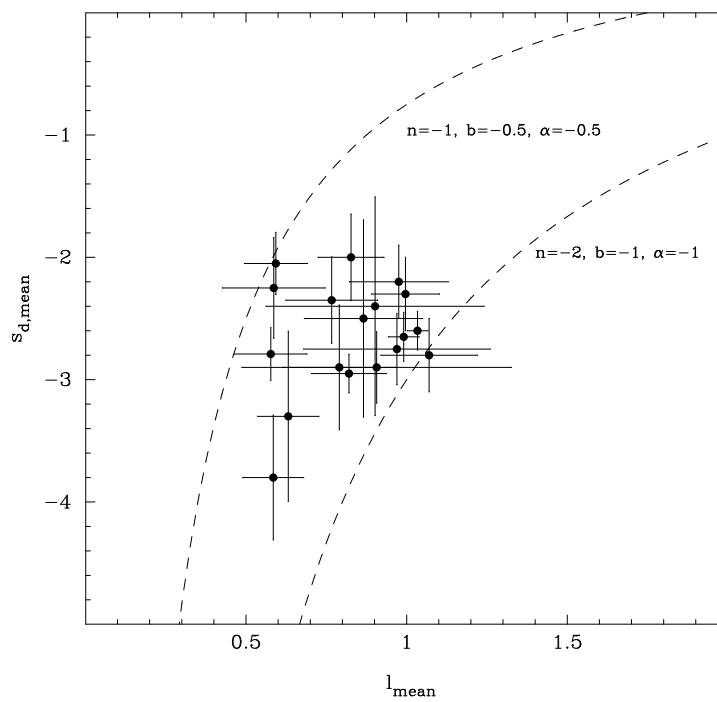
Figure C.10: The mean power-law index s_d as a function of the mean measured value of l. The dashed lines indicate the expected dependence on l for some values of n, b, and α.

Summary and outlook: In this chapter, a method has been presented to derive characteristic jet parameters describing the jet geometry and the distributions of electron density and the magnetic field, from VLBI measured brightness temperature gradients along the jets on parsec scales. This method is "untypical" because brightness temperatures are more commonly used to investigate the most compact regions in jets (i.e., the cores) while, here, we explicitly assume resolved structures along the jet with optically thin synchrotron spectra. Moreover, the basic assumption that the jets can be sufficiently described by Equation C.3 is surprisingly simple and in view of the variety of different structures seen in VLBI hybrid-mapping images at high frequencies certainly only a rough approximation. However, this simple models describes consistently the relationship between its basic parameters showing that the individual jet components in the sources selected for this study can be considered as *probes of a more or less steady jet at a given distance from the jet core.* The fact the not all sources from the initial sample showed a simple power-law dependence of T_b on core distance suggests that not all jet components can be seen in this way. Major plasma ejections, associated with considerable source flux density outbursts may lead to jet components with brightness temperatures well above the values extrapolated from more distant components and relatively bright structures at large distances from the core may be the relics of such major outbursts in the past. The example of component E 1 in 3C 111 (see Sect. 6.4) shows that in such cases the brightness temperature of an unusually bright and compact jet component can be treated in a similar way as the jets investigated in this chapter by tracing the development of T_b in time as the component travels away from the jet core. The example of NGC 1052 (see Sect. 6.3) shows that local deviations from an otherwise "standard power-law distribution" can reveal free-free absorbing regions along the jet or rapidly changing density gradients of the jet ambient medium. The differences between the measured gradients at different frequencies, in particular deviations from the expected ν^{-2} dependence, may reflect changes of α making a T_b-gradient analysis in principle sensitive to spectral curvature.

The presented model considers only the gradients of T_b and ignores the absolute brightness temperatures of the jets and their cores. The lack of an absolute position along the jet, as e.g., the 1 pc distance to the (invisible) central engine, makes it difficult to account for the absolute values of T_b. It is interesting to speculate whether this argument can be turned around and the brightness temperature distribution along the jets might reveal a "characteristic position" along the jets at which one can compare them. The cores cannot be used for this task since these are unresolved in nearly all cases and their offset to the physical central engine are not *a-priori* known. Solving these issues is beyond the scope of this PhD thesis.

D Sub-milliarcsecond Imaging of Quasars and Active Galactic Nuclei

The following introduction the *VLBA 2 cm Survey* project has been adopted from Zensus et al. (2003). In this conference contribution we reported on the status of the 2 cm survey in early 2003. The citations in the cited text are cross-referenced to the bibliography of this thesis and the cited tables are reproduced at the end of this introductive chapter.

> *"[The] radio morphologies of AGN can usually be classified as being either "extended" (e.g., spatially resolved) or "compact" (e.g., unresolved at 1' resolution). The extended sources can be as large as Megaparsecs and are transparent to their own radio synchrotron emission, whereas, due to self-absorption, the compact sources can have flat or even inverted spectra. VLBI probes the compact regions typically with resolutions of the order of 1 milliarcsecond (mas), which correspond to parsec scales (see Zensus 1997). VLBI is thus the key tool to study the relativistic outflows. [...]*
>
> *There have been various surveys to study the nature of AGN physics (see Table D.1 and Green et al. 2002). In spite of the extensive body of observational data and the sophisticated theoretical models which have been discussed in the last decades, major questions remain unanswered related to the nature of AGN jets. For example, it is not clear whether the flows are ballistic, that is, if individual features have straight trajectories, or if they follow the curvature of the jet. It also remains unclear if the changes in speed or direction of features as they propagate down the jet are typical or if they occur only under special circumstances. The different classes of AGN may present different characteristic Lorentz factors.*
>
> *Individual, selected sources have been observed intensively in order to address these questions (e.g., 3C 345: Ros et al. 2000; 3C 273: Lobanov and Zensus 2001; 3C 120: Gómez et al. 2000; 3C 279: Homan (2003) and Homan et al. (2003); 4C +12.50: Lister et al. 2003b). In particular, variability studies, multi-frequency monitoring, and observations of polarized emission have been important in understanding the physical conditions within individual sources. Our intent [...] is to study a representative sample of objects, carrying out a long-term, systematic monitoring of relativistic motion in AGN jets on parsec scales. We seek a significant improvement over previous surveys in terms of image resolution and fidelity, sample size, and statistical completeness. The goals of our program are to test and characterize the kinematics of these AGN jets and to determine how these are related to other source prop-*

erties. We try to provide the basis for a comprehensive physical theory to relate the distribution of Lorentz factors and bends and other morphological characteristics, the internal temperatures, and the spectral behavior.

Since 1994, we have been using the NRAO Very Long Baseline Array (VLBA) at 15 GHz (2 cm) to study the relativistic outflows in a sample of AGN (see description in Kellermann et al. 1998a and Zensus et al. 2002). Our sample is based on the 1 Jy catalog (Kuehr et al. 1981), and considers sources with flat spectra ($\alpha > -0.5$ for $S_\nu = \nu^{+\alpha}$ above 500 MHz) and flux densities $S_{15\,\mathrm{GHz}} > 1.5$ Jy for $\delta > 0°$, and $S_{15\,\mathrm{GHz}} > 2$ Jy for $-20° < \delta < 0°$. Some additional sources have been added, particularly those classified as compact symmetric objects or lobe-dominated sources with a strong core. The current 2 cm survey source list (complete up to February 2003) is shown in Table D.2. The sources observed so far are tabulated under the column labeled with "O". [...]

We maintain a data bank of images from these observations, accessible at `http://www.nrao.edu/2cmsurvey`*. Each source has been observed at least once per year. The observations typically consisted of multiple snapshots spread over 8 hours with a total integration time of 50 minutes. The root-mean-square noise level in each image is typically less than 1 mJy/beam. In other words, the dynamic ranges achieved are better than 1000:1, sufficient to determine the kinematics of the features in the sources by comparing images made at different epochs. The typical synthesized beam is 1 mas $\times$ 0.5 mas in position angle $P.A. = 0°$. Automatic imaging procedures proved to be sufficient in many of the cases (applying loops of clean and phase self-calibration) using the difmap software package.*

The results of the survey have been published in several papers and conference proceedings. A description of the survey including contour plots for each of the sources is given in Kellermann et al. (1998a) Zensus et al. (2002). General results from the Survey were presented in Kellermann et al. (1997; 1998b; 1999b; 2000; 2003), Kellermann (2002; and 2003), Cohen et al. (2003b), Ros et al. (2002), Ros (2003), and Lister et al. (2003a). Studies on individual sources have been presented: Kellermann et al. (1999a), Vermeulen et al. (2003b; 2003c; and 2003d): NGC 1052, Homan (2002), Homan et al. (2003 and 2003): 3C 279; Lister et al. (2002), Lister (2002; 2003b): 4C +12.50; and Lister et al. (2002): 2134+004 and OQ 208."[1]

---

[1]The cited list of published VLBA 2 cm Survey papers is complete until February 2003. Since then, the following additional works have been published: Arshakian et al. (2005), Cohen et al. (2003b), Cohen et al. (2003a) Kadler et al. (2004b), Kellermann et al. (2004), and Ros (2004).

Table D.1: Selected AGN Surveys (Table updated from the original in Zensus et al. 2003).

	Name	Refs.
Radio		
VLBI ($\lambda\lambda$ 18/6 cm)	Pearson-Readhead & Caltech-Jodrell Bank	Pearson and Readhead (1988); Taylor et al. (1994); Taylor et al. (1996) ; Polatidis et al. (1995); Thakkar et al. (1995); Xu et al. (1995); Henstock et al. (1995); Vermeulen et al. (2003a)
VLBI (13/3.6/2)	Radio Optical Reference Frame	Fey et al. (1996); Fey and Charlot (1997, 2000)
VLBI (6)	VSOP Pre-Launch	Fomalont et al. (2000)
VLBI (0.7)		Jorstad et al. (2001)
VLBI (0.3)	MPIfR	Lobanov et al. (2000)
Variability (6/3.6/2)	UMRAO	Aller et al. (2003)
Variability	Effelsberg	Kraus et al. (2003)
Variability (1.3)	Northern 2 Jy	Valtaoja et al. (1992)
X-Ray		
Soft X-Rays	*ROSAT*	Brinkmann et al. (1997b & 1997a); Yuan et al. (1998); Lamer et al. (1996)
Soft–Medium X-Rays	*ASCA*, *Chandra*, *XMM-Newton*	Sambruna et al. (1999a); Reeves and Turner (2000); Terashima et al. (2002); Terashima and Wilson (2003); Sambruna et al. (2004); Marshall et al. (2005); Galbiati et al. (2005)
Hard X-Rays	*Beppo*Sax	Donato et al. (2001); Padovani et al. (2002)
γ-Ray		
EGRET	3rd Catalog	Hartman et al. (1999)

Table D.2: 2 cm Survey Source List (adopted from Zensus et al. (2003) and updated as of February 2005)

Name	O[a]	K[b]	M[c]	Name	O	K	M	Name	O	K	M	Name	O	K	M
0003−066	✓	✓	✓	0615+820	✓	✓		1150+812			✓	1741−038	✓	✓	✓
0007+106	✓	✓	✓	0642+449	✓	✓	✓	1155+251	✓			1749+096	✓		✓
0016+731	✓	✓	✓	0648−165			✓	1156+295	✓	✓	✓	1749+701	✓	✓	
0026+346	✓	✓		0707+476	✓	✓		1213−172			✓	1751+288			✓
0035+413	✓	✓		0710+439	✓	✓		1219+044			✓	1758+388	✓	✓	✓
0048−097	✓		✓	0716+714	✓	✓	✓	1219+285	✓	✓		1800+440	✓	✓	✓
0055+300	✓	✓		0723−008	✓	✓		1222+216			✓	1803+784	✓	✓	✓
0059+581			✓	0727−115	✓	✓	✓	1226+023	✓	✓	✓	1807+698	✓	✓	
0106+013	✓	✓	✓	0730+504			✓	1228+126	✓	✓	✓	1823+568	✓	✓	✓
0108+358	✓	✓		0735+178	✓	✓	✓	1253−055	✓	✓	✓	1828+487	✓	✓	✓
0109+224			✓	0736+017	✓	✓	✓	1302−102	✓	✓		1845+797	✓	✓	
0112−017	✓	✓		0738+313	✓	✓	✓	1308+326	✓	✓	✓	1849+670	✓		✓
0119+041	✓	✓		0742+103	✓	✓		1323+321	✓	✓		1901+319	✓	✓	
0119+115	✓	✓	✓	0745+241	✓	✓		1324+224			✓	1921−293	✓		
0133+476	✓	✓	✓	0748+126	✓	✓	✓	1328+254	✓			1928+738	✓	✓	✓
0149+218	✓	✓		0754+100	✓	✓	✓	1328+307	✓			1936−155			✓
0153+744	✓	✓		0804+499	✓	✓	✓	1334−127	✓	✓	✓	1954+513	✓	✓	
0201+113	✓	✓		0805−077			✓	1345+125	✓	✓		1957+405	✓	✓	✓
0202+149	✓	✓	✓	0808+019	✓	✓	✓	1354+196	✓	✓		1958−179			✓
0202+319	✓	✓	✓	0814+425	✓	✓	✓	1354−152	✓	✓		2005+403	✓	✓	✓
0212+735	✓	✓	✓	0821+394				1404+286	✓	✓		2007+776	✓	✓	
0215+015			✓	0823+033	✓	✓	✓	1413+135	✓	✓	✓	2008−159	✓		✓
0218+357	✓			0827+243			✓	1417+385			✓	2021+317	✓	✓	✓
0221+067	✓	✓		0829+046	✓	✓	✓	1418+546				2021+614	✓	✓	✓
0224+671			✓	0834−201	✓	✓		1424+366	✓	✓		2037+511			✓
0234+285	✓	✓	✓	0836+710	✓	✓	✓	1458+718	✓	✓	✓	2113+293	✓	✓	
0235+164	✓		✓	0850+581	✓	✓		1502+106	✓	✓	✓	2121+053	✓	✓	✓
0238−084	✓	✓	✓	0851+202	✓	✓	✓	1504+377	✓	✓		2128+048	✓		
0300+470			✓	0859+470	✓	✓		1504−167	✓	✓	✓	2128−123	✓	✓	✓
0310+013	✓			0859−140	✓	✓		1508−055	✓	✓		2131−021	✓	✓	✓
0316+161	✓			0906+015	✓	✓	✓	1510−089	✓	✓	✓	2134+004	✓	✓	✓
0316+413			✓	0917+449	✓	✓		1511−100	✓	✓		2136+141	✓	✓	✓
0333+321	✓	✓	✓	0917+624			✓	1514−241	✓	✓		2144+092	✓	✓	
0336−019	✓	✓	✓	0923+392	✓	✓	✓	1519−273	✓			2145+067	✓	✓	✓
0355+508	✓	✓		0945+408	✓	✓	✓	1532+016	✓	✓		2155−152	✓	✓	✓
0403−132			✓	0953+254	✓	✓		1538+149	✓	✓	✓	2200+420	✓	✓	✓
0405−385	✓	✓		0954+658			✓	1546+027	✓	✓	✓	2201+171	✓		✓
0415+379	✓	✓	✓	0955+476			✓	1548+056	✓	✓	✓	2201+315	✓	✓	✓
0420+022	✓	✓		1012+232	✓	✓		1555+001	✓	✓		2209+236	✓	✓	✓
0420−014	✓	✓	✓	1015+359	✓	✓		1606+106	✓	✓	✓	2216−038			✓
0422+004			✓	1032−199	✓			1611+343	✓	✓	✓	2223−052	✓	✓	✓
0430+052	✓	✓	✓	1036+054			✓	1622−253	✓	✓		2227−088	✓		✓
0440−003	✓	✓		1038+064			✓	1633+382	✓	✓	✓	2230+114	✓	✓	✓
0446+112			✓	1045−188			✓	1637+574			✓	2234+282	✓	✓	
0454+844	✓	✓		1049+215	✓	✓		1638+398	✓	✓	✓	2243−123	✓	✓	✓
0458−020	✓	✓	✓	1055+018	✓	✓	✓	1641+399	✓	✓	✓	2251+158	✓	✓	✓
0521−365	✓	✓		1055+201	✓	✓		1642+690	✓	✓		2255−282	✓	✓	
0528+134	✓	✓	✓	1101+384	✓	✓		1652+398	✓	✓		2318+049	✓	✓	
0529+075			✓	1124−186	✓		✓	1655+077	✓	✓	✓	2331+073			✓
0529+483			✓	1127−145	✓	✓	✓	1656+053	✓	✓		2345−167	✓	✓	✓
0552+398	✓		✓	1128+385	✓	✓		1656+477	✓	✓		2351+456			✓
0602+673	✓			1144+402				1726+455			✓				
0605−085	✓	✓	✓	1145−071	✓			1730−130	✓	✓	✓				
0607−157	✓	✓	✓	1148−001	✓			1739+522	✓		✓				

[a]: Included originally in the 2 cm survey (for selection criteria, see Zensus et al. 2002: sect. 2).
[b]: Kinematic analysis performed. (Excludes sources with only one observing epoch or unresolved structure.)
[c]: Included in the MOJAVE sample (see Zensus et al. 2002, sect. 4).

D.1   Kinematics of Parsec-Scale Radio Jets

Sub-Milliarcsecond Imaging of Quasars and Active Galactic Nuclei. III. Kinematics of Parsec-Scale Radio Jets, K.I. Kellermann, M.L. Lister, D.C. Homan, R.C. Vermeulen, M.H. Cohen, E. Ros, M. Kadler, J.A. Zensus, Y.Y. Kovalev, Astrophysical Journal, 609, 539–563 (2004)

In this paper, we present the kinematical results of the 2cm Survey program, begun in 1994 and continuing with multi-epoch observations at 15 GHz, to study the outflow in radio jets ejected from quasars and active galaxies. Our observations directly measure highly collimated relativistic motion in both quasars and active galaxies with apparent velocity typically between 0 and 8c, but for quasars we observe a tail extending up to $34\,c$. Source-characteristic speeds are found in a large fraction of the sources. These characteristic speed of individual jet features can be interpreted as the result of an underlying continuous jet flow. In some sources, however, stationary and even apparently inward-moving components are found. The observed distribution of linear velocities rules out simple ballistic models but suggests a broad range of Lorentz factors, a significant difference between the velocity of the bulk relativistic flow and the pattern speed of underlying shocks, or a combination of these effects. We find evidence for a steep power-law distribution of intrinsic Lorentz factors, an isotropic distribution of orientations of the parent population, and intrinsic brightness temperatures about an order of magnitude below the canonical inverse Compton limit. It appears that the parent population of radio jets is not dominated by highly relativistic flows, and contrary to the assumption of simple unified models, not all sources have intrinsic speeds close to c.

Many jets exhibit strong bending and non-radial motions aligned with the local jet direction but not aligned with the direction back to the core. This suggests that the jet flow occurs along preexisting bent channels. In a few cases we have observed a clear change in the direction of a feature as it flows along the jet. Radio jets that are also strong gamma-ray sources detected by EGRET appear to have significantly faster speeds than the non-EGRET sources, consistent with the idea that gamma-ray sources have larger Doppler factors than non-gamma-ray sources. Sources at high redshift have systematically lower angular speeds than low-redshift jets, consistent with standard cosmologies.

Determination of source kinematics in sources with complicated structure: The confidence of component cross-identification between different epochs depends crucially on both the source structure and the time sampling. Ideally, a source is modeled by a small number of well-separated components located at characteristic positions along the jet and traveling with a speed low enough to identify the components unambiguously at the different epochs. If the flux densities of the different model components in one source differ they can be used to verify the cross-identification from which the source kinematics are derived. However, in many sources these ideal conditions do not apply. In some cases the component proper motions may be too large between the observing epochs (resulting to "stroboscopic" effects) so that no unique multi-epoch model can be found to describe the source. Moreover, the gaps between the different observing epochs are in some cases much longer than 1 yr making the identification difficult also in some sources with smaller apparent velocities. Finally, complex source structures may not allow a simple and unique

source parametrization if, e.g., two adjacent components with similar flux densities travel along different paths or with different velocities. The last problem can in principle be overcome by (u, v)-modelfitting, which is superior to image-plane-fitting in the case of complex source structures. The image-plane-fitting, that was applied for the derivation of the most other jet-component speeds for the 2 cm Survey kinematical study, yielded ambiguous results in several cases. For those sources, (u, v)-modelfitting was done using DIFMAP by fitting the amplitudes and phases of the measured visibilities by elliptical Gaussian components. In general, the ellipticity of the individual model components was allowed to vary. In some cases, however, circular Gaussians were used to reduce the number of free parameters.

In 18 out of 110 cases, the (u, v)-modelfitting yielded results superior to image-plane-fitting, so that the latter were dismissed and the former were incorporated in the statistical study. These cases (0238−084, 0716+714, 0823+033, 0851+202, 0906+015, 0953+254, 1101+384, 1128+385, 1302–102, 1323+321, 1345+125, 1606+106, 1749+096, 1921–293, 1957+405, 2113+293, 2131–021, and 2145+067) are marked in Fig. 1 of Kellermann et al. (2004) by asterisks[2].

Here, 8 cases are discussed in more detail than in Kellermann et al. (2004). The distances of the various model components to the VLBI core in these 8 sources as a function of the observing epoch is shown in Fig. D.1. In contrast to Fig. 1 of Kellermann et al. (2004), all components are shown and not only the ones with 3 or more epochs to illustrate possible ambiguities. Throughout the section, the manner-of-labeling of Kellermann et al. (2004) is adopted: Component B (filled triangles), C (filled five-point star), D (filled circle), E (filled six-point star), F (cross), G (open five-point star), H (square), I (triangle).

0716+714 The parsec-scale jet kinematics of 0716+714 were discussed in Sect. 6.5 of this work.

0851+202 (OJ 287) 5 epochs of observations of OJ 287 between April 1995 and October 1998 were model-fitted. An additional epoch in January 2001 was discarded from the analysis due to the long period elapsed since the previous epoch. The parsec-scale structure of this source is very complex and approximating the (u, v)-data with a small number of model components (3 to 5) leaves significant peaks in the residual map. It was tried to achieve the best compromise between a too poor fit and a too large and confusing number of model components. The models with the smallest possible number of components, for which the component parameters are not substantially affected by the introduction of additional components, were used. Thus, the derived models represent the brightest and most significant features along the jet of OJ 287. This approach does sufficiently parametrize the jet in order to study its kinematics although it does not account for the faint details in the jet structure. Jorstad et al. (2001) reported the presence of two stationary components located at a distance of ∼0.2 mas and ∼1.2 mas from the core and moving components with velocities of 0.43–0.67 mas yr^{-1}. In contrast to this, no evidence for a stationary component at 1.2 mas is found from the analysis presented here. The most natural component identification contains only 5 moving components with velocities between 0.3 and 0.5 mas yr^{-1}. However, the innermost component at ∼0.25 mas might as well be interpreted as a stationary feature. In this case, however, the flux density

---

[2]Due to an error in editing, the three sources 1128+385, 1302–102, and 1606+106 are not properly labeled as (u, v)-modelfitted sources in Kellermann et al. (2004).
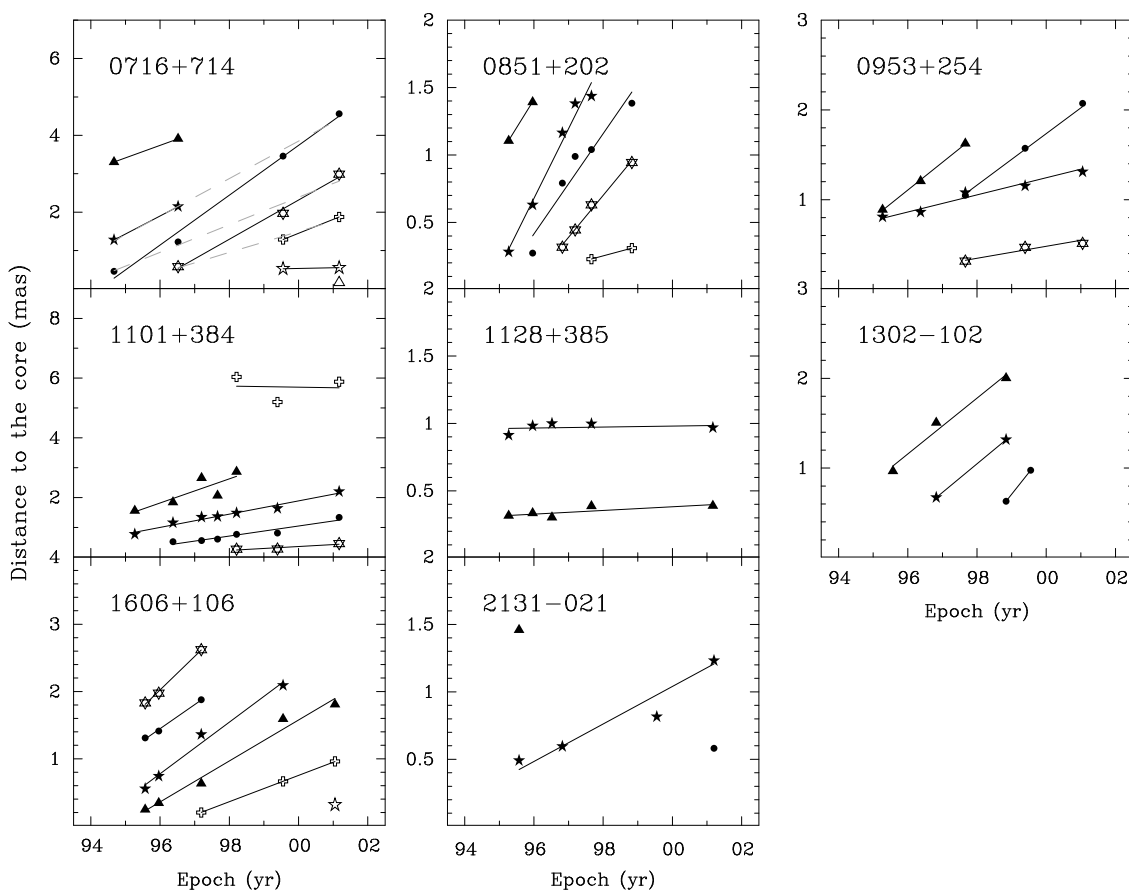
Figure D.1: Plots showing the change in separation from the core with time for components in 8 sources obtained from (u, v)-modelfitting. An alternative component identification scenario is indicated by dashed lines in the case of 0716+714.

of the stationary component varies significantly between 50 mJy and 1.1 Jy. Figure D.2 shows the flux density evolution of the fitted model components as a function of distance to the core. Two components (C and E) exhibit a pronounced minimum in flux density at a distance of $\sim$0.6 mas from the core. This might be interpreted as reduced Doppler boosting due to bending away from the line of sight.

0953+254 (OK 290) The varying source structure of OK 290 between April 1995 and January 2001 can be described with 4 moving components. Figure D.3 shows the images at the 6 observing epochs with the positions of the model components. The two brightest components (C and E) travel southeastwards (see Fig. D.4) with velocities of 0.09 mas yr^{-1} and 0.06 mas yr^{-1}, respectively. In contrast to this, the two weaker components (B and D) move faster with $\sim$0.3 mas yr^{-1} eastwards. This corresponds to a difference in apparent velocity between 2–3 c for the components C and E and 12 c for B and D. Moreover, their flux density decreases rapidly with time while the decrease of component C is much slower and component E remains virtually constant in flux density. Component D seems not to be emerged from the core but splits off from component C in 1997. Thus, the data suggests the existence of two distinct channels within the jet flow of OK 290 with different velocity fields and possibly different Doppler factors.

1101+384 (Mrk 421) Almost all of the flux density of this TeV blazar is contained

273
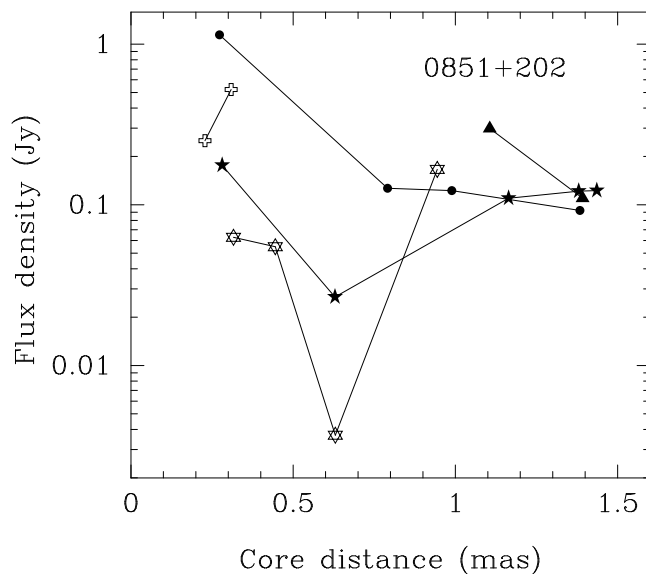
Figure D.2: Flux density of different model components in 0851+202 as a function of core distance (see Fig. D.1 for the positions).

within the core of the source ($\sim 90\%$), while the jet is weak, short and shows no prominent isolated components. Marscher (1999) reported speeds of 0.9–1.35 mas yr^{-1} or ~ 0.15 mas yr^{-1} depending on the component identification scenario. The VLBA 2 cm Survey data obtained from 7 epochs between April 1995 and March 2001 shows 4 moving components with velocities of 0.1–0.4 mas yr^{-1}. This supports the finding that the apparent superluminal motion in some TeV blazars is too small to explain the large Lorentz factors postulated by TeV-emission models (see Marscher 1999).

1128+385 This source shows a very compact structure which, however, cannot be approximated by a single Gaussian component adequately well. The best fit is achieved with a core- plus two jet-components for all epochs. However, in two epochs the 3-component fit is not significantly better than a 2-component fit from the statistical point of view. Thus, an alternative scenario with very rapid outward motion (> 0.4 mas yr^{-1}) cannot be excluded. However, the model with 2 stationary components ($\mu < 0.02$ mas yr^{-1}) is preferred because it offers an easier and more consistent explanation. Moreover, the fitted flux densities of both jet components are almost stable over the epochs with 30–70 mJy for component C and 90–110 mJy for component B.

1302−102 Three moving jet components are found between July 1995 and July 1999 with velocities of ~ 0.3 mas yr^{-1}. While the components B and C are comparatively weak, a new, extraordinarily bright component (D) is visible from October 1998 on. It moves with the same speed and on the same path to the northwest as the components B and C, but its flux density even exceeds the core flux density in October 1998 and July 1999. This component is also visible in a later epoch at the position expected from a linear extrapolation with 0.3 mas yr^{-1} with a comparable brightness.

1606+106 While Jorstad et al. (2001) detected no motion of jet components at 22 GHz, the VLBA 2 cm Survey data between July 1995 and January 2001 show several moving components with velocities of 0.2–0.5 mas yr^{-1}. All of them travel along a strongly curved path starting towards the east and turning towards the northeast beyond a distance
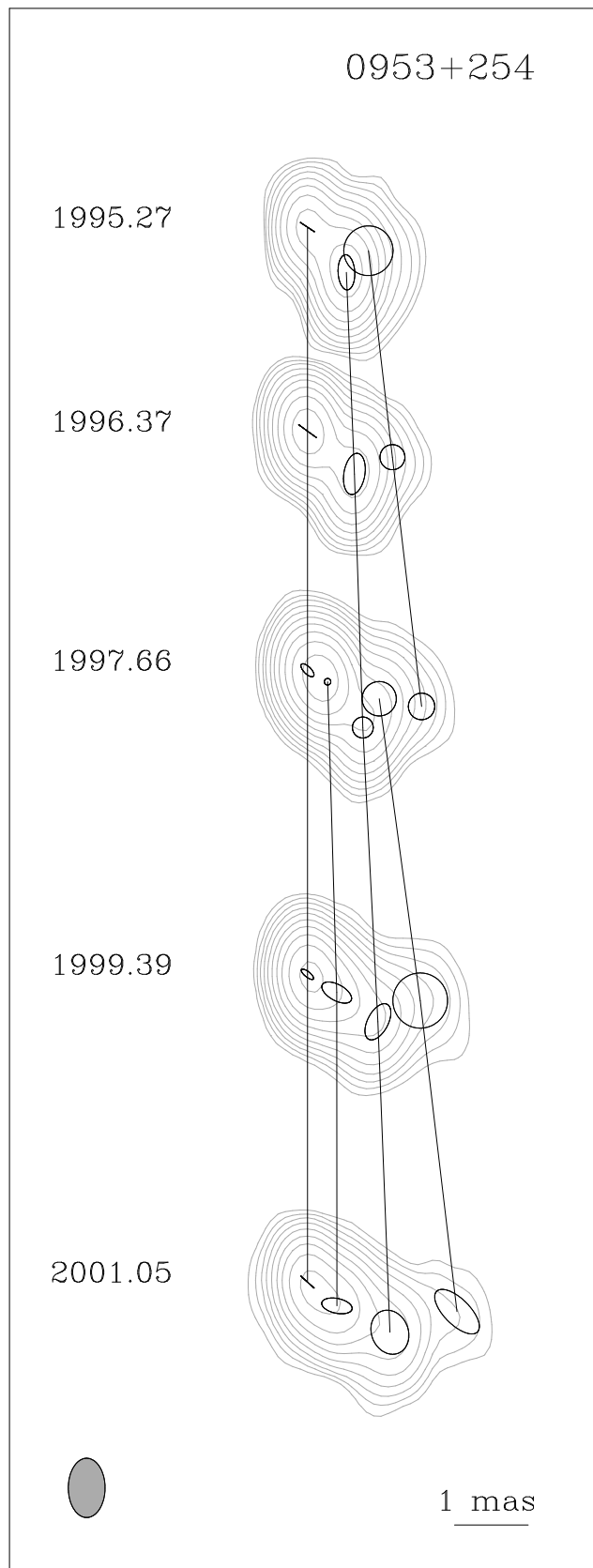
Figure D.3: Images showing the varying source structure of 0953+254. The positions of the various model components are indicated by open ellipses.
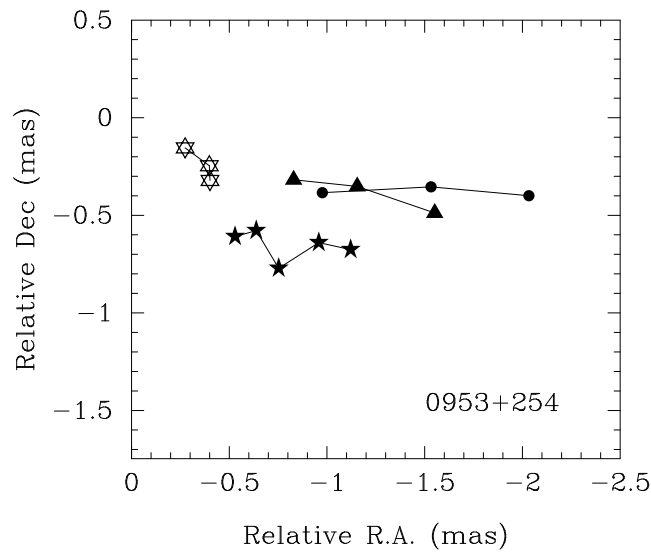
Figure D.4: Positions of the various model components in 0953+254 at the different epochs in the plane of the sky.

of 1 mas from the core. The measured velocities correspond to 12–30 c while Piner and Kingham (1998) find velocities of 2.4–8 c.

2131−021 This source can be approximated well with a two-component model at all epochs. A significantly better fit, however, is obtained by adding an additional jet component to the first epoch in July 1995 and to the last epoch in March 2001. While the simpler model used in the image-plane fitting resulted to a poor kinematical model with one formally inward moving jet component, the latter model implies a moving and expanding component (C) traveling with ∼0.15 mas yr^{-1} to the west. In addition to this, an extended component is implied in the first epoch that has vanished in the later epochs (B) and a new, bright component (D) that is only visible in the last epoch.

SUB-MILLIARCSECOND IMAGING OF QUASARS AND ACTIVE GALACTIC NUCLEI. III. KINEMATICS OF PARSEC-SCALE RADIO JETS

K. I. KELLERMANN, M. L. LISTER,[1,2] AND D. C. HOMAN[1,3]

National Radio Astronomy Observatory, 520 Edgemont Road, Charlottesville, VA 22903-2475;
kkellerm@nrao.edu, mlister@physics.purdue.edu, homand@denison.edu

R. C. VERMEULEN

Netherlands Foundation Research in Astronomy (ASTRON), Postbus 2, NL-7990 AA Dwingeloo, Netherlands; rvermeulen@astron.nl

M. H. COHEN

Department of Astronomy, MS 105-24, California Institute of Technology, Pasadena, CA 91125; mhc@astro.caltech.edu

E. ROS AND M. KADLER

Max-Planck-Institut für Radioastronomie, Auf dem Hügel 69, D-53121 Bonn, Germany; eros@mpifr-bonn.mpg.de, mkadler@mpifr-bonn.mpg.de

J. A. ZENSUS

Max-Planck-Institut für Radioastronomie, Auf dem Hügel 69, D-53121 Bonn, Germany; and National Radio Astronomy Observatory, 520 Edgemont Road, Charlottesville, VA 22903-2475; azensus@mpifr-bonn.mpg.de

AND

Y. Y. KOVALEV[1]

National Radio Astronomy Observatory, P.O. Box 2, Green Bank, WV 24944; and Astro Space Center of P. N. Lebedev Physical Institute, Profsoyuznaya 84/32, 117997 Moscow, Russia; ykovalev@nrao.edu

ABSTRACT

We report the results of a 15 GHz (2 cm) multiepoch Very Long Baseline Array (VLBA) program, begun in 1994 to study the outflow in radio jets ejected from quasars and active galaxies. The observed flow of 208 distinct features measured in 110 quasars, active galaxies, and BL Lac objects shows highly collimated relativistic motion with apparent transverse velocities typically between zero and about $15c$, with a tail extending up to about $34c$. Within individual jets, different features appear to move with a similar characteristic velocity that can represent an underlying continuous jet flow, but we also see some stationary and even apparently inward-moving features that coexist with the main features. Comparison of our observations with published data at other wavelengths suggests that there is a systematic decrease in apparent velocity with increasing wavelength, probably because the observations at different wavelengths sample different parts of the jet structure.

The observed distribution of linear velocities is not consistent with any simple ballistic model. Either there is a rather broad range of Lorentz factors, a significant difference between the velocity of the bulk relativistic flow and the pattern speed of underlying shocks, or a combination of these options. Assuming a ballistic flow, comparison of observed apparent velocities and Doppler factors computed from the timescale of flux density variations is consistent with a steep power-law distribution of intrinsic Lorentz factors, an isotropic distribution of orientations of the parent population, and intrinsic brightness temperatures about an order of magnitude below the canonical inverse Compton limit. It appears that the parent population of radio jets is not dominated by highly relativistic flows, and contrary to the assumption of simple unified models, not all sources have intrinsic speeds close to c.

Usually, the observed jet flow is in the general direction of an established jet. However, many jets show significant bends and twists, where the observed motions are nonradial but are aligned with the local jet direction, suggesting that the jet flow occurs along preexisting bent channels. In a few cases we have observed a clear change in the direction of a feature as it flows along the jet. Radio jets that are also strong gamma-ray sources detected by EGRET appear to have significantly faster speeds than the non-EGRET sources, consistent with the idea that gamma-ray sources have larger Doppler factors than non–gamma-ray sources. Sources at high redshift have systematically lower angular speeds than low-redshift jets, consistent with standard cosmologies.

Subject headings: galaxies: active — galaxies: jets — quasars: general — radio continuum: galaxies

On-line material: machine-readable tables

1. INTRODUCTION

The discovery in the mid-1960s of rapid variability in extragalactic radio sources (Sholomitskii 1965; Dent 1965; Pauliny-Toth & Kellermann 1966) appeared difficult to explain in terms of conventional synchrotron radiation theory. These early observations showed changes by as much as 25%

---

[1] Karl Jansky Fellow.
[2] Current address: Department of Physics, Purdue University, 525 Northwestern Avenue, West Lafayette, IN 47907.
[3] Current address: Department of Physics and Astronomy, Denison University, Granville, OH 43023.

over a few weeks, as well as significant day-to-day variations (Pauliny-Toth & Kellermann 1966). It was quickly realized (e.g., Hoyle et al. 1966) that the observed rapid variability implied such small linear dimensions that the relativistic electron population would be rapidly extinguished by inverse Compton scattering. Later, Kellermann & Pauliny-Toth (1969) put these arguments on a quantitative observational basis, showing that as a result of inverse Compton cooling, the maximum sustainable brightness temperature for an incoherent source of electron synchrotron radiation is less than 10^{12} K.

However, Woltjer (1966) and Rees (1966, 1967) pointed out that if there is relativistic bulk motion of the emitting material, since the radiation is then beamed along the direction of motion, the apparent luminosity in that direction is enhanced, while at the same time the cross section for inverse Compton scattering is reduced. Additionally, since the radiating source nearly catches up with its radiation, for a favorably positioned observer, the apparent transverse motion can exceed the speed of light. Early VLBI observations (Whitney et al. 1971; Cohen et al. 1971) showed evidence of the predicted high-velocity outflow; however, the arguments were indirect, and one had to have faith in the interpretation of the very limited radio interferometric data, which did not fully sample the source structure (e.g., Dent 1972). Subsequent higher quality VLBI observations confirmed the existence of superluminal motion in the well-collimated radio jets, found in the nuclei of many quasars and in nearby active galaxies (Cohen et al. 1977).

VLBI observations provide a direct method to investigate aspects of the formation, acceleration, and propagation of extragalactic radio jets. Early studies discussing apparent jet speeds were statistically unreliable because they were largely based on the analysis of published observations of only a few tens of sources made at different times, often at only two or three epochs, by different groups, using different antenna array configurations and different observing/data reduction strategies. The dynamic range of the images was often inadequate to identify individual features, especially for the more complex sources, and spacings in time between successive observations were frequently too long to uniquely identify and track moving jet features from epoch to epoch. Moreover, the source selection criteria for many previously published studies of superluminal motion were not well defined. A systematic study by Vermeulen (1995) of 81 sources from the flux density–limited 6 cm Caltech–Jodrell Bank Survey indicated smaller typical speeds than in earlier reports. This suggested that earlier studies preferentially tended to observe and/or report only sources in which rapid motion was detected or suspected.

In 1994 we began a systematic 15 GHz Very Long Baseline Array (VLBA) survey of relativistic outflows in a sample of over 100 quasar and active galaxy radio jets. Our motivation was to study the distributions of velocities, bending, pattern motions, accelerations, and other complexities of the jet kinematics that may exist, as well as changes in the strength and morphology of features as they propagate along the jet. These observations have provided the homogeneity, resolution, and dynamic range to reliably distinguish and identify individual components between different epochs. The central VLBA antennas provide short interferometric spacings that have allowed us to (1) track features moving for some distance down the jet where they become more diffuse and (2) observe the continuous jet rather than just the bright features that are often referred to as "components" or "blobs."

We chose 15 GHz as a compromise between achieving the best angular resolution and the better sensitivity and immunity from weather conditions found at lower frequencies. At this observing frequency the resolution of the VLBA is approximately 0.5 mas in right ascension and between 0.5 and 1 mas in declination. We therefore have sufficient angular resolution in many cases to resolve the two-dimensional jet transverse to its flow, which allows for tests of some theoretical models. In addition, individual features can often be recognized at significantly smaller separations from the origin. On the other hand, our observations are less sensitive to structure and motions of the more diffuse features located far out along the jet or within 0.5 mas of the core.

Our 15 GHz data represent a significant improvement over previous studies of superluminal motion in active galactic nuclei (AGNs). First, our sample of sources is large, and the sample membership was based on criteria other than observed superluminal motion. Second, the speeds are better determined because (1) our data are well sampled and span a longer time period and (2) our higher image resolution results in less blending of features.

In Kellermann et al. (1998, hereafter Paper I) we described the parsec-scale structure of 132 of the strongest known radio jets based on a single epoch of observation. In Zensus et al. (2002, hereafter Paper II) we discussed the structure of an additional 39 sources. Contour maps of all of our multiepoch observations are available on our Web site[4] along with kinematic and other data on each source. In this paper we discuss our multiepoch observations made through 2001 March 15 and the kinematics derived from these observations.

Some preliminary results of our program have already been published (Kellermann et al. 1999, 2000, 2003; Kellermann 2002; Ros et al. 2002; Cohen et al. 2003; Kovalev 2003; Zensus et al. 2003). We have also discussed the kinematics of several individual sources, including PKS 1345+125 (Lister et al. 2003), NGC 1052 (Vermeulen et al. 2003b), and 3C 279 (Homan et al. 2003).

In § 2 we describe our sample and source selection criteria, and in § 3 we discuss the details of our observational program. In § 4.1 we summarize the predictions of relativistic beaming models, while in § 4.2 we present the observed jet kinematics. In §§ 4.3 and 4.4 we discuss the implications of our observations for the nature of the relativistic flow. In § 4.5 we discuss the angular velocity–redshift relation, and in § 5 we summarize our results and describe our ongoing observing program.

Throughout this paper we use the following cosmological parameters: $H_0 = 70$ km s^{-1} Mpc^{-1}, $\Omega_m = 0.3$, and $\Omega_\Lambda = 0.7$.

2. SAMPLE DEFINITION

2.1. *The Full Sample*

Our original source sample (see Paper I) was based on the Kühr 1 Jy catalog (Kühr et al. 1981) as supplemented by Stickel et al. (1994). Our goal was to include all known sources in the Stickel et al. (1994) catalog that have a flat spectral index ($\alpha > -0.5$ for $S_\nu \sim \nu^\alpha$) anywhere above 500 MHz and a total flux density at 15 GHz, observed at least at one epoch, greater than 1.5 Jy for sources north of the celestial equator or greater than 2 Jy for sources between declinations $-20°$ and the equator. Since the Stickel et al. (1994) catalog is complete only at 5 GHz, we used other measurements at 15 GHz or extrapolations from lower frequencies to augment the Kühr sample.

_____
[4] Available at http://www.nrao.edu/2cmsurvey.

While we attempted to be complete for flat-spectrum, core-dominated sources that met our selection criteria, we also included a number of other sources of special interest as follows:

1. Six compact steep-spectrum (CSS) sources as indicated in Table 1. These sources generally have steep radio spectra and angular sizes smaller than $\sim 1''$ on the sky.

2. Four lobe-dominated sources with core components that would satisfy our criteria if they did not also have strong extended steep-spectrum structure. Two other sources, NGC 1052 (0238$-$084) and 3C 120 (0430+052), also have prominent double-lobe structure, but since they are core dominated on arcsecond scales at 15 GHz, they met our spectral index selection criterion.

3. Ten gigahertz-peaked spectrum (GPS) sources, some of which have two-sided jet structure (Lister et al. 2002; M. L. Lister et al. 2004, in preparation). However, many of the GPS sources we observed turned out to be merely flat-spectrum sources whose spectrum was temporarily dominated by a bright, synchrotron self-absorbed component in the jet. Our "peaked" classification in Table 1 is given only to sources that to our knowledge have always met the GPS spectral criteria given by de Vries et al. (1997). For a few sources, our classification differs from that previously published (e.g., O'Dea 1998); however, we believe that our classification is more robust (Kovalev 2004; Y. Y. Kovalev et al. 2004, in preparation).

Table 1 summarizes the properties of each source discussed in this paper. All of these sources were introduced in Papers I and II; however, 37 sources included in Papers I and II are not discussed now because they were observed only once or twice. These have subsequently been observed and will be discussed in a separate paper (E. Ros et al. 2004, in preparation). One source listed in Paper I is gravitationally lensed (0218+357), so we have chosen not to include it in our statistical discussion. Eight other sources had no detectable jet above our sensitivity limit. They are labeled as "naked cores" in Table 1, and we report no motions for these sources. Three sources, 0316+162, 1328+254, and 1328+307 reported in Papers I or II, are not discussed here as they have complex structure that we could not adequately image.

Columns (1) and (2) of Table 1 give the IAU source designation and, where appropriate, a commonly used alias. Column (3) indicates whether or not the source is a member of the representative flux density–limited sample that we describe in § 2.2. The optical classification and redshift as given mainly by Véron-Cetty & Véron (2001) are given in columns (4) and (5), respectively. In column (6) we give a radio spectral classification for each source based on RATAN-600 telescope observations of broadband instantaneous spectra from 1 to 22 GHz as described by Kovalev et al. (1999). These spectra are available on our web site. For a few sources not observed at the RATAN-600 telescope, we used published (nonsimultaneous) radio flux densities taken from the literature. We consider a radio spectrum to be "flat" if any portion of its spectrum in the range 0.6–22 GHz has a spectral index flatter than -0.5 and "steep" if the radio spectral index is steeper than -0.5 over this entire region. Column (7) shows the parsec-scale radio morphology taken from Papers I and II, column (8) shows the largest total flux density seen on any of our VLBA images, and column (9) gives an indication of whether or not the radio source is associated with a gamma-ray detection by EGRET.

2.2. The Representative Flux Density–limited Subsample

The full sample of sources described in the previous section is useful for investigating jet kinematics in a cross section of known AGN classes. However, in order to compare with the theoretical predictions of relativistic beaming models, a well-defined sample selected on the basis of beamed (not total) flux density is needed. Past surveys (e.g., Taylor et al. 1996; Lister 2001) have attempted to accomplish this by means of a spectral flatness criterion. However, we found that this method eliminates some lobe-dominated active galaxies such as those described in § 2.1. We also found that the extrapolated 15 GHz flux density based on nonsimultaneous lower frequency measurements was often grossly in error because of spectral curvature or variability.

We have therefore assembled a flux density–limited subsample from the full 15 GHz VLBA survey by using our measured VLBA flux densities as the main selection criterion. All sources that had a total CLEAN VLBA flux density exceeding 1.5 Jy (2 Jy for southern sources) *at any epoch since 1994* are included in this subsample. We excluded any sources that were observed on at least four occasions and never exceeded this limit. For survey sources with fewer than four VLBA epochs, we estimated the VLBA flux density at various epochs during this period using the source compactness and data from the flux density monitoring programs at the RATAN-600 radio telescope (Kovalev et al. 1999) or the University of Michigan Radio Astronomy Observatory[5] (Aller et al. 1992, 2003).

It is important to note that this subsample, although flux density–limited, is not complete; that is, there are additional compact sources that fulfill our selection criteria. This is partly due to the lack of a complete all-sky survey at 15 GHz and also to the variable nature of AGNs. We have therefore identified a list of candidate sources from other recent high-frequency radio surveys, made since our original list was compiled in 1994. These include the *WMAP* survey (Bennett et al. 2003), the VLBA calibrator survey (Beasley et al. 2002), RATAN-600 observations (Kovalev et al. 1999), and the high-frequency peaker survey (Dallacasa et al. 2000). We have made new VLBA observations of these sources in order to assemble a complete flux density–limited, core-selected sample. There are 133 sources in this complete flux density–limited sample, but so far we have multiepoch observations and derived speeds for only 71 of these sources, which we define as the representative subsample. For the purposes of the statistical analysis presented here, we consider our present subsample to be *representative* of a complete sample, since the general properties of the missing sources should not be substantially different from the whole. We have compared the 15 GHz luminosity distributions of our representative subsample and the missing sources from the full sample using a Kolmogorov-Smirnov (K-S) test and find no significant difference between the two samples.

Although our subsample selection method is somewhat complex, it is based on the directly measured compact flux density and does not use an often unreliable spectral index criterion. In addition, since the survey membership is not determined from a single "snapshot" epoch, we are not excluding potentially interesting or highly variable sources simply because they happened to be in a low state at the time of the original investigation. This increases the size of the

---

[5] See http://www.astro.lsa.umich.edu/obs/radiotel/umrao.html.

TABLE 1
GENERAL SOURCE PROPERTIES

IAU Name (1)	Alias (2)	Subsample Member (3)	Optical Class (4)	Redshift (5)	Radio Spectrum (6)	Radio Morphology (7)	S_{VLBI} (Jy) (8)	EGRET ID (9)
0003−066	NRAO 005	Y	B	0.347	Flat	CJ	2.84	N
0007+106	III Zw 2, Mrk 1501	Y	G	0.0893	Flat	N	1.29	N
0016+731		Y	Q	1.781	Flat	CJ	0.98	N
0026+346		N	G^a	0.517	Flat	CJ	0.65	N
0035+413		N	Q	1.353	Flat	CJ	0.53	N
0048−097		Y	B	. . .	Flat	N	1.65	N
0055+300	NGC 315	N	G	0.0165	Flat	CJ	0.82	N
0106+013		Y	Q	2.107	Flat	CJ	2.97	N
0112−017..............		N	Q	1.365	Flat	CJ	0.82	N
0119+041		N	Q	0.637	Flat	CJ	1.28	N
0133+476	DA 55	Y	Q	0.859	Flat	CJ	4.95	N
0149+218		N	Q	1.320	Flat	CJ	1.42	N
0153+744		N	Q	2.341	Flat	CJ	0.37	N
0202+149	4C +15.05	Y	Q^b	0.405	Flat	CJ	2.29	Y
0202+319		Y	Q	1.466	Flat	CJ	2.27	N
0212+735		Y	Q	2.367	Flat	CJ	2.69	N
0218+357^e..............		N	B^a	0.96	Flat	CJ	0.70	N
0234+285	CTD 20	Y	Q	1.213	Flat	CJ	4.04	Y
0235+164		Y	B^d	0.940	Flat	N	1.62	Y
0238−084	NGC 1052	Y	G	0.00490	Flat	2S	2.48	N
0316+162^e..............	CTA 21	N	G	. . .	Peaked	CJ	0.34	N
0316+413^f..............	3C 84	Y	G	0.01756	Flat	CJ	10.59	N
0333+321	NRAO 140	Y	Q	1.263	Flat	CJ	2.24	N
0336−019	CTA 26	Y	Q	0.852	Flat	CJ	3.44	Y
0355+508	NRAO 150	N	U	. . .	Flat	CJ	7.11	N
0415+379	3C 111	Y	G	0.0485	Steep	CJ, LD	5.98	N
0420−014		Y	Q	0.915	Flat	CJ	10.60	Y
0430+052	3C 120	Y	G	0.033	Flat	CJ	4.41	N
0440−003	NRAO 190	N	Q	0.844	Flat	CJ	1.20	Y
0454+844		N	B	. . .	Flat	CJ	0.34	N
0458−020		Y	Q	2.286	Flat	CJ	2.33	Y
0528+134		Y	Q	2.070	Flat	CJ	7.95	Y
0552+398	DA 193	Y	Q	2.363	Peaked	N	5.02	N
0602+673		N	Q	1.970	Flat	N	0.97	N
0605−085		Y	Q	0.872	Flat	CJ	2.80	N
0607−157		Y	Q	0.324	Flat	CJ	7.26	N
0615+820		N	Q	0.710	Flat	N	0.48	N
0642+449	OH 471	Y	Q	3.408	Peaked	CJ	4.31	N
0707+476		N	Q	1.292	Flat	CJ	0.63	N
0710+439		N	G	0.518	Peaked	2S	0.61	N
0716+714		Y	B	. . .	Flat	CJ	1.25	Y
0727−115..............		Y	Q^a	1.591	Flat	CJ	5.30	N
0735+178		Y	B	. . .	Flat	CJ	1.64	Y
0736+017		Y	Q	0.191	Flat	CJ	2.58	N
0738+313	OI 363	Y	Q	0.630	Flat	CJ	2.87	N
0742+103		Y	G^a	. . .	Peaked	CJ	1.50	N
0745+241		N	Q^b	0.409	Flat	CJ	0.95	N
0748+126		Y	Q	0.889	Flat	CJ	3.25	N
0754+100		Y	B	0.266	Flat	CJ	1.83	N
0804+499		Y	Q	1.432	Flat	CJ	1.14	N
0808+019		Y	B	. . .	Flat	CJ	1.34	N
0814+425		Y	B	0.245	Flat	CJ	1.28	N
0823+033		Y	B	0.506	Flat	CJ	1.40	N
0829+046		Y	B	0.180	Flat	CJ	1.35	Y
0850+581		N	Q	1.322	Flat	CJ	0.61	N
0851+202	OJ 287	Y	B	0.306	Flat	CJ	4.12	Y
0859−140		N	Q	1.339	Steep	CJ, CSS	1.58	N
0906+015	4C +01.24	Y	Q	1.018	Flat	CJ	2.73	N
0917+449		N	Q	2.180	Flat	CJ	1.43	P
0923+392	4C +39.25	Y	Q	0.698	Flat	CJ	12.68	N
0945+408		Y	Q	1.252	Flat	CJ	1.59	N
0953+254		N	Q	0.712	Flat	CJ	1.31	N
1012+232	4C +23.24	N	Q	0.565	Flat	CJ	1.16	N

542

280

TABLE 1—*Continued*

IAU Name (1)	Alias (2)	Subsample Member (3)	Optical Class (4)	Redshift (5)	Radio Spectrum (6)	Radio Morphology (7)	S_{VLBI} (Jy) (8)	EGRET ID (9)
1015+359		N	Q	1.226	Flat	CJ	0.82	N
1049+215	4C +21.28	N	Q	1.300	Flat	CJ	1.45	N
1055+018	4C +01.28	Y	Q	0.888	Flat	CJ	5.30	N
1055+201	4C +20.24	N	Q	1.110	Flat	CJ	0.38	N
1101+384	Mrk 421	N	B	0.031	Flat	CJ	0.53	Y
1127−145		Y	Q	1.187	Flat	CJ	3.39	N
1128+385		N	Q	1.733	Flat	CJ	1.13	N
1155+251		N	G$^{\text{a}}$	0.202	Flat	CJ	0.24	N
1156+295	4C +29.45	Y	Q	0.729	Flat	CJ	2.36	P
1219+285	W Comae	N	B	0.102	Flat	CJ	0.60	P
1226+023	3C 273	Y	Q	0.158	Flat	CJ	41.40	Y
1228+126	M87	Y	G	0.0044	Steep	CJ, LD	2.97	N
1253−055	3C 279	Y	Q	0.538	Flat	CJ	24.89	Y
1302−102		N	Q	0.286	Flat	CJ	0.71	N
1308+326		Y	Q	0.997	Flat	CJ	3.98	N
1323+321	4C +32.44	N	G$^{\text{a}}$	0.370	Peaked	2S	0.65	N
1328+254$^{\text{e}}$	3C 287	N	Q	1.055	Steep	CJ, CSS	0.09	N
1328+307$^{\text{e}}$	3C 286	N	Q	0.846	Steep	CJ, CSS	1.23	N
1334−127		Y	Q	0.539	Flat	CJ	8.87	Y
1345+125	4C +12.50	N	G	0.121	Peaked	2S	0.99	N
1404+286	OQ 208, Mrk 668	N	G	0.077	Peaked	2S	1.20	N
1413+135		Y	B	0.247	Flat	2S	1.72	N
1424+366		N	Q	1.091	Flat	N	0.61	P
1508−055		N	Q	1.191	Steep	CJ, CSS	0.73	N
1510−089		Y	Q	0.360	Flat	CJ	2.93	Y
1532+016		N	Q	1.420	Flat	CJ	0.76	N
1546+027		Y	Q	0.412	Flat	CJ	2.83	N
1548+056	4C +05.64	Y	Q	1.422	Flat	CJ	2.92	N
1606+106	4C +10.45	Y	Q	1.226	Flat	CJ	1.93	Y
1611+343	DA 406	Y	Q	1.401	Flat	CJ	4.52	Y
1633+382	4C +38.41	Y	Q	1.807	Flat	CJ	4.28	Y
1638+398	NRAO 512	Y	Q	1.666	Flat	N	1.61	N
1641+399	3C 345	Y	Q	0.594	Flat	CJ	8.73	N
1642+690	4C +69.21	N	Q$^{\text{b}}$	0.751	Flat	CJ	1.34	N
1652+398	Mrk 501	N	B	0.033	Flat	CJ	0.90	N
1655+077		Y	Q	0.621	Flat	CJ	2.09	N
1656+053		N	Q	0.879	Flat	CJ	0.69	N
1656+477		N	Q	1.622	Flat	CJ	1.14	N
1730−130	NRAO 530	Y	Q	0.902	Flat	CJ	10.97	Y
1749+096	4C +09.57	Y	B$^{\text{d}}$	0.320	Flat	CJ	5.58	N
1749+701		N	B	0.770	Flat	CJ	0.79	N
1758+388		Y	Q	2.092	Peaked	CJ	1.75	N
1800+440		Y	Q	0.663	Flat	CJ	1.50	N
1803+784		Y	B$^{\text{d}}$	0.680	Flat	CJ	2.54	N
1807+698	3C 371	N	B	0.050	Flat	CJ	1.38	N
1823+568	4C +56.27	Y	B$^{\text{d}}$	0.663	Flat	CJ	2.31	N
1828+487	3C 380	Y	Q	0.692	Steep	CJ, CSS	2.01	N
1845+797	3C 390.3	N	G	0.057	Steep	CJ, LD	0.47	N
1901+319	3C 395	N	Q	0.635	Steep	CJ, CSS	1.35	N
1921−293		N	Q	0.352	Flat	CJ	14.39	N
1928+738	4C +73.18	Y	Q	0.303	Flat	CJ	3.92	N
1957+405	Cygnus A	Y	G	0.056	Steep	2S, LD	1.68	N
2005+403		Y	Q	1.736	Flat	CJ	2.79	N
2007+777		N	B	0.342	Flat	CJ	1.16	N
2021+317	4C +31.56	Y	U	. . .	Flat	CJ	2.16	N
2021+614		Y	Q$^{\text{b}}$	0.227	Flat	CJ	2.73	N
2113+293		N	Q	1.514	Flat	CJ	0.94	N
2128−123		Y	Q	0.501	Flat	CJ	3.18	N
2131−021	4C −02.81	Y	B$^{\text{d}}$	1.285	Flat	CJ	2.21	N
2134+004		Y	Q	1.932	Peaked	CJ	6.34	N
2136+141	OX 161	Y	Q	2.427	Flat	CJ	2.75	N
2144+092		N	Q	1.113	Flat	CJ	0.81	N
2145+067	4C +06.69	Y	Q	0.999	Flat	CJ	10.37	N
2200+420	BL Lac	Y	B	0.069	Flat	CJ	5.67	Y

543

TABLE 1—*Continued*

IAU Name (1)	Alias (2)	Subsample Member (3)	Optical Class (4)	Redshift (5)	Radio Spectrum (6)	Radio Morphology (7)	S_{VLBI} (Jy) (8)	EGRET ID (9)
2201+315	4C +31.63	Y	Q	0.298	Flat	CJ	3.28	N
2209+236		Y	Q[a]	1.125	Flat	CJ	1.62	Y
2223−052	3C 446	Y	Q	1.404	Flat	CJ	6.57	N
2230+114	CTA 102	Y	Q	1.037	Flat	CJ	4.86	P
2234+282	CTD 135	N	Q	0.795	Flat	CJ	1.44	N
2243−123		Y	Q	0.630	Flat	CJ	2.56	N
2251+158	3C 454.3	Y	Q	0.859	Flat	CJ	12.08	Y
2345−167		Y	Q	0.576	Flat	CJ	2.54	N

Notes.—Col. (1): IAU name (B1950.0). Col. (2): Other name. Col. (3): Indicator for the flux density–limited subsample (see § 2). Col. (4): Optical classification according to the Véron-Cetty & Véron (2001) catalog, where Q = quasar, B = BL Lac object, G = active galaxy, and U = unidentified. Col. (5): Redshift from Véron-Cetty & Véron (2001) (the redshifts for 0026+346, 0727−115 and 1155+251 are from Paper II, that of 0202+149 is from Stickel et al. 1996, that of 0218+357 is from Lawrence 1996, that of 0754+100 is from Carangelo et al. 2003, and that of 2209+236 is from Sowards-Emmerd et al. 2003). Col. (6): Description of radio spectrum (see § 2). Col. (7): Radio morphology classification, where CJ = core jet, 2S = two-sided jet, N = naked core, LD = lobe dominated, and CSS = compact steep-spectrum object. Col. (8): Strongest 2 cm total cleaned VLBI flux density at any epoch, in Jy. Col. (9): EGRET gamma-ray source identification according to Mattox et al. (2001) and Sowards-Emmerd et al. (2003), where Y = highly probable identification, P = probable identification, N = no identification. Table 1 is also available in machine-readable form in the electronic edition of the *Astrophysical Journal*.

 [a] Source not in the Véron-Cetty & Véron (2001) catalog.
 [b] Source classified as a galaxy in the Véron-Cetty & Véron (2001) catalog.
 [c] The source 0218+357 is a gravitationally lensed AGN that we do not include in our statistical analysis.
 [d] Source classified as a quasar in the Véron-Cetty & Véron (2001) catalog.
 [e] Source has large or diffuse structures that are not adequately sampled by our observations.
 [f] The complex source 0316+413 (3C 84) satisfies our selection criteria but was observed as part of a separate monitoring program (Walker et al. 2000). It is included in our statistical analysis for completeness.

sample and the robustness of statistical tests on source properties. Of the 71 sources in our representative subsample, there are 53 quasars, 12 BL Lac objects, and six galaxies.

3. THE OBSERVATIONS AND ANALYSIS

Our observations were made during 29 separate observing sessions between 1994 and 2001. Typically, we obtained images of each source at three to seven epochs over this 7 yr period. Sources were usually observed at 6–18 month intervals. Those with known rapid motion were observed more frequently, while those with no observed jet or with only small observed motions were observed less often. Each observing session lasted between 8 and 24 hr. In general we tried to observe only at elevations above $10°$ to minimize the effect of tropospheric absorption, phase errors, and excessive ground radiation. Except for sources at low declinations, where the hour angle coverage is restricted, we observed each source once per hour for 6–8 minutes over a range of 8 hr in hour angle. In general, all 10 VLBA antennas were used for each observation, except when restricted by elevation. We rarely used less than eight antennas. Papers I and II, as well as our Web site, give logs of the observations.

Some additional observations were made in 1998 and 1999 by L. I. Gurvits et al. (2004, in preparation) as part of a different program to compare 15 GHz source structure measured with the VLBA to the 5 GHz structure measured using the Japanese *HALCA* space VLBI satellite (Hirabayashi et al. 1998). We have used these data to supplement our own as the observations were made using the same observing and data reduction procedures as used for the present program. These images are also available on our Web site.

Data reduction was done using a combination of AIPS and DIFMAP as described in Paper I. Each image was analyzed using the AIPS task JMFIT or MAXFIT to determine the relative positions of each definable feature at each epoch, and these positions were then used to calculate velocities relative to a presumed core component. We have assumed that the bright

unresolved feature typically found at the end of so-called core-jet sources is the stationary core. Generally, the choice of the core is clear because of its high brightness temperature and location. However, in a few cases, the location of the core is ambiguous, particularly in some sources where the component motions appear two-sided about a centrally located core. As an aid in identifying components from one epoch to the next, we examined each image for continuity in position, flux density, and structure. Usually, this procedure is more reliable than fitting independent models to the (u, v) data at each epoch, and with the possible exception of a few isolated cases, we believe that we have correctly cross-identified features as they evolve from epoch to epoch. However, for those sources where the jet is barely resolved from the VLBA core, we fit models to the data in the (u, v)-plane in order to exploit the full interferometric resolution of the VLBA.

In Figures 1 and 2 we show the angular motion in the jets of the 120 sources for which we have been able to determine motions with three or more epochs of observation. Of these 120 sources, there are 110 sources with good-quality data and measured redshifts for which we have been able to determine the linear velocity of at least one jet feature. These comprise 13 active galaxies, 79 quasars, and 18 BL Lac objects. In all, we have been able to determine reliable values for 208 separate features found in these 110 jets.

We have determined the radial angular speed, μ, of each definable jet feature using a linear least-squares fit to the measured component positions, relative to the presumed core. Our measured values of μ are given in Table 2. In Figures 1 and 2 the slope of the line corresponds to the best-fitting least-squares fit to the speed, which is shown in column (6) of Table 2. Figure 1 shows the plots for the one-sided jets and Figure 2 the two-sided ones. For well-defined components the formal uncertainty in the relative position is small, generally less than 0.02 mas. Frequently, however, the jets have a complex brightness distribution with regions of enhanced intensity that can brighten and fade with time. In some sources,
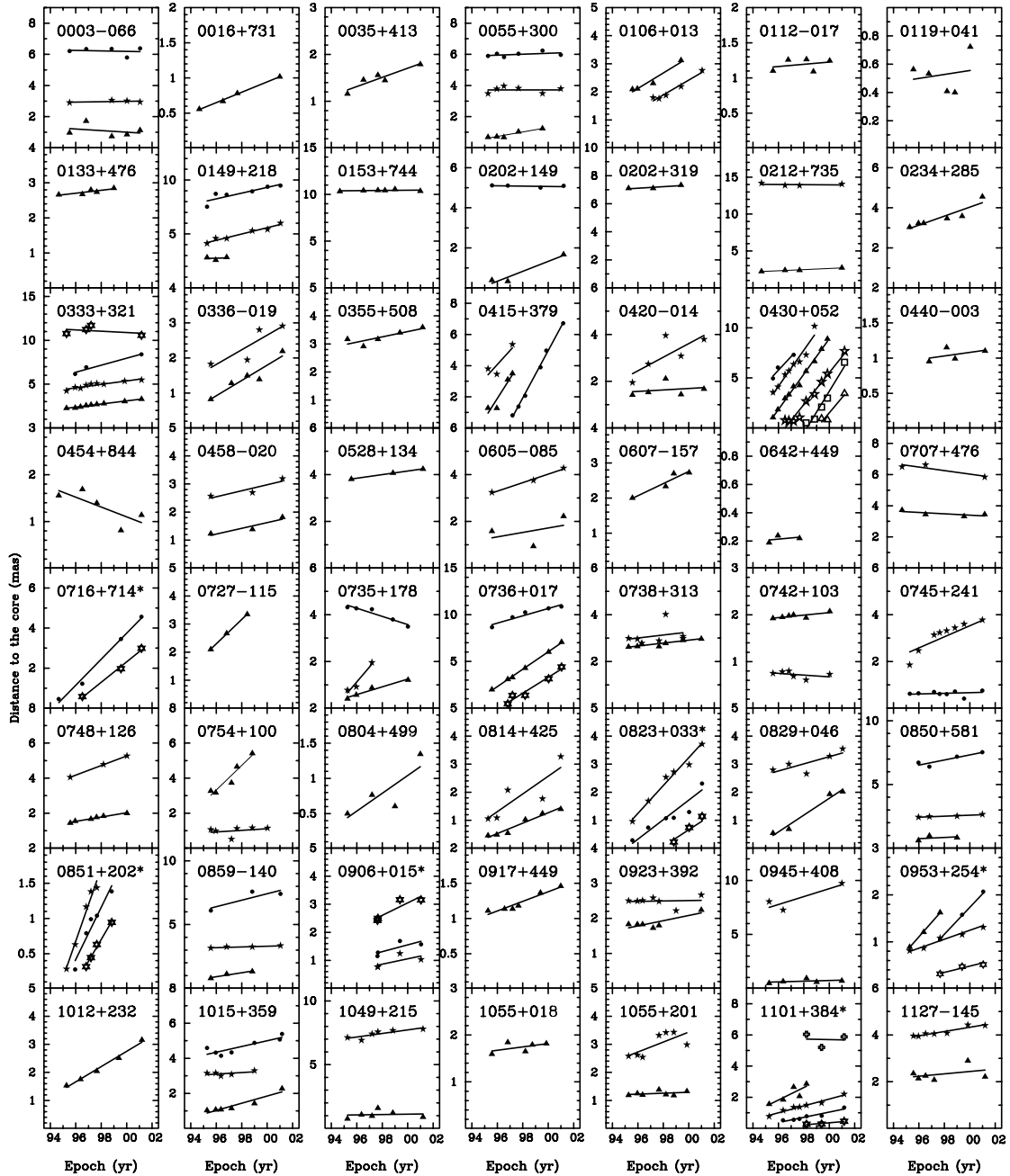
Fig. 1.—Plots showing the change in separation with time of features of one-sided jets for which we have measured a velocity from observations at three or more epochs. An asterisk denotes sources that were model fitted in the (u, v)-plane rather than in the image plane. Different symbols are used for each component as follows: B (*filled triangle*), C (*filled five-point star*), D (*filled circle*), E (*filled six-point star*), F (*cross*), G (*open five-point star*), H (*square*), I (*triangle*), J (*circle with cross*), K (*circle with dot*), L (*open circle*). The solid lines denote the best least-squares linear fit to the data, and the slope represents the proper motion, μ, tabulated in Table 2.
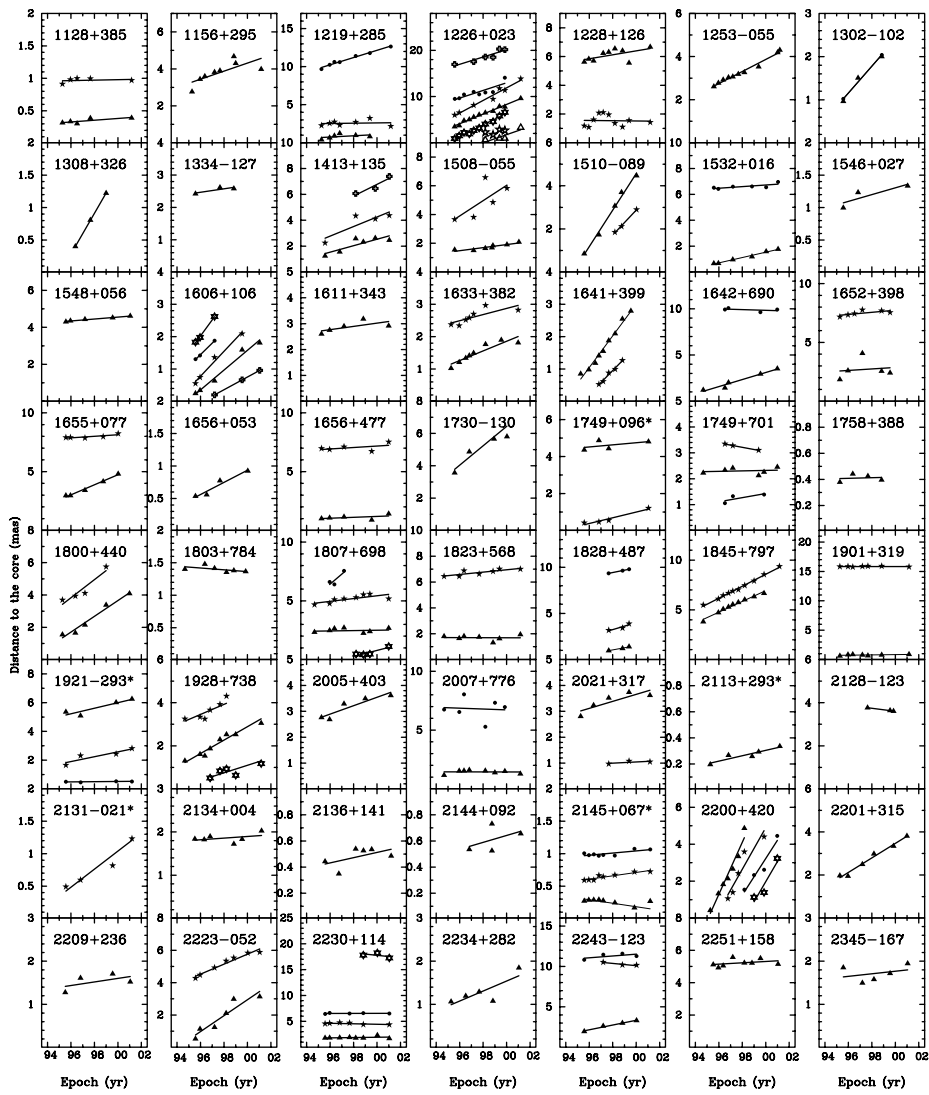
Fɪɢ. 1.—*Continued*
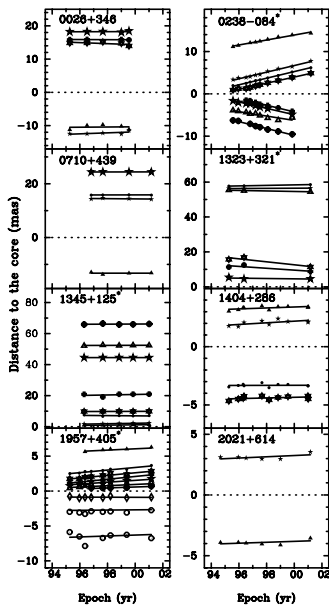
Fig. 2.—Same as Fig. 1, but for two-sided sources only. The points shown for 0238−084 (NGC 1052) are the brightest four components located on each side of the center of symmetry. No central component is visible for these sources, so the measured component positions are referred to a virtual center of symmetry as discussed by Vermeulen et al. (2003b).

instead of a well-collimated jet, there is a broad plume or more complex two-dimensional structure. Not only is the centroid of these components poorly defined, but changes in the brightness distribution with time complicate the definition of their motion. Some features appear to move, while others appear stationary. Some may break up into two or more separate features, and it is often unclear how these moving features are related to the underlying relativistic flow. In some sources, the moving features are not well resolved from each other, especially when they are close to the core. These issues all affect our ability to make a unique identification of components from epoch to epoch. In a few cases in which there are fast moving components, our observations may be too widely spaced in time to uniquely define their speed. Ambiguities exist, but we believe that most of our component identifications are robust and that component speeds are reliably determined.

We have based our error estimates of the angular velocity on the dispersion about the best-fit linear relation between the measured feature positions and time. The accuracy of each fit depends on the strength and size of the feature, the number of epochs, and the range of time covered by the observations. We note, however, that the measured dispersion of points about the best-fit line will overestimate the true scatter in component positions if there is acceleration such as observed for 3C 279 (Homan et al. 2003). Additionally, the measured radial speed may be an underestimate of the true speed if there is a significant nonradial component to the motion. However, we show in § 4.2.3 that while nonradial motions are common, the vector speeds do not differ significantly from the radial speeds, except in the case of 1548+056.

We use the following criteria to classify the quality of each measured velocity:

1. The component position is determined at four or more observations.

2. The component is a well-defined feature whose position can be unambiguously determined to a small fraction of the VLBA beamwidth.

3. The best-fitting angular speed is determined to high accuracy, defined by an uncertainty of ≤ 0.08 mas yr^{-1} or a significance[6] of ≥ 5 σ.

We then assign a "quality code" to each component motion as follows:

1. E (Excellent) denotes motions that satisfy all three of the above criteria.

2. G (Good) denotes motions that satisfy any two of the above criteria.

3. F (Fair) denotes motions that satisfy only one of the above criteria.

4. P (Poor) denotes motions that do not satisfy any of the above criteria or that the uncertainty in the fitted speed is greater than 0.15 mas yr^{-1} (except for the ≥ 5 σ cases described above).

These codes and the measured proper motions are tabulated in Table 2.

4. DISCUSSION

4.1. *Superluminal Motion and Relativistic Beaming*

We interpret the structural changes seen in the AGNs of our sample in terms of the twin relativistic jet model of Blandford & Rees (1974). In this framework, the bulk velocity of the relativistic flow, in units of the speed of light, c, is usually denoted as β_b, and γ_b is the corresponding Lorentz factor defined by $\gamma_b = (1 - \beta_b^2)^{-1/2}$. For a jet flow at an angle θ to the observer's line of sight, the Doppler factor, δ, is given by $\delta = \gamma_b^{-1}(1 - \beta_b \cos \theta)^{-1}$.

Three important observational consequences of relativistic motion in synchrotron sources are as follows:

1. A Doppler frequency shift of the radiation, where the ratio of observed frequency ν to the emitted frequency ν_e is given by

$$\nu/\nu_e = \delta. \qquad (1)$$

2. A change in the observed transverse velocity due to the apparent time compression. The apparent transverse velocity, in units of c, is given by

$$\beta_{\mathrm{app}} = \beta_p \sin \theta / (1 - \beta_p \cos \theta), \qquad (2)$$

where $\beta_p = v_p/c$ is the pattern velocity. We make this distinction between pattern and bulk velocities because jet features can move with significantly different velocity than the bulk jet flow (see, e.g., Lind & Blandford 1985; Zensus et al. 1995; Vermeulen & Cohen 1994). This could be the case, for example, if the pattern motion is due to the propagation of shocks. By studying 25 core-dominated quasars selected from the literature, Vermeulen & Cohen (1994) showed that the

_____

[6] The ≥ 5 σ requirement is necessary to accommodate nearby sources with very high angular speed features that may have large absolute uncertainties.

TABLE 2
Proper Motions

Object (1)	Component (2)	N (3)	$\langle R \rangle$ (mas) (4)	$\langle \vartheta \rangle$ (deg) (5)	μ_r (mas yr^{-1}) (6)	β_{app} (7)	t_0 (yr) (8)	Distinct Component (9)	Rating (10)
0003−066[a]	B[b]	5	1.1	−72	−0.05 ± 0.09	−1.1 ± 2.0	...	Y	G
	C	4	3.0	−77	0.01 ± 0.02	0.3 ± 0.4	...	Y	E
	D	5	6.2	−78	−0.02 ± 0.06	−0.3 ± 1.3	...	Y	E
0016+731[a]	B[b]	4	0.8	−50	0.074 ± 0.003	5.7 ± 0.2	1987.2 ± 0.5	N	G
0026+346	B	5	10.4	−124	0.03 ± 0.23	0.9 ± 7.0	...	N	P
	C[b]	5	12.2	−129	0.15 ± 0.12	4.7 ± 3.8	...	Y	G
	E	5	14.7	56	−0.16 ± 0.12	−4.8 ± 3.6	...	Y	G
	F	4	15.8	56	−0.02 ± 0.02	−0.6 ± 0.6	...	Y	E
	G	5	18.2	59	0.02 ± 0.05	0.5 ± 1.5	...	Y	E
0035+413	B[b]	5	1.5	104	0.10 ± 0.02	6.3 ± 1.5	1982.6 ± 3.5	Y	E
0055+300	B[b]	5	0.9	−54	0.14 ± 0.03	0.16 ± 0.03	1991.0 ± 1.1	N	G
	C	6	3.7	−51	0.00 ± 0.04	0.00 ± 0.05	...	Y	E
	D	6	6.0	−51	0.03 ± 0.03	0.03 ± 0.03	...	Y	E
0106+013[a]	B[b]	4	2.4	−119	0.28 ± 0.04	23.3 ± 3.6	1988.3 ± 1.4	Y	E
	C	5	2.1	−113	0.27 ± 0.03	22.3 ± 2.7	1990.9 ± 1.0	N	G
0112−017	B[b]	5	1.2	118	0.02 ± 0.03	1.0 ± 1.8	...	Y	E
0119+041	B[b]	5	0.4	124	0.01 ± 0.04	0.5 ± 1.6	...	N	G
0133+476[a]	B[b]	5	2.7	143	0.04 ± 0.01	2.0 ± 0.7	...	Y	E
0149+218	B	3	2.8	−13	0.03 ± 0.18	1.9 ± 11.7	...	Y	P
	C	6	5.0	−22	0.29 ± 0.03	18.4 ± 1.9	1980.8 ± 1.8	Y	E
	D[b]	6	8.8	−12	0.27 ± 0.07	16.8 ± 4.6	1964.9 ± 9.0	Y	E
0153+744	B[b]	6	10.4	152	0.01 ± 0.02	1.0 ± 1.5	...	Y	E
0202+149[a]	B	3	0.8	−67	0.25 ± 0.06	6.2 ± 1.6	1994.7 ± 1.0	N	F
	D[b]	4	5.1	−59	−0.01 ± 0.01	−0.2 ± 0.3	...	Y	E
0202+319[a]	B[b]	3	7.2	−2	0.06 ± 0.03	3.9 ± 2.0	...	Y	G
0212+735[a]	B[b]	4	2.4	104	0.08 ± 0.01	7.0 ± 1.0	1966.1 ± 4.5	Y	E
	C	4	14.0	92	−0.01 ± 0.04	−1.1 ± 3.8	...	Y	E
0234+285[a]	B[b]	6	3.5	−13	0.23 ± 0.05	13.5 ± 2.9	1982.0 ± 3.4	Y	E
0238−084[a,c]	E08	7	...	...	0.68 ± 0.10	0.23 ± 0.03	1967.7 ± 4.5	Y	E
	E17	8	...	...	0.75 ± 0.12	0.25 ± 0.04	1991.4 ± 0.9	Y	E
	E20[b]	7	...	...	0.79 ± 0.12	0.26 ± 0.04	1992.7 ± 0.7	Y	E
	E23	8	...	...	0.76 ± 0.12	0.25 ± 0.04	1994.1 ± 0.5	Y	E
	W07	7	...	...	0.82 ± 0.13	0.27 ± 0.04	1984.7 ± 2.0	Y	E
	W10	7	...	...	0.72 ± 0.11	0.24 ± 0.04	1991.2 ± 1.0	Y	E
	W14	7	...	...	0.75 ± 0.12	0.25 ± 0.04	1993.4 ± 0.7	Y	E
	W16	6	...	...	0.80 ± 0.12	0.27 ± 0.04	1995.4 ± 0.4	Y	E
0316+413[a,c]	B[b]	3	...	...	0.19 ± 0.05	0.2 ± 0.1	1960.0 ± 5.0	Y	E
0333+321[a]	B[b]	9	2.7	123	0.18 ± 0.01	11.0 ± 0.5	1982.7 ± 0.7	Y	E
	C	9	4.9	126	0.20 ± 0.03	12.0 ± 1.7	1972.5 ± 3.5	Y	E
	D	3	7.2	128	0.40 ± 0.07	24.5 ± 4.5	1980.0 ± 3.3	Y	G
	E	4	11.1	131	−0.08 ± 0.13	−4.7 ± 8.1	...	N	F
0336−019[a]	B[b]	5	1.4	67	0.22 ± 0.04	10.1 ± 2.0	1991.8 ± 1.4	Y	E
	C	4	1.6	46	0.21 ± 0.08	9.7 ± 3.9	...	Y	G
0355+508	B[b]	5	3.2	46	0.09 ± 0.03	...	...	Y	E
0415+379[a]	B	4	2.3	65	1.29 ± 0.32	4.2 ± 1.0	1994.5 ± 0.5	Y	P
	C	3	4.2	70	0.90 ± 0.53	2.9 ± 1.7	...	Y	P
	D[b]	6	3.3	66	1.52 ± 0.05	4.9 ± 0.2	1996.7 ± 0.1	Y	E
0420−014[a]	B[b]	5	1.6	−163	0.03 ± 0.07	1.5 ± 3.6	...	N	G
	C	5	3.1	170	0.29 ± 0.14	14.2 ± 6.6	...	Y	G
0430+052[a]	B[b]	10	4.7	−111	1.77 ± 0.06	3.9 ± 0.1	1995.0 ± 0.1	Y	E
	C	8	6.1	−106	1.80 ± 0.19	4.0 ± 0.4	1993.7 ± 0.4	Y	E
	D	3	6.1	−110	1.36 ± 0.35	3.0 ± 0.8	1991.8 ± 1.2	Y	P
	G	9	3.0	−112	1.59 ± 0.11	3.5 ± 0.2	1996.5 ± 0.2	Y	E
	I	3	1.7	−125	1.51 ± 0.44	3.4 ± 1.0	1999.0 ± 0.4	Y	P
	H	5	2.6	−118	2.08 ± 0.24	4.6 ± 0.5	1998.2 ± 0.2	Y	E
0440−003	B[b]	4	1.1	−120	0.03 ± 0.03	1.1 ± 1.4	...	Y	E
0454+844	B[b]	5	1.3	162	−0.10 ± 0.05	...	...	Y	E
0458−020[a]	B[b]	3	1.5	−43	0.10 ± 0.04	8.9 ± 3.3	...	Y	G
	C	3	2.8	−51	0.11 ± 0.05	9.4 ± 4.1	...	Y	G
0528+134[a]	B[b]	3	4.0	23	0.077 ± 0.002	6.4 ± 0.2	1946.0 ± 1.6	Y	G
0605−085[a]	B	3	1.6	123	0.10 ± 0.21	4.5 ± 9.8	...	N	P
	C[b]	3	3.8	110	0.18 ± 0.02	8.6 ± 0.8	1977.9 ± 2.0	Y	G
0607−157[a]	B[b]	4	2.4	88	0.17 ± 0.04	3.5 ± 0.8	1984.1 ± 3.3	Y	E

548

286

TABLE 2—*Continued*

Object (1)	Component (2)	N (3)	$\langle R \rangle$ (mas) (4)	$\langle \vartheta \rangle$ (deg) (5)	μ_r (mas yr^{-1}) (6)	β_{app} (7)	t_0 (yr) (8)	Distinct Component (9)	Rating (10)
0642+449[a]	B[b]	3	0.2	92	0.01 ± 0.02	0.9 ± 2.0	. . .	N	F
0707+476	B[b]	4	3.5	5	-0.04 ± 0.03	-2.8 ± 1.7	. . .	Y	E
	C	3	6.3	24	-0.11 ± 0.05	-7.1 ± 3.3	. . .	Y	G
0710+439	B[b]	4	13.3	3	0.01 ± 0.13	0.2 ± 3.9	. . .	Y	G
	C	4	14.4	3	-0.05 ± 0.07	-1.4 ± 2.0	. . .	N	G
	D	4	15.8	4	0.00 ± 0.02	0.0 ± 0.5	. . .	Y	E
	G	4	24.4	1	0.00 ± 0.01	0.0 ± 0.3	. . .	Y	E
0716+714[a]	D[b]	4	2.4	14	0.65 ± 0.04	. . .	1994.2 ± 0.3	N	G
	E	3	1.8	11	0.51 ± 0.04	. . .	1995.5 ± 0.3	N	F
0727−115[a]	B[b]	3	2.7	−52	0.44 ± 0.01	31.2 ± 0.6	1990.7 ± 0.1	Y	G
0735+178[a]	B[b]	4	0.7	72	0.17 ± 0.02	. . .	1992.5 ± 0.7	N	G
	C	3	1.2	59	0.64 ± 0.16	. . .	1994.2 ± 0.5	N	P
	D	5	4.0	64	-0.18 ± 0.03	. . .	. . .	Y	E
0736+017[a]	B	6	4.2	−70	0.93 ± 0.02	11.5 ± 0.2	1993.5 ± 0.1	Y	E
	D	5	10.0	−88	0.39 ± 0.06	4.8 ± 0.8	1972.7 ± 4.1	Y	E
	E[b]	5	2.1	−68	0.85 ± 0.10	10.5 ± 1.3	1996.1 ± 0.4	Y	E
0738+313[a]	B[b]	8	2.8	179	0.06 ± 0.01	2.3 ± 0.4	1953.8 ± 8.0	Y	E
	C	7	3.1	170	0.07 ± 0.10	2.4 ± 3.8	. . .	N	F
0742+103[a]	B[b]	6	2.0	−5	0.03 ± 0.01	. . .	. . .	N	G
	C	6	0.7	−38	-0.02 ± 0.02	. . .	. . .	N	G
0745+241	C[b]	8	3.1	−63	0.32 ± 0.05	7.9 ± 1.3	1988.2 ± 1.6	Y	E
	D	8	0.6	−64	0.003 ± 0.022	0.1 ± 0.6	. . .	N	G
0748+126[a]	B[b]	6	1.7	120	0.12 ± 0.01	5.9 ± 0.5	1983.5 ± 1.1	Y	E
	C	3	4.7	111	0.274 ± 0.004	13.1 ± 0.2	1980.8 ± 0.2	Y	G
0754+100[a]	B[b]	5	4.0	15	0.70 ± 0.12	11.9 ± 2.1	1991.3 ± 1.0	Y	E
	C	6	0.9	17	0.05 ± 0.07	0.8 ± 1.2	. . .	N	G
0804+499[a]	B[b]	4	0.8	134	0.13 ± 0.06	8.5 ± 4.2	. . .	N	G
0808+019[a]	B[b]	3	0.4	−175	0.11 ± 0.01	. . .	1993.1 ± 0.5	N	F
	C	3	4.8	−173	-0.20 ± 0.18	. . .	. . .	Y	P
0814+425[a]	B[b]	6	0.9	90	0.18 ± 0.02	2.9 ± 0.3	1993.2 ± 0.5	N	G
	C	5	1.7	129	0.32 ± 0.11	4.9 ± 1.7	. . .	N	F
0823+033[a]	C	6	2.4	14	0.48 ± 0.04	14.4 ± 1.1	1993.3 ± 0.4	N	G
	D[b]	6	1.1	32	0.31 ± 0.06	9.5 ± 1.8	1994.8 ± 0.8	N	G
	E	3	0.7	32	0.41 ± 0.01	12.3 ± 0.4	1998.2 ± 0.1	N	F
0829+046[a]	B	4	1.3	66	0.30 ± 0.04	3.5 ± 0.4	1994.0 ± 0.6	N	G
	C[b]	5	3.0	66	0.13 ± 0.06	1.5 ± 0.7	. . .	Y	E
0850+581	B	3	0.8	174	0.05 ± 0.11	3.0 ± 7.1	. . .	N	P
	C[b]	4	2.5	152	0.04 ± 0.01	2.5 ± 0.5	1935.6 ± 12.5	Y	E
	D	4	7.0	151	0.20 ± 0.07	12.7 ± 4.1	1963.5 ± 11.3	Y	E
0851+202[a]	C	5	1.0	−92	0.52 ± 0.04	9.9 ± 0.9	1994.7 ± 0.2	N	G
	D[b]	5	0.9	−102	0.37 ± 0.06	7.1 ± 1.1	1994.9 ± 0.4	N	G
	E	4	0.6	−116	0.31 ± 0.02	6.0 ± 0.4	1995.7 ± 0.1	N	G
0859−140	B	3	1.1	160	0.16 ± 0.04	10.1 ± 2.8	1990.3 ± 1.9	N	F
	C[b]	4	3.2	−155	0.03 ± 0.01	1.9 ± 0.6	1889.8 ± 32.2	Y	E
	D	3	7.0	158	0.26 ± 0.15	16.3 ± 9.4	. . .	Y	F
0906+015[a]	C[b]	4	0.9	38	0.10 ± 0.07	5.1 ± 3.9	. . .	N	G
	D	4	1.4	40	0.12 ± 0.07	6.4 ± 3.5	. . .	N	G
	E	4	2.8	45	0.22 ± 0.07	11.8 ± 3.9	1986.3 ± 4.3	N	G
0917+449	B[b]	6	1.2	178	0.07 ± 0.01	5.8 ± 0.9	1979.8 ± 2.6	Y	E
0923+392[a]	B[b]	6	1.9	−78	0.07 ± 0.03	2.9 ± 1.0	. . .	Y	E
	C	7	2.5	−79	0.01 ± 0.03	0.2 ± 1.2	. . .	N	G
0945+408[a]	B[b]	5	0.1	−83	0.03 ± 0.04	2.0 ± 2.4	. . .	N	G
	C	3	8.3	119	0.37 ± 0.20	22.5 ± 12.1	. . .	N	P
0953+254	B	3	1.2	−108	0.31 ± 0.01	12.4 ± 0.4	1992.4 ± 0.1	N	F
	C[b]	5	1.0	−129	0.09 ± 0.01	3.5 ± 0.4	1986.1 ± 1.3	N	G
	D	3	1.6	−104	0.301 ± 0.001	12.09 ± 0.04	1994.17 ± 0.02	N	F
	E	3	0.4	−124	0.06 ± 0.02	2.4 ± 0.7	1992.0 ± 2.2	N	F
1012+232	B[b]	5	2.2	110	0.27 ± 0.02	9.0 ± 0.6	1989.9 ± 0.5	Y	E
1015+359	B[b]	6	1.3	−172	0.20 ± 0.04	12.4 ± 2.2	1991.0 ± 1.2	N	G
	C	5	3.1	−178	0.04 ± 0.04	2.6 ± 2.2	. . .	Y	E
	D	7	4.7	−178	0.16 ± 0.04	9.9 ± 2.5	1969.4 ± 7.1	Y	E
1049+215	B[b]	6	1.1	106	0.01 ± 0.07	0.9 ± 4.4	. . .	N	G
	C	6	7.4	112	0.14 ± 0.04	8.8 ± 2.6	1944.7 ± 16.1	Y	E
1055+018[a]	B[b]	5	1.7	−49	0.04 ± 0.03	1.7 ± 1.6	. . .	Y	E

549

TABLE 2—*Continued*

Object (1)	Component (2)	N (3)	$\langle R \rangle$ (mas) (4)	$\langle \vartheta \rangle$ (deg) (5)	μ_r (mas yr^{-1}) (6)	β_{app} (7)	t_0 (yr) (8)	Distinct Component (9)	Rating (10)
1055+201	B[b]	7	1.2	−10	0.02 ± 0.02	0.9 ± 1.1	...	N	G
	C	7	3.0	−5	0.18 ± 0.08	10.0 ± 4.3	...	Y	E
1101+384	B	5	2.2	−40	0.40 ± 0.15	0.8 ± 0.3	...	N	F
	C	7	1.4	−39	0.22 ± 0.02	0.46 ± 0.04	1991.5 ± 0.5	N	G
	D[b]	6	0.8	−30	0.17 ± 0.03	0.4 ± 0.1	1993.8 ± 0.7	N	G
	E	3	0.3	0	0.07 ± 0.03	0.1 ± 0.1	...	N	F
	F	3	5.7	−44	−0.02 ± 0.30	0.0 ± 0.6	...	N	P
1127−145[a]	B	6	2.3	82	0.05 ± 0.06	3.0 ± 3.5	...	Y	E
	C[b]	7	4.1	83	0.09 ± 0.01	5.4 ± 0.8	1952.5 ± 6.9	Y	E
1128+385	B[b]	5	0.3	−168	0.01 ± 0.01	1.1 ± 0.5	...	N	G
	C	5	1.0	−155	0.004 ± 0.008	0.3 ± 0.6	...	N	G
1155+251	B	3	10.2	8	0.02 ± 0.17	0.2 ± 2.2	...	N	P
	C	3	10.2	20	−0.17 ± 0.14	−2.2 ± 1.9	...	N	P
	D	3	8.0	14	0.00 ± 0.33	0.0 ± 4.3	...	N	P
	E[b]	3	3.4	21	0.03 ± 0.03	0.3 ± 0.4	...	Y	G
	F	3	4.5	−83	−0.06 ± 0.20	−0.7 ± 2.5	...	N	P
	G	3	3.0	−51	0.01 ± 0.02	0.1 ± 0.3	...	N	F
	I	3	1.2	−24	−0.03 ± 0.04	−0.4 ± 0.6	...	N	F
1156+295[a]	B[b]	8	3.8	−2	0.22 ± 0.08	8.9 ± 3.4	...	Y	G
1219+285	B	6	0.8	101	0.08 ± 0.08	0.5 ± 0.6	...	N	F
	C	7	2.5	107	0.02 ± 0.08	0.1 ± 0.5	...	Y	E
	D[b]	7	11.0	107	0.48 ± 0.03	3.2 ± 0.2	1974.5 ± 1.4	Y	E
1226+023[a]	B[b]	11	6.1	−113	1.05 ± 0.04	10.8 ± 0.5	1992.1 ± 0.3	Y	E
	C	7	9.6	−120	1.36 ± 0.11	14.1 ± 1.1	1991.3 ± 0.6	Y	E
	D	8	10.8	−119	0.83 ± 0.20	8.6 ± 2.0	1984.3 ± 3.1	Y	P
	E	10	3.3	−116	1.27 ± 0.07	13.1 ± 0.8	1995.0 ± 0.2	Y	E
	F	6	18.7	−123	0.79 ± 0.15	8.2 ± 1.6	1974.6 ± 4.6	Y	E
	G	4	2.3	−122	0.41 ± 0.39	4.2 ± 4.0	...	Y	P
	I	4	1.4	−122	0.88 ± 0.32	9.1 ± 3.3	...	Y	P
1228+126[a]	B	9	6.0	−76	0.14 ± 0.07	0.04 ± 0.02	...	N	G
	C[b]	10	1.5	−78	−0.01 ± 0.08	0.00 ± 0.02	...	N	G
1253−055[a]	B[b]	10	3.3	−116	0.28 ± 0.01	8.9 ± 0.4	1986.2 ± 0.6	Y	E
1302−102	B[b]	3	1.5	30	0.31 ± 0.05	5.6 ± 0.9	1992.3 ± 0.8	N	F
1308+326[a]	B[b]	3	0.8	−80	0.313 ± 0.002	16.3 ± 0.1	1995.08 ± 0.01	Y	G
1323+321	C	3	56.4	−51	0.04 ± 0.03	0.9 ± 0.8	...	N	F
	D	3	58.0	−50	0.142 ± 0.001	3.25 ± 0.02	1588.5 ± 1.4	N	F
	E	3	14.6	−46	−0.86 ± 0.35	−19.7 ± 8.0	...	N	P
	F	3	10.8	−41	−0.54 ± 0.28	−12.3 ± 6.5	...	N	P
	G	3	4.8	−35	−0.10 ± 0.12	−2.2 ± 2.8	...	N	P
	I[b]	3	55.0	−50	−0.15 ± 0.03	−3.4 ± 0.7	...	N	F
1334−127[a]	B[b]	3	2.5	156	0.05 ± 0.03	1.7 ± 1.0	...	N	F
1345+125	B	5	1.1	168	0.09 ± 0.02	0.7 ± 0.2	1986.8 ± 3.2	Y	E
	C	5	2.0	164	0.15 ± 0.02	1.2 ± 0.1	1985.7 ± 1.5	Y	E
	D	5	7.1	171	−0.07 ± 0.09	−0.6 ± 0.7	...	Y	G
	E[b]	5	9.8	162	0.03 ± 0.01	0.2 ± 0.1	...	Y	E
	F	5	20.6	156	0.16 ± 0.23	1.3 ± 1.9	...	Y	P
	G	5	44.5	155	−0.01 ± 0.01	−0.06 ± 0.05	...	Y	E
	I	5	52.4	161	0.02 ± 0.05	0.1 ± 0.4	...	Y	E
	J	5	66.1	177	0.03 ± 0.08	0.2 ± 0.6	...	Y	E
1404+286	B[b]	10	3.3	53	0.04 ± 0.02	0.2 ± 0.1	...	Y	E
	C	9	2.0	62	0.06 ± 0.03	0.3 ± 0.2	...	Y	E
	D	10	3.3	−127	0.00 ± 0.02	0.0 ± 0.1	...	Y	E
	E	10	4.4	−111	0.03 ± 0.02	0.1 ± 0.1	...	Y	E
1413+135[a]	B[b]	6	2.1	−113	0.25 ± 0.08	3.9 ± 1.2	1989.8 ± 2.7	Y	E
	C	4	3.8	−111	0.37 ± 0.15	5.8 ± 2.4	...	Y	P
	F	3	6.6	−109	0.45 ± 0.15	7.1 ± 2.4	1984.9 ± 4.9	Y	F
1508−055	B[b]	7	1.7	85	0.10 ± 0.02	6.2 ± 1.2	1981.9 ± 3.2	Y	E
	C	5	4.9	83	0.53 ± 0.30	31.4 ± 18.1	...	Y	P
1510−089[a]	B[b]	5	2.8	−26	0.85 ± 0.05	18.9 ± 1.0	1994.6 ± 0.2	Y	E
	C	3	2.3	−32	0.57 ± 0.03	12.8 ± 0.7	1995.0 ± 0.2	N	F
1532+016	B[b]	6	1.1	130	0.21 ± 0.01	13.7 ± 0.9	1992.6 ± 0.4	Y	E
	D	6	6.6	143	0.06 ± 0.03	4.1 ± 1.9	...	N	G
1546+027[a]	B[b]	3	1.2	175	0.05 ± 0.03	1.3 ± 0.8	...	N	F
1548+056[a]	B[b]	5	4.4	10	0.052 ± 0.004	3.5 ± 0.3	1912.6 ± 7.0	Y	E

550

TABLE 2—*Continued*

Object (1)	Component (2)	N (3)	$\langle R \rangle$ (mas) (4)	$\langle \vartheta \rangle$ (deg) (5)	μ_r (mas yr^{-1}) (6)	β_{app} (7)	t_0 (yr) (8)	Distinct Component (9)	Rating (10)
1606+106[a]	B[b]	5	0.9	−58	0.30 ± 0.02	18.4 ± 1.4	1994.8 ± 0.3	N	G
	C	4	1.2	−53	0.38 ± 0.03	23.2 ± 2.1	1994.0 ± 0.3	N	G
	D	3	1.5	−52	0.36 ± 0.02	21.6 ± 1.3	1991.9 ± 0.2	N	F
	E	3	2.1	−40	0.50 ± 0.03	30.1 ± 1.6	1991.9 ± 0.2	N	F
	F	3	0.6	−61	0.196 ± 0.001	11.8 ± 0.1	1996.16 ± 0.00	N	F
1611+343[a]	B[b]	5	2.9	173	0.06 ± 0.04	4.2 ± 2.6	. . .	Y	E
1633+382[a]	B[b]	8	1.5	−86	0.15 ± 0.03	11.5 ± 2.0	1987.5 ± 1.8	Y	E
	C	7	2.6	−82	0.10 ± 0.03	7.3 ± 2.6	. . .	N	G
1641+399[a]	B[b]	9	1.7	−95	0.49 ± 0.03	17.0 ± 0.9	1993.9 ± 0.2	Y	E
	C	5	0.9	−101	0.37 ± 0.03	12.8 ± 1.0	1995.4 ± 0.2	Y	E
1642+690	B[b]	5	2.2	−162	0.38 ± 0.04	16.0 ± 1.8	1991.9 ± 0.7	Y	E
	D	4	9.9	−166	−0.04 ± 0.05	−1.6 ± 2.3	. . .	Y	E
1652+398	B	5	2.7	142	0.06 ± 0.26	0.1 ± 0.6	. . .	Y	P
	C[b]	6	7.5	109	0.09 ± 0.05	0.2 ± 0.1	. . .	Y	E
1655+077[a]	B	5	3.7	−38	0.43 ± 0.03	15.3 ± 1.0	1988.9 ± 0.6	Y	E
	C[b]	5	8.0	−44	0.07 ± 0.03	2.4 ± 0.9	. . .	Y	E
1656+053	B[b]	4	0.7	72	0.09 ± 0.02	4.4 ± 0.8	1990.0 ± 1.4	N	G
1656+477	B[b]	5	1.1	0	0.04 ± 0.04	2.8 ± 3.0	. . .	N	G
	C	5	7.0	−19	0.06 ± 0.06	4.5 ± 4.6	. . .	Y	E
1730−130[a]	B[b]	4	5.0	17	0.48 ± 0.12	23.3 ± 5.6	1987.5 ± 2.5	Y	G
1749+096[a]	B	4	4.6	29	0.06 ± 0.07	1.2 ± 1.3	. . .	Y	E
	C[b]	4	0.7	34	0.15 ± 0.03	3.1 ± 0.5	1993.5 ± 0.8	N	G
1749+701	B[b]	6	2.3	−66	0.01 ± 0.03	0.4 ± 1.1	. . .	Y	E
	C	3	3.2	−58	−0.084 ± 0.003	−3.6 ± 0.1	. . .	N	F
	D	3	1.3	−76	0.08 ± 0.06	3.4 ± 2.6	. . .	N	F
1758+388[a]	B[b]	4	0.4	−98	0.002 ± 0.013	0.2 ± 1.1	. . .	N	G
1800+440[a]	B[b]	5	2.6	−163	0.49 ± 0.05	18.5 ± 2.0	1992.5 ± 0.6	Y	E
	C	4	4.4	−155	0.56 ± 0.14	21.2 ± 5.3	1989.1 ± 2.0	Y	G
1803+784[a]	B[b]	6	1.4	−94	−0.01 ± 0.01	−0.5 ± 0.4	. . .	Y	E
1807+698	B[b]	7	2.5	−96	0.01 ± 0.04	0.0 ± 0.1	. . .	Y	E
	C	8	5.2	−94	0.12 ± 0.04	0.4 ± 0.1	. . .	Y	E
	D	3	6.8	−97	0.85 ± 0.47	2.9 ± 1.6	. . .	Y	P
	E	4	0.6	−97	0.26 ± 0.08	0.9 ± 0.3	1996.9 ± 0.8	N	F
1823+568[a]	B[b]	7	1.7	−158	−0.003 ± 0.040	−0.1 ± 1.5	. . .	Y	E
	C	7	6.7	−161	0.09 ± 0.03	3.4 ± 1.1	1923.0 ± 23.4	Y	E
1828+487[a]	B	3	1.2	−20	0.23 ± 0.03	9.2 ± 1.3	1993.5 ± 0.7	N	F
	C	3	3.5	−23	0.38 ± 0.15	14.8 ± 5.8	. . .	Y	F
	D[b]	3	9.6	−32	0.26 ± 0.01	10.1 ± 0.4	1961.5 ± 1.6	Y	G
1845+797	B	9	5.5	−41	0.54 ± 0.03	2.1 ± 0.1	1987.2 ± 0.6	Y	E
	C[b]	10	7.2	−36	0.60 ± 0.01	2.3 ± 0.1	1985.7 ± 0.3	Y	E
1901+319	B[b]	7	0.8	122	0.03 ± 0.02	0.9 ± 0.7	. . .	N	G
	C	7	15.8	120	0.00 ± 0.01	0.0 ± 0.5	. . .	Y	E
1921−293	B	4	5.7	24	0.19 ± 0.06	4.2 ± 1.3	1968.9 ± 8.9	Y	E
	C	4	2.3	−1	0.17 ± 0.06	3.7 ± 1.2	1984.7 ± 4.5	N	G
	D[b]	4	0.5	−29	0.01 ± 0.01	0.2 ± 0.2	. . .	N	G
1928+738[a]	B[b]	8	2.1	165	0.29 ± 0.03	5.6 ± 0.6	1990.3 ± 0.7	Y	E
	C	6	3.6	161	0.30 ± 0.08	5.8 ± 1.5	1984.7 ± 3.1	Y	E
	E	5	0.8	156	0.12 ± 0.06	2.3 ± 1.1	. . .	Y	E
1957+405[a]	B	5	6.0	−78	0.12 ± 0.02	0.5 ± 0.1	1950.6 ± 8.0	N	G
	D	8	3.0	−79	0.18 ± 0.02	0.7 ± 0.1	1981.4 ± 1.6	N	G
	E	8	2.2	−80	0.19 ± 0.03	0.7 ± 0.1	1986.0 ± 1.6	N	G
	F	6	1.7	−79	0.22 ± 0.03	0.8 ± 0.1	1990.3 ± 1.1	N	G
	G[b]	8	1.2	−79	0.16 ± 0.03	0.6 ± 0.1	1990.0 ± 1.6	N	G
	I	7	0.8	−79	0.10 ± 0.02	0.4 ± 0.1	1990.6 ± 1.6	N	G
	J	5	0.5	−123	0.05 ± 0.02	0.2 ± 0.1	1989.6 ± 3.1	N	G
	K	7	6.6	109	0.00 ± 0.14	0.0 ± 0.5	. . .	Y	G
	L	8	3.0	115	0.05 ± 0.03	0.2 ± 0.1	. . .	Y	E
2005+403[a]	B[b]	5	3.2	120	0.16 ± 0.04	12.3 ± 3.0	1978.2 ± 4.8	Y	E
2007+776	B[b]	8	1.4	−92	0.00 ± 0.03	0.0 ± 0.6	. . .	Y	E
	D	6	6.8	−91	−0.04 ± 0.23	−0.8 ± 4.9	. . .	Y	P
2021+317[a]	B[b]	5	3.4	166	0.14 ± 0.05	. . .	. . .	Y	E
	C	3	1.0	−172	0.02 ± 0.02	. . .	. . .	N	F
2021+614[a]	B	6	3.9	34	0.04 ± 0.04	0.6 ± 0.5	. . .	Y	E
	C[b]	6	3.1	−149	0.05 ± 0.04	0.8 ± 0.6	. . .	Y	E

551

289

TABLE 2—*Continued*

Object (1)	Component (2)	N (3)	$\langle R \rangle$ (mas) (4)	$\langle \vartheta \rangle$ (deg) (5)	μ_r (mas yr^{-1}) (6)	β_{app} (7)	t_0 (yr) (8)	Distinct Component (9)	Rating (10)
2113+293	B[b]	5	0.3	177	0.02 ± 0.01	1.4 ± 0.3	1985.1 ± 3.2	N	G
2128−123[a]	B[b]	3	3.7	−143	-0.07 ± 0.01	-2.0 ± 0.2	...	Y	G
2131−021[a]	C[b]	4	0.8	105	0.12 ± 0.03	7.7 ± 1.6	1991.9 ± 1.4	N	G
2134+004[a]	B[b]	6	1.9	−99	0.02 ± 0.02	1.5 ± 1.7	...	Y	E
2136+141[a]	B[b]	6	0.3	−72	0.02 ± 0.01	1.8 ± 1.4	...	N	G
2144+092	B[b]	3	0.6	83	0.03 ± 0.04	1.5 ± 2.0	...	N	F
2145+067[a]	B	8	0.3	−95	-0.01 ± 0.01	-0.6 ± 0.4	...	N	G
	C[b]	8	0.6	−119	0.027 ± 0.003	1.4 ± 0.2	1974.2 ± 2.3	N	G
	D	8	1.0	−118	0.03 ± 0.01	1.4 ± 0.4	1960.4 ± 9.6	N	G
2200+420[a]	B[b]	7	2.4	−172	1.41 ± 0.13	6.5 ± 0.6	1995.1 ± 0.2	Y	E
	C	5	2.5	−171	1.12 ± 0.22	5.2 ± 1.0	1995.6 ± 0.5	Y	E
	D	4	2.7	−172	0.99 ± 0.18	4.5 ± 0.8	1996.7 ± 0.5	Y	E
	E	3	1.9	−161	1.09 ± 0.37	5.0 ± 1.7	...	Y	P
2201+315[a]	B[b]	6	2.8	−145	0.34 ± 0.02	6.3 ± 0.5	1989.7 ± 0.6	Y	E
2209+236[a]	B[b]	4	1.5	18	0.04 ± 0.04	2.3 ± 2.4	...	N	G
2223−052[a]	B[b]	6	1.9	102	0.49 ± 0.09	32.5 ± 6.0	1994.0 ± 0.8	Y	E
	C	7	5.2	98	0.31 ± 0.03	20.4 ± 1.9	1981.4 ± 1.6	Y	E
2230+114[a]	B[b]	8	1.9	143	0.03 ± 0.04	1.4 ± 2.1	...	Y	E
	C	6	4.6	166	-0.05 ± 0.03	-2.7 ± 1.6	...	Y	E
	D	5	6.5	156	0.00 ± 0.01	0.0 ± 0.8	...	Y	E
	E	3	17.8	141	-0.23 ± 0.37	-12.3 ± 19.9	...	N	P
2234+282	B[b]	5	1.2	−97	0.12 ± 0.05	5.1 ± 2.2	...	Y	E
2243−123[a]	B[b]	4	2.7	15	0.29 ± 0.03	10.7 ± 1.1	1988.7 ± 0.9	Y	E
	C	3	10.3	25	-0.14 ± 0.05	-4.9 ± 1.9	...	Y	G
	D	4	11.3	33	0.11 ± 0.10	4.1 ± 3.5	...	Y	G
2251+158[a]	B[b]	8	5.2	−86	0.04 ± 0.04	1.9 ± 2.1	...	Y	E
2345−167[a]	B[b]	5	1.7	124	0.03 ± 0.05	1.0 ± 1.6	...	Y	E

NOTES.—Col. (1): IAU name. Col. (2): Component identifier. Col. (3): Number of epochs with measured position. Col. (4): Mean radial position, relative to the core. Col. (5): Mean structural position angle, relative to the core. Col. (6): Angular radial speed and 1 σ uncertainty. Col. (7): Radial speed in units of the speed of light and 1 σ uncertainty, computed assuming $H_0 = 70$ km s^{-1} Mpc^{-1}, $\Omega_m = 0.3$, and $\Omega_\Lambda = 0.7$. Col. (8): Extrapolated epoch of origin and uncertainty. Col. (9): Does the component satisfy the second criterion in § 3, i.e., is it a well-defined feature? Col. (10): Overall quality rating. Table 2 is also available in machine-readable form in the electronic edition of the *Astrophysical Journal*.

[a] Source is a member of the representative sample.

[b] Component is the brightest.

[c] Motions for 0316+413 that are taken from unpublished data do not appear in Fig. 1. The motions for 0238−084 are from Vermeulen et al. (2003b).

simplest model, which has only one value of γ that is the same in all sources and also has $\beta_b = \beta_p$ in all sources, is not tenable. They showed that either there must be a distribution of γ among the sources, or $\beta_b \neq \beta_p$. Most likely, there is both some distribution of γ and also a difference between γ_p and γ_b.

The apparent transverse velocity of an approaching component with a pattern Lorentz factor γ_p reaches a maximum apparent speed $\beta_p\gamma_p$ when the component moves at an angle $\sin\theta = 1/\gamma_p$ to the line of sight. For the corresponding component in the receding jet, the observed velocity is $\beta_p/2$.

3. A change in the apparent flux density, S, of a moving component over its stationary value, S_0, by a factor

$$S/S_0 = \delta^{x-\alpha}, \qquad (3)$$

where α is the spectral index and x has a value of 2 for a continuous jet or 3 for discrete components (see, e.g., Urry & Padovani 1995).

The Doppler factor is sharply peaked along the direction of motion, so sources with highly relativistic jets that happen to be pointed close to the line of sight will appear strongly boosted and hence are likely to be selected in a flux-limited sample. Although the jets may be intrinsically two-sided, unless they are very close to the plane of the sky, they

will appear highly asymmetric (i.e., one-sided) since the radiation from the receding jet is highly beamed away from the observer.

Equation (3) has the important consequence that the strongest, most compact radio sources we observe tend to have highly relativistic jets that are aligned close to the line of sight, and they will therefore likely display superluminal motion. The most probable angle for sources selected on the basis of beamed flux density alone is close to $(2\gamma)^{-1}$, where $\beta_{app} \sim \gamma/2$ (Vermeulen & Cohen 1994). The distribution of observed speeds and flux densities is dependent on the distributions of γ, redshift, and the intrinsic luminosity function.

This is illustrated in Figure 3, where we show the predicted distribution of apparent velocities for three different models. If the effect of Doppler boosting is ignored, for example, if the observed motions are due to the propagation of shocks rather than actual bulk motion, then most jets will lie close to the plane of the sky and have apparent speeds β_{app} close to β_p. If we take into account the effect of Doppler boosting, then, in a flux-limited sample, with a single Lorentz factor, most sources are found to lie close to the line of sight and have an apparent velocity $\beta_{app} \sim \beta_p\gamma$. In the typical situation that we consider, where $\beta_p \sim 1$, in the absence of Doppler boosting most sources appear to have an apparent velocity close to c,
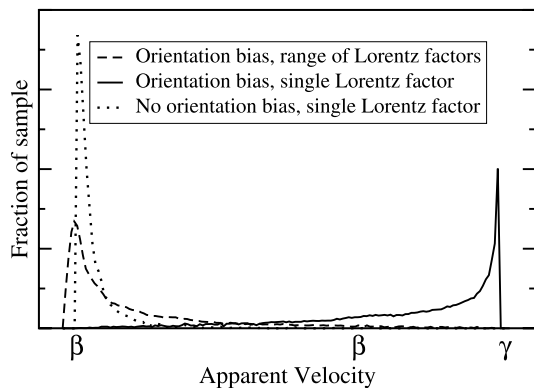
Fig. 3.—Predicted distributions of β_{app} when the sample has randomly oriented jets all with the same Lorentz factor γ (*dotted line*), when the sample has sources drawn from such a jet population but based on flux density that can be enhanced by Doppler boosting (*solid line*), and for a Doppler boosting with a range of Lorentz factors that favors low values of the Lorentz factor (*dashed line*).

whereas in the Doppler boosted case most sources have an apparent velocity close to γc. Note that in the absence of Doppler boosting there are virtually no sources with apparent speeds less than βc since this would require rare end-on orientations. The randomly oriented model also drops much more sharply with increasing β than the model with a range of Lorentz factors.

Blandford & König (1979) suggested that one of the observed jet components might be the stationary feature of the approaching jet at the point where it becomes optically thin, so that the flux density of this "core" component, as well as the moving component, is Doppler boosted. The observed overall spectrum is typically flat, which may be due to the superposition of different parts of the jet, which each have different Doppler factors, causing the synchrotron cutoff to appear at different frequencies. Consideration of differential Doppler boosting led to the concept of unified models (e.g., Orr & Browne 1982; Barthel 1989; Urry & Padovani 1995), which is usually invoked to understand the observed differences in the properties of quasars, active galaxies, and BL Lac objects as due to the orientation of the relativistic beam and an obscuring torus with respect to the line of sight. Thus, comparison of apparent jet speeds with optical classification is an effective test of these unified models and also serves to refine their parameters.

4.2. *Jet Kinematics*

The motion statistics collected for our sample address many physical questions related to relativistic jets. The process of their formation, that is, the initial acceleration and collimation of the flow, can be constrained by studying the speeds as a function of distance from the beginning of the visible jet (often referred to as the "core") and also by comparing the times when flares occur with the back-extrapolated epochs at which moving features appear to originate. Long-term multi-epoch observations can show whether there are accelerations or decelerations farther down the jets and whether radio features follow straight or curved trajectories.

In order to discriminate between various jet models and then to refine the relevant ones, it is important to establish whether jets exist as predefined channels, along which mul-

tiple moving features can be seen, or whether instead successive components follow different trajectories, at either the same or at different speeds. Viable models of jet formation will also need to be able to reproduce the observed Lorentz factor distribution. The moving features may in fact be patterns, caused by the propagation of shocks rather than the flow of matter. This can be studied by comparing the Lorentz factors inferred from the motions to the Lorentz factors estimated by other means, such as variability, brightness temperature, and (possibly) the presence of X-ray and gamma-ray emission. By probing for correlations between the apparent velocities and other quantities such as the radio or X-ray luminosity, more can be learned about the physical parameters relevant for jet formation. Finally, studying the distribution of velocities as a function of optical host type is relevant to constraining unification models.

Most of the jets in our study are well collimated and are unresolved transverse to their flow, although there often is significant curvature. In some radio galaxies with two-sided structure, the appearance of the source is very frequency dependent, suggesting free-free absorption in a disk or torus, probably associated with the accretion disk surrounding the central engine.

We found several jet features to have apparent negative velocities; that is, they appear to be approaching rather than receding from the core. Most of these apparently negative velocities are consistent, within the errors, with no significant motion. Observations extending over a longer time frame are needed to determine if these inward motions are real. Apparent inward motion may be produced if there is a newly emerging jet feature that is ejected from the core and the combination is not resolved by our beam. This would cause a shift in the measured position of the centroid and a corresponding decrease with time in the apparent separation of the core and other jet features. It is also possible that the true core is not seen, possibly as a result of absorption, and that the only observed features are parts of a jet that are moving with different velocities. If the farthest component is moving with a slower velocity than the one closest to the obscured core, then they will appear to be approaching each other. The apparent decrease in component separation from the core could also be due to component motion away from the core along a highly curved jet that bends back toward the line of sight, so that the projected separation from the core appears to decrease with time. Finally, the moving features could be only patterns in the flow, some of which might even be moving backward. Istomin & Pariev (1996) have discussed an electron-positron jet model where an observer located close to the direction of motion will see backward-moving knots. We note that any model involving patterns must account for the very large numbers of observed outward motions, as opposed to inward ones. For this reason, many of the simplest "moving marquee" models for superluminal motion have already been ruled out. In the case of 0735+178, the most distant feature appears to be moving inward, but this is probably an artifact of the complex brightness distribution whose centroid shifts when the intensity distribution changes.

4.2.1. *Velocity Distributions*

Figure 4 shows the distribution of the observed values of $\beta_{app} = 1.58 \times 10^{-2}\mu D_A(1 + z)$, where D_A is the angular size distance to the radio source in megaparsecs and the angular velocity, μ, is in mas yr^{-1}. Figure 5 shows the same distributions for those jets found in the representative subsample
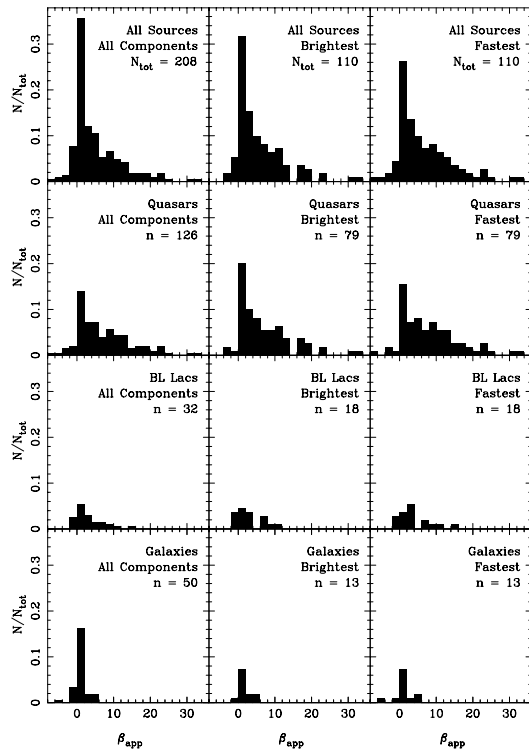
Fig. 4.—Distribution of the apparent linear velocity in all sources with a quality code E or G and that have measured redshifts. The left panels display the distribution for all individual features that we have observed. Distributions in the middle and right panels show only one feature per source, the brightest or the fastest, respectively. Sources are divided by optical class in the second, third, and fourth rows of the figure.

Fig. 5.—Same distributions as in Fig. 4, except that only those sources contained in our representative flux density–limited subsample are included.

described in § 2.2. We include in these figures only those jet features that we have been able to measure with a quality code of E or G and that have measured redshifts.

The middle and right panels of Figures 4 and 5 show the motions of only one feature per source, the brightest and the fastest, respectively. The brightest feature in each jet is defined as the one with the largest peak flux density at the epoch for which the source image was presented in Papers I and II, although in nearly all cases this does not change over the period covered by these observations. These features generally have well-determined motions; however, in a few cases, the brightest jet feature does not have an E or G quality code, usually because it has a large diffuse structure. In these cases, we have substituted the brightest component that did have an E or G quality code. For the right panels of Figure 4, the fastest feature within a source is simply defined as the one with the largest (absolute) linear speed with a quality code of either E or G.

K-S tests indicate that at a 95% confidence level there is no difference in the distribution of the jet speeds, independent of whether we consider the brightest, fastest, or even all the jet features within a source. We consider the brightest feature of each source to be the most representative for our analysis, since in the case of sources with weak secondary features

observations having a limited sensitivity or dynamic range might only detect the brightest jet feature.

The distributions shown in Figures 4 and 5 are also subdivided according to optical class. We find that the velocity distributions for the quasars, radio galaxies, and BL Lac objects are mostly concentrated in the same range ($0 < \beta_{app} < 15$). However, the quasars have a tail ranging up to $\beta_{app} \sim 34$, while jets associated with active galaxies have a narrow range of velocities with $\beta_{app} \leq 6$. A K-S test confirms at the 98% confidence level that the quasars have a different speed distribution than the galaxies and BL Lac objects, while the distributions of speeds for the galaxies and BL Lac objects are statistically indistinguishable. Examination of Figures 4 and 5 suggests that the distribution of quasar velocities may be bimodal with a minimum near $\beta_{app} \sim 5$. We have compared our observed distributions with one and two Gaussian distributions and find in each case a significantly lower value of reduced χ^2 for the two-component distribution for all of the quasar distributions. However, we are reluctant to quantify this further, as the observed distributions are clearly more complex than can be represented by two Gaussians.

We have also compared the dispersion in the speed of different features within each jet with the dispersion of the average jet speeds. We find that the dispersion of the average jet speeds among the 50 sources with two or more features with quality factors E or G is 6.3c, whereas in all but four jets
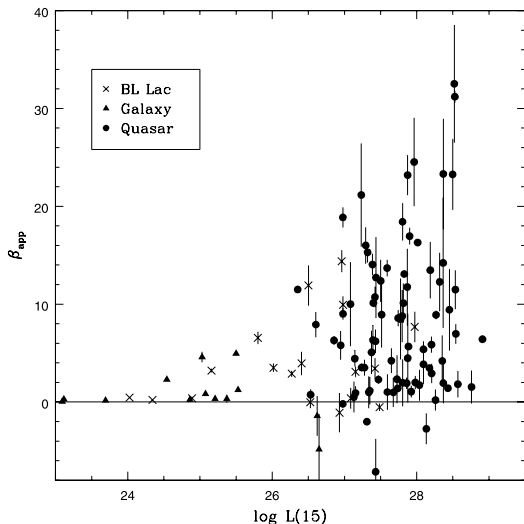
Fig. 6.—Apparent speed of the fastest feature found in 110 jets as a function of the radio luminosity.

(92%) the dispersion in the speed of individual jet features is smaller than this value. This suggests that there is an underlying flow, characteristic of each jet, that determines the speed of individual features with the jet.

4.2.2. *Apparent Speed and Apparent Luminosity*

Figure 6 shows the relation between β_{app} and apparent VLBA core luminosity at 15 GHz. There is a distinct upper envelope to the distribution, which is very similar to that found at 5 GHz in the Caltech-Jodrell flat-spectrum survey by Vermeulen (1995). In particular, the low-luminosity sources all have slow apparent speeds. If we divide the sources at the median luminosity of $L_{15} < 10^{27.4}$ W Hz^{-1}, a K-S test yields less than a 1% probability that speed distributions for the brightest components of the high- and low-luminosity sources have the same parent distribution. We note that if the apparent jet speeds that we are measuring are simply random patterns, then no envelope would be expected in Figure 6.

As discussed by Lister & Marscher (1997), the presence of this envelope does not necessarily imply that *intrinsically* faint jets have low *intrinsic* speeds. As discussed in § 4.3.1, in practice there is likely to be a spread in Lorentz factors. The lowest luminosity sources in a flux-limited sample will tend to lie at low redshifts, where the comoving volume element is small. Ignoring evolutionary effects and assuming a constant comoving space density and a steep luminosity function, these sources will therefore be representative of the most common jets in the parent population. The probability of any of them having *both* a high Lorentz factor and a small viewing angle will be very small, especially if the parent population is dominated by low Lorentz factor jets [i.e., $n(\gamma) \propto \gamma^{-1.5}$ as found by Lister & Marscher 1997]. This may therefore explain why none of the low-luminosity sources in Figure 6 are highly superluminal.

4.2.3. *Nonradial and Bent Trajectories*

For most of the sources in our sample we have determined only the radial speed and position angle of the motion with respect to the assumed core component. For those sources

with sufficiently high quality data, we also computed the full two-dimensional vector proper motion on the sky. This was accomplished by fitting separately for the proper motion in both right ascension and declination. These results were combined to form a vector velocity, determined by the speed, μ, and the direction, ϕ, on the sky relative to the radio core. We are particularly interested in comparing the direction of motion, ϕ, to the mean structural position angle of the jet, $\langle \vartheta \rangle$.

Table 3 compiles the vector proper motions for all jet components in our sample that have at least five epochs of observation and for which the vector velocity is of at least 5 σ significance. These criteria guarantee that only the highest quality vector motions are used in our comparison of velocity direction to structural position angle. Of the 60 component motions that meet these criteria, we find that 20 are significantly "nonradial," meaning that the velocity direction, ϕ, differs by at least 3 σ from the mean structural position angle, $\langle \vartheta \rangle$. These nonradial motions are highlighted in bold in Table 3.

Nonradial motions do not follow a direction that extrapolates back to the jet origin and are by definition considered nonballistic. The occurrence of such nonballistic motions in approximately one-third of the highest quality motions we examined is striking. Assuming that the observed velocities trace the underlying jet flow, this result indicates that bends in jet direction and/or jet collimation are common. The actual bends may be small, only a few degrees, but the observed bends can be large, of the order of 90°, since they appear amplified by projection.

In Figure 7 we show tracks in the right ascension–declination plane of several sources that have clearly defined nonradial or bent trajectories. In general, the trajectories are bent toward the next structure down the jet, whether seen directly in our maps or in published larger scale images. This suggests that jet features may trace out a flow in a preexisting curved channel. Sources 1226+023 (3C 273), 1219+285, 1532+016, and 2200+420 (BL Lac) are excellent examples of this trend. In 1548+056, the component motion appears to be transverse to the main jet direction that is known from lower resolution images, and is hinted at in our images, to lie to the north. However, the motion we observe is directed toward the small extension toward the east, and looking back toward the core, the jet ridgeline appears to curve into the component from the opposite direction.

In 3C 390.3 (1845+797) the two most prominent features appear to be moving with a similar speed of about 2.5c but along slightly different trajectories of 27° and 30°. Neither trajectory is aligned with the direction of the core or with the narrow 60″ jet that points toward one of the distant hot spots in position angle 35° (Alef et al. 1996). This is a clear exception to the trend identified above.

In general we do not have sufficient data to robustly detect changes in velocity, although the high incidence of nonballistic motion implies that such changes must occur. However, in BL Lac, there is evidence that the moving feature traces the curved ridgeline of the jet. Moreover, we have previously reported an abrupt change in both speed and direction in 3C 279 that occurred in 1998 (Homan et al. 2003).

4.2.4. *Two-sided Sources*

Seven sources in Table 2 display two-sided structure in which the jet flow appears bidirectional away from a central core. We have previously reported our results on the two-sided source NGC 1052 (Vermeulen et al. 2003b), where the component motion is close to the plane of the sky and multiple

293

TABLE 3
VECTOR PROPER-MOTION RESULTS

Object (1)	Component (2)	N (3)	$\langle R \rangle$ (mas) (4)	$\langle \vartheta \rangle$ (deg) (5)	μ (mas yr^{-1}) (6)	ϕ (deg) (7)	β_{app} (8)	$\|\langle \vartheta \rangle - \phi\|$ (deg) (9)
0035+413	B	5	1.5 ± 0.0	103.7 ± 0.8	0.10 ± 0.02	121.8 ± 8.2	6.6 ± 1.2	18.1 ± 8.2
0055+300	B	5	0.9 ± 0.0	−54.2 ± 1.6	0.14 ± 0.02	−52.3 ± 7.3	0.2 ± 0.0	1.9 ± 7.5
0106+013	C	5	2.1 ± 0.0	−112.7 ± 1.2	0.27 ± 0.03	−119.6 ± 7.4	22.4 ± 2.1	6.9 ± 7.5
0149+218	C	6	5.0 ± 0.1	−21.9 ± 1.1	0.29 ± 0.04	−26.3 ± 9.9	18.7 ± 2.3	4.5 ± 9.9
0234+285	**B**	**6**	**3.5 ± 0.1**	**−12.6 ± 0.6**	**0.25 ± 0.05**	**11.6 ± 4.2**	**14.7 ± 2.8**	**24.2 ± 4.3**
0333+321	B	9	2.7 ± 0.0	123.3 ± 0.2	0.18 ± 0.01	120.3 ± 1.8	11.0 ± 0.4	3.0 ± 1.8
	C	9	4.9 ± 0.0	126.0 ± 0.5	0.20 ± 0.02	135.0 ± 6.8	12.2 ± 1.4	9.0 ± 6.8
0336−019	B	5	1.4 ± 0.1	66.9 ± 1.8	0.22 ± 0.04	67.1 ± 7.0	10.1 ± 1.7	0.2 ± 7.2
0415+379	D	6	3.3 ± 0.1	65.9 ± 0.8	1.52 ± 0.04	65.3 ± 1.4	4.9 ± 0.1	0.6 ± 1.6
0430+052	B	10	4.7 ± 0.1	−110.8 ± 0.6	1.77 ± 0.06	−108.7 ± 1.1	3.9 ± 0.1	2.1 ± 1.3
	C	8	6.1 ± 0.2	−105.9 ± 1.1	1.81 ± 0.17	−100.0 ± 3.7	4.0 ± 0.4	5.9 ± 3.8
	G	9	3.0 ± 0.1	−112.0 ± 1.9	1.59 ± 0.10	−105.9 ± 2.5	3.5 ± 0.2	6.1 ± 3.2
	H	5	2.6 ± 0.2	−118.4 ± 2.6	2.08 ± 0.20	−114.8 ± 3.5	4.6 ± 0.4	3.6 ± 4.4
0735+178	**D**	**5**	**4.0 ± 0.1**	**63.9 ± 0.9**	**0.18 ± 0.03**	**−119.1 ± 12.6**	**...**	**177.0 ± 12.7**
0736+017	**B**	**6**	**4.2 ± 0.1**	**−70.0 ± 1.6**	**0.96 ± 0.04**	**−87.3 ± 4.3**	**11.9 ± 0.5**	**17.4 ± 4.6**
	D	5	10.0 ± 0.1	−87.8 ± 0.2	0.39 ± 0.06	−86.1 ± 3.1	4.8 ± 0.8	1.7 ± 3.1
	E	5	2.1 ± 0.1	−67.8 ± 2.2	0.86 ± 0.09	−72.0 ± 3.8	10.6 ± 1.1	4.2 ± 4.4
0738+313	B	8	2.8 ± 0.0	179.4 ± 0.3	0.07 ± 0.01	157.7 ± 7.6	2.5 ± 0.4	21.6 ± 7.6
0745+241	C	8	3.1 ± 0.1	−63.1 ± 1.0	0.33 ± 0.04	−50.0 ± 6.5	8.2 ± 1.0	13.1 ± 6.5
0748+126	B	6	1.7 ± 0.0	120.1 ± 0.4	0.12 ± 0.01	129.3 ± 4.5	5.9 ± 0.5	9.3 ± 4.5
0754+100	**B**	**5**	**4.0 ± 0.1**	**14.6 ± 0.9**	**0.76 ± 0.13**	**−7.1 ± 4.5**	**12.9 ± 2.1**	**21.7 ± 4.6**
0814+425	B	6	0.9 ± 0.0	89.6 ± 0.8	0.18 ± 0.02	86.5 ± 2.0	2.9 ± 0.3	3.1 ± 2.1
0823+033	C	6	2.4 ± 0.1	14.1 ± 0.6	0.48 ± 0.04	10.8 ± 1.6	14.5 ± 1.1	3.3 ± 1.7
	D	6	1.1 ± 0.1	31.9 ± 3.0	0.31 ± 0.05	31.3 ± 6.4	9.4 ± 1.5	0.6 ± 7.1
0851+202	C	5	1.0 ± 0.0	−91.9 ± 1.0	0.52 ± 0.04	−90.6 ± 2.5	9.9 ± 0.9	1.2 ± 2.7
	D	5	0.9 ± 0.1	−102.4 ± 1.5	0.38 ± 0.06	−111.4 ± 5.0	7.2 ± 1.1	9.0 ± 5.3
0917+449	B	6	1.2 ± 0.0	177.7 ± 0.5	0.07 ± 0.01	−176.1 ± 5.7	5.9 ± 0.8	6.2 ± 5.7
0953+254	**C**	**5**	**1.0 ± 0.0**	**−129.3 ± 1.4**	**0.10 ± 0.00**	**−96.6 ± 9.5**	**4.2 ± 0.1**	**32.7 ± 9.6**
1012+232	B	5	2.2 ± 0.0	109.7 ± 0.4	0.27 ± 0.02	111.7 ± 1.8	9.0 ± 0.6	2.0 ± 1.8
1015+359	**B**	**6**	**1.3 ± 0.1**	**−172.3 ± 0.4**	**0.21 ± 0.04**	**177.2 ± 0.6**	**12.6 ± 2.2**	**10.4 ± 0.7**
1101+384	**C**	**7**	**1.4 ± 0.0**	**−38.8 ± 1.3**	**0.23 ± 0.02**	**−57.1 ± 3.8**	**0.5 ± 0.0**	**18.3 ± 4.0**
	D	6	0.8 ± 0.0	−30.3 ± 2.8	0.17 ± 0.02	−26.8 ± 9.2	0.4 ± 0.0	3.5 ± 9.7
1127−145	**C**	**7**	**4.1 ± 0.0**	**83.0 ± 0.1**	**0.09 ± 0.01**	**70.4 ± 3.1**	**5.5 ± 0.8**	**12.6 ± 3.1**
1219+285	**D**	**7**	**11.0 ± 0.1**	**106.8 ± 0.3**	**0.59 ± 0.03**	**143.6 ± 3.0**	**4.0 ± 0.2**	**36.7 ± 3.0**
1226+023	**B**	**11**	**6.1 ± 0.1**	**−112.7 ± 0.4**	**1.05 ± 0.04**	**−119.6 ± 1.6**	**10.9 ± 0.4**	**6.9 ± 1.7**
	C	7	9.6 ± 0.1	−120.2 ± 0.7	1.36 ± 0.08	−119.1 ± 2.9	14.1 ± 0.9	1.1 ± 3.0
	D	8	10.8 ± 0.2	−119.5 ± 1.0	0.83 ± 0.16	−119.7 ± 10.3	8.6 ± 1.7	0.2 ± 10.3
	E	10	3.3 ± 0.1	−116.1 ± 1.1	1.27 ± 0.07	−115.4 ± 2.3	13.1 ± 0.8	0.7 ± 2.5
	F	6	18.7 ± 0.2	−123.1 ± 0.6	0.83 ± 0.14	−140.5 ± 10.6	8.5 ± 1.5	17.4 ± 10.6
1253−055	**B**	**10**	**3.3 ± 0.0**	**−115.9 ± 0.5**	**0.29 ± 0.01**	**−130.3 ± 3.1**	**9.1 ± 0.4**	**14.4 ± 3.1**
1345+125	C	5	2.0 ± 0.0	164.2 ± 0.8	0.16 ± 0.01	173.3 ± 7.3	1.2 ± 0.1	9.1 ± 7.3
	E	**5**	**9.8 ± 0.1**	**161.8 ± 0.1**	**0.04 ± 0.01**	**114.3 ± 15.1**	**0.3 ± 0.1**	**47.5 ± 15.1**
1510−089	B	5	2.8 ± 0.1	−26.5 ± 0.9	0.85 ± 0.04	−23.2 ± 2.1	19.0 ± 0.8	3.3 ± 2.3
1532+016	**B**	**6**	**1.1 ± 0.0**	**130.4 ± 1.0**	**0.21 ± 0.01**	**146.8 ± 2.5**	**14.3 ± 0.7**	**16.4 ± 2.7**
1548+056	**B**	**5**	**4.4 ± 0.0**	**10.4 ± 0.3**	**0.12 ± 0.01**	**74.4 ± 2.9**	**7.7 ± 0.8**	**64.1 ± 2.9**
1606+106	B	5	0.9 ± 0.0	−58.0 ± 2.5	0.31 ± 0.02	−47.8 ± 4.0	18.7 ± 1.3	10.2 ± 4.7
1633+382	B	8	1.5 ± 0.0	−86.2 ± 0.8	0.15 ± 0.03	−86.2 ± 3.0	11.4 ± 1.9	0.0 ± 3.1
1641+399	B	9	1.7 ± 0.0	−95.0 ± 0.6	0.49 ± 0.02	−99.9 ± 1.7	17.0 ± 0.8	5.0 ± 1.8
	C	5	0.9 ± 0.0	−100.6 ± 0.7	0.37 ± 0.03	−92.9 ± 2.5	12.9 ± 0.9	7.7 ± 2.6
1642+690	B	5	2.2 ± 0.1	−162.4 ± 1.6	0.38 ± 0.04	−161.0 ± 4.8	16.0 ± 1.6	1.4 ± 5.0
1655+077	B	5	3.7 ± 0.0	−38.4 ± 0.6	0.43 ± 0.03	−46.6 ± 3.4	15.4 ± 1.0	8.2 ± 3.5
	C	**5**	**8.0 ± 0.0**	**−44.2 ± 0.2**	**0.14 ± 0.02**	**17.1 ± 6.1**	**4.9 ± 0.9**	**61.3 ± 6.1**
1800+440	B	5	2.6 ± 0.1	−163.1 ± 1.4	0.49 ± 0.04	−155.7 ± 4.3	18.6 ± 1.6	7.4 ± 4.5
1845+797	**B**	**9**	**5.5 ± 0.0**	**−40.9 ± 0.3**	**0.55 ± 0.03**	**−29.9 ± 2.2**	**2.1 ± 0.1**	**10.9 ± 2.2**
	C	**10**	**7.2 ± 0.0**	**−36.0 ± 0.2**	**0.61 ± 0.02**	**−26.6 ± 1.0**	**2.3 ± 0.1**	**9.3 ± 1.0**
1928+738	B	8	2.1 ± 0.1	165.3 ± 0.7	0.29 ± 0.03	158.4 ± 3.2	5.6 ± 0.6	7.0 ± 3.3
1957+405	D	8	3.0 ± 0.0	−78.6 ± 0.2	0.18 ± 0.02	−78.2 ± 2.0	0.7 ± 0.1	0.4 ± 2.0
	E	8	2.2 ± 0.0	−79.7 ± 0.4	0.19 ± 0.03	−75.6 ± 3.1	0.7 ± 0.1	4.1 ± 3.1
	F	6	1.7 ± 0.1	−79.4 ± 0.5	0.22 ± 0.03	−79.5 ± 1.9	0.8 ± 0.1	0.1 ± 2.0
	G	8	1.2 ± 0.1	−79.0 ± 0.7	0.16 ± 0.03	−80.2 ± 2.9	0.6 ± 0.1	1.2 ± 2.9
2005+403	B	5	3.2 ± 0.1	119.8 ± 1.4	0.20 ± 0.03	83.6 ± 13.6	14.9 ± 2.1	36.2 ± 13.7
2113+293	**B**	**5**	**0.3 ± 0.0**	**177.0 ± 2.2**	**0.04 ± 0.01**	**−131.3 ± 8.2**	**2.4 ± 0.3**	**51.7 ± 8.5**
2145+067	**C**	**8**	**0.6 ± 0.0**	**−119.4 ± 0.7**	**0.03 ± 0.01**	**−156.4 ± 5.3**	**1.8 ± 0.3**	**37.0 ± 5.3**

TABLE 3—*Continued*

Object (1)	Component (2)	N (3)	$\langle R \rangle$ (mas) (4)	$\langle \vartheta \rangle$ (deg) (5)	μ (mas yr^{-1}) (6)	ϕ (deg) (7)	β_{app} (8)	$\|\langle \vartheta \rangle - \phi\|$ (deg) (9)
2200+420	B	7	2.4 ± 0.1	-171.6 ± 1.6	1.41 ± 0.12	-170.7 ± 3.1	6.5 ± 0.6	0.9 ± 3.5
	C	**5**	**2.5 ± 0.2**	**-171.4 ± 1.5**	**1.16 ± 0.22**	**172.8 ± 3.4**	**5.3 ± 1.0**	**15.8 ± 3.7**
2201+315	B	6	2.8 ± 0.0	-144.5 ± 1.2	0.34 ± 0.03	-142.7 ± 5.3	6.3 ± 0.5	1.8 ± 5.4
2223−052	B	6	1.9 ± 0.1	102.4 ± 2.8	0.50 ± 0.08	107.3 ± 6.4	32.9 ± 5.4	4.9 ± 7.0
	C	7	5.2 ± 0.1	98.0 ± 0.3	0.31 ± 0.03	90.6 ± 3.3	20.6 ± 1.8	7.4 ± 3.3

Notes.—Sources with significant nonradial motion are shown in bold print. Col. (1): IAU name (B1950.0). Col. (2): Component identifier. Col. (3): Number of epochs with measured position. Col. (4): Mean radial position, relative to the core. Col. (5): Mean structural position angle, relative to the core. Col. (6): Angular velocity. Col. (7): Direction of velocity. Col. (8): Linear speed in units of the speed of light. Col. (9): Misalignment angle.

components move in opposite directions from the core with a velocity, $\beta \sim 0.26$, that is only mildly relativistic. Plots of component position versus time for all of the two-sided jets are shown in Figure 2. For most of these sources we were able to identify the central component at each epoch and so determine the motion of individual features away from the center. In a few cases, however, such as 1404+286 (epochs 1998.83 and 1999.55), the central core was not detected at one or more epochs, either because it was weak or because the dynamic range was limited for that observation. In these cases we have interpolated from the positions of the outer features, to find the "virtual" center, and we have used that to determine the motion of the individual outer features. For the source 1323+321 even that procedure was not possible since the structure appears to be two-sided, but we do not see the core at any epoch. Moreover, our imaging of this source is not completely satisfactory as a result of its large angular size and the limited interferometer spacings sampled by our data.

4.2.5. *Peaked Spectrum Sources*

GPS sources are characterized by their sharp low-frequency cutoff and general absence of prominent large-scale structure. There is no consensus as to whether the observed spectral cutoff in these sources is due to synchrotron self-absorption or free-free absorption (Shaffer et al. 1999). Previous VLBI observations have suggested that GPS sources have a simple double-structure morphology with little or no significant motions (e.g., O'Dea 1998). Thirteen of our sources are classified as GPS sources, of which we, so far, have observations of eight at three or more epochs. Of these, only 1345+125 shows superluminal motion. The mean velocity observed for the GPS sources in our sample is only $(0.5 \pm 1.5)c$. None of the GPS sources have $\beta_{app} > 1.5$.

The existence of a sharp peak in the spectra of these sources implies that the individual components each peak up at about the same frequency. This means that the different components probably have comparable Doppler shifts, and if the spectral cutoff is due to synchrotron self-absorption, they should have comparable brightness temperatures. Some GPS sources, such as 0552+398 and 0642+449, contain a single unresolved strong component, and so an interpretation in terms of synchrotron self-absorption is required for any reasonable magnetic field strength. However, for other GPS sources we note the very different appearance of the core and jet components; nevertheless, they have a common cutoff frequency. Moreover, many of the peaked spectrum sources included in our study have sharply bent jet structure suggesting very different amounts of Doppler boosting and frequency shift of the self-absorption peak. Free-free absorption probably plays an

important role in determining the spectra of these sources. Since many of the core-jet GPS sources show little or no motion, we suggest that possibly the jet flow in these sources is nonrelativistic or that these sources are seen at very large viewing angles, rather than that the measured velocity is the advance speed of a young double-lobe radio galaxy as suggested by Owsianik & Conway (1998). Either of these scenarios would imply a small Doppler shift. GPS sources do not have any extended double-lobe structure, which may be a consequence of the slow jets that do not carry sufficient energy to form extended radio lobes.

We note that in some cases, such as CTA 102, which had a peaked spectrum in the past, there are large variations in the total flux density (Kovalev et al. 2002), which probably reflects significant relativistic boosting. Lister (2003) and Kovalev (2004) have argued that these sources are not bona fide GPS sources but "masquerading blazars" that often contain bright transient jet features that dominate their radio spectrum.

4.2.6. *Sources with Extended Double Structure*

As a result of our selection criteria, most of the sources included in our study are dominated by their flat-spectrum compact structure; they are mostly identified with quasars. Some quasars, however, also have extended structure with relatively steep radio spectra, in addition to their flat-spectrum compact core. We have included a few of these lobe-dominated sources in our study, although they did not meet our selection criteria. Extended structure is more common among the active galaxies. The following sources in Table 2 have significant double-lobe steep-spectrum extended structure: NGC 315 (0055+300), NGC 1052 (0238−084), 3C 111 (0415+379), 3C 120 (0430+052), M87 (1228+126), 3C 390.3 (1845+797), and Cygnus A (1945+405). All are identified with galaxies containing a relatively strong AGN. All but NGC 1052 and 3C 120 are dominated by the extended steep-spectrum double-lobe structure even at 15 GHz. In the framework of standard relativistic beaming models, radio galaxies and lobe-dominated sources are presumed to lie close to the plane of the sky and thus should show values of $\beta_{app} \sim 1$. However, 3C 111, 3C 120, and 3C 390.3 each show rather large apparent motions, and it is not clear how they fit into standard unification models.

These objects are all broad-line radio galaxies (BLRGs), although 3C 120 has also been classified as a narrow-line radio galaxy (NLRG). The NLRGs are thought to lie at rather large angles to the line of sight, and polarimetry shows that in some cases they contain a central quasar and a broad-line region that are hidden by a dusty torus. The NLRGs do not show strong superluminal motion. Sources 3C 111, 3C 120, and 3C 390.3 do show superluminal motion and hence must
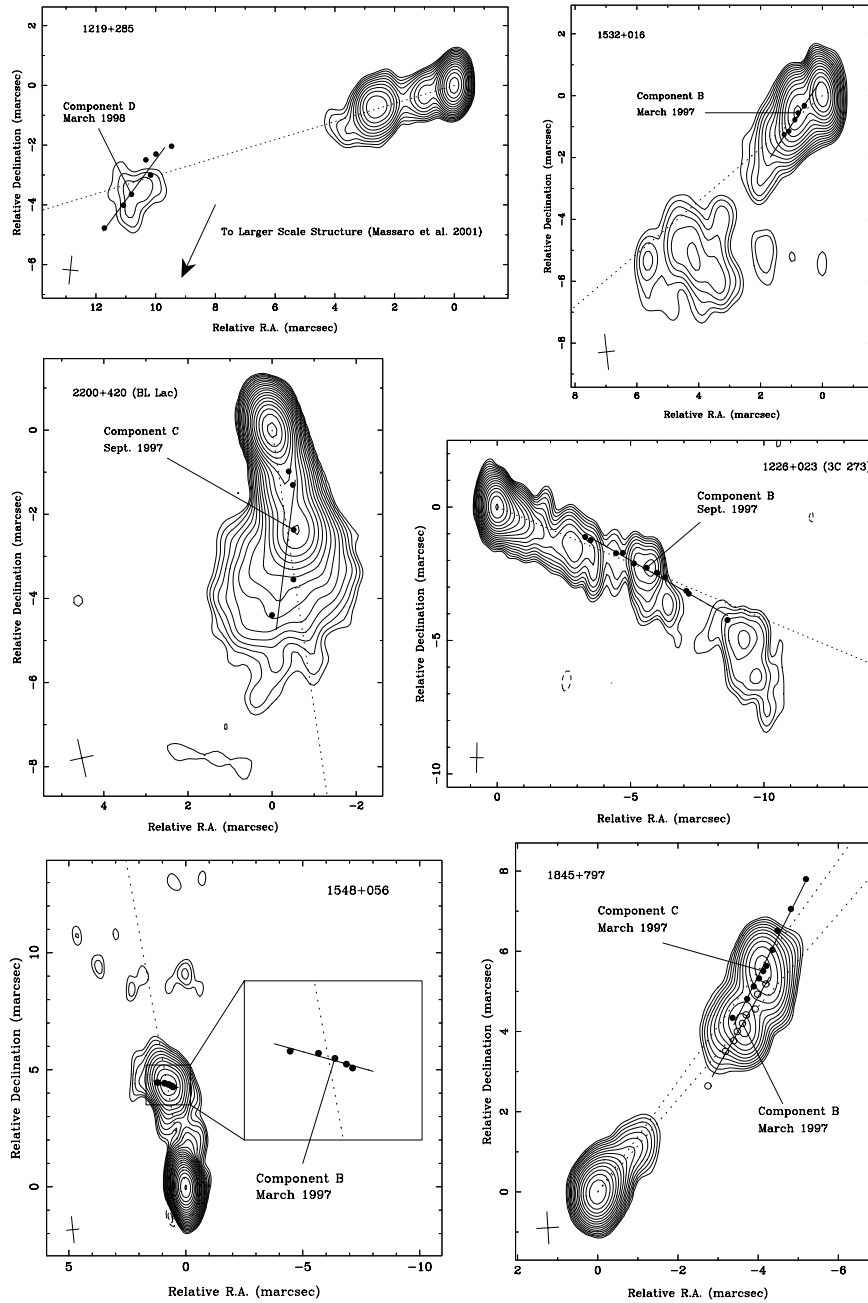
Fɪɢ. 7.—Selected images of sources with jets that show nonballistic component motion. Measured component positions for each epoch are superimposed on the images along with the vector motion (*solid lines*) in the right ascension–declination plane. Dashed lines represent the mean structural position angles, $\langle\vartheta\rangle$, for each component.

be at small angles to the line of sight (less than about 11° for 3C 111). The BLRGs are not well understood, and they may have a wide range of intrinsic luminosity and orientation (Dennett-Thorpe et al. 2000).

On the other hand, the jets of other lobe-dominated sources appear to be subrelativistic. The powerful radio galaxy Cygnus A contains twin jets pointed toward the distant hot spots. The approaching and receding jets appear to propagate with velocities of $0.7c$ and $0.2c$, respectively, and we find relatively slow speeds of $(0.16 \pm 0.03)c$ in the parsec-scale jet of NGC 315. In the case of the radio galaxy NGC 1052, we have reported a two-sided flow with subrelativistic jet speeds of only $0.26c$ (Vermeulen et al. 2003b) on both sides of the core. At least in these radio galaxies, the intrinsic jet flow close to the core appears to have only moderate speeds with $\beta_{app} \ll 1$. Thus, it appears that the observed distribution of speeds and/or degree of jet asymmetry cannot be interpreted simply in terms of the orientation of a twin relativistic jet with $\beta \sim 1$, unless the observed speeds do not reflect the actual jet flow speed, or the radiation from a high-speed inner spine is not observed as a result of a more slowly moving outer sheath that dominates the emission at large angles from the jet direction. As we show in § 4.4.1, highly relativistic jets are relatively rare among the general population of radio jets.

4.2.7. *Comparison with Other Velocity Studies*

Other recent VLBA monitoring observations (e.g., Jorstad et al. 2001a, 2001b; Britzen et al. 2001; Homan et al. 2001; Vermeulen et al. 2003a) made at other wavelengths with different resolution and with different sampling intervals are complementary to our observations and may be used to extend the range of size and timescales over which jet kinematics may be studied.

Jorstad et al. (2001a, 2001b) have used the VLBA to study the motions in a sample of strong sources at 7 and 13 mm. These observations probe the source structure and motions on a scale about 3 times smaller than our 2 cm observations, but as a result of the decreased surface brightness at 7 mm, they are generally not able to trace the motions beyond a few milliarcseconds from the core. From the comparison of the observed motions for the sources in common to our two studies, it is possible to trace the motions of individual components over a wider range of scales than is possible from either set of observations alone.

We have compared our velocities determined at 15 GHz with those of Jorstad et al. (2001a, 2001b). There appears to be little agreement in the individual source speeds found by the two studies. On average, the Jorstad et al. (2001a, 2001b) speeds appear systematically higher, possibly because their observations were carried out at shorter wavelengths and probed jet regions closer to the core.

Britzen et al. (1999, 2001) and Vermeulen et al. (2003a) have discussed jet motions in a large sample of sources at 6 cm, taken from the Caltech-Jodrell CJ surveys covering declinations greater than +35°. These observations have lower angular resolution than ours and are thus more sensitive to the lower surface brightness structure located downstream. Vermeulen et al. (2003a) quote a mean velocity for quasar and galaxy jets of $2.9c$ and $0.9c$, respectively. This appears to be less than the values of $(7.3 \pm 0.8)c$ and $(1.7 \pm 0.8)c$ that we measure at 2 cm for the brightest features in each source. On the other hand, Jorstad et al. (2001b), working primarily at 0.7 and 1.3 cm, find systematically faster velocities in those

sources where our samples overlap. These results suggest that there is a systematic decrease in β_{app} with increasing wavelength, probably because the observations at different wavelengths sample different parts of jet structure. In a separate paper (R. C. Vermeulen et al. 2004, in preparation) we will discuss, in more detail, the motions of those sources in common to the 6 and 2 cm samples.

4.3. *Implications for Relativistic Beaming Models*

4.3.1. *Ballistic Models*

The simplest model to consider is a pure ballistic model with a common flow velocity for all sources, with $\beta_p = \beta_b \sim 1$, and a flow that is intrinsically symmetric. In this simple case, observations of the apparent velocities, as well as the ratio of flux densities of approaching and receding components, can, in principle, be used to solve uniquely for γ and θ and thus provide a test of the hypothesis that $\beta_p = \beta_b$. However, even early VLBI data indicated that this simple model is not tenable (Vermeulen & Cohen 1994; Lister & Marscher 1997).

In a flux density–limited sample, the combined effect of available solid angle and Doppler boosting leads to a distribution of β_{app} with many values close to γ (Vermeulen & Cohen 1994). On the other hand, if Doppler boosting is not an important selection mechanism, then in most cases $\beta_{app} \sim 1$. Figure 3 shows the expected distribution of apparent velocities for the case in which $\gamma_p = \gamma_b$ (see § 4.1) along with the corresponding distribution for a randomly oriented sample. None of the distributions shown in Figure 4 or Figure 5 are consistent with either of these two simple ballistic models as there is neither evidence of the peak at $\beta_{app} \sim \gamma$ characteristic of the simple Doppler boosted models nor evidence of the sharp low-speed cutoff at $\beta_{app} \sim 1$ characteristic of models that ignore Doppler boosting.

How do we reconcile the difference between the observed and predicted distributions? There must be either a spread in intrinsic velocity (e.g., Lister & Marscher 1997) or a difference between the bulk flow velocity and the pattern velocity, so that there is less Doppler bias in favor of observing beams that are oriented close to the critical angle (Vermeulen & Cohen 1994). In Figure 3 we plot a model with a spread of intrinsic velocity such that $n(\gamma) \propto \gamma^{-1.5}$. This model has equal pattern and bulk velocities and reproduces the general characteristics of the observed distribution of superluminal speeds. A more detailed analysis will be discussed by M. L. Lister et al. (2004, in preparation).

4.3.2. *Randomly Oriented Samples*

Based on earlier observations of apparent velocity distributions, Ekers & Liang (1990) suggested that the simple model with no Doppler bias provided an adequate fit to the observed distributions of β_{app} with only a slight adjustment needed, which was satisfied by introducing an obscuring torus. However, comparison of our data with models that do not include Doppler boosting shows poor agreement, since, as shown in Figure 3, in the absence of Doppler boosting, most sources are expected to lie close to the plane of the sky where $\beta_{app} \sim 1$. This appears to be inconsistent with the tail of the velocity distribution that we find extending toward larger apparent velocities. Following the discussion of Cohen (1990), a detailed analysis of the observed velocities shows that the probability of the sources having been picked at random from a parent population that is isotropically distributed is less than
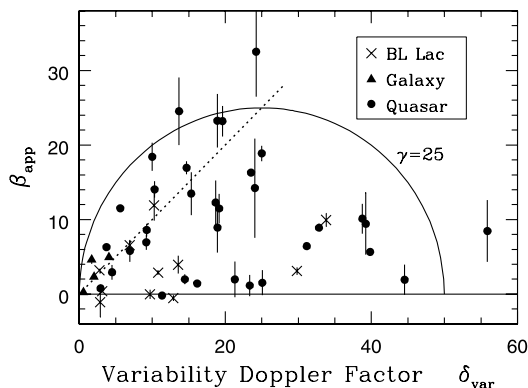
FIG. 8.—Apparent velocity, β_{app}, plotted against variability Doppler factor, δ_{var}, for the fastest component found in 49 sources calculated using the method of Lähteenmäki & Valtaoja (1999) with an intrinsic brightness temperature $T_b^{int} = 2 \times 10^{10}$ K. The solid line shows the expected locus of points for Lorentz factor values of 25. The dotted line represents the $1/\gamma$ cone where $\delta_{var} = \beta_{app}$.

10^{-5}. We therefore conclude that the sources are preferentially aligned along the line of sight, as would be expected if Doppler boosting is in fact important.

4.4. Comparison with Other Relativistic Velocity Indicators

While the actual observation of superluminal motion in radio source jets remains the most direct way of establishing the existence of relativistic motion, comparison of the observed values of β_{app} with other velocity indicators also provides important tests of beaming models and specifically the relation between pattern and bulk flow speeds. This includes flux density variability (Hughes et al. 1992; Lähteenmäki & Valtaoja 1999; Lähteenmäki et al. 1999), maximum brightness temperature (Kellermann & Pauliny-Toth 1969; Readhead 1994; Guijosa & Daly 1996), the ratio of core to extended radio luminosity (Orr & Browne 1982), the gamma-ray luminosity (von Montigny et al. 1995; Hartman et al. 1999; Mattox et al. 1997, 2001), or observations of inverse Compton X-rays (Ghisellini et al. 1993). Relativistic boosting also affects the radio source counts and luminosity functions (Padovani & Urry 1992; Wall & Jackson 1997), which provide a consistency check on beaming models.

4.4.1. Relation between Observed Velocity and Flux Density Variations

Flux density changes are commonly seen in superluminal sources, and their short timescale is generally taken to imply high brightness temperatures. The variability timescale and the timescale for apparent transverse motion are both compressed as a result of the forward motion; hence, we might expect to see a relation between β_{app} and the flux density variability provided that β_b is related to β_p. Lähteenmäki & Valtaoja (1999) used variability data at 1.3 cm and 8 mm from the Metsähovi Observatory to calculate a variability Doppler factor, δ_{var}, assuming an intrinsic brightness temperature characteristic of a self-absorbed synchrotron source in which the particle and magnetic energy are in equilibrium. We have recalculated their values using the cosmology given in § 1 and for different values of intrinsic brightness temperature. Since δ_{var} varies inversely as the cube root of the assumed intrinsic

temperature in the synchrotron plasma, T_b^{int}, δ_{var} is relatively insensitive to the assumed value of T_b^{int}.

In Figure 8 we plot β_{app} against δ_{var} for the 49 sources in common to the Metsähovi and VLBA samples. We calculate $\delta_{var} = (T_b^{var}/T_b^{int})^{1/3}$ assuming a spectral index of zero and where T_b^{var} is the apparent brightness temperature calculated from the variability timescale, by assuming that it is limited by the size of the source divided by the speed of light. Five sources that only have components located at a bend in the jet were excluded, as they probably reflect a standing shock wave, or perhaps a stationary location in a helical jet where the flow is closest to the line of sight and hence is boosted most strongly. In either case the measured velocity is a poor indicator of the flow velocity and not relevant in discussing relativistic effects. The sample we use contains five active galaxies, 14 BL Lac objects, and 30 quasars. Most points lie inside the "$1/\gamma$ cone" ($\beta_{app} = \delta_{var}$) as they should for a flux density–limited sample (Vermeulen & Cohen 1994).

Cohen et al. (2003) have compared Figure 8 with the results of a simulation generated by randomly picking a flux-limited sample from an isotropically distributed population with power-law distributions of luminosity and γ and for several values of T_b^{int} over the range 4×10^9–1×10^{11} K. The value $T_b^{int} \sim 2 \times 10^{10}$ K gives the best fit between the measured and simulated data. However, although there does appear to be an upper limit to β_{app} that is close to the expected locus for components with $\gamma = 25$, the detailed distribution is not well matched to that expected from the simulation (Lister & Marscher 1997).

Calculations of the variability Doppler factor using values of T_b^{int} closer to the inverse Compton limit, $\sim 10^{12}$ K, lead to distributions on the β_{app}-δ_{var} plane that are very different from those expected from the simulations. We conclude that T_b^{int} is perhaps an order of magnitude below the inverse Compton limit.

For this application, we have used the *fastest* feature for each source, on the grounds that these velocities should be more representative of the true flow velocities. Slower moving components, especially those located at a bend in the jet, may be dominated by standing shock waves. Forward shock waves might also exist, and trying to understand their role is a goal of our study. Other geometries have been suggested for the jet, including a fast "spine," which we would preferentially see, surrounded by a slower shell. In this case, the spine would probably also control the flux variations, so that using the fastest (spine) velocity for β_{app} is appropriate.

We have also examined values of δ_{var} calculated from the UMRAO database at our wavelength of 2 cm and noted a large dispersion between Doppler factors deduced from these data and the shorter wavelength Metsähovi data. Thus, the robustness of the Doppler factors calculated in this way appears to be uncertain. The Michigan data cover a longer time span but are at longer wavelengths where individual outbursts appear to overlap in time.

The Lorentz factor γ in a superluminal jet is important because it is intrinsic to the jet, whereas β_{app} and δ_{var} are the observables that depend on the jet orientation. The distribution of γ may give information on the physics of the collimation region. From the values of β_{app} and δ shown in Figure 8 we calculate the actual Lorentz factors, shown as a histogram in Figure 9. We believe that the apparent deficit in the first bin of Figure 9 for the quasars may be a selection effect or just due to small number statistics. To be fully consistent with the analysis above and the choice $T_b^{int} = 2 \times 10^{10}$ K, the Lorentz
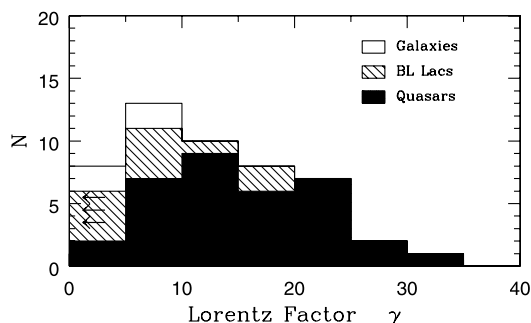
Fig. 9.—Histogram of Lorentz factors for 49 sources, calculated from β_{app} and δ_{var} based on $T_b^{int} = 2 \times 10^{10}$ K.

Fig. 10.—Histogram of the brightest component speed in EGRET-detected and non–EGRET-detected sources for our representative flux density–limited sample.

factors should have a power-law distribution. However, the number of objects is too small and the errors too uncertain to make a meaningful comparison. A small Lorentz factor implies a low velocity and small flux density variations, and the latter especially is less likely to be measurable. However, the calculated Lorentz factors are useful in showing that there must be a wide range of γ in the superluminal sources. The galaxies all have rather low Lorentz factors, while the quasars have a broad distribution up to $\gamma \approx 30$.

4.4.2. Gamma-Ray Sources

Many of the sources included in our study have been cataloged as strong gamma-ray sources according to measurements made by the EGRET detector on board the *Compton Gamma Ray Observatory* (von Montigny et al. 1995; Hartman et al. 1999; Mattox et al. 1997, 2001; Sowards-Emmerd et al. 2003). It is generally thought that the gamma-ray emission occurs deep within the relativistic jet. Arguments based on size limits deduced from time variability and the cross section for pair production suggest that the gamma-ray emission, like the radio emission, is Doppler boosted (Dermer & Schlickeiser 1994). In fact, the gamma rays may be even more strongly beamed than the radio emission since the former generally have a steeper spectral index, α, and the flux density boosting varies as $\delta^{(2-\alpha)}$ for continuous jets. Furthermore, Dermer (1995) has shown that if the bulk of the gamma rays are produced by external Compton scattering off photons associated with the accretion disk, the resulting gamma-ray emission will be boosted by an additional factor of $\delta^{(1-\alpha)}$.

If gamma-ray–loud AGNs do indeed have systematically high Doppler factors, then we might expect to see a different apparent speed distribution for them than for AGNs that have not been detected in gamma rays. The situation is complicated by the possibility that the gamma-ray–loud jets may be seen inside the critical angle for maximizing superluminal motion ($1/\gamma$) and therefore might have slow apparent projected speeds. However, Monte Carlo simulations based on a simple linear relationship between radio and gamma-ray luminosity (e.g., Lister & Marscher 1999; Lister 1999) confirm that in a flux density–limited radio sample, AGNs detected by EGRET should have typically higher speeds than those that were not detected in gamma rays.

Jorstad et al. (2001b) recently measured the apparent speeds of 33 EGRET-detected AGNs. They found a mean value of 16c for the fastest component in each source and concluded that the gamma-ray sources have larger Lorentz factors than the general population of radio sources. However, Jorstad et al.
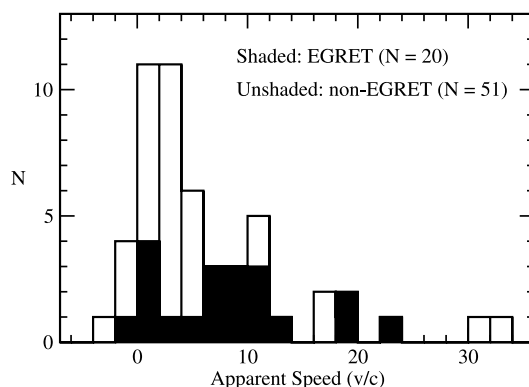
(2001b) did not have a non–gamma-ray control sample observed in the same way and at the same wavelength with which to compare their results.

We have classified our sample into EGRET and non-EGRET sources based on the list of Mattox et al. (2001) and recently modified by Sowards-Emmerd et al. (2003). These authors classify gamma-ray sources from the third EGRET catalog (Hartman et al. 1999) as "highly probable" and "plausible" AGN identifications, based on Bayesian statistics and their proximity to bright flat-spectrum radio sources. In Figure 10 we show the distribution of measured speeds for the EGRET-detected and nondetected sources. For the brightest jet component found in the 18 EGRET sources in our representative sample we found a median speed of $(8.0 \pm 1.6)c$ compared with a value of $(3.9 \pm 1.1)c$ for the 53 sources with no EGRET detections. A K-S test suggests that the difference appears significant at the 90% level. For the purpose of this analysis we have included the two "plausible" EGRET sources, 2230+114 and 1156+295, as detections. Reclassifying them as nondetections had no effect on our results, and neither did excluding the sources with negative velocities from our analysis.

These results are consistent with the idea that the radio emission from gamma-ray quasars is indeed more strongly beamed than for the whole radio quasar population. However, our samples are incomplete and may therefore be biased.

4.5. The Angular Velocity–Redshift Relation

Figure 11 shows the measured values of angular velocity μ versus redshift for the fastest E or G rated component found in the sources in Table 2. The line represents μ_{max}, the fastest proper motion a source can display if it has $\gamma = 25$. The variables are the observables, uncontaminated by modeling, and hence are of value in showing directly that (1) at all redshifts, the observed velocities are not clustered near the maximum value as expected from the simple ballistic models with a single Lorentz factor for all sources, (2) low values of μ are seen at all z, and (3) high values of μ are seen only at low z. This is true for galaxies, BL Lac objects, and quasars and appears inconsistent with noncosmological interpretation of quasar redshifts as proposed by Burbidge (2004).

An early version of this plot (Cohen et al. 1988) was used to show that the standard paradigm for superluminal motion provided a crude upper bound to the points in Figure 11 and

299
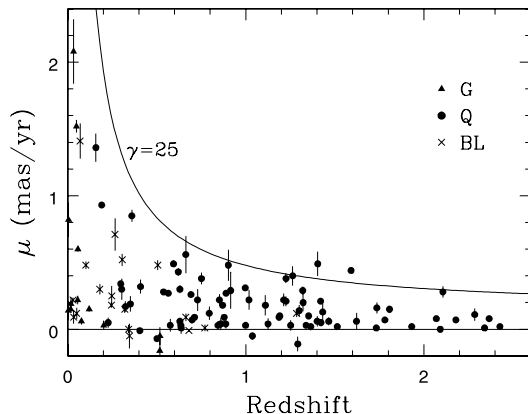
Fig. 11.—The μ-z diagram showing the distribution of angular velocity for the fastest component of the 110 sources that has a quality factor of G or E. The solid line is the maximum value of β_{app} for $\gamma = 25$.

that the maximum value of β_{app} in 32 sources was about 13 ($H_0 = 70$, $q_0 = 0.5$). The μ_{max} line in Figure 11 is, similarly, a crude upper bound to the measured points and shows that $\beta_{app,max} \sim 25$. Note that the cosmology used in this paper makes β_{app} somewhat larger than for a cosmology with $\Omega_m = 1$ and $\Omega_\Lambda = 0$.

The data in Cohen et al. (1988) were compiled at assorted frequencies, mostly below 15 GHz, and corresponded to measurements made at different distances from the core, which may explain the difference in $\beta_{app,max}$. As we have discussed in § 4.2.7, there is some evidence that observations at high frequencies give higher values of μ than observations at lower frequencies.

Vermeulen & Cohen (1994) and Lister & Marscher (1997) have shown that if Doppler boosting is important, then even rather small samples of superluminal sources will show $\beta_{app,max}$ near the maximum value of the distribution of γ, γ_{max}. Hence, we expect that $\gamma_{max} \sim 25$ for the sample shown in Figure 11. This is marginally consistent with Figure 9, reflecting that Lorentz factors calculated according to the method in § 4.4.1 have rather large uncertainties.

5. SUMMARY

We have studied the kinematics of a large well-defined sample of 110 quasar and active galaxy jets and find a distribution of apparent velocities typically between 0 and 14c but ranging up to about 34c. There is evidence of a characteristic velocity in each jet that may represent the true plasma flow velocity. We have found that quasar jets generally have larger apparent velocities than jets associated with BL Lac objects and active galaxies, although the distributions overlap. Our measured values of β_{app} are consistent with the Doppler factors, δ_{var}, calculated from time variability and a parent population having a steep power-law distribution of intrinsic Lorentz factors extending down to moderate velocities and an intrinsic brightness temperature close to 2×10^{10} K. This is close to the value expected if the particle and magnetic energy densities in the jet are comparable (Readhead 1994; Singal & Gopal-Krishna 1985).

In approximately one-third of the well-studied jets, we find evidence of nonballistic motion; that is, the flow is not along the direction away from the core. In most of the jets, we find

no deviation from a constant speed, but in a few sources, we do see evidence of changes in speed and direction of individual features. Mostly, the flow appears to lie along the direction of the local jet orientation. However, in some cases the flow has a significant nonradial component, which points toward more distant parts of the jet. This suggests that there is a continuous flow along a preexisting channel. Contrary to the assumption of the simple unified models, in some jets, the intrinsic flow appears to be with speeds much less than c.

Observations made at higher frequencies sample jet features located closer to the core, and they typically show larger apparent velocities than we observe at 15 GHz, while lower frequency observations show yet smaller speeds. Sources with stable GPS spectra show little or no motion; the jet flow in these sources may be nonrelativistic or lie in the plane of the sky with a correspondingly small Doppler shift.

We find that jets of quasars that have been observed as strong gamma-ray sources have marginally higher speeds than those that are not gamma-ray sources. This is consistent with models where the gamma-ray sources have more highly relativistic jets and are aligned closer to the line of sight. However, our analysis is limited by both small number statistics and the uncertainties in the ever-changing analysis of the EGRET catalogs. In addition, with the limited range of flux density observed by EGRET, there is no well-defined class of gamma-ray–loud and gamma-ray–quiet sources analogous to the radio-loud and radio-quiet classifications. More sensitive observations with the next generation of gamma-ray observatories, such as GLAST, combined with jet speed data for our complete radio sample of 133 radio sources, should be very useful for investigating gamma-ray production mechanisms in AGN jets and relating the gamma-ray properties to the observed jet outflow.

E. Ros et al. (2004, in preparation) have extended these observations and analysis through 2001 and 2002. M. L. Lister et al. (2004, in preparation) have defined a more complete sample of 133 sources and are continuing the observations of these sources including linear and circular polarization (D. C. Homan et al. 2004, in preparation). Observations with this new sample will allow a more robust comparison with models, a better estimate of the distribution of intrinsic Lorentz factors, and a start to understanding the evolution of jet magnetic fields.

REFERENCES

Alef, W., Wu, S. Y., Preuss, E., Kellermann, K. I., & Qiu, Y. H. 1996, A&A, 308, 376
Aller, M. F., Aller, H. D., & Hughes, P. A. 1992, ApJ, 399, 16
———. 2003, in ASP Conf. Ser. 300, Radio Astronomy at the Fringe, ed. J. A. Zensus, M. H. Cohen, & E. Ros (San Francisco: ASP), 159
Barthel, P. D. 1989, ApJ, 336, 606
Beasley, A. J., Gordon, D., Peck, A. B., Petrov, L., MacMillan, D. S., Fomalont, E. B., & Ma, C. 2002, ApJS, 141, 13
Bennett, C. L., et al. 2003, ApJS, 148, 97
Blandford, R. D., & Königl, A. 1979, ApJ, 232, 34
Blandford, R. D., & Rees, M. J. 1974, MNRAS, 169, 395
Britzen, S., Vermeulen, R. C., Taylor, G. B., Campbell, R. M., Browne, I. W. A., Wilkinson, P. N., Pearson, T. J., & Readhead, A. C. S. 2001, in IAU Symp. 205, Galaxies and Their Constituents at the Highest Angular Resolutions, ed. R. T. Schilizzi, S. Vogel, F. Paresce, & M. Elvis (San Francisco: ASP), 106
Britzen, S., Vermeulen, R. C., Taylor, G. B., Pearson, T. J., Readhead, A. C. S., Wilkinson, P. N., & Browne, I. W. A. 1999, in ASP Conf. Ser. 159, BL Lac Phenomenon, ed. L. O. Takalo & A. Sillanpää (San Francisco: ASP), 431
Burbidge, G. 2004, ApJ, 603, 28
Carangelo, N., Falomo, R., Kotilainen, J., Treves, A., & Ulrich, M.-H. 2003, A&A, 412, 651
Cohen, M. H. 1990, in Parsec-scale Radio Jets, ed. J. A. Zensus & T. J. Pearson (Cambridge: Cambridge Univ. Press), 317
Cohen, M. H., Barthel, P. D., Pearson, T. J., & Zensus, J. A. 1988, ApJ, 329, 1
Cohen, M. H., Cannon, W., Purcell, G. H., Shaffer, D. B., Broderick, J. J., Kellermann, K. I., & Jauncey, D. L. 1971, ApJ, 170, 207
Cohen, M. H., et al. 1977, Nature, 268, 405
———. 2003, in ASP Conf. Ser. 300, Radio Astronomy at the Fringe, ed. J. A. Zensus, M. H. Cohen, & E. Ros (San Francisco: ASP), 27
Dallacasa, D., Stanghellini, C., Centonza, M., & Fanti, R. 2000, A&A, 363, 887
Dennett-Thorpe, J., Barthel, P. D., & van Bemmel, I. M. 2000, A&A, 364, 501
Dent, W. A. 1965, Science, 148, 1458
———. 1972, Science, 175, 1105
Dermer, C. D. 1995, ApJ, 446, L63
Dermer, C. D., & Schlickeiser, R. 1994, ApJS, 90, 945
de Vries, W. H., Barthel, P. D., & O'Dea, C. P. 1997, A&A, 321, 105
Ekers, R., & Liang, H. 1990, in Parsec-scale Radio Jets, ed. J. A. Zensus, & T. J. Pearson (Cambridge: Cambridge Univ. Press), 333
Ghisellini, G., Padovani, P., Celotti, A., & Maraschi, L. 1993, ApJ, 407, 65
Guijosa, A., & Daly, R. A. 1996, ApJ, 461, 600
Hartman, R. C., et al. 1999, ApJS, 123, 79
Hirabayashi, H., et al. 1998, Science, 281, 1825
Homan, D. C., Lister, M. L., Kellermann, K. I., Cohen, M. C., Ros, E., Zensus, J. A., Kadler, M., & Vermeulen, R. C. 2003, ApJ, 589, L9
Homan, D. C., Ojha, R., Wardle, J. F. C., Roberts, D. H., Aller, M. F., Aller, H. D., & Hughes, P. A. 2001, ApJ, 549, 840
Hoyle, F., Burbidge, G. R., & Sargent, W. 1966, Nature, 209, 751
Hughes, P. A., Aller, H. D., & Aller, M. F. 1992, ApJ, 396, 469
Istomin, Y. N., & Pariev, V. I. 1996, MNRAS, 281, 1
Jorstad, S. G., Marscher, A. P., Mattox, J. R., Aller, M. F., Aller, H. D., Wehrle, A. E., & Bloom, S. D. 2001a, ApJ, 556, 738
Jorstad, S. G., Marscher, A. P., Mattox, J. R., Wehrle, A. E., Bloom, S. D., & Yurchenko, A. V. 2001b, ApJS, 134, 181
Kellermann, K. I. 2002, Publ. Astron. Soc. Australia, 19, 77
Kellermann, K. I., & Pauliny-Toth, I. I. K. 1969, ApJ, 155, L71
Kellermann, K. I., Vermeulen, R. C., Zensus, J. A., & Cohen, M. H. 1998, AJ, 115, 1295 (Paper I)
———. 2000, in Astrophysical Phenomena Revealed by Space VLBI, ed. H. Hirabayashi, P. G. Edwards, & D. W. Murphy (Sagamihara: ISAS), 159
Kellermann, K. I., et al. 1999, NewA Rev., 43, 757
———. 2003, in ASP Conf. Ser. 299, High Energy Blazar Astronomy, ed. L. O. Takalo & E. Valtaoja (San Francisco: ASP), 117
Kovalev, Y. Y. 2003, in ASP Conf. Ser. 300, Radio Astronomy at the Fringe, ed. J. A. Zensus, M. H. Cohen, & E. Ros (San Francisco: ASP), 65
———. 2004, Baltic Astron., in press
Kovalev, Y. Y., Kovalev, Yu. A., Nizhelsky, N. A., & Bogdantsov, A. V. 2002, Publ. Astron. Soc. Australia, 19, 83

Kovalev, Y. Y., Nizhelsky, N. A., Kovalev, Y. A., Berlin, A. B., Zhekanis, G. V., Mingaliev, M. G., & Bogdantsov, A. V. 1999, A&AS, 139, 545
Kühr, H., Witzel, A., Pauliny-Toth, I. I. K., & Nauber, U. 1981, A&AS, 45, 367
Lähteenmäki, A., & Valtaoja, E. 1999, ApJ, 521, 493
Lähteenmäki, A., Valtaoja, E., & Wiik, K. 1999, ApJ, 511, 112
Lawrence, C. L. 1996, in IAU Symp. 173, Astrophysical Applications of Gravitational Lensing, ed. C. S. Kochanek & J. N. Hewitt (Dordrecht: Kluwer), 299
Lind, K. R., & Blandford, R. D. 1985, ApJ, 295, 358
Lister, M. L. 1999, Ph.D. thesis, Boston Univ.
———. 2001, ApJ, 562, 208
———. 2003, in ASP Conf. Ser. 300, Radio Astronomy at the Fringe, ed. J. A. Zensus, M. H. Cohen, & E. Ros (San Francisco: ASP), 71
Lister, M. L., Kellermann, K. I., & Pauliny-Toth, I. I. K. 2002, in Proc. of the 6th European VLBI Network Symp., ed. E. Ros, R. W. Porcas, A. P. Lobanov, & J. A. Zensus (Bonn: MPIfR), 135
Lister, M. L., Kellermann, K. I., Vermeulen, R. C., Cohen, M. H., Zensus, J. A., & Ros, E. 2003, ApJ, 584, 135
Lister, M. L., & Marscher, A. P. 1997, ApJ, 476, 572
———. 1999, Astropart. Phys., 11, 65
Mattox, J. R., Hartman, R. C., & Reimer, O. 2001, ApJS, 135, 155
Mattox, J. R., Schachter, J., Molnar, L., Hartman, R. C., & Patnaik, A. R. 1997, ApJ, 481, 95
O'Dea, C. P. 1998, PASP, 110, 493
Orr, M. J. L., & Browne, I. W. A. 1982, MNRAS, 200, 1067
Owsianik, I., & Conway, J. E. 1998, A&A, 337, 69
Padovani, P., & Urry, C. M. 1992, ApJ, 387, 449
Pauliny-Toth, I. I. K., & Kellermann, K. I. 1966, ApJ, 146, 634
Readhead, A. C. S. 1994, ApJ, 426, 51
Rees, M. J. 1966, Nature, 211, 468
———. 1967, MNRAS, 135, 345
Ros, E., Kellermann, K. I., Lister, M. L., Zensus, J. A., Cohen, M. H., Vermeulen, R. C., Kadler, M., & Homan, D. C. 2002, in Proc. of the 6th European VLBI Network Symp., ed. E. Ros, R. W. Porcas, A. P. Lobanov, & J. A. Zensus (Bonn: MPIfR), 105
Shaffer, D. B., Kellermann, K. I., & Cornwell, T. J. 1999, ApJ, 515, 558
Sholomitskii, G. B. 1965, AZh, 42, 673 (English transl. in Soviet Astron., 9, 516)
Singal, K. A., & Gopal-Krishna 1985, MNRAS, 215, 383
Sowards-Emmerd, D., Romani, R. W., & Michelson, P. F. 2003, ApJ, 590, 109
Stickel, M., Meisenheimer, K., & Kühr, H. 1994, A&AS, 105, 211
Stickel, M., Rieke, G. H., Kuehr, H., & Rieke, M. J. 1996, ApJ, 468, 556
Taylor, G. B., Vermeulen, R. C., Readhead, A. C. S., Pearson, T. J., Henstock, D. R., & Wilkinson, P. N. 1996, ApJS, 107, 37
Urry, C. M., & Padovani, P. 1995, PASP, 107, 803
Vermeulen, R. C. 1995, Proc. Natl. Acad. Sci., 92, 11385
Vermeulen, R. C., Britzen, S., Taylor, G. B., Pearson, T. J., Readhead, A. C. S., Wilkinson, P. N., & Browne, I. W. A. 2003a, in ASP Conf. Ser. 300, Radio Astronomy at the Fringe, ed. J. A. Zensus, M. H. Cohen, & E. Ros (San Francisco: ASP), 43
Vermeulen, R. C., & Cohen, M. H. 1994, ApJ, 430, 467
Vermeulen, R. C., Ros, E., Kellermann, K. I., Cohen, M. H., Zensus, J. A., & van Langevelde, H. J. 2003b, A&A, 401, 113
Véron-Cetty, M.-P., & Véron, P. 2001, A&A, 374, 92
von Montigny, C., et al. 1995, ApJ, 440, 525
Walker, R. C., Dhawan, V., Romney, J. D., Kellermann, K. I., & Vermeulen, R. C. 2000, ApJ, 530, 233
Wall, J. V., & Jackson, C. A. 1997, MNRAS, 290, L17
Whitney, A. R., et al. 1971, Science, 173, 225
Woltjer, L. 1966, ApJ, 146, 597
Zensus, J. A., Cohen, M. H., & Unwin, S. C. 1995, ApJ, 443, 35
Zensus, J. A., Ros, E., Kadler, M., Kellermann, K. I., Lister, M. L., Homan, D. C., Cohen, M. H., & Vermeulen, R. C. 2003, in ASP Conf. Ser. 300, Radio Astronomy at the Fringe, ed. J. A. Zensus, M. H. Cohen, & E. Ros (San Francisco: ASP), 27
Zensus, J. A., Ros, E., Kellermann, K. I., Cohen, M. H., & Vermeulen, R. C. 2002, AJ, 124, 662 (Paper II)

E   3C 390.3

3C 390.3 is part of the VLBA 2 cm Survey sample but does not belong to the MOJAVE sample and as such not a member of the *2 cm-X-Sample.* Here, its X-ray spectrum is presented because of its relevance in the context of broad iron line emission from radio-loud AGN. Sambruna et al. (1999a) reported that the *ASCA* spectrum of 3C 390.3 can be significantly better approximated by a relativistic iron-line model rather than by a narrow or broad Gaussian line component.

Here, the highest signal-to-noise X-ray spectrum of 3C 390.3 so far obtained, from a 35 ksec *Chandra* observation, is presented. In Fig. E.1, the X-ray spectrum of 3C 390.3 is shown together with its rich large-scale X-ray brightness distribution. Several knots in the north-west and south-east of the nucleus can be found, some of them corresponding to knots or hot-spots in the radio structure.

The comparably flat X-ray spectrum ($\Gamma \sim 1.4$ for a simple absorbed-power-law fit), is best approximated by either an absorbed broken power law or a high-energy-reflected power-law spectrum with an intrinsic photon index of 1.6 to 1.7 in both cases. The residuals (bottom panel at the top right illustration in Fig. E.1) show no obvious evidence for excess iron-line emission. For both models the fit is not improve significantly when an additional line component is added to the model. Thus, the *CHANDRA* data do not support the relativistic iron-line scenario for 3C 390.3.

Decl.(J2000)

CHANDRA (Greyscale)   VLA (Contours)

R.A.(J2000)
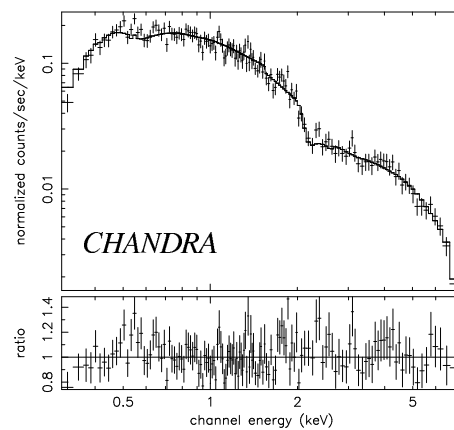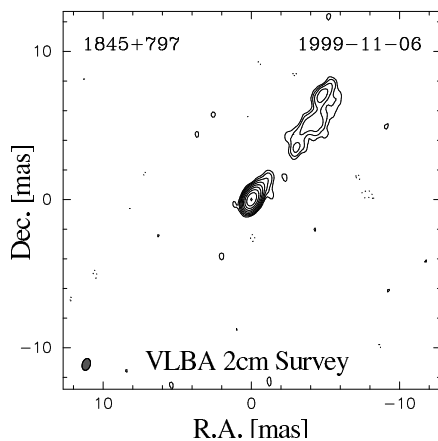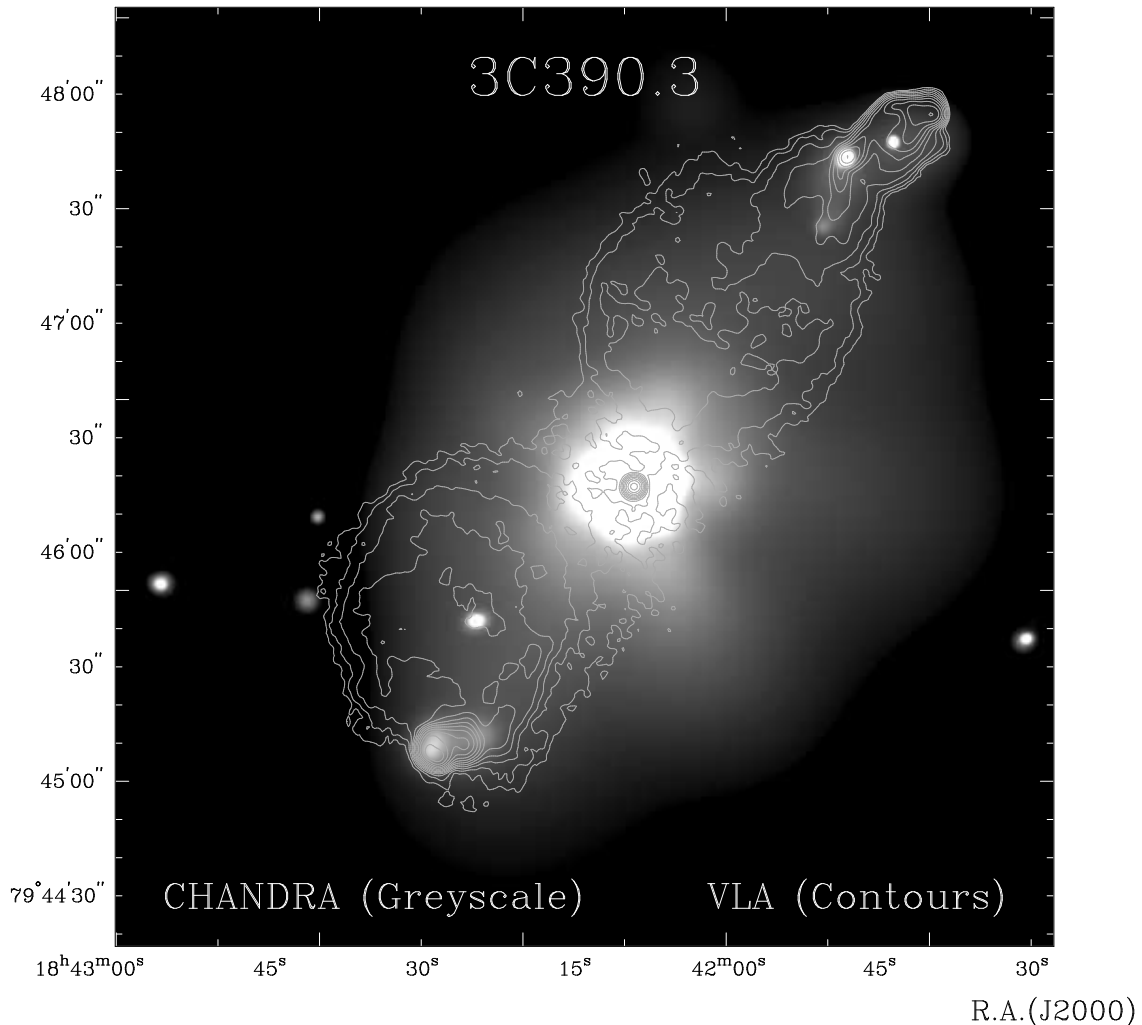
Figure E.1: Top: The kpc-scale radio- and X-ray structure of 3C 390.3. The 1.6 GHz radio jet (taken from the NED archive and previously published by Leahy & Perley Leahy and Perley (1991)) is superimposed on the integrated 0.2 keV to 8 keV X-ray brightness distribution from a 35 ksec *CHANDRA* observation (PI: S. Wagner). Bottom left: The milliarcsecond structure of the nuclear radio jet in November 1999. Bottom right: X-ray spectrum of 3C 390.3 and residuals after subtracting a high-energy-reflected power-law spectrum model.

F Compact Radio Cores in Radio-Quiet Broad-Iron-Line Seyfert Galaxies

F.1 Introduction

The study of relativistically broadened iron lines in the X-ray regime allows the very closest neighborhood of black holes to be explored: their accretion disks. These are thought to provide the "fuel" for the jet production in radio-loud AGN. It is commonly accepted that broad iron lines arise from fluorescent Kα emission when the accretion disks of AGNs are irradiated by hard X-rays from their coronae. Due to the strong relativistic effects in the inner disk, the iron-line profile is broadened and skewed (e.g., Fabian et al. 2000). If measured precisely enough, it reveals properties of the accretion disk, in particular the orientation, extent and emissivity gradient radially outward from the black hole. Accretion events that might trigger enhanced jet-production activity are expected to cause changes in the line profile. Thus, combined jet and broad-iron-line monitoring can in principle disclose the physical processes in accretion disks that lead to jet production.

The apparent lack of significantly broadened iron X-ray emission lines in radio-loud AGN (Sambruna et al. 1999, Gambill et al. 2003), has been explained by either dominant beamed jet components, very high ionization of the disks, or optically-thin, radiatively-inefficient accretion flows (e.g., Fabian et al. 2000a). Contrary to this expectation, in Sect. 6.3.3 the detection of a highly relativistic, broad iron line from the nucleus of the elliptical galaxy NGC 1052 (see Fig. F.1) has been reported. Not only is there a broad line, but a change in the line profile coincides with an epoch of jet-plasma ejection (see Sect. 6.3.4).

At present NGC 1052 is the only strong radio source known for which straightforward observational input can be gained from combined high-angular-resolution VLBI observations and X-ray iron-line monitoring. Thus, it is worthwhile to review the known radio-core properties of the so-called "radio-quiet" broad-iron-line Seyfert galaxies. In this section it is shown that these sources are not so quiet after all at radio wavelengths but comprise a sample suitable for coordinated X-ray and VLBI monitoring.
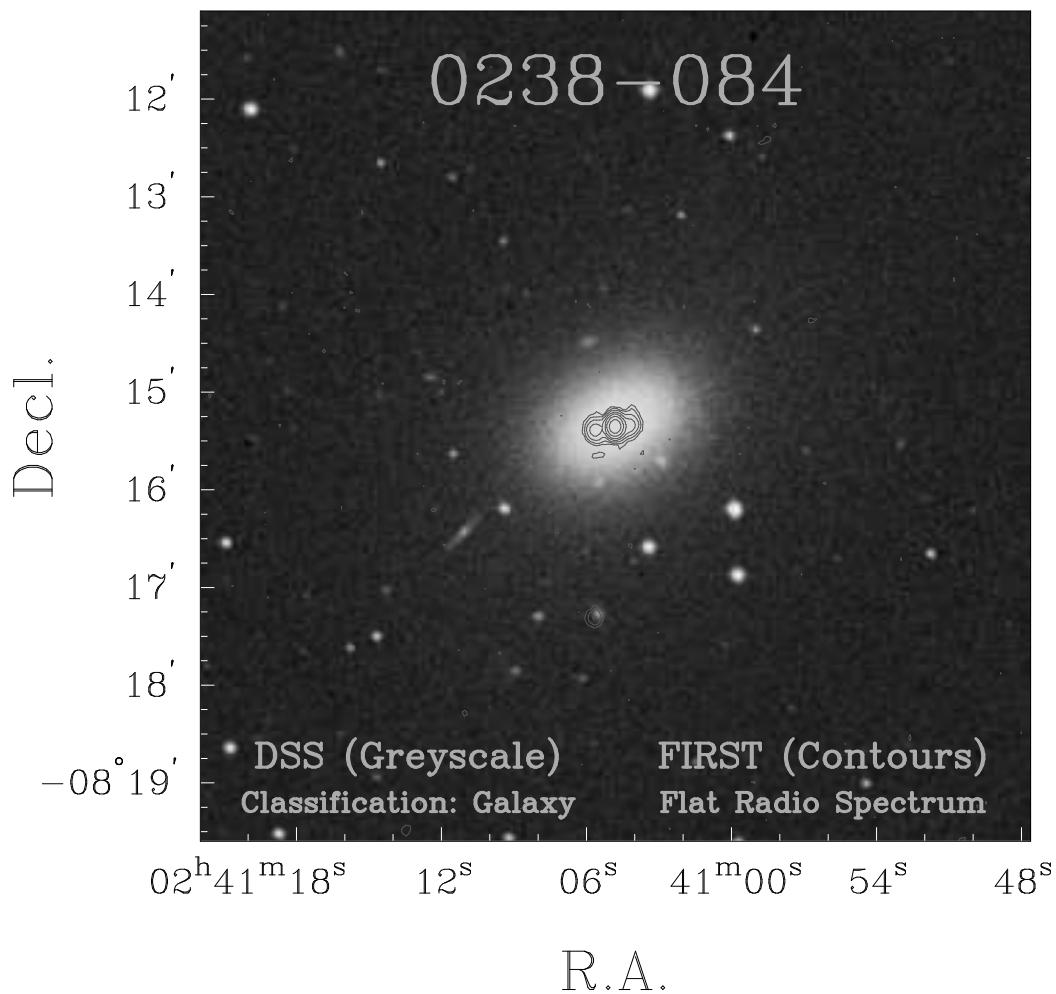
Figure F.1: The kiloparsec-scale radio-jet system of NGC 1052 embedded into its elliptical host galaxy.

F.2   The Compact Radio Cores in Broad-Iron-Line Seyfert Galaxies

After the first detection of an extragalactic broad iron line associated with the Seyfert galaxy MCG −6−30−15 (Tanaka et al. 1995) there followed a boom of follow-up *ASCA* detections in other Seyfert galaxies and relativistic iron lines seemed to become a common ingredient of Seyfert X-ray spectra. However, in several cases *XMM-Newton* could not verify the broad, relativistic red wings. Firm *XMM-Newton* detections of broad iron lines have been reported only for MCG −6−30−15, MCG −5−23−16, NGC 3516, Mrk 335, and Mrk 766 (see Table 1 for references). It is not clear at present, whether insufficient data quality from *ASCA* and over-simplified spectral models have led to the discrepancy between the apparent presence of broad lines in IC 4329a, NGC 4051, NGC 4151, and NGC 5548 or if intrinsic line variability in these sources might have played a crucial
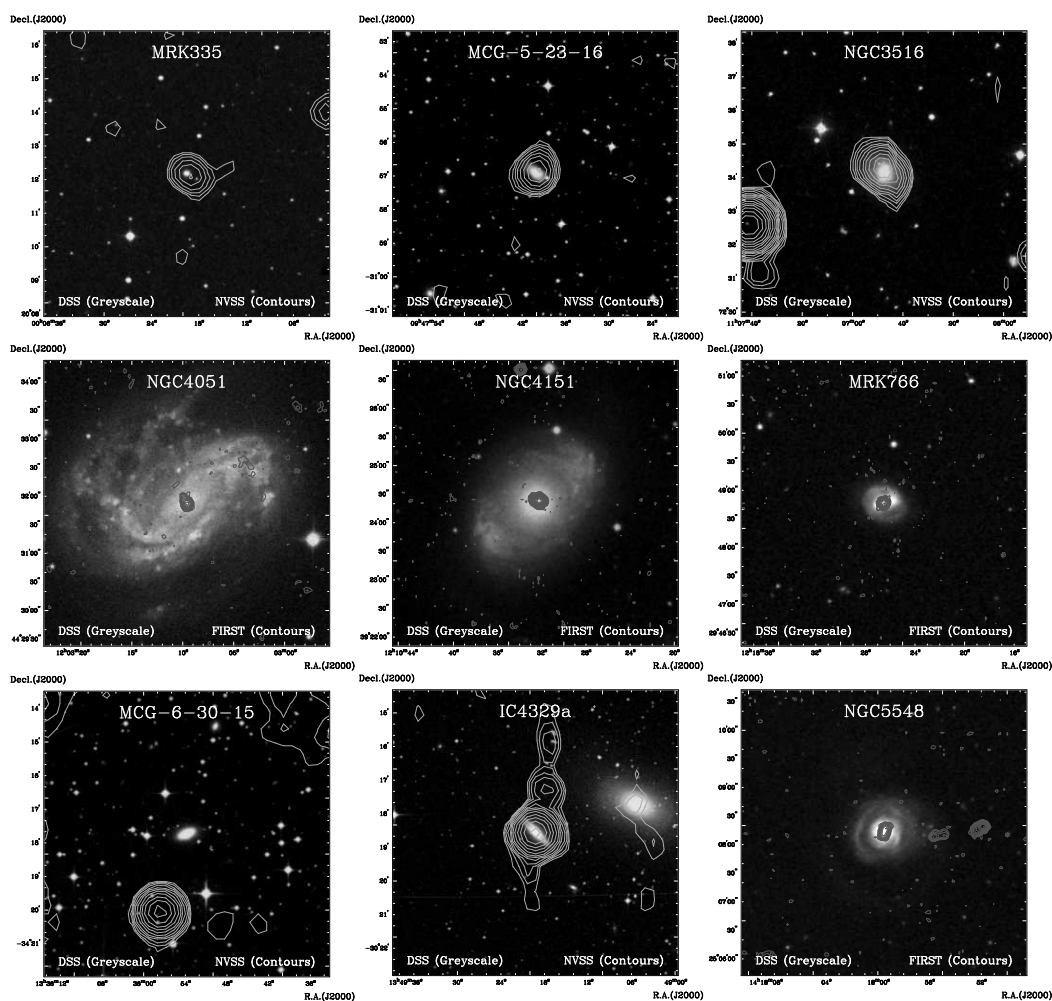
Figure F.2: Compact radio cores in "radio-quiet" Seyfert galaxies. Images display the optical host galaxies (DSS2 data), while contours show the radio structure at 1.4 GHz (FIRST and NVSS data, respectively). Integrated flux densities at $\lambda 6$ cm are given in Table 1.

role. In Fig. F.2 the arcsecond-scale radio structure[1] of those Seyfert galaxies is shown superimposed on optical images from the Digitized Sky Survey[2] compiled by using *Sky View*[3]. All sources in this sample harbor compact radio cores at their centers. Only in the case of MCG $-6-30-15$ does the flux density lie below the detection limit of the NVSS. Several authors, however, report the detection of a weak but possibly highly variable flat-spectrum radio core in MCG $-6-30-15$, e.g., Ulvestad and Wilson (1984) report 1.7 mJy at $\lambda 20$ cm whilst Nagar et al. (1999) measure 4.0 mJy.

---

[1]Where available, we used radio images from the FIRST survey (`http://sundog.stsci.edu`), otherwise we used images from the NVSS (`http://www.cv.nrao.edu/nvss`)

[2]The Digitized Sky Survey was produced at the Space Telescope Science Institute under U.S. Government grant NAG W-2166. The images of these surveys are based on photographic data obtained using the Oschin Schmidt Telescope on Palomar Mountain and the UK Schmidt Telescope. The plates were processed into the present compressed digital form with the permission of these institutions.

[3]`http://skyview.gsfc.nasa.gov`

Table F.1: General radio and X-ray properties of the confirmed and disputed broad-iron-line Seyfert galaxies discussed here.

Source	S_{6cm}^{VLA} [mJy]	$F_{(2-10)\,keV}$ [erg cm^{-2} s^{-1}/10^{11}]	Broad Iron Line	Notes
Mrk 335	4.3[a]	1.7[b]	Yes[c]	Seyfert 1. Steep X-ray continuum with photon index of $\sim$2.3$^{(c)}$. Line profile might indicate a highly ionized, innermost region of the accretion disk around a rotating black hole.
MCG −5−23−16[d]	6.0[a]	7.5[e]	Yes[e]	Seyfert 1.9. Broad iron line emission, variable on timescales of months[e]. Time stable narrow fine-scale features. VLBI-unobserved.
NGC 3516	4.3[a]	5.0[b]	Yes[f]	Narrow fine scale features indicate injection of material with a speed of 0.25 c[f].
NGC 4051	6.0[a]	2.0[b]	Disputed[g,h]	X-ray and radio variability[i]. Correlation between the (accretion dynamics dominated) X-ray flux and the (jet dominated) radio flux.
NGC 4151	125.0[a]	0.2[b]	Disputed[j]	*XMM-Newton* spectrum does not require a relativistically broadened iron line. Narrow and variable Fe line, with amplitude of $\sim$25%. Compact jet[k,l]
Mrk 766	15.8[m]	1.9[b]	Yes[n]	Broadened iron emission lines at 6.4 keV and 6.7 keV. Unconfirmed highly relativistic "red wing"[n]. Blueshifted Fe absorption edge at 8.7 keV, suggesting ejected material at speeds of 15,000 km s^{-1} ($\beta \sim 0.05$). Only barely resolved with VLBI[o]
MCG −6−30−15	1.0[a]	3.8[b]	Yes[p]	The archetypical broad-iron-line galaxy. Broad and variable profile, fine structure[q]. Compact VLA structure. VLBI-unobserved.
IC 4329a	31.5[m]	8.3[b]	Disputed[r]	Disk possibly truncated shortly before reaching the innermost stable orbit around the central black hole[s]. VLBI-unobserved.
NGC 5548	10.5[m]	6.0[t]	Disputed[t]	Soft excess varies more strongly than the high-energy continuum[u]. The spectrum shows reflection and fluorescence from neutral iron distant from the central source[t]. Rapid radio variability[v].

[a] Ulvestad and Wilson (1984); [b] HEASARC website: `http://heasarc.gsfc.nasa.gov/`; [c] Gondoin et al. (2002); [d] see Fabian et al. (2000a) for a review; [e] Dewangan et al. (2003); [f] Turner et al. (2002); [g] Wang et al. (1999); [h] Pounds et al. (2004); [i] McHardy et al. (2004, & priv. comm.); [j] Schurch et al. (2003); [k] Ulvestad et al. (1998); [l] Mundell et al. (2003); [m] Rush et al. (1996); [n] Pounds et al. (2003b); [o] Lal et al. (2004); [p] Fabian et al. (2002); [q] Wang et al. (2004); [r] Gondoin et al. (2001); [s] Done et al. (2000); [t] Pounds et al. (2003a); [u] Done et al. (1995); [v] Wrobel (2000)

Figure F.3 displays the positions in the radio-flux-density vs. X-ray-flux plane[4] of the undisputed broad-iron-line Seyfert galaxies MCG−6−30−15 (Fabian et al. 2002; Wilms et al. 2001), MCG−5−23−16 (Dewangan et al. 2003), NGC 3516 (Turner et al. 2002), Mrk 335 (Gondoin et al. 2002), and Mrk 766 (Pounds et al. 2003a). In addition, the sources IC 4329a (Gondoin et al. 2001; McKernan and Yaqoob 2004), and NGC 4151

---

[4]Fluxes are taken from Fomalont et al. (2000), Giovannini et al. (2001), Gregory and Condon (1991), Morganti et al. (1999), Rush et al. (1996), Sambruna et al. (1999a), Stickel et al. (1994), Ulvestad and Wilson (1984), and the HEASARC website.

(Schurch et al. 2003) are shown, in which *ASCA* detected broad iron lines which could not be confirmed by *XMM-Newton* or are disputed. Finally, the radio-loud sources 3C 120 (Ogle et al. 2005), 3C 273 (Page et al. 2004; Yaqoob and Serlemitsos 2000), 3C 382 (Sambruna et al. 1999a), 3C 390.3 (Sambruna et al. 1999a and Sect. E), and NGC 1052 (see Sect. 6.3) are also plotted. Figure F.3 shows that not only the radio-loud AGN are accessible by VLBI, but also the so-called radio-quiet Seyfert galaxies. In particular, the EVN with its large antennas provides enough sensitivity to image, e.g., the parsec-scale structure of the possibly most interesting broad-iron-line Seyfert galaxy MCG$-6-30-15$, given that it harbors a compact nucleus on milliarcsecond scales.

The qualification of an object being radio-loud or radio-quiet depends crucially on the definition of the actual considered "source" of the radio emission. While, e.g., the integrated single-dish radio flux of NGC 4151 indicates a borderline object, the comparably marginal flux being emitted from the core of the parsec-scale jet of only $\sim$1 mJy reveals a very radio-quiet nucleus. On the other hand, the radio emission of NGC 1052 at 6 cm wavelength is totally dominated by the nuclear radio emission being emitted on milliarcsecond scales. Even the core component of the eastern jet of the nuclear twin-jet system alone is bright enough to make the active galactic nucleus in NGC 1052 radio-loud, while the more classical radio-loudness criterion of Kellermann et al. (1989) that compares the radio with the optical luminosity (including all the star light from the well resolved and nearby host galaxy of this low-luminosity AGN) classifies NGC 1052 as a radio-quiet or at most borderline object. Again, this consideration underlines the importance of a careful sample definition if one aims to investigate statistically the characteristic X-ray peculiarities of jet-forming radio-loud AGN.
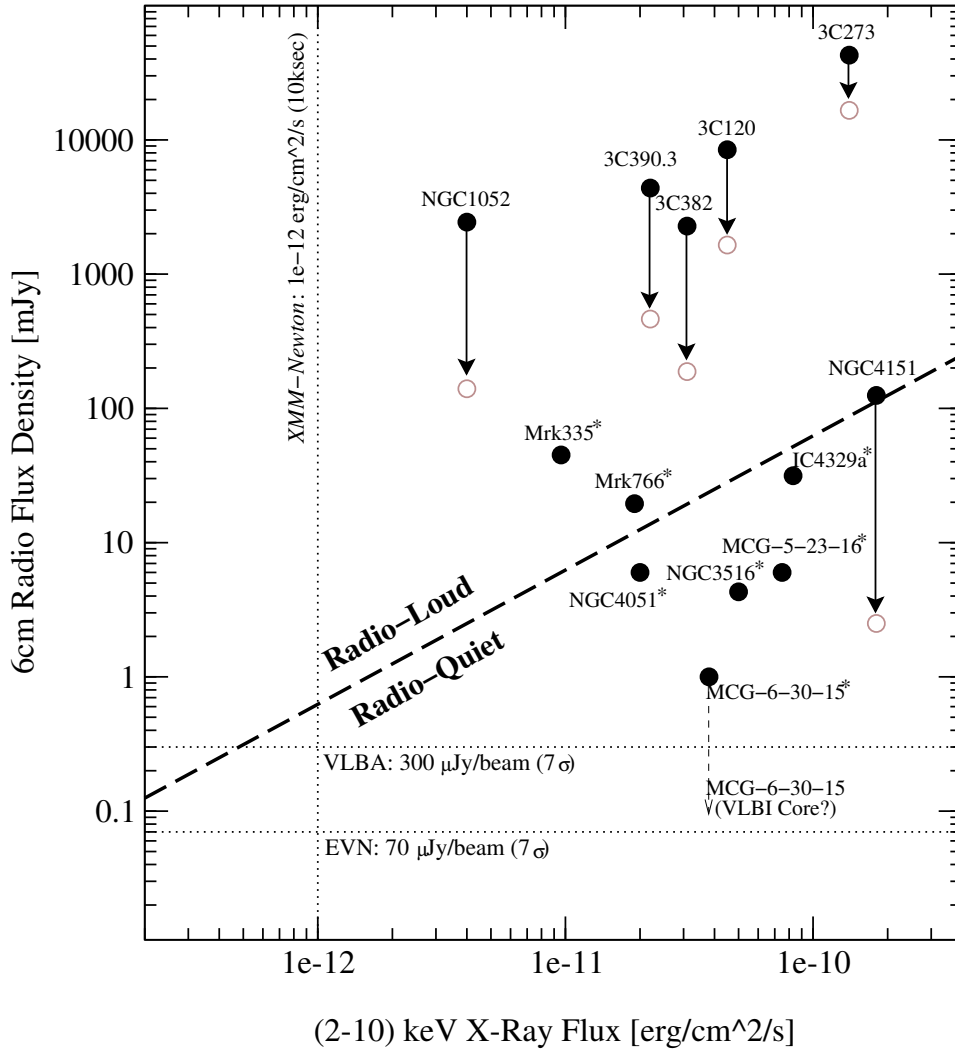
Figure F.3: Radio and X-ray fluxes of confirmed and disputed broad-iron-line AGN systems. The radio-loud/quiet dividing line follows the definition of Terashima and Wilson (2003). The arrows indicate the range from integrated (single-dish: filled circles) flux density to VLBI-core flux density (open circles). Only integrated (VLA) flux densities are given for the radio-quiet objects (marked by an asterisk). The arrow for MCG−6−30−15 indicates that the flux density of the compact core component might be well below the integrated (although compact on VLA scales) value. Approximate sensitivity limits for the EVN, the VLBA, and *XMM-Newton* are shown. The EVN and VLBA limits correspond to deep 5 hour integrations with 1024 Mbps (EVN) and 256 Mbps and a 7σ detection of an unresolved image feature. The *XMM-Newton* limit at $10^{-12}\,\mathrm{erg\,cm^{-2}\,s^{-1}}$ corresponds to the minimal source flux for which a 1000-photon spectrum can be obtained in a 10 ksec pointing.

G Glossary of Acronyms

Many of the acronym explanations are taken from the HEASARC (see below) website (`http://heasarc.gsfc.nasa.gov/`).

- **AO** – 1. (e.g., AO 0235+16) This name prefix indicates sources originally discovered by Arecibo occultation studies (see, e.g., Argue et al. 1973); 2. **A**nnouncement of **O**pportunity to apply for observing time with an astronomical facility. Commonly used in the case of X-ray telescopes (compare **CfP**).

- **ARF** – **A**ncillary **R**esponse **F**ile. Common file extension for data files containing the combined telescope/filter/detector areas and efficiencies as a function of energy averaged over time. Sometimes combined with a RMF file into a single response file (RSP).

- **ASCA** – **A**dvanced **T**elescope for **C**osmology and **A**strophysics. See Tanaka et al. (1994). Japan's fourth X-ray Astronomy mission (1993 – 2001).

- **ACIS** – **A**dvanced **C**amera for **I**maging and **S**pectroscopy. (Formerly *AXAF* CCD **I**maging **S**pectrograph). Detector type onboard *Chandra*. Contains two arrays: a square for imaging (ACIS-I) and a narrower strip, primarily for readout of the diffraction gratings (ACIS-S), particularly the HETG.

- **Astro A** – The pre-launch name for *Hinotori* (Launch: 1981), Japanese for "phoenix". A Japanese satellite, launched to investigate X-rays from the Sun. In this sense, not(!) Japan's first X-ray Astronomy mission, which was *Hakucho*.

- **Astro B** – The pre-launch name for *Tenma*.

- **Astro C** – The pre-launch name for *Ginga*.

- **Astro D** – The pre-launch name for *ASCA*.

- **Astro E** – Planned fifth Japanese X-ray Astronomy mission, which was lost after launch in February 2000. Due to a problem with the first stage of the carrier rocket, *Astro-E* could not obtain the necessary altitude for a proper orbit. As a result, the satellite was declared unusable.

- **Astro E2** – Japan's fifth X-ray Astronomy mission. Recovery mission from the original *ASTRO-E* mission. The pre-launch name for *Suzaku*. See `http://heasarc.gsfc.nasa.gov/docs/astroe/` and links on that website.

- **AXAF** – **A**dvanced *X*-ray **A**strophysics **F**acility. The pre-launch name for *Chandra*.

- **BeppoSax** – Italian/Dutch X-ray astronomy mission (1996 – 2002). See Boella et al. (1997a).

- **CfP** – **C**all **f**or **P**roposals. Commonly used in the case of radio astronomical facility (compare **AO**)

- **Corsa B** – The pre-launch name for *Hakucho*.

- **Chandra** – NASA X-ray astronomy mission (1999 – present). See http://chandra.harvard.edu/.

- **Einstein** – NASA X-ray astronomy mission (1978 – 1981).

- **EPIC** – **E**uropean **P**hoton **I**maging **C**amera. CCD detectors onboard *XMM-Newton*. There are two MOS and one PN detector.

- **EVN** – **E**uropean **VLBI** **N**etwork. The EVN is a collaboration of the major radio astronomical institutes in Europe, Asia and South Africa. See http://www.evlbi.org/.

- **Ginga** – Japan's third X-ray Astronomy mission (1987 – 1991). Japanese for "galaxy".

- **GIS** – **G**as **I**maging **S**pectrometer. See Ohashi et al. (1996). A type of detector on *ASCA*. There are two GISs called GIS2 and GIS3.

- **GSPC** – **G**as **S**cintillation **P**roportional **C**ounter.

- **Hakucho** – Japan's first X-ray Astronomy mission (1979 – 1985). Japanese for "swan".

- **HEAO 1** – The first of NASA's three **H**igh **E**nergy **A**strophysical **O**bservatories (1977 – 1979).

- **HEAO 2** – The second of NASA's three **H**igh **E**nergy **A**strophysical **O**bservatories. Pre-launch name for *Einstein*.

- **HEAO 3** – The third of NASA's three **H**igh **E**nergy **A**strophysical **O**bservatories (1979 – 1981). Survey mission operating in the hard X-ray and gamma-ray band.

- **HEASARC** – **H**igh **E**nergy **A**strophysics **S**cience **A**rchive **R**esearch **C**enter. The primary archive for high-energy astronomy missions, in the extreme ultraviolet, X-ray and gamma-ray wavelengths.

- **HET/HETG** – **H**igh **E**nergy **T**ransmission **G**rating (**S**pectrometer) on *Chandra*. The dispersed spectrum is normally read out by the ACIS-S.

- **HEXTE** – **H**igh **E**nergy **X**-ray **T**iming **E**xperiment. A type of detector on *RXTE*.

- **HRC** – **H**igh **R**esolution **C**amera onboard *Chandra*. Contains two arrays: a square for imaging (HRC-I) and a narrower strip, primarily for readout of the diffraction gratings (HRC-S) especially LETG, and for high time resolution observations using the central element of HRC-S only.

- **LECS** – **L**ow **E**nergy **C**oncentrator **S**pectrometer. A type of detector on *Beppo*Sax. See Parmar et al. (1997).

- **LET/LETG** – **L**ow **E**nergy **T**ransmission **G**rating (**S**pectrometer) on *Chandra*. The dispersed spectrum is normally read out by the HRC-S.

- **MECS** – **M**edium **E**nergy **C**oncentrator **S**pectrometer. A type of detector onboard *Beppo*Sax. See Boella et al. (1997b).

- **MERLIN** – The **M**ulti **E**lement **R**adio **L**inked **I**nterferometer **N**etwork is operated by Jodrell Bank Observatory. See `http://www.jb.man.ac.uk/merlin/`.

- **MOS** – **M**etal **O**xide **S**ilicon. Two of the three EPIC detectors onboard *XMM-Newton* are of the MOS type.

- **NFI** – **N**arrow **F**ield **I**nstruments onboard *Beppo*Sax.

- **Non-Thermal Emission** – Emission with a spectral distribution that does not reproduce the expected shape from a plasma in thermal equilibrium. Examples: synchrotron emission, inverse-Compton emission,...

- **OM** – **O**ptical **M**onitor onboard *XMM-Newton*.

- **PCA** – **P**roportional **C**ounter **A**rray. A type of detector on *RXTE*.

- **PDS** – **P**hoswich **D**etection **S**ystem. A type of detector on *Beppo*Sax. See Frontera et al. (1997).

- **PN** – Detector type onboard *XMM-Newton*. A fully depleted PN CCD.

- **PSPC** – **P**osition **S**ensitive **P**roportional **C**ounter. A type of detector on *ROSAT*.

- **RGS** – **R**eflection **G**rating **S**pectrometer onboard *XMM-Newton*.

- **RMF** – **R**edistribution **M**atrix **F**ile. Common file extension for data files containing information on the non-perfect detector properties. Neccessary to translate detector channels into energy bins. Sometimes combined with a ARF file into a single response file (RSP).

- **ROSAT** – From the German word *Röntgensatellit*. German/British/US X-ray observatory (1990 – 1999). See `http://wave.xray.mpe.mpg.de/rosat/` and links on that website.

- **RXTE** – **R**ossi **X**-ray **T**iming **E**xplorer (1995 – present). See `http://heasarc.gsfc.nasa.gov/docs/xte/`.

- **SAX** – Italian for **S**atellite per **A**stronomia **X**. The pre-launch name for *Beppo*Sax.

- **SIS** – **S**olid-state **I**maging **S**pectrometer. See Gendreau (1995). A type of detector on *ASCA*. There are two SISs called SIS0 and SIS1.

- **SNR** – Signal-to-noise ratio.

- **Suzaku** – Japan's fifth X-ray Astronomy mission. Recovery mission from the *ASTRO-E* mission. Launched in 2005. Red sparrow like bird in Chinese mythology.

- **Tenma** – Japan's second X-ray Astronomy mission (1983 – 1985). Japanese for "Pegasus".

- **Thermal Emission** – Emission from a Plasma that can be fully described by its temperature. See Sect. 2.1.1, Page 15.

- **VLA** – **V**ery **L**arge **A**rray (Napier et al. 1983). See http://www.vla.nrao.edu/.

- **VLBA** – **V**ery **L**ong **B**aseline **A**rray. The VLBA is a national research facility, funded by the National Science Foundation. See http://www.vlba.nrao.edu/.

- **VLBI** – **V**ery **L**ong **B**aseline **I**nterferometry. See Kellermann and Moran (2001) for a review on the history of VLBI

- **Warm Absorber** — This term, introduced by Halpern (1984), denote X-ray absorption by partially ionized, optically thin material, along the line of sight to AGN. Most prominent are often the O VII and O VIII absorption edges at rest energies of 0.74 keV and 0.87 keV, respectively.

- **XMM-Newton** – **X**-ray **M**ulti-**M**irror Mission. ESA X-ray observatory (1999 – present). See http://xmm.vilspa.esa.es/.

- **XTE** – The pre-launch name of *RXTE*.

- **WFC** – **W**ide **F**ield **C**amera onboard *Beppo*Sax.

Bibliography

Abraham, Z., 2000, Precession, beaming and the periodic light curve of OJ287, Astron. & Astrophys., 355, 915–921

Agudo, I., Gómez, J., Martí, J., Ibáñez, J., Marscher, A. P., Alberdi, A., Aloy, M., Hardee, P. E., 2001, Jet Stability and the Generation of Superluminal and Stationary Components, Astrophys. J., 549, L183–L186

Agudo, I., Gómez, J. L., Gabuzda, D. C., Alberdi, A., Marscher, A. P., Jorstad, S. G., 2002, Multi-frequency VLBI observations of the BL Lac 0735+178, in Proceedings of the 6th EVN Symposium, p. 115

Akritas, M. G., Siebert, J., 1996, A test for partial correlation with censored astronomical data, Monthly Not. Roy. Astron. Soc., 278, 919–924

Alef, W., Preuss, E., Kellermann, K. I., Gabuzda, D., 1998, Sub-milliarcsec Structure of 3C 111 at 0.7 and 3.6 CM, in ASP Conf. Ser. 144: IAU Colloq. 164: Radio Emission from Galactic and Extragalactic Compact Sources, p. 129

Aller, M. F., Aller, H. D., Hughes, P. A., Latimer, G. E., 1999, Centimeter-Wavelength Total Flux and Linear Polarization Properties of Radio-loud BL Lacertae Objects, Astrophys. J., 512, 601–622

Aller, M. F., Aller, H. D., Hughes, P. A., 2003, Survey of Variability, in Astronomical Society of the Pacific Conference Series, p. 159

Antonucci, R. R. J., 1986, Deep radio maps of BL Lacertae and 3C 446, Astrophys. J., 304, 634–636

Argue, A. N., Kenworthy, C. M., Stewart, P. M., 1973, Optical Positions for 24 Radio Sources, Astrophys. Let., 14, 99

Arshakian, T. G., Chavushyan, V. H., Ros, E., Kadler, M., Zensus, J. A., 2005, Radio-optical scrutiny of the central engine in compact AGN, Memorie della Societa Astronomica Italiana, 76, 35

Aschenbach, B., 1985, X-ray telescopes, Reports of Progress in Physics, 48, 579–629

Bach, U., Krichbaum, T. P., Ros, E., Britzen, S., Tian, W. W., Kraus, A., Witzel, A., Zensus, J. A., 2005, Kinematic study of the blazar S5 0716+714, Astron. & Astrophys., 433, 815–825

Baker, J. C., Hunstead, R. W., Brinkmann, W., 1995, Radio and X-ray beaming in steep-spectrum quasars, Monthly Not. Roy. Astron. Soc., 277, 553–560

Ballo, L., Maraschi, L., Tavecchio, F., Celotti, A., Fossati, G., Ghisellini, G., Pian, E., Raiteri, C. M., Tagliaferri, G., Treves, A., Urry, C. M., Villata, M., 2002, Spectral Energy Distributions of 3C 279 Revisited: BeppoSAX Observations and Variability Models, Astrophys. J., 567, 50–57

Bania, T. M., Marscher, A. P., Barvainis, R., 1991, Observations of local interstellar CO toward four compact extragalactic radio sources, Astron. J., 101, 2147–2150

Bechtold, J., Siemiginowska, A., Aldcroft, T. L., Elvis, M., Dobrzycki, A., 2001, Chandra Detection of X-Ray Absorption Associated with a Damped Lyα System, Astrophys. J., 562, 133–138

Belsole, E., Sauvageot, J. L., Böhringer, H., Worrall, D. M., Matsushita, K., Mushotzky, R. F., Sakelliou, I., Molendi, S., Ehle, M., Kennea, J., Stewart, G., Vestrand, W. T., 2001, An XMM-Newton study of the sub-structure in M 87's halo, Astron. & Astrophys., 365, L188–L194

Best, P. N., Peacock, J. A., Brookes, M. H., Dowsett, R. E., Röttgering, H. J. A., Dunlop, J. S., Lehnert, M. D., 2003, The final two redshifts for radio sources from the equatorial BRL sample, Monthly Not. Roy. Astron. Soc., 346, 1021–1024

Biermann, P., Duerbeck, H., Eckart, A., Fricke, K., Johnston, K. J., Kuhr, H., Liebert, J., Pauliny-Toth, I. I. K., Schleicher, H., Stockman, H., Strittmatter, P. A., Witzel, A., 1981, Observations of six flat spectrum sources from the 5 GHz survey, Astrophys. J., 247, L53–L56

Blandford, R. D., Königl, A., 1979, "relativistic jets as compact radio sources", Astrophys. J., 232, 34–48

Boella, G., Butler, R. C., Perola, G. C., Piro, L., Scarsi, L., Bleeker, J. A. M., 1997a, BeppoSAX, the wide band mission for X-ray astronomy, Astron. &. Astrophys. Suppl., 122, 299–307

Boella, G., Chiappetti, L., Conti, G., Cusumano, G., del Sordo, S., La Rosa, G., Maccarone, M. C., Mineo, T., Molendi, S., Re, S., Sacco, B., Tripiciano, M., 1997b, The medium-energy concentrator spectrometer on board the BeppoSAX X-ray astronomy satellite, Astron. &. Astrophys. Suppl., 122, 327–340

Briggs, F. H., Wolfe, A. M., Liszt, H. S., Davis, M. M., Turner, K. L., 1989, The spatial extent of the Z = 2.04 absorber in the spectrum of PKS 0458-020, Astrophys. J., 341, 650–657

Brinkmann, W., Siebert, J., Feigelson, E. D., Kollgaard, R. I., Laurent-Muehleisen, S. A., Reich, W., Fuerst, E., Reich, P., Voges, W., Truemper, J., McMahon, R., 1997a, Radio-loud active galaxies in the northern ROSAT All-Sky Survey. II. Multi-frequency properties of unidentified sources., Astron. & Astrophys., 323, 739–748

Brinkmann, W., Yuan, W., Siebert, J., 1997b, Broad band energy distribution of ROSAT detected quasars. I. Radio-loud objects., Astron. & Astrophys., 319, 413–429

Brinkmann, W., Papadakis, I. E., den Herder, J. W. A., Haberl, F., 2003, Temporal variability of Mrk 421 from XMM-Newton observations, Astron. & Astrophys., 402, 929–947

Brunthaler, A., Falcke, H., Bower, G. C., Aller, M. F., Aller, H. D., Teräsranta, H., Lobanov, A. P., Krichbaum, T. P., Patnaik, A. R., 2000, III Zw 2, the first superluminal jet in a Seyfert galaxy, Astron. & Astrophys., 357, L45–L48

Cappi, M., Matsuoka, M., Comastri, A., Brinkmann, W., Elvis, M., Palumbo, G. G. C., Vignali, C., 1997, ASCA and ROSAT X-Ray Spectra of High-Redshift Radio-loud Quasars, Astrophys. J., 478, 492

Carangelo, N., Falomo, R., Kotilainen, J., Treves, A., Ulrich, M.-H., 2003, Optical spectroscopy of BL Lac objects: New redshifts and mis-identified sources, Astron. & Astrophys., 412, 651–655

Carswell, R. F., Strittmatter, P. A., Williams, R. E., Kinman, T. D., Serkowski, K., 1974, Optical Observations of the Radio Source 0735+178, Astrophys. J., 190, L101+

Castander, F. J., Treister, E., Maza, J., Coppi, P. S., Maccarone, T. J., Zepf, S. E., Guzmán, R., Ruiz, M. T., 2003, The CYDER survey: first results, Astronomische Nachrichten, 324, 40–43

Chen, Y. J., Zhang, F. J., Sjouwerman, L. O., 1999, Is the jet of AO 0235+164 rotating?, New Astronomy Review, 43, 707–710

Chu, L. B., Baath, F. T., Rantakyroe, F. J., Zhang, H. S., Nicholson, G., 1996, VLBI observations of the puzzling BL Lacertae object 0235+164., Astron. & Astrophys., 307, 15

Churazov, E., Forman, W., Jones, C., Sunyaev, R., Böhringer, H., 2004, XMM-Newton observations of the Perseus cluster - II. Evidence for gas motions in the core, Monthly Not. Roy. Astron. Soc., 347, 29–35

Cohen, M., Russo, M., Homan, D., Kellermann, K., Lister, M., Vermeulen, R., Ros, E., Zensus, A., 2003a, Compact Sources: Velocity and Variability, Quasar Cores and Jets, 25th meeting of the IAU, Joint Discussion 18, 23-24 July 2003, Sydney, Australia, 18

Cohen, M. H., Russo, M. A., Homan, D. C., Kellermann, K. I., Lister, M. L., Vermeulen, R. C., Ros, E., Zensus, J. A., 2003b, Variability and Velocity of Superluminal Sources, in Astronomical Society of the Pacific Conference Series, p. 177

Comastri, A., Setti, G., Zamorani, G., Elvis, M., Wilkes, B. J., McDowell, J. C., Giommi, P., 1992, EXOSAT X-ray spectra of quasars, Astrophys. J., 384, 62–71

Comastri, A., Fossati, G., Ghisellini, G., Molendi, S., 1997, On the Soft X-Ray Spectra of gamma -loud Blazars, Astrophys. J., 480, 534

Czerny, B., Elvis, M., 1987, Constraints on quasar accretion disks from the optical/ultraviolet/soft X-ray big bump, Astrophys. J., 321, 305–320

Davis, J. E., 2001, Event Pileup in Charge-coupled Devices, Astrophys. J., 562, 575–582

Dennett-Thorpe, J., de Bruyn, A. G., 2000, The Discovery of a Microarcsecond Quasar: J1819+3845, Astrophys. J., 529, L65–L68

Dewangan, G. C., Griffiths, R. E., Schurch, N. J., 2003, XMM-Newton Observations of Broad Iron Kα Emission from Seyfert 1.9 Galaxy MCG -5-23-16, Astrophys. J., 592, 52–61

Dickey, J. M., Lockman, F. J., 1990, H I in the Galaxy, Annu. Rev. Astron. Astrophys., 28, 215–261

Donato, D., Ghisellini, G., Tagliaferri, G., Fossati, G., 2001, Hard X-ray properties of blazars, Astron. & Astrophys., 375, 739–751

Donato, D., Gliozzi, M., Sambruna, R. M., Pesce, J. E., 2003, Chandra observations of the X-ray environment of BL Lacs, Astron. & Astrophys., 407, 503–513

Donato, D., Sambruna, R. M., Gliozzi, M., 2005, Six years of BeppoSAX observations of blazars: A spectral catalog, Astron. & Astrophys., 433, 1163–1169

Done, C., Pounds, K. A., Nandra, K., Fabian, A. C., 1995, The complex variable soft X-ray spectrum of NGC 5548, Monthly Not. Roy. Astron. Soc., 275, 417–428

Done, C., Madejski, G. M., Życki, P. T., 2000, The Relativistic Iron Line Profile in the Seyfert 1 Galaxy IC 4329A, Astrophys. J., 536, 213–224

Drinkwater, M. J., Webster, R. L., Francis, P. J., Condon, J. J., Ellison, S. L., Jauncey, D. L., Lovell, J., Peterson, B. A., Savage, A., 1997, The Parkes Half-Jansky Flat-Spectrum Sample, Monthly Not. Roy. Astron. Soc., 284, 85–125

Eckart, A., Witzel, A., Biermann, P., Johnston, K. J., Simon, R., Schalinski, C., Kuhr, H., 1986, Investigation of a complete sample of flat spectrum radio sources from the S5 survey, Astron. & Astrophys., 168, 17–24

Ezawa, H., Yamasaki, N. Y., Ohashi, T., Fukazawa, Y., Hirayama, M., Honda, H., Kamae, T., Kikuchi, K., Shibata, R., 2001, ASCA Observations of the Temperature Structure and Metal Distribution in the Perseus Cluster of Galaxies, Publ. Astron. Soc. Japan, 53, 595–604

Fabian, A. C., Iwasawa, K., Reynolds, C. S., Young, A. J., 2000a, Broad Iron Lines in Active Galactic Nuclei, Publ. Astron. Soc. Pacific, 112, 1145–1161

Fabian, A. C., Sanders, J. S., Ettori, S., Taylor, G. B., Allen, S. W., Crawford, C. S., Iwasawa, K., Johnstone, R. M., Ogle, P. M., 2000b, Chandra imaging of the complex X-ray core of the Perseus cluster, Monthly Not. Roy. Astron. Soc., 318, L65–L68

Fabian, A. C., Ballantyne, D. R., Merloni, A., Vaughan, S., Iwasawa, K., Boller, T., 2002, How the X-ray spectrum of a narrow-line Seyfert 1 galaxy may be reflection-dominated, Monthly Not. Roy. Astron. Soc., 331, L35–L39

Fabian, A. C., Sanders, J. S., Allen, S. W., Crawford, C. S., Iwasawa, K., Johnstone, R. M., Schmidt, R. W., Taylor, G. B., 2003, A deep Chandra observation of the Perseus cluster: shocks and ripples, Monthly Not. Roy. Astron. Soc., 344, L43–L47

Falcke, H., 2001, The Silent Majority – Jets and Radio Cores from Low-Luminosity Black Holes, Reviews of Modern Astronomy, 14, 15

Falcke, H., Biermann, P. L., 1995, "the jet-disk symbiosis. i. radio to x-ray emission models for quasars.", Astron. & Astrophys., 293, 665–682

Falomo, R., 1996, Host galaxy and close environment of BL Lacertae objects., Monthly Not. Roy. Astron. Soc., 283, 241–250

Fang, T., Marshall, H. L., Bryan, G. L., Canizares, C. R., 2001, Chandra Observations of Two High-Redshift Quasars, Astrophys. J., 555, 356–363

Feigelson, E. D., Berg, C. J., 1983, X-ray observations of 20 3CR radio galaxies and their environs, Astrophys. J., 269, 400–415

Fey, A. L., Charlot, P., 1997, VLBA Observations of Radio Reference Frame Sources. II. Astrometric Suitability Based on Observed Structure, Astrophys. J. Suppl., 111, 95

Fey, A. L., Charlot, P., 2000, VLBA Observations of Radio Reference Frame Sources. III. Astrometric Suitability of an Additional 225 Sources, Astrophys. J. Suppl., 128, 17–83

Fey, A. L., Clegg, A. W., Fomalont, E. B., 1996, VLBA Observations of Radio Reference Frame Sources. I., Astrophys. J. Suppl., 105, 299

Fiore, F., Guainazzi, M., Grandi, P., 1999, Cookbook for BeppoSAX NFI Spectral Analysis, v. 1.2.,

Fomalont, E. B., Frey, S., Paragi, Z., Gurvits, L. I., Scott, W. K., Taylor, A. R., Edwards, P. G., Hirabayashi, H., 2000, The VSOP 5 GHZ Continuum Survey: The Prelaunch VLBA Observations, Astrophys. J. Suppl., 131, 95–183

Fossati, G., Maraschi, L., Celotti, A., Comastri, A., Ghisellini, G., 1998, A unifying view of the spectral energy distributions of blazars, Monthly Not. Roy. Astron. Soc., 299, 433–448

Fossati, G., Celotti, A., Chiaberge, M., Zhang, Y. H., Chiappetti, L., Ghisellini, G., Maraschi, L., Tavecchio, F., Pian, E., Treves, A., 2000, X-Ray Emission of Markarian 421: New Clues from Its Spectral Evolution. II. Spectral Analysis and Physical Constraints, Astrophys. J., 541, 166–179

Frey, S., Gurvits, L. I., Altschuler, D. R., Davis, M. M., Perillat, P., Salter, C. J., Aller, H. D., Aller, M. F., Hirabayashi, H., 2000, Dual-Frequency VSOP Observations of AO 0235+164, Publ. Astron. Soc. Japan, 52, 975–

Frontera, F., Costa, E., dal Fiume, D., Feroci, M., Nicastro, L., Orlandini, M., Palazzi, E., Zavattini, G., 1997, The high energy instrument PDS on-board the BeppoSAX X–ray astronomy satellite, Astron. &. Astrophys. Suppl., 122, 357–369

Gómez, J., Marscher, A. P., Alberdi, A., Gabuzda, D. C., 1999, The Twisted Parsec-Scale Structure of 0735+178, Astrophys. J., 519, 642–646

Gómez, J., Marscher, A. P., Alberdi, A., Jorstad, S. G., Agudo, I., 2001a, Monthly 43 GHz VLBA Polarimetric Monitoring of 3C 120 over 16 Epochs: Evidence for Trailing Shocks in a Relativistic Jet, Astrophys. J., 561, L161–L164

Gómez, J. L., Marscher, A. P., Alberdi, A., Jorstad, S. G., García-Miró, C., 2000, Flashing Superluminal Components in the Jet of the Radio Galaxy 3C120, Science, 289, 2317–2320

Gómez, J. L., Guirado, J. C., Agudo, I., Marscher, A. P., Alberdi, A., Marcaide, J. M., Gabuzda, D. C., 2001b, Changes in the trajectory of the radio jet in 0735+178?, Monthly Not. Roy. Astron. Soc., 328, 873–881

Gabel, J. R., Bruhweiler, F. C., Crenshaw, D. M., Kraemer, S. B., Miskey, C. L., 1999, The Ionization Mechanism of LINER Galaxy NGC1052, Bulletin of the American Astronomical Society, 31, 893

Gabuzda, D. C., Kollgaard, R. I., Roberts, D. H., Wardle, J. F. C., 1993, Is 1308+326 A BL Lacertae object or a quasar?, Astrophys. J., 410, 39–43

Gabuzda, D. C., Kovalev, Y. Y., Krichbaum, T. P., Alef, W., Kraus, A., Witzel, A., Quirrenbach, A., 1998, VLBI polarization observations of the rapidly variable BL Lacertae object BL 0716+714, Astron. & Astrophys., 333, 445–451

Gabuzda, D. C., Pushkarev, A. B., Cawthorne, T. V., 1999, The lambda=6cm VLBI polarization structure of nine BL Lacertae objects, Monthly Not. Roy. Astron. Soc., 307, 725–736

Gabuzda, D. C., Gómez, J. L., Agudo, I., 2001, Evidence for parsec-scale absorption from VSOP observations of the BL Lacertae object 0735+178, Monthly Not. Roy. Astron. Soc., 328, 719–725

Galbiati, E., Caccianiga, A., Maccacaro, T., Braito, V., Della Ceca, R., Severgnini, P., Brunner, H., Lehmann, I., Page, M. J., 2005, XMM-Newton spectroscopy of an X-ray selected sample of RL AGNs, Astron. & Astrophys., 430, 927–940

Gambill, J. K., Sambruna, R. M., Chartas, G., Cheung, C. C., Maraschi, L., Tavecchio, F., Urry, C. M., Pesce, J. E., 2003, Chandra observations of nuclear X-ray emission from a sample of radio sources, Astron. & Astrophys., 401, 505–517

Gendreau, K. C., 1995, X-Ray Ccds for Space Applications: Calibration, Radiation Hardness, and Use for Measuring the Spectrum of the Cosmic X-Ray Background, Ph.D. Thesis

George, I. M., Nandra, K., Turner, T. J., Celotti, A., 1994, The X-ray spectrum of the highly polarized quasar PKS 1502+106, Astrophys. J., 436, L59–L62

George, I. M., Turner, T. J., Yaqoob, T., Netzer, H., Laor, A., Mushotzky, R. F., Nandra, K., Takahashi, T., 2000, X-Ray Observations of Optically Selected, Radio-quiet Quasars. I. The ASCA Results, Astrophys. J., 531, 52–80

Ghisellini, G., Madau, P., 1996, On the origin of the gamma-ray emission in blazars, Monthly Not. Roy. Astron. Soc., 280, 67–76

Ghisellini, G., Costamante, L., Tagliaferri, G., Maraschi, L., Celotti, A., Fossati, G., Pian, E., Comastri, A., de Francesco, G., Lanteri, L., Raiteri, C. M., Sobrito, G., Villata, M., Glass, I. S., Grandi, P., Perola, C., Treves, A., 1999, The blazar PKS 0528+134: new results from BeppoSAX observations, Astron. & Astrophys., 348, 63–70

Ghosh, K. K., Soundararajaperumal, S., 1995, Multifrequency Spectra of EXOSAT Blazars, Astrophys. J. Suppl., 100, 37

Giommi, P., Massaro, E., Chiappetti, L., Ferrara, E. C., Ghisellini, G., Jang, M., Maesano, M., Miller, H. R., Montagni, F., Nesci, R., Padovani, P., Perlman, E., Raiteri, C. M., Sclavi, S., Tagliaferri, G., Tosti, G., Villata, M., 1999, Synchrotron and inverse Compton variability in the BL Lacertae object S5 0716+714, Astron. & Astrophys., 351, 59–64

Giovannini, G., Cotton, W. D., Feretti, L., Lara, L., Venturi, T., 2001, VLBI Observations of a Complete Sample of Radio Galaxies: 10 Years Later, Astrophys. J., 552, 508–526

Goetz, M. M. A., Preuss, E., Alef, W., Kellermann, K. I., 1987, Strong structural variability in the lobe-dominated radio galaxy 3 C 111, Astron. & Astrophys., 176, 171–174

Gondoin, P., Barr, P., Lumb, D., Oosterbroek, T., Orr, A., Parmar, A. N., 2001, Simultaneous XMM-Newton and BeppoSAX observation of the Seyfert I galaxy IC 4329A, Astron. & Astrophys., 378, 806–816

Gondoin, P., Orr, A., Lumb, D., Santos-Lleo, M., 2002, XMM-Newton observations of the Seyfert 1 galaxy Mrk 335, Astron. & Astrophys., 388, 74–87

Grandi, P., Palumbo, G. G. C., 2004, Jet and Accretion-Disk Emission Untangled in 3C 273, Science, 306, 998–1002

Green, R. F., Khachikian, E. Y., Sanders, D. B. (Eds.), 2002, IAU Colloquium 184: AGN Surveys

Gregory, P. C., Condon, J. J., 1991, The 87GB catalog of radio sources covering delta between O and + 75 deg at 4.85 GHz, Astrophys. J. Suppl., 75, 1011–1291

Guainazzi, M., Antonelli, L. A., 1999, The flat X-ray spectrum of the LINER NGC 1052, Monthly Not. Roy. Astron. Soc., 304, L15–L19

Guainazzi, M., Oosterbroek, T., Antonelli, L. A., Matt, G., 2000, On the hypothesis of an advection-dominated flow in the core of NGC 1052: new constraints from a BeppoSAX observation, Astron. & Astrophys., 364, L80–L84

Haardt, F., Maraschi, L., 1993, X-ray spectra from two-phase accretion disks, Astrophys. J., 413, 507–517

Halpern, J. P., 1984, Variable X-ray absorption in the QSO MR 2251 - 178, Astrophys. J., 281, 90–94

Hartman, R. C., Bertsch, D. L., Bloom, S. D., Chen, A. W., Deines-Jones, P., Esposito, J. A., Fichtel, C. E., Friedlander, D. P., Hunter, S. D., McDonald, L. M., Sreekumar, P., Thompson, D. J., Jones, B. B., Lin, Y. C., Michelson, P. F., Nolan, P. L., Tompkins, W. F., Kanbach, G., Mayer-Hasselwander, H. A., Mücke, A., Pohl, M., Reimer, O., Kniffen, D. A., Schneid, E. J., von Montigny, C., Mukherjee, R., Dingus, B. L., 1999, The Third EGRET Catalog of High-Energy Gamma-Ray Sources, Astrophys. J. Suppl., 123, 79–202

Hartmann, D., Burton, W. B., 1997, Atlas of galactic neutral hydrogen, Cambridge; New York: Cambridge University Press, ISBN 0521471117

Hazard, C., Mackey, M. B., Shimmins, A. J., 1963, Investigation of the Radio Source 3C273 by the method of Lunar Occultations, Nature, 197, 1037

Heeschen, D. S., Krichbaum, T., Schalinski, C. J., Witzel, A., 1987, Rapid variability of extragalactic radio sources, Astron. J., 94, 1493–1507

Henstock, D. R., Browne, I. W. A., Wilkinson, P. N., Taylor, G. B., Vermeulen, R. C., Pearson, T. J., Readhead, A. C. S., 1995, The Second Caltech–Jodrell Bank VLBI Survey. II. Observations of 102 of 193 Sources, Astrophys. J. Suppl., 100, 1

Hill, G. J., Goodrich, R. W., Depoy, D. L., 1996, Observations of Paschen alpha in a Complete Sample of Radio Galaxies, Astrophys. J., 462, 163

Homan, D. C., 2002, Non-Ballistic Motions in Relativistic Jets, Bulletin of the American Astronomical Society, 34, 1245

Homan, D. C., 2003, Jet Collimation: 3C 279 Caught in the Act, in Astronomical Society of the Pacific Conference Series, p. 35

Homan, D. C., Lister, M. L., Kellermann, K. I., Cohen, M. H., Ros, E., Zensus, J. A., Kadler, M., Vermeulen, R. C., 2003, Jet Collimation in Action: Realignment on Kiloparsec Scales in 3C 279, Astrophys. J., 589, L9–L12

Hughes, P. A., Aller, H. D., Aller, M. F., 1998, Extraordinary Activity in the BL Lacertae Object OJ 287, Astrophys. J., 503, 662

Idesawa, E., Tashiro, M., Makishima, K., Kubo, H., Otani, C., Fujimoto, R., Kii, T., Makino, F., Takahashi, T., Ueda, Y., Ohashi, T., 1997, X-Ray Observations of the BL Lacertae Object OJ 287 with ASCA, Publ. Astron. Soc. Japan, 49, 631–637

Isobe, N., Tashiro, M., Sugiho, M., Makishima, K., 2001, ASCA Observations of the BL Lacertae Object OJ 287 in 1997 April and November, Publ. Astron. Soc. Japan, 53, 79–84

Jackson, C. A., Wall, J. V., Shaver, P. A., Kellermann, K. I., Hook, I. M., Hawkins, M. R. S., 2002, The Parkes quarter-Jansky flat-spectrum sample. I. Sample selection and source identifications, Astron. & Astrophys., 386, 97–113

Jansen, F., Lumb, D., Altieri, B., Clavel, J., Ehle, M., Erd, C., Gabriel, C., Guainazzi, M., Gondoin, P., Much, R., Munoz, R., Santos, M., Schartel, N., Texier, D., Vacanti, G., 2001, XMM-Newton observatory. I. The spacecraft and operations, Astron. & Astrophys., 365, L1–L6

Jones, T. W., O'dell, S. L., Stein, W. A., 1974, Physics of Compact Nonthermal Sources. H. Determination of Physical Parameters, Astrophys. J., 192, 261–278

Jorstad, S. G., Marscher, A. P., 2004, The Highly Relativistic Kiloparsec-Scale Jet of the Gamma-Ray Quasar 0827+243, Astrophys. J., 614, 615–625

Jorstad, S. G., Marscher, A. P., Mattox, J. R., Wehrle, A. E., Bloom, S. D., Yurchenko, A. V., 2001, Multiepoch Very Long Baseline Array Observations of EGRET-detected Quasars and BL Lacertae Objects: Superluminal Motion of Gamma-Ray Bright Blazars, Astrophys. J. Suppl., 134, 181–240

Jorstad, S. G., Marscher, A. P., Lister, M. L., Stirling, A. M., Cawthorne, T. V., Gear, W. K., Gomez, J. L., Stevens, J. A., Smith, P. S., Forster, J. R., Robson, E. I., 2005, Polarimetric Observations of 15 Active Galactic Nuclei at High Frequencies: Jet Kinematics from Bimonthly Monitoring with the Very Long Baseline Array, ArXiv Astrophysics e-prints, `arXiv:astro-ph/0502501`

Junkkarinen, V. T., Cohen, R. D., Beaver, E. A., Burbidge, E. M., Lyons, R. W., Madejski, G., 2004, Dust and Diffuse Interstellar Bands in the z = 0.524 Absorption System toward AO 0235+164, Astrophys. J., 614, 658–670

Kadler, M., 2002, NGC1052 – A study of the parsec-scale twin jet, Diplomarbeit, Rheinische Friedrich-Wilhelms-Universität Bonn, Germany

Kadler, M., Kerp, J., Ros, E., Falcke, H., Pogge, R. W., Zensus, J. A., 2004a, Jet emission in NGC 1052 at radio, optical, and X-ray frequencies, Astron. & Astrophys., 420, 467–474

Kadler, M., Ros, E., Kerp, J., Kovalev, Y., Zensus, J. A., 2004b, Combined VLBI- and X-ray Observations of Active Galactic Nuclei, in European VLBI Network on New Developments in VLBI Science and Technology, pp. 23–26

Kadler, M., Ros, E., Lobanov, A. P., Falcke, H., Zensus, J. A., 2004c, The twin-jet system in NGC 1052: VLBI-scrutiny of the obscuring torus, Astron. & Astrophys., 426, 481–493

Kalberla, P. M. W., Burton, W. B., Hartmann, D., Arnal, E. M., Bajaja, E., Morras, R., Poppel, W. G. L., 2005, The Leiden/Argentine/Bonn (LAB) Survey of Galactic HI: Final data release of the combined LDS and IAR surveys with improved stray-radiation corrections, ArXiv Astrophysics e-prints, `arXiv:astro-ph/0504140`

Kameno, S., Sawada-Satoh, S., Inoue, M., Shen, Z., Wajima, K., 2001, The Dense Plasma Torus around the Nucleus of an Active Galaxy NGC1052, Publ. Astron. Soc. Japan, 53, 169–178

Kataoka, J., Takahashi, T., Makino, F., Inoue, S., Madejski, G. M., Tashiro, M., Urry, C. M., Kubo, H., 2000, Variability Pattern and the Spectral Evolution of the BL Lacertae Object PKS 2155-304, Astrophys. J., 528, 243–253

Kellermann, K. I., 2002, Brightness Temperature Constraints to Compact Synchrotron Source Radiation Obtained from IDV and VLBI Observations, Publications of the Astronomical Society of Australia, 19, 77–82

Kellermann, K. I., 2003, Variability, Brightness Temperature, Superluminal Motion, Doppler Boosting, and Related Issues, in Astronomical Society of the Pacific Conference Series, p. 185

Kellermann, K. I., Moran, J. M., 2001, The Development of High-Resolution Imaging in Radio Astronomy, Annu. Rev. Astron. Astrophys., 39, 457–509

Kellermann, K. I., Pauliny-Toth, I. I. K., 1969, The Spectra of Opaque Radio Sources, Astrophys. J., 155, L71+

Kellermann, K. I., Sramek, R., Schmidt, M., Shaffer, D. B., Green, R., 1989, VLA observations of objects in the Palomar Bright Quasar Survey, Astron. J., 98, 1195–1207

Kellermann, K. I., Vermeulen, R. C., Zensus, A., Cohen, M. H., 1997, Parsec-Scale Imaging of Quasars and AGN, Bulletin of the American Astronomical Society, 29, 1257

Kellermann, K. I., Vermeulen, R. C., Zensus, J. A., Cohen, M. H., 1998a, "submilliarcsecond imaging of quasars and active galactic nuclei", Astron. J., 115, 1295–1318

Kellermann, K. I., Zensus, J. A., Vermeulen, R. C., Cohen, M. H., 1998b, The Submilliarcsecond Structure of Quasars and AGN, in Astronomical Society of the Pacific Conference Series, p. 153

Kellermann, K. I., Vermeulen, R. C., Cohen, M. H., Zensus, J. A., 1999a, "the shroud around the twin jets of ngc 1052", in American Astronomical Society Meeting, vol. 194, p. #20.02

Kellermann, K. I., Vermeulen, R. C., Zensus, J. A., Cohen, M. H., West, A., 1999b, Kinematics of quasars and AGN, New Astronomy Review, 43, 757–760

324

Kellermann, K. I., Vermeulen, R. C., Zensus, J. A., Cohen, M. H., 2000, Observations of Relativistic Outflow in AGN and the Brightness Temperature of Synchrotron Sources, in Astrophysical Phenomena Revealed by Space VLBI, Proceedings of the VSOP Symposium, held at the Institute of Space and astronautical Science, Sagamihara, Kanagawa, Japan, January 19 - 21, 2000, Eds.: H. Hirabayashi, P.G. Edwards, and D.W. Murphy, Published by the Institute of Space and Astronautical Science, p. 159-166., pp. 159–166

Kellermann, K. I., Lister, M. L., Homan, D. C., Ros, E., Zensus, J. A., Cohen, M. H., Russo, M., Vermeulen, R. C., 2003, Superluminal Motion and Relativistic Beaming in Blazar Jets, in Astronomical Society of the Pacific Conference Series, p. 117

Kellermann, K. I., Lister, M. L., Homan, D. C., Vermeulen, R. C., Cohen, M. H., Ros, E., Kadler, M., Zensus, J. A., Kovalev, Y. Y., 2004, Sub-Milliarcsecond Imaging of Quasars and Active Galactic Nuclei. III. Kinematics of Parsec-scale Radio Jets, Astrophys. J., 609, 539–563

Kelly, B. C., Hughes, P. A., Aller, H. D., Aller, M. F., 2003, The Cross-Wavelet Transform and Analysis of Quasi-periodic Behavior in the Pearson-Readhead VLBI Survey Sources, Astrophys. J., 591, 695–713

Kharb, P., Gabuzda, D., Alef, W., Preuss, E., Shastri, P., 2003, Magnetic field geometry of the broad line radio galaxy 3C111, New Astronomy Review, 47, 621–624

Kovalev, Y. Y., Kellermann, K. I., Lister, M. L., Homan, D. C., Vermeulen, R. C., Cohen, M. H., Ros, E., Kadler, M., Lobanov, A. P., Zensus, J. A., Kardashev, N. S., Gurvits, L. I., Aller, M. F., Aller, H. D., 2005, Sub-milliarcsecond Imaging of Quasars and Active Galactic Nuclei. IV. Fine Scale Structure, ArXiv Astrophysics e-prints, `arXiv: astro-ph/0505536`

Kraus, A., Quirrenbach, A., Lobanov, A. P., Krichbaum, T. P., Risse, M., Schneider, P., Qian, S. J., Wagner, S. J., Witzel, A., Zensus, J. A., Heidt, J., Bock, H., Aller, M., Aller, H., 1999, Unusual radio variability in the BL Lacertae object 0235+164, Astron. & Astrophys., 344, 807–816

Kraus, A., Krichbaum, T. P., Wegner, R., Witzel, A., Cimò, G., Quirrenbach, A., Britzen, S., Fuhrmann, L., Lobanov, A. P., Naundorf, C. E., Otterbein, K., Peng, B., Risse, M., Ros, E., Zensus, J. A., 2003, Intraday variability in compact extragalactic radio sources. II. Observations with the Effelsberg 100 m radio telescope, Astron. & Astrophys., 401, 161–172

Krolik, J. H., 1999, Active galactic nuclei : from the central black hole to the galactic environment, Princeton, NJ, USA : Princeton University Press, 1999.

Kubo, H., Takahashi, T., Madejski, G., Tashiro, M., Makino, F., Inoue, S., Takahara, F., 1998, ASCA Observations of Blazars and Multiband Analysis, Astrophys. J., 504, 693

Kuehr, H., Witzel, A., Pauliny-Toth, I. I. K., Nauber, U., 1981, A catalogue of extragalactic radio sources having flux densities greater than 1 Jy at 5 GHz, Astron. &. Astrophys. Suppl., 45, 367–430

Lähteenmäki, A., Valtaoja, E., 1999, Total Flux Density Variations in Extragalactic Radio Sources. III. Doppler Boosting Factors, Lorentz Factors, and Viewing Angles for Active Galactic Nuclei, Astrophys. J., 521, 493–501

Lal, D. V., Shastri, P., Gabuzda, D. C., 2004, Milliarcsec-scale radio structure of a matched sample of Seyfert 1 and Seyfert 2 galaxies, Astron. & Astrophys., 425, 99–108

Lamer, G., Brunner, H., Staubert, R., 1996, ROSAT observations of BL Lacertae objects., Astron. & Astrophys., 311, 384–392

Leahy, J. P., Perley, R. A., 1991, VLA images of 23 extragalactic radio sources, Astron. J., 102, 537–561

Lewis, K. T., Eracleous, M., Gliozzi, M., Sambruna, R. M., Mushotzky, R. F., 2005, A Simultaneous RXTE and XMM-Newton Observation of the Broad-Line Radio Galaxy 3C 111, Astrophys. J., 622, 816–829

Linfield, R., Perley, R., 1984, 3C 111 - A luminous radio galaxy with a highly collimated jet, Astrophys. J., 279, 60–73

Lister, M., 2002, Relativistic Jet Kinematics of the GPS Source PKS 1345+125, Bulletin of the American Astronomical Society, 34, 715

Lister, M. L., Homan, D. C., 2005, MOJAVE: Monitoring of Jets in AGN with VLBA Experiments - I. First-Epoch 15 GHz Linear Polarization Images, ArXiv Astrophysics e-prints, `arXiv:astro-ph/0503152`

Lister, M. L., Kellermann, K. I., Pauliny-Toth, I. I. K., 2002, The Diverse Properties of GPS Sources, in Proceedings of the 6th EVN Symposium, p. 135

Lister, M. L., Kellermann, K. I., Homan, D. C., Ros, E., Zensus, J. A., Kadler, M., Cohen, M. H., Russo, M., Vermeulen, R. C., 2003a, Kinematics of Relativistic Jets in Active Galactic Nuclei: The 2 cm VLBA Survey, in Astronomical Society of the Pacific Conference Series, p. 345

Lister, M. L., Kellermann, K. I., Vermeulen, R. C., Cohen, M. H., Zensus, J. A., Ros, E., 2003b, 4C +12.50: A Superluminal Precessing Jet in the Recent Merger System IRAS 13451+1232, Astrophys. J., 584, 135–146

Lobanov, A. P., 1998, "ultracompact jets in active galactic nuclei", Astron. & Astrophys., 330, 79–89

Lobanov, A. P., Zensus, J. A., 2001, A Cosmic Double Helix in the Archetypical Quasar 3C273, Science, 294, 128–131

Lobanov, A. P., Krichbaum, T. P., Graham, D. A., Witzel, A., Kraus, A., Zensus, J. A., Britzen, S., Greve, A., Grewing, M., 2000, 86 GHz VLBI survey of compact radio sources, Astron. & Astrophys., 364, 391–408

Lomb, N. R., 1976, Least-squares frequency analysis of unequally spaced data, Astrophys. & Space Science, 39, 447–462

Lucas, R., Liszt, H. S., 1993, Plateau-De Observations of Millimeter-Wave Molecular Absorption Toward Bl-Lacertae, Astron. & Astrophys., 276, L33+

Madejski, G., 1994, Soft X-ray spectrum of BL Lacertae object AO 0235+164 as a tracer of elemental abundances at Z approximately 0.5, Astrophys. J., 432, 554–559

Madejski, G., Takahashi, T., Tashiro, M., Kubo, H., Hartman, R., Kallman, T., Sikora, M., 1996, Simultaneous Soft X-Ray and GeV Gamma-Ray Observations of BL Lacertae Object AO 0235+164, Astrophys. J., 459, 156

Magdziarz, P., Zdziarski, A. A., 1995, Angle-dependent Compton reflection of X-rays and gamma-rays, Monthly Not. Roy. Astron. Soc., 273, 837–848

Maisack, M., Staubert, R., Otterbein, K., Witzel, A., Wagner, S. J., Heines, A., 1996, CGRO, radio and optical observations of the quasar NRAO 140., Astron. &. Astrophys. Suppl., 120, C533+

Mannheim, K., Biermann, P. L., 1989, Photomeson production in active galactic nuclei, Astron. & Astrophys., 221, 211–220

Marscher, A. P., 1988, Contemporaneous X-ray and VLBI radio observations of the quasar NRAO 140, Astrophys. J., 334, 552–559

Marscher, A. P., 1999, The compact jets of TeV blazars, Astroparticle Physics, 11, 19–25

Marscher, A. P., Jorstad, S. G., Gómez, J., Aller, M. F., Teräsranta, H., Lister, M. L., Stirling, A. M., 2002, Observational evidence for the accretion-disk origin for a radio jet in an active galaxy, Nature, 417, 625–627

Marshall, H. L., Cheung, T., Canizares, C. R., Fang, T., 2003, The Large Scale X-ray Jet in 3C 279, American Astronomical Society Meeting Abstracts, 202, 42.13

Marshall, H. L., Schwartz, D. A., Lovell, J. E. J., Murphy, D. W., Worrall, D. M., Birkinshaw, M., Gelbord, J. M., Perlman, E. S., Jauncey, D. L., 2005, A Chandra Survey of Quasar Jets: First Results, Astrophys. J. Suppl., 156, 13–33

Massaro, E., Giommi, P., Perri, M., Tagliaferri, G., Nesci, R., Tosti, G., Ciprini, S., Montagni, F., Ravasio, M., Ghisellini, G., Frasca, A., Marilli, E., Valentini, G., Kurtanidze, O. M., Nikolashvili, M. G., 2003, Optical and X-ray observations of the two BL Lac objects OJ 287 and MS 1458+22, Astron. & Astrophys., 399, 33–38

McHardy, I. M., Papadakis, I. E., Uttley, P., Page, M. J., Mason, K. O., 2004, Combined long and short time-scale X-ray variability of NGC 4051 with RXTE and XMM-Newton, Monthly Not. Roy. Astron. Soc., 348, 783–801

McKernan, B., Yaqoob, T., 2004, High-Resolution X-Ray Spectroscopy of the Fe K Complex in IC 4329A, Astrophys. J., 608, 157–165

Meier, D. L., Koide, S., Uchida, Y., 2001, Magnetohydrodynamic Production of Relativistic Jets, Science, 291, 84–92

Merloni, A., Fabian, A. C., 2002, Coronal outflow dominated accretion discs: a new possibility for low-luminosity black holes?, Monthly Not. Roy. Astron. Soc., 332, 165–175

Mirabel, I. F., Rodríguez, L. F., 1999, Sources of Relativistic Jets in the Galaxy, Annu. Rev. Astron. Astrophys., 37, 409–443

Mirabel, I. F., Rodriguez, L. F., 1998, Microquasars in our Galaxy., Nature, 392, 673–676

Morganti, R., Tsvetanov, Z. I., Gallimore, J., Allen, M. G., 1999, Radio continuum morphology of southern Seyfert galaxies, Astron. &. Astrophys. Suppl., 137, 457–471

Mundell, C. G., Wrobel, J. M., Pedlar, A., Gallimore, J. F., 2003, The Nuclear Regions of the Seyfert Galaxy NGC 4151: Parsec-Scale H I Absorption and a Remarkable Radio Jet, Astrophys. J., 583, 192–204

Murphy, D. W., Browne, I. W. A., Perley, R. A., 1993, VLA Observations of a Complete Sample of Core-Dominated Radio Sources, Monthly Not. Roy. Astron. Soc., 264, 298

Nagar, N. M., Wilson, A. S., Mulchaey, J. S., Gallimore, J. F., 1999, Radio Structures of Seyfert Galaxies. VIII. A Distance- and Magnitude-Limited Sample of Early-Type Galaxies, Astrophys. J. Suppl., 120, 209–245

Nandra, K., Pounds, K. A., 1994, GINGA Observations of the X-Ray Spectra of Seyfert Galaxies, Monthly Not. Roy. Astron. Soc., 268, 405

Napier, P. J., Thompson, A. R., Ekers, R. D., 1983, The Very Large Array - Design and performance of a modern synthesis radio telescope, IEEE Proceedings, 71, 1295–1320

Nilsson, K., Pursimo, T., Heidt, J., Takalo, L. O., Sillanpää, A., Brinkmann, W., 2003, R-band imaging of the host galaxies of RGB BL Lacertae objects, Astron. & Astrophys., 400, 95–118

Ogle, P. M., Davis, S. W., Antonucci, R. R. J., Colbert, J. W., Malkan, M. A., Page, M. J., Sasseen, T. P., Tornikoski, M., 2005, Multiwavelength Observations of Radio Galaxy 3C 120 with XMM-Newton, Astrophys. J., 618, 139–154

Ohashi, T., Ebisawa, K., Fukazawa, Y., Hiyoshi, K., Horii, M., Ikebe, Y., Ikeda, H., Inoue, H., Ishida, M., Ishisaki, Y., Ishizuka, T., Kamijo, S., Kaneda, H., Kohmura, Y., Makishima, K., Mihara, T., Tashiro, M., Murakami, T., Shoumura, R., Tanaka, Y., Ueda, Y., Taguchi, K., Tsuru, T., Takeshima, T., 1996, The Gas Imaging Spectrometer on Board ASCA, Publ. Astron. Soc. Japan, 48, 157–170

Ostorero, L., Villata, M., Raiteri, C. M., 2004, Helical jets in blazars. Interpretation of the multifrequency long-term variability of AO 0235+16, Astron. & Astrophys., 419, 913–925

Ott, M., Witzel, A., Quirrenbach, A., Krichbaum, T. P., Standke, K. J., Schalinski, C. J., Hummel, C. A., 1994, An updated list of radio flux density calibrators, Astron. & Astrophys., 284, 331–339

Padovani, P., Costamante, L., Giommi, P., Ghisellini, G., Comastri, A., Wolter, A., Maraschi, L., Tagliaferri, G., Megan Urry, C., 2001, BeppoSAX observations of 1-Jy BL Lacertae objects - I, Monthly Not. Roy. Astron. Soc., 328, 931–943

Padovani, P., Costamante, L., Ghisellini, G., Giommi, P., Perlman, E., 2002, BeppoSAX Observations of Synchrotron X-Ray Emission from Radio Quasars, Astrophys. J., 581, 895–911

Padovani, P., Costamante, L., Giommi, P., Ghisellini, G., Celotti, A., Wolter, A., 2004, BeppoSAX observations of 1-Jy BL Lacertae objects - II, Monthly Not. Roy. Astron. Soc., 347, 1282–1293

Page, K. L., Turner, M. J. L., Done, C., O'Brien, P. T., Reeves, J. N., Sembay, S., Stuhlinger, M., 2004, XMM-Newton observations of 3C 273, Monthly Not. Roy. Astron. Soc., 349, 57–67

Paragi, Z., Frey, S., Fejes, I., Murphy, D. W., 2000, Space VLBI observations reveal a parsec scale misalignment in the jet of 0458-020, in EVN Symposium 2000, Proceedings of the 5th european VLBI Network Symposium, p. 43

Parmar, A. N., Martin, D. D. E., Bavdaz, M., Favata, F., Kuulkers, E., Vacanti, G., Lammers, U., Peacock, A., Taylor, B. G., 1997, The low-energy concentrator spectrometer on-board the BeppoSAX X-ray astronomy satellite, Astron. &. Astrophys. Suppl., 122, 309–326

Pearson, T. J., Readhead, A. C. S., 1988, The milliarcsecond structure of a complete sample of radio sources. II - First-epoch maps at 5 GHz, Astrophys. J., 328, 114–142

Perley, R. A., Schwab, F. R., Bridle, A. H. (Eds.), 1989, Synthesis imaging in radio astronomy

Perlman, E. S., Stocke, J. T., Carilli, C. L., Sugiho, M., Tashiro, M., Madejski, G., Wang, Q. D., Conway, J., 2002, The Apparent Host Galaxy of PKS 1413+135: Hubble Space Telescope, ASCA, and Very Long Baseline Array Observations, Astron. J., 124, 2401–2412

Peterson, L. E., 1973, Hard Cosmic X-Ray Sources, in IAU Symp. 55: X- and Gamma-Ray Astronomy, p. 51

Pian, E., Foschini, L., Beckmann, V., Sillanpää, A., Soldi, S., Tagliaferri, G., Takalo, L., Barr, P., Ghisellini, G., Malaguti, G., Maraschi, L., Palumbo, G. G. C., Treves, A., Courvoisier, T. J.-L., Di Cocco, G., Gehrels, N., Giommi, P., Hudec, R., Lindfors, E., Marcowith, A., Nilsson, K., Pasanen, M., Pursimo, T., Raiteri, C. M., Savolainen, T., Sikora, M., Tornikoski, M., Tosti, G., Türler, M., Valtaoja, E., Villata, M., Walter, R., 2005, INTEGRAL observations of the field of the BL Lacertae object S5 0716+714, Astron. & Astrophys., 429, 427–431

Piconcelli, E., Jimenez-Bailón, E., Guainazzi, M., Schartel, N., Rodríguez-Pascual, P. M., Santos-Lleó, M., 2005, The XMM-Newton view of PG quasars. I. X-ray continuum and absorption, Astron. & Astrophys., 432, 15–30

Piner, B. G., Kingham, K. A., 1998, Geodetic VLBI Observations of EGRET Blazars, Astrophys. J., 507, 706–725

Polatidis, A. G., Wilkinson, P. N., Xu, W., Readhead, A. C. S., Pearson, T. J., Taylor, G. B., Vermeulen, R. C., 1995, The First Caltech–Jodrell Bank VLBI Survey. I. lambda = 18 Centimeter Observations of 87 Sources, Astrophys. J. Suppl., 98, 1

Pounds, K. A., Reeves, J. N., Page, K. L., Wynn, G. A., O'Brien, P. T., 2003a, Fe K emission and absorption features in XMM-Newton spectra of Markarian 766: evidence for reprocessing in flare ejecta, Monthly Not. Roy. Astron. Soc., 342, 1147–1155

Pounds, K. A., Reeves, J. N., Page, K. L., Wynn, G. A., O'Brien, P. T., 2003b, Fe K emission and absorption features in XMM-Newton spectra of Markarian 766: evidence for reprocessing in flare ejecta, Monthly Not. Roy. Astron. Soc., 342, 1147–1155

Pounds, K. A., Reeves, J. N., King, A. R., Page, K. L., 2004, Exploring the complex X-ray spectrum of NGC 4051, Monthly Not. Roy. Astron. Soc., 350, 10–20

Preuss, E., Alef, W., Kellermann, K. I., 1988, Superluminal Behavior of the Double-Lobed Radio Galaxy 3C111, in IAU Symp. 129: The Impact of VLBI on Astrophysics and Geophysics, p. 105

Primini, F. A., Basinska, E., Howe, S. K., Lang, F., Levine, A. M., Lewin, W. H. G., Rothschild, R., Baity, W. A., Gruber, D. E., Knight, F. K., Matteson, J. L., Lea, S. M., Reichert, G. A., 1981, HEAO 1 observations of the Perseus cluster above 10 keV, Astrophys. J., 243, L13–L17

Protassov, R., van Dyk, D. A., Connors, A., Kashyap, V. L., Siemiginowska, A., 2002, Statistics, Handle with Care: Detecting Multiple Model Components with the Likelihood Ratio Test, Astrophys. J., 571, 545–559

Qian, S., Li, X., Wegner, R., Witzel, A., Krichbaum, T. P., 1996, Implications of the correlation between the optical and radio intraday variations in BLO 0716+714, Chinese Astronomy and Astrophysics, 20, 15–25

Quirrenbach, A., Witzel, A., Wagner, S., Sanchez-Pons, F., Krichbaum, T. P., Wegner, R., Anton, K., Erkens, U., Haehnelt, M., Zensus, J. A., Johnston, K. J., 1991, Correlated radio and optical variability in the BL Lacertae object 0716 + 714, Astrophys. J., 372, L71–L74

Quirrenbach, A., Witzel, A., Kirchbaum, T. P., Hummel, C. A., Wegner, R., Schalinski, C. J., Ott, M., Alberdi, A., Rioja, M., 1992, Statistics of intraday variability in extragalactic radio sources, Astron. & Astrophys., 258, 279–284

Raiteri, C. M., Villata, M., Aller, H. D., Aller, M. F., Heidt, J., Kurtanidze, O. M., Lanteri, L., Maesano, M., Massaro, E., Montagni, F., Nesci, R., Nilsson, K., Nikolashvili, M. G., Nurmi, P., Ostorero, L., Pursimo, T., Rekola, R., Sillanpää, A., Takalo, L. O., Teräsranta, H., Tosti, G., Balonek, T. J., Feldt, M., Heines, A., Heisler, C., Hu, J., Kidger, M., Mattox, J. R., McGrath, E. J., Pati, A., Robb, R., Sadun, A. C., Shastri,

P., Wagner, S. J., Wei, J., Wu, X., 2001, Optical and radio variability of the BL Lacertae object AO 0235+16: A possible 5-6 year periodicity, Astron. & Astrophys., 377, 396–412

Raiteri, C. M., Villata, M., Ibrahimov, M. A., Larionov, V. M., Kadler, M., Aller, H. D., Aller, M. F., Kovalev, Y. Y., Lanteri, L., Nilsson, K., Papadakis, I. E., Pursimo, T., Romero, G. E., Teräsranta, H., Tornikoski, M., Arkharov, A. A., Barnaby, D., Berdyugin, A., Böttcher, M., Byckling, K., Carini, M. T., Carosati, D., Cellone, S. A., Ciprini, S., Combi, J. A., Crapanzano, S., Crowe, R., di Paola, A., Dolci, M., Fuhrmann, L., Gu, M., Hagen-Thorn, V. A., Hakala, P., Impellizzeri, V., Jorstad, S., Kerp, J., Kimeridze, G. N., Kovalev, Y. A., Kraus, A., Krichbaum, T. P., Kurtanidze, O. M., Lähteenmäki, A., Lindfors, E., Mingaliev, M. G., Nesci, R., Nikolashvili, M. G., Ohlert, J., Orio, M., Ostorero, L., Pasanen, M., Pati, A., Poteet, C., Ros, E., Ros, J. A., Shastri, P., Sigua, L. A., Sillanpää, A., Smith, N., Takalo, L. O., Tosti, G., Vasileva, A., Wagner, S. J., Walters, R., Webb, J. R., Wills, W., Witzel, A., Xilouris, E., 2005, The WEBT campaign to observe AO 0235+16 in the 2003-2004 observing season. Results from radio-to-optical monitoring and XMM-Newton observations, Astron. & Astrophys., 438, 39–53

Ravasio, M., Tagliaferri, G., Ghisellini, G., Giommi, P., Nesci, R., Massaro, E., Chiappetti, L., Celotti, A., Costamante, L., Maraschi, L., Tavecchio, F., Tosti, G., Treves, A., Wolter, A., Balonek, T., Carini, M., Kato, T., Kurtanidze, O., Montagni, F., Nikolashvili, M., Noble, J., Nucciarelli, G., Raiteri, C. M., Sclavi, S., Uemura, M., Villata, M., 2002, BL Lacertae: Complex spectral variability and rapid synchrotron flare detected with BeppoSAX, Astron. & Astrophys., 383, 763–772

Ravasio, M., Tagliaferri, G., Ghisellini, G., Tavecchio, F., Böttcher, M., Sikora, M., 2003, BeppoSAX and multiwavelength observations of BL Lacertae in 2000, Astron. & Astrophys., 408, 479–491

Readhead, A. C. S., 1994, Equipartition brightness temperature and the inverse Compton catastrophe, Astrophys. J., 426, 51–59

Reeves, J. N., Turner, M. J. L., 2000, X-ray spectra of a large sample of quasars with ASCA, Monthly Not. Roy. Astron. Soc., 316, 234–248

Reynolds, C. S., 1996, X-Ray Emission and Absorption in Active Galaxies, Ph.D. Thesis, University of Cambridge

Reynolds, C. S., Nowak, M. A., 2003, Fluorescent iron lines as a probe of astrophysical black hole systems, Physics Reports, 377, 389–466

Rickett, B. J., 1986, Refractive interstellar scintillation of radio sources, Astrophys. J., 307, 564–574

Romero, G. E., Cellone, S. A., Combi, J. A., 2000, Extreme intranight variability in the BL Lacertae object AO 0235+164, Astron. & Astrophys., 360, L47–L50

Ros, E., 1997, Astrometría diferencial de precisión con VLBI en el triángulo de Draco (y estudios de SN 1993J), València, Spain: Servicio de Publicaciones, Universitat de València

Ros, E., 2003, The VLBA 2cm Survey: Kinematics of pc-Scale Structures in Active Galactic Nuclei, in Highlights in Spanish Astrophysics III, (Ed.) N. C. Gallego, J. Zamorano, pp. 235–238, Kluwer Academic Publishers

Ros, E., 2004, Extending and Exploring the 2 cm Survey Sample, in Proceerings of the 7th EVN Symposium, p. 27

Ros, E., Zensus, J. A., Lobanov, A. P., 2000, Total intensity and polarized emission of the parsec-scale jet in 3C 345, Astron. & Astrophys., 354, 55–66

Ros, E., Kellermann, K. I., Lister, M. L., Zensus, J. A., Cohen, M. H., Vermeulen, R. C., Kadler, M., Homan, D. C., 2002, Kinematics of parsec-scale structures in AGN: the 2cm VLBA Survey, in Proceedings of the 6th EVN Symposium, p. 105

Rothschild, R. E., Baity, W. A., Marscher, A. P., Wheaton, W. A., 1981, Nonthermal hard X-ray emission from the nucleus of NGC 1275, Astrophys. J., 243, L9–L12

Rush, B., Malkan, M. A., Edelson, R. A., 1996, The Radio Properties of Seyfert Galaxies in the 12 Micron and CfA Samples, Astrophys. J., 473, 130

Rybicki, G. B., Lightman, A. P., 1979, Radiative Processes in Astrophysics, New York, USA: Wiley-Interscience

Salvi, N. J., Page, M. J., Stevens, J. A., Wu, K., Mason, K. O., Aller, M. F., Aller, H. D., Teräsranta, H., Romero-Colmenero, E., Cordova, F. A., Priedhorsky, W. C., 2002, Correlated multiwavelength emission from the X-ray-bright Seyfert galaxy III Zw 2, Monthly Not. Roy. Astron. Soc., 335, 177–188

Sambruna, R. M., Urry, C. M., Maraschi, L., Ghisellini, G., Mukherjee, R., Pesce, J. E., Wagner, S. J., Wehrle, A. E., Hartman, R. C., Lin, Y. C., von Montigny, C., 1997, The High-Energy Continuum Emission of the Gamma-Ray Blazar PKS 0528+134, Astrophys. J., 474, 639

Sambruna, R. M., Eracleous, M., Mushotzky, R. F., 1999a, An X-Ray Spectral Survey of Radio-loud Active Galactic Nuclei with ASCA, Astrophys. J., 526, 60–96

Sambruna, R. M., Ghisellini, G., Hooper, E., Kollgaard, R. I., Pesce, J. E., Urry, C. M., 1999b, ASCA and Contemporaneous Ground-based Observations of the BL Lacertae Objects 1749+096 and 2200+420 (BL Lac), Astrophys. J., 515, 140–152

Sambruna, R. M., Chou, L. L., Urry, C. M., 2000, Testing the Blazar Paradigm: ASCA Observations of Flat-Spectrum Radio Quasars with Steep Soft X-Ray Spectra, Astrophys. J., 533, 650–657

Sambruna, R. M., Eracleous, M., Mushotzky, R. F., 2002, Constraining the central engine of radio-loud AGNs, New Astronomy Review, 46, 215–220

Sambruna, R. M., Gambill, J. K., Maraschi, L., Tavecchio, F., Cerutti, R., Cheung, C. C., Urry, C. M., Chartas, G., 2004, A Survey of Extended Radio Jets with Chandra and the Hubble Space Telescope, Astrophys. J., 608, 698–720

Scargle, J. D., 1982, Studies in astronomical time series analysis. II - Statistical aspects of spectral analysis of unevenly spaced data, Astrophys. J., 263, 835–853

Schlegel, D. J., Finkbeiner, D. P., Davis, M., 1998, Maps of Dust Infrared Emission for Use in Estimation of Reddening and Cosmic Microwave Background Radiation Foregrounds, Astrophys. J., 500, 525

Schmidt, M., 1963, 3C 273: a star-like object with large red-shift., Nature, 197, 1040–1040

Schurch, N. J., Warwick, R. S., Griffiths, R. E., Sembay, S., 2003, Iron K-features in the hard X-ray XMM-Newton spectrum of NGC 4151, Monthly Not. Roy. Astron. Soc., 345, 423–428

Shen, Z.-Q., Wan, T.-S., Moran, J. M., Jauncey, D. L., Reynolds, J. E., Tzioumis, A. K., Gough, R. G., Ferris, R. H., Sinclair, M. W., Jiang, D.-R., Hong, X.-Y., Liang, S.-G., Costa, M. E., Tingay, S. J., McCulloch, P. M., Lovell, J. E. J., King, E. A., Nicolson, G. D., Murphy, D. W., Meier, D. L., van Ommen, R. D., Edwards, P. G., White, G. L., 1997, A 5-GHz Southern Hemishere VLBI Survey of Compact Radio Sources.I., Astron. J., 114, 1999

Siebert, J., Brinkmann, W., Morganti, R., Tadhunter, C. N., Danziger, I. J., Fosbury, R. A. E., di Serego Alighieri, S., 1996, The soft X-ray properties of a complete sample of radio sources., Monthly Not. Roy. Astron. Soc., 279, 1331–1344

Siebert, J., Brinkmann, W., Drinkwater, M. J., Yuan, W., Francis, P. J., Peterson, B. A., Webster, R. L., 1998, X-ray properties of the Parkes sample of flat-spectrum radio sources: dust in radio-loud quasars?, Monthly Not. Roy. Astron. Soc., 301, 261–279

Siemiginowska, A., Bechtold, J., Aldcroft, T. L., Elvis, M., Harris, D. E., Dobrzycki, A., 2002, Chandra Discovery of a 300 Kiloparsec X-Ray Jet in the Gigahertz-peaked Spectrum Quasar PKS 1127-145, Astrophys. J., 570, 543–556

Siemiginowska, A., Stanghellini, C., Brunetti, G., Fiore, F., Aldcroft, T. L., Bechtold, J., Elvis, M., Murray, S. S., Antonelli, L. A., Colafrancesco, S., 2003, Chandra Discovery of an X-Ray Jet and Extended X-Ray Structure in the z = 0.63 Quasar B2 0738+313, Astrophys. J., 595, 643–655

Singh, K. P., Shrader, C. R., George, I. M., 1997, X-Ray Spectrum of the High-Polarization Quasar PKS 1510-089, Astrophys. J., 491, 515

Sowards-Emmerd, D., Romani, R. W., Michelson, P. F., 2003, The Gamma-Ray Blazar Content of the Northern Sky, Astrophys. J., 590, 109–122

Stickel, M., Fried, J. W., Kuehr, H., 1988, AO 0235+164 - The case of a gravitationally microlensed BL Lac object, Astron. & Astrophys., 198, L13–L16

Stickel, M., Meisenheimer, K., Kuehr, H., 1994, The optical identification status of the 1 Jy radio source catalogue, Astron. &. Astrophys. Suppl., 105, 211–234

Stickel, M., Rieke, G. H., Kuehr, H., Rieke, M. J., 1996, Flat-Spectrum Radio Sources with Faint Optical Counterparts, Astrophys. J., 468, 556

Stirling, A. M., Cawthorne, T. V., Stevens, J. A., Jorstad, S. G., Marscher, A. P., Lister, M. L., Gómez, J. L., Smith, P. S., Agudo, I., Gabuzda, D. C., Robson, E. I., Gear, W. K., 2003, Discovery of a precessing jet nozzle in BL Lacertae, Monthly Not. Roy. Astron. Soc., 341, 405–422

Strüder, L., Briel, U., Dennerl, K., Hartmann, R., Kendziorra, E., Meidinger, N., Pfeffermann, E., Reppin, C., Aschenbach, B., Bornemann, W., Bräuninger, H., Burkert, W., Elender, M., Freyberg, M., Haberl, F., Hartner, G., Heuschmann, F., Hippmann, H., Kastelic, E., Kemmer, S., Kettenring, G., Kink, W., Krause, N., Müller, S., Oppitz, A., Pietsch, W., Popp, M., Predehl, P., Read, A., Stephan, K. H., Stötter, D., Trümper, J., Holl, P., Kemmer, J., Soltau, H., Stötter, R., Weber, U., Weichert, U., von Zanthier, C., Carathanassis, D., Lutz, G., Richter, R. H., Solc, P., Böttcher, H., Kuster, M., Staubert, R., Abbey, A., Holland, A., Turner, M., Balasini, M., Bignami, G. F., La Palombara, N., Villa, G., Buttler, W., Gianini, F., Lainé, R., Lumb, D., Dhez, P., 2001, The European Photon Imaging Camera on XMM-Newton: The pn-CCD camera, Astron. & Astrophys., 365, L18–L26

Sutherland, R. S., Dopita, M. A., 1993, Cooling functions for low-density astrophysical plasmas, Astrophys. J. Suppl., 88, 253–327

Tagliaferri, G., Ravasio, M., Ghisellini, G., Giommi, P., Massaro, E., Nesci, R., Tosti, G., Aller, M. F., Aller, H. D., Celotti, A., Maraschi, L., Tavecchio, F., Wolter, A., 2003, The BL Lacertae objects OQ 530 and S5 0716+714. Simultaneous observations in the X-rays, radio, optical and TeV bands, Astron. & Astrophys., 400, 477–486

Takahashi, T., Kataoka, J., Madejski, G., Mattox, J., Urry, C. M., Wagner, S., Aharonian, F., Catanese, M., Chiappetti, L., Coppi, P., Degrange, B., Fossati, G., Kubo, H., Krawczynski, H., Makino, F., Marshall, H., Maraschi, L., Piron, F., Remillard, R., Takahara, F., Tashiro, M., Terasranta, H., Weekes, T., 2000, Complex Spectral Variability from Intensive Multiwavelength Monitoring of Markarian 421 in 1998, Astrophys. J., 542, L105–L109

Takalo, L. O., Kidger, M. R., de Diego, J. A., Sillanpaa, A., Nilsson, K., 1992, Near infrared monitoring of a sample of blazars with the Carlos Sanchez Telescope., Astron. J., 104, 40–52

Tanaka, Y., Inoue, H., Holt, S. S., 1994, The X-ray astronomy satellite ASCA, Publ. Astron. Soc. Japan, 46, L37–L41

Tanihata, C., Urry, C. M., Takahashi, T., Kataoka, J., Wagner, S. J., Madejski, G. M., Tashiro, M., Kouda, M., 2001, Variability Timescales of TeV Blazars Observed in the ASCA Continuous Long-Look X-Ray Monitoring, Astrophys. J., 563, 569–581

Tavecchio, F., Maraschi, L., Ghisellini, G., Celotti, A., Chiappetti, L., Comastri, A., Fossati, G., Grandi, P., Pian, E., Tagliaferri, G., Treves, A., Raiteri, C. M., Sambruna, R., Villata, M., 2000, Gamma-loud Quasars: A View with BeppoSAX, Astrophys. J., 543, 535–544

Tavecchio, F., Maraschi, L., Ghisellini, G., Celotti, A., Chiappetti, L., Comastri, A., Fossati, G., Grandi, P., Pian, E., Tagliaferri, G., Treves, A., Sambruna, R., 2002, Spectral Energy Distributions of Flat-Spectrum Radio Quasars Observed with BeppoSAX, Astrophys. J., 575, 137–144

Taylor, G. B., Vermeulen, R. C., Pearson, T. J., Readhead, A. C. S., Henstock, D. R., Browne, I. W. A., Wilkinson, P. N., 1994, The second Caltech-Jodrell Bank VLBI survey. 1: Observations of 91 of 193 sources, Astrophys. J. Suppl., 95, 345–369

Taylor, G. B., Vermeulen, R. C., Readhead, A. C. S., Pearson, T. J., Henstock, D. R., Wilkinson, P. N., 1996, A Complete Flux-Density–limited VLBI Survey of 293 Flat-Spectrum Radio Sources, Astrophys. J. Suppl., 107, 37

Taylor, G. B., Carilli, C. L., Perley, R. A. (Eds.), 1999, Synthesis Imaging in Radio Astronomy II

Teräsranta, H., Achren, J., Hanski, M., Heikkilä, J., Holopainen, J., Joutsamo, O., Juhola, M., Karlamaa, K., Katajainen, S., Keinänen, P., Koivisto, P., Koskimies, M., Könönen, P., Lainela, M., Lähtenmäki, A., Mäkinen, K., Niemelä, T., Nurmi, P., Pursimo, T., Rekola, R., Savolainen, T., Tornikoski, M., Torppa, J., Valtonen, T., Varjonen, N., Vilenius, E., Virtanen, J., Wiren, S., 2004, Twenty years monitoring of extragalactic sources at 22, 37 and 87 GHz, Astron. & Astrophys., 427, 769–771

Terashima, Y., Wilson, A. S., 2003, Chandra Snapshot Observations of Low-Luminosity Active Galactic Nuclei with a Compact Radio Source, Astrophys. J., 583, 145–158

Terashima, Y., Iyomoto, N., Ho, L. C., Ptak, A. F., 2002, X-Ray Properties of LINERs and Low-Luminosity Seyfert Galaxies Observed with ASCA. I. Observations and Results, Astrophys. J. Suppl., 139, 1–36

Thakkar, D. D., Xu, W., Readhead, A. C. S., Pearson, T. J., Taylor, G. B., Vermeulen, R. C., Polatidis, A. G., Wilkinson, P. N., 1995, The First Caltech–Jodrell Bank VLBI Survey. II. lambda = 18 Centimeter Observations of 25 Sources, Astrophys. J. Suppl., 98, 33

Thompson, A. R., Moran, J. M., Swenson, G. W., 1986, Interferometry and synthesis in radio astronomy, New York, Wiley-Interscience

Turner, M. J. L., Abbey, A., Arnaud, M., Balasini, M., Barbera, M., Belsole, E., Bennie, P. J., Bernard, J. P., Bignami, G. F., Boer, M., Briel, U., Butler, I., Cara, C., Chabaud, C., Cole, R., Collura, A., Conte, M., Cros, A., Denby, M., Dhez, P., Di Coco, G., Dowson, J., Ferrando, P., Ghizzardi, S., Gianotti, F., Goodall, C. V., Gretton, L., Griffiths, R. G., Hainaut, O., Hochedez, J. F., Holland, A. D., Jourdain, E., Kendziorra, E., Lagostina, A., Laine, R., La Palombara, N., Lortholary, M., Lumb, D., Marty, P., Molendi, S., Pigot, C., Poindron, E., Pounds, K. A., Reeves, J. N., Reppin, C., Rothenflug, R., Salvetat, P., Sauvageot, J. L., Schmitt, D., Sembay, S., Short, A. D. T., Spragg, J., Stephen, J., Strüder, L., Tiengo, A., Trifoglio, M., Trümper, J., Vercellone, S., Vigroux, L., Villa, G., Ward, M. J., Whitehead, S., Zonca, E., 2001a, The European Photon Imaging Camera on XMM-Newton: The MOS cameras : The MOS cameras, Astron. & Astrophys., 365, L27–L35

Turner, T. J., George, I. M., Madejski, G. M., Kitamoto, S., Suzuki, T., 1995, ASCA and ROSAT observations of NRAO 140 and IX Persei, Astrophys. J., 445, 660–665

Turner, T. J., Nandra, K., Turcan, D., George, I. M., 2001b, Tartarus-An ASCA AGN database, AIP Conf. Proc. 599: X-ray Astronomy: Stellar Endpoints, AGN, and the Diffuse X-ray Background, 599, 991–994

Turner, T. J., Mushotzky, R. F., Yaqoob, T., George, I. M., Snowden, S. L., Netzer, H., Kraemer, S. B., Nandra, K., Chelouche, D., 2002, Narrow Components within the Fe Kα Profile of NGC 3516: Evidence of the Importance of General Relativistic Effects?, Astrophys. J., 574, L123–L127

Ulrich, M., Maraschi, L., Urry, C. M., 1997, Variability of Active Galactic Nuclei, Annu. Rev. Astron. Astrophys., 35, 445–502

Ulvestad, J. S., Wilson, A. S., 1984, Radio structures of Seyfert galaxies. VI - VLA observations of a nearby sample, Astrophys. J., 285, 439–452

Ulvestad, J. S., Roy, A. L., Colbert, E. J. M., Wilson, A. S., 1998, A Subparsec Radio Jet or Disk in NGC 4151, Astrophys. J., 496, 196

Véron-Cetty, M.-P., Véron, P., 2003, A catalogue of quasars and active nuclei: 11th edition, Astron. & Astrophys., 412, 399–403

Valtaoja, E., Lahteenmaki, A., Terasranta, H., 1992, A northern 2 Jy sample of compact extragalactic radio sources suitable for millimeter and space VLBI observations, Astron. &. Astrophys. Suppl., 95, 73–85

Venturi, T., Dallacasa, D., Orfei, A., Bondi, M., Fanti, R., Gregorini, L., Mantovani, F., Stanghellini, C., Trigilio, C., Umana, G., 2001, Radio monitoring of a sample of X- and gamma-ray loud blazars, Astron. & Astrophys., 379, 755–766

Vermeulen, R. C., Britzen, S., Taylor, G. B., Pearson, T. J., Readhead, A. C. S., Wilkinson, P. N., Browne, I. W. A., 2003a, Motion Statistics in the CJ Survey - The Status in October 2002, in Astronomical Society of the Pacific Conference Series, p. 43

Vermeulen, R. C., Ros, E., Kellermann, K. I., Cohen, M. H., Zensus, J. A., van Langevelde, H. J., 2003b, The shroud around the twin radio jets in NGC 1052, Astron. & Astrophys., 401, 113–127

Vermeulen, R. C., Ros, E., Kellermann, K. I., Cohen, M. H., Zensus, J. A., van Langevelde, H. J., 2003c, The Shroud around the 'Compact, Symmetric' Radio Jets in NGC1052, Publications of the Astronomical Society of Australia, 20, 65–68

Vermeulen, R. C., Ros, E., Zensus, J. A., Kellermann, K. I., Cohen, M. H., van Langevelde, H. J., 2003d, Ionised, Atomic, and Molecular Gas around the Twin Radio Jets of NGC 1052, in Astronomical Society of the Pacific Conference Series, p. 119

Voges, W., 1994, The First ROSAT Source Catalogue of Pointed Observations with the PSPC, in ROSAT News, No.32

Wagner, S. J., Witzel, A., 1995, Intraday Variability In Quasars and BL Lac Objects, Annu. Rev. Astron. Astrophys., 33, 163–198

Wagner, S. J., Witzel, A., Heidt, J., Krichbaum, T. P., Qian, S. J., Quirrenbach, A., Wegner, R., Aller, H., Aller, M., Anton, K., Appenzeller, I., Eckart, A., Kraus, A., Naundorf, C., Kneer, R., Steffen, W., Zensusj, A., 1996, Rapid Variability in S5 0716+714 Across the Electromagnetic Spectrum, Astron. J., 111, 2187

Wang, J., Watarai, K., Mineshige, S., 2004, The Hot Disk Corona and Magnetic Turbulence in Radio-quiet Active Galactic Nuclei: Observational Constraints, Astrophys. J., 607, L107–L110

Wang, J. X., Zhou, Y. Y., Xu, H. G., Wang, T. G., 1999, Rapidly Variable Fe Kalpha Line in NGC 4051, Astrophys. J., 516, L65–L68

Watson, D., Smith, N., Hanlon, L., McBreen, B., Quilligan, F., Tashiro, M., Metcalfe, L., Doyle, P., Teräsranta, H., Carramiñana, A., Guichard, J., 2000, ASCA and other contemporaneous observations { } of the blazar B2 1308+326, Astron. & Astrophys., 364, 43–52

Weaver, K. A., Wilson, A. S., Henkel, C., Braatz, J. A., 1999, X-Ray Emission from the Prototypical LINER Galaxy NGC 1052, Astrophys. J., 520, 130–136

Webb, J. R., Howard, E., Benítez, E., Balonek, T., McGrath, E., Shrader, C., Robson, I., Jenkins, P., 2000, The 1997 Outburst of AO 0235+164: Evidence for a Microlensing Event?, Astron. J., 120, 41–46

Wilkes, B. J., Elvis, M., 1987, Quasar energy distributions. I - Soft X-ray spectra of quasars, Astrophys. J., 323, 243–262

Wilms, J., Reynolds, C. S., Begelman, M. C., Reeves, J., Molendi, S., Staubert, R., Kendziorra, E., 2001, XMM-EPIC observation of MCG-6-30-15: direct evidence for the extraction of energy from a spinning black hole?, Monthly Not. Roy. Astron. Soc., 328, L27–L31

Witzel, A., Heeschen, D. S., Schalinski, C., Krichbaum, T., 1986, Kurzzeit-Variabilität extragalaktischer Radioquellen, Mitteilungen der Astronomischen Gesellschaft Hamburg, 65, 239

Witzel, A., Schalinski, C. J., Johnston, K. J., Biermann, P. L., Krichbaum, T. P., Hummel, C. A., Eckart, A., 1988, The occurrence of bulk relativistic motion in compact radio sources, Astron. & Astrophys., 206, 245–252

Wolfe, A. M., Briggs, F. H., Turnshek, D. A., Davis, M. M., Smith, H. E., Cohen, R. D., 1985, Detection of 21 centimeter absorption at Z = 2.04 in the QSO PKS 0458-02, Astrophys. J., 294, L67–L72

Wolfe, A. M., Turnshek, D. A., Smith, H. E., Cohen, R. D., 1986, Damped Lyman-alpha absorption by disk galaxies with large redshifts. I - The Lick survey, Astrophys. J. Suppl., 61, 249–304

Woo, J., Urry, C. M., 2002, Active Galactic Nucleus Black Hole Masses and Bolometric Luminosities, Astrophys. J., 579, 530–544

Worrall, D. M., Birkinshaw, M., 1994, Multiple X-ray emission components in low-power radio galaxies, Astrophys. J., 427, 134–139

Worrall, D. M., Wilkes, B. J., 1990, X-ray spectra of compact extragalactic radio sources, Astrophys. J., 360, 396–407

Wrobel, J. M., 1984, Radio continuum activity in the elliptical galaxy NGC 1052, Astrophys. J., 284, 531–543

Wrobel, J. M., 2000, Photometric Variability and Astrometric Stability of the Radio Continuum Nucleus in the Seyfert Galaxy NGC 5548, Astrophys. J., 531, 716–726

Xu, W., Readhead, A. C. S., Pearson, T. J., Polatidis, A. G., Wilkinson, P. N., 1995, The First Caltech–Jodrell Bank VLBI Survey. III. VLBI and MERLIN Observations at 5 GHz and VLA Observations at 1.4 GHz, Astrophys. J. Suppl., 99, 297

Yamasaki, N. Y., Ishikawa, T., Ohashi, T., 2000, ASCA Observation of the Lyman-Limit Quasar PKS 2145+067, Publ. Astron. Soc. Japan, 52, 763–767

Yaqoob, T., Serlemitsos, P., 2000, A Broad Fe Kα Emission Line in the X-Ray Spectrum of the Quasar 3C 273, Astrophys. J., 544, L95–L99

Young, A. J., Wilson, A. S., Terashima, Y., Arnaud, K. A., Smith, D. A., 2002, A Chandra X-Ray Study of Cygnus A. II. The Nucleus, Astrophys. J., 564, 176–189

Yuan, W., Brinkmann, W., Siebert, J., Voges, W., 1998, Broad band energy distribution of ROSAT detected quasars. II. Radio-quiet objects, Astron. & Astrophys., 330, 108–122

Yuan, W., Brinkmann, W., Gliozzi, M., Zhao, Y., Matsuoka, M., 2000, X-ray observation of the super-luminal quasar 4C +73.18 (1928+738) by ASCA, Astron. & Astrophys., 362, 19–26

Zensus, J. A., 1997, "parsec-scale jets in extragalactic radio sources", Annu. Rev. Astron. Astrophys., 35, 607–636

Zensus, J. A., Ros, E., Kellermann, K. I., Cohen, M. H., Vermeulen, R. C., Kadler, M., 2002, Sub-milliarcsecond Imaging of Quasars and Active Galactic Nuclei. II. Additional Sources, Astron. J., 124, 662–674

Zensus, J. A., Ros, E., Kadler, M., Kellermann, K. I., Lister, M. L., Homan, D. C., Cohen, M. H., Vermeulen, R. C., 2003, The 2 cm VLBA Survey, in Astronomical Society of the Pacific Conference Series, p. 27

Zhang, Y. H., Celotti, A., Treves, A., Chiappetti, L., Ghisellini, G., Maraschi, L., Pian, E., Tagliaferri, G., Tavecchio, F., Urry, C. M., 1999, Rapid X-Ray Variability of the BL Lacertae Object PKS 2155-304, Astrophys. J., 527, 719–732

List of Figures

List of Tables

Danksagung

Zum Abschluss möchte ich mich bei allen bedanken, die zum Gelingen dieser Arbeit beigetragen haben:

Ich danke den Mitgliedern der Promotionskommission, den beiden Referenten PD Dr. Jürgen Kerp und Prof. Dr. Uli Klein, sowie den beiden weiteren Kommissionsmitgliedern Prof. Dr. Peter Herzog und Prof. Dr. Christel Baier, für ihre Bereitschaft zur Begutachtung meiner Arbeit und der Teilnahme am Promotionskolloquium und der Disputation. Mein besonderer Dank gilt PD Dr. Jürgen Kerp, der mich während der letzten Jahre und insbesondere während der letzten Monate der Doktorarbeit auf vielfältige Weise unterstützt hat und mir stets beratend zur Seite gestanden hat.

Die tiefe Dankbarkeit auszudrücken, die ich meinem MPI Betreuer Dr. Eduardo Ros gegenüber empfinde ist kaum möglich. Seiner Hilfe, den Diskussionen und Anregungen im Zusammenhang mit dieser Arbeit sowie den Problemen im wissenschaftlichen Alltag, habe ich vieles zu verdanken. Besonders dankbar bin ich aber auch dafür, in Eduardo einen guten Freund gefunden zu haben.

Ich bin dankbar, dass mir die Gelegenheit gegeben wurde, meine Arbeit im Rahmen der International Max Planck Research School anfertigen zu können. Besonders danke ich Dr. J. Anton Zensus für seine Unterstützung und die Möglichkeit während der letzten Jahre in seiner Gruppe am Max-Planck-Institut für Radioastronomie zu arbeiten. Nichtzuletzt ermöglichte er es mir durch die Einbindung in die Aktivitäten des VLBA 2 cm Survey Teams, meine Arbeit im Umfeld dieses Projektes zu definieren.

Wichtige Teile dieser Arbeit sind in Zusammenarbeit mit Kollegen ausserhalb Deutschlands entstanden. Von besonderer Bedeutung waren die inspirierende Zusammenarbeit mit Prof. Alan P. Marscher, Dr. Claudia M. Raiteri, und Dr. Kimberly A. Weaver, der ich insbesondere auch für ihre Unterstützung bei der Planung und Gestaltung der Zeit nach der Doktorarbeit danke.

Den Team-Mitgliedern des VLBA 2 cm Survey danke ich für die gute Zusammenarbeit und die Impulse, die von dieser Kollaboration ausgegangen sind. Besonderes Dr. Ken I. Kellermann, Dr. Yuri Y. Kovalev, Dr. Margo F. Aller, und Dr. Hugh D. Aller haben meine Arbeit an verschiedenen Punkten stark beeinflusst.

Meinen Kollegen in Bonn möchte ich herzlich für die langjährige gute Zusammenarbeit danken. Unter ihnen, möchte ich vor allem diejenigen hervorheben, die durch ihre

345

Refereed Publications

- Zensus, J.A., Ros, E., Kellermann, K.I., Cohen, M.H., Vermeulen, R.C., **Kadler, M.** 2002, *Sub-Milliarcsecond Imaging of Quasars and Active Galactic Nuclei II. Additional Sources*, AJ, 124, 662

- Homan, D.C., Lister, M.L., Kellermann, K.I., Cohen, M.H., Ros, E., Zensus, J.A., **Kadler, M.**, Vermeulen, R.C. 2003, *Jet Collimation in Action: The Case of 3C 279*, ApJ, 589, L9

- **Kadler, M.**, Kerp, J., Ros, E., Falcke, H., Pogge, R.W., Zensus, J.A. 2004, *Jet Emission in NGC 1052 at Radio, Optical, and X-Ray Frequencies*, A&A, 420, 467

- **Kadler M.**, Ros, E., Lobanov, A.P., Falcke, H., Zensus, J.A. 2004, *The Twin-Jet System in NGC 1052: VLBI-Scrutiny of the Obscuring Torus*, A&A, 426, 481

- Kellermann, K.I., Lister, M.L., Homan, D.C., Vermeulen, R.C., Cohen, M.H., Ros, E., **Kadler, M.**, Zensus, J.A., Kovalev, Y.Y. 2004, *Sub-Milliarcsecond Imaging of Quasars and Active Galactic Nuclei III. Kinematics*, ApJ, 609, 539

- Raiteri, C. M., Villata, M., Ibrahimov, M. A., Larionov, V. M., **Kadler, M.**, Aller, H. D., Aller, M. F., Kovalev, Y. Y., Lanteri, L., Nilsson, K., Papadakis, I. E., Pursimo, T., Romero, G. E., Tersranta, H., Tornikoski, M., Arkharov, A. A., Barnaby, D., Berdyugin, A., Bttcher, M., Byckling, K., Carini, M. T., Carosati, D., Cellone, S. A., Ciprini, S., Combi, J. A., Crapanzano, S., Crowe, R., di Paola, A., Dolci, M., Fuhrmann, L., Gu, M., Hagen-Thorn, V. A., Hakala, P., Impellizzeri, V., Jorstad, S., Kerp, J., Kimeridze, G. N., Kovalev, Yu. A., Kraus, A., Krichbaum, T. P., Kurtanidze, O. M., Lhteenmki, A., Lindfors, E., Mingaliev, M. G., Nesci, R., Nikolashvili, M. G., Ohlert, J., Orio, M., Ostorero, L., Pasanen, M., Pati, A., Poteet, C., Ros, E., Ros, J. A., Shastri, P., Sigua, L. A., Sillanp, A., Smith, N., Takalo, L. O., Tosti, G., Vasileva, A., Wagner, S. J., Walters, R., Webb, J. R., Wills, W., Witzel, A., Xilouris, E. 2005, *The WEBT campaign on AO 0235+164 in the 2003-2004 observing season: Results from radio-to-optical monitoring and XMM-Newton observations*, A&A, 438, 39

- Kovalev, Y.Y., Kellermann, K.I., Lister, M.L., Homan, D.C., Vermeulen, R.C., Cohen, M.H., Ros, E., **Kadler, M.**, Lobanov, A.P., Zensus, J.A., Kardashev, N.S., Gurvits, L.I., Aller, M.F., Aller, H.D., 2005, *Sub-Milliarcsecond Imaging of Quasars and Active Galactic Nuclei IV. Fine Scale Structure*, 2005, AJ, in press

Curriculum Vitae

Persönliche Daten

Name   Matthias Kadler

Anschrift   Vom Stein Strasse 2c, 53757 Sankt Augustin, Deutschland

Geburtsdatum   28. August 1975

Geburtsort   Brake (Unterweser), Deutschland

Familienstand   verheiratet mit Agnes Johanna Kadler, geb. Jamroziak, gemeinsamer Sohn Finn Kadler

Staatsangehörigkeit   Deutsch

Wissenschaftlicher Werdegang

1987–1995   Gymnasium Brake mit dem Abschluss der Allgemeinen Hochschulreife im Juli 1995

1995–2002   Studium der Physik an der Universität Hamburg und der Rheinischen Friedrich-Wilhelms-Universität Bonn

1998–2002   Studentische Hilfskraft in den Arbeitsgruppen Infrarot-Interferometrie und Very Long Baseline Interferometry des Max-Planck-Instituts für Radioastronomie

20.06.2002   Abschluss des Studiums mit der Diplomarbeit "NGC 1052: A study of the parsec-scale twin jet", durchgeführt in der Very Long Baseline Interferometry Gruppe des Max-Planck-Instituts für Radioastronomie und betreut durch Dr. E. Ros; Referenten: PD Dr. H. Falcke und Prof. Dr. U. Klein

21.06.2002–20.06.2005   Doktorand in der Very Long Baseline Interferometry Gruppe des Max-Planck-Instituts für Radioastronomie, gefördert durch ein Stipendium der Max-Planck International Research School (IMPRS) for Radio and Infrared Astronomy

21.06.2005–   Stipendiat am Radioastronomischen Institut der Universität Bonn und Gast in der Very Long Baseline Interferometry Gruppe des Max-Planck-Instituts für Radioastronomie

Bonn, November 9, 2005